

VOLUME 103
NOVEMBER 25, 1999
NUMBER 47

ON THE WEB
pubs.acs.org/JPCA

The Journal of

Physical Chemistry A

DISTRIBUTION STATEMENT A
Approved for Public Release
Distribution Unlimited

Time-Dependent
Quantum Molecular
Dynamics Workshop
Brian Head, Utah
March 13–17, 1999



PUBLISHED WEEKLY BY THE AMERICAN CHEMICAL SOCIETY

The Journal of Physical Chemistry A (ISSN 1089-5639) is published weekly except for the last week in December by the American Chemical Society at 1155 16th St., N.W., Washington, DC 20036. Periodicals postage paid at Washington, DC, and at additional mailing offices. POSTMASTER: Send address changes to *The Journal of Physical Chemistry A*, Member & Subscriber Services, P.O. Box 3337, Columbus, OH 43210.

American Chemical Society

1155 16th St., N.W.
Washington, DC 20036
(202) 872-4614
TDD (202) 872-6076
Fax (202) 776-8264

Publishing Operations

American Chemical Society
2540 Olentangy River Road
P.O. Box 3330, Columbus, OH 43210
(614) 447-3665
Fax (614) 447-3745; Telex 6842086
E-mail acsproof@acs.org

Member & Subscriber Services

American Chemical Society
P.O. Box 3337, Columbus, OH 43210
(614) 447-3776; (800) 333-9511
Fax (614) 447-3671
E-mail service@acs.org

Advertising Office

Centcom, Ltd.
676 East Swedesford Road
Suite 202, Wayne, PA 19087-1612
(610) 964-8061

Publications Division

Robert D. Bovenschulte, Director

Publishing Operations

Mary E. Scanlan, Director

Journal Publications

Anne C. O'Melia, Manager; Kathleen E. Duffy, Journals Editing Manager; Ann G. Turpie, Senior Associate Editor; Stephanie R. Harrell, Ramaswami Ravi, and Loretta M. Yam, Associate Editors; Cristina C. Ingenito, Assistant Editor; Daniel E. Luehrs and Leslie A. Walker, Staff Editors

Circulation Office

Justin Spence, Manager



Canadian GST Reg. No. 127571347
Printed in the USA

Copyright Permission: See copyright status form for certain rights (<http://pubs.acs.org>). Reprographic copying beyond that permitted by Section 107 or 108 of the U.S. Copyright Act is allowed, provided that \$18.00 per article is paid to the Copyright Clearance Center, 222 Rosewood Drive, Danvers, MA 01923. Republication or reproduction for sale of articles or abstracts in this journal is permitted only by written permission from the Copyright Office, ACS, Washington, DC. Tel: (202) 872-4368. Fax: (202) 872-6060. E-mail: copyright@acs.org.

Subscription Donations: Members may donate/share their personal subscriptions to/with libraries but only after 5 years from publication.

Editorial Information

Instructions for Authors and Copyright Status Form: See the first issue of each volume or visit the Publications Division Web site (<http://pubs.acs.org>). Please conform to these instructions when submitting manuscripts.

Manuscript Submission: Send manuscripts to the Editor, Mostafa A. El-Sayed, *The Journal of Physical Chemistry A*, School of Chemistry and Biochemistry, Georgia Institute of Technology, Atlanta, GA 30332-0400.

Accepted Papers and Proofs: Direct correspondence to Publishing Operations, Columbus, OH. Tel: (614) 447-3665. Fax: (614) 447-3745. E-mail: acsproof@acs.org.

Page Charges: A \$25.00 per page fee may be paid for papers published in this journal except for Letters, which are free of charge. Payment does not affect acceptance or scheduling of papers.

Journal Policies: The American Chemical Society and its Editors assume no responsibility for the statements and opinions advanced by contributors. Registered names and trademarks, etc., used in this publication, even without specific indication thereof, are not to be considered unprotected by law.

Document Number: At the end of each document is a 9-character code that serves as a link between the printed and electronic products and facilitates retrieval of the document in electronic form.

Digital Object Identifier (DOI): The DOI identification system for digital media has been designed to provide persistent and reliable identification of digital objects. Information on the DOI and its governing body, the International DOI Foundation, can be found at <http://www.doi.org>. In the Web editions of ACS journals, the DOI appears at the top of the HTML version of an article and at the bottom of the first page in its PDF version; in the print editions, the DOI appears in the same location as in the PDF version.

1999 Subscription and Ordering Information

		USA	Canada, Mexico	Europe*	All Other Countries*
Printed Edition (A and B)	Members	\$ 160	\$ 356	\$ 566	\$ 696
	Student Members	\$ 120	\$ 316	\$ 526	\$ 656
	Nonmembers	\$ 430	\$ 626	\$ 836	\$ 966
	Institutional	\$2354	\$2550	\$2760	\$2890
Printed Edition (A or B)	Members	\$ 85	\$ 183	\$ 288	\$ 353
	Student Members	\$ 63	\$ 161	\$ 266	\$ 331
	Nonmembers	\$ 228	\$ 326	\$ 431	\$ 496
Web Edition† (A or B)	Members	\$ 94	\$ 192	\$ 297	\$ 362
	Nonmembers	\$ 251	\$ 349	\$ 454	\$ 519
Print/Web Combination† (A or B)	Members	\$ 123	\$ 221	\$ 326	\$ 391
	Nonmembers	\$ 331	\$ 429	\$ 534	\$ 599

* Air service included. † For Institutional rates, call Member & Subscriber Services.

Web Edition: This journal is available to subscribers via the Internet. Contact Member & Subscriber Services [Tel: (614) 447-3776 or (800) 333-9511. Fax: (614) 447-3671. E-mail: service@acs.org] or visit the Publications Division Web site (<http://pubs.acs.org>) for additional details.

New and Renewal Subscriptions: Send with payment to American Chemical Society, Department L-0011, Columbus, OH 43268-0011. Institutional subscribers in Japan must enter subscription orders with Maruzen Company Ltd., 3-10 Nihonbashi 2-chome, Chuo-ku, Tokyo 103, Japan. Tel: (03) 272-7211.

Change of Address: Notify Member & Subscriber Services, ACS, Columbus, OH. Tel: (614) 447-3776 or (800) 333-9511. Fax: (614) 447-3671. E-mail: address@acs.org. Include both old and new addresses and a mailing label from a recent issue.

Microfilm, Microfiche, Back Issue, and Printed Edition Single Issue Orders: Send requests to Publications Support Services, ACS, Washington, DC. Tel: (202) 872-4376. Fax: (202) 872-6325. Printed edition not available prior to 1995.

Bulk Reprint Orders: For quotes and information, contact CJS Reprint Services. Tel: (888) 257-2134 or (410) 819-3991. Fax: (410) 820-9765.

Claims for Issues Not Received: Claims will be honored only if submitted within 90 days of the issue date (subscribers in North America) or within 180 days of the issue date (all other subscribers). Send requests to Member & Subscriber Services, ACS, Columbus, OH. Tel: (614) 447-3776 or (800) 333-9511. Fax: (614) 447-3671. E-mail: service@acs.org.

Supporting Information (SI): SI is available free of charge via the Internet (<http://pubs.acs.org>). For information on electronic access, send E-mail to si-help@acs.org or phone (202) 872-6333. For SI prior to 1999, contact Publications Support Services. Tel: (202) 872-4376. Fax: (202) 872-6325.

© Copyright 1999 American Chemical Society-

REPORT DOCUMENTATION PAGEForm Approved
OMB No. 0704-0188

Public reporting burden for this collection of information is estimated to average 1 hour per response, including the time for reviewing instructions, searching data sources, gathering and maintaining the data needed, and completing and reviewing the collection of information. Send comments regarding this burden estimate or any other aspect of this collection of information, including suggestions for reducing this burden to Washington Headquarters Service, Directorate for Information Operations and Reports, 1215 Jefferson Davis Highway, Suite 1204, Arlington, VA 22202-4302, and to the Office of Management and Budget, Paperwork Reduction Project (0704-0188) Washington, DC 20503.

PLEASE DO NOT RETURN YOUR FORM TO THE ABOVE ADDRESS.

1. REPORT DATE (DD-MM-YYYY) 11-01-2000		2. REPORT DATE		3. DATES COVERED (From - To)	
4. TITLE AND SUBTITLE Workshop on Time-Dependent Quantum Molecular Dynamics				5a. CONTRACT NUMBER	
				5b. GRANT NUMBER N00014-99-1-0128	
				5c. PROGRAM ELEMENT NUMBER	
6. AUTHOR(S) Y. Ohrn and J. L. Krause				5d. PROJECT NUMBER	
				5e. TASK NUMBER	
				5f. WORK UNIT NUMBER	
7. PERFORMING ORGANIZATION NAME(S) AND ADDRESS(ES) Univeristy of Florida Quantum Theory Project 2301 NPB #92 PO Box 118435 Gainesville, FL 32611-8435				8. PERFORMING ORGANIZATION REPORT NUMBER 1	
9. SPONSORING/MONITORING AGENCY NAME(S) AND ADDRESS(ES)				10. SPONSOR/MONITOR'S ACRONYM(S)	
				11. SPONSORING/MONITORING AGENCY REPORT NUMBER	
12. DISTRIBUTION AVAILABILITY STATEMENT Public Availability					
13. SUPPLEMENTARY NOTES					
14. ABSTRACT Proceedings of Workshop					
15. SUBJECT TERMS					
16. SECURITY CLASSIFICATION OF:			17. LIMITATION OF ABSTRACT	18. NUMBER OF PAGES	19a. NAME OF RESPONSIBLE PERSON
a. REPORT	b. ABSTRACT	c. THIS PAGE			Yngve Ohrn
					19b. TELEPHONE NUMBER (Include area code) 352-392-1597

The Journal of Physical Chemistry A

EDITOR-IN-CHIEF MOSTAFA A. EL-SAYED

School of Chemistry and Biochemistry, Georgia Institute of Technology, Atlanta, Georgia 30332-0400
(404) 894-0293; Fax (404) 894-0294; E-mail jphyschm@chemistry.gatech.edu

SENIOR EDITORS

Michael A. Duncan, *University of Georgia*
Martin Gruebele, *University of Illinois at Urbana-Champaign*
Charles Knobler, *University of California, Los Angeles*
Arthur J. Nozik, *National Renewable Energy Laboratory*

George C. Schatz, *Northwestern University*
Ellen B. Stechel, *Ford Motor Company*
Steve Webber, *University of Texas, Austin*
Paul H. Wine, *Georgia Institute of Technology*

ADVISORY BOARD

Paul Alivisatos
University of California, Berkeley

George W. Flynn
Columbia University

Dan Neumark
University of California, Berkeley

Paul Barbara
University of Texas, Austin

Richard A. Friesner
Columbia University

Bengt Norden
Chalmers University of Technology, Sweden

Robert Birge
Syracuse University

Mark Gordon
Iowa State University

Mark Ratner
Northwestern University

Steven G. Boxer
Stanford University

William Hase
Wayne State University

Hanna Reisler
University of Southern California

A. L. Buchachenko
Russian Academy of Sciences

Manfred Kappes
Universitaet Karlsruhe

John Simon
Duke University

Udo Buck
*Max-Planck-Institut für
Stromungsforschung, Germany*

Uzi Landman
Georgia Institute of Technology

Gerald J. Small
*Iowa State University of Science
and Technology*

Laurie Butler
University of Chicago

Jean Marie Lehn
College de France

Richard Stratt
Brown University

Emily Carter
University of California, Los Angeles

Marsha Lester
University of Pennsylvania

Jack A. Syage
Syagen Technology Inc.

C. R. A. Catlow
*Royal Institution of Great Britain,
U.K.*

M. C. Lin
Emory University

R. van Grondelle
Vrije University, The Netherlands

D. C. Clary
University College London, U.K.

Hiroshi Masuhara
Osaka University

Albert Wagner
Argonne National Laboratory

William A. Eaton
National Institutes of Health

Richard A. Mathies
University of California, Berkeley

Michael Weaver
Purdue University

Barbara Finlayson-Pitts
University of California, Irvine

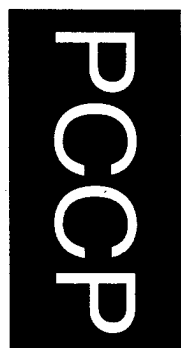
Dan Meisel
University of Notre Dame

Brigitta Whaley
University of California, Berkeley

Graham R. Fleming
University of California, Berkeley

John Miller
Oak Ridge National Laboratory

George Whitesides
Harvard University



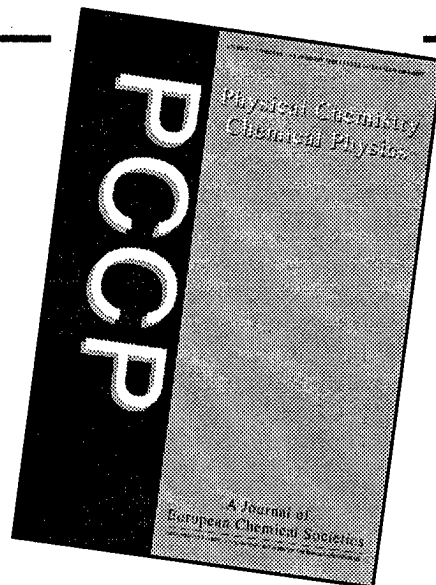
Physical Chemistry Chemical Physics

A Journal of European Chemical Societies

*Formed by the merger of Europe's leading physical
chemistry journals*

***Faraday Transactions and
Berichte der Bunsen-Gesellschaft***

Interdisciplinary, with a broad subject base, PCCP encompasses all aspects of physical chemistry, biophysical chemistry and chemical physics. It is jointly owned by The Royal Society of Chemistry, Deutsche Bunsen-Gesellschaft für Physikalische Chemie, Società Chimica Italiana and Koninklijke Nederlandse Chemische Vereniging.



Key features and benefits

- Excellent value
- Rapid publication times
- Wide circulation and author base
- High quality papers
- FREE online access to full institutional rate subscribers

For submission details, author guidelines, contents lists and much more,
visit www.rsc.org/pccp

1999 prices (24 issues)

Print (ISSN 1463-9076) £1154/\$2038 Includes FREE online access

Personal rate £132/\$214 Available only at a site where a full institutional rate subscription exists

Online (ISSN 1463-9084) £1154/\$2038

Members of the participating societies should contact their relevant society for details of members' prices.

Orders can be sent to: **Turpin Distribution Services Ltd, Blackhorse Road, Letchworth, Herts SG6 1HN, UK**

Tel: +44 (0)1462 672555 • Fax: +44 (0)1462 480947 • E-mail: turpin@rsc.org

K\SEP98\PCCP\18099840

Further details of this or any other RSC product can be found on
www.rsc.org or contact the **Sales and Promotion Department, Royal Society of Chemistry,**
Thomas Graham House, Science Park, Milton Road, Cambridge CB4 0WF (e-mail: sales@rsc.org)

20000124 014

Time-Dependent Quantum Molecular Dynamics

ARTICLES

- Workshop on Time-Dependent Quantum Molecular Dynamics **Gregory A. Voth** 9383
- Generalization of the Linearized Approximation to the Semiclassical Initial Value Representation for Reactive Flux Correlation Functions **William H. Miller** 9384
- A Direct Transition State Theory Based Study of Methyl Radical Recombination Kinetics
Stephen J. Klippenstein* and Lawrence B. Harding* 9388
- Improvement of the Internal Consistency in Trajectory Surface Hopping **Jian-Yun Fang and Sharon Hammes-Schiffer*** 9399
- Time-Domain and Tunneling Pictures of Nonadiabatic Induced Electron Ejection in Molecular Anions **Jack Simons** 9408
- Short-Range Coherence in the Energy Transfer of Photosynthetic Light-Harvesting Systems **Jonaki Ray and Nancy Makri*** 9417
- Electron Dynamics in Dendrimers **T. Sean Elicker and Deborah G. Evans*** 9423
- Computer Simulation of the Excited State Dynamics of Betaine-30 in Acetonitrile **John Lobaugh and Peter J. Rossky*** 9432
- Quantum Wave Packet Study of Nonadiabatic Effects in $\text{O}(^1\text{D}) + \text{H}_2 \rightarrow \text{OH} + \text{H}$
Stephen K. Gray,* Carlo Petrongolo, Karen Drukker, and George C. Schatz 9448
- Electronic Coherence in Mixed-Valence Systems: Spectral Analysis **Younjoon Jung, Robert J. Silbey, and Jianshu Cao*** 9460
- Semiclassical Wave Packet Dynamics with Electronic Structure Computed on the Fly: Application to Photophysics of Electronic Excited States in Condensed Phase
Alfredo E. Cárdenas, Roman Krems, and Rob D. Coalson* 9469
- Propagation Matrices from the Finite Element Method **Bjørn R. Jensen and Jan Linderberg*** 9475
- Forward-Backward Semiclassical Dynamics with Linear Scaling **Jiushu Shao and Nancy Makri*** 9479
- Forward-Backward Semiclassical Calculation of Spectral Line Shapes: I_2 in a Rare Gas Cluster
Oliver Kühn and Nancy Makri* 9487
- Quantum Dynamics and Vibrational Relaxation **S. A. Egorov, K. F. Everitt, and J. L. Skinner*** 9494
- On Obtaining Reactive Potential Energy Surfaces from Transition State Photodetachment Spectra. I. Sensitivity Analysis
Ward H. Thompson 9500
- On Obtaining Reactive Potential Energy Surfaces from Transition State Photodetachment Spectra. II. Inversion of Spectra in Model Systems
Ward H. Thompson 9506
- Quantum Molecular Dynamics Simulations of Low-Temperature High Energy Density Matter: Solid $\text{p-H}_2/\text{Li}$ and $\text{p-H}_2/\text{B}$
Soonmin Jang, Seogjoo Jang, and Gregory A. Voth* 9512
- Dimensional Strategies and the Minimization Problem: Barrier-Avoiding Algorithms
Daniel B. Faken, A. F. Voter, David L. Freeman, and J. D. Doll* 9521
- A Modification of Path Integral Quantum Transition State Theory for Asymmetric and Metastable Potentials
Seogjoo Jang, Charles D. Schwieters, and Gregory A. Voth* 9527



AMERICAN CHEMICAL SOCIETY

Science That Matters.

How can ACS Web Edition subscribers instantly access abstracts of article references from the CAS database?

[CAS]



just click this

Now, ACS Web Edition subscribers can immediately link from references in all ACS Web Edition articles to the relevant Chemical Abstracts Service (CAS) record, gaining instant access to the abstract and bibliographic information, regardless of article publisher.

Available exclusively from the American Chemical Society, this new capability greatly enriches and extends the value of the original article, enabling scientists, librarians and academicians to achieve significantly faster and more productive results.

Visit an article from the first edition of *Organic Letters* today at
<http://pubs.acs.org/reflink>
and simply click on the CAS tag in the references to try out this exciting new feature.
It's that easy.

ACS Web Edition Subscribers: use the HTML version to avail of this new reference-linking capability—available now for all ACS Web Editions.

ACS  WEB EDITIONS
Know it Now!
<http://pubs.acs.org>

American Chemical Society Publications Division

Member & Subscriber Services, P.O. Box 3337, Columbus, OH 43210

Phone: (800) 333-9511 (US & Canada); (614) 447-3776

Fax: (614) 447-3671 • E-mail: service@acs.org • <http://pubs.acs.org>

- Classical Approximation to Nonradiative Electronic Relaxation in Condensed Phase Systems
Eran Rabani, S. A. Egorov, and B. J. Berne* 9539
- Toward an ab Initio Treatment of the Time-Dependent Schrödinger Equation of Molecular Systems
Yngve Öhrn* and Erik Deumens 9545
- Vibrational Dynamics of the I₃ Radical: A Semiempirical Potential Surface, and Semiclassical Calculation of the Anion Photoelectron Spectrum
C. J. Margulis, D. A. Horner, S. Bonella, and D. F. Coker* 9552

ADDITIONS AND CORRECTIONS

- Classical Approximation to Nonradiative Electronic Relaxation in Condensed Phase Systems
Eran Rabani, S. A. Egorov, and B. J. Berne* 9564

There is no Supporting Information for this issue.

* In papers with more than one author, the asterisk indicates the name of the author to whom inquiries about the paper should be addressed.

AUTHOR INDEX

- | | | | | |
|---------------------------------|---------------------------|---------------------------|-----------------------------|-------------------------------|
| Berne, B. J., 9539, 9564 | Elicker, T. S., 9423 | Horner, D. A., 9552 | Makri, N., 9417, 9479, 9487 | Schwieters, C. D., 9527 |
| Bonella, S., 9552 | Evans, D. G., 9423 | Jang, S., 9512, 9527 | Margulis, C. J., 9552 | Shao, J., 9479 |
| Cao, J., 9460 | Everitt, K. F., 9494 | Jensen, B. R., 9475 | Miller, W. H., 9384 | Silbey, R. J., 9460 |
| Cárdenas, A. E., 9469 | Faken, D. B., 9521 | Jung, Y., 9460 | Öhrn, Y., 9545 | Simons, J., 9408 |
| Coalson, R. D., 9469 | Fang, J.-Y., 9399 | Klippenstein, S. J., 9388 | Petrongolo, C., 9448 | Skinner, J. L., 9494 |
| Coker, D. F., 9552 | Freeman, D. L., 9521 | Krems, R., 9469 | Rabani, E., 9539, 9564 | Thompson, W. H., 9500, 9506 |
| Deumens, E., 9545 | Gray, S. K., 9448 | Kühn, O., 9487 | Ray, J., 9417 | Voter, A. F., 9521 |
| Doll, J. D., 9521 | Hammes-Schiffer, S., 9399 | Linderberg, J., 9475 | Rossky, P. J., 9432 | Voth, G. A., 9383, 9512, 9527 |
| Drukker, K., 9448 | Harding, L. B., 9388 | Lobaugh, J., 9432 | Schatz, G. C., 9448 | |
| Egorov, S. A., 9494, 9539, 9564 | | | | |

A cumulative author index for the current volume is published in the first issue of each month.

Digital Object Identifier (DOI): The DOI appears at the bottom of the first page of each article. We suggest that you include the DOI in all CCC reporting and document delivery requests. See the masthead of this journal or our Web site at <http://pubs.acs.org> for more details.

Workshop on Time-Dependent Quantum Molecular Dynamics

Brian Head Utah, March 13–17, 1999
Organizers: Gregory A. Voth and Jack Simons

During the period March 13–17, 1999, the Henry Eyring Center for Theoretical Chemistry organized and hosted a workshop on time-dependent quantum molecular dynamics in Brian Head, Utah. The workshop was financially co-sponsored by the Henry Eyring Center, the Office of Naval Research, the IBM Corporation, the University of Florida Quantum Theory Project, and the University of Utah Center for High Performance Computing. The goal of the workshop was to bring together leading researchers from the theoretical chemistry community in the general area of quantum molecular dynamics. The underlying concept behind the meeting, however, was the notion that the solution of the time-dependent Schrödinger equation, in a variety of different contexts, is likely to become one of the central efforts in theoretical chemistry in the 21st century. It was felt by the two workshop organizers, Jack Simons and myself, that a “critical mass” of researchers and ideas is now in place in order for this effort to progress forward in full force. In addition, there seems to be no doubt that the effort to deal with quantum dynamics through both accurate and efficient theoretical and numerical methods is timely in light of the demands of the larger chemistry community. One needs only to explore the rapidly growing experimental literature in the areas of charge migration (e.g., electron and proton transfer), vibrational dynamics and energy relaxation, nonadiabatic transitions, chemical reaction dynamics, and surface and bulk diffusion, to name a few. These fundamental processes occur not only in the traditional areas of chemistry, but they are also increasingly being revealed as important in biological, atmospheric, and materials science research. A common underlying theme in all of these important research areas is the need to solve the time-dependent Schrödinger equation, or at least a requirement to extract some degree of useful information from it.

During the latter half of this century, a primary concern of many theoretical chemists has been the solution of the *time-independent* Schrödinger equation for electrons in atoms and molecules, i.e., quantum chemistry. While much remains to be

done on that very important problem, one can confidently assert that much has already been accomplished over 50 or more years of research. Evidence for this assertion may be found from many sources, and the recent Nobel Prize to John Pople and Walter Kohn is but one example. The *time-dependent* Schrödinger equation, however, has yielded significantly less progress to researchers (though no doubt there *has* been significant progress). In no small part, this lack of progress is because of the vast diversity of contexts in which the equation is found. To put it more technically, the potential energy functions which serve as input into the equation vary widely from system to system. Usually, they are the result of the application of the Born–Oppenheimer approximation and, as such, have few general principles which govern their final form and behavior. It is an inescapable fact that in most important cases the potential energy function is highly nonlinear and many-dimensional. The normal mode (harmonic) approximation for which exact solutions exist was found many years ago to be severely limited in real applications. It is also well known that a frontal numerical assault on the quantum dynamics problem runs into complications extremely rapidly as the dimensionality of the system increases. In fact, the numerical effort becomes “exponentially complex.” Therefore, the need for insightful, accurate, and efficient approximation schemes becomes very great, perhaps like few other problems in the field of theoretical chemistry.

In this special issue of *The Journal of Physical Chemistry*, one will find contributions submitted by many of the invited workshop participants, as well as from others who attended the meeting. Taken as a whole, the various methods and problems described herein provide an overview of the state-of-the-art in the very challenging and rapidly evolving field of time-dependent quantum molecular dynamics.

Gregory A. Voth

*Director, Henry Eyring Center for Theoretical Chemistry,
University of Utah*

ARTICLES

Generalization of the Linearized Approximation to the Semiclassical Initial Value Representation for Reactive Flux Correlation Functions

William H. Miller

*Department of Chemistry, University of California, and Chemical Sciences Division, Lawrence Berkeley National Laboratory Berkeley, California 94720-1460**Received: May 7, 1999; In Final Form: July 8, 1999*

The semiclassical (SC) initial value representation (IVR) provides a general and practical approach for including quantum effects in classical molecular dynamics simulations. The linearized approximation (LA) to the SC-IVR simplifies the description much further, reducing it to the well-known classical Wigner model (i.e., a classical trajectory calculation with a Wigner distribution of initial conditions); the LA is able to describe quantum effects well for short times ($t \lesssim \hbar\beta$) but not so for longer times. It is shown here how the full SC-IVR approach, which is able to describe quantum effects for long times, can be cast in a form very similar in structure to the LA, with specific application to flux correlation functions relevant to chemical reaction rates. This formulation may thus make it possible to carry out full SC-IVR calculations while still retaining much of the simplifying aspects of its linearized approximation.

I. Introduction

There has been a rebirth of interest among several research groups in using semiclassical (SC) theory as a practical way for including quantum interference and tunneling effects in classical molecular dynamics (CMD) simulations.^{1–8} These recent efforts make use of an initial value representation (IVR)⁹ to implement the semiclassical approximation, thus reducing the calculation to an average over the initial conditions of classical trajectories. The primary difference of an SC-IVR calculation from a conventional CMD one is that there is phase information in the semiclassical calculation, from which the quantum effects arise but which also makes the calculation more difficult. Applications^{1–8} to a number of simple molecular systems have shown that the SC-IVR provides a very useful description of essentially all quantum effects in molecular dynamics, so there is an intense ongoing effort to make these calculations as practical as possible so that they can be used for more complex molecular systems.

In a previous paper^{6f} it was shown that a particular kind of *linearization* of the general SC-IVR expression for the reactive flux correlation function (which is related¹⁰ to thermal rate constants for chemical reactions) leads to an extremely simple result for the correlation function, namely, the classical Wigner model that has been obtained many times before from a variety of approaches.^{11–14} Within this approximation the only difference from a conventional CMD, or classical trajectory calculation, is that the initial conditions are weighted by the Wigner function corresponding to the Boltzmannized flux operator rather than the classical Boltzmann and flux functions themselves. (This is reviewed in section II below.) This linearized approximation to the SC-IVR is thus practical for systems with many degrees of freedom, and in fact it has been applied^{6c,i} to

several problems involving a reaction coordinate (or a two level system^{6h}) coupled to an infinite bath of harmonic oscillators and found to give excellent results for the thermal rate constant (by comparison to accurate quantum path integral calculations^{15,16}). A more detailed study,^{6g} however, showed that though the linearized approximation to the SC-IVR describes quantum effects in the flux correlation function accurately for *short* times ($t \lesssim \hbar\beta$), its description of longer time dynamics is that of classical, not quantum, mechanics. This means that it is good for describing quantum effects in direct barrier-crossing dynamics, i.e., transition state theory-type dynamics,¹⁷ but not for describing quantum effects in more complex phenomena, e.g., recrossing dynamics that violate transition-state theory behavior.

Because the linearized approximation to the SC-IVR, i.e., the classical Wigner model, does some things quite well, it is desirable to exploit its possibilities and build thereon. In this paper I thus show how the full SC-IVR expression for the flux correlation function can be written in the same form as its linearized approximation, with a generalized distribution function replacing the Wigner function. This development is carried out in section II, and section III concludes with a discussion of further ways one may be able to simplify and implement it.

II. SC-IVR for the Flux-Side Correlation Function

The flux-side correlation function is defined by the following quantum trace expression:¹⁰

$$C_{fs}(t) = \text{Tr}[\hat{F}(\beta) e^{i\hat{H}t/\hbar} \hat{h}_e^{-i\hat{H}t/\hbar}] \quad (2.1)$$

The thermal rate constant $k(T)$ for a chemical reaction is given by its long time limit

$$k(T) = Q_r(T)^{-1} \lim_{t \rightarrow \infty} C_{fs}(t) \quad (2.2)$$

where Q_r is the reactant partition function (per unit volume for a bimolecular reaction). In eq 2.1 \hat{H} is the total molecular Hamiltonian and $\hat{h} = h(\mathbf{q})$ is a Heaviside function that is 0 (1) on the reactant (product) side of a surface that divides reactants from products, where \mathbf{q} denotes all the coordinates of the system. $\hat{F}(\beta)$ is the Boltzmannized flux operator,

$$\hat{F}(\beta) \equiv e^{-(\beta/2)\hat{H}} \hat{F} e^{-(\beta/2)\hat{H}} \quad (2.3)$$

where β is related to temperature in the usual way, $\beta = (k_B T)^{-1}$, and \hat{F} is the flux operator

$$\hat{F} = \frac{i}{\hbar} [\hat{H}, \hat{h}] \quad (2.4)$$

The standard expression for the coordinate space, or Van Vleck SC-IVR for the time evolution operator, is^{6a}

$$e^{-i\hat{H}t/\hbar} = \int d\mathbf{p}_0 \int d\mathbf{q}_0 \left[\left| \frac{\partial \mathbf{q}_t(\mathbf{p}_0, \mathbf{q}_0)}{\partial \mathbf{p}_0} \right| / (2\pi i \hbar)^F \right]^{1/2} \times e^{iS_t(\mathbf{p}_0, \mathbf{q}_0)/\hbar} |\mathbf{q}_t\rangle \langle \mathbf{q}_0| \quad (2.5)$$

where the integration variables $(\mathbf{p}_0, \mathbf{q}_0)$ are the initial conditions for classical trajectories, $\mathbf{q}_t \equiv \mathbf{q}(\mathbf{p}_0, \mathbf{q}_0, t)$ is the coordinate at time t that results from these initial conditions, and S_t the action integral along it,

$$S_t(\mathbf{p}_0, \mathbf{q}_0) = \int_0^t dt' [\mathbf{p}(t') \cdot \dot{\mathbf{q}}(t') - H] \quad (2.6)$$

(F is the number of degrees of freedom of the system.) For present purposes, however, it is useful for the moment to consider trajectories running backward in time from t to 0; thus, the operator

$$e^{i\hat{H}t/\hbar} \equiv e^{-iH(0-t)/\hbar} \quad (2.6a)$$

propagates from t to 0, and use of eq 2.5 gives

$$e^{i\hat{H}t/\hbar} = \int d\mathbf{p}_t \int d\mathbf{q}_t \left[\left| \frac{\partial \mathbf{q}_0(\mathbf{p}_t, \mathbf{q}_t)}{\partial \mathbf{p}_t} \right| / (2\pi i \hbar)^F \right]^{1/2} \times e^{iS_{-t}(\mathbf{p}_t, \mathbf{q}_t)/\hbar} |\mathbf{q}_0\rangle \langle \mathbf{q}_t| \quad (2.6b)$$

where here $(\mathbf{p}_t, \mathbf{q}_t)$ are thought of as the initial conditions and $\mathbf{q}_0 \equiv \mathbf{q}_0(\mathbf{p}_t, \mathbf{q}_t)$ the final position; the action integral S_{-t} is

$$S_{-t}(\mathbf{p}_t, \mathbf{q}_t) = \int_t^0 dt' [\mathbf{p}(t') \cdot \dot{\mathbf{q}}(t') - H] \quad (2.7)$$

where the integrand is the trajectory determined by the "initial conditions" $(\mathbf{p}_t, \mathbf{q}_t)$. By adjoining eq 2.6b, one has

$$e^{-i\hat{H}t/\hbar} = \int d\mathbf{p}_t' \int d\mathbf{q}_t' \left[\left| \frac{\partial \mathbf{q}_0(\mathbf{p}_t', \mathbf{q}_t')}{\partial \mathbf{p}_t'} \right| / (-2\pi i \hbar)^F \right]^{1/2} \times e^{-iS_{-t}(\mathbf{p}_t', \mathbf{q}_t')/\hbar} |\mathbf{q}_t'\rangle \langle \mathbf{q}_0'| \quad (2.8)$$

where we have used primed variables as the integration variables and $\mathbf{q}_0' \equiv \mathbf{q}_0(\mathbf{p}_t', \mathbf{q}_t')$. (Equation 2.8 is also obtainable directly from the "standard" expression, eq 2.5, by using Liouville's theorem, i.e., that $\int d\mathbf{p}_0 \int d\mathbf{q}_0 = \int d\mathbf{p}_t \int d\mathbf{p}_t$, and also that $d\mathbf{q}_t/d\mathbf{p}_0 = -\partial \mathbf{q}_0/\partial \mathbf{p}_t$.)

Equations 2.6b and 2.8 are now used for the propagators in the flux correlation function, eq 2.1, to give

$$C_{fs}(t) = \frac{\int d\mathbf{q}_t \int d\mathbf{p}_t \int d\mathbf{p}_t' \left| \frac{\partial \mathbf{q}_0(\mathbf{p}_t, \mathbf{q}_t)}{\partial \mathbf{p}_t} \right|^{1/2} \left| \frac{\partial \mathbf{q}_0(\mathbf{p}_t', \mathbf{q}_t')}{\partial \mathbf{p}_t'} \right|^{1/2} \times h(\mathbf{q}_t) \langle \mathbf{q}_0' | \hat{F}(\beta) | \mathbf{q}_0 \rangle e^{i[S_{-t}(\mathbf{p}_t, \mathbf{q}_t) - S_{-t}(\mathbf{p}_t', \mathbf{q}_t')]/\hbar}}{(2\pi \hbar)^F} \quad (2.9)$$

with $\mathbf{q}_0 = \mathbf{q}_0(\mathbf{p}_t, \mathbf{q}_t)$, $\mathbf{q}_0' = \mathbf{q}_0(\mathbf{p}_t', \mathbf{q}_t')$. Next one performs a sum and difference transformation of the integration variables \mathbf{p}_t and \mathbf{p}_t' .

$$\mathbf{p}_t = \bar{\mathbf{p}}_t - \frac{\Delta \mathbf{p}}{2}$$

$$\mathbf{p}_t' = \bar{\mathbf{p}}_t + \frac{\Delta \mathbf{p}}{2}$$

to give

$$C_{fs}(t) = \frac{\int d\mathbf{q}_t \int d\bar{\mathbf{p}}_t \int d\Delta \mathbf{p} \left| \frac{\partial \mathbf{q}_0^+}{\partial \bar{\mathbf{p}}_t} \right|^{1/2} \left| \frac{\partial \mathbf{q}_0^-}{\partial \bar{\mathbf{p}}_t} \right|^{1/2} h(\mathbf{q}_t) \langle \mathbf{q}_0^+ | \hat{F}(\beta) | \mathbf{q}_0^- \rangle e^{i[S_{-t}(\bar{\mathbf{p}}_t, \mathbf{q}_t) - S_{-t}(\bar{\mathbf{p}}_t, \mathbf{q}_t)]/\hbar}}{(2\pi \hbar)^F} \quad (2.10a)$$

where

$$\mathbf{q}_0^\pm = \mathbf{q}_0\left(\bar{\mathbf{p}}_t \pm \frac{\Delta \mathbf{p}}{2}, \mathbf{q}_t\right) \quad (2.10b)$$

$$S_{-t}^\pm = S_{-t}\left(\bar{\mathbf{p}}_t \pm \frac{\Delta \mathbf{p}}{2}, \mathbf{q}_t\right) \quad (2.10c)$$

Finally, we use Liouville's theorem to change integration variables in eq 2.10a from $(\bar{\mathbf{p}}_t, \mathbf{q}_t)$ to $(\mathbf{p}_0, \mathbf{q}_0)$, which are connected to $(\bar{\mathbf{p}}_t, \mathbf{q}_t)$ by the trajectory from 0 to t , giving

$$C_{fs}(t) = \frac{\int d\mathbf{p}_0 \int d\mathbf{q}_0}{(2\pi \hbar)^F} h[\mathbf{q}_t(\mathbf{p}_0, \mathbf{q}_0)] F_{\text{eff}}(\mathbf{p}_0, \mathbf{q}_0) \quad (2.11a)$$

where

$$F_{\text{eff}}(\mathbf{p}_0, \mathbf{q}_0) = \int d\Delta \mathbf{p} \left| \frac{\partial \mathbf{q}_0^+}{\partial \bar{\mathbf{p}}_t} \right|^{1/2} \left| \frac{\partial \mathbf{q}_0^-}{\partial \bar{\mathbf{p}}_t} \right|^{1/2} \times \langle \mathbf{q}_0^+ | \hat{F}(\beta) | \mathbf{q}_0^- \rangle e^{i[S_{-t}(\bar{\mathbf{p}}_t, \mathbf{q}_t) - S_{-t}(\bar{\mathbf{p}}_t, \mathbf{q}_t)]/\hbar} \quad (2.11b)$$

with $\mathbf{q}_t = \mathbf{q}_t(\mathbf{p}_0, \mathbf{q}_0)$, $\bar{\mathbf{p}}_t(\mathbf{p}_0, \mathbf{q}_0)$, and \mathbf{q}_0^\pm and S_{-t}^\pm from eqs 2.10b and 2.10c. The meaning of eq 2.11 is indicated pictorially in Figure 1. Given initial conditions $(\mathbf{p}_0, \mathbf{q}_0)$ (at time $t = 0$), one integrates to time t , arriving at the phase point $(\bar{\mathbf{p}}_t, \mathbf{q}_t)$; one now integrates back to time 0 with "initial conditions" (at time t) $(\bar{\mathbf{p}}_t \pm \Delta \mathbf{p}/2, \mathbf{q}_t)$ arriving at positions \mathbf{q}_0^\pm . The action integrals S_{-t}^\pm are along the two "backward" trajectories.

The linearized approximation^{6f} is obtained by linearizing \mathbf{q}_0^\pm and S_{-t}^\pm in the variable $\Delta \mathbf{p}$:

$$\begin{aligned} \mathbf{q}_0^\pm &\equiv \mathbf{q}_0\left(\bar{\mathbf{p}}_t \pm \frac{\Delta \mathbf{p}}{2}, \mathbf{q}_t\right) \\ &\approx \mathbf{q}_0(\bar{\mathbf{p}}_t, \mathbf{q}_t) \pm \frac{1}{2} \frac{\partial \mathbf{q}_0(\mathbf{p}_t, \mathbf{q}_t)}{\partial \bar{\mathbf{p}}_t} \cdot \Delta \mathbf{p} \end{aligned} \quad (2.12a)$$

$$\begin{aligned} S_{-t}^\pm &\equiv S_{-t}\left(\bar{\mathbf{p}}_t \pm \frac{\Delta \mathbf{p}}{2}, \mathbf{q}_t\right) \\ &\approx S_{-t}(\bar{\mathbf{p}}_t, \mathbf{q}_t) \pm \frac{1}{2} \mathbf{p}_0(\bar{\mathbf{p}}_t, \mathbf{q}_t) \cdot \frac{\partial \mathbf{q}_0(\bar{\mathbf{p}}_t, \mathbf{q}_t)}{\partial \bar{\mathbf{p}}_t} \cdot \Delta \mathbf{p} \end{aligned} \quad (2.12b)$$

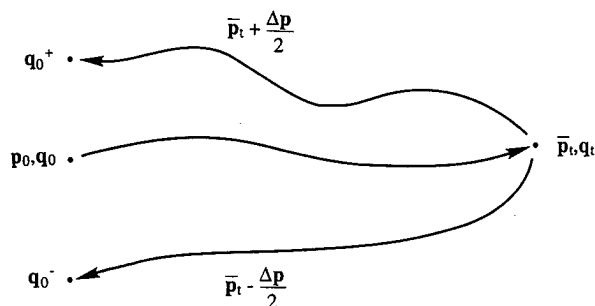


Figure 1. Schematic depiction of the classical trajectories relevant to eq 2.11. The trajectory begins at time t with initial conditions $(\mathbf{q}_0, \mathbf{p}_0)$ and evolves to the phase point $(\mathbf{q}_t, \mathbf{p}_t)$ at time t ; two trajectories are then integrated backward in time, from t to 0 , starting from position \mathbf{q}_t but with momenta $\bar{\mathbf{p}}_t \pm \Delta \mathbf{p}/2$, arriving at positions \mathbf{q}_0^\pm .

and we note that $\mathbf{q}_0(\bar{\mathbf{p}}_t, \mathbf{q}_t)$ and $\bar{\mathbf{p}}_0(\mathbf{p}_t, \mathbf{q}_t)$ are equal to \mathbf{q}_0 and \mathbf{p}_0 , respectively, the integration variables in eq 2.11a. With the linearized approximations in eq 2.12, and neglecting the $\Delta \mathbf{p}$ dependence of the Jacobian determinants in eq 2.11b, the function F_{eff} of eq 2.11b becomes

$$F_{\text{eff}}(\mathbf{p}_0, \mathbf{q}_0) \approx \int d\Delta \mathbf{p} \left| \frac{\partial \mathbf{q}_0}{\partial \bar{\mathbf{p}}_t} \right| \left\langle \mathbf{q}_0 + \frac{1}{2} \frac{\partial \mathbf{q}_0}{\partial \bar{\mathbf{p}}} \cdot \Delta \mathbf{p} \left| \hat{F}(\beta) \right| \mathbf{q}_0 - \frac{1}{2} \frac{\partial \mathbf{q}_0}{\partial \bar{\mathbf{p}}} \cdot \Delta \mathbf{p} \right\rangle e^{-i\mathbf{p}_0 \cdot (\partial \mathbf{q}_0 / \partial \bar{\mathbf{p}}_t) \Delta \mathbf{p} / \hbar} \quad (2.13a)$$

Changing integration variables from $\Delta \mathbf{p}$ to $\Delta \mathbf{q}$,

$$\Delta \mathbf{q} \equiv \frac{\partial \mathbf{q}_0}{\partial \bar{\mathbf{p}}_t} \cdot \Delta \mathbf{p} \quad (2.13c)$$

then gives the Wigner function¹⁸ for F_{eff} in this linearized approximation,

$$F_w(\mathbf{p}_0, \mathbf{q}_0) \equiv \int d\Delta \mathbf{q} \left\langle \mathbf{q}_0 + \frac{1}{2} \Delta \mathbf{q} \left| \hat{F}(\beta) \right| \mathbf{q}_0 - \frac{1}{2} \Delta \mathbf{q} \right\rangle e^{-i\mathbf{p}_0 \cdot \Delta \mathbf{q} / \hbar} \quad (2.13c)$$

The linearized approximation has the great advantage that the Jacobian factor $|\partial \mathbf{q}_0(\mathbf{p}_t, \mathbf{q}_t) / \partial \bar{\mathbf{p}}_t|$ completely cancels out; not only does this simplify matters by not having to calculate it but it also eliminates problems that arise in long-time and/or chaotic dynamics when this factor becomes very large. The fact that it totally cancels out in the linearized approximation suggests that its effects may be small even in the full version of the SC-IVR if it is handled appropriately.

Equation 2.11 is thus the desired result of the present work. It expresses the full SC-IVR for the flux-side correlation function, i.e., there are no approximations involved in going from eq 2.9 to eq. 2.11, in precisely the same form as its linearized approximation, with the function $F_{\text{eff}}(\mathbf{p}_0, \mathbf{q}_0)$ replacing the Wigner function. This formulation also suggests a convenient way of evaluating eq 2.11. Using Monte Carlo sampling based on the Wigner function $F_w(\mathbf{p}_0, \mathbf{q}_0)$, eq 2.11a can be written as

$$C_{\text{fs}}(t) = C_{\text{fs}}^{\text{LA}}(t) \cdot \Delta C(t) \quad (2.14a)$$

where $C_{\text{fs}}^{\text{LA}}(t)$ is the linearized approximation for the correlation function (i.e., the classical Wigner model) and the correction factor $\Delta C(t)$ is given by a Monte Carlo average of

$$[F_{\text{eff}}(\mathbf{p}_0, \mathbf{q}_0) / F_w(\mathbf{p}_0, \mathbf{q}_0)] \quad (2.14b)$$

Another possibly useful variation is to use the Kubo version of $\hat{F}(\beta)$ rather than the split operator version in eq 2.3. This is¹⁹

$$\hat{F}_{\text{Kubo}}(\beta) = \frac{i}{\hbar \beta} [\hat{h}, e^{-\beta \hat{H}}]$$

so that eq 2.11b becomes

$$F_{\text{eff}}(\mathbf{p}_0, \mathbf{q}_0) = \frac{i}{\hbar \beta} \int d\Delta \mathbf{p} \left| \frac{\partial \mathbf{p}_0^+}{\partial \bar{\mathbf{p}}_t} \right|^{1/2} \left| \frac{\partial \mathbf{q}_0^-}{\partial \bar{\mathbf{p}}_t} \right|^{1/2} (h(\mathbf{q}_0^+) - h(\mathbf{q}_0^-)) \langle \mathbf{q}_0^+ | e^{-\beta \hat{H}} | \mathbf{q}_0^- \rangle e^{i[S_{-t}^- - S_{-t}^+] / \hbar} \quad (2.11c)$$

with $\mathbf{q}_t = \mathbf{q}_t(\mathbf{p}_0, \mathbf{q}_0)$, $\bar{\mathbf{p}}_t = \mathbf{p}_t(\mathbf{p}_0, \mathbf{q}_0)$. In this case one would first integrate the trajectory with initial conditions $(\mathbf{p}_0, \mathbf{q}_0)$ from 0 to t . From eq 2.11a, it is required that \mathbf{q}_t be on the product side of the dividing surface. One then integrates from t back to 0 , with initial conditions $(\bar{\mathbf{p}}_t \pm \Delta \mathbf{p}/2, \mathbf{q}_t)$; \mathbf{q}_0^+ and \mathbf{q}_0^- must lie on different sides of the dividing surface, or else the integrand of eq 2.11c is zero. These conditions, along with the matrix element of the Boltzmann operator, limit the range of the integration variables.

Finally, it is useful to illustrate the basic result for F_{eff} , eq 2.11b, for the elementary example of a one-dimensional free particle. Here, the $0 \rightarrow t$ trajectory gives

$$q_t = q_0 + p_0 \left(\frac{t}{m} \right) \\ \bar{p}_t = p_0$$

and the two backward trajectories, $t \rightarrow 0$, give

$$q_0^\pm = q_t + \left(\bar{p}_t \pm \frac{\Delta p}{2} \right) \left(-\frac{t}{m} \right)$$

so that

$$q_0^\pm = q_0 \mp \frac{\Delta p}{2} \frac{t}{m}$$

and

$$S_{-t}^\pm = -\frac{t}{2m} \left(p_0 \pm \frac{\Delta p}{2} \right)^2$$

With the split operator version of $\hat{F}(\beta)$, for example, eq 2.11b thus gives

$$F_{\text{eff}}(p_0, q_0) = \int d\Delta p \frac{t}{m} \frac{m}{\pi \hbar^2 \beta} \frac{\Delta p t}{m \hbar \beta} \times \exp \left\{ \frac{-m}{\hbar^2 \beta} \left[2q_0^2 + \frac{1}{2} \left(\frac{\Delta p t}{m} \right)^2 \right] \right\} e^{-i p_0 \Delta p / (\hbar m)}$$

or with the change of integration variable to $\Delta q = \Delta p t / m$,

$$F_{\text{eff}}(p_0, q_0) = \int d\Delta q \frac{m}{\pi \hbar^2 \beta} \frac{\Delta q}{m \hbar \beta} \times \exp \left[\frac{-m}{\hbar^2 \beta} \left(2q_0^2 + \frac{1}{2} \Delta q^2 \right) \right] e^{-i p_0 \Delta q / \hbar}$$

which is identical to the Wigner function in this case. The

important thing to notice is that the integration over Δp (or Δq) is well localized.

III. Concluding Remarks

The purpose of this short note has been to show that the SC-IVR expression for the flux-side correlation function can be cast in a form very similar to its linearized approximation. This suggests new computational approaches that may have advantages over existing ones. We also note some similarities in structure of the present formulation to the "forward-backward" IVR presented before,^{6m} though it is not equivalent to it. At the present time one is still investigating various strategies for implementing the SC-IVR approach, so various formulations may suggest useful approaches or other approximations.

For example, it may be useful to make part of the linearized approximation but not all of it. Thus, suppose one neglects the Δp dependence in the Jacobian factors in eq 2.11b but retains it elsewhere, then

$$\frac{\partial q_0^\pm}{\partial \bar{p}_t} = \frac{\partial q_0(\bar{p}_t, q_t)}{\partial \bar{p}_t} = - \frac{\partial q_t(p_0, q_0)}{\partial p_0}$$

so that one can change integration variables in eq 2.11b from Δp to Δq ,

$$\begin{aligned} \Delta q &\equiv \frac{\partial q_0(\bar{p}_t, q_t)}{\partial p_t} \cdot \Delta p \\ &= - \frac{\partial q_t(p_0, q_0)}{\partial p_0} \cdot \Delta p \end{aligned}$$

and the expression for the effective distribution function becomes

$$F_{\text{eff}}(p_0, q_0) = \int d\Delta q \langle q_0^+ | \hat{F}(\beta) | q_0^- \rangle \cdot e^{i[S_{-t} - S_{-t}^+]/\hbar} \quad (3.1)$$

with q_0^\pm and S_{-t}^\pm still given by eqs 2.10b and 2.10c, and

$$\bar{p}_t = p_t(p_0, q_0)$$

$$q_t = q_t(p_0, q_0)$$

$$\Delta p = - \left(\frac{\partial q_t(p_0, q_0)}{\partial p_0} \right)^{-1} \cdot \Delta q$$

One expects the dependence on the Jacobian factor, $\partial q_t / \partial p_0$, to be weak, since there is no dependence at all in the linearized approximation.

Acknowledgment. This work has been supported by the Director, Office of Science, Office of Basic Energy Sciences, Chemical Sciences Division of the U.S. Department of Energy under Contract No. DE-AC03-76SF00098, Lawrence Berkeley National Laboratory, and also by the National Science Foundation under Grant No. CHE97-32758.

References and Notes

- (1) (a) Herman, M. F.; Kluk, E. *Chem. Phys.* **1984**, *91*, 27. (b) Kluk, E.; Herman, M. F.; Davis, H. L. *J. Chem. Phys.* **1986**, *84*, 326. (c) Herman, M. F. *Chem. Phys. Lett.* **1997**, *275*, 445. (d) Guerin, B. E.; Herman, M. F. *Chem. Phys. Lett.* **1998**, *286*, 361. (e) Herman, M. F. *Annu. Rev. Phys. Chem.* **1994**, *45*, 83.
- (2) (a) Heller, E. J. *J. Chem. Phys.* **1991**, *94*, 2723; **1991**, *95*, 9431. (b) Tomsovic, J.; Heller, E. J. *Phys. Rev. Lett.* **1991**, *67*, 664. (c) Sepulveda, M. A.; Tomsovic, S.; Heller, E. J. *Phys. Rev. Lett.* **1992**, *69*, 402. (d) Tomsovic, S.; Heller, E. J. *Phys. Rev. E* **1993**, *47*, 282. (e) Grossman, F.; Heller, E. J. *Chem. Phys. Lett.* **1995**, *241*, 45. (f) Maitra, N. T.; Heller, E. J. *Phys. Rev. Lett.* **1997**, *78*, 3035.
- (3) (a) Kay, K. G. *J. Chem. Phys.* **1994**, *100*, 4377. (b) Kay, K. G. *J. Chem. Phys.* **1994**, *100*, 44332. (c) Kay, K. G. *J. Chem. Phys.* **1994**, *101*, 2250. (d) Kay, K. G. *J. Chem. Phys.* **1997**, *107*, 2313. (e) Elran, Y.; Kay, K. G. *J. Chem. Phys.* **1999**, *110*, 3653. (f) Elran, Y.; Kay, K. G. *J. Chem. Phys.* **1999**, *110*, 8912.
- (4) (a) Campolieti, G.; Brumer, P. *Phys. Rev. A* **1994**, *50*, 997. (b) Campolieti, G.; Brumer, P. *Phys. Rev. A* **1996**, *53*, 2958. (c) Campolieti, G.; Brumer, P. *J. Chem. Phys.* **1992**, *96*, 5969. (d) Campolieti, G.; Brumer, P. *J. Chem. Phys.* **1997**, *107*, 791. (e) Campolieti, G.; Brumer, P. *J. Chem. Phys.* **1998**, *109*, 2999. (f) Provost, D.; Brumer, P. *Phys. Rev. Lett.* **1995**, *74*, 250.
- (5) (a) Garashchuk, S.; Tannor, D. J. *Chem. Phys. Lett.* **1996**, *262*, 477. (b) Garashchuk, S.; Tannor, D. J. *J. Chem. Phys.* **1998**, *109*, 3028. (c) Garashchuk, S.; Tannor, D. J. *Phys. Chem. Chem. Phys.* **1999**, *1*, 1081. (d) Garashchuk, S.; Grossmann, F.; Tannor, D. J. *J. Chem. Soc., Faraday Trans.* **1997**, *93*, 781.
- (6) (a) Miller, W. H. *J. Chem. Phys.* **1991**, *95*, 9428. (b) Spath, B. W.; Miller, W. H. *J. Chem. Phys.* **1996**, *104*, 95. (c) Sun, X.; Miller, W. H. *J. Chem. Phys.* **1997**, *106*, 916. (d) Sun, X.; Miller, W. H. *J. Chem. Phys.* **1997**, *106*, 6346. (e) Sun, X.; Miller, W. H. *J. Chem. Phys.* **1998**, *108*, 8870. (f) Wang, H.; Sun, X.; Miller, W. H. *J. Chem. Phys.* **1998**, *108*, 9726. (g) Sun, X.; Wang, H.; Miller, W. H. *J. Chem. Phys.* **1998**, *109*, 4190. (h) Sun, X.; Wang, H.; Miller, W. H. *J. Chem. Phys.* **1998**, *109*, 7064. (i) Wang, H.; Song, X.; Chandler, D.; Miller, W. H. *J. Chem. Phys.* **1999**, *110*, 4828. (j) Miller, W. H. *Faraday Discuss. Chem. Soc.* **1998**, *1998*, *110*, 1. (k) Skinner, D.; Miller, W. H. *Chem. Phys. Lett.* **1999**, *300*, 20. (l) Batista, V. S.; Zanni, M. T.; Greenblatt, B. J.; Neumark, D. M.; Miller, W. H. *J. Chem. Phys.* **1999**, *110*, 3736. (m) Sun, X.; Miller, W. H. *J. Chem. Phys.* **1999**, *110*, 6635. (n) Guallar, V.; Batista, V. S.; Miller, W. H. *J. Chem. Phys.* **1999**, *111*, 9922.
- (7) (a) Walton, A. R.; Manolopoulos, D. E. *Mol. Phys.* **1996**, *87*, 961. (b) Walton, A. R.; Manolopoulos, D. E. *Chem. Phys. Lett.* **1995**, *244*, 448. (c) Brewer, M. L.; Hulme, J. S.; Manolopoulos, D. E. *J. Chem. Phys.* **1997**, *106*, 4832.
- (8) Shalashilin, D. V.; Jackson, B. *Chem. Phys. Lett.* **1998**, *291*, 143.
- (9) Miller, W. H. *J. Chem. Phys.* **1970**, *53*, 3578.
- (10) (a) Miller, W. H. *J. Chem. Phys.* **1974**, *61*, 1823. (b) Miller, W. H.; Schwartz, S. D.; Tromp, J. W. *J. Chem. Phys.* **1983**, *79*, 4889.
- (11) (a) Cao, J. S.; Voth, G. A. *J. Chem. Phys.* **1996**, *104*, 273. (b) Cline, R. E., Jr.; Wolynes, P. G. *J. Chem. Phys.* **1988**, *88*, 4334. (c) Khidekel, V.; Chernyak, V.; Mukamel, S. *Femtochemistry: Ultrafast Chemical and Physical Processes in Molecular Systems*; Chergui, M., Ed.; World Scientific: Singapore, 1996, 507.
- (12) (a) Heller, E. J. *J. Chem. Phys.* **1976**, *65*, 1289. (b) Brown, R. C.; Heller, E. J. *J. Chem. Phys.* **1981**, *75*, 186.
- (13) Lee, H. W.; Scully, M. O. *J. Chem. Phys.* **1988**, *73*, 2238.
- (14) (a) Filinov, V. S.; Medvedev, Y. V.; Kamskyri, V. L. *Mol. Phys.* **1995**, *85*, 711. (b) Filinov, V. S. *Mol. Phys.* **1996**, *88*, 1517. (c) Filinov, V. S. *Mol. Phys.* **1996**, *88*, 1529.
- (15) Topaler, M.; Makri, N. *J. Chem. Phys.* **1994**, *101*, 7500.
- (16) Mak, C. H.; Chandler, D. *Phys. Rev. A* **1991**, *44*, 2352.
- (17) (a) Pollak, E.; Liao, J. L. *J. Chem. Phys.* **1998**, *108*, 2733. (b) Shao, J.; Liao, J. L.; Pollak, E. *J. Chem. Phys.* **1998**, *108*, 9711. (c) Liao, J. L.; Pollak, E. *J. Chem. Phys.* **1999**, *110*, 80. (d) Pollak, E.; Eckhardt, B. *Phys. Rev. E* **1998**, *58*, 5436.
- (18) For a review, see the following. Hillery, M.; O'Connell, R. F.; Scully, M. O.; Wigner, E. P.; *Phys. Rep.* **1984**, *106*, 121.
- (19) Voth, G. A.; Chandler, D.; Miller, W. H. *J. Chem. Phys.* **1989**, *93*, 7009.

A Direct Transition State Theory Based Study of Methyl Radical Recombination Kinetics

Stephen J. Klippenstein*

Chemistry Department, Case Western Reserve University, Cleveland, Ohio 44106-7078

Lawrence B. Harding*

Theoretical Chemistry Group, Argonne National Laboratory, 9700 South Cass Avenue, Argonne, Illinois 60439

Received: May 14, 1999; In Final Form: July 26, 1999

Multireference configuration interaction based quantum chemical estimates are directly implemented in a variational transition state theory based analysis of the kinetics of methyl radical recombination. Separations ranging from 5.5 to 1.9 Å are considered for two separate forms for the reaction coordinate. The *a priori* prediction for the high-pressure limit rate constant gradually decreases with increasing temperature, with a net decrease of a factor of 1.7 from 300 to 1700 K. Near room temperature, this theoretical estimate is in quantitative agreement with the experimental data. At higher temperatures, comparison between theory and experiment requires a model for the pressure dependence. Master equation calculations employing the exponential down energy transfer model suggest that the theoretical and experimental high-pressure limits gradually diverge with increasing temperature, with the former being about 3 times greater than the latter at 1700 K. The comparison with experiment also suggests that the energy transfer coefficient, $\langle \Delta E_{\text{down}} \rangle$, increases with increasing temperature.

I. Introduction

The accurate *a priori* prediction of rate constants for reactions of polyatomic species remains a difficult and important goal. One of the primary difficulties involves the development of sufficiently accurate representations of the multidimensional potential energy surface. Direct dynamics approaches (see, e.g., refs 1–3) bypass one aspect of this difficulty by obtaining an *ab initio* quantum chemical estimate of the potential for each configuration sampled in the dynamics. One is then limited only by the accuracy of the underlying quantum chemical evaluations and dynamical simulations. Unfortunately, such direct dynamical procedures generally require vast CPU times due to the enormous number of potential energy evaluations in typical dynamical simulation procedures. The representation of the potential in terms of an expansion about some selected geometries provides one route for reducing the number of *ab initio* energetic evaluations.^{4,5}

Alternatively, replacing the dynamical simulation with a transition state theory (TST) based simulation can yield an even greater reduction in the number of required calls to the potential. For example, within reaction path Hamiltonian based approaches, one typically requires only the potential, its gradient, and its second derivative, at a limited number of points along the reaction path.^{6,7} For barrierless reactions the situation is more complicated since many of the modes are in the process of changing from free rotors to nearly harmonic bending motions. As a result, simple quadratic representations of the potential and the corresponding rigid-rotor harmonic oscillator estimates for the energetics seem inadequate.

Phase space integral based representations of the transition state partition function have provided a means for accurately treating the anharmonicities and kinetic couplings of these “transitional” modes, but require a global potential for them.^{8,9} However, with Monte Carlo integration techniques one may obtain reasonably well converged results with only a limited number of configurational samplings and corresponding poten-

tial energy evaluations. For example, convergence to about 10% can be obtained with simple random sampling of about 1000 sets of the transitional mode coordinates.¹⁰ Consideration of about 10 different reaction coordinates will often provide a reasonably satisfactory optimization of the transition state dividing surface. Thus, a total of about 10^4 *ab initio* evaluations may be used to obtain direct variational TST estimates for the rate constant which include the full anharmonicity and mode–mode couplings for the transitional modes. Also, importance sampling schemes may provide a means for further reducing the number of required potential energy calls.

In this work, we present a direct TST-based study of the prototypical methyl–methyl radical recombination reaction. This reaction, which is of considerable importance in combustion processes, has been the subject of a large number of both experimental^{11–20} and theoretical^{16,21–42} studies. Currently available experimental measurements span the range from 200 to 1700 K with pressures ranging from 0.3 to 10^5 Torr.⁴³ This wide ranging experimental data set provides a valuable database for examining the quantitative accuracy of the theoretical predictions.

The present study focuses on the temperature dependence for the high-pressure limiting rate constants [$k_{\infty}(T)$] since an accurate understanding of this behavior is of some utility in extrapolating related experimental data from room temperature to the higher temperatures of interest in combustion chemistry. Unfortunately, the experimental studies are unable to reach the high-pressure limit for temperatures above about 400 K.³⁷ Thus, a direct comparison with experiment requires a model for the pressure dependence. This pressure dependence is treated here via a one-dimensional master equation²⁹ employing a range of energy transfer coefficients within the exponential down model.

The accuracy of the theoretical predictions for $k_{\infty}(T)$ depends on both the accuracy of the *ab initio* estimates for the potential energy surface and the validity of the statistical assumptions inherent in TST. In this work we strive to minimize the errors

in the former in order to address the latter accuracy in as meaningful a fashion as feasible. Thus, multireference configuration interaction (MR-CI) based techniques have been employed in the determination of the energetics and various corrections for basis set and geometry relaxation effects are incorporated. A detailed description of the quantum chemical methodology employed here is provided in section II. The qualitative characteristics of the potential are also summarized therein.

A meaningful analysis of the validity of TST requires an accurate procedure for evaluating the transition state partition functions. In this work, we employ the variable reaction coordinate TST formalism.^{44,45} The MR-CI calculated energetics are directly incorporated in the evaluation of the phase space integrals inherent to this formalism. The details of the current implementation of the VRC-TST formalism, and of the master equation treatment of the overall kinetics, are reviewed in section III.

There have been numerous prior theoretical studies of this reaction, including *ab initio* quantum chemical studies of the energetics,^{26,30,34,42} as well as TST-based and other model studies of the kinetics.^{16,21–25,27–33,35–42} The present study proceeds substantially beyond these studies in a variety of ways. In particular, the *ab initio* energetics are generated for orders of magnitude more geometries than in any of the prior studies, and the energetics along the reaction path are generated at a higher level. Furthermore, the direct incorporation of the energetics bypasses the uncertainties in the fitting of the potential energy surfaces for the transitional modes. Finally, the modeling of the pressure dependence via a one-dimensional master equation allows for a more direct comparison of the theoretical and experimental results. This comparison is provided in section IV and some concluding remarks are then made in section V.

II. Potential Surface Calculations

A. Methodology. The basis set used in most calculations was the correlation-consistent, polarized valence double- ζ (cc-pvdz) basis set of Dunning.^{46–48} All of the electronic structure results reported here come from multireference configuration interaction (MR-CI) calculations employing orbitals from complete active space, self-consistent field (CASSCF) calculations. The CASSCF reference wave function consists of two active electrons and two active orbitals (the two radical orbitals of the reactants). This is the minimum necessary to correctly describe the reactant asymptote. The CASSCF orbitals were used in multireference configuration interaction (CAS+1+2) calculations to which a multireference Davidson⁴⁹ correction was added to account for the effects of higher order excitations. To estimate the error associated with the use of the relatively small cc-pvdz basis set, additional calculations were carried out along the staggered D_{3d} path using an aug-pvtz basis set. This basis is the same as the Dunning aug-cc-pvtz basis set except that the diffuse carbon f functions and the diffuse hydrogen d functions were eliminated to make the calculations more tractable. All calculations were carried out using the COLUMBUS package of codes.⁵⁰

One problem in doing a direct dynamics calculation using Monte Carlo methods is that the geometries are chosen randomly and consequently a starting guess for one calculation is not always appropriate for the next calculation. In doing these calculations we found 5–10% of the CASSCF calculations converged incorrectly due to poor starting guesses. However, it proved to be relatively straightforward to detect these points by monitoring the overlap of the CI wave function with the CASSCF wave function. Points having suspiciously low overlap were redone using different starting guesses.

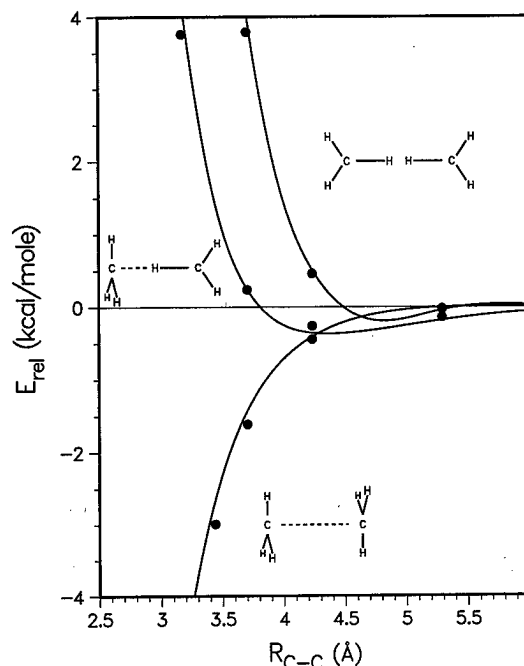


Figure 1. Plots of the energy as a function of the CC distance for three fixed orientations (as shown). The lines are the results of calculations using the cc-pvdz basis set. The solid circles denote results from aug-pvtz calculations. For all calculations the geometries of the two methyl fragments are kept frozen (planar).

B. Results. In the majority of the calculations the geometries of the two methyl radical fragments were kept frozen. Figure 1 shows comparisons of cc-pvdz and aug-pvtz calculations as a function of the C–C distance for three fixed orientations of the two methyl fragments. From this plot it can be seen that at large C–C distances (>4.5 Å) the preferred orientation is one in which one methyl fragment is perpendicular to the CC axis and the other is parallel. This is the orientation favored by the quadrupole–quadrupole interaction. At shorter distances the preferred orientation is one in which both methyls are perpendicular to the CC axis, in a face-to-face orientation. From this plot it can also be seen that at large distances the difference between the cc-pvdz and aug-pvtz interaction energies is quite small.

To further assess the difference between the cc-pvdz and aug-pvtz results, potential curves for the face-to-face orientation were evaluated using both basis sets over a wider range of CC distances. The results are compared in Figure 2. From this plot it can be seen that the interaction energies calculated with these two basis sets are quite similar. Even at the shortest distances examined, 2.5 Å, the aug-pvtz interaction energy is only 1.1 kcal/mol (8%) more attractive. In the dynamical calculations that follow the difference between these two curves will be used as an orientation independent basis set correction to the cc-pvdz potential surfaces. Also compared in Figure 2 are potential curves with and without the Davidson correction for higher order correlations. Including the Davidson correction leads to a somewhat more attractive potential. The dynamical results reported here will employ the Davidson-corrected energies.

To assess the importance of allowing the low-frequency inversion mode of the methyl radicals to relax as the radicals approach, calculations were carried out in which the umbrella angle was optimized as a function of the CC distance. Figure 3 shows a plot of the optimum umbrella angle as a function of CC distance and Figure 4 compares the potential from this calculation to the potential obtained when the geometry of the

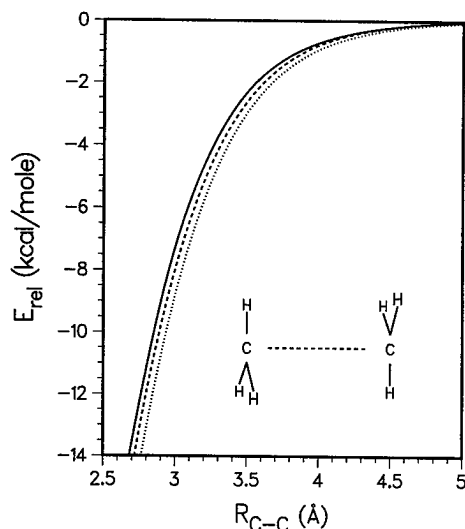


Figure 2. Plot of the energy as a function of the CC distance for the D_{3d} , face-to-face, staggered orientation (as shown). The solid line is the CAS+1+2/cc-pvdz result; the dashed line CAS+1+2/aug-pvtz; and the dotted line, CAS+1+2+QC/aug-pvtz. For all calculations the geometries of the two methyl fragments are kept frozen (planar).

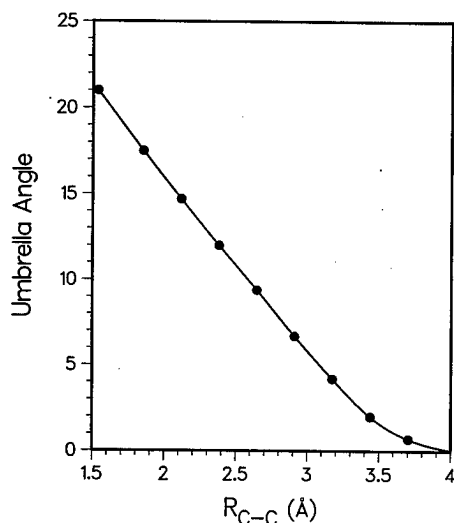


Figure 3. Optimum methyl umbrella angle as a function of the CC distance from CAS+1+2/cc-pvdz calculations. An angle of 0° corresponds to planar radicals. The molecule is constrained to be of D_{3d} symmetry.

methyl fragments is not allowed to relax. From these plots it can be seen that significant deviations from planarity start to occur at CC distances < 3.5 Å. At a distance of ~ 3 Å, allowing the methyls to relax leads to an interaction energy that is ~ 1 kcal/mol (10%) more attractive. The difference between the two curves in Figure 4 will be used as an orientation independent correction for geometry relaxation in the dynamical calculations reported below.

To get a better understanding of the overall topology of this surface, several two-dimensional cuts were evaluated in which the CC distance was held fixed and the relative orientations of the two methyls were allowed to vary. In Figure 5 we show three plots in which the methyls are each allowed to spin about one of their CH bonds. In each case the CH bond which forms the axis of rotation is kept fixed with a CCH angle of 90° and the dihedral angle between the two axis CH bonds is fixed at 180° . For large CC distances this figure shows a potential having diagonal troughs with shallow minima at orientations where one methyl is parallel to the CC axis ($\phi = 0^\circ$) and the other is

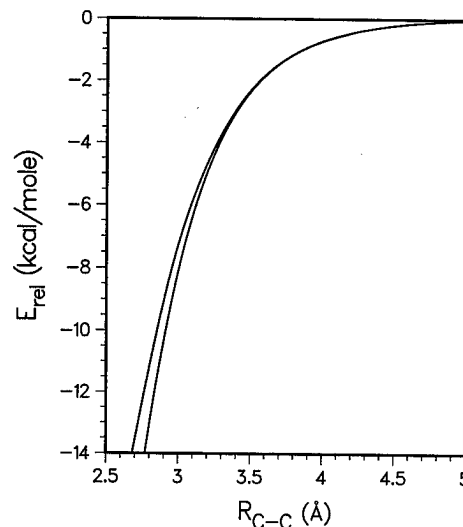


Figure 4. Comparison of D_{3d} potential curves from calculations in which the methyl radicals were kept planar (upper curve) to calculations in which methyls were allowed to distort from planarity (lower curve).

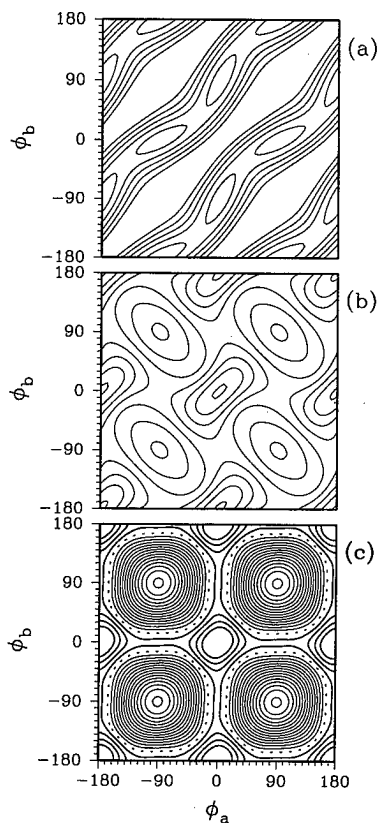


Figure 5. Contour plots of the orientation dependence of the energy for fixed CC distances. The internal geometries of the methyl radicals are kept fixed and the relative orientation of two CH bonds ($C_a H_a$ and $C_b H_b$) are kept fixed with HCC angles of 90° and an $H_a C_a C_b H_b$ dihedral angle of 180° . The plotting coordinates, ϕ_a and ϕ_b , are dihedral angles between the CH_3 planes and the CC axis (see text). Heavy solid contours denote repulsive regions (energies higher than that of the reactant asymptote), light solid contours denote attractive regions, and the dotted contours denote the energy of the reactant asymptote. The contour increments and CC distances are as follows: (a) $R_{CC} = 9$ au, inc = 0.02 kcal/mol; (b) $R_{CC} = 8$ au, inc = 0.05 kcal/mol; (c) $R_{CC} = 7$ au, inc = 0.1 kcal/mol.

perpendicular ($\phi = 90^\circ$). As the CC distance is shortened the potential gradually deforms to one having four equivalent minima, in which both methyls are perpendicular to the CC bond. One surprising aspect of these plots is that at the shortest

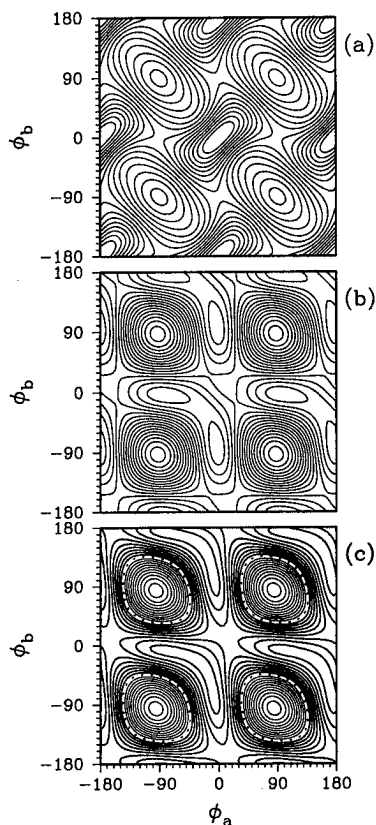


Figure 6. Same as Figure 5, only $H_aCC = H_bCC = 60^\circ$ and $H_aC_aC_bH_b = 60^\circ$. The contour increments and CC distances are as follows: (a) $R_{CC} = 8$ au, inc = 0.02 kcal/mol; (b) $R_{CC} = 7$ au, inc = 0.05 kcal/mol; (c) $R_{CC} = 6$ au, inc = 0.2 kcal/mol.

CC distance it appears as though the preferred path to go from one of the four minima to another involves the stepwise rotation of one methyl at a time (in this plot single rotations correspond to moving either vertically or horizontally). The simultaneous rotation of both methyls in either a conrotatory (the positively sloped diagonal in the plot) or disrotatory (the negatively sloped diagonal) manner requires several kcal/mol more energy. The reason for this appears to be that in this orientation, at these relatively large CC separations, nonbonded repulsions involving the CH bonds are more important in determining the shape of the hindered-rotor potentials than covalent overlap between the two radical orbitals. This picture changes if we orient the methyls in such a way as to minimize nonbonded repulsions. In Figure 6 we show similar plots in which the axis CH bonds are now fixed with CCH angles of 60° and the dihedral angle between the two axis CH bonds is 60° . In these plots it can be seen that for a given CC distance the hindered rotor barriers are smaller than those in Figure 5 and the disrotatory path is preferred.

To allow for an estimate of the possible contribution from the triplet state, a triplet potential curve for the face-to-face orientation was evaluated at the CAS+1+2/cc-pvdz level. This triplet curve is compared with the corresponding singlet curve in Figure 7. The splitting between these two curves is used as an orientation-independent singlet-triplet splitting in generating a crude triplet potential energy surface for the transition state theory calculations.

III. Kinetic Methodology

A. Master Equation Formalism. The effective bimolecular rate constant for methyl radical recombination corresponds to

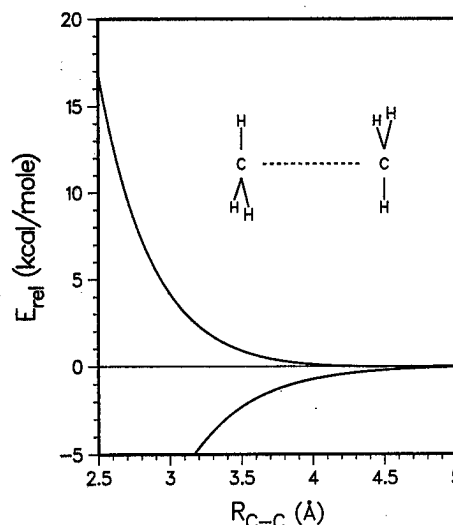


Figure 7. Comparison of CAS+1+2/cc-pvdz, D_{3d} potential curves for the singlet state (lower curve) and triplet state (upper curve). The internal coordinates of the methyl radicals are kept fixed.

a thermal average of the initial rate of formation of energized ethane complexes, $k_f(E, J)$, at energy E and total angular momentum J , times the probability of collisional stabilization at each E and J . Since a single collision does not always yield a stabilized complex, the accurate determination of the latter stabilization probability requires an analysis of the time dependence of the populations in each E and J state, as in the master equation approach.⁵¹ For computational simplicity, a one-dimensional form of the master equation is employed here in which the J dependence of the populations is averaged over according to the scheme of Smith and Gilbert.²⁹

Within this scheme, the E and J resolved dissociation rate constants, $k(E, J)$, are reduced to E resolved rate constants, $k(E)$, via the relation

$$k(E) = \frac{\int dJ P_{\text{comp}}(J) k(E, J) [\omega + k(E, J)]}{\int dJ P_{\text{comp}}(J) [\omega + k(E, J)]} \quad (1)$$

where ω is the collision frequency, and $P_{\text{comp}}(J)$ denotes the thermal equilibrium probability for the complex to have a total angular momentum of J . As discussed by Smith and Gilbert,²⁹ this reduction scheme, which corresponds to a strong collision assumption for the rotational degrees of freedom and assumes a decoupling of the transition probabilities in E and J , provides the correct limiting behavior in both the low- and high-pressure limits.

The present implementation of eq 1 employs the total energy and total angular momentum as variables rather than the vibrational and rotational energy employed in ref 29. These variables provide a more appropriate separation for the rate constants and are the natural variables for the present TST calculations. It is perhaps worth noting that, at least for the temperature and pressure ranges of interest here, employing the alternative reduction scheme based on simply averaging the rate constants with the $P_{\text{comp}}(J)$ weighting function yields essentially identical results. However, there are other reactions where the two reduction schemes produce dramatically different results.

The time dependence of the population, P_i , of the complex in energy state i may be written as

$$\frac{dP_i}{dt} = \omega \sum_j (R_{ij}P_j - R_{ji}P_i) - k_i P_i + v_i \quad (2)$$

where R_{ij} is the probability of making a transition from state i to state j during a collision with the bath gas. The first term on the right-hand side of eq 2 represents the rate of transfer from state j into state i via collisions. The second term represents the corresponding rate of transfer out of state i into state j . The third term represents the rate of loss of the complex in state i due to dissociation, while v_i is the source term describing the rate of formation of ethane in energy state i from the free methyl radicals.

The effective bimolecular rate constants are ultimately obtained via direct numerical inversion of the steady state representation of eq 2.⁵¹ The reduced matrix procedure of ref 52 is employed and the energy transfer rate coefficients are evaluated on the basis of the exponential down model. A variety of energy transfer parameters ($\langle \Delta E_{\text{down}} \rangle$) ranging from 100 to 1600 cm^{-1} are considered since there is no suitable *a priori* means for obtaining quantitative estimates for the average energy transfer. For reference purposes we note here that for temperatures of 200, 296, 407, 474, 577, 810, 1305, 1525, and 1700 K, $\langle \Delta E_{\text{down}} \rangle = 100 \text{ cm}^{-1}$ corresponds (at the ethane dissociation threshold) to an average total energy transferred, $\langle \Delta E_{\text{tot}} \rangle$, of -40, -31, -24, -21, -17, -12, -6.2, -5.1, and -4.2 cm^{-1} , respectively. $\langle \Delta E_{\text{down}} \rangle = 200 \text{ cm}^{-1}$ corresponds to $\langle \Delta E_{\text{tot}} \rangle$ of -110, -94, -77, -69, -59, -43, -23, -19, and -16 cm^{-1} , respectively. $\langle \Delta E_{\text{down}} \rangle = 400 \text{ cm}^{-1}$ corresponds to $\langle \Delta E_{\text{tot}} \rangle$ of -290, -260, -220, -200, -180, -140, -83, -71, and -60 cm^{-1} , respectively. $\langle \Delta E_{\text{down}} \rangle = 800 \text{ cm}^{-1}$ corresponds to $\langle \Delta E_{\text{tot}} \rangle$ of -670, -620, -570, -540, -500, -420, -280, -240, and -210 cm^{-1} , respectively. $\langle \Delta E_{\text{down}} \rangle = 1600 \text{ cm}^{-1}$ corresponds to $\langle \Delta E_{\text{tot}} \rangle$ of -1460, -1400, -1330, -1290, -1230, -1100, -830, -740, and -670 cm^{-1} , respectively.

A Lennard-Jones model for the $\text{Ar} \cdots \text{C}_2\text{H}_6$ collision frequency, ω , is employed (cf. eqs 5.5.14 and 5.5.17 of ref 51), with σ and ϵ values of 3.9 Å and 160 K, respectively. An energy grain size of 100 cm^{-1} provides numerically converged results for all temperatures studied here with the energies spanning the range from -20 000 cm^{-1} below to 22 000 cm^{-1} above the threshold. Total angular momentum quantum numbers ranging up to 138 are considered with a step size of 4.

The underlying dissociation rate constants, $k(E, J)$, are obtained from RRKM theory

$$k(E, J) = \frac{N_{\text{EJ}}^{\ddagger}}{h\rho_{\text{EJ}}} \quad (3)$$

where N_{EJ}^{\ddagger} is the transition state number of states. Rigid rotor harmonic oscillator assumptions were employed for all but the torsional mode in the evaluation of ρ_{EJ} , the density of states for the complex, and for the corresponding canonical partition function. For the torsional mode, calculations for harmonic oscillator, free rotor, and hindered rotor representations were found to differ by less than 5% for the temperatures and pressures of interest here. The pressure-dependent rate constants plotted below are for a free rotor treatment of this mode.

Symmetry numbers of 18, 72, and 72 were employed for the reactants, the transition state, and the products of the recombination reaction, respectively. The reaction was generally assumed to occur on only the ground singlet state. Thus, electronic degeneracies of 4, 1, and 1 were employed for the reactants, the transition state, and the products. Some discussion is given

below of the possible contribution of the triplet state to the association kinetics.

The final results plotted here are for a dissociation energy of 87.5 kcal/mol. Various sources suggest values ranging from about 87.5 to 88.5 kcal/mol.²⁸ Sample calculations for the higher value were qualitatively similar yielding rates that differed by 15% or less in the range of temperature and pressures of interest here. Furthermore, the shapes of the curves were essentially identical thus yielding only a small downward shift in the magnitude of the fitted energy transfer coefficient.

B. High-Pressure Limit Rate Constant, $k_{\infty}(T)$. In the high-pressure limit, where the stabilization probability is unity, the effective bimolecular rate constant simplifies to

$$k_{\infty}(T) = \frac{1}{hQ_{\text{reactants}}(T)} \int dE dJ N_{\text{EJ}} \exp(-E/k_{\text{B}}T) \quad (4)$$

where $Q_{\text{reactants}}$ is the partition function for the reactants. In TST one considers the number of available states for the motion on a dividing surface which separates reactants from products. Within a statistical framework this number of states is an upper bound to the true cumulative reaction probability. The minimum in this number of states with respect to a given family of dividing surfaces, N_{EJ}^{\ddagger} , provides the TST approximation to the true cumulative reaction probability, N_{EJ} .

The variationally optimized dividing surface properly depends on both the total energy E and the total angular momentum J , since they are both strictly conserved between collisions. A useful simplification arises when one assumes that this transition state dividing surface depends only on temperature. In this case, the TST approximation to $k_{\infty}(T)$ reduces to

$$k_{\infty}^{\text{can}}(T) = \frac{k_{\text{B}}T}{h} \frac{Q^{\ddagger}(T)}{Q_{\text{reactants}}(T)} \quad (5)$$

where $Q^{\ddagger}(T)$ is now the minimum in the canonical partition function for the motion on any proper dividing surface.

In the present study, the transition state number of states and rate constants are generally evaluated at the E/J resolved level. For comparison, evaluations at the canonical level yield rate constants which are typically about 15–30% greater. The reasonably small deviation between these two quantities allows us to focus on solely the canonical variations of various factors in our qualitative discussions.

C. Variable Reaction Coordinate TST. In any recombination reaction a number of the modes transform from free rotational to nearly harmonic bending motions. In the transition state region, which typically lies at separations of about 2–5 Å, these modes are intermediate in their transformation. As a result, neither harmonic bending nor free rotational descriptions are generally correct. Instead, one must generally consider these modes as strongly coupled hindered rotors; with the extent of the hindering depending on the location of the transition state and the details of the fragment–fragment interaction potential.

Within the variable reaction coordinate TST approach^{44,45} the contribution to N_{EJ}^{\ddagger} from these “transitional” modes is evaluated on the basis of classical phase space integrals, thereby obtaining an accurate description of the mode–mode couplings and also of angular momentum conservation. Sample calculations indicate that the quantum corrections for these modes are generally negligible due to the combination of their low effective frequency and the additional energy available from the fragment–fragment attractive interactions.^{27,53} An assumed decoupling of the remaining “conserved” modes, which correspond

to the internal vibrations of the free fragments, allows for a quantum treatment of their contribution.

The transitional mode phase space integrals are evaluated here at the energy, E , and total angular momentum J resolved level according to the algorithm described in ref 45. This algorithm employs crude Monte Carlo integration and requires an interaction potential for each relative orientation of the two reacting fragments that is generated in the random sampling for a given transition state dividing surface. A prior study suggested that only a limited number of such configurational samplings (e.g., 100–1000) provide satisfactory convergence (i.e., 10%) within Monte Carlo based evaluations of these integrals.¹⁰ This observation provided the motivation for the present direct implementation of the CAS+1+2 quantum chemical estimates for the required interactions energies.

Any implementation of transition state theory requires the specification of a dividing surface which separates reactants from products. Within variational TST one then minimizes the partition function for motion on a given dividing surface within a family of such surfaces. In this work the dividing surface is specified in terms of a fixed distance between arbitrarily chosen pivot points on each of the fragments, and two separate choices for the pivot point locations are considered. Choosing the pivot points at the centers of mass of the methyl groups provides the appropriate separation of motions at large separations and is thus a useful first choice. At shorter separations the optimum dividing surface may correspond more closely to the separation between the centers of the two radical orbitals involved in the incipient bond. Choosing the pivot points to lie 0.4 Å away from the C atoms, along the C_3 symmetry axis of the methyl fragment, should yield a reasonable first approximation to the latter dividing surface.

Ideally, one would consider a more complete set of pivot point locations (e.g., 0, 0.2, 0.4, 0.6 Å, away from the C atom). However, within the present approach, the net number of ab initio evaluations is proportional to the number of different pivot point locations considered. Thus, in the interest of computational efficiency, only the 0 (center of mass) and 0.4 Å pivot point separations were considered. For both of these choices interfragment separations ranging from 4.0 to 8.0 bohr, in 0.5 bohr spacings, were considered. For the center-of-mass reaction coordinate, larger separations of 8.5, 9.0, 9.5, 10.5, 11.5, 12.5, 14.0, and 16.0 bohr were also considered. In each case the number of configurations generated was designed to produce a net Monte Carlo integration uncertainty of about 10% or less. At the shorter separations approximately 1000 configurations were considered while only 50 configurations are required for the largest separations due to the more nearly symmetrical potential at large separations. Altogether, a total of 14 600 configurations were sampled over.

As might be expected, there is some correlation between the full interaction energy V_{int} for a given geometry and the repulsivity of the interactions between the H atoms on the two separate fragments, for that geometry. This correlation was used to obtain a modest reduction in the number of geometries for which explicit quantum chemical simulations were required. In particular, the factor

$$V_{\text{rep}} = \sum_{ij} \exp(-0.5 \text{ Å}/r_{ij}) \quad (6)$$

where r_{ij} is the distance between the H atoms on the separate fragments, was used as a crude representation of the repulsivity. The correlation observed in plots of V_{int} versus V_{rep} for a limited set of sampled geometries allowed for the subsequent prere-

jection of points with too large a V_{rep} . These prerejected points were included in the sampling but the potential was simply assumed to be infinite and no ab initio quantum chemical simulation was performed.

For large separations, little reduction could be obtained since the repulsive contribution is not dominant. However, for the shortest separation with the 0.4 Å pivot point separation, this prerejection reduced the number of required quantum chemical evaluations by a factor of 3. The sample plots also provided an extra benefit in clearly illustrating a few undetected instances where the quantum chemical simulations had converged to an incorrect electronic state. Such convergence errors were quite uncommon, occurring less than 1% of the time, and were corrected for by the generation of the appropriate energies.

A perfect separation of the conserved modes from the transitional modes and reaction coordinate would imply that the methyl radical geometry is unchanging during the course of the reaction. In reality, this geometry has a substantial variation from planar to tetrahedral during the recombination. Furthermore, the optimal geometry is a function not only of how far apart the methyl radicals are but also of their relative orientation.

In the transition state the structure tends to be more like the separated methyl radicals than like ethane. Thus, the former geometry was generally employed in the random samplings for the Monte Carlo integration of the phase space integrals. The effects of the variation in the rovibrational properties of the methyl radical were then examined and correction factors were incorporated as appropriate.

The variation in the effective moments of inertia leads to changes in the kinetic energies for the transitional modes. The variation of the product of the three moments of inertia provides a reasonable first approximation to the effect of this aspect. This product was found to vary by only about 1% from the free fragments to the transition state region and so this aspect of the variation was neglected.

A more important effect of the variation is on the interaction energies. To account for this effect, the optimum geometry and corresponding relaxation energy were determined as a function of the CC separation. This energetic relaxation was added in as an orientation independent correction to the interaction energies. The reference orientation for this correction was taken as the optimal orientation for the equivalent CC atom–atom separation. At the shorter separations, this correction is quite sizable and leads to significant variations in the estimated rate constants.

The vibrational frequencies of the conserved modes also vary along the reaction path, with that for the umbrella mode being especially large. The quantum chemical study of Robertson et al. provided GVB/3-21G estimates for the dependence of these frequencies on the CC separation.³⁴ This predicted variation in the conserved mode frequencies is incorporated at the harmonic oscillator level for all but the umbrella mode. For the latter mode, a one-dimensional WKB treatment is instead incorporated, again employing the data from ref 34.

The above-described correction factors are based on the optimum geometry for a given separation. In reality, the optimal geometry depends also on the relative orientation. The quantitative examination of the energetic relaxation and conserved mode vibrational frequencies for each geometry sampled in the phase space integrations is computationally intractable. However, some indication of the effect may be obtained from a limited sampling. Thus, relaxation energies and umbrella mode vibrational force fields were obtained for 39 configurations at a CC separation of 5 bohr, which corresponds to the transition state location for a temperature of 3000 K. Incorporating these relaxation energies

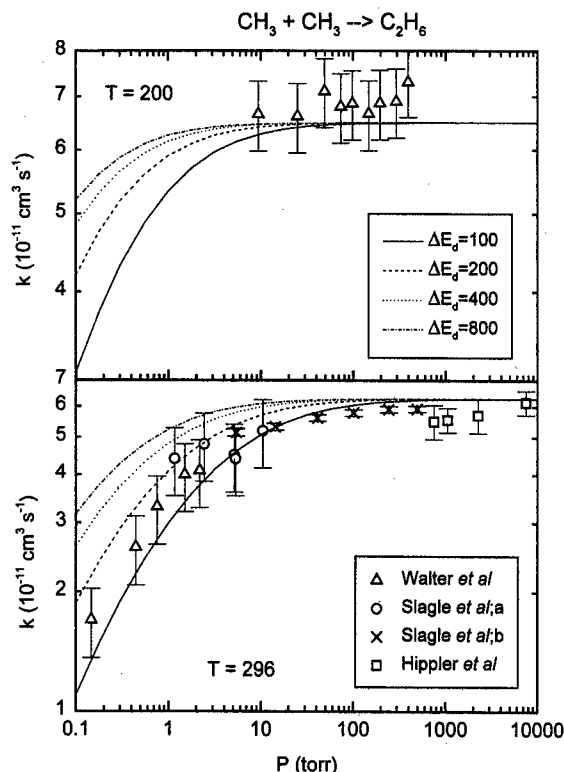


Figure 8. Plot of the pressure dependence of the rate constant for temperatures of 200 and 296 K. The squares denote the experimental data of Hippler *et al.*,¹⁴ the circles and crosses of Slagle *et al.*,¹⁵ and the triangles of Walter *et al.*¹⁶ The lines denote the present theoretical results for various $\langle \Delta E_{\text{down}} \rangle$ values.

and vibrational frequencies in place of those for the reference geometries yielded an increase in the transitional mode canonical partition function at 3000 K of only 10%, which is certainly less than the uncertainty arising from the limited sampling. The smallness of this correction suggests that the orientation dependence of the corrections is relatively minor.

IV. Kinetics Results

A. Pressure Dependence. Illustrative plots of the pressure dependence of the bimolecular rate constants are provided in Figures 8–14. In each case, the available experimental data are plotted along with the theoretical predictions for $\langle \Delta E_{\text{down}} \rangle$ values of 100, 200, 400, and 800 cm^{-1} . At 200 K (cf. Figure 8) both the absolute rate constants and the predicted negligible dependence on pressure above 10 Torr are in good agreement with the experimental observations.

At 296 K (cf. Figure 8) the experimental pressure range extends to low enough pressures (i.e., 0.1 Torr) to produce a falloff in the rate constant (from its infinite pressure limit) by a factor of 4. The theoretical predictions for energy transfer coefficients $\langle \Delta E_{\text{down}} \rangle$ ranging from about 100 to 200 cm^{-1} are in quantitative agreement with the observations. Higher energy transfer coefficients do not produce sufficient falloff in the rate constant with decreasing pressure.

At 407 K (cf. Figure 9) the optimum agreement between theory and experiment occurs for a $\langle \Delta E_{\text{down}} \rangle$ value of about 200 cm^{-1} . At 474 K (cf. Figure 9) the optimum $\langle \Delta E_{\text{down}} \rangle$ value is again near 200 cm^{-1} . However, at the latter temperature there is some discrepancy between the theoretical and experimental falloff curves. Furthermore, for both these temperatures, the high-pressure limit of the theoretical predictions appears to lie slightly (i.e., about 10–20%) above the experimental limit.

By 577 K (cf. Figure 10) the experimental measurements at

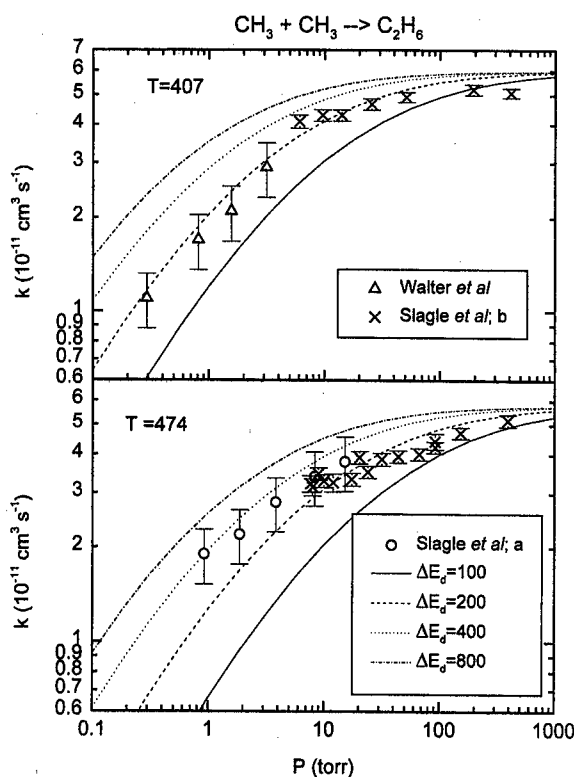


Figure 9. As in Figure 8, but for temperatures of 407 and 474 K.

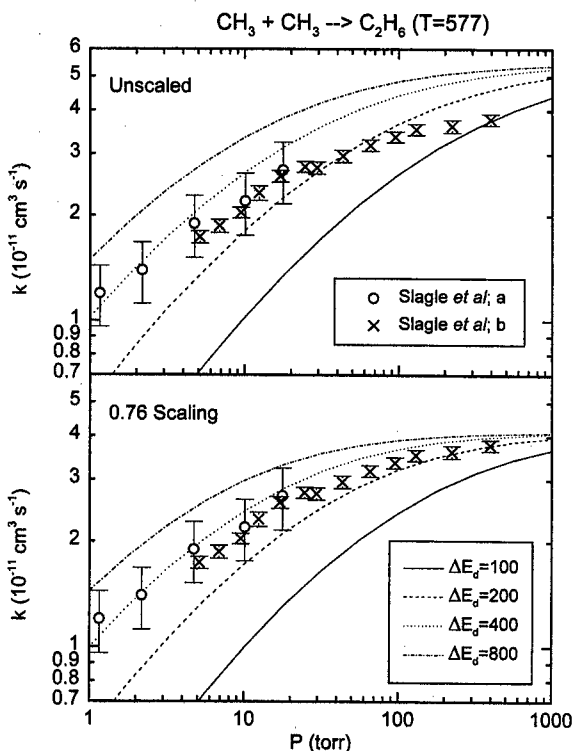


Figure 10. As in Figure 8, but for a temperature of 577 K. The theoretical results in the lower plot employ a transition state number of states which are scaled to yield a high-pressure thermal rate constant which is 0.76 times as large. The upper plot provides the unscaled theoretical results.

the highest pressures are not quite at the high-pressure limit. Regardless, the theoretical predictions now appear to lie measurably above the experimental measurements at the highest pressures, perhaps by about 30%. The optimum agreement between theory and experiment is not very good and now occurs for $\langle \Delta E_{\text{down}} \rangle$ values of 200–400 cm^{-1} .

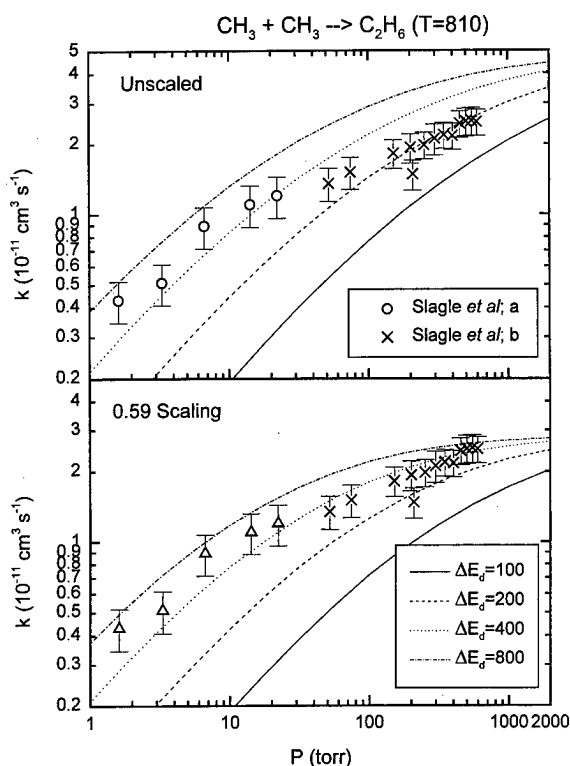


Figure 11. As in Figure 10, but for a temperature of 810 K. At this temperature the scaling reduces the high-pressure thermal rate constant by a factor of 0.59.

These discrepancies between the theoretical and experimental predictions could be indicative of various errors. Either the theoretical predictions or the experimental measurements for the high-pressure limit may simply be slightly inaccurate. Alternatively, the particular model employed here for the pressure dependence of the kinetics (i.e., the exponential down model for energy transfer within the one-dimensional master equation) may be inadequate. It is instructive to consider to what extent the theoretical predictions for the high-pressure limit would need to be in error in order to obtain a satisfactory reproduction of the experimental observations. Thus, for temperatures of 577 K and higher we have also plotted theoretical predictions for the pressure dependence which employ an energy-dependent scaling of the transition state number of states. This empirical scaling takes the form $[1 - 0.65 \tan h(E/3500)^2]$, where E is the excess energy relative to the dissociation threshold in cm^{-1} . This form, which varies from no correction at low temperature to a maximum correction of 0.35 at high temperature, has no fundamental physical basis. Instead, it was simply designed to produce an average scaling which increases with temperature and to an extent which yields improved agreement with the experimental results for the full range of temperatures considered here. The scale factors printed on the plots indicate the effect of this scaling on the thermal high-pressure limit rate constant for the given temperature. Implementing this scaling for 577 K clearly improves the agreement between theory and experiment.

At 810 K (cf. Figure 11) this empirical scaling results in good agreement between theory and experiment for a $\langle \Delta E_{\text{down}} \rangle$ value of about 400 cm^{-1} . In contrast, the optimum falloff curve for the unscaled theoretical result differs significantly from the experimental results. At temperatures of 474 and 407 K the thermal scale factors of 0.83 and 0.88, arising from this same energy-dependent scaling, also result in improved agreement between the theoretical and experimental observations. Although

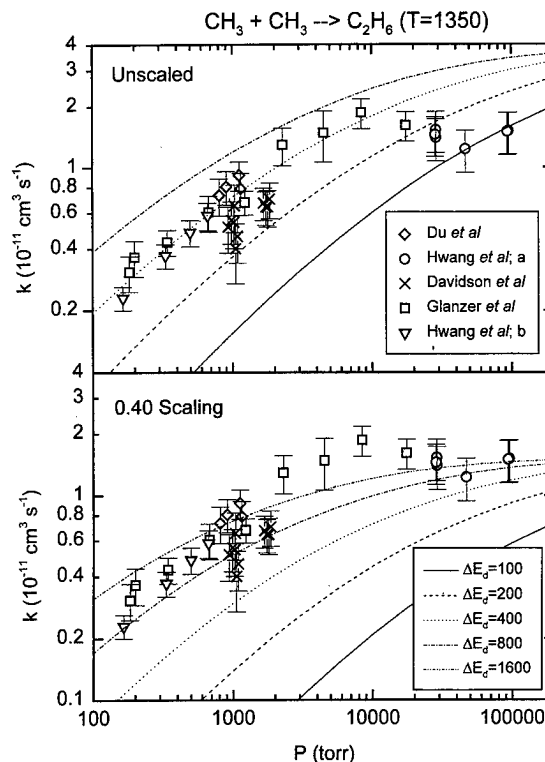


Figure 12. As in Figure 10, but for a temperature of 1350 K, and for different sets of experimental data. The diamonds denote the experimental data of Du et al.,²⁰ the circles of Hwang et al.,¹⁷ the crosses of Davidson et al.,¹⁹ the squares of Glanzer et al.,¹³ and the triangles of Hwang et al.¹⁸ At this temperature the scaling reduces the high-pressure thermal rate constant by a factor of 0.40.

not plotted here, this same improvement in the agreement between the theoretical and experimental falloff curves is found for the scaled results for other temperatures in this region (e.g., 700 and 910 K).

A similar situation exists for the higher temperatures of 1200, 1350, 1525, and 1700 K (cf. Figures 12–14). However, for these temperatures the scatter in the experimental data is somewhat greater, and the rate constants for the highest pressures studied appear to be further from the high-pressure limit. As a result, the comparison between the theoretical and experimental results is less definitive. Nevertheless, the scaled results still show a marked improvement in the overall agreement. For these scaled results the optimum $\langle \Delta E_{\text{down}} \rangle$ value is near 800 cm^{-1} .

The present pressure-dependent calculations are restricted to temperatures of 1700 K and below, since additional dissociative processes (i.e., to $\text{C}_2\text{H}_5 + \text{H}$, and $\text{C}_2\text{H}_4 + \text{H}_2$) begin to contribute above this range. The potential energy surface and kinetic estimates generated in our study of the $\text{H} + \text{C}_2\text{H}_5$ radical reaction⁵⁴ could be employed in an extension of this work to such higher temperatures. However, this extension is sufficiently time consuming that we have chosen to leave it for future work.

B. T Dependence of k_{∞} . A priori VRC-TST predictions for the temperature dependence of the high-pressure limiting rate constant, $k_{\infty}(T)$, were performed for a somewhat wider temperature range of 200–3000 K. However, the region from 300 to 1700 K is of primary interest and thus our discussion again focuses on this temperature region. The results of these calculations are provided in Table 1 and plotted in Figure 15, together with some related theoretical estimates.

Also plotted in Figure 15 are the corresponding experimental data^{14–16} for temperatures of 407 K and lower, where the extrapolation to the high-pressure limit is reasonably secure (cf.

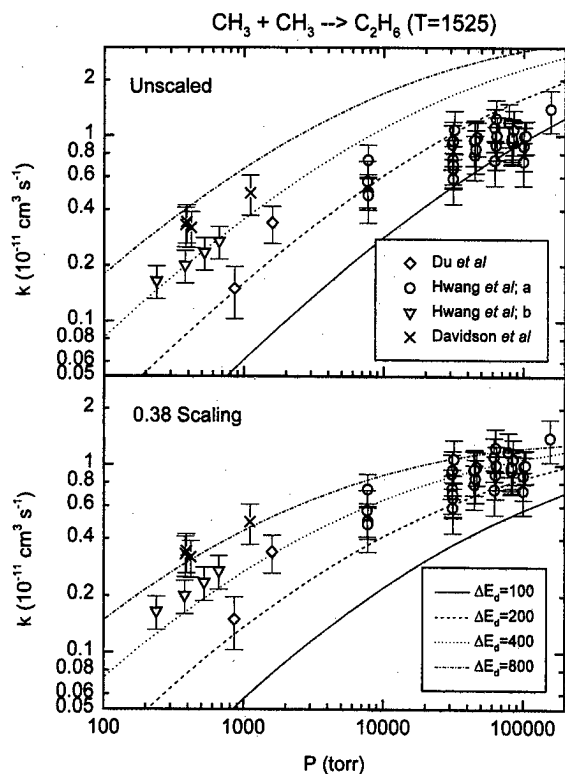


Figure 13. As in Figure 12, but for a temperature of 1525 K. At this temperature the scaling reduces the high-pressure thermal rate constant by a factor of 0.38.

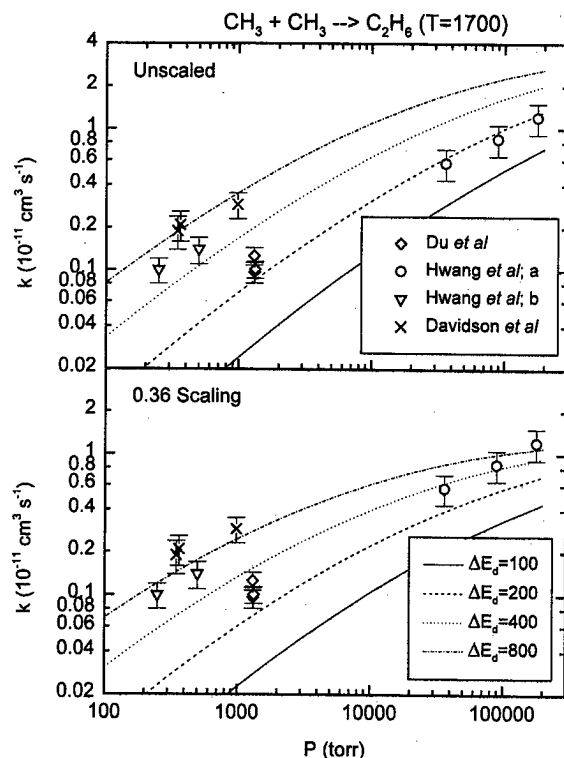


Figure 14. As in Figure 12, but for a temperature of 1700 K. At this temperature the scaling reduces the high-pressure thermal rate constant by a factor of 0.36.

Figures 8–14). For these temperatures, the agreement between the present a priori VRC-TST estimates and the experimental data is remarkable. Unfortunately, as discussed above, the results for the pressure dependence at higher temperatures suggest that this agreement does not persist.

TABLE 1. High-Pressure Association Rate Constants

T (K)	k (10^{-11} cm 3 s $^{-1}$)	T (K)	k (10^{-11} cm 3 s $^{-1}$)
200	6.44	906	4.44
245	6.4	1050	4.22
296	6.28	1200	4.04
370	6.06	1350	3.88
407	5.93	1525	3.74
474	5.7	1700	3.6
513	5.55	1950	3.43
539	5.46	2250	3.24
577	5.31	2600	3.05
700	4.92	3000	2.8
810	4.64		

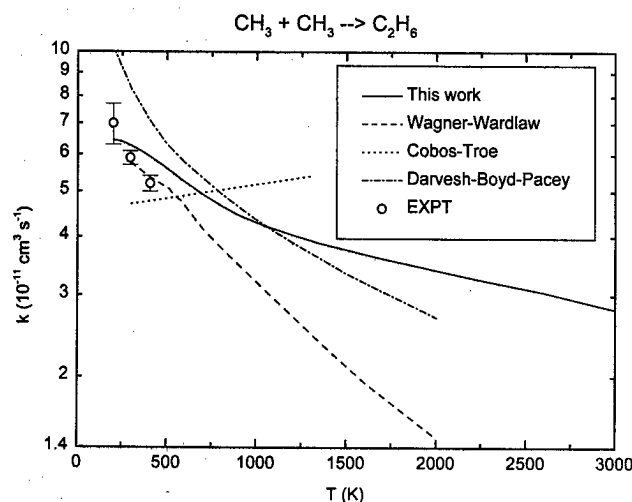


Figure 15. Plot of the temperature dependence of the high-pressure limiting rate constant for methyl radical association. The solid, the dashed, and the dashed-dotted lines represent the TST calculations from this work, from ref 28, and from ref 30. The dotted line denotes the SACM calculations from ref 23. The circles denote the experimental results from refs 14–16.

A variety of other theoretical results are also plotted in Figure 15. The study of Pacey and co-workers³⁰ is based on a TST method similar to the present one, but employs a potential based on a fit to a limited set of ab initio data. Perhaps not surprisingly, their results are similar to the present ones.

The study of Wagner and Wardlaw²⁸ is based on an earlier TST-based study of Wardlaw and Marcus.²⁵ The primary difference between these studies^{25,28} and that of Pacey and co-workers³⁰ is in the use of a more empirical potential energy surface. A key parameter in the study of Wagner and Wardlaw was adjusted to allow their RRKM based calculations to accurately reproduce the pressure-dependent rate constants from ref 15. Thus, the discrepancy between the present results and those of ref 28 is another indication of our apparent overestimate of the high-pressure limit rate constant for high temperatures. Although not shown here, the hindered Gorin model calculations of ref 31 are similar to those of Wagner and Wardlaw.

Cobos and Troe²³ have provided empirical statistical adiabatic channel model (SACM) results which are clearly the most distinctly different from the present ones. In these SACM calculations the α and β parameters that characterize the potential were adjusted to produce a small rise in the high-pressure rate constant with increasing temperature. In contrast, the present a priori TST calculations suggest a decrease by a factor of 1.7 from 300 to 1700 K. Due to the difficulty of measuring the high-pressure limit at temperatures above 500 K, it is currently not possible to resolve the question of the temperature dependence of k_∞ from experimental data alone.

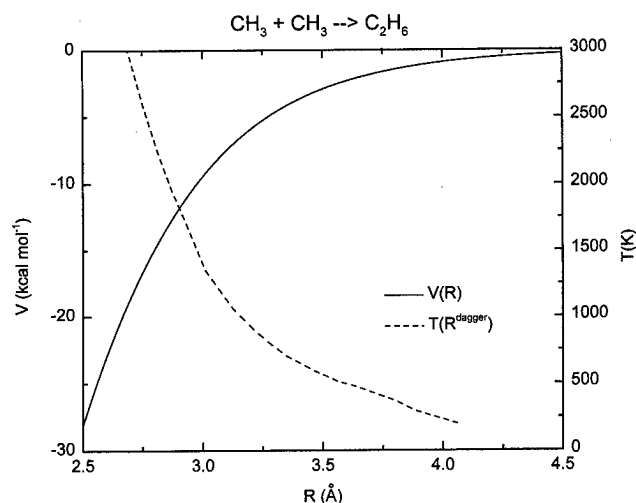


Figure 16. Plot of the temperature dependence of the transition state location (dashed line; right axis) and the interaction potential along the reaction path (solid line; left axis).

The sign and the magnitude of this temperature dependence for radical radical recombinations are of considerable fundamental interest. The separation into the conserved and transitional modes allows one to consider the individual contributions to this temperature dependence. Considering only the transitional modes (i.e., ignoring both the effect of the geometric relaxation of the methyl radicals on the energies and the variations of the methyl radical vibrational frequencies) leads to a predicted drop by a factor of 2.9 over this same temperature range. This drop is due to the increasing hindrance of the relative orientational motions of the two fragments as the interfragment separation decreases.

The conserved mode variations have two competing effects on the temperature dependence. The relaxation energy (arising from the geometric relaxation of the internal coordinates of the methyl radicals) yields a rise in the rate constant by a factor of 2.2 over this temperature range, while the variation in their frequencies leads to a decrease by a factor of 1.3. The umbrella mode is the dominant component in both these variations. The net effect of the conserved mode variations corresponds to an increase by a factor of 1.7 from 300 to 1700 K.

The variation of the CC separation at the transition state with temperature is illustrated in Figure 16. The results plotted therein are for the optimum CC separation with the pivot points 0.4 Å away from the C atoms. The canonical rate constants for the center-of-mass pivot points were generally higher, but only by a few percent. The transition state location is seen to decrease quite dramatically with decreasing separation, decreasing from about 4.0 Å near room temperature to 3.0 Å near 1500 K. The minimum-energy path potential at these separations is remarkably large.

The present calculations have focused on the contribution from solely the ground singlet state. The lowest triplet state is asymptotically degenerate with the ground singlet state. Thus, at large separations, the triplet state may make a nonnegligible contribution to the reactive flux. The size of this contribution is limited in part by the rate of intersystem crossing to the ground singlet state. The maximum contribution would arise for rapid electronic equilibration throughout the transition state region. In this instance, the transition state number of states may be equated with the minimum in the sum of the number of available states for motion on both the singlet and triplet states, including an electronic degeneracy factor of 3 for the triplet state:

$$N_{EJ}^{\dagger} = \min\{N_{EJ}(V_{\text{singlet}}^{\dagger}, R) + 3N_{EJ}(V_{\text{triplet}}^{\dagger}, R); R\} \quad (6)$$

The evaluation of the triplet potential along the reaction path (cf. Figure 7) allows for a crude estimate of the maximum contribution from the triplet state. This estimate employed a triplet state potential given by the sum of the orientation-dependent singlet state potential and the orientation-independent singlet-triplet splitting along the reaction path. This maximum contribution decreases from 60% of the singlet state contribution at 200 K to 40% at 300 K and 20% at 500 K, and continues to decrease with increasing temperature. The good agreement observed between theory and experiment for the singlet rate near room temperature suggests that the triplet state contribution is likely much smaller due to a slow intersystem crossing rate. Similar observations were made for the H + ethyl and H + vinyl reactions.

The primary results here employ both a Davidson correction for multiple excitations and an orientation-independent reaction path basis set correction. The effect of these corrections provides some indication of the uncertainties due to the accuracy of the ab initio potential. Neglecting the basis set correction yielded rate constants which were 25–40% lower. Further basis set corrections would be expected to yield substantially smaller corrections. The calculations employ an unnormalized Davidson correction which has the effect of increasing the rate by 20–30%. A rough estimate of the probable error in this correction can be made by repeating the calculations using a normalized Davidson correction (unnormalized Davidson corrections typically underestimate the effect of higher order correlations while normalized Davidson corrections often overestimate the importance of these effects). In this case, using the normalized Davidson correction increases the rate by 3–7% relative to using the unnormalized Davidson correction.

V. Concluding Remarks

The direct implementation of 14 600 ab initio data points within a phase space integral based version of VTST yields high-pressure bimolecular rate constants, $k_{\infty}(T)$, which are in quantitative agreement with experiment near room temperature. The generation of this many data points yields Monte Carlo integration uncertainties on the order of 10% or less for each of the transition state dividing surfaces considered. The underlying quantum chemical estimates are based on calculations at the CAS+1+2/cc-pvdz level but also include corrections for basis set limitations and higher level excitations. The modest variations for neglect of basis set corrections and/or Davidson corrections suggest that any errors in the quantum chemical estimates are likely of only minor importance.

The present a priori theoretical estimates provide strong evidence for a decrease in $k_{\infty}(T)$ with increasing temperature. The increasing hindrance of the relative orientational modes is the dominant factor in this decrease which amounts to an overall decrease by a factor of 1.7 from 300 to 1700 K. Changes in the umbrella mode geometry and vibrational frequency actually yield a contribution which increases with temperature.

The theoretical and experimental results for the pressure dependence of the bimolecular rate become increasingly discordant as the temperature rises. Such discrepancies may be indicative of failures in either the model for the pressure dependence or of an overestimate of $k_{\infty}(T)$ at higher temperatures. Sample calculations illustrated that the latter explanation would require an overestimate by about a factor of 2–3 for temperatures of about 1200–1700 K. An empirical reduction of the underlying transition state number of states yielded

pressure-dependent rate constants which were in good agreement with the experimental data.

It is interesting to consider the possible failures in the theoretical calculations which might lead to such an overestimate of $k_{\infty}(T)$. One possibility is simply that the underlying quantum chemistry is not accurate enough. However, the basis set and Davidson corrections are small enough to suggest that this is unlikely. Alternatively, the transition state evaluations may not be accurate enough. For example, the coupling of the conserved and transitional modes becomes more important as the temperature rises. This coupling has been approximately accounted for via the incorporation of the geometrical relaxation effects and the variation of the conserved mode frequencies along the reaction path. However, such corrections may be inadequate. The consideration of only two different forms for the transition state dividing surface might also lead to some overestimate of the association rate constant. The present model for the pressure dependence of the kinetics may also be inadequate.

Each of the above-mentioned inadequacies, while not necessarily insignificant, do not seem likely to yield the necessary major corrections. An intriguing alternative possibility is that the fraction of trajectories which are directly repulsive increases with temperature ultimately becoming the dominant fraction. These directly repulsive trajectories would be high collision energy trajectories which come in to a close separation and then immediately turn around and dissociate back to reactants. Such trajectories would cross any configuration-based dividing surface and thus result in an overestimate of the effective association rate constant. In the true infinite pressure limit, such trajectories could also be stabilized. However, the immediacy of their return suggests that such stabilization would generally not arise for realistic experimental pressure ranges. The $H + O_2$ reaction provides an interesting example of a case where such trajectories do appear to occupy a major fraction of phase space.^{55,56} An empirical model for correcting for the effect of such repulsive trajectories has been provided by Truhlar.⁵⁷

Acknowledgment. This work was supported by the U.S. Department of Energy, Office of Basic Energy Sciences, Division of Chemical Sciences, under Contract W-31-109-ENG-38 (L.B.H. and S.J.K.) and through NSF grant CHE-9423725 (S.J.K.). Helpful discussions with Jan Hessler, Al Wagner, and Dave Wardlaw are gratefully acknowledged.

References and Notes

- Helgaker, T.; Uggerud, E.; Jensen, H. J. A. *Chem. Phys. Lett.* **1990**, 173, 145.
- Hartke, B.; Carter, E. A. *Chem. Phys. Lett.* **1992**, 189, 358.
- Chen, W.; Hase, W. L.; Schlegel, H. B. *Chem. Phys. Lett.* **1994**, 228, 436.
- Collins, M. A.; *Adv. Chem. Phys.* **1996**, 93, 389. Bettens, R. P. A.; Collins, M. A. *J. Chem. Phys.* **1998**, 109, 9728.
- Schatz, G. C.; Papaioannou, A.; Pederson, L. A.; Harding, L. B.; Hollebeck, T.; Ho, T. S.; Rabitz, H. *J. Chem. Phys.* **1997**, 107, 2340. Ho, T. S.; Hollebeck, T.; Rabitz, H.; Harding, L. B.; Schatz, G. C.; *J. Chem. Phys.* **1996**, 105, 10472.
- Truhlar, D. G. In *The Reaction Path in Chemistry: Current Approaches and Perspectives*; Heidrich, D., Ed.; Kluwer: Dordrecht, The Netherlands, 1995; pp 229–255.
- Duncan, W. T.; Bell, R. L.; Truong, T. N. *J. Comput. Chem.* **1998**, 19, 1039. Truong, T. N.; Duncan, W. T.; Bell, R. L. *ACS Symp. Ser.* **1996**, 629, 85.
- Wardlaw, D. M.; Marcus, R. A. *Adv. Chem. Phys.* **1988**, 70, Part 2, 231.
- Klippenstein, S. J. In *Advances in Physical Chemistry: The Chemical Dynamics and Kinetics of Small Radicals*; Liu, K.; Wagner, A. F., Eds.; World Scientific: Singapore, 1995; Part 1.
- Klippenstein, S. J.; Allen, W. D. *Ber. Bunsen. Phys. Chem.* **1997**, 101, 423. Klippenstein, S. J.; East, A. L. L.; Allen, W. D. *J. Chem. Phys.* **1996**, 105, 118.
- Mallard, W. G. NIST Chemical Kinetics Database, 1992, and references therein.
- Glänzer, K.; Quack, M.; Troe, J. *Chem. Phys. Lett.* **1976**, 39, 304.
- Glänzer, K.; Quack, M.; Troe, J. In *Sixteenth Symposium (International) Combustion*; The Combustion Institute: Seattle, WA, 1977; p 949.
- Hippler, H.; Luther, K.; Ravishankara, A. R.; Troe, J. *Z. Phys. Chem. NF* **1984**, 142, 1.
- Slagle, I. R.; Gutman, D.; Davies, J. W.; Pilling, M. J. *J. Phys. Chem.* **1988**, 92, 2455.
- Walter, D.; Grotheer, H.-H.; Davies, J. W.; Pilling, M. J.; Wagner, A. F. In *Twenty-Third Symp. (Int.) Combust.*; The Combustion Institute: Seattle, WA, 1990; p 107.
- Hwang, S. M.; Wagner, H. G.; Wolff, T. In *Twenty-Third Symp. (Int.) Combust.*; The Combustion Institute: Seattle, WA, 1990; p 99.
- Hwang, S. M.; Rabinowitz, M. J.; Gardiner, Jr., W. C. *Chem. Phys. Lett.* **1993**, 205, 157.
- Davidson, D. F.; DiRosa, M. D.; Chang, E. J.; Hanson, R. K.; Bowman, C. T. *Int. J. Chem. Kinet.* **1995**, 27, 1179.
- Du, H.; Hessler, J. P.; Ogren, P. J. *J. Phys. Chem.* **1996**, 100, 974.
- Gorin, E. *J. Chem. Phys.* **1939**, 7, 256.
- Quack, M.; Troe, J. *Ber. Bunsen-Ges. Phys. Chem.* **1977**, 81, 329.
- Cobos, C. J.; Troe, J. *J. Chem. Phys.* **1985**, 83, 1010.
- Wardlaw, D. M.; Marcus, R. A. *J. Chem. Phys.* **1985**, 83, 3462.
- Wardlaw, D. M.; Marcus, R. A. *J. Phys. Chem.* **1986**, 90, 5383.
- Evleth, E. M.; Kassab, E. *Chem. Phys. Lett.* **1986**, 131, 475.
- Klippenstein, S. J.; Marcus, R. A. *J. Chem. Phys.* **1987**, 87, 3410.
- Wagner, A. F.; Wardlaw, D. M. *J. Phys. Chem.* **1988**, 92, 2462.
- Smith, S. C.; Gilbert, R. G. *Int. J. Chem. Kinet.* **1988**, 20, 307, 979.
- Darvesh, K. V.; Boyd, R. J.; Pacey, P. D. *J. Phys. Chem.* **1989**, 93, 4772.
- Stewart, P. H.; Larson, C. W.; Golden, D. M. *Combust. Flame* **1989**, 75, 25.
- Aubanel, E. E.; Robertson, S. H.; Wardlaw, D. M. *J. Chem. Soc., Faraday Trans.* **1991**, 87, 2291.
- Forst, W. *J. Phys. Chem.* **1991**, 95, 3612.
- Robertson, S. H.; Wardlaw, D. M.; Hirst, D. M. *J. Chem. Phys.* **1993**, 99, 7748.
- Pitt, I. G.; Gilbert, R. G.; Ryan, K. R. *J. Phys. Chem.* **1995**, 99, 239.
- Robertson, S. H.; Pilling, M. J.; Baulch, D. L.; Green, N. J. B. *J. Phys. Chem.* **1995**, 99, 13452.
- Hessler, J. P.; Ogren, P. J. *J. Phys. Chem.* **1996**, 100, 984.
- Hessler, J. P. *J. Phys. Chem.* **1996**, 100, 2141.
- Jeffrey, S. J.; Gates, K. E.; Smith, S. C. *J. Phys. Chem.* **1996**, 100, 7090.
- Pesa, M.; Pilling, M. J.; Robertson, S. H.; Wardlaw, D. M. *J. Phys. Chem. A* **1998**, 102, 8526.
- Pacey, P. D. *J. Phys. Chem. A* **1998**, 102, 8541.
- Naroznik, M. *J. Chem. Soc., Faraday Trans.* **1998**, 94, 2531.
- The experimental data for temperatures greater than about 1700 K (cf. ref 19 and references therein) includes a significant contribution from the $H + C_2H_5$ channel and thus will not be considered here.
- Klippenstein, S. J. *Chem. Phys. Lett.* **1990**, 170, 71; *J. Chem. Phys.* **1991**, 94, 6469; **1992**, 96, 367.
- Klippenstein, S. J. *J. Phys. Chem.* **1994**, 98, 11459.
- Dunning, T. H., Jr. *J. Chem. Phys.* **1989**, 90, 1007.
- Kendall, R. A.; Dunning, T. H., Jr.; Harrison, R. J. *J. Chem. Phys.* **1992**, 96, 6796.
- Woon, D. E.; Dunning, T. H., Jr. *J. Chem. Phys.* **1993**, 98, 1358.
- Langhoff, S. R.; Davidson, E. R. *Int. J. Quantum Chem.* **1974**, 8, 61. Silver, D. W.; Davidson, E. R. *Chem. Phys. Lett.* **1978**, 52, 403.
- Shepard, R.; Shavitt, I.; Pitzer, R. M.; Comeau, D. C.; Pepper, M.; Lischka, H.; Szalay, P. G.; Ahlrichs, R.; Brown, F. B.; Zhao, J.-G. *Int. J. Quantum Chem.* **1988**, S22, 149.
- Gilbert, R. G.; Smith, S. C. *Theory of Unimolecular Recombination Reactions*, Blackwell Scientific: Oxford, UK, 1990; Holbrook, R. A.; Pilling, M. J.; Robertson, S. H. *Unimolecular Reactions*, 2nd ed.; Wiley: Chichester, UK, 1996.
- Robertson, S. H.; Pilling, M. J.; Baulch, D. L.; Green, N. J. B. *J. Phys. Chem.* **1995**, 99, 13452.
- Yu, J.; Klippenstein, S. J. *J. Phys. Chem.* **1991**, 95, 9882.
- Harding, L. B.; Klippenstein, S. J. *27th Symp. (Int.) Combust.* **1998**, 151.
- Yang, C.-Y.; Klippenstein, S. J. *J. Chem. Phys.* **1995**, 103, 7287.
- Dobbyn, A. J.; Stumpf, M.; Keller, H.-M.; Schinke, R. *J. Chem. Phys.* **1996**, 104, 8357.
- Truhlar, D. G. *J. Am. Chem. Soc.* **1975**, 97, 6310.

Improvement of the Internal Consistency in Trajectory Surface Hopping

Jian-Yun Fang and Sharon Hammes-Schiffer*

Department of Chemistry and Biochemistry, University of Notre Dame, Notre Dame, Indiana 46556-5670

Received: May 17, 1999; In Final Form: July 9, 1999

This paper addresses the issue of internal consistency in the molecular dynamics with quantum transitions (MDQT) surface hopping method. The MDQT method is based on Tully's fewest switches algorithm, which is designed to ensure that the fraction of trajectories on each surface is equivalent to the corresponding average quantum probability determined by coherent propagation of the quantum amplitudes. For many systems, however, this internal consistency is not maintained. Two reasons for this discrepancy are the existence of classically forbidden transitions and the divergence of the independent trajectories. This paper presents a modified MDQT method that improves the internal consistency. The classically forbidden switches are eliminated by utilizing modified velocities for the integration of the quantum amplitudes, and the difficulties due to divergent trajectories are alleviated by removing the coherence of the quantum amplitudes when each trajectory leaves a nonadiabatic coupling region. The standard and modified MDQT methods are compared to fully quantum calculations for a classic model for ultrafast electronic relaxation (i.e., a two-state three-mode model of the conically intersecting S_1 and S_2 excited states of pyrazine). The standard MDQT calculations exhibit significant discrepancies between the fraction of trajectories in each state and the corresponding average quantum probability. The modified MDQT method leads to remarkable internal consistency for this model system.

I. Introduction

Trajectory surface hopping methods have been used extensively to study processes occurring on multiple coupled potential energy surfaces. In these methods the system is divided into a quantum and a classical subsystem. The classical subsystem is approximated as an ensemble of independent trajectories, and each trajectory moves classically on a single potential energy surface with the possibility of instantaneous transitions among the surfaces. The various surface hopping methods^{1–31} differ mainly in how these transitions are incorporated. This paper centers on the molecular dynamics with quantum transitions (MDQT) method, which is based on Tully's stochastic fewest switches algorithm.¹⁴ In this algorithm the quantum amplitudes for all surfaces are propagated coherently along each independent trajectory, and the probability of a transition depends on the rate of change of the quantum probabilities determined from the quantum amplitudes. The number of transitions is minimized by specifying that the flux of trajectories switching from one state to another is unidirectional over a specified time interval. This algorithm is designed to ensure that the fraction of trajectories on each surface is equivalent to the corresponding average quantum probability. As has been noticed in the literature, however, this internal consistency is not always maintained.^{32,33} The goal of this paper is to identify the reasons for this discrepancy and to develop methods for improving the internal consistency of MDQT. These new methods are applied to a model of the conically intersecting S_1 and S_2 excited states of pyrazine. This model system was chosen because it is a classic example of ultrafast electronic relaxation^{34–40} and was previously found to exhibit a significant discrepancy between the fraction of trajectories in each state and the corresponding average quantum probability in MDQT calculations.³³

The reason often cited for the internal inconsistency in MDQT is the existence of classically forbidden transitions. In MDQT, energy is conserved during a transition by adjusting the classical velocities as if they were subjected to a force in the direction of the nonadiabatic coupling vector. If there is not enough velocity in this direction to maintain energy conservation, then the transition is classically forbidden and is not allowed to occur. (In this case, the component of velocity in the direction of the nonadiabatic coupling is reversed¹⁵ or, in some implementations, the velocity is not changed.³³) Such classically forbidden transitions lead to an inconsistency between the fraction of trajectories in each state and the corresponding average quantum probability. The most rigorous way to fix this problem is to increase the size of the quantum mechanical subsystem or to use semiclassical formulations. Unfortunately, a sufficiently large quantum mechanical subsystem is often computationally impractical and, although a number of promising semiclassical formulations have been developed recently,^{41–49} the surface hopping approach is still appealing due to its conceptual simplicity and computational speed.

Classically forbidden transitions can be eliminated in the framework of the MDQT method in a number of ways. One hypothesis is that the forbidden transitions should occur and that the fundamental limitation is the method of velocity adjustment. In this case, classically forbidden transitions can be eliminated by taking energy from other components of the velocities, delaying the transition until the energy is available in the appropriate component of the velocities, or, if all else fails, violating energy conservation. An alternative hypothesis is that the forbidden transitions should not occur and that the fundamental limitation is the method of integrating the quantum amplitudes. In support of this alternative view, Müller and Stock³³ found that for the pyrazine model the agreement with exact quantum calculations was much better for the fraction of

* Corresponding author. E-mail: hammes-schiffer.1@nd.edu.

trajectories in each state than for the corresponding average quantum probability.

Adopting this alternative view, in a previous paper⁵⁰ we presented a modification of MDQT (denoted MDQT*) that eliminates classically forbidden transitions by utilizing modified velocities for the integration of the quantum amplitudes. In this approach, the nonadiabatic coupling between two states vanishes if a switch to the unoccupied state would be classically forbidden. As a result, the quantum amplitudes between these two states are uncoupled so population is not transferred between these two states. According to the fewest switches algorithm, in this case the probability of a transition between these two states vanishes. In ref 50 we applied both MDQT and MDQT* to models representing single and double proton transfer and found that both MDQT and MDQT* maintained internal consistency. In this paper we apply MDQT* to the pyrazine model system to provide a more rigorous test of MDQT*. We show that even in the absence of classically forbidden switches the MDQT* method does not maintain internal consistency for this model system.

Another reason for the lack of internal consistency in MDQT is that the divergence of independent trajectories may lead to a breakdown in the basic assumption of the fewest switches algorithm. This basic assumption is that when a trajectory passes through a nonadiabatic coupling region with nonzero quantum amplitudes for the other surfaces, an ensemble of virtually identical trajectories (i.e., with similar quantum amplitudes and classical coordinates and momenta) are apportioned among the other surfaces according to these quantum amplitudes. (Note that the trajectories are expected to vary slightly due to different initial conditions.) Typically, this assumption is valid for one-dimensional systems involving a single pass through a single nonadiabatic coupling region. Unfortunately, this assumption is violated in many other situations.⁵¹

A dramatic example of the breakdown of the fewest switches algorithm can be illustrated with a two-state model with two nonadiabatic coupling regions. Assume all of the population starts on the upper state, and when it passes through the first nonadiabatic coupling region some of the population transfers down to the lower state. Assume also that there is a barrier on the lower state preventing the lower state population from reaching the second nonadiabatic coupling region. In this case, when the upper state population passes through the second nonadiabatic coupling region the quantum amplitudes of the trajectories are nonzero for the lower state, but there are no trajectories on the lower state in this nonadiabatic coupling region. As a result, the population flux determined by the net change in quantum probabilities for the trajectories on the upper state is inaccurate. (See ref 51 for a clear and comprehensive analysis of such situations.)

A breakdown of the fewest switches algorithm could also occur for a single pass through a single nonadiabatic coupling region if the potential energy surfaces are of very different character in this region (leading to different quantum amplitudes and classical coordinates and momenta of the trajectories on each state). Figure 1 depicts a schematic illustration of such a situation for a two-state model, where P_2 and F_2 indicate the average quantum probability and fraction of trajectories, respectively, for the upper state in an MDQT simulation. As shown in Figure 1a, all of the population is assumed to start on the upper state. As the population passes through the nonadiabatic coupling region, it starts to transfer down to the lower state. If the lower and upper state surfaces are similar throughout the nonadiabatic coupling region, the internal consistency will

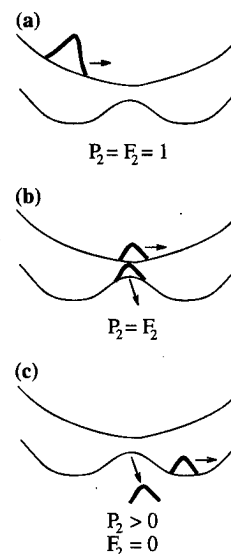


Figure 1. A schematic picture of the effects of divergent trajectories in MDQT simulations, where P_2 and F_2 denote the average quantum probability and the fraction of trajectories, respectively, in the upper state. The populations for the two states are shown for (a) the initial time, (b) an intermediate time, and (c) the final time. The different orientations of the arrows within (b) and (c) indicate that the trajectories are moving in different directions.

be maintained. If the two surfaces differ, however, the trajectories on the lower state may diverge and follow different paths as they leave the nonadiabatic coupling region. In Figure 1, the internal consistency is maintained between the time shown in Figure 1a and the time shown in Figure 1b. The arrows in Figure 1, b and c, indicate that after the time shown in Figure 1b, the trajectories on the lower state move out of the nonadiabatic coupling region before the trajectories on the upper state have passed through the nonadiabatic coupling region. The orientations of the arrows indicate that the trajectories on the lower state are moving in a different direction than those on the upper state. Note that this situation is more likely for multidimensional systems. If the population flux is unidirectional (i.e., from the upper to the lower state) throughout the coupling region, this divergence will not affect the final fraction of trajectories in each state. On the other hand, this divergence will lead to an internal inconsistency because the quantum amplitudes of the divergent trajectories will not be consistent with the quantum amplitudes of the trajectories that continued to move on the excited state. Thus, as illustrated in Figure 1c, the fraction of trajectories on each state may be correct after passing through this nonadiabatic coupling region, but the internal consistency will not be maintained. In this paper we present evidence that this is the main source of the discrepancies noticed by Müller and Stock for the pyrazine model system.

This inconsistency can be alleviated by eliminating the coherence of the quantum amplitudes between well-separated regions of nonadiabatic coupling. In this paper we present a method in which the quantum amplitudes are reset so that the occupied state has a quantum probability of unity after each trajectory has left the nonadiabatic coupling region. (Note that this type of resetting of the quantum amplitudes was also proposed in ref 51. Also note that the resetting of the quantum amplitudes will affect the number of classically forbidden transitions.) We emphasize that resetting the quantum amplitudes is not a general solution to this inherent problem of mixed quantum/classical methods. Clearly this prescription would be inappropriate for systems where the quantum interference between nonadiabatic coupling regions is important.^{29,31} For

many systems, however, such quantum interference effects are washed out due to decoherence in condensed phase systems or averaging over a range of initial conditions. In these cases this method for promoting internal consistency in MDQT is physically justified. We point out that similar methods involving the removal of the coherence of the quantum amplitudes have been applied previously in conjunction with a variety of surface hopping methods.^{4,17,24} Moreover, Rossky and co-workers have performed a thorough analysis of the treatment of coherence in surface hopping.^{52,53}

An outline of this paper is as follows. Section II presents the model system for internal conversion in pyrazine, including the diabatic and adiabatic Hamiltonian matrices for this system. Section III describes the methodology for fully quantum dynamical and mixed quantum/classical MDQT calculations. This section also presents modifications of MDQT to eliminate classically forbidden transitions and to remove the coherence of the quantum amplitudes far from regions of nonadiabatic coupling. Section IV presents the results and compares the various methods, and section V presents our conclusions.

II. Model System

The model system investigated in this paper is a two-state three-mode model of the conical intersection of the $S_1[{}^1B_{3u}(n\pi^*)]$ and $S_2[{}^1B_{2u}(\pi\pi^*)]$ excited states of pyrazine. This conical intersection has been shown to trigger an ultrafast $S_2 \rightarrow S_1$ internal conversion process and a dephasing of the vibrational motion on a femtosecond time scale.^{34,36} The model used in this paper includes a single vibronic coupling mode ν_{10a} and two totally symmetric tuning modes ν_1 , ν_{6a} (which modulate the energetic separation of the electronic states). This model invokes the following standard simplifications:^{38,39} (1) the model Hamiltonian is constructed in a diabatic electronic basis; (2) the harmonic approximation is invoked for the diabatic potential energy surfaces and the vibrational frequencies are assumed to be equal for all of the unperturbed surfaces; and (3) interstate and intrastate coupling terms are approximated by linear terms in the normal coordinates. This model has been used throughout the literature as a standard example of ultrafast electronic relaxation.³⁴⁻³⁹ (Note that other models for conical intersections have also been studied with similar methods.⁵⁴)

The Hamiltonian is defined in terms of the two diabatic electronic basis states $|\psi_1^{\text{dia}}\rangle$ and $|\psi_2^{\text{dia}}\rangle$ that represent the two lowest excited singlet states (S_1 and S_2) of pyrazine. The Hamiltonian matrix in the diabatic representation can be expressed as

$$\tilde{H}^{\text{dia}} = (T_N + V_0)\tilde{I} + \begin{pmatrix} E_1 + \sum_{j=1}^2 \kappa_j^{(1)} x_j & \lambda x_3 \\ \lambda x_3 & E_2 + \sum_{j=1}^2 \kappa_j^{(2)} x_j \end{pmatrix} \quad (1)$$

In the first term, T_N is the kinetic energy expressed as

$$T_N = \frac{1}{2} \sum_{j=1}^3 \omega_j p_j^2 \quad (2)$$

and V_0 is a harmonic oscillator potential with respect to the electronic ground state equilibrium geometry

$$V_0 = \frac{1}{2} \sum_{j=1}^3 \omega_j x_j^2 \quad (3)$$

Here ω_j is the vibrational frequency and x_j and p_j are the position and momentum of the j th vibrational mode, where $j = 1$ represents the tuning mode ν_1 , $j = 2$ represents the tuning mode ν_{6a} , and $j = 3$ represents the vibronic coupling mode ν_{10a} . For this model the mass corresponding to mode j is $m_j = 1/\omega_j$ with the appropriate units conversion. In this paper the coordinates of the modes are expressed in vector notation as $\mathbf{x} = (x_1, x_2, x_3)$, \tilde{I} is the identity matrix, and $\hbar = 1$. In the state-dependent part of the Hamiltonian, E_k is the vertical transition energy of the diabatic state k and $\kappa_j^{(k)}$ is the gradient of the excited state potential k with respect to x_j at the ground state equilibrium geometry. The off-diagonal term λx_3 is responsible for the vibronic coupling between the two electronic states. The values of the parameters for this model are given in Table I of ref 33.

Although the diabatic representation is useful for fully quantum dynamical calculations, the adiabatic representation is more appropriate for surface hopping calculations. As shown in ref 55, the transformation from the diabatic to the adiabatic representation is given by

$$\psi^{\text{ad}}(\mathbf{x}) = \tilde{S}^\dagger(\mathbf{x})\psi^{\text{dia}} \quad (4)$$

where the adiabatic basis states are expressed in vector notation as

$$\psi^{\text{ad}}(\mathbf{x}) = \begin{pmatrix} \psi_1^{\text{ad}}(\mathbf{x}) \\ \psi_2^{\text{ad}}(\mathbf{x}) \end{pmatrix} \quad (5)$$

and the diabatic basis states are expressed in vector notation as

$$\psi^{\text{dia}} = \begin{pmatrix} \psi_1^{\text{dia}} \\ \psi_2^{\text{dia}} \end{pmatrix} \quad (6)$$

The transformation matrix can be expressed as

$$\tilde{S}(\mathbf{x}) = \begin{pmatrix} \cos \phi & \sin \phi \\ -\sin \phi & \cos \phi \end{pmatrix} \quad (7)$$

where ϕ is defined by

$$\begin{aligned} \sin(2\phi) &= \frac{\lambda x_3}{(\Delta^2 + \lambda^2 x_3^2)^{1/2}} \\ \cos(2\phi) &= \frac{\Delta}{(\Delta^2 + \lambda^2 x_3^2)^{1/2}} \end{aligned} \quad (8)$$

and Δ is half the energy gap between the diabatic electronic surfaces at \mathbf{x} :

$$\Delta = \frac{1}{2} \left[\left(E_2 + \sum_{j=1}^2 \kappa_j^{(2)} x_j \right) - \left(E_1 + \sum_{j=1}^2 \kappa_j^{(1)} x_j \right) \right] \quad (9)$$

Note that the S matrix is a double-valued function of the coordinates \mathbf{x} . In this paper we define a unique S matrix by following the prescription given in ref 56 of setting the signs of S_{11} and S_{22} equal to the sign of x_3 .

Invoking the Born–Oppenheimer approximation, the adiabatic Hamiltonian matrix is

$$\tilde{H}^{\text{ad}} = (T_N + V_0)\tilde{I} + \begin{pmatrix} \bar{E} - (\Delta^2 + \lambda^2 x_3^2)^{1/2} & 0 \\ 0 & \bar{E} + (\Delta^2 + \lambda^2 x_3^2)^{1/2} \end{pmatrix} \quad (10)$$

where

$$\bar{E} = \frac{1}{2} \left[\left(E_2 + \sum_{j=1}^2 \kappa_j^{(2)} x_j \right) + \left(E_1 + \sum_{j=1}^2 \kappa_j^{(1)} x_j \right) \right] \quad (11)$$

The two adiabatic Born–Oppenheimer potential energy surfaces are described by

$$W_k(\mathbf{x}) = H_{kk}^{\text{ad}} - T_N \quad (12)$$

(See ref 56 for a discussion of the non-Born–Oppenheimer terms in the adiabatic Hamiltonian.)

III. Methods

A. Fully Quantum Dynamical Method. The fully quantum dynamical calculations were performed in the diabatic representation to avoid numerical difficulties associated with the double-valued nature of the S matrix. The time-dependent wave function $\Psi(\mathbf{x}, t)$ can be expressed in terms of the diabatic basis states as

$$\Psi(\mathbf{x}, t) = \chi_1(\mathbf{x}, t) \psi_1^{\text{dia}} + \chi_2(\mathbf{x}, t) \psi_2^{\text{dia}} \quad (13)$$

where $\chi_k(\mathbf{x}, t)$ is the vibrational wave function corresponding to the diabatic state $|\psi_k^{\text{dia}}\rangle$. Substituting this equation for $\Psi(\mathbf{x}, t)$ into the time-dependent Schrödinger equation using the diabatic Hamiltonian matrix given in eq 10 leads to the two coupled equations of motion

$$\begin{aligned} i\dot{\chi}_1^{\text{dia}}(\mathbf{x}, t) &= V_{11}(\mathbf{x})\chi_1^{\text{dia}}(\mathbf{x}, t) + V_{12}(\mathbf{x})\chi_2^{\text{dia}}(\mathbf{x}, t) \\ i\dot{\chi}_2^{\text{dia}}(\mathbf{x}, t) &= V_{21}(\mathbf{x})\chi_1^{\text{dia}}(\mathbf{x}, t) + V_{22}(\mathbf{x})\chi_2^{\text{dia}}(\mathbf{x}, t) \end{aligned} \quad (14)$$

where V_{ij} are matrix elements of the matrix $\tilde{\mathbf{H}}^{\text{dia}} - T_N \tilde{\mathbf{I}}$. We solve these equations of motion using the predictor–corrector method with the discrete variable representation. These results are converted to the adiabatic representation for comparison to the surface hopping results using the projector operator defined in ref 55.

B. Surface Hopping Methods. 1. Standard MDQT Method. In surface hopping methods the classical subsystem moves according to the standard classical equations of motion

$$m_j \ddot{x}_j = - \frac{\partial W_k(\mathbf{x})}{\partial x_j} \quad (15)$$

where $W_k(\mathbf{x})$ (defined in eq 12) is the potential energy of the occupied adiabatic state. The time-dependent wave function describing the quantum mechanical state at time t is expanded in terms of the two adiabatic states

$$\Psi(\mathbf{x}, t) = C_1(t) \psi_1^{\text{ad}}(\mathbf{x}) + C_2(t) \psi_2^{\text{ad}}(\mathbf{x}) \quad (16)$$

where $C_i(t)$ are complex-valued expansion coefficients (i.e., quantum amplitudes). Note that the adiabatic states are also time-dependent through the classical trajectory $\mathbf{x}(t)$. Substitution of the wave function $\Psi(\mathbf{x}, t)$ into the time-dependent Schrödinger equation using the adiabatic Hamiltonian matrix $\tilde{\mathbf{H}}^{\text{ad}}$ given in eq 10 leads to the following equations of motion for the quantum amplitudes:

$$\dot{C}_k = -iC_k W_k - \sum_{j=1}^2 C_j \dot{\mathbf{x}} \cdot \mathbf{d}_{kj} \quad (17)$$

where $\dot{\mathbf{x}}$ denotes the time derivatives of the coordinates \mathbf{x} and \mathbf{d}_{kj} is the nonadiabatic coupling vector defined as

$$\mathbf{d}_{kj} = \langle \psi_k^{\text{ad}} | \nabla_{\mathbf{x}} \psi_j^{\text{ad}} \rangle = \sum_{i=1}^2 S_{ik} \nabla_{\mathbf{x}} S_{ij} \quad (18)$$

for $j \neq k$ and $\mathbf{d}_{kk} = 0$. In density matrix notation, the density matrix elements are defined as $a_{kj} = C_k C_j^*$, where the diagonal density matrix elements a_{kk} are the occupation probabilities of the adiabatic states, and the off-diagonal elements a_{kj} describe the coherence. In practice, eqs 15 and 17 are integrated numerically to simultaneously propagate the coordinates and momenta (\mathbf{x}, \mathbf{p}) and the quantum amplitudes C_j .

The surface hopping calculations in this paper are based on the molecular dynamics with quantum transitions (MDQT) surface hopping method.^{14,15} The MDQT method implements Tully's fewest switches algorithm,¹⁴ which is designed to correctly apportion trajectories among the states according to the quantum probabilities $|C_j(t)|^2$ with the minimum required number of quantum transitions. In this algorithm the probability of switching states is defined in terms of the rate of change of the occupation probabilities, which can be derived from eq 17 to be

$$\dot{a}_{kk} = \sum_{j \neq k} b_{kj} \quad (19)$$

where

$$b_{jk} = -2\text{Re}(a_{jk}^* \dot{\mathbf{x}} \cdot \mathbf{d}_{jk}) \quad (20)$$

The rate of change of the occupation probability for state k due to coupling with state j is b_{kj} , so the change in the occupation probability for state k due to coupling with state j over a short time interval δt is $b_{kj} \delta t$. The number of state switches is minimized by assuming that the flux of probability between each pair of states results from probability transferring in only one direction. According to this algorithm, the probability of switching from the current state k to another state j during the time interval between t and $t + \delta t$ is

$$g_{kj}(t, \delta t) = \max\left(0, \frac{b_{jk} \delta t}{a_{kk}}\right) \quad (21)$$

where b_{jk} and a_{kk} are assumed to remain approximately constant during the short time interval δt and thus can be evaluated either at time t or at time $t + \delta t$. If $b_{jk} < 0$ then the occupation probability of the occupied state k can be viewed as increasing due to coupling with state j , so the probability of switching from state k to state j is zero. On the other hand, if $b_{jk} > 0$ then the occupation probability of the occupied state k can be viewed as decreasing due to coupling with state j , so the probability of switching from state k to state j is $b_{jk} \delta t / a_{kk}$. References 14 and 22 illustrate that this algorithm achieves the correct statistical populations of the states for model systems.

In order to determine whether a switch to any state j will occur, a uniform random number ξ ($0 < \xi < 1$) is selected at each time step in the trajectory. For example, for a two-state system, if the occupied state $k = 1$ then a switch to state 2 will occur if $\xi < g_{12}$. If a switch to a different state j does occur and if $W_k \neq W_j$, then the velocities must be adjusted in order to conserve total energy. The velocities should be adjusted as if they were subjected to a force in the direction of the nonadiabatic coupling vector.¹⁴ As derived in ref 15, the new velocities $\dot{\mathbf{x}}'$

can be calculated as follows:

$$\dot{x}'_i = \dot{x}_i - \gamma_{kj} \mathbf{d}_{kj}^i / m_i \quad (22)$$

where \mathbf{d}_{kj}^i specifies the i th component of the three-dimensional vector \mathbf{d}_{kj} , and

$$\gamma_{kj} \equiv \frac{\beta_{kj} + \sqrt{\beta_{kj}^2 + 4\alpha_{kj}[W_k(\mathbf{x}) - W_j(\mathbf{x})]}}{2\alpha_{kj}}, \quad \beta_{kj} < 0 \quad (23)$$

$$\gamma_{kj} \equiv \frac{\beta_{kj} - \sqrt{\beta_{kj}^2 + 4\alpha_{kj}[W_k(\mathbf{x}) - W_j(\mathbf{x})]}}{2\alpha_{kj}}, \quad \beta_{kj} \geq 0 \quad (24)$$

where

$$\alpha_{kj} \equiv \frac{1}{2} \sum_{i=1}^3 m_i^{-1} (\mathbf{d}_{kj}^i)^2 \quad (25)$$

and

$$\beta_{kj} \equiv \sum_{i=1}^3 \dot{x}_i \mathbf{d}_{kj}^i \quad (26)$$

Note that a switch can occur only if

$$\beta_{kj}^2 + 4\alpha_{kj}[W_k(\mathbf{x}) - W_j(\mathbf{x})] \geq 0 \quad (27)$$

Otherwise, there is not enough velocity in the direction of the nonadiabatic coupling vector to maintain energy conservation, and the system remains in the initial quantum state. This situation is denoted a classically forbidden transition. Within the framework of standard MDQT, there are two different approaches for determining the velocities after classically forbidden transitions. In the first approach, the component of velocity in the direction of the nonadiabatic coupling vector is reversed; i.e., the velocities are changed according to eq 22 with $\gamma_{kj} = \beta_{kj}/\alpha_{kj}$.¹⁵ In the second approach, the velocities are not adjusted.³³ In either approach, these classically forbidden transitions lead to inconsistencies between the fraction of trajectories $F_i(t)$ in each state i and the corresponding average quantum probability $\langle |C_i(t)|^2 \rangle$.

2. MDQT* Method for Eliminating Classically Forbidden Switches. Recently we presented a modified MDQT method (denoted MDQT*) originally proposed by Tully⁵⁷ to eliminate classically forbidden transitions. In MDQT* the quantum amplitudes are integrated using modified velocities $\dot{\mathbf{x}}_{ij}$:

$$\dot{C}_i = -iC_i W_i - \sum_{j=1}^2 C_j \dot{\mathbf{x}}_{ij} \cdot \mathbf{d}_{ij} \quad (28)$$

and the velocity $\dot{\mathbf{x}}_{jk}$ replaces $\dot{\mathbf{x}}$ in eq 20 for the calculation of b_{jk} used to calculate the probability of switching from state k to state j . The modified velocities are defined as

$$\dot{\mathbf{x}}_{ij} = \sqrt{\dot{x}'_i \dot{x}'_j} \frac{\dot{\mathbf{x}}}{\dot{x}} \quad (29)$$

where $\dot{\mathbf{x}}$ is the classical velocity for the occupied state k , and \dot{x}'_i , \dot{x}'_j , and \dot{x} are the magnitudes of the three-dimensional vectors $\dot{\mathbf{x}}'_i$, $\dot{\mathbf{x}}'_j$, and $\dot{\mathbf{x}}$, respectively. (Note that $\dot{\mathbf{x}}_{ij} = \dot{\mathbf{x}}_{ji}$.)

In this paper we examine two different approaches for defining the modified velocities within the framework of MDQT*. In both approaches, $\dot{x}'_j = 0$ if a switch from the

occupied state k to state j would be classically forbidden (i.e., if eq 27 is not satisfied). Otherwise, in the first approach $\dot{\mathbf{x}}'_j$ is the velocity that would be obtained using the prescription in eq 22 to conserve total energy for a transition from the occupied state k to state j , and in the second approach $\dot{\mathbf{x}}'_j = \dot{\mathbf{x}}$. (Note that in both approaches $\dot{\mathbf{x}}'_k = \dot{\mathbf{x}}$.) In both MDQT* approaches, if a hop from state k to state j would be classically forbidden, the nonadiabatic coupling between states k and j vanishes (i.e., all components of $\dot{\mathbf{x}}_{kj}$ are zero) so the flux of quantum probability from state k to state j vanishes (i.e., $b_{jk} = 0$). According to the fewest switches algorithm, in this case the probability of switching from state k to state j is zero (i.e., $g_{kj} = 0$). Thus, the classically forbidden transitions are eliminated.

We emphasize that MDQT* is not based on rigorous theoretical grounds, but rather is a minor modification that eliminates the classically forbidden transitions while maintaining the appealing simplicity and computational speed of MDQT. MDQT* is the same as MDQT in that the classical subsystem moves according to standard classical equations of motion using the positions \mathbf{x} and velocities $\dot{\mathbf{x}}$ on the occupied state k . Moreover, MDQT and MDQT* use the same fewest switches algorithm and the same method for scaling velocities after a state switch to conserve total energy. MDQT* differs from MDQT only in the integration of the quantum amplitudes, which invokes the modified velocities. In the first MDQT* approach, the modified velocities are geometric averages of the velocities in different states. In the second MDQT* approach, the modified velocities are identical to the standard velocity used in MDQT (i.e., the velocity for the occupied state) except that the modified velocity is set to zero if a transition would be classically forbidden. The second MDQT* approach is more appealing in that it is identical to standard MDQT in the absence of classically forbidden transitions. In both MDQT* approaches, however, MDQT* is virtually identical to MDQT far from the nonadiabatic coupling region (since the nonadiabatic coupling vanishes) and in the strong coupling region (since the energy difference between the coupled states is so small that the velocity adjustment due to a transition would be negligible). Furthermore, the results in ref 50 and in this paper indicate that the MDQT and MDQT* methods lead to virtually identical adiabatic populations (determined by the fraction of trajectories in each adiabatic state) for a variety of model systems.

3. Removal of Coherence of the Quantum Amplitudes. As discussed in the Introduction, even in the absence of classically forbidden switches, the fewest switches algorithm does not always maintain consistency between the fraction of trajectories $F_i(t)$ and the average quantum probability $\langle |C_i|^2 \rangle$. In standard MDQT the quantum amplitudes are propagated coherently throughout each trajectory. When independent trajectories diverge, this coherent propagation may lead to an inconsistency between the fraction of trajectories in each state and the corresponding average quantum probability. This internal inconsistency can be improved if the quantum amplitudes are reset so that the quantum amplitude of the occupied state is unity after passing through a nonadiabatic coupling region. In this paper the quantum amplitudes are reset when the magnitude of the nonadiabatic coupling vector $|\mathbf{d}_{12}|$ between the two adiabatic states becomes smaller than a specified tolerance. Clearly this resetting of the quantum amplitudes is not appropriate for systems where the quantum interference between nonadiabatic coupling regions is important.^{29,31} This resetting of the quantum amplitudes is physically justified, however, if the quantum interference effects between the nonadiabatic coupling regions are washed out by decoherence effects or by

averaging over a range of initial conditions. In this paper the resetting of the quantum amplitudes is used as a numerical tool to correct a deficiency of the MDQT method.

C. Initial Conditions. The fully quantum calculations were performed in the diabatic representation. In this case, the initial wavepacket is a Gaussian wavepacket on the second diabatic electronic state:

$$\begin{aligned}\psi_1^{\text{dia}}(\mathbf{x}) &= 0 \\ \psi_2^{\text{dia}}(\mathbf{x}) &= A \exp[-1/2(x_1^2 + x_2^2 + x_3^2)]\end{aligned}\quad (30)$$

where A is a normalization factor. Note that the exponential also includes a units conversion factor from use of the identity $\omega_j m_j = 1$.

The MDQT calculations were performed in the adiabatic representation. In this case, the initial conditions for the nuclear variables were obtained from classical action-angle variables:^{33,58}

$$\begin{aligned}x_j(0) &= \sin \alpha_j \\ p_j(0) &= \cos \alpha_j\end{aligned}\quad (31)$$

where the angles α_j are randomly picked from the interval $[0, 2\pi]$. Again, these expressions include a units conversion factor from use of the identity $\omega_j m_j = 1$. Note that these initial conditions were chosen to allow direct comparison to the results in ref 33. Discrepancies between the fully quantum and MDQT initial conditions for the nuclear variables may be responsible for small differences between the MDQT and fully quantum calculations. The initial conditions for the quantum probabilities in the adiabatic representation were obtained by applying the projection operator defined in ref 55 to the initial wavepacket in the diabatic representation. The fraction of trajectories starting in each adiabatic state was chosen to be consistent with these quantum probabilities, and the phases of the initial quantum amplitudes were set to zero. 5000 trajectories were propagated with a time step of 0.012 fs for each calculation.

IV. Results

In this section we present the results of the application of the methods discussed in section III to the model system for internal conversion in pyrazine described in section II. Figure 2 depicts the time evolution of the population (i.e., the occupation probability) of the upper adiabatic state. For the fully quantum results we plot $\int dx |\psi_2^{\text{ad}}(\mathbf{x}, t)|^2$, and for the surface hopping results we plot both the average quantum probability $\langle |C_2(t)|^2 \rangle$ and the fraction of trajectories $F_2(t)$. The fully quantum results are shown with solid lines and the surface hopping results are shown with dashed lines. In all cases the population of the upper adiabatic state exhibits an ultrafast initial decay within less than 50 fs, followed by a number of weak recurrences.

Figure 2a,b depicts the results of the standard MDQT method, where in Figure 2a the component of velocity in the direction of the nonadiabatic coupling vector is reversed after a classically forbidden transition and in Figure 2b the velocities are not altered after a classically forbidden transition. In both cases the fraction of trajectories in the upper state for the MDQT calculations agrees qualitatively with the fully quantum results. As shown previously,³³ the quantitative agreement is better for the algorithm in which the velocities are not adjusted after classically forbidden transitions. In particular, for the results with velocity reversal (Figure 2a), the first few recurrences are

weaker, and the recurrences are completely damped out at later times. In both MDQT methods, however, the quantum probability does not agree well with the fraction of trajectories, indicating a significant internal inconsistency.

As discussed in the Introduction, the reason most often cited for this lack of internal consistency in MDQT is the existence of classically forbidden transitions. Figure 3 depicts the time evolution of the total number of classically forbidden transitions for 5000 trajectories (corresponding to the results in Figure 2b). The classically forbidden transitions start to occur at ~ 5 fs and continue to occur at a constant rate of 0.02 fs^{-1} per trajectory (i.e., 2% of the trajectories exhibit a classically forbidden transition each femtosecond). The absence of a significant number of classically forbidden transitions before ~ 5 fs is due to the use of initial conditions with 96% of the trajectories starting on the upper state. (All transitions from the upper to the lower state are allowed.) The substantial number of classically forbidden switches occurring after ~ 5 fs suggests that this may be a cause of the internal inconsistency in these calculations. On the other hand, the number of classically forbidden transitions increases at a constant rate, whereas the discrepancy between the quantum probability and the fraction of trajectories becomes virtually constant after 200 fs. This observation suggests that the classically forbidden transitions may not be the main cause of this discrepancy.

To determine the degree to which the classically forbidden transitions are responsible for the significant internal inconsistency illustrated in Figure 2a,b, we applied the MDQT* method to this model system. Figure 2, c and d, depicts the results of the standard MDQT* method using the two different prescriptions discussed in section III. The results are virtually identical for the two different prescriptions and are similar to the results of Figure 2b. The quantum probability still does not agree well with the fraction of trajectories for the MDQT* method. Thus, these results indicate that the classically forbidden transitions are not responsible for the large internal inconsistency.

As discussed in the Introduction, another cause of internal inconsistency is the divergence of the independent trajectories in the ensemble, which may lead to a breakdown of the basic assumption of the fewest switches algorithm. If the independent trajectories diverge while the ensemble is passing through the nonadiabatic coupling region and the flux of population is predominantly unidirectional throughout this region, the fraction of trajectories in each state could be accurate while the average quantum probabilities are inconsistent. In support of this hypothesis, Figure 4 depicts the distribution of quantum probabilities $|C_2(t)|^2$ after the ensemble has first passed through the nonadiabatic coupling region ($t = 67.7$ fs) for the calculations shown in Figure 2d. Although $\sim 30\%$ of the trajectories have a quantum probability less than 0.1, the remaining trajectories have quantum probabilities ranging from 0.1 to 0.95. These trajectories must have followed divergent paths when the ensemble passed through the region of nonadiabatic coupling. As a result, their quantum amplitudes are not representative of the ensemble.

This source of the internal inconsistency can be eliminated by removing the coherence of the quantum amplitudes when each trajectory leaves the nonadiabatic coupling region. As discussed in section III, in our calculations the criterion for resetting the quantum amplitudes to unity for the occupied state is the magnitude of the nonadiabatic coupling vector $|\mathbf{d}_{12}|$ becoming less than a specified tolerance. In our calculations, we used a tolerance of 0.1 au. To justify this choice, Figure 5 depicts the magnitude of the nonadiabatic coupling vector for

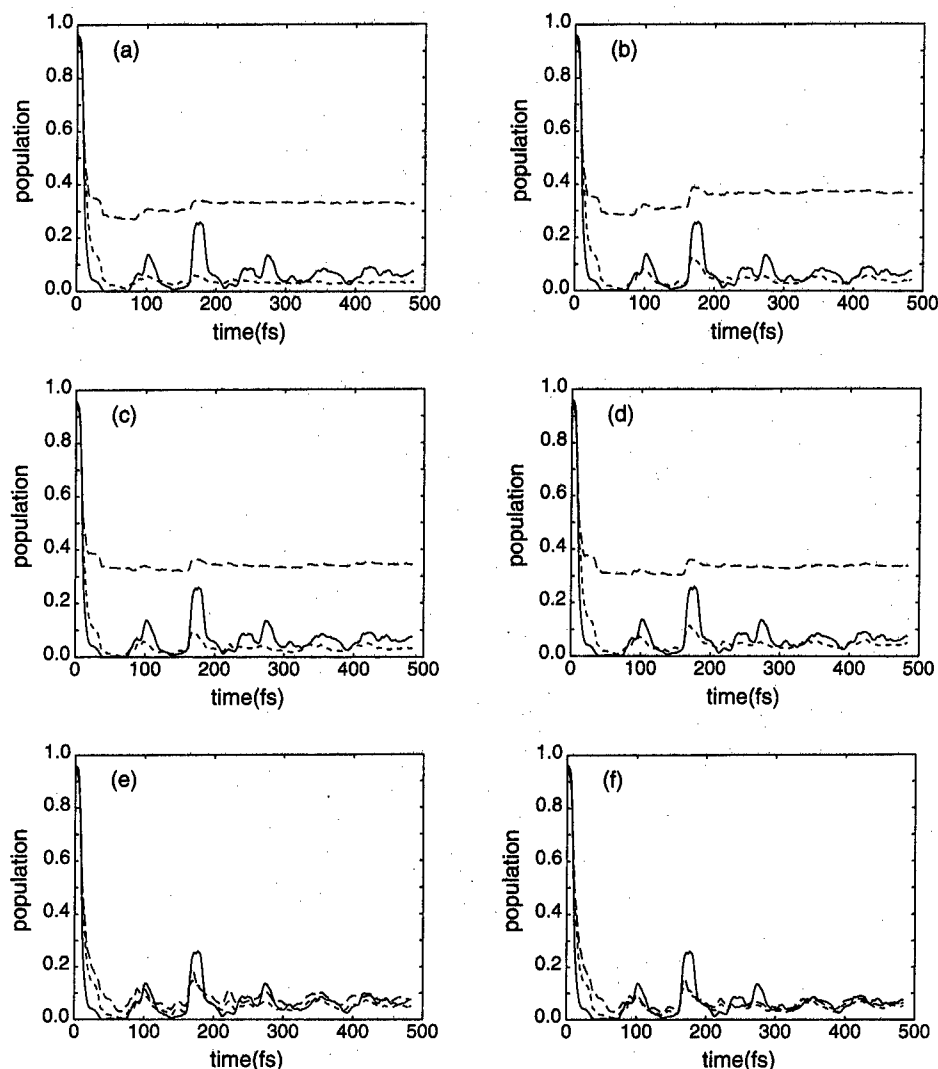


Figure 2. Time evolution of the population (i.e., the occupation probability) of the upper adiabatic state for fully quantum and surface hopping calculations. The fully quantum results depict $\int dx |\psi_2^{\text{ad}}(\mathbf{x}, t)|^2$ (solid line), and the surface hopping results depict both the average quantum probability $\langle |C_2(t)|^2 \rangle$ (long dashed line) and the fraction of trajectories $F_2(t)$ (short dashed line). (a) Standard MDQT with the component of velocity in the direction of the nonadiabatic coupling vector reversed after classically forbidden transitions; (b) standard MDQT with no modification of the velocities after classically forbidden transitions; (c) standard MDQT* with the modified velocity defined such that \dot{x}_j (used in eq 29) is set to zero if a transition to state j would be classically forbidden and to the magnitude of the velocity that would be obtained by conserving total energy after a transition to state j otherwise; (d) standard MDQT* with the modified velocity defined such that \dot{x}_j (used in eq 29) is set to zero if a transition to state j would be classically forbidden and to \dot{x} otherwise; (e) MDQT method of Figure 2b with quantum amplitudes reset so that the quantum probability of the occupied state is unity when $|\mathbf{d}_{12}| < 0.1$ au; (f) MDQT* method of Figure 2d with quantum amplitudes reset so that the quantum probability of the occupied state is unity when $|\mathbf{d}_{12}| < 0.1$ au.

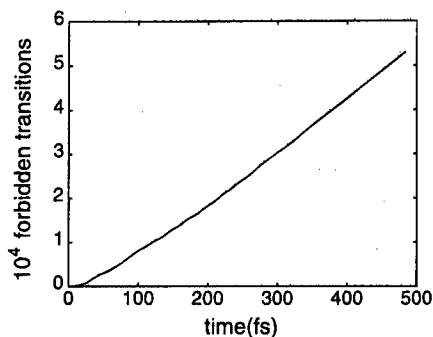


Figure 3. Time evolution of the total number of classically forbidden transitions for the 5000 MDQT trajectories corresponding to Figure 2b.

three representative trajectories. Note that the tolerance was chosen to be close to the minimum value of $|\mathbf{d}_{12}|$ for these representative trajectories. Figure 2, e and f, depicts the results of the MDQT and MDQT* methods (corresponding to Figure

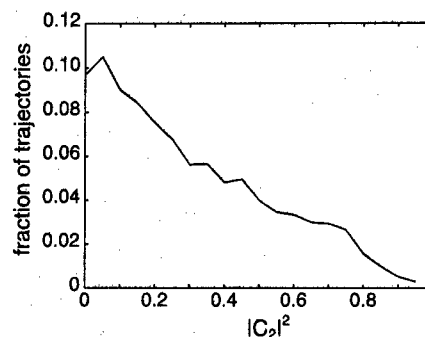


Figure 4. A normalized distribution of the quantum probabilities at time $t = 67.7$ fs for the MDQT* results shown in Figure 2d.

2, b and d) with the coherence removed using this method. In this case, the quantum probability agrees extremely well with the fraction of trajectories. We emphasize that the resetting of the quantum amplitudes enforces the internal consistency by construction. As shown in Figure 2, however, this resetting of

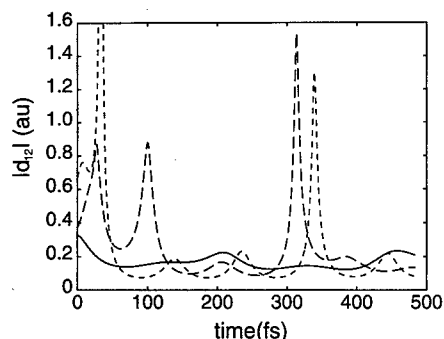


Figure 5. Time evolution of the magnitude of the nonadiabatic coupling vector $|d_{12}|$ for three representative MDQT* trajectories corresponding to Figure 2d. The solid curve corresponds to a trajectory that started on the lower adiabatic state, and the dashed curves correspond to trajectories that started on the upper adiabatic state.

the quantum amplitudes not only improves the internal consistency but also slightly improves the agreement between the surface hopping and the exact quantum results for the adiabatic populations.

These results indicate that the internal inconsistency is due mainly to the breakdown of the fewest switches algorithm resulting from diverging trajectories. On the other hand, a comparison of Figure 2, e and f, indicates that the internal consistency is better for MDQT* than for MDQT. Specifically, the value of the difference between the quantum probability and the fraction of trajectories averaged over times greater than 100 fs is 0.011 for MDQT* (Figure 2f) and 0.024 for MDQT (Figure 2e). Thus, the elimination of classically forbidden switches is also a significant aspect of maintaining internal consistency.

V. Conclusions

In this paper we identified two reasons for discrepancies between the fraction of trajectories in each state and the corresponding average quantum probability in MDQT calculations. One reason for this discrepancy is the existence of classically forbidden transitions. Another reason for this discrepancy is that divergence of the independent trajectories may lead to a breakdown of the basic assumption of the fewest switches algorithm. We presented modifications of MDQT to improve the internal consistency. In these methods the classically forbidden switches are eliminated by using modified velocities for the integration of the quantum amplitudes, and the difficulties due to divergent trajectories are alleviated by removing the coherence of the quantum amplitudes when each trajectory leaves the nonadiabatic coupling region. We compared the standard and modified MDQT methods to fully quantum calculations for a classic model for ultrafast electronic relaxation (i.e., a two-state three-mode model of the conically intersecting S_1 and S_2 excited states of pyrazine). For this model, the standard MDQT calculations exhibited significant discrepancies between the fraction of trajectories in each state and the corresponding average quantum probability. Our results indicate that for this model the divergence of independent trajectories is mainly responsible for this large internal inconsistency, although the classically forbidden transitions also cause minor discrepancies. The modified MDQT method improving both aspects resulted in remarkable internal consistency for this model system. Thus, this modified MDQT method should be useful for future surface hopping calculations on similar systems that are vibronically coupled through a conical intersection.

Surface hopping methods such as MDQT are appealing due to their conceptual simplicity and computational speed. Com-

parisons of MDQT to fully quantum calculations for simple one-dimensional model systems illustrate the potential accuracy of these methods.^{14,24,25} On the other hand, surface hopping methods have been shown to be inaccurate for certain types of systems.^{27–29} For example, surface hopping methods are problematic for processes involving an extended nonadiabatic coupling region or a large number of successive recrossings of a nonadiabatic coupling region.^{29,31} Moreover, surface hopping methods are not appropriate when tunneling of the classical degrees of freedom is important (i.e., for processes involving classically treated reacting H atoms). To determine when surface hopping methods are accurate, these methods should be compared to fully quantum results for a wide range of different types of models. Future work will center on testing the modified MDQT method presented in this paper for other model systems to determine the extent of its applicability.

Acknowledgment. We gratefully acknowledge useful discussions with John Tully about surface hopping methods and with Gerhard Stock about the model system studied in this paper. In addition, we acknowledge financial support from the AFOSR Grant No. F49620-98-1-0209 and the NSF Grant No. CHE-9623813. S.H.S. is a recipient of an Alfred P. Sloan Foundation Research Fellowship and a Camille Dreyfus Teacher Scholar Award.

References and Notes

- (1) Tully, J. C.; Preston, R. K. *J. Chem. Phys.* **1971**, *55*, 562.
- (2) Miller, W. H.; George, T. F. *J. Chem. Phys.* **1972**, *56*, 5637.
- (3) Stine, J. R.; Muckerman, J. T. *J. Chem. Phys.* **1976**, *65*, 3975.
- (4) Blais, N. C.; Truhlar, D. G. *J. Chem. Phys.* **1983**, *79*, 1334.
- (5) Dunne, L. J.; Murrell, J. N.; Stamper, J. G. *Chem. Phys. Lett.* **1984**, *112*, 497.
- (6) Parlant, G.; Gislason, E. A. *J. Chem. Phys.* **1989**, *91*, 4416.
- (7) Parlant, G.; Alexander, M. H. *J. Chem. Phys.* **1990**, *92*, 2287.
- (8) Kuntz, P. J. *J. Chem. Phys.* **1991**, *95*, 141.
- (9) Kuntz, P. J.; Hogreve, J. J. *J. Chem. Phys.* **1991**, *95*, 156.
- (10) Herman, M. F. *J. Chem. Phys.* **1984**, *81*, 754.
- (11) Herman, M. F. *J. Chem. Phys.* **1984**, *81*, 764.
- (12) Herman, M. F.; Arce, J. C. *Chem. Phys.* **1994**, *183*, 335.
- (13) Arce, J. C.; Herman, M. F. *J. Chem. Phys.* **1994**, *101*, 7520.
- (14) Tully, J. C. *J. Chem. Phys.* **1990**, *93*, 1061.
- (15) Hammes-Schiffer, S.; Tully, J. C. *J. Chem. Phys.* **1994**, *101*, 4657.
- (16) Webster, F. J.; Schnitker, J.; Friedrichs, M. S.; Friesner, R.; Rossky, P. *Phys. Rev. Lett.* **1991**, *66*, 3172.
- (17) Webster, F.; Rossky, P. J.; Friesner, R. A. *Comput. Phys. Commun.* **1991**, *63*, 494.
- (18) Webster, F.; Wang, E. T.; Rossky, P. J.; Friesner, R. A. *J. Chem. Phys.* **1994**, *100*, 4835.
- (19) Space, B.; Coker, D. F. *J. Chem. Phys.* **1991**, *94*, 1976.
- (20) Space, B.; Coker, D. F. *J. Chem. Phys.* **1992**, *96*, 652.
- (21) Coker, D. F.; Xiao, L. *J. Chem. Phys.* **1995**, *102*, 496.
- (22) Coker, D. F. In *Computer Simulation in Chemical Physics*; Allen, M. P.; Tildesley, D. J., Eds.; Kluwer Academic: Dordrecht, 1993; p 315.
- (23) Prezhdov, O. V.; Rossky, P. J. *J. Chem. Phys.* **1997**, *107*, 825.
- (24) Morelli, J.; Hammes-Schiffer, S. *Chem. Phys. Lett.* **1997**, *269*, 161.
- (25) Fang, J.-Y.; Hammes-Schiffer, S. *J. Chem. Phys.* **1997**, *107*, 8933.
- (26) Hammes-Schiffer, S. *J. Phys. Chem. A* **1998**, *102*, 10443.
- (27) Topaler, M. S.; Allison, T. C.; Schwenke, D. W.; Truhlar, D. G. *J. Phys. Chem. A* **1998**, *102*, 1666.
- (28) Topaler, M. S.; Allison, T.; Schwenke, D. W.; Truhlar, D. G. *J. Chem. Phys.* **1998**, *109*, 3321.
- (29) Kohen, D.; Stillinger, F. H.; Tully, J. C. *J. Chem. Phys.* **1998**, *109*, 4713.
- (30) Sholl, D. S.; Tully, J. C. *J. Chem. Phys.* **1998**, *109*, 7702.
- (31) Tully, J. C. *Faraday Discuss.* **1998**, *110*, 407.
- (32) Neria, E.; Nitzan, A. *J. Chem. Phys.* **1993**, *99*, 1109.
- (33) Müller, U.; Stock, G. *J. Chem. Phys.* **1997**, *107*, 6230.
- (34) Schneider, R.; Domcke, W. *Chem. Phys. Lett.* **1988**, *150*, 235.
- (35) Stock, G.; Schneider, R.; Domcke, W. *J. Chem. Phys.* **1989**, *90*, 7184.
- (36) Schneider, R.; Domcke, W.; Koppel, H. *J. Chem. Phys.* **1990**, *92*, 1045.
- (37) Stock, G. *J. Chem. Phys.* **1995**, *103*, 2888.
- (38) Prasad, M. D. *Chem. Phys. Lett.* **1992**, *194*, 27.

- (39) Latha, G. S.; Prasad, M. D. *J. Chem. Phys.* **1996**, *105*, 2972.
(40) Stock, G.; Woywod, C.; Domcke, W.; Swinney, T.; Hudson, B. S. *J. Chem. Phys.* **1995**, *103*, 6851.
(41) Herman, M. F. *J. Chem. Phys.* **1995**, *103*, 8081.
(42) Martinez, T. J.; Ben-Nun, M.; Levine, R. D. *J. Phys. Chem.* **1996**, *100*, 7884.
(43) Sun, X.; Miller, W. H. *J. Chem. Phys.* **1997**, *106*, 6346.
(44) Xiong, S.; Haobin, W.; Miller, W. H. *J. Chem. Phys.* **1998**, *109*, 7064.
(45) Haobin, W.; Song, X.; Chandler, D.; Miller, W. H. *J. Chem. Phys.* **1999**, *110*, 4824.
(46) Herman, M. F. *Int. J. Quantum Chem.* **1998**, *70*, 897.
(47) Herman, M. F. *J. Chem. Phys.* **1999**, *110*, 4141.
(48) Ben-Nun, M.; Martinez, T. *J. Chem. Phys.* **1998**, *108*, 7244.
(49) Ben-Nun, M.; Martinez, T. *J. Chem. Phys.* **1999**, *110*, 4134.
(50) Fang, J.-Y.; Hammes-Schiffer, S. *J. Chem. Phys.* **1999**, *110*, 11166.
(51) Thachuk, M.; Ivanov, M. Y.; Wardlaw, D. M. *J. Chem. Phys.* **1998**, *109*, 5747.
(52) Bittner, E. R.; Rossky, P. J. *J. Chem. Phys.* **1995**, *103*, 8130.
(53) Schwartz, B. J.; Bittner, E. R.; Prezhdo, O. V.; Rossky, P. J. *J. Chem. Phys.* **1996**, *104*, 5942.
(54) Cattaneo, P.; Persico, M. *J. Phys. Chem. A* **1997**, *101*, 3454.
(55) Manthe, U.; Koppel, H. *J. Chem. Phys.* **1990**, *93*, 345.
(56) Koppel, H.; Domcke, W.; Cederbaum, L. S. *Adv. Chem. Phys.* **1984**, *57*, 59.
(57) Tully, J. C., private communication.
(58) Child, M. S. *Theory of Chemical Reaction Dynamics*; CRC Press: Boca Raton, FL, 1985; Vol. III.

Time-Domain and Tunneling Pictures of Nonadiabatic Induced Electron Ejection in Molecular Anions

Jack Simons*

Henry Eyring Center for Theoretical Chemistry, Chemistry Department, University of Utah, Salt Lake City, Utah 84112

Received: June 1, 1999; In Final Form: July 15, 1999

Molecular anions possessing excess internal vibrational and/or rotational energy can eject their “extra” electron through radiationless transitions involving non-Born–Oppenheimer coupling. In such processes, there is an interplay between the nuclear and electronic motions that allows energy to be transferred from the former to the latter and that permits momentum and/or angular momentum to also be transferred in a manner that preserves total energy, momentum, and angular momentum. There are well established quantum mechanical expressions for the rates of this kind of radiationless process, and these expressions have been used successfully to compute electron ejection rates. In this paper, we recast the state-to-state quantum rate equation into the time domain and into a form in which the departing electron tunnels through a radial potential. The time domain expressions are especially useful for polyatomic systems where the multidimensional time correlation function decays to zero on a very short time scale. The tunneling framework is more appropriate when the perturbative assumptions, upon which the time-domain expressions are based, are questionable.

I. Introduction

A. Relation to Experiments. Numerous spectroscopy experiments have been carried out over a number of years in the Lineberger,¹ Brauman,² and Beauchamp³ laboratories in which electronically stable negative molecular ions prepared in excited vibrational–rotational states have been observed to eject their “extra” electron. For the anions considered in those experiments, it is unlikely that the anion and neutral molecule potential energy surfaces undergo crossings at geometries accessed by their vibrational motions. It is therefore believed that the mechanism of electron ejection must involve vibration–rotation to electronic energy transfer in which couplings between nuclear motions and electronic motions known as non-Born–Oppenheimer (BO) couplings cause the electron ejection rather than curve crossings in which the anion’s energy surface intersects that of the neutral at some geometries.

In earlier works, we⁴ and others⁵ have formulated (within a first-order Fermi “golden rule” perturbative framework)⁶ and computed non-BO coupling strengths for several of the anion systems that have been studied experimentally including the following.

(1) Dipole-bound anions^{4f,5a,b} in which the extra electron is attracted primarily by the dipole force field of the polar molecule and for which rotation-to-electronic coupling is most important in inducing electron ejection.

(2) NH^- ($\text{X}^2\Pi$) for which^{4d} vibration of the N–H bond couples only weakly to the nonbonding $2p_\pi$ orbital and for which rotation-to-electronic coupling can be dominant in causing electron ejection for high rotational levels.

(3) Enolate anions^{4c} that have been “heated” by infrared multiple photon absorption for which torsional motion about the $\text{H}_2\text{C}-\text{C}$ bond, which destabilizes the π orbital containing the extra electron, is the mode contributing most to vibration-to-electronic energy transfer and thus to ejection.

Our calculations have been successful in interpreting trends that are seen in the experimentally observed rates of electron ejection. However, in our opinion, there is a need to extend the theoretical framework in two directions. First, the time-independent state-to-state golden rule expressions used to date are too cumbersome for use in highly excited polyatomic anions (containing N atoms); it is simply not feasible to compute the $3N-6$ -dimensional vibrational wave functions at high internal energies. Second, a tool that does not rely on the perturbative treatment upon which the golden rule expressions are based is needed; this is essential whenever the non-BO couplings are not weak enough to be viewed as weak perturbations.

It is the purpose of this paper to effect such extensions in the theoretical frameworks by recasting the rate equations both (a) in the time domain rather than state-to-state expressions and (b) using a radial electron tunneling framework⁵ that does not require perturbative assumptions.

B. Review of State-to-State Quantum Rate Expression. Within the Born–Oppenheimer approximation, the electronic Schrödinger equation

$$h_e(r|Q) \psi_k(r|Q) = E_k(Q) \psi_k(r|Q) \quad (1)$$

is solved to obtain electronic wave functions $\psi_k(r|Q)$, which are functions of the molecule’s electronic coordinates (collectively denoted r) and atomic coordinates (denoted Q), and the corresponding electronic energies $E_k(Q)$, which are functions of the Q coordinates. The electronic Hamiltonian

$$h_e(r|Q) = \sum_i \left\{ -\hbar^2/2m_e \nabla_i^2 + \frac{1}{2} \sum_{j \neq i} e^2/r_{ij} - \sum_a Z_a e^2/r_{ia} \right\} + \frac{1}{2} \sum_{a \neq b} Z_a Z_b e^2/R_{a,b} \quad (2)$$

contains, respectively, the sum of the kinetic energies of the electrons, the electron–electron repulsion, the electron–nuclear Coulomb attraction, and the nuclear–nuclear repulsion energy.

The rate R (sec^{-1}) of transition from a Born–Oppenheimer initial state $\Psi_i = \psi_i \chi_i$ (ψ_i is the anion electronic function and χ_i is the anion vibration/rotation function) to a final state $\Psi_f = \psi_f \chi_f$ (ψ_f and χ_f are the neutral plus ejected electron electronic and vibration/rotation functions) is given, via first-order perturbation theory,^{4,6} as

$$R = (2\pi/\hbar) \int |\langle \chi_i | \langle \psi_i | P | \psi_f \rangle \langle P/\mu | \chi_f \rangle|^2 \delta(\epsilon_f + E - \epsilon_i) \rho(E) dE \quad (3)$$

Here, $\epsilon_{i,f}$ are the vibration–rotation energies of the initial (anion) and final (neutral) vibration–rotation states (χ_i and χ_f , respectively), and E is the kinetic energy carried away by the ejected electron (e.g., the initial state corresponds to an anion and the final state to a neutral molecule plus an ejected electron). The density ρ of translational energy states of the ejected electron is related to the kinetic energy by $\rho(E) = 4\pi m_e L^3 (2m_e E)^{1/2} / \hbar$. Here and elsewhere, we use the short-hand notation $P\psi P\chi/\mu$ to symbolize the action of the multidimensional derivative operators arising in the non-BO couplings:

$$(P\psi_f)(P/\mu\chi_f) = \sum_a (-i\hbar \partial\psi_f/\partial R_a)(-i\hbar \partial\chi_f/\partial R_a)/m_a \quad (4)$$

where R_a runs over the Cartesian coordinates (X_a, Y_a, Z_a) of the a th atom whose mass is m_a .

It should be noted that the energy conserving $\delta(\epsilon_f + E - \epsilon_i)$ appearing in eq 3 does *not* imply a crossing between the anion and neutral energy surfaces $E_i(Q)$ and $E_f(Q)$, respectively. For all of the anions discussed in this paper, the anion's electronic energy $E_i(Q)$ lies below the neutral's electronic energy $E_f(Q)$ for all geometries Q accessed by vibrational/rotational motion of the anion. However, because the anion has "excess" vibrational and/or rotational energy, its *total* energy ϵ_i exceeds the total energy ϵ_f of the (vibrationally/rotationally) colder neutral. As a result, the *total* energy conservation condition $\delta(\epsilon_f + E - \epsilon_i)$ can be fulfilled when the ejected electron carries away the excess energy E as its asymptotic kinetic energy.

C. The Electronic Non-BO Matrix Elements. The integrals over the anion and neutral plus free electron electronic states

$$m_{i,f} = \langle \psi_f | P | \psi_i \rangle \quad (5)$$

are known to be large in magnitude only under the following special circumstances.

(1) The orbital of the anion from which an electron is ejected to form the state ψ_f of the neutral (usually the anion's highest occupied molecular orbital (HOMO)) must be *strongly modulated* or affected by movement of the molecule in one or more directions (Q). That is, $\partial\psi_i/\partial Q$, which appears in $P\psi_i$, must be significant or the above integral will be small.

(2) The state-to-state energy gap, $\epsilon_i - \epsilon_f$, which is equal to the kinetic energy E of the ejected electron, must not be too large; otherwise, the spatial oscillations in the ejected electron's wave function ψ_f will be so rapid as to render overlap with $\partial\psi_i/\partial Q$ negligible, again making the above integral small.

Moreover, symmetry can cause $m_{i,f} = \langle \psi_f | P | \psi_i \rangle$ to vanish if the direct product of the symmetry of ψ_i and of $\partial\psi_i/\partial Q$ do not match that of ψ_f . Viewed another way, the direct product of the HOMO's symmetry and the symmetry of the vibration or rotation coordinate (Q) from which energy is transferred determines the symmetry of the ejected electron's continuum orbital which, in turn, determines the angular distribution of the ejected electron.

The derivatives (i.e., the dynamic responses) of the anion's orbitals to nuclear motions $\partial\psi_i/\partial Q$ arise from two sources.

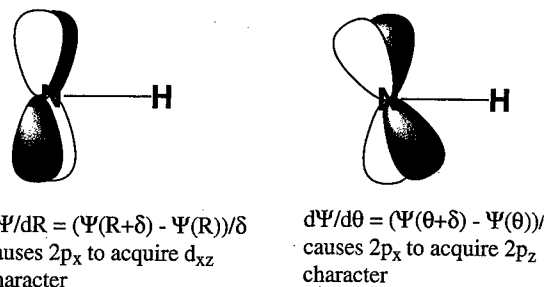


Figure 1. Orbital response of NH^- 's $2p_x$ orbital to (a) vibration of the N–H bond (left) and (b) rotation of the N–H bond (right).

(1) An orbital's LCAO–MO coefficients depend on the positions of the atoms (or, equivalently, on the anion's bond lengths and internal angles). For example, the π^* orbital of an olefin anion that contains the "extra" electron is affected by stretching or twisting the C–C bond involving this orbital because the LCAO–MO coefficients depend on the bond length and twist angle. As the bond stretches or twists, the π^* orbital's LCAO–MO coefficients vary, as a result of which the orbital's energy, radial extent, and other properties also vary.

(2) The atomic orbitals (AOs, which are denoted χ_μ) themselves dynamically respond to the motions of the atomic centers. These dynamical responses occur in $\partial\psi/\partial Q$ as $\partial\chi_\mu/\partial Q$, which can be evaluated using the same analytical derivative methods that have made computation of potential energy gradients and Hessians powerful tools in quantum chemistry. For example, vibration of the $\text{X}^2\Pi$ NH^- anion's N–H bond induces d_x character into the $2p_x$ orbital containing the extra electron as shown in Figure 1, because the radial derivative of a p_x orbital, $\partial p_x/\partial R$, produces a function of d_{xz} symmetry. Alternatively, rotation of this anion's N–H bond axis causes the $2p_x$ HOMO to acquire some $2p_z$ character because $\partial p_x/\partial \theta$ contains terms of p_z character (see Figure 1 for a pictorial explanation).

Further insight into how the LCAO–MO coefficients vary with geometry can be achieved by way of the Hellmann–Feynman theorem in the form

$$\langle \psi_f | -i\hbar \partial h_e / \partial Q | \psi_i \rangle / (E_i - E_f - E) = \langle \psi_f | -i\hbar \partial / \partial Q | \psi_i \rangle = \langle \psi_f | P | \psi_i \rangle = m_{i,f} \quad (6)$$

One sees that the electronic non-BO matrix elements will be enhanced at geometries where the anion and neutral potential surfaces approach closely. Note that this requirement (of small $E_i - E_f$) meaning that the energy surfaces are close says nothing about the anion-to-neutral state-to-state energy gap $\epsilon_i - \epsilon_f$, which determines the kinetic energy E carried away by the electron. Enhancement is also effected when the initial and final states have a strong matrix element of the "force operator" $\partial h_e / \partial Q$. The latter is effectively a *one-electron* operator involving derivatives of the electron–nuclear Coulomb attraction potential $\sum_i \sum_a Z_a e^2 / r_{i,a}$, so the matrix element $\langle \psi_f | \partial h_e / \partial Q | \psi_i \rangle$ can be visualized as $\langle \phi_f | \partial h_e / \partial Q | \phi_i \rangle$, where ϕ_i is the anion's HOMO and ϕ_f is the continuum orbital of the ejected electron. At geometries where the anion–neutral energy surfaces are far removed, the denominator in eq 6 will attenuate the coupling. If the state-to-state energy difference $\epsilon_i - \epsilon_f = E$ accompanying the electron ejection is large, the integral $\langle \phi_f | \partial h_e / \partial Q | \phi_i \rangle$ will be small because the continuum orbital ϕ_f will be highly oscillatory and thus will not overlap well with $(\partial h_e / \partial Q) \phi_i$.

In summary, for non-BO coupling to be significant,⁴ the anion's HOMO must be strongly modulated by a motion (vibration or rotation) of the molecule's nuclear framework and

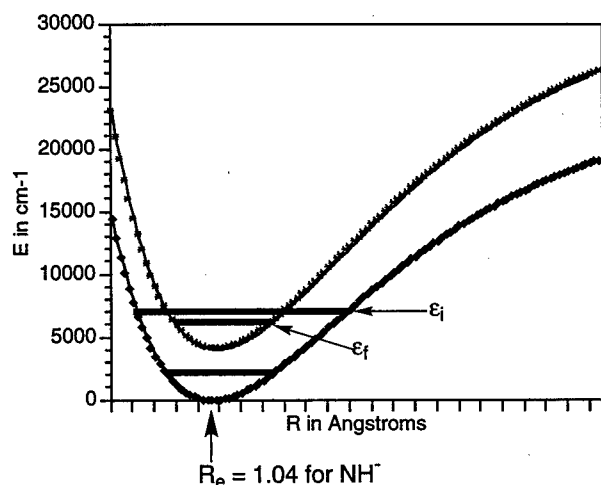


Figure 2. Anion (lower) and neutral (upper) potential energy surfaces illustrative of NH^- where the surface spacing does not vary strongly along R .

the state-to-state energy gap must not be too large as to render the HOMO-to-continuum orbital overlap insignificant. For the HOMO to be strongly modulated, it is helpful if the anion and neutral energy surfaces approach closely at some accessible geometries.

It should be emphasized that it is necessary but not sufficient for $E_f(Q) - E_i(Q)$ to be small over an appreciable range of geometries; this only guarantees that the denominator in eq 6 is small. It is also necessary that $E_f(Q) - E_i(Q)$ decrease at a significant rate as the point of closest approach is reached; this is why we say the surfaces must **approach** closely. If $E_f(Q) - E_i(Q)$ were small yet unvarying over some range of geometries, then the HOMO's electron binding energy (and thus radial extent) would remain unchanged over this range of geometries. In such a case, movement along Q would not *modulate* the HOMO, and thus $\partial\psi/\partial Q$ would vanish. Let us consider a few examples to further illustrate.

D. A Few Examples. In Figure 2 are depicted anion and neutral potential curves that are qualitatively illustrative of^{1b,4d} the $\text{X}^2\Pi \text{NH}^-$ case mentioned earlier. In this anion, the HOMO is a nonbonding $2p_\pi$ orbital localized almost entirely on the N atom. As such, its LCAO-MO coefficients are not strongly affected by vibration of the N-H bond (because it is a nonbonding orbital). Moreover, the anion and neutral surfaces have nearly identical R_e and ω_e values, and similar D_e values, as a result of which these two surfaces are nearly parallel to one another over a wide range of internuclear distances and are separated by ca. 0.4 eV or more than 3000 cm^{-1} at their minima. It has been seen experimentally that excitation of NH^- to the low rotational states of the $v = 1$ vibrational level (which lies above $v = 0$ NH of the neutral and thus has enough energy to eject the electron) results in very slow (e.g., ca. 10^8 s^{-1}) electron ejection, corresponding to 1 million vibrational periods before detachment occurs. However, excitation to high rotational levels (e.g., $J = 40$) of $v = 1$ produces much more rapid electron ejection (10^9 – 10^{10} s^{-1}). These data have been interpreted as saying that vibrational coupling is weak (i.e., $\partial\psi/\partial R$ is small) because of the nonbonding nature of the $2p_\pi$ MO, while rotational coupling becomes significant (i.e., $\partial\psi/\partial\theta$ large) for high J .

In Figure 3 are shown anion and neutral potential curves, as functions of the "twist" angle of the $\text{H}_2\text{C}-\text{C}$ bond in a typical enolate anion^{2,4c} such as acetaldehyde enolate H_2CCHO^- . Angles near $\theta = 0$ correspond to geometries where the p_π orbital

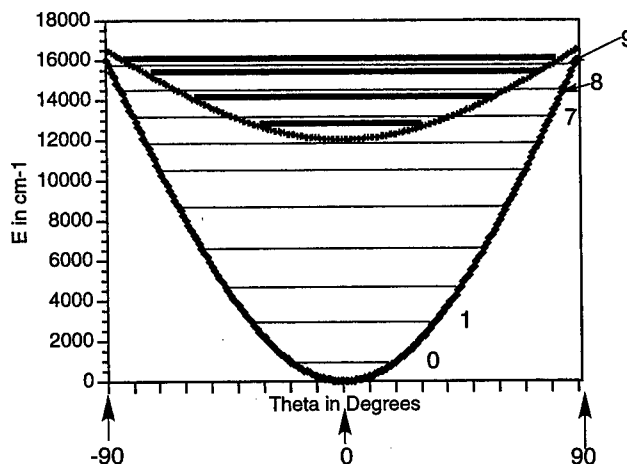


Figure 3. Anion (lower) and neutral (upper) potential energy surfaces illustrative of enolate cases where the surface spacing varies strongly along the $\text{H}_2\text{C}-\text{C}$ torsion angle θ and becomes very small near $\theta = 90^\circ$.

of the H_2C moiety is delocalized over the two p_π orbitals of the neighboring C and O atoms, thus forming a delocalized π HOMO. At angles near $\theta = 90^\circ$, the p_π orbital of the H_2C group is no longer stabilized by delocalization, so the HOMO's energy is much higher. In this case, excitation of, for example, $v = 7$ in the $\text{H}_2\text{C}-\text{C}$ torsional mode of the anion might be expected to produce electron ejection because $v = 7$ of the anion lies above $v = 0$ of the neutral. However, over the range of θ values accessible to both the $v = 7$ vibrational function of the anion and the $v = 0$ function of the neutral, the anion-neutral energy surface gap is quite large (i.e., $E_f(Q) - E_i(Q)$ is large even though $\epsilon_i - \epsilon_f$ is small). In contrast, excitation of $v = 9$ of the anion could produce more rapid electron ejection (to $v = 2$ of the neutral, but not to $v = 0$ of the neutral) because for the $v = 9 \rightarrow v = 2$ transition there are angles accessed by both $v = 9$ anion and $v = 2$ neutral vibrational functions for which $E_f(Q) - E_i(Q)$ is small and changing; moreover, the state-to-state gap $\epsilon_i - \epsilon_f$ is also small in this case.

II. Time Correlation Function Expression for Rates

1. Time Domain Expression for Electron Ejection Rates

We begin with the^{6,4g} Wentzel-Fermi "golden rule" expression given in eq 3 for the transition rate between electronic states $\psi_{i,f}$ and corresponding vibration-rotation states $\chi_{i,f}$ appropriate to the non-BO case. We recall that $\epsilon_{i,f}$ are the vibration-rotation energies of the molecule in the anion and neutral molecule states, E denotes the kinetic energy carried away by the ejected electron, and the density of translational energy states of the ejected electron is $\rho(E)$. Also recall that we use the short hand notation to symbolize the multidimensional derivative operators that embody the momentum exchange between the vibration/rotation and electronic degrees of freedom:

$$(P\psi_f)(P/\mu\chi_f) = \sum_a (-i\hbar\partial\psi_f/\partial R_a)(-i\hbar\partial\chi_f/\partial R_a)/m_a \quad (4)$$

where R_a is one of the Cartesian coordinates (X_a, Y_a, Z_a) of the a th atom whose mass is m_a .

In the event that some subset $\{Q_j\}$ of internal vibration or rotation coordinates have been identified as inducing the radiationless transition, $(P\psi_f)(P/\mu\chi_f)$ would represent $\sum_j (-i\hbar\partial\psi_f/\partial Q_j)(-i\hbar\partial\chi_f/\partial Q_j)/(\mu_j)$, where μ_j is the reduced mass associated with the coordinate Q_j . It is usually straightforward to identify which distortional modes need to be considered by noting which modes most strongly *modulate the anion's HOMO*. So, for the

remainder of this work, we will assume that such active modes have been identified as a result of which the sum $\sum_j (-i\hbar \partial \psi_i / \partial Q_j) (-i\hbar \partial \chi_f / \partial Q_j) / (\mu_j)$ will include only these modes. The integration over all of the other vibration/rotation coordinates contained in the matrix element $\langle \chi_i | \langle \psi_i | P | \psi_f \rangle \langle P | \mu | \chi_f \rangle$ can then be carried out (assuming the electronic element $\langle \psi_i | P | \psi_f \rangle$ to not depend significantly on these coordinates) to produce an effective Franck-Condon like factor (FC) for these inactive:

$$\begin{aligned} \langle \chi_i | \langle \psi_i | P | \psi_f \rangle \langle P | \mu | \chi_f \rangle &= \\ \prod_{j=\text{inactive}} \int dQ_j \langle \chi_{i,j} | \chi_{f,j} \rangle \prod_{j=\text{active}} \int dQ_j \langle \chi_{i,j} | \langle \psi_i | P | \psi_f \rangle & \\ \langle P | \mu | \chi_{f,j} \rangle &= \text{FC} \prod_{j=\text{active}} \int dQ_j \langle \chi_{i,j} | \langle \psi_i | P | \psi_f \rangle \langle P | \mu | \chi_{f,j} \rangle \quad (7) \end{aligned}$$

Since, by assumption, the anion and neutral molecule do not differ significantly in their geometries (and vibrational frequencies) along the coordinates contributing to the FC factor (otherwise, the anion-neutral energy gap would depend substantially on these modes), the FC factor is probably close to unity in magnitude. Hence, for the remainder of this paper, we will focus only on the active-mode part of this expression and will do so assuming only one such mode is operative (i.e., we treat one active mode at a time).

Recalling the definition of the electronic coupling matrix element $m_{i,f} = \langle \psi_f | P | \psi_i \rangle$, and realizing that P is a Hermitian operator, allows the non-BO rate R to be rewritten as

$$R = (2\pi/\hbar) \int \langle (P/\mu) \chi_i | m_{i,f}^* | \chi_f \rangle \langle \chi_f | m_{i,f} (P/\mu) \chi_i \rangle \delta(\epsilon_f + E - \epsilon_i) \rho(E) dE \quad (8)$$

If the Fourier integral representation of the δ function is introduced and the sum over all possible final-state vibration-rotation states $\{\chi_f\}$ is carried out, the *total* rate R_T can be expressed as

$$R_T = (2\pi/\hbar) \sum_f \int (1/2\pi\hbar) \int \exp[i t(\epsilon_f - \epsilon_i + E)/\hbar] \langle (P/\mu) \chi_i | m_{i,f}^* | \chi_f \rangle \langle \chi_f | m_{i,f} (P/\mu) \chi_i \rangle dt \rho(E) dE \quad (9)$$

Using $(\epsilon_f + E) \chi_f = \chi_f (T + V_f + E)$, $(\epsilon_i) \chi_i = |(T + V_i) \chi_i|$, and $\sum_f |\chi_f| \langle \chi_f | = 1$, gives

$$R_T = (2\pi/\hbar) \int (1/2\pi\hbar) \int \rho(E) \langle m_{i,f} (P/\mu) \exp(-it(T + V_i)/\hbar) \chi_i | \exp(-it(T + V_f)/\hbar) m_{i,f}^* (P/\mu) \chi_i \rangle dt \exp(-itE/\hbar) dE \quad (10)$$

In this form, the rate expression looks much like that given for the photon absorption rate given in many sources,⁷ but with $m_{i,f}(P/\mu)$ replacing the molecule-photon electronic transition matrix element $\mu_{i,f}$. That is, R_T is given as the *Fourier transform of the overlap of two time propagated functions* F_i and F_f .

(a) F_i is the initial vibration-rotation state χ_i upon which the non-BO perturbation $m_{i,f}(P/\mu)$ acts after which propagation on the *neutral* molecule's potential surface V_f is effected via $\exp(-it(T + V_i)/\hbar)$.

(b) F_f is the initial function χ_i propagated on the anion's surface V_i via $\exp(-it(T + V_i)/\hbar)$ (producing, of course, $\exp(-it\epsilon_i/\hbar) \chi_i$) after which the perturbation $m_{i,f}(P/\mu)$ is allowed to act. The time correlation function $\langle F_2 | F_1 \rangle$ is then Fourier transformed at energy $E = \epsilon_i - \epsilon_f$ and multiplied by the density of states $\rho(E)$ appropriate to the electron ejected with kinetic energy E .

2. Electron Ejection is Not Closely Analogous to Photon Emission. It is tempting to conclude that the process of electron

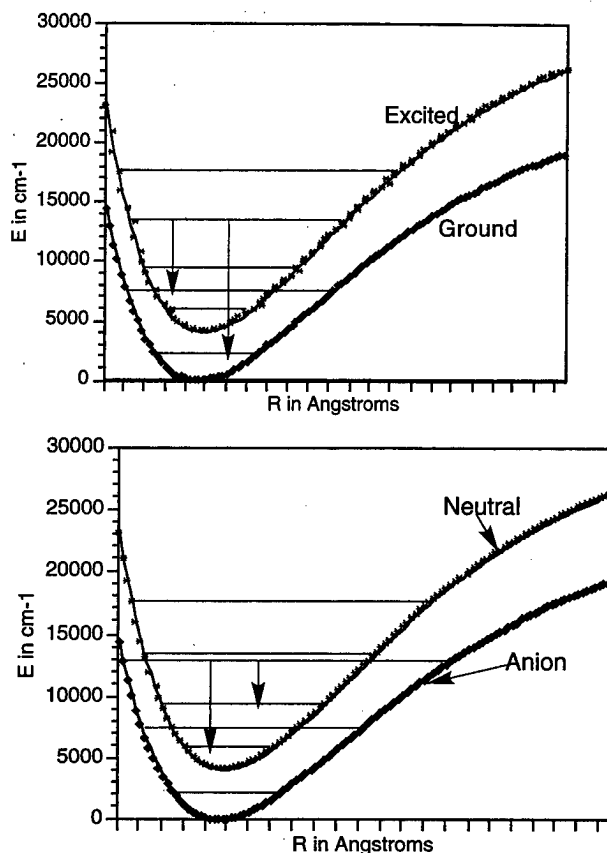


Figure 4. (a) Ground (lowest) and excited (upper) potential energy surfaces arising in the photon emission case. (b) Anion (lower) and neutral (upper) potential energy surfaces for the electron ejection case.

ejection induced by non-BO coupling can be viewed as very similar to photon emission. However, such is not at all the case, as we now illustrate (also consult Figure 4). The rate of photon emission from an excited state with energy ϵ_i to a final state with energy ϵ_f is expressed in many sources^{6,7} as

$$R = (2\pi/\hbar) |\langle \psi_i \chi_i | V | \psi_f \chi_f \rangle|^2 \delta(\epsilon_f - \epsilon_i + \hbar\omega) \quad (11)$$

Introducing the electronic dipole transition matrix element $\mu_{i,f} = \langle \psi_f | V | \psi_i \rangle$ and using identities analogous to those employed above to move from the state-to-state to the time domain, this rate expression can be reduced to

$$R_T = (2\pi/\hbar) (1/2\pi\hbar) \int \exp[-it\omega] \langle \mu_{i,f} \exp(-ith_f/\hbar) \chi_i | \exp(-ith_f/\hbar) \mu_{i,f}^* | \chi_i \rangle dt \quad (12)$$

which is the photon-emission analogue of eq 10.

If one makes the (classical) assumption that the nuclear motion kinetic energy operator T commutes with $V_{i,f}$ and with $m_{i,f}$ in the non-BO case and with $\mu_{i,f}$ in the photon case, the time integrations can be carried out and the following expressions are obtained from eqs 10 and 12:

$$R_T = (2\pi/\hbar) \int \rho(E) \langle m_{i,f} (P/\mu) \chi_i | \delta(V_f + E - V_i) m_{i,f}^* (P/\mu) \chi_i \rangle dE \quad (10a)$$

$$R_T = (2\pi/\hbar) \langle \mu_{i,f} \chi_i | \delta(V_f + \hbar\omega - V_i) \mu_{i,f}^* | \chi_i \rangle \quad (12a)$$

For anions that are electronically bound, the anion's electronic energy $V_i(Q)$ lies *below* the neutral molecule's electronic energy $V_f(Q)$ as depicted in Figures 2–4. As a result, $V_f(Q) - V_i(Q)$ is

positive at all geometries, and because E is also a positive quantity, there are no values of Q for which the argument of the δ function in eq 10a vanishes. In contrast, in the photon emission case, the final (ground) state surface $V_f(Q)$ lies below the initial (excited) state surface $V_i(Q)$, so $V_f - V_i$ is a negative quantity. Therefore, values of (the positive) $\hbar\omega$ can be found for which the argument of the δ function in eq 12a vanishes.

The fact that the simplest (purely classical) picture of the electron ejection and photon emission events produce entirely different results (the former predicts a vanishing rate, the latter does not) indicates that these two processes are not analogous. The essential difference lies in how the total electronic energy changes in the two events.

(a) In photon emission, a positive energy photon is ejected, and the system moves from a state of higher electronic energy to a state of lower electronic energy. The vibration/rotation energy is altered only in a secondary way (i.e., because the forces experienced on the nuclei changes once the electronic state changes).

(b) In the electron ejection case, a positive energy electron is ejected, but the system moves from a state of lower electronic energy (the anion) to a state of higher electronic energy (the neutral). The vibration/rotation energy plays an *essential* role because its depletion provides the energy (and momentum) that allows the electronic energy to increase.

3. When is the Time-Domain Expression Useful? The rate expressions given in eqs 3 and 10 are formally identical. However, the practical implementation of eq 10 will be favorable when one is treating polyatomic molecules and, especially, if one can identify specific geometries (Q^*) near which the electronic non-BO matrix elements $m_{i,f}$ are most strongly focused. Examples of two such situations are shown in Figure 5. In these cases, the initial ($t = 0$) wave function $m_{i,f}(P/\mu)\chi_i$ to be propagated on the final (neutral) energy surface will be localized to those regions (Q^*) where $m_{i,f}$ is localized. The other time-evolved function entering into the correlation function of eq 10 is $m_{i,f}(P/\mu) \exp(-it(T + V_i)/\hbar)\chi_i$, which is equal to $\exp(-it(\epsilon_f/\hbar)m_{i,f}(P/\mu)\chi_i)$; this function is also spatially localized because $m_{i,f}$ is. As a result of this localization, the time correlation function

$$C(t) = \exp(it\epsilon_f/\hbar) \langle m_{i,f}(P/\mu)\chi_i | \exp(-it(T + V_f)/\hbar) m_{i,f}(P/\mu)\chi_i \rangle \quad (13)$$

will rapidly (i.e., on a time scale of the molecular vibrations that are most important in promoting the non-BO coupling) decay to zero. $C(t)$ will display nonzero values again at later times as the time evolving function $\exp(-it(T + V_f)/\hbar) m_{i,f}(P/\mu)\chi_i$ returns to near where it started at $t = 0$. However, especially in polyatomic anions, these recurrences will contribute little amplitude to $C(t)$ because of rapid dephasing along each of the $3N - 6$ vibrational modes.

Because of the rapid decay of $C(t)$ and because of the availability of efficient tools^{8,9} for handling short-time quantum wave function propagation even in multidimensional systems, the time-dependent prescription given in eq 10 will be favored over the state-to-state time-independent eq 3 when treating polyatomic anions. However, both eqs 3 and 10 are based on a perturbative treatment of the non-BO coupling and, thus, are expected to be restricted to cases where the perturbation is weak as reflected in the fact that the rate of electron ejection is orders of magnitude slower than rates of vibrations or rotations. For the examples discussed earlier (e.g., NH^- , enolates, etc.), it was indeed the case that electron ejection rates were much slower

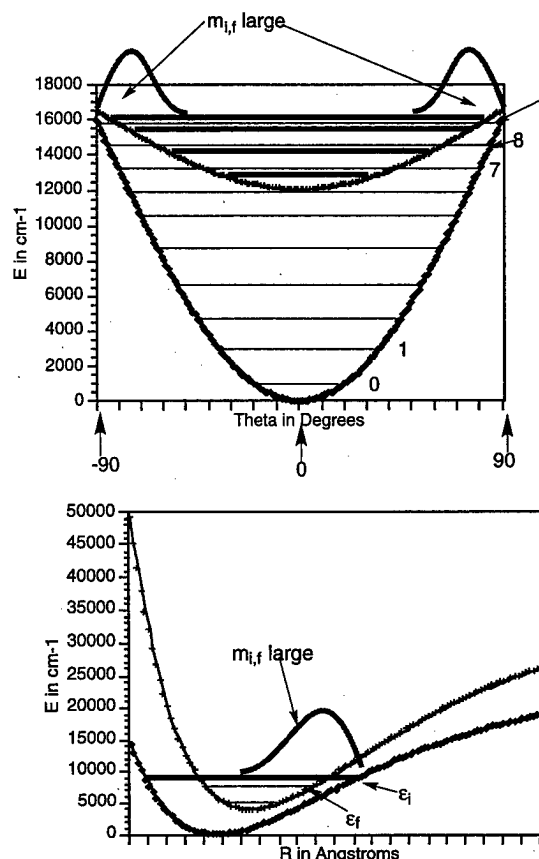


Figure 5. Two illustrations of how the electronic non-BO matrix element $m_{i,f}$ tends to be largest at geometries where the anion and neutral surfaces approach closely.

than even rotations, so the golden rule perturbative approach could be used.

However, there are species for which the electron is so weakly bound (and thus the separation in time scales between rotation/vibration motion and electronic motions is not large) that a perturbative approach likely will not work. We now turn our attention to a framework that allows such extreme cases to be more adequately addressed.

III. Tunneling View of Electron Ejection

When considering anions with very weakly bound (e.g., $1-100 \text{ cm}^{-1}$) electrons, it may be more appropriate to reverse the conventional assumption of fast moving electrons and slow moving nuclei as postulated in the BO approximation. In particular, in such systems, it is useful to introduce potential energy surfaces that describe the interaction of an electron (at a fixed location r, θ, ϕ) with a neutral molecule whose geometry is averaged over its vibrational motion. Let us proceed to explore this role-reversed point of view.

The following Hamiltonian is used⁵ to describe the neutral molecule (whose vibrational and orientational coordinates are collectively denoted Q) and the "extra" electron (whose spatial coordinates are r, θ, ϕ) and the interaction potential V between the electron and the neutral:

$$H = h(Q) + L^2(\theta, \phi)r^{-2}/2m_e + V(r, Q) - \hbar r^{-2} \nabla^2 \quad (14)$$

The electronic (n), vibrational (v), and rotational¹⁰ (J, M) eigenstates $\{\psi_{n,v,J,M}\}$ of the neutral are solutions of the Schrö-

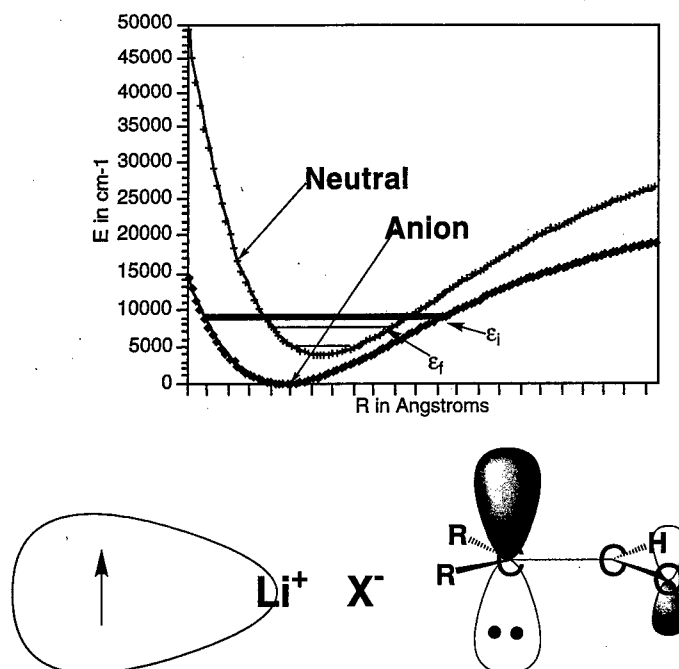


Figure 6. Anion and neutral energy curves (top) representative of the alkali halide species together with a depiction of the anion HOMO of such LiX species (bottom left) and of the anion HOMO of an enolate (bottom right).

dinger equation for which $h(Q)$ is the Hamiltonian

$$h(Q)\psi_{n,v,J,M} = E_{n,v,J,M}\psi_{n,v,J,M} \quad (15)$$

and the $E_{n,v,J,M}$ are the electronic/vibrational/rotational energy levels of the neutral molecule.

To generate a series of "diabatic" energy surfaces that describe the potential energy of interaction of the extra electron with the neutral molecule *averaged* over the internal (electronic, vibrational, and rotational) motions of the neutral, we evaluate the diagonal elements of the Hamiltonian that contains all terms in eq 14 except the radial motion of the extra electron $H' = h(Q) + L^2(\theta, \phi)/2m_e r^2 + V(r, Q)$ within a basis $\{\Psi_{a,l,m,n,v,J,M} = Y_{l,m}(\theta_a, \phi_a)\psi_{n,v,J,M}(Q)\}$ consisting of products of neutral molecule functions $\psi_{n,v,J,M}(Q)$ and angular functions $Y_{l,m}$ for the extra electron (relative to each atomic center a in the molecule).

In this product basis, the *diagonal elements* of the Hamiltonian H' are labeled by the quantum numbers of the neutral molecule (n, v, J, M) as well as by the atomic center (a) and electronic angular momentum quantum numbers l and m and are given by

$$H_{n,v,J,M,a,l,m} = E_{n,v,J,M} + \hbar^2 l(l+1)/2m_e r_a^2 + \int |Y_{l,m}(\theta_a, \phi_a)|^2 |\psi_{n,v,J,M}(Q)|^2 V(r_a, \theta_a, \phi_a, Q) dQ \sin \theta_a d\theta_a d\phi_a \quad (16)$$

For notational simplicity in describing how these diagonal elements and the off diagonal elements discussed below couple to generate diabatic energy surfaces, we use a single index (v) to represent the neutral molecule quantum numbers (n, v, J, M). Each neutral molecule level with product wave function $\Psi_{v,a,l,m}$ is coupled through $V(Q, r)$ to other levels $\Psi_{v',a',l',m'}$ as reflected in the off-diagonal elements of this same Hamiltonian:

$$H_{v,a,l,m,v',a',l',m'} = \int \Psi_{v,a,l,m}^* V(Q, r, \theta, \phi) \Psi_{v',a',l',m'} dQ \sin \theta d\theta d\phi \quad (17)$$

Both the diagonal and off-diagonal matrix elements remain

functions of r , the radial distance of the extra electron from the neutral molecule.

The nature and strength of the coupling elements $H_{v,l,m,v',a',l',m'}$ is governed by how V depends on (a) the angular location of the extra electron θ_a, ϕ_a relative to the atomic centers a , (b) the distance of the extra electron r_a from these centers, and (c) the variation of V along the $3N - 6$ internal vibrational modes of the neutral. The latter dependence is often represented in terms of a series expansion of V about some reference geometry (Q^0) (usually some equilibrium geometry):

$$V(Q, r) = V(Q^0, r) + \sum_{k=1, 3N-6} (\partial V / \partial Q_k)(r)(Q_k - Q_k^0) + \sum_{k,m} (\partial^2 V / \partial Q_k \partial Q_m)(r)(Q_k - Q_k^0)(Q_m - Q_m^0) + \dots \quad (18)$$

The characteristics of V described above in (a) and (b) allow V to couple basis states belonging to the *same* neutral molecule level (n, v, J, M) but having different atomic centers a and different angular dependence l, m to produce what we will call *diabatic* states (for reasons made clear later). Let us consider an example to illustrate such couplings. In Figure 6 are shown the conventional Born–Oppenheimer energy surfaces for a typical alkali halide (LiX) and its anion in which the extra electron is bound to the positive end of the polar LiX molecule in an orbital consisting primarily of s and p_σ atomic orbitals on the Li center. This bound orbital results from the coupling of $l = 0, m = 0$ and $l = 1, m = 0$ basis orbitals located primarily on the Li atom. Also shown in Figure 6 is the anion orbital of a typical enolate. This orbital results from coupling $l = 1$ orbitals (having $m = 0$ with the z -axis directed perpendicular to the molecular plane) on the left C, middle C, and O centers. In terms of the diabatic states discussed above, these orbitals are solutions $F(r)$ to a radial Schrödinger equation

$$-\hbar^2/2m_e r^2 \{ \partial / \partial r (r^2 \partial / \partial r) F \} + E_{\text{diabatic}}(r)F = \epsilon F \quad (19)$$

where $E_{\text{diabatic}}(r)$ is the attractive diabatic potential obtained by coupling basis states having identical n, v, J, M quantum numbers but different a, l, m values, and ϵ is the orbital energy of the HOMO orbital(s) shown in Figure 6.

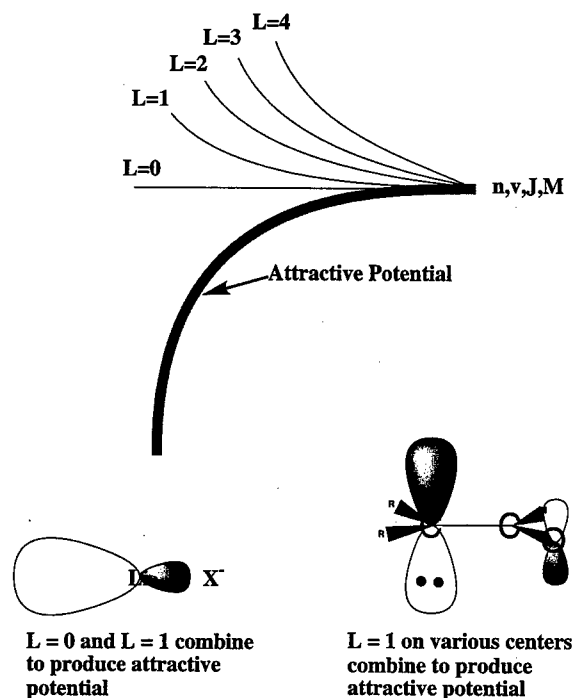


Figure 7. Family of one attractive and many repulsive curves generated for each n, v, J, M neutral molecule level by coupling various a, l, m values. Couplings that arise in alkali halide (bottom left) and enolate (bottom right) cases.

Because it is rare for a neutral molecule to support more than one bound anion state (i.e., to have more than one bound virtual orbital), the effects discussed in (a) and (b) most commonly will couple basis states having common n, v, J, M quantum numbers to produce only one attractive diabatic potential plus a family of repulsive potentials. Each of the repulsive surfaces can be labeled by an l quantum number because, at large electron-molecule distances, these surfaces vary with r as $l(l+1)\hbar^2/2m_e r^2$. This situation is illustrated in Figure 7 where the single attractive and many repulsive surfaces are shown for one n, v, J, M level.

The above discussion covered how $V(Q, r)$ couples basis states with different a, l, m but with identical n, v, J, M (i.e., all states derived from a given state of the neutral molecule). However, V also couples states having different n, v, J , and M quantum numbers; in fact, it is only through such interactions that transitions among various internal states of the neutral occur and, hence, energy flows to the extra electron. It is by way of these interactions that the diabatic curves discussed in the preceding two paragraphs evolve into adiabatic curves that we detail further below.

The strength of the coupling to various internal states depends on the magnitudes of the derivatives appearing in eq 18. For example, in the LiX systems, radial vibrational motion modulates the anion's HOMO most strongly, so $\partial V/\partial R$ is the dominant term in the expansion of eq 18. In the enolate cases, twisting motion (θ) of the R_2C group is the primary source of HOMO modulation, so $\partial V/\partial \theta$ is largest. If a dominant motion can be identified as in these two examples, then one can approximate the effect of V in terms of a single contribution ($\partial V/\partial Q$) ($Q - Q^0$) to first order. Such terms can be expected to give rise to couplings between internal states of the neutral which differ (by unity, within the harmonic approximation) in their quantum numbers that label that motion (Q) which dominates $\partial V/\partial Q$. Again considering the LiX and enolate cases, states with

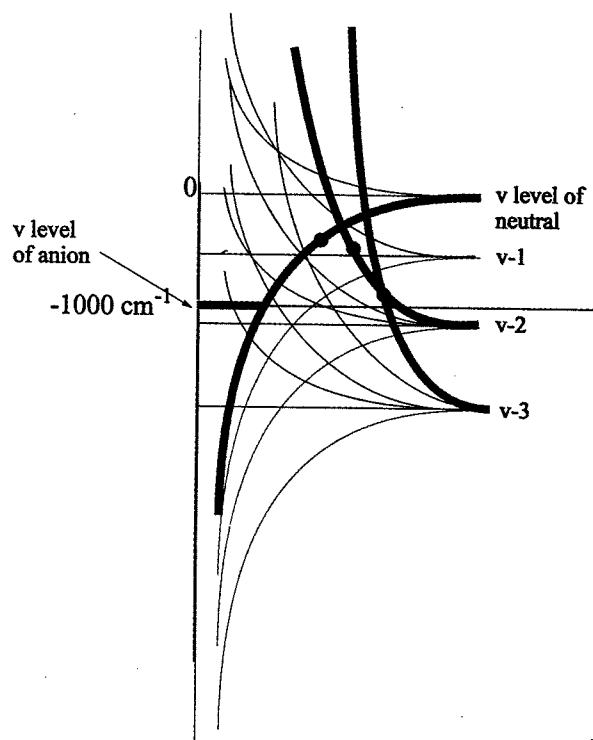


Figure 8. Families of attractive and repulsive curves arising from neutral molecule levels $v, v-1, v-2$, and $v-3$ showing the crossings of repulsive curves from lower v levels with attractive curves from higher v levels. For the anion level labeled v , the crossings indicated by dots show how the attractive diabatic curve (connecting to the neutral level v) acquires $v-1, v-2$, and $v-3$ components as r increases.

different bond stretching (LiX) or torsional (enolate) vibrational quantum numbers should experience the most important couplings.

In Figure 8, are shown the *families of diabatic curves* (one attractive and numerous repulsive for each v level of the neutral) appropriate for the LiX case where radial vibrational motion dominates. The attractive diabatic curve that connects, at large r , to the v th level of LiX undergoes crossings with various repulsive diabatic curves connecting to $v-1, v-2$, and $v-3$ of LiX. Because $(\partial V/\partial R)$ ($R - R^0$) is linear in the bond length displacement, within a harmonic treatment, (a) those crossings of diabatic curves whose v quantum numbers differ by one will be coupled and (b) those crossings whose v quantum numbers differ by 2 or more will not be coupled. As a result, the attractive curve of the v th level will interact (to undergo an *avoided crossing*) at the left-most dot in Figure 8 to acquire $v-1$ character (simultaneously causing the electronic function to acquire more $l=1$ character). At larger r , near the second dot, this evolving *adiabatic curve* will acquire $v-2$ character (and the electron will gain $l=2$ nature) and so forth until, at the last dot, the $v-3$ character is gained (as the electron gains even higher l dependence). It is through this sequence of avoided crossings that (a) the *diabatic curves generate an adiabatic curve* through which the extra electron must tunnel radially, (b) the vibrational energy decreases from v , to $v-1, v-2$, and $v-3$ while the electron gains energy (and angular momentum) as it detaches.

To determine the rate of electron ejection from the anion (diabatic) level having quantum numbers n, v, J , and M (represented by the single quantum number v in Figure 8), one must solve for the rate at which tunneling occurs on the corresponding adiabatic curve by solving the Schrödinger equation

$$-\hbar/2m_e r^2 \{ \partial/\partial r (r^2 \partial/\partial r) \} F(r) + V(r)F(r) = \epsilon^-_\nu F(r) \quad (20)$$

where $V(r)$ is the adiabatic curve (shown as the evolving red/yellow/blue/fucia curve in Figure 8). The energy ϵ^-_ν is found by solving the bound-state radial Schrödinger equation in which $V(r)$ is the corresponding attractive diabatic potential (shown in red in Figure 8).

In practice, the (red) diabatic surface can be found, using conventional quantum chemistry tools, as follows.

(1) One obtains the anion's (bound) HOMO $\psi(r, \theta, \phi)$ and its orbital energy ϵ^- as well as the neutral molecule's occupied molecular orbitals $\{\psi_i\}$ using conventional BO quantum chemistry. These orbitals are expressed as expansions (e.g., for the HOMO, $\psi(r, \theta, \phi) = \sum_{a,l,m,j} C_{a,l,m,j} Y_{l,m}(\theta, \phi) R_{a,j}(r_a)$) in terms of angular and radial basis functions centered on the various atoms (a). Of course, the LCAO-MO coefficients and the orbital energies depend on the geometry (\mathbf{Q}) at which this calculation is performed.

(2) One can next define an electron-molecule interaction potential $V(\mathbf{Q}, \mathbf{r})$ in terms of the Coulomb minus exchange potential generated by the neutral's occupied orbitals $\{\psi_i\}$ plus the Coulomb attraction potential of the underlying neutral's nuclei:

$$V(\mathbf{Q}, \mathbf{r}) = \sum_a \{ -Z_a e^2 / |\mathbf{r} - \mathbf{R}_a| \} + \sum_j \int \psi_j(\mathbf{r}')^* e^2 / |\mathbf{r} - \mathbf{r}'| (1 - P_{r,r'}) \psi_j(\mathbf{r}') d\mathbf{r}' \quad (21)$$

(3) The diabatic surface $V(r)$ appropriate to the neutral molecule in a specified internal state (n, ν, J, M) is obtained from $V(\mathbf{Q}, \mathbf{r})$ by (a) averaging over the \mathbf{Q} coordinates using the square of the neutral's vibration/rotation wave function $\psi_{n,\nu,J,M}(\mathbf{Q})$ as the weighting factor, (b) averaging over the extra electron's angular coordinates θ, ϕ using $|\psi(r, \theta, \phi)|^2$ as the weighting, and (c) adding in the electronic angular kinetic energy (i.e., the centrifugal potential) for the extra electron occupying ψ :

$$V(r) = \int |\psi(r, \theta, \phi)|^2 |\psi_{n,\nu,J,M}(\mathbf{Q})|^2 V(\mathbf{Q}, r, \theta, \phi) d\mathbf{Q} \sin \theta d\theta d\phi + 1/(2m_e r^2) \int \psi^* L^2 \psi \sin \theta d\theta d\phi \quad (22)$$

Because the HOMO $\psi(r, \theta, \phi)$ has been obtained by mixing basis functions on all centers and with various l, m values, it explicitly contains all of the couplings among basis states with fixed n, ν, J , and M but with various a, l , and m quantum numbers. It is this $V(r)$ function that the red curve in Figure 8 represents; it is the potential that the extra electron experiences as the nuclei in the molecule undergo their motions if there were no couplings between the internal (i.e., electronic, vibrational, rotational) energy of the molecule and of the extra electron.

The adiabatic curve derived from each such diabatic curve can be approximated by finding where the (red) diabatic curve (computed as detailed above) belonging to a given internal level (e.g., the level denoted ν in Figure 8) intersects the first repulsive diabatic curve connecting to the nearest lying lower level (e.g., that denoted $\nu - 1$ in Figure 8). This first repulsive curve can be approximated in terms of the asymptotic energy of the underlying ($\nu - 1$ in Figure 8) neutral level plus the extra electron's centrifugal potential corresponding to $l = 1$, $E_{\nu-1} + 1(1 + 1)\hbar/2m_e r_a^2$, and where it crosses the (red) diabatic curve can easily be determined. Likewise, the location of the second crossing (the second dot in Figure 8) can be estimated by finding where $E_{\nu-1} + 1(1 + 1)\hbar/2m_e r_a^2$ and $E_{\nu-2} + 2(2 + 1)\hbar/2m_e r_a^2$ intersect. In this manner, it is possible to "piece together" a description of the red/yellow/blue/fucia adiabatic curve by

following the red diabatic curve until the first dot, moving to the yellow curve until the second dot, then on to the blue curve until the third dot, and, finally, on to the fucia curve ($E_{\nu-3} + 3(3 + 1)\hbar/2m_e r_a^2$) from then on.

The rate of electron ejection is then obtained by computing the radial tunneling rate on the red/yellow/blue/fucia curve at an energy ϵ^-_ν obtained by solving the Schrödinger equation (eq 20) for the radial motion of the extra electron on the red diabatic curve. It is through this process that one can evaluate⁵ electron ejection rates in terms of tunneling. As stated earlier, this framework is especially useful when the extra electron is so weakly attached that it makes sense to reverse the conventional separation of electronic and nuclear motion time scales.

IV. Summary

The rate of ejection of electrons from anions induced by non-BO couplings can be expressed rigorously and quantum mechanically as a Fourier transform of an overlap function between two functions

$$R_T = (2\pi/\hbar) \int (1/2\pi\hbar) \int \rho(E) \langle m_{i,f}(P/\mu) \exp(-it(T + V_i)/\hbar) \chi_i | \exp(-it(T + V_f)/\hbar) m_{i,f}(P/\mu) \chi_i \rangle dt \exp(-itE/\hbar) dE \quad (10)$$

one of which is the anion vibration-rotation function χ_i acted on by the non-BO perturbation $m_{i,f}(P/\mu)$ and then propagated on the neutral molecule surface, the other being the initial χ_i propagated on the anion surface and then acted on by $m_{i,f}(P/\mu)$. In computer applications involving polyatomic anions, it is especially efficient to compute R_T in this manner using short-time quantum wave function propagation techniques.

For an anion having a very weakly bound extra electron, it can prove more fruitful to evaluate the rate of non-BO induced electron detachment in terms of the radial tunneling of this electron through an adiabatic potential. This approach arises when one reverses the conventional BO assumption of fast electrons and slow nuclei and introduces families of diabatic radial potentials (for each electronic, vibrational, rotational level of the daughter neutral molecule) that are coupled by the electron-molecule interaction potential to generate adiabatic radial potentials through which the electron tunnels.

Acknowledgment. This work has been supported by NSF Grant CHE-9618904 and by proceeds of the Henry Eyring Endowed Chair.

References and Notes

- (1) (a) Lykke, K. R.; Neumark, D. M.; Ansen, T.; Trapa, V. J.; Lineberger, W. C. *J. Chem. Phys.* **1987**, *87*, 6842. (b) Neumark, D. M.; Lykke, K. R.; Andersen, T.; Lineberger, W. C. *J. Chem. Phys.* **1985**, *83*, 4364. (c) Andersen, T.; Lykke, K. R.; Neumark, D. M.; Lineberger, W. C. *J. Chem. Phys.* **1987**, *86*, 1858.
- (2) (a) Marks, J.; Wentzel, D. M.; Comita, P. B.; Brauman, J. I. *J. Chem. Phys.* **1986**, *86*, 5284. (b) Meyer, F. K.; Jasinski, J. M.; Rosenfeld, R. N.; Brauman, J. I. *J. Am. Chem. Soc.* **1982**, *104*, 663. (c) Rosenfeld, R. N.; Jasinski, J. M.; Brauman, J. I. *J. Chem. Phys.* **1979**, *71*, 1030. (d) Mead, R. D.; Lykke, K. R.; Lineberger, W. C.; Marks, J.; Brauman, J. I. *J. Chem. Phys.* **1984**, *81*, 4883. (e) Jackson, R. L.; Zimmerman, A. H.; Brauman, J. I. *J. Chem. Phys.* **1979**, *71*, 2088. (f) Zimmerman, A. H.; Reed, K. J.; Brauman, J. I. *J. Am. Chem. Soc.* **1977**, *99*, 7203. (g) Zimmerman, A. H.; Brauman, J. I. *J. Chem. Phys.* **1977**, *66*, 5823.
- (3) Wight, C. A.; Beauchamp, J. L. *J. Am. Chem. Soc.* **1981**, *103*, 6501.
- (4) (a) Acharya, P. K.; Kendall, R.; Simons, J. *SASP* **1984**, *84*. (b) Acharya, P. K.; Kendall, R.; Rick, A.; Simons, J. *J. Am. Chem. Soc.* **1984**, *106*, 3402. (c) Acharya, P. K.; Kendall, R.; Simons, J. *J. Chem. Phys.* **1985**, *83*, 3888. (d) Chalasinski, G.; Kendall, R. A.; Taylor, H.; Simons, J. J.

Phys. Chem. **1988**, 92, 3086. (e) O'Neal, D., Simons, J. *J. Phys. Chem.* **1988**, 93, 58. (f) Simons, J. *J. Chem. Phys.* **1989**, 91, 6858. (g) Simons, J. *J. Am. Chem. Soc.* **1981**, 103, 3971.

(5) (a) Clary, D. L. *J. Phys. Chem.* 92, 3173 1988. (b) Clary, D. L. *Phys. Rev.* **1989**, A40, 4392.

(6) Berry, R. S. *J. Chem. Phys.* **1966**, 45, 1228. This paper discusses how a similar approach can be used to treat vibrational and rotational autoionization of Rydberg states of H_2 molecules.

(7) (a) A good textbook treatment of how time correlation functions relate to photon absorption and other rates is given in the following: McQuarrie, D. A. *Statistical Mechanics*; Harper and Row: New York, 1976.

(b) Gordon, R. G. *Adv. Magn. Reson.* **1968**, 3, 1. (c) Heller, E. J. *Acc. Chem. Res.* **1981**, 14, 368. (d) Bergsma, J. P.; Berens, P. H.; Wilson, K.

R.; Fredkin, D. R.; Heller, E. J. *J. Phys. Chem.* **1984**, 88, 612. (e) Heller, E. J.; Brown, R. C. *J. Chem. Phys.* **1983**, 79, 3336. (f) Heller, E. J. *J. Chem. Phys.* **1978**, 68, 2066. (g) Heller, E. J. *J. Chem. Phys.* **1978**, 68, 3891.

(8) See, for example: Allen, M. P.; Tildesley, D. J. *Computer Simulations of Liquids*; Oxford Science Publishers: New York, 1987; Chapter 10. *Time-Dependent Quantum Molecular Dynamics*; Broeckhove, J., Lathouwers, L., Eds.; NATO ASI Series, Series B, Vol. 299; Plenum Press: New York, 1992.

(9) Jensen, B.; Linderberg, J. Propagation Matrices from the Finite Element Method. *J. Phys. Chem.*, in press.

(10) We use the quantum numbers J and M , which are appropriate for diatomic species; for larger ions, the three quantum numbers J , M , and K should be used instead.

Short-Range Coherence in the Energy Transfer of Photosynthetic Light-Harvesting Systems

Jonaki Ray

School of Chemical Sciences, University of Illinois, 601 S. Goodwin Avenue, Urbana, Illinois 61801

Nancy Makri*

School of Chemical Sciences, University of Illinois, 601 S. Goodwin Avenue, Urbana, Illinois 61801 and
Theoretical and Physical Chemistry Institute, National Hellenic Research Foundation,
48 Vassileos Constantinou Avenue, Athens, Greece 11635

Received: May 24, 1999; In Final Form: August 24, 1999

We employ a simple model for the electronic excitations and the exciton–vibration coupling characterizing the B850 ring of the light-harvesting complex in photosynthetic bacteria to investigate the possibility of coherence in the energy transfer within the system. The structure of the equilibrium density matrix is studied using the path integral formulation of quantum statistical mechanics. The calculated mean coherence length is computed from the average root-mean-square deviation of closed imaginary time paths that are sampled via a Monte Carlo procedure. This procedure allows simultaneous examination of the effects of thermal averaging and dynamic and static disorder in a single calculation. The mean coherence length is found to be about two to three chlorophyll monomers at room temperature. The principal factor responsible for this localization is thermal averaging, although static and dynamic disorder further destabilize extended states. At low temperatures the circular arrangement of the pigments favors coherence with respect to the situation in a linear aggregate. Visual inspection of typical paths offers an intuitive picture of the extent of coherent energy delocalization in biological antenna systems.

I. Introduction

The process of energy transduction in the membranes of photosynthetic bacteria begins with the absorption of visible light by light-harvesting antennas which then funnel the energy into the reaction center.^{1–6} The light-harvesting complexes are molecular aggregates composed of several units that contain peptides, chlorophyll molecules, and carotenoids. These building blocks are organized in symmetric structures that assume the shape of a ring. The light-harvesting complex I (LH-I) immediately surrounds the reaction center, while a second type of light-harvesting complex (LH-II) channels energy to the reaction center through LH-I.

The structure and electronic arrangement of *Rps. acidophila* and *Rs. molischianum* were determined in recent experimental and theoretical studies.^{7,8} The basic unit of LH-II is a heterodimer consisting of two small protein subunits referred to as the α - and β -apoproteins. The α heterodimers bind three bacteriochlorophyll (BChl) molecules, two of which are in close contact. These dimers form a ring (see Figure 1) that absorbs around 850 nm. The third BChl of the structural unit is located about 19 Å away on an outer ring whose absorption maximum lies at 800 nm. Carotenoid molecules in proximity to the outer BChl ring harvest light in a different spectral range and also prevent photooxidation of the chlorophylls. The LH-II of the above species is composed of eight or nine such units.

This article is concerned with the energy-transfer process within the inner ring of these LH-II systems. In the absence of static disorder, the eigenstates of the 16 singly excited BChl

molecules of *Rs. molischianum* form two exciton bands. Only the degenerate second and third excited states carry oscillator strength, and thus, initial excitation at zero temperature should produce a delocalized linear combination of these. Femtosecond pump–probe experiments have monitored the subsequent energy flow and found that intraband relaxation occurs within less than 50 fs at room temperature.^{9–13} Whether the energy deposited in the ring remains delocalized under biological conditions is a matter of considerable debate. Static disorder, caused by structural inhomogeneity,^{14–18} and also exciton–vibration coupling and temperature are factors expected to favor localization. The energy-transfer process within the LH-II system has been studied by fluorescence, transient absorption, and time-resolved fluorescence anisotropy techniques.^{15,19,18,20,21} Because of the complexity of these systems, the interpretation of the measured superradiance and emission anisotropy has been elusive and the reported estimates of the coherence lengths vary from one to two subunits to a substantial portion of the ring. Some groups have reported evidence of delocalized states at all temperatures,^{22–24} while the findings of others indicate incoherent energy transfer between monomers or dimers even under cryogenic conditions.^{15,25} These apparent discrepancies have been attributed²⁶ to a strong temperature dependence of the superradiance enhancement factor not accounted for in the interpretation of these experiments. Theoretical investigations have assessed the effect of static disorder on the coherence of the exciton eigenstates in an isolated ring and found it to be small.²⁷ The effects of static and dynamic disorder on the resulting superradiance have been examined using adiabatic and polaron models.²⁸ Other recent work has employed a multilevel Redfield description to follow the dynamics of the photoexcited state in

* To whom correspondence should be addressed. Address: School of Chemical Sciences, University of Illinois, 601 S. Goodwin Avenue, Urbana, Illinois 61801.

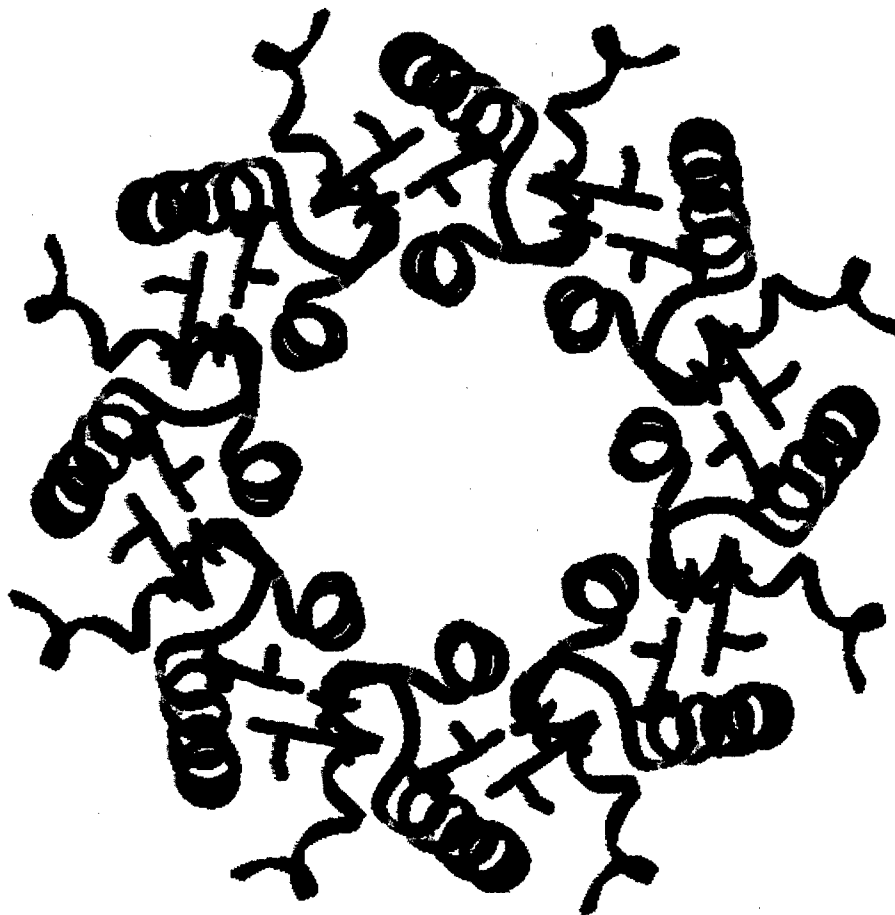


Figure 1. Top view of the B850 ring of the LH-II in *Rs. molischianum*. The 16 bacteriochlorophyll monomers are shown in red, while the α and β heterodimers are depicted in green.

the presence of coupling to vibrations modeled in terms of a dissipative bath and estimated the exciton coherence domain.^{29–31}

In the present paper we adopt the imaginary time path integral formulation of quantum statistical mechanics³² to investigate the equilibrium properties of the excited LH-II complex. The Monte Carlo path integral description of light-harvesting systems is appealing for several reasons: it can take into account the effects of ensemble averaging at a given temperature, exciton–vibration coupling, and static disorder automatically in a single calculation; in addition, it leads to simple pictures that allow easy visualization of the pertinent coherence length.

In section II we use a simple two-level-system paradigm to motivate the path integral analysis of the coherence length in LH-II. Section III describes the model and the discretized path integral representation of the quantum partition function, which we adopt. The results of our calculations are presented in section IV. That section reports the mean coherence length that we obtain as a function of temperature and dynamic disorder. Further, graphical representation of typical paths provides an intuitive picture of the coherence in the energy transfer. Finally, some concluding remarks are given in section V.

II. Theoretical Analysis

To motivate the calculation and facilitate the analysis of the results presented in the next section, it is instructive to consider the equilibrium distribution of an isolated two-level system (TLS). In the site representation the Hamiltonian reads

$$H = -\hbar\Omega(|L\rangle\langle R| + |R\rangle\langle L|) \quad (2.1)$$

where $|L\rangle$ and $|R\rangle$ are left- and right-localized states and the

tunneling splitting is $2\hbar\Omega$. Coherences are associated with the off-diagonal elements of the density matrix in the site basis. To obtain a quantitative measure for the significance of these off-diagonal elements, we examine their contribution to the canonical partition function. The latter is given by the expression

$$Z = \text{Tr} e^{-\beta H} = \langle L|e^{-\beta H}|L\rangle + \langle R|e^{-\beta H}|R\rangle = 2\langle L|e^{-\beta H}|L\rangle \quad (2.2)$$

where the last step follows from the symmetry of the Hamiltonian. By use of the path integral representation of the imaginary time propagator, this element takes the form

$$\langle L|e^{-\beta H}|L\rangle = \sum_{k_1=L,R} \dots \sum_{k_{N-1}=L,R} \langle L|e^{-\beta H/N}|\sigma_{k_1}\rangle \langle \sigma_{k_1}|e^{-\beta H/N}|\sigma_{k_2}\rangle \dots \langle \sigma_{k_{N-1}}|e^{-\beta H/N}|L\rangle \quad (2.3)$$

where $\sigma_k = L, R$ and N is the number of imaginary time steps. As is well-known, each realization $L, \sigma_{k_1}, \sigma_{k_2}, \dots, \sigma_{k_{N-1}}, L$ of localized states defines a closed path. Coherence prevails if the paths that contribute most to the partition function alternate between the two sites. On the other hand, if most statistically significant paths are localized for the most part, the equilibrium distribution is characterized by lack of coherence.

To obtain a feel for the nature of the coherent and incoherent contributions, we examine the terms that enter the path sum for $N = 2$. We choose this particular value of N because it is the smallest value that allows paths to visit both accessible sites. A straightforward calculation leads to the following result for the contributions of localized vs delocalized paths:

$$\langle L | e^{-\beta H/2} | L \rangle \langle L | e^{-\beta H/2} | L \rangle = \left\{ \frac{1}{2} e^{-\beta E_g/2} (1 + e^{-\hbar\beta\Omega}) \right\}^2 \quad (2.4a)$$

$$\langle L | e^{-\beta H/2} | R \rangle \langle R | e^{-\beta H/2} | L \rangle = \left\{ \frac{1}{2} e^{-\beta E_g/2} (1 - e^{-\hbar\beta\Omega}) \right\}^2 \quad (2.4b)$$

From these expressions it follows that localized and delocalized paths make equal contributions to the partition function at zero temperature. In the opposite limit of infinite temperature the weight of the delocalized path vanishes and the partition function is dominated by paths that remain on one site.

We define the coherence length of a path as twice the root-mean-square deviation of the path from its centroid. Restricting attention to the above two types of paths, the mean coherence length (MCL) at a given temperature becomes

$$l = w_{\text{loc}} \lambda_{\text{loc}} + w_{\text{deloc}} \lambda_{\text{deloc}} \quad (2.5)$$

where w_{loc} , w_{deloc} are the weights of the localized and delocalized paths and λ_{loc} , λ_{deloc} are the corresponding lengths. In the TLS example one finds

$$l = \frac{d}{\sqrt{1 + \gamma^2}} \quad (2.6a)$$

where d is the distance between left and right sites and

$$\gamma = \coth(\hbar\Omega\beta/2) \quad (2.6b)$$

Applying eq 2.6, one concludes that $l = 0$ at infinite temperature, while the zero temperature coherence length is found to be $l = d/\sqrt{2}$. Note that even at zero temperature the MCL is smaller than the site-to-site separation with the present definition. Other workers have adopted different measures where the MCL is defined as the inverse participation ratio or the autocorrelation function of the exciton wave function. Finally, at a temperature $\beta^{-1} = 2\hbar\Omega$ the TLS coherence length is $l \approx 0.24d$. Given that the population of the excited state is only 0.37 at this temperature, one might expect a higher degree of coherence. The reason for the short delocalization length predicted by eq 2.6 is the cyclic nature of equilibrium paths; as a consequence, the actual distance traversed by such a path is double the site-to-site distance.

III. Model and Computational Procedure

We model the photosynthetic antenna system by an n -state model in the basis of localized single excitations. This Hamiltonian is coupled diagonally to a dissipative heat bath comprising the vibrational and torsional modes of the pigments and their protein-water environment. In the absence of static or dynamic disorder the system is completely symmetric and takes the form

$$H_0 = \epsilon \sum_{i=1}^n |u_i\rangle \langle u_i| + \sum_{i \neq j} \Delta_{ij} |u_i\rangle \langle u_j| \quad (3.1)$$

where $n = 16$ for the B850 ring of LH-II in *Rs. molischianum*. Here, $|u_i\rangle$ denote single excitations of individual chlorophylls, ϵ is the corresponding excitation energy, and Δ_{ij} are the couplings that are due primarily to dipolar interactions. Symmetry implies that $\Delta_{2k+i, 2k+j} = \Delta_{ij}$. Hu et al.²⁷ have parametrized this Hamiltonian by fitting the corresponding eigenvalues to results of ZINDO electronic structure calculations.³³ The resulting parameters are given in Table 1.

A qualitative description of the effects of exciton-vibration coupling on the dynamics of energy transfer is obtained by

TABLE 1: Parameterization of Eq 3.1 As Obtained by Hu et al.^a

ϵ	13059
Δ_{12}	806
Δ_{23}	377
Δ_{13}	-152
Δ_{24}	-102

^a All Parameters are in cm^{-1}

modeling the nuclear motion of the complex in terms of a dissipative bath of effective harmonic modes whose coordinates x_j are denoted collectively by the vector \mathbf{x} . The harmonic bath picture is justified by virtue of the linear response approximation³⁴ as in the case of electron transfer.^{35,36} The total Hamiltonian takes the form

$$H = H_0 + \sum_{j=1}^n \frac{p_j^2}{2m_j} + \frac{1}{2} m_j \omega_j^2 \left(x_j - \frac{c_j}{m_j \omega_j^2} \sum_{k=1}^n \sigma_k |u_k\rangle \langle u_k| \right)^2 \quad (3.2)$$

As is well-known, only the collective characteristics of the bath, rather than the individual mode frequencies ω_j and coupling constants c_j , affect the ring dynamics with this Hamiltonian. These collective features are contained in the spectral density

$$J(\omega) = \frac{\pi}{2} \sum_j \frac{c_j^2}{m_j \omega_j} \delta(\omega - \omega_j) \quad (3.3)$$

which can be obtained from the force-force autocorrelation function of the medium.^{34,37,38} Since molecular dynamics calculations of the LH-II correlation function have not been reported, we employ a simple model of a generic Ohmic bath whose spectral density takes the form

$$J(\omega) = 2\pi\hbar\xi\omega e^{-\omega/\omega_c} \quad (3.4)$$

This function has a maximum at $\omega_c = 100 \text{ cm}^{-1}$.^{39,30} The reorganization energy between two adjacent chlorophyll monomers is related to the exciton-vibration coupling characterized by ξ through the expression

$$E_r = \frac{1}{\pi} (\sigma_k - \sigma_{k-1})^2 \int_0^\infty \frac{J(\omega)}{\omega} d\omega = 2\hbar\xi\omega_c (\sigma_k - \sigma_{k-1})^2 \quad (3.5)$$

Given the unequal separations of neighboring chlorophyll monomers that belong to a single or to adjacent dimers, we expect the intra- and interdimer reorganization energies to have somewhat different values. Knowledge of these reorganization energies would uniquely determine the parameters ξ and σ_k that are needed to complete the model. A rough estimate of the reorganization energy can be obtained from the dynamic Stokes shift, which has been found^{40,10} to be about 80 cm^{-1} . Ultrafast experiments¹⁰ also revealed that the electronic excitations are coupled to nuclear motions with frequencies ranging from 20 to 1000 cm^{-1} . We thus choose $\omega_c = 100 \text{ cm}^{-1}$. In the absence of more detailed information, we set σ_k equal to the chlorophyll monomer index k with periodic boundary conditions, i.e., $\sigma_{n+1} = \sigma_1$. We have verified that the coherence length reported in section IV remains essentially unchanged if a slightly nonuniform choice of σ_k is made. Finally, we present results for the values $\xi = 0.1$ and 0.25 , which describe exciton-vibration coupling corresponding to reorganization energies equal to 20 and 50 cm^{-1} , respectively.

The off-diagonal coupling elements obtained by Hu et al. are likely to be too large.⁴¹⁻⁴³ For this reason we also report results

for couplings that have been scaled down compared to those given in Table 1 by a factor of 2.

The calculation is performed in the site basis u_k . The partition function is given by the expression

$$Z = \text{Tr} e^{-\beta H} = \sum_{i=1}^n \int_{-\infty}^{\infty} dx \langle u_i | x | e^{-\beta H} | x u_i \rangle \quad (3.6)$$

which is written in the discretized path integral representation:

$$Z = \sum_{k_1=1}^n \sum_{k_2=1}^n \dots \sum_{k_N=1}^n \int_{-\infty}^{\infty} dx_1 \int_{-\infty}^{\infty} dx_2 \dots \int_{-\infty}^{\infty} dx_N \langle u_N | x_N | e^{-\beta H/N} | x_{N-1} u_{N-1} \rangle \dots \langle u_2 | x_2 | e^{-\beta H/N} | x_1 u_1 \rangle \langle u_1 | x_1 | e^{-\beta H/N} | x_N u_N \rangle \quad (3.7)$$

The imaginary time propagator is split symmetrically using the isolated exciton Hamiltonian as the reference.⁴⁴

$$\langle u_i | x_i | e^{-\beta H} | x_j u_j \rangle = \langle x_i | e^{-[\beta/(2N)][H(\sigma_i) - H_0]} e^{-[\beta/(2N)][H(\sigma_j) - H_0]} | x_j \rangle \langle u_i | e^{-\beta H_0/N} | u_j \rangle \quad (3.8)$$

In turn, the isolated exciton propagator is calculated in terms of the eigenstates Φ_k and eigenvalues E_k of eq 3.1:

$$\langle u_i | e^{-\beta H_0/N} | u_j \rangle = \sum_{k=1}^n \langle u_i | \Phi_k \rangle e^{-\beta E_k/N} \langle \Phi_k | u_j \rangle \quad (3.9)$$

With the present harmonic model for the nuclear vibrations, the integrals in eq 3.5 are of the Gaussian form and can be performed analytically. The result is⁴⁵

$$Z = \sum_{k_1=1}^n \sum_{k_2=1}^n \dots \sum_{k_N=1}^n \langle u_N | e^{-\beta H_0/N} | u_{N-1} \rangle \dots \langle u_2 | e^{-\beta H_0/N} | u_1 \rangle \langle u_1 | e^{-\beta H_0/N} | u_N \rangle F(\sigma_1, \sigma_2, \dots, \sigma_N) \quad (3.10)$$

where F is the influence functional and is given by the expression

$$F(\sigma_1, \sigma_2, \dots, \sigma_N) = \exp\left(-\sum_{k=1}^N \sum_{k'=1}^N \eta_{kk'} \sigma_k \sigma_{k'}\right) \quad (3.11)$$

The coefficients $\eta_{kk'}$ are given through integrals of the spectral density.

Because paths entering the path integral expression of the partition function are closed, these paths can be thought of as a necklace whose beads correspond to the auxiliary variables of eq 3.8.⁴⁶ In the present case each bead can occupy one of the n lattice sites of the LH-II ring. This correspondence allows straightforward visual examination of the system's coherence.

Paths contributing to eq 3.10 are sampled via a Metropolis procedure using the entire integrand as the sampling function. The coherence length of a path is obtained from the expression i.e.,

$$l = 2 \sum_{k_1=1}^n \sum_{k_2=1}^n \dots \sum_{k_N=1}^n \langle u_N | e^{-\beta H_0/N} | u_{N-1} \rangle \dots \langle u_2 | e^{-\beta H_0/N} | u_1 \rangle \langle u_1 | e^{-\beta H_0/N} | u_N \rangle F(\sigma_1, \sigma_2, \dots, \sigma_N) [(\sigma_1 - \sigma_c)^2 + (\sigma_2 - \sigma_c)^2 + \dots + (\sigma_N - \sigma_c)^2]^{1/2} \quad (3.12)$$

where σ_c is the centroid of the closed path $\{\sigma_1, \sigma_2, \dots, \sigma_N\}$.

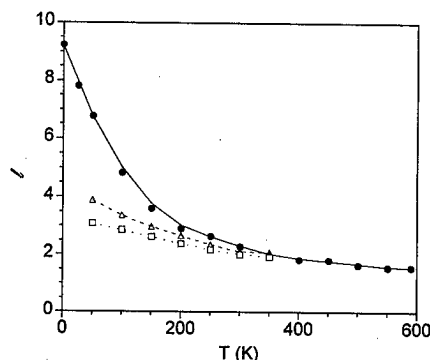


Figure 2. Coherence length as a function of temperature for the LH-II model with couplings from Table 1: (solid circles) isolated ring ($\xi = 0$); (hollow triangles) very weak exciton-vibration coupling ($\xi = 0.1$); (hollow squares) weak exciton-vibration coupling ($\xi = 0.25$). The lines are guides to the eye.

The effects of static diagonal disorder can be evaluated by replacing the parameter ϵ in eq 3.1 by the individual site energies ϵ_i , which are chosen from a Gaussian distribution with variance D . The MCL is then obtained from the ensemble average of l with respect to the fluctuation of the site energy. Interestingly, the integration associated with the inhomogeneous broadening of the ensemble can be combined with the Monte Carlo search for cyclic paths such that the effects of static disorder can be assessed within a *single random walk*. In this case the Boltzmann matrix elements of the reference Hamiltonian must be reevaluated for each choice of site energies.

In the next section we report the mean coherence length of the random walk and sketch typical paths for various parameters.

IV. Results

In this section we present the results of the path integral simulations described in section III. Figure 2 shows the coherence length in a 16-unit model of LH-II as a function of temperature for the isolated ring and also in the presence of small dissipation corresponding to $\xi = 0.1$ and $\xi = 0.25$. These calculations are performed without including disorder, using the coupling parameters of Table 1 for $N = 32$ path integral slices and 50 000 Monte Carlo points per integration variable after an equilibration step of equal length. At absolute zero the eigenstates are entirely delocalized. Dominant paths reflecting this delocalized structure exhibit coherence. The centroid of a completely delocalized path ($\sigma_k = \text{int}(kn/N)$, $k = 1, \dots, n$) is equal to

$$\sigma_c = \frac{n+1}{2} \quad (4.1)$$

and (taking $N = n$ for simplicity), the coherence length is

$$l = 2 \sqrt{\frac{1}{n} \sum_{k=1}^n (k - \sigma_c)^2} = \sqrt{\frac{1}{3}(n^2 - 1)} \quad (4.2)$$

which for $n = 16$ equals 9.22. At low temperatures and in the absence of any disorder the system exhibits moderate coherence, reflecting the delocalized nature of the eigenstates. This is illustrated in Figure 3, which shows typical paths having coherence length within one unit of the calculated MCL at $T = 50$ K. Clearly, the delocalized exciton picture is relevant at or below this temperature. However, even in the case of an isolated,

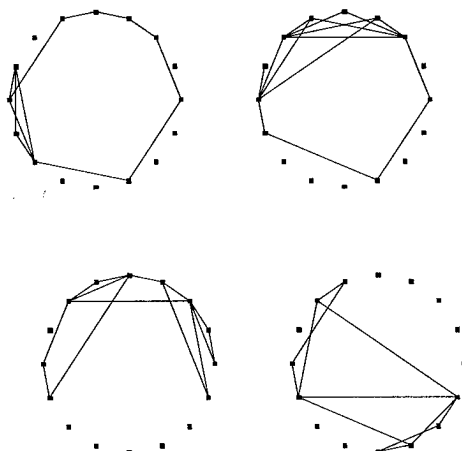


Figure 3. Typical paths for the isolated LH-II system ($\xi = 0$, no static disorder) at $T = 50$ K with the parameters shown in Table 1. The markers represent the chlorophyll monomers.

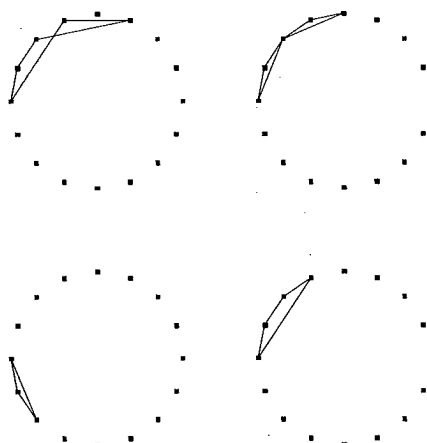


Figure 4. Typical paths for the isolated LH-II system ($\xi = 0$, no static disorder) at $T = 300$ K with the parameters shown in Table 1. The markers represent the chlorophyll monomers.

perfectly symmetric ring, only at very low temperatures does the path integral necklace begin to extend over the entire domain of the ring. As seen in Figure 2, thermal averaging has a dramatic effect on energy localization. At room temperature the coherence length is only 2.3 in the absence of any disorder. Typical paths at $T = 300$ K are shown in Figure 4. These paths now extend over only a few chlorophyll units. Note that these paths appear more delocalized than they actually are, since significant portions of the path integral necklace have collapsed on a single chlorophyll unit, an effect that cannot be discerned in the graphs. Coupling the ring to a weakly dissipative environment induces further localization, leading to $l = 2.1$ with $\xi = 0.1$ and $l = 2.0$ if $\xi = 0.25$ at 300 K. Still, coherence spans one to two dimers at room temperature, so hopping between individual monomers does not provide a faithful representation of energy transfer. At low temperatures where the perfect ring exhibits a high degree of coherence the effects of dissipation are more dramatic, as can be seen from Figure 2. Finally, inclusion of static disorder further enhances localization, although this effect is rather small, since the standard deviation of the site energies is small compared to the off-diagonal elements of the ring Hamiltonian.^{27,47}

As alluded to in the previous section, the coupling parameters obtained by Hu et al. are deemed too large. For this reason we repeat the calculation of the MCL using coupling parameters that are scaled by a factor of $1/2$ with respect to those presented in Table 1. The resulting MCL is shown in Figure 5. Even

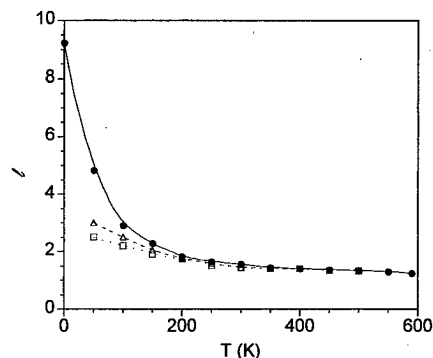


Figure 5. Coherence length as a function of temperature for the LH-II model with couplings from Table 1 scaled by 0.5: (solid circles) isolated ring ($\xi = 0$); (hollow triangles) very weak exciton-vibration coupling ($\xi = 0.1$); (hollow squares) weak exciton-vibration coupling ($\xi = 0.25$). The lines are guides to the eye.

though the MCL at zero temperature (where the ensemble is dominated by the ground state) is still given by eq 4.2, the MCL now decreases faster with increasing temperature and is equal to $l = 1.5$ at 300 K. The effects of dynamic disorder are again significant at low temperature, but given the very small extent of the paths at $T \geq 250$ K, this effect is negligible at room temperature.

From the results of these calculations it is evident that the coherence characterizing the exciton eigenstates of a perfect light-harvesting ring prevails only at very low temperatures. The calculated low-temperature MCL is in agreement with the estimate of Fleming and co-workers.⁴⁸ The major contributor to the localization observed at room temperature is thermal averaging, which destroys the coherent nature of individual eigenstates. Although static and dynamic disorder induce further localization, they are not crucial for disruption of coherence at biological temperatures. For this reason the conclusions reached on the basis of the simple model employing a harmonic dissipative bath appear robust and rather general.

In contrast to the localizing effects of the environment (temperature and static and dynamic disorder), the geometry of light-harvesting rings favors coherent energy transfer at low temperatures. Compared to a linear aggregate, the circular arrangement of the chlorophyll molecules eliminates the penalty in the Boltzmann factor associated with closing the path integral necklace for a path extending over at least half of the ring units. Choosing, for example, $N = n$, a completely delocalized path with $\sigma_k = k$, $k = 1, \dots, n$ enters the partition function with exactly the same weight as the path

$$\begin{aligned} \sigma_k &= k, \quad k = 1, \dots, n/2 \\ &= n + 1 - k, \quad k = n/2 + 1, \dots, n \end{aligned}$$

This would not be the case if the pigments were arranged in an open shape. Since the coherence length of the first of these paths is larger, the overall MCL is increased. The geometric enhancement of coherence is modest under conditions that already favor delocalized paths, i.e., at low temperatures and weak disorder, but does not have an observable effect under biological conditions where coherence appears to span a small portion of the ring.

V. Concluding Remarks

In the absence of static disorder, the energy absorbed by the B850 ring of the LH-II system is used to excite a pair of degenerate exciton states that are delocalized over the entire

ring. However, coherence does not survive thermalization. At room temperature, the onset of thermal equilibrium is characterized by an incoherent ensemble of excitations that extend over two to three chlorophyll units. At very low temperatures coherence spans a significant portion of the ring and is enhanced by the circular arrangement of the pigments.

Although these conclusions were reached on the basis of a very simple model, they appear quite robust and insensitive to the details of the calculation. We employed the Hamiltonian of Hu et al. and a simple model for the effects of exciton-vibration coupling to describe the equilibrium properties of the LH-II ring. Despite the strong couplings in this parametrization, which certainly favor delocalization, we find that *at room temperature the coherence length is reduced by a factor of 4 with regard to the zero temperature case*. Our estimate of the room-temperature MCL is in reasonable agreement with the conclusions reached by the groups of van Grondelle^{15,25} and Sundström,^{2,28,30,31} who report a coherence domain of three to four monomers. If the couplings of the model are scaled down to more likely values, localization is even more pronounced. Addition of exciton-vibration coupling enhances localization. In the present work this coupling was modeled in terms of a dissipative harmonic bath. Although anharmonicity of the vibrational degrees of freedom may weaken the localizing effects of dynamic disorder, such motion should nevertheless destabilize extended states. It is thus hard to imagine the more intricate motion of the pigments and protein atoms resulting in a different outcome. Finally, if static disorder is also taken into consideration, the resulting MCL becomes even shorter. Thus, energy delocalization over the entire ring appears extremely improbable under biological conditions, although within a dimer and probably across two dimers coherence appears to prevail.

Acknowledgment. This material is based on work supported by the Research Corporation through a Cottrell Scholar Award and by the National Science Foundation through Award No. 93-57102. N.M. is grateful to the Director and the Faculty of the National Hellenic Research Foundation for their hospitality during her sabbatical leave from the University of Illinois.

References and Notes

- (1) van Grondelle, R.; Dekker, J. P.; Gillbro, T.; Sundström, V. *Biochim. Biophys. Acta* **1994**, *1187*, 1–65.
- (2) Pullerits, T.; Sundström, V. *Acc. Chem. Res.* **1996**, *29*, 381–389.
- (3) Frank, H. A.; Cogdell, R. J. *Photochem. Photobiol.* **1996**, *63*, 257–264.
- (4) Kühn, O.; Renger, T.; May, V.; Voigt, J.; Pullerits, T.; Sundström, V. *Trends Photochem. Photobiol.* **1997**, *4*, 213–256.
- (5) *Resonance energy transfer*; Gnanakaran, S.; Haran, G.; Kumble, R.; Hochstrasser, R. M., Eds.; John Wiley and Sons: Chichester, 1999; pp 308–365.
- (6) Sundström, V.; Pullerits, T.; van Grondelle, R. *J. Phys. Chem. B* **1999**, *103*, 2327–2346.
- (7) McDermott, G.; Prince, S.; Freer, A.; Hawthornthwaite-Lawless, A.; Papiz, M.; Cogdell, R.; Isaacs, N. *Nature* **1995**, *374*, 517.
- (8) Hu, X.; Xu, D.; Hamer, K.; Schulten, K.; Koepke, J.; Michel, H. *Protein Sci.* **1995**, *4*, 1670–1682.
- (9) Nagarajan, V.; Alden, R. G.; Williams, J. C.; Parson, W. W. *Proc. Natl. Acad. Sci. U.S.A.* **1996**, *93*, 13774.
- (10) Kumble, R.; Palese, S.; Visschers, R. W.; Dutton, P. L.; Hochstrasser, R. M. *Chem. Phys. Lett.* **1996**, *262*, 396–404.
- (11) Arnett, D. C.; Kumble, R.; Visschers, R. W.; Dutton, P. L.; Hochstrasser, R. M.; Scherer, N. F. *Laser techniques for condensed phase and biological systems*. *SPIE Proc.* **1998**.
- (12) Freiberg, A.; Jackson, J. A.; Lin, S.; Woodbury, N. W. *J. Phys. Chem. A* **1998**, *102*, 4372–4380.
- (13) Kennis, J. T. M.; Streltsov, A. M.; Permentier, H.; Aartsma, T. J.; Amesz, J. *J. Phys. Chem. B* **1997**, *101*, 8367–8372.
- (14) Reddy, N. R. S.; Small, G. J.; Seibert, M.; Picorel, R. *Chem. Phys. Lett.* **1991**, *181*, 391–399.
- (15) van Mourik, F.; Visschers, R. W.; v. Grondelle, R. *Chem. Phys. Lett.* **1992**, *193*, 1–7.
- (16) Reddy, N. R. S.; Codgell, R. J.; Zhao, L.; Small, G. J. *Photochem. Photobiol.* **1993**, *57*, 35.
- (17) Visschers, R. W.; van Mourik, F.; Monshouwer, R.; van Grondelle, R. *Biochim. Biophys. Acta* **1993**, *1141*, 238.
- (18) Bradforth, S. E.; Jimenez, R.; van Mourik, F.; van Grondelle, R.; Fleming, G. R. *J. Phys. Chem.* **1995**, *99*, 16179.
- (19) Pullerits, T.; Visscher, K. J.; Hess, S.; Sundström, V.; Freiberg, A.; Timpmann, K.; van Grondelle, R. *Biophys. J.* **1994**, *66*, 236.
- (20) Monshouwer, R.; van Grondelle, R. *Biochim. Biophys. Acta* **1996**, *1275*, 70–75.
- (21) Hess, S.; Chachisvilis, M.; Timpmann, K.; Jones, M. R.; Fowler, G. J. S.; Hunter, C. N.; Sundström, V. *Proc. Natl. Acad. Sci. U.S.A.* **1995**, *92*, 12333–12337.
- (22) Xiao, W. H.; Lin, S.; Taguchi, K. W.; Woodbury, N. W. *Biochemistry* **1994**, *33*, 8313–8222.
- (23) Wu, H.-M.; Ratsep, M.; Lee, I.-J.; Cogdell, R. J.; Small, G. J. *J. Phys. Chem. B* **1997**, *101*, 7654–7663.
- (24) Kennis, J. T. M.; Streltsov, A. M.; Aartsma, T. J.; Nozawa, T.; Amesz, J. *J. Phys. Chem.* **1996**, *100*, 2438–2442.
- (25) Monshouwer, R.; Abrahamsson, M.; van Mourik, F.; van Grondelle, R. *J. Phys. Chem. B* **1997**, *101*, 7241–7248.
- (26) Meier, T.; Chernyak, V.; Mukamel, S. *J. Phys. Chem. B* **1997**, *101*, 7332–7342.
- (27) Hu, X.; Ritz, T.; Damjanovic, A.; Schulten, K. *J. Phys. Chem. B* **1997**, *101*, 3854–3871.
- (28) Meier, T.; Zhao, Y.; Chernyak, V.; Mukamel, S. *J. Chem. Phys.* **1997**, *107*, 3876–3893.
- (29) Kühn, O.; Sundström, V. *J. Phys. Chem. B* **1997**, *101*, 3432–3440.
- (30) Kühn, O.; Sundström, V. *J. Chem. Phys.* **1997**, *107*, 4154–4164.
- (31) Chachisvilis, M.; Kühn, O.; Pullerits, T.; Sundström, V. *J. Phys. Chem. B* **1997**, *101*, 7275–7283.
- (32) Feynman, R. P. *Statistical Mechanics*; Addison-Wesley: Redwood City, CA, 1972.
- (33) Cory, M. G.; Zerner, M. C.; Hu, X.; Schulten, K. *J. Phys. Chem. B* **1998**, *102*, 7640–7650.
- (34) Makri, N. *J. Phys. Chem. B* **1999**, *103*, 2823–2829.
- (35) Marcus, R. A.; Sutin, N. *Biochim. Biophys. Acta* **1985**, *811*, 265–322.
- (36) Onuchic, J. N.; Wolynes, P. G. *J. Chem. Phys.* **1993**, *98*, 2218–2224.
- (37) Warshel, A.; Hwang, J.-K. *J. Chem. Phys.* **1986**, *84*, 4938–4957.
- (38) Schulten, K.; Tesch, M. *Chem. Phys.* **1991**, *158*, 421–446.
- (39) Pullerits, T.; Van Mourik, F.; Monshouwer, R.; Visschers, R. W.; Van Grondelle, R. *J. Lumin.* **1994**, *58*, 168.
- (40) Visser, H. M.; Somsen, O. J. G.; van Mourik, F.; Lin, S.; van Stokkum, I. H. M.; van Grondelle, R. *Biophys. J.* **1995**, *69*, 1083.
- (41) Sauer, K.; Cogdell, R. J.; Prince, S. M.; Isaacs, N. W.; Scheer, H. *Photochem. Photobiol.* **1996**, *64*, 564.
- (42) Pullerits, T.; Hess, S.; Herek, J.; Sundström, V. *J. Phys. Chem. B* **1997**, *101*, 10560–10567.
- (43) Krueger, B. P.; Scholes, G. D.; Fleming, G. R. *J. Phys. Chem. B* **1998**, *102*, 5378–5386.
- (44) Makri, N. *Chem. Phys. Lett.* **1992**, *193*, 435–444.
- (45) Feynman, R. P.; Vernon, J. *Ann. Phys.* **1963**, *24*, 118–173.
- (46) Chandler, D.; Wolynes, P. G. *J. Chem. Phys.* **1981**, *74*, 4078–4095.
- (47) Wu, H.-M.; Reddy, N. R. S.; Small, G. J. *J. Phys. Chem. B* **1997**, *101*, 651–656.
- (48) Jimenez, R.; Dikshit, S. N.; Bradforth, S. E.; Fleming, G. R. *J. Phys. Chem.* **1996**, *100*, 6825–6834.

Electron Dynamics in Dendrimers

T. Sean Elicker and Deborah G. Evans*

Quantum Chemistry Research Group, Albuquerque High-Performance Computing Center and Department of Chemistry, University of New Mexico, Albuquerque, New Mexico 87131

Received: May 17, 1999; In Final Form: September 2, 1999

Electron transfer dynamics in extensively branched macromolecules (dendrimers) is studied using time-dependent quantum mechanical techniques. A split operator method that fully exploits the Cayley tree topology of these macromolecules is developed within a tight-binding model Hamiltonian. Solvent effects are simulated by time-dependent random fluctuations; this dephasing eliminates the localized oscillations that characterize the nonsolvated dynamics, and results in decay of the electron density from an initially photoexcited state. Electron transfer is asymmetric depending on the site of initial excitation, and solvent fluctuations in general enhance the directed transport within the structure. Some dendrimers, particularly those with a certain extended structures show enhanced transport toward their central nodes. The efficiency of electron transfer to the central node depends on both the dendrimer structure and the characteristics of the solvent fluctuations.

I. Introduction

Dendrimers have been the topic of numerous synthetic studies in the last few years. Sophisticated molecules with a wide range of monomer units ranging from silicon to porphyrins have been assembled with extensively branched tree structures.¹ They are currently the only synthetic realizations of the Cayley tree structure;² this novel topology, along with the existence of precise control over the size of the product molecule, makes dendrimers a useful model for investigating the dependence of physical properties on molecular size and topology. Recent experiments examining the physical and spectroscopic properties of certain classes of dendrimers provide preliminary evidence that some dendrimers may have applications in molecular electronics, as LEDs³ and single-molecule photonic antennae.⁴

A number of theoretical papers have focused on the classical simulation of dendrimer structure.⁵ Molecular dynamics simulations of large dendrimers in solvent have successfully explained phenomena like the uptake of small chromophores into a dendrimer structure, for example.⁶ Effective coupling matrix elements for electron transfer have been studied by Risser et al.⁷ They have shown that the connectivity gives rise to different electronic properties from those of corresponding linear polymers. By focusing on the electron pathways model of electron transfer⁸ in macromolecules, Risser et al.⁷ were able to show that at certain levels of static disorder in the dendrimer Hamiltonian, there is a growth of strong paths to the dendrimer surface in comparison with their linear counterparts. Interestingly, they have found that static disorder in dendrimers may therefore increase coupling between the donor and acceptor sites.

Recent spectroscopic studies on two classes of dendrimer structures have provided interesting results.^{9–11} The structures are phenyl dendrimers, where the branching nodes are 1,3,5-trisubstituted benzene and the node-to-node linkage is via various bridging systems (see for example, ref 9). These macromolecules are generally synthesized by a convergent method,¹² in which each of the three main branches are formed independently. The final step of the synthesis then couples these branches to a central molecule. This method is known to be superior to divergent methods,¹³ where the dendrimer is grown

outward from an initial core; indeed, convergent synthesis practically guarantees a Cayley tree structure in the product, and the size limitations of that product are due solely to steric interactions between elements of the outermost layer, or "generation". By modifying the synthesis slightly, a selected number of paradisubstituted benzenes (and accompanying bridging groups) may be inserted between successive generations of branching nodes. These structures, called extended Cayley dendrimers, manifest different spectroscopic properties from their compact counterparts. In extended structures, the electronic absorption peak maximum exhibits a red shift with increasing generation number, whereas in compact dendrimers no such shift occurs. This energy gradient could be exploited to create an energy funnel in these structures.⁹ The collective electronic oscillator approach¹⁴ for calculating the absorption spectrum has been applied to a series of these phenylacetylene-type dendrimers.¹⁵ It has been shown that the electron-hole pairs that contribute to the elementary collective excitations are well-localized. This has enabled the calculation of the absorption spectra of a series of dendrimers to be approximated from the absorption profiles of the independent constituent oligomers, and these show a red shift commensurate with the experimental data.

Intermolecular electron transfer studies have been conducted on a variety of systems. For example, encapsulated electroactive molecules have been synthesized with iron–sulfur cluster cores.¹⁶ Photoinduced electron transfer rates from metalloporphyrin dendrimers to solvated MV²⁺ ions have been recorded spectroscopically¹⁷ and electron transfer from dendrimeric metallophthalocyanines to MV²⁺ has been monitored via fluorescence quenching.¹⁸ Other studies have used electron spin resonance to study electron transfer from carboxylated dendrimers to C₆₀ as a function of the number of dendrimer generations.¹⁹ Recently, intermolecular photoinduced experiments have been carried out on a series of phenylacetylene dendrimers with geometries very similar to the phenylacetylene dendrimers studied spectroscopically as photonic antennae.²⁰ These measurements are a prelude to studies on intramolecular electron transfer with suitable donor and acceptor functionalities.

These studies demonstrate that dendrimers can act as suitable bridging media for electron transfer between redox centers, and indicate the feasibility to effect photoinduced electron transfer in dendrimers with a suitable choice of electron/donor functionality at the core and on the periphery.

A study of electron transfer within dendrimers is therefore timely. In particular, this study focuses on the electron dynamics of photoinduced electron transfer in both condensed and extended dendrimeric structures. The role of solvent fluctuations on electron transfer is examined and the behavior compared with linear donor-bridge-acceptor molecules. Unlike the work of Risser et al.,¹⁷ our research focuses on the time evolution of electron population dynamics within the dendrimeric structure. In order to extend this to more sophisticated models in the future, we have developed a split-operator method that exploits the unique dendrimer connectivity, and incorporates time-dependent solvent fluctuations as discussed in Section II. In Section III, the electron transfer dynamics is simulated for several classes of condensed and extended dendrimer structures. The effects of changes in dendrimer size, and particularly geometry, are examined. Changes induced by solvent fluctuations are studied both in terms of the magnitude and time scales of the solvent fluctuations. A discussion of the experimental ramifications of these results is presented in the final section.

II. Methods

We have devised an algorithm for the time evolution of an initial photoexcited state. The algorithm, DEVO (*dendrimer evolution*), is a split operator method and it is specifically designed to perform quantum-dynamic simulations of electron transport in dendrimers. Although DEVO is applicable to both electron and exciton dynamics, this study is concerned exclusively with electron dynamics following photoexcitation. The tight-binding Hamiltonian for electron transport in a dendrimer is written as

$$\hat{H} = \sum_{ij} \beta_{ij} (a_i^\dagger a_j + a_j^\dagger a_i) + \sum_i \epsilon_i a_i^\dagger a_i + \Phi(t) \quad (1)$$

where we use the parameter values of Felts et al.:²¹ $\epsilon = 1500 \text{ cm}^{-1}$ for the donor and acceptor sites and zero for all other sites; $\beta = 300 \text{ cm}^{-1}$ for nearest neighbors and zero otherwise. Further details on the workings of the DEVO algorithm may be found in Appendix A.

The $\Phi(t)$ term represents the influence of the solvent on the electron process

$$\Phi(t) = \sum_i \phi_i a_i^\dagger a_i + \sum_{ij} \mu_{ij} (a_i^\dagger a_j + a_j^\dagger a_i) \quad (2)$$

Both the on-site ϕ_i and off-diagonal μ_{ij} components are described as uncorrelated Gaussian noise, and in this model represent a way of incorporating the solvent influences into a calculation of the electron dynamics. Unlike more phenomenological approaches,²³ these effects can be incorporated into the model using further calculations. For example, for electron transfer in a particular dendrimer in a specific solvent, these fluctuating matrix elements can be obtained from simulations of the system. In particular, on-site fluctuations could be determined from *ab initio* reaction field calculations and off-diagonal coupling matrix elements could be determined by calculating the fluctuating site-site distances using classical molecular dynamics simulations and correlating these with changes in the bond integral.²² We represented different solvents by changing the magnitude of the fluctuations and/or the

characteristic updating time τ_{solv} of the fluctuations. The three different solvation regimes are characterized by the magnitude of the standard deviations of the two types of fluctuations: $\langle \phi_i(t), \phi_i(t') \rangle = \sigma_i \cdot \delta(t - t')$ and $\langle \mu_{ij}(t), \mu_{ij}(t') \rangle = \sigma_{ij} \cdot \delta(t - t')$. We set $\sigma_i = 0.04\epsilon_i$ and $\sigma_{ij} = 0.0001\beta_{ij}$ in the nearly-coherent regime I; $\sigma_i = 0.1\epsilon_i$ and $\sigma_{ij} = 0.01\beta_{ij}$ in regime II; finally, $\sigma_i = 0.25\epsilon_i$ and $\sigma_{ij} = \beta_{ij}$ for the strongly solvated regime III. The organometallic center and radially symmetric arrangement of organic centers is reminiscent of donor/acceptor models in linear conjugated systems, which motivated our choice of energetic parameters from earlier work on such linear systems.^{21,23}

In our simulations, we have examined the nature of the evolution of electron density through a series of structurally distinct dendrimers, and the spatial character of the evolving electron density in these structures. Using DEVO to compute the wavefunction at each time step enables the evaluation of electron probability density on each node in the dendrimer, as well as the total density on each generation. In order to investigate possible wavefunction localization, we have calculated the inverse participation ratio.^{24,25}

$$P^{-1} = \sum_i (\Psi_i \Psi_i^*)^2$$

In a system with N sites, this ratio is unity for a perfectly localized state, and equal to $1/N$ for a completely delocalized state. Therefore, P (the participation number) gives a rough estimate of the extent of wavefunction delocalization over the dendrimer sites. We also compute the ratios of the site densities to the value $1/N$, to study how the asymptotic probability distribution varies from the perfectly delocalized state.

III. Results and Discussion

In order to focus on the general properties of dendrimers with a certain geometrical structure, our study is confined to a class of synthetically well known phenyl-based dendrimers with an organometallic central node. As shown in Appendix A, there is no loss of generality in modeling these dendrimers as benzene nodes with no bridging groups. Recent experimental work has shown that interesting spectroscopic behavior occurs in dendrimers with extended structures,⁹ which is different to the behavior observed for condensed, or self-similar structures. To determine whether dendrimers with these different geometries can display radically different behavior in electron transfer experiments, we studied electron transfer dynamics in both condensed and extended dendrimers. Our simulations include condensed dendrimers with three, four, and five generations, denoted hereafter as $3N$, $4N$, and $5N$ and a set of three qualitatively different three-generation extended dendrimers: (14), (33), and (52). Schematics of the six structures are shown in Figure 1. The first number in the ordered pair is the size (in terms of nodes) of the three interstitial groups between the center and first branching nodes, while the second number in the ordered pair is the size of the six interstitial groups between these first branching nodes and the outer nodes in the three-generation dendrimer. These particular extended geometries have been selected because each one involves the addition of exactly 27 interstitial nodes to a three-generation dendrimer. This excludes the possibility that variations in dynamics are due to a change in the total number of nodes in the dendrimer. The electron density following photoexcitation is monitored for 100 fs in these simulations, and the solvent-induced fluctuations are updated (on average) every 15 fs. The final data sets are averaged over an ensemble of solvent fluctuations.

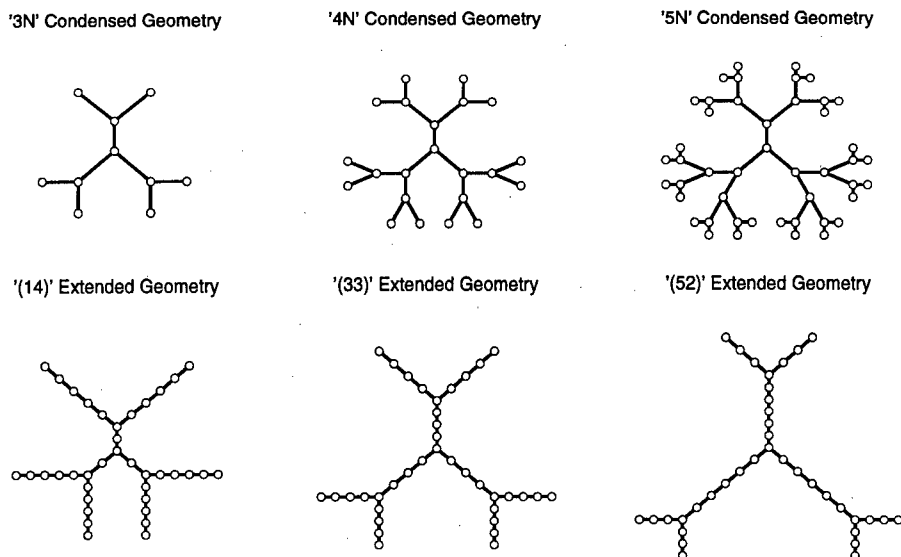


Figure 1. Schematic diagrams of the six dendrimer geometries studied (circles represent chemical units).

Dendrimers in which the outer generation of benzene rings is replaced with a generation of nodes chemically identical to the center node are also studied; such structures are analogous to linear conjugated donor/acceptor systems that have been well-studied elsewhere. Linear systems at high solvent coupling exhibit the phenomenon of bridge trapping, where the measurable electron density is found on the intermediate bridge sites. Figure 2 shows the values of ρ_B/ρ_{B0} for the various dendrimer geometries; ρ_B is the asymptotic total density on all the intermediate (bridge) nodes of the dendrimer, and the zero subscript denotes data from simulations without an outer acceptor layer. Bridge-trapping behavior is observed in those simulations where the electron starts on the center node ($SN = 1$), but not in those simulations where the electron starts on the outer layer ($SN = N$). In the $SN = 1$ case, the Cayley tree topology ensures that all paths from the donor (center) to an acceptor are equivalent in length, and the electron transfer system is analogous to linear donor-bridge-acceptor systems. In all solvent regimes, evidence for bridge trapping is found, unlike previous studies on linear systems. This is due to the fact that this model incorporates both on-site and site-site fluctuations which dephase the electron wavefunction on the bridge even at relatively small solvent fluctuations. The $SN = N$ case lacks the symmetry of the $SN = 1$ case, and electron transfer is different from linear systems if the dephasing time scale is longer than it takes for the electron on one of the periphery sites to move to the center and then be transferred to alternative branches. In fact, the natural bias in the dendrimer geometry for outward movement of quasiparticles in the incoherent (strong solvent coupling) regime has previously been illustrated using simple rate equations.¹⁰ That our results differ for $SN = 1$ or N tends to support that this is also the situation for typical electron transfer in dendrimeric bridge molecules for a range of solvent regimes where the fluctuations are on the order of 10–15 femtoseconds. Thus, the $SN = N$ system is not analogous to a linear donor-acceptor system, and the dynamics of these systems is asymmetric in terms of where the excitations are initiated. As shown in Figure 2, ρ_B/ρ_{B0} is less than one for the $SN = N$ simulations, which is evidence that less electron density is found on the bridge sites in those simulations with an outer layer of acceptor nodes. This suggests that for the case with no acceptor nodes on the periphery, electron transfer to the center takes place, and then the less efficient back transfer to the outer nodes occurs, creating a

buildup of electron density on the bridge sites as the dynamics is dephased by the solvent-induced fluctuations.

There is evidence of substantial localization in all of our simulations. Figure 3 shows the participation number P in dendrimers of various geometries, as compared to the total number of nodes in the dendrimer. In all cases, the number of nodes participating in the wavefunction is much less than the total number of nodes. P increases as the stochastic fluctuations increase, indicating that the destruction of interferences in these finite systems have more impact on localization than the structural distortion induced by the solvent. The degree of localization was much smaller for simulations in which the excitation begins on the outer layer of the dendrimer; this provides further evidence that the spatial anisotropy of such simulations has a real effect on the observed asymmetric dynamics.

Photoinduced electron transfer experiments have recently demonstrated intermolecular electron transfer between phenylacetylene dendrimers and donor molecules in the surrounding solution.²⁰ The following section is therefore focused on in dendrimers without an outer acceptor layer, and the exploration of the possibility that certain structures may be capable of directed electron transport of the electron density from the outer layers to the center node. To compare the relative abilities of the various structures to do this, $\rho_{tot} = \int_0^{t_f} \rho_c(t) dt$, where the integral is over the entire time interval $[0, t_f]$ of the simulation, is calculated. For $SN = N$ simulations, this integral provides a measure of how effectively the electron density is transferred from the outer layer to the central node, and could be observed as the integrated emission intensity from a fluorescent central core over this time period. Figure 4 shows ρ_{tot} for the six structures in this set of experiments. The efficiency of direct electron density to the central nodes of the condensed structures decreases exponentially with the generation number, but this may be a consequence of the number of nodes between the center and outer layer of the dendrimer. Casting the dependence in terms of this radius r_N allows for a direct comparison of the condensed and extended structures. The lack of relative difference in efficiency between the three extended structures is expected, because their large r_N values (6, 7, and 8) lead to small efficiency differences. This result is supported by examining the effective coupling elements between an outer-layer node and the central node for the three extended structures. As shown

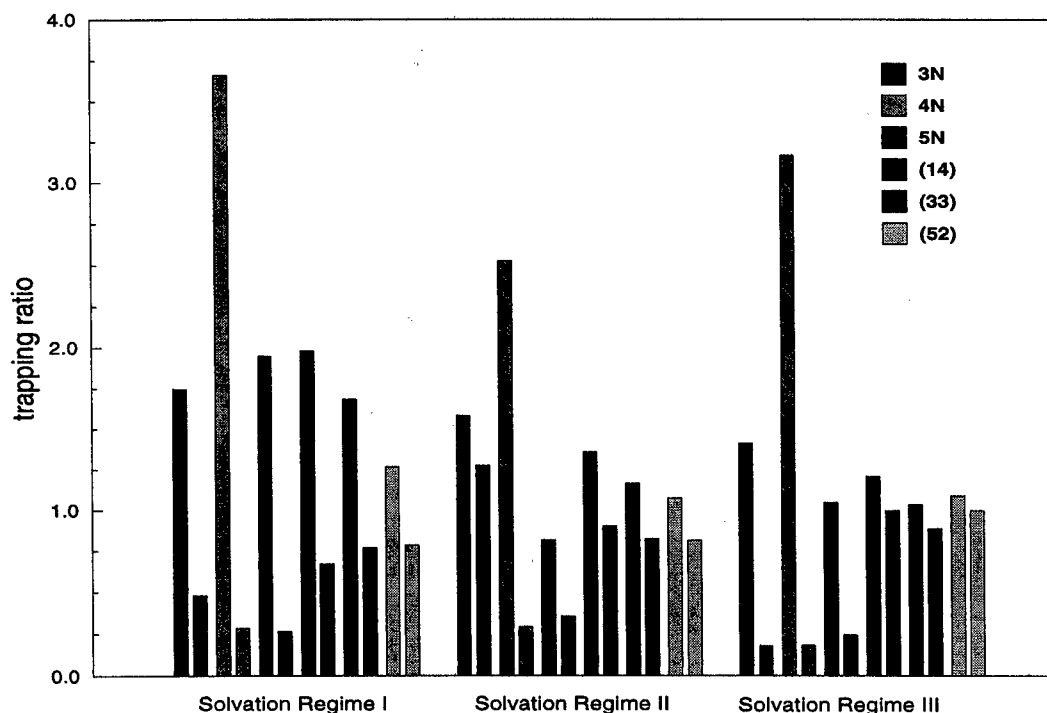


Figure 2. Trapping ratio (ρ/ρ_0) for various dendrimer geometries with $SN = 1$ (left-hand bar) and $SN = N$ (right-hand bar).

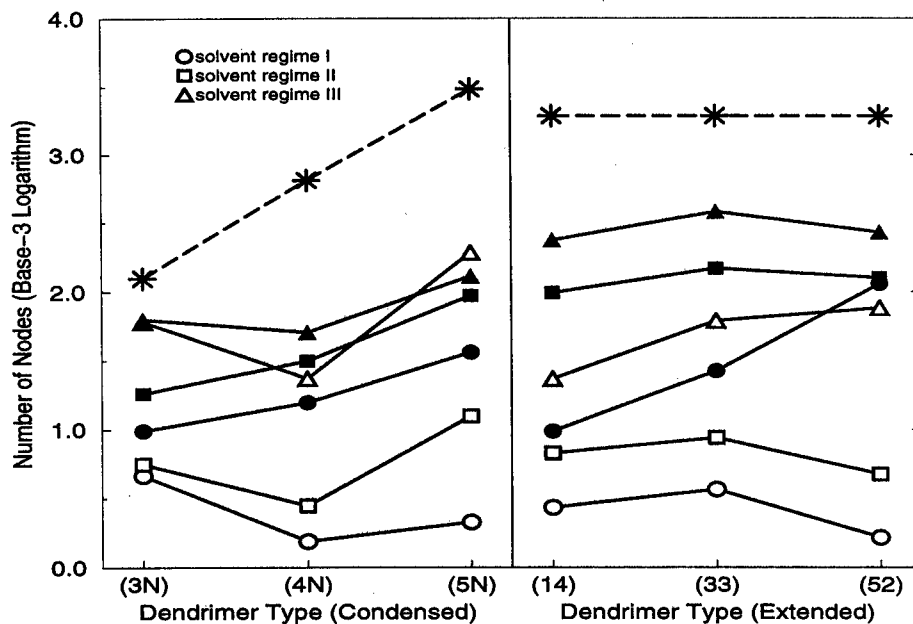


Figure 3. Comparison of participation number for simulations in the three solvent regimes described in Section II. Open symbols denote simulations with $STARTNODE = 1$, filled symbols denote simulations with $STARTNODE = N$, and asterisks denote the total number of nodes in the dendrimer.

in Appendix B, there is a negligible difference between the three effective couplings for $|\beta|$ values less than one-half of the magnitude of the on-site energies. Nevertheless, the efficiency of the (52) structure is higher than expected, given its increased r_N , in comparison with the condensed geometry. The increased efficiencies of the extended structures must therefore arise from other considerations.

The electron densities on each dendrimer node vary in an oscillatory manner in the absence of solvent; although explicit oscillations are not apparent in the stronger solvent regimes, the timescales of the unsolvated recurrences will affect the observed electron dynamics in the solvated system. Figure 5 shows the total generation densities for four three-generation structures in an unsolvated dendrimer. The behavior for the three

extended structures is qualitatively similar, but the timescales for various components of the dynamics vary. For example, Figure 6 graphs the timescales for two components: (i) the first minimum of the density of the initial node, and (ii) the first maximum in the density of the branching node nearest to the initial node for four similar dendrimers. The relationship between structure and time scales is easily seen: decay out of the initial node is independent of the dendrimer size, while the growth on the first branching node depends on the number of monomer spacers in a regular fashion.

The results shown in Figure 4 are obtained by updating the solvent fluctuations every 15 fs (realistic for a generic polar solvent). Different solvents will have different relaxation times, and the variation of dendrimer timescales shown above indicates

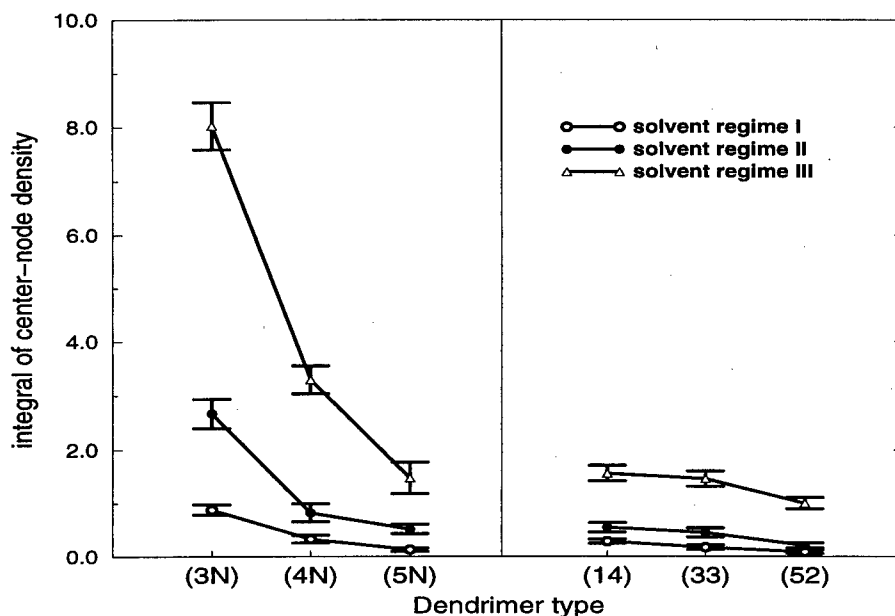


Figure 4. Comparison of ρ_{tot} values for six dendrimers, in the three solvent regimes described in Section II.

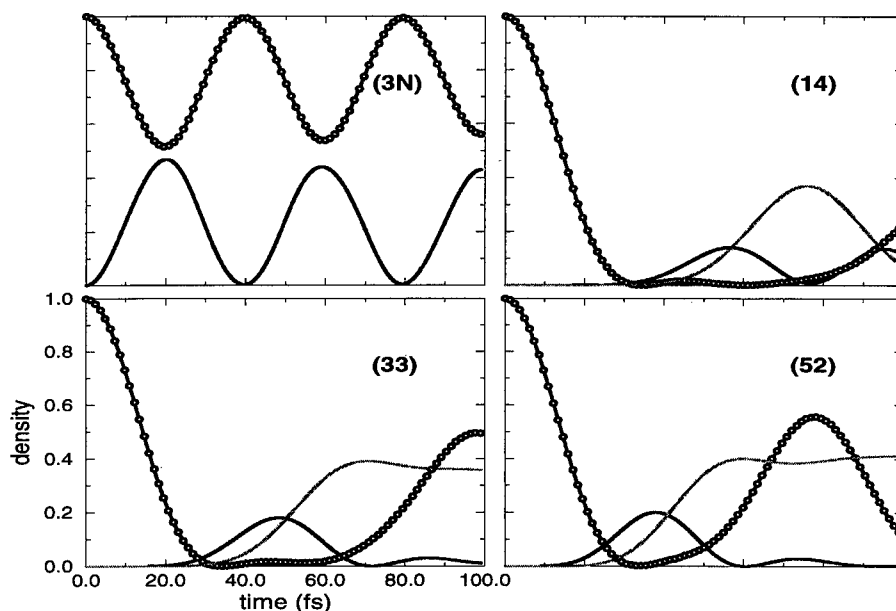


Figure 5. Unsolvated dynamics of (3N), (14), (33), and (52), showing the total density on the initial node (circles), the inner branching nodes (solid), and the inner group of interstitial nodes (gray).

that the dynamics is closely linked to the statistics of the solvent. Figures 7 and 8 show ρ_{tot} for the dendrimer families ($5m$) ($1 \leq m \leq 4$) and ($m2$) ($1 \leq m \leq 5$). For each structure, ρ_{tot} was calculated in four different solvents, with equivalent fluctuation magnitudes but different timescales. The update times for the fluctuations of the four solvents are $\tau_{\text{solv}} = 7, 15, 30$, and 60 fs respectively. For a fixed value of τ_{solv} , the efficiency tends to decrease as r_N increases. The increasing radius increases the recurrence timescales for densities of the inner nodes, so that solvent relaxation results in less electron density trapped near the center of the dendrimer in structures with larger r_N . In such structures, density moves to the center via repeated trapping, and the overall efficiency is lower. This effect vanishes as τ_{solv} increases, for two reasons: the longer solvent timescale allows for significant trapping in the inner regions even for those structures with longer recurrence timescales; also, there are far fewer relaxation steps in the simulation for large τ_{solv} , so structural differences are less important.

The r_N dependence is important; in the 15 fs solvent, the efficiency of the three-generation condensed structure is many times greater than any of the ($5m$) structures, and more than twice as great as the most efficient structures in the ($m2$) family. This may not translate into a preference for condensed structures in devices, however; we expect that molecular volume will also be an important characteristic for directed transfer applications, and (for example) (52) has 4 times as many benzene nodes as (3N).

Along with the strong dependence of efficiency on r_N , the relative sizes of the two interstitial groups are also important. For example, the data for ($n2$) shows that, in all four solvents, the drop off in efficiency between (22) and (32) is less than the drop off between (32) and (42). In three-generation structures where r_N does not change by more than one, those dendrimers with more interstitial nodes in the innermost group were more efficient at funneling electron density to the center. Table 1 shows comparison of (22) with various structures having the

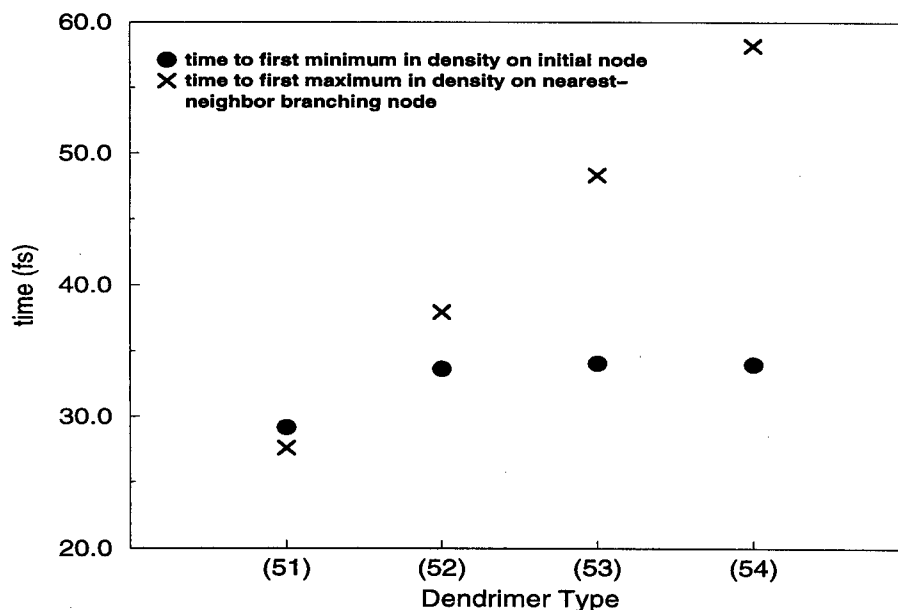


Figure 6. Comparison of two particular timescales for the $(5n)$ family of extended dendrimers, $n = 1, 2, 3, 4$.

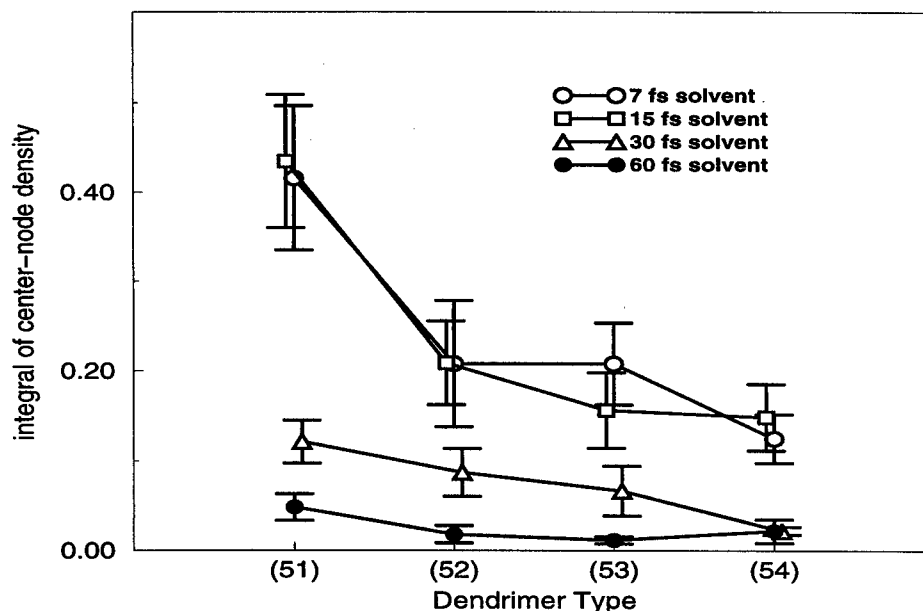


Figure 7. ρ_{tot} values for the $(5n)$ family of extended dendrimers, $n = 1, 2, 3, 4$.

same r_N value. The efficiencies of (13) and (22) are comparable, while (31) is nearly 150% more efficient. The trend does not continue, however; (40) is only about 60% as efficient as (22); the complete absence of one interstitial group changes the underlying topology in addition to altering the recurrence time scales.

This importance of the relative sizes of the interstitial groups can also be seen in four-generation dendrimers. In Table 2, three structures that (as above) have the same r_N value are compared in a 15 fs solvent.

The (321) structure is more than twice as efficient as either the (420) or the (402) structures, which is consistent with our hypothesis that structures like (n_1, n_2, \dots, n_K) with $n_i > n_i + 1$ are the most efficient among those with the same r_N value. Note that, to a lesser extent, (420) is more efficient than (402), although the presence of the null interstitial groups complicates a direct comparison. Indeed, the efficiency of (302) is less than that of (321), despite the fact that the latter structure has a larger radius.

IV. Conclusions

This study examines the electron transfer dynamics in various dendrimer structures and the effects solvent fluctuations have on those dynamics. To perform these calculations on large dendrimers at the atomistic scale and include time-dependent solvent fluctuations, we have developed a split-operator algorithm (DEVO) to study electron dynamics in dendrimers. This algorithm exploits the Cayley tree structure of dendrimers and is consistently about 40% faster than the checkerboard algorithm. However, DEVO is particularly well-suited to parallelization, and simple scaling arguments increase its efficiency over the checkerboard algorithm to several orders of magnitude for reasonable-sized dendrimers of 7–8 generations.

Intermolecular electron transfer in analogs of phenylacetylene dendrimers has recently been observed,²⁰ and given a suitable choice of donor and acceptor sites, it appears that intramolecular electron transfer in dendrimers will soon be effected. Experimental⁹ and theoretical¹⁵ work on the spectroscopic behavior

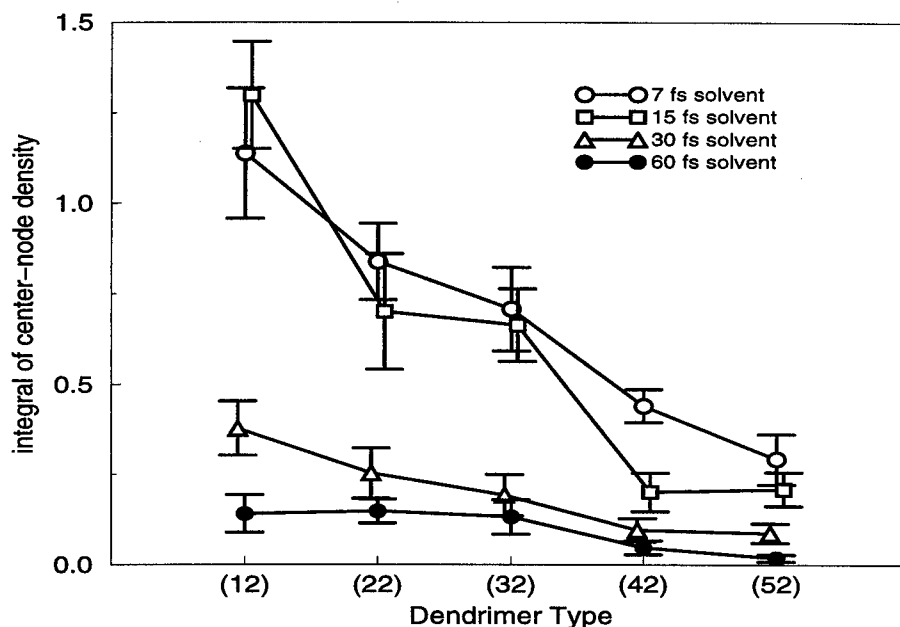


Figure 8. ρ_{tot} values for the $(n2)$ family of extended dendrimers, $n = 1, 2, 3, 4, 5$.

TABLE 1: Efficiencies for a Family of Dendrimers with $r_N = 5$, in a 15 fs Solvent

structure	r_N	$\rho_{\text{tot}}(\tau_{\text{solv}} = 15 \text{ fs})$
(22)	5	0.7010 ± 0.15916
(13)	5	0.7939 ± 0.09751
(31)	5	1.0353 ± 0.14736
(40)	5	0.4849 ± 0.08159

TABLE 2: Values of ρ_{tot} for a Group of Four-Generation Extended Dendrimers

structure	radius	$\rho_{\text{tot}}(\tau_{\text{solv}} = 15 \text{ fs})$
(420)	8	0.1243 ± 0.03259
(402)	8	0.1024 ± 0.03446
(321)	8	0.2525 ± 0.04472
(302)	7	0.2284 ± 0.04849

of phenylacetylene dendrimers has shown that for dendrimers of a particular extended geometry, energy funneling can occur. It has been demonstrated that the spectroscopic behavior of these extended dendrimers is quite different from those with condensed geometries. In this study we have focused on determining whether these two types of dendrimer structure show different electron transfer behavior as well. In particular, we have examined a number of geometries in order to determine if the extended structures are more efficient in transferring an electron from the periphery to the center in a photoinduced electron transfer process.

We have studied electron transfer in dendrimers with organometallic donor sites at the core, both with and without electroactive groups on the periphery. All these structures have trisubstituted benzene molecules as the regular nodes of the dendrimer branches. Our study focuses on the behavior of four related families of geometric arrangements: the first set of simulations were performed on condensed dendrimers with three, four, and five generations, as well as three different extended geometries that have disubstituted nodes between successive generations of branching nodes. All our simulations included solvent effects through stochastic fluctuations of the Hamiltonian matrix elements; the magnitudes of these effects—along with the values of the matrix elements—were taken from previous studies on electron transfer in donor-acceptor linear conjugated systems.^{21,23}

When a layer of trapping acceptor nodes was placed at the outer edge of these dendrimers, we found analogies between the resulting dynamics and the dynamics of the linear donor-acceptor systems. In particular, we found evidence of bridge trapping, where significant electron density is found on the nodes between the center and the outer acceptor layer in simulations where the electron density was initially on the central node. If the electron density was initially located on one of the outer nodes, no bridge-trapping occurs as the electron transfer to the center and subsequent branches is now inherently asymmetric, and unlike the linear donor-acceptor bridge systems.

Our studies indicate that strong solvent fluctuations may increase the efficiency of electron transfer to the central core, and that the different types of extended dendrimers do indeed display different behavior for electron transport to the central node in simulations where the electron density was initially at the periphery. We found that, in general, the efficiency of both condensed and extended dendrimers decreases as the radius (number of nodes between the outer node and the center) increases, but the efficiency of extended structures is larger than that of a condensed dendrimer with the same radius. Our data on nonsolvated dynamics shows a strong correlation between the size of interstitial groups and the timescales of electron density recurrences for the various generations in the dendrimer. In many of the structures we studied, the relationship between these recurrence timescales and the relaxation time of the solvent can be directly linked to the directed electron transport to the dendrimer core. There are also specific structural considerations: for example, the decrease in efficiency from (22) to (32) is smaller than between other pairs of successive structures in the $(n2)$ family, and among dendrimers of equal radius those with interstitial groups that decrease with distance from the center tend to have higher efficiency of transport to the center.

Attempts to increase the sophistication of describing the solvation effects on the electron transfer are currently underway. Using the DEVO algorithm with solvent fluctuation data extracted from classical molecular dynamics simulations, specific experimental systems (e.g., Fe-S cluster dendrimers¹⁶) can be described realistically. These results can then be compared with phenomenological approaches²³ and the dissipative

Redfield models of long range electron transfer used by Friesner et al.²¹

Acknowledgment. The authors would like to thank the National Science Foundation (NSF-CAREER), the donors of the Petroleum Research Fund administered by the American Chemical Society, and The Albuquerque High-Performance Computing Center for their support of this research, and Mark Mothersbaugh and his group for their contribution.

Appendix A

The DEVO algorithm decomposes the Hamiltonian (eq 1) in a way that facilitates construction of the propagator for the associated time-dependent Schrödinger equation. DEVO is a simple extension of the checkerboard algorithm,^{24,26} where the Hamiltonian is shredded into pairs of interactions and the full propagator $\hat{A} = \exp[-i\hat{H}(t)\cdot\delta t]$ is evaluated using split operator techniques. As in other studies,^{7,28} this algorithm specifically exploits the topology of the dendrimer. However, DEVO is a split-operator method that replaces the full short-time propagator with an product of simpler propagators that update the evolution of those wavevector coefficients corresponding to a particular subset of nodes. DEVO decomposes the overall propagator \hat{A} into $\hat{A}_0 \cdot \Pi_i \hat{B}_i$. The operator $\hat{A}_0 = \exp[-i\hat{H}_0(t)\cdot\delta t]$ describes the evolution of the central node and the three benzene nodes adjacent to those connector sites. The sub-Hamiltonian matrix for constructing this evolution operator is

$$\hat{H}_0 = \begin{vmatrix} \epsilon_0 & \beta_0 & \beta_0 & \beta_0 \\ \beta_0 & \epsilon_1 & 0 & 0 \\ \beta_0 & 0 & \epsilon_1 & 0 \\ \beta_0 & 0 & 0 & \epsilon_1 \end{vmatrix}$$

where ϵ_0 is the on-site energy of the central node, ϵ_1 is the on-site energy of the neighboring benzene nodes, and β_0 is the overlap between the central node and its neighbors. Similarly, the \hat{B}_i describe the evolution for each branching node and the two adjacent benzene nodes in the next generation outward. These three-node evolution operators are constructed from sub-Hamiltonian matrices similar to the above matrix

$$\hat{H}_i = \begin{vmatrix} 0 & \beta & \beta \\ \beta & \epsilon_1 & 0 \\ \beta & 0 & \epsilon_1 \end{vmatrix}$$

with β the overlap between two benzene nodes. Note that the (1,1) entry of \hat{H}_i is set to zero, to avoid double-counting; that matrix element is already accounted for in either the (2,2) or the (3,3) entry of the submatrix from the next generation inward. Operating on the full-system wavevector with this outward cascade of evolution operators is thus an approximation of the total propagator for the system. Figure 9 is a schematic of how this cascade is performed in a three-generation dendrimer. In a typical dendrimer, the problem of diagonalizing a $(3 \cdot 2^{N-1} - 2) \times (3 \cdot 2^{N-1} - 2)$ matrix is replaced by the diagonalization of a single 4×4 matrix and $3 \cdot (2^{N-2} - 1) \times 3$ matrices.

Many dendrimers have connectors (e.g., oxygen centers and acetylene groups) between adjacent nodes, but DEVO is easily adapted to such systems. In our formalism, such a bridging group is treated as a single interstitial node, so that the sub-Hamiltonian matrices for the bridged dendrimer are

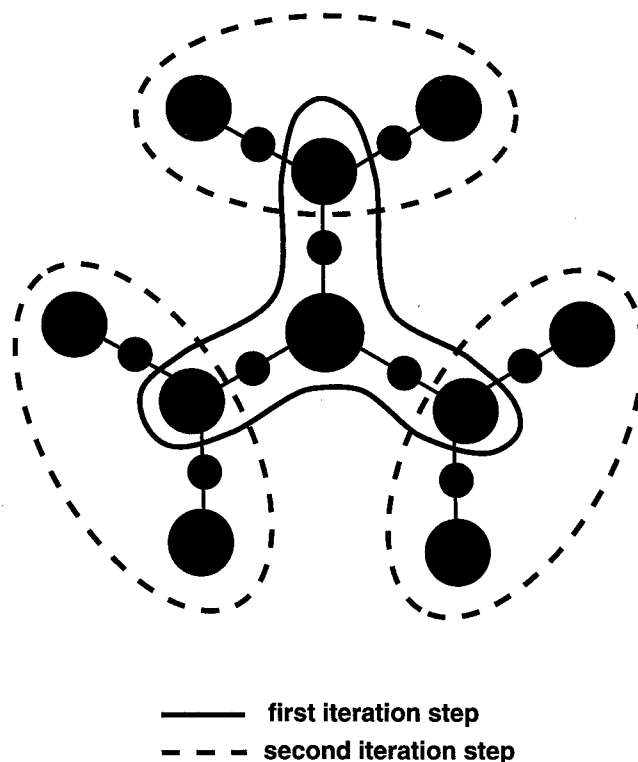


Figure 9. Decomposition scheme for a three-generation dendrimer with connector nodes.

$$\hat{H}_0 = \begin{vmatrix} \epsilon_0 & \beta_0 & \beta_0 & \beta_0 & 0 & 0 & 0 \\ \beta_0 & \epsilon_2 & 0 & 0 & \beta_1 & 0 & 0 \\ \beta_0 & 0 & \epsilon_2 & 0 & 0 & \beta_1 & 0 \\ \beta_0 & 0 & 0 & \epsilon_2 & 0 & 0 & \beta_1 \\ 0 & \beta_1 & 0 & 0 & \epsilon_1 & 0 & 0 \\ 0 & 0 & \beta_1 & 0 & 0 & \epsilon_1 & 0 \\ 0 & 0 & 0 & \beta_1 & 0 & 0 & \epsilon_1 \end{vmatrix}$$

and

$$\hat{H}_i = \begin{vmatrix} 0 & \beta_1 & \beta_1 & 0 & 0 \\ \beta_1 & \epsilon_2 & 0 & \beta_1 & 0 \\ \beta_1 & 0 & \epsilon_2 & 0 & \beta_1 \\ 0 & \beta_1 & 0 & \epsilon_1 & 0 \\ 0 & 0 & \beta_1 & 0 & \epsilon_1 \end{vmatrix}$$

where the on-site energies of the central, benzene, and bridging nodes are given (respectively) by ϵ_0 , ϵ_1 , and ϵ_2 ; the central-bridging and bridging-benzene overlaps are given by β_0 and β_1 . These two matrices may now be reduced to 4×4 and 3×3 matrices via Löwdin decomposition;²⁷ the reduced matrices will have the same form as the matrices in the DEVO algorithm, with the non-zero entries now algebraic combinations of the various elements of the original matrices. The DEVO algorithm only requires that the two matrices have the form shown above, so it works perfectly well with the reduced matrices of the bridged dendrimer.

DEVO is also applicable for extended dendrimers, which have a number of disubstituted benzene nodes between branching benzene nodes of successive generations. We chose to include these disubstituted nodes directly in the algorithm (rather than calculating effective matrix elements as above) because the electron population of these new nodes was of interest to us. Each set of interstitial nodes introduces a tridiagonal matrix into the decomposition of the Hamiltonian, since these new nodes—

along with the branching nodes at each end—form a linear chain. These tridiagonal matrices are used to construct sub-propagators which are inserted at the proper place in the DEVO evolution cascade.

The development of a time-evolution algorithm like DEVO is motivated by the fact that the Hamiltonian is explicitly time-dependent as a result of the solvent induced fluctuations; the use of many small matrices speeds up the diagonalization process, allowing several updates without making the simulation run-time prohibitively long. This formalism also works well in simulations where, due to steric or other factors, the effect of the solvent is spatially anisotropic.

Appendix B

For the three different three-generation extended structures—(14), (33), and (52)—explicit algebraic formulae for the effective coupling elements (ECE) between the central node and a node in the outer generation can be calculated. This is done via the Lowdin decomposition;²⁷ in each case the Hamiltonian matrix representing an entire branch of the dendrimer is reduced to a 4×4 matrix for the central node, the single branching node, and the two nodes on the outer layer. (For details on these structures, see Figure 1.) In the following formulae, the on-site energy of benzene nodes is denoted by a ; the energy scale is assumed to be shifted such that the on-site energy of the donor-acceptor nodes is zero. The benzene-benzene overlap is given by b , and B is the overlap between a benzene node and a donor-acceptor node (although the outer layer of nodes in most of our simulations were benzenes, we included the more general case in these calculations for completeness.). For clarity, D_n denotes the determinant of an $n \times n$ tridiagonal matrix with a on the main diagonal and b on both subdiagonals.

The three ECE are

$$(14) = \frac{\left(\frac{B^2 D_3}{D_4}\right) \left(\frac{Bb}{a}\right) \left(\frac{Bb^4}{D_4}\right)}{\left[a - \frac{b^2}{a} - \frac{2b^2 D_3}{D_4}\right] \left(\frac{B^2 D_3}{D_4}\right) + \left(\frac{Bb^4}{D_4}\right)^2}$$

$$(33) = \frac{\left(\frac{B^2 D_2}{D_3}\right) \left(\frac{Bb^3}{D_3}\right)^2}{\left[\frac{3bD_2}{D_3} - a\right] \left(\frac{B^2 D_2}{D_3}\right) - \left(\frac{Bb^3}{D_3}\right)^2}$$

$$(52) = \frac{\left(\frac{aB^2 b^3}{D_5}\right) \left(\frac{Bb^2}{D_2}\right)^2}{\left[\frac{2ab^2}{D_2} + \frac{b^2 D_4}{D_5} - a\right] \left(\frac{aB^2}{D_2}\right) - \left(\frac{Bb^2}{D_2}\right)^2}$$

For the relative energies used in our simulations (the magnitude of the overlap matrix elements never more than 25% of the on-site energy) the difference between these three ECE is negligible. There are quantitative changes if the outer layers are taken to be benzene rings rather than acceptor nodes, but

the difference between the ECE for these three structures are still essentially equal in magnitude.

References and Notes

- (1) (a) Wooley, K. L.; Hawker, C. J.; Pochan, J. M.; Frechet, J. M. J. *Macromolecules* **1993**, *26*, 1515; (b) Tomalia, D. A.; Naylor, A. M.; Goddard, W. A. III. *Angew. Chem. Int. Ed. Engl.* **1990**, *29*, 138; (c) Tomalia, D. A.; Durst, H. D. *Top. Curr. Chem.* **1993**, *165*, 192; (d) Mansfield, M. L. *Polymer* **1997**, *38*, 1827.
- (2) Ziman, J. M. *Models of Disorder*; Cambridge University Press, Cambridge, U.K., 1979.
- (3) Moore, J. S.; Wang, P.; Liu, Y.; Devadoss, C.; Bharathi, P. *Adv. Mater.* **1996**, *8*, 237.
- (4) (a) Barhaim, A.; Klafter, J.; Kopelman, R. *J. Am. Chem. Soc.* **1997**, *119*, 6197; (b) Barhaim, A.; Klafter, J. *J. Phys. Chem. B* **1998**, *102*, 1662; (c) Barhaim, A.; Klafter, J. *J. of Lumin.* **1998**, *76*, 197.
- (5) (a) Murat, M.; Grest, G. S. *Macromolecules*, **1996**, *29*, 1278; (b) Mansfield, M. L.; Klushin, L. I. *Macromolecules* **1993**, *26*, 4262.
- (6) Miklis, P.; Cagin, T.; Goddard, W. A. *J. Am. Chem. Soc.* **1997**, *119*, 7458.
- (7) Risser, S. M.; Beratan, D. N.; Onuchic, J. N. *J. Phys. Chem.* **1993**, *97*, 4523.
- (8) Skourtis, S. S.; Onuchic, J. N.; Beratan, D. N. *Inorg. Chim. Acta* **1996**, *243*, 167.
- (9) (a) Shortreed, M. R.; Swallen, S. F.; Shi, Z. Y.; Tan, W. H.; Xu, Z. F.; Devadoss, C.; Moore, J. S.; Kopelman, R. *J. Phys. Chem. B* **1997**, *101*, 6318; (b) Shortreed, M. R.; Shi, Z. Y.; Kopelman, R. *Mol. Cryst. and Liq. Cryst. Sci. Tech. A*, **1996**, *283*, 95.
- (10) Barhaim, A.; Klafter, J. *J. Chem. Phys.* **1998**, *109*, 5187.
- (11) Kopelman, R.; Shortreed, M.; Shi, Z. Y.; Tan, W. H.; Xu, Z. F.; Moore, J. S.; Barhaim, A.; Klafter, J. *Phys. Rev. Lett.* **1997**, *78*, 1239.
- (12) For example: (a) Tomalia, D. A.; Baker, H.; Dewald, J. R.; Hall, M.; Kallos, G.; Martin, S.; Roeck, J.; Ryder, J.; Smith, P. *Polym. J.* **1985**, *17*, 117; (b) Jayaraman, M.; Frechet, J. M. J. *J. Am. Chem. Soc.* **1998**, *120*, 12996.
- (13) For example: (a) Hawker, C. J.; Wooley, K. L.; Frechet, J. M.; *J. Chem. Soc., Perkin Trans.* **1993**, *12*, 1287. (b) Huck, W. T. S.; Prins, L. J.; Fokkens, R. H.; Nibbering, N. M. M.; Vanveggel, F. C. J. M.; Reinhoudt, D. N. *J. Am. Chem. Soc.* **1998**, *120*, 6240.
- (14) (a) Mukamel, S.; Tretiak, S.; Wagersreiter, T.; Chernyak, V. *Science* **1997**, *277*, 781. (b) Chernyak, V.; Mukamel, S. *J. Chem. Phys.* **1996**, *104*, 444. (c) Tretiak, S.; Chernyak, V.; Mukamel, S. *J. Chem. Phys.* **1996**, *105*, 8914.
- (15) Tretiak, S.; Chernyak, V.; Mukamel, S. *J. Phys. Chem. B* **1998**, *102*, 3310.
- (16) (a) Gorman, C. B. *Adv. Mater.* **1997**, *9*, 1117. (b) Gorman, C. B.; Parkhurst, B. L.; Su, W. Y.; Chen, K-Y. *J. Am. Chem. Soc.* **1997**, *119*, 1141.
- (17) Sadamoto, R.; Tomioka, N.; Aida, T. *J. Am. Chem. Soc.* **1996**, *118*, 3978.
- (18) Kimura, M.; Nakada, K.; Yamaguchi, Y.; Hanabusa, K.; Shirai, H.; Kobayashi, N. *Chem. Comm.* **1997**, *13*, 1215.
- (19) Janssen, R. A.; Jansen, J.; van Haare, J. A. E. H.; Meijer, E. W. *Adv. Mater.* **1996**, *8*, 494.
- (20) Devadoss, C.; Bharathi, P.; Moore, J. S. *Macromolecules* **1998**, *31*, 8091.
- (21) (a) Felts, A. K.; Pollard, W. T.; Friesner, R. A. *J. Phys. Chem.* **1995**, *99*, 2929. (b) Pollard, W. T.; Friesner, R. A. *J. Chem. Phys.* **1994**, *100*, 5054.
- (22) Yates, K. *Huckel Molecular Orbital Theory*; Academic Press, New York, 1978.
- (23) Davis, W. B.; Wasielewski, M. R.; Ratner, M. A.; Mujica, V.; Nitzan, A. *J. Phys. Chem. A* **1997**, *101*, 6158.
- (24) (a) Evensky, D. A.; Scalettar, R. T.; Wolynes, P. G. *J. Phys. Chem. B* **1990**, *94*, 1149. (b) Evensky, D. A.; Wolynes, P. G. *Chem. Phys. Lett.* **1993**, *209*, 185.
- (25) Economou, E. N. *Green's Functions in Quantum Physics*; Springer: New York, 1994.
- (26) (a) Hill, N. A.; Whaley, K. B. *Chem. Phys.* **1996**, *210*, 117; (b) Hill, N. A.; Whaley, B. *J. Chem. Phys.* **1993**, *99*, 3707.
- (27) Löwdin, P. O. *J. Mol. Spectrosc.* **1963**, *10*, 12; *J. Math. Phys.* **1962**, *3*, 969.
- (28) Poliakov, E. Y.; Chernyak, V.; Tretiak, S.; Mukamel, S. *J. Chem. Phys.* **1999**, *110*, 8161.

Computer Simulation of the Excited State Dynamics of Betaine-30 in Acetonitrile

John Lobaugh and Peter J. Rossky*

Department of Chemistry and Biochemistry, University of Texas at Austin, Austin, Texas 78712-1167

Received: May 17, 1999

Time-dependent studies of the excited state dynamics of betaine-30 in acetonitrile at room temperature have been carried out using a mixed classical/quantum molecular dynamics simulation methodology. The π -electron system of the solute molecule is treated quantum mechanically using the semiempirical Pariser–Parr–Pople Hamiltonian, including the solvent influence on electronic structure. The remaining interactions are treated via empirical potentials. Transition probabilities between adiabatic electronic states are evaluated using surface hopping methods, including all nuclear degrees of freedom in the coupling. The dynamics treats the (rigid) solvent and the dihedral angles for relative rotation of rings of an otherwise rigid solute classically. The contribution of all remaining solute intramolecular vibrations is included in the nonadiabatic coupling via an approximate, but purely quantum mechanical, treatment. Analysis of the dynamics reveals that, after excitation to the first excited state, the energy gap between ground and first excited states of the molecule exhibits an ultrafast (~ 100 fs) decrease due to the inertial response of the solvent that accounts for about 70% of the solvent response, followed immediately by a further subpicosecond solvent component. The times and amplitudes of these solvation components are in accord with the results inferred from resonance Raman spectra, and the solvent contribution to the Stokes shift observed is in accord with values inferred from ground state absorption spectral line shape analysis. However, we also find that the energy gap exhibits a slower picosecond time scale response of comparable magnitude due to relative rotation of the central phenolate and pyridinium rings. This relaxation has not been previously noted or incorporated in corresponding electron transfer models. Analysis of contributions to the electronic nonadiabatic coupling shows that this is dominated by a small set of high-frequency intramolecular modes of the betaine-30 molecule, with the solvent making a relatively very small contribution, also in agreement with previous experimental inference.

I. Introduction

Both ultrafast spectroscopy and modern theory have played major roles in the elucidation of the details and mechanisms of intramolecular electron transfer (ET) in solution. In particular, over the last 2 decades, the elucidation of the relative importance of the contributions of solvent dynamics and of intramolecular modes to ET rates is an issue that has been pursued in numerous theoretical and experimental studies.¹ Contemporary theories of ET have typically treated the role of solvent on the level of a dielectric continuum characterized by a Debye relaxation spectrum with a single characteristic relaxation time. The inclusion of inner sphere vibrational modes has been done classically^{2,3} or quantum mechanically.⁴ A common feature of these theories is that they predict a strong correlation of the ET rate in barrierless cases with the relaxation time characteristic of the solvent.^{5–8} Nonetheless, a number of ultrafast ET reactions have been found to exhibit rates that vastly exceed time scales for diffusional solvation dynamics.^{9–13} Ultrafast components of solvent dynamics as well as inner sphere modes or intramolecular vibrations have been posited as mechanisms that can give rise to ET times that are faster than solvent diffusional relaxation times.^{1,14}

A particular molecular solute where the kinetics of ET have been explored in a relatively comprehensive series of experiments is betaine-30. The betaines consist of a covalently bound, charge separated, ground state, shown schematically in Figure 1. The large sensitivity of the lowest energy electronic transition to the local molecular environment has been exploited as the

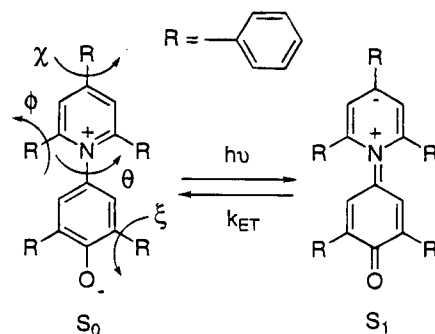


Figure 1. Schematic of the optically induced ground to first excited state electronic transition and the subsequent reverse electron transfer.

basis for the E_T solvent polarity scales,^{15,16} as a probe of micelle/solution interfaces,¹⁷ and as a probe in other applications in analytical chemistry.^{18,19} ET occurs after photoexcitation of the highly polar S_0 ground state to the less polar S_1 state of the molecule, as shown schematically in Figure 1. The subsequent kinetics of the photoexcited system have been measured via ultrafast absorption spectroscopy in a series of experiments in polar aprotic solvents^{20–26} and alcohols.¹¹ In these experiments, it was found that the rates for the $S_1 \rightarrow S_0$ relaxation followed characteristic average solvent response times in polar aprotic solvents,¹¹ with the ET rates in fast aprotic solvents comparable to the solvent dynamical times. However, in slow solvents, these ET rates were found to far exceed inverse solvation times. In alcohols, an additional faster solvent dynamical contribution was inferred to contribute to the ET dynamics.¹¹

The observed ET kinetics of the system have been interpreted in terms of a hierarchy of theoretical formalisms for ET rates which focus on the quantitative role of medium dynamics and of solute intramolecular modes. The limitations and successes of each description in reproducing experimental trends have been effectively used to delineate underlying mechanistic aspects of the rates and to point out remaining uncertainties. It is these uncertainties that motivate large scale simulations of the type we pursue in the present work. To delineate the key open issues, as well as to point out those results that one should expect to be correctly described by a valid model, we briefly review various theoretical modeling efforts. The formulation of Sumi and Marcus^{2,3} treats the reaction dynamics via a medium coordinate dependent ET rate with a diffusional evolution of the medium coordinate and treats all modes classically. Application of the formulation, with appropriate modification for the nonequilibrium initial conditions appropriate to the photo-initiated ultrafast experiments,²⁴ was found to fall short of the observed rates by orders of magnitude. This result was not surprising since the enhancement of the rate of ET in the strongly inverted regime via high-frequency inner sphere/intramolecular modes had been appreciated earlier. In particular, for the inverted regime, high-frequency vibrationally excited states of the product manifold can provide reaction channels with relatively small activation energies. The explicit incorporation of this effect into a theory which also incorporates solvent dynamics (at the level of a single characteristic solvent response time) was accomplished in the formulation of Jortner and Bixon.⁴ There, the rate is described as a sum over product vibronic channels of a rate that incorporates solvent diffusional dynamics. Although the rates for the betaine-30 transition evaluated via this formulation were much greater than those obtained via the Sumi-Marcus expression, the rates failed to manifest the apparent transition in the rate-limiting process from solvent dynamical control in fast solvents to one relying primarily on high-frequency intramolecular vibrations at low temperature, where the solvent response is far slower than the ET rate.²⁴

A hybrid model formulated by Barbara and collaborators^{20,24} incorporates the diffusive dynamics of the Sumi-Marcus model, the vibronic channels of the Jortner-Bixon model, and a very rapidly responding classical intramolecular relaxation of the solute. The low-frequency intramolecular component provides a Gaussian energy width to the individual vibronic channels for any value of the solvent coordinate. This model was able to capture the temperature and solvent dependence of the experimental data in polar aprotic solvents using parameters derived from modeling of static spectra. Nevertheless, it was argued more recently^{27,28} that, to properly describe the ET dynamics of these systems, one must include the fact that the solvents relax on multiple time scales, a potential limitation of the simple hybrid model that had been noted by its developers.²⁴ In particular, it is widely appreciated that the response of polar solvents to rapid perturbation in the solute-solvent interaction includes at least one relaxation time that is far faster than the diffusive time scale of the complete relaxation.²⁹ This very rapid component can account for a majority of the solvent relaxation dynamics. In many cases, this is the initial so-called inertial, or Gaussian, time scale, but it need not be, as in methanol, where a subpicosecond exponential component is manifest. These results for solvation dynamics have been demonstrated in numerous ways, through experimental transient Stokes shift measurements,³⁰⁻³³ via molecular dynamics (MD) simulations,³⁴⁻³⁶ and via molecular theories of solvation dynamics.³⁷⁻⁴⁰

If the use of a multiple time scale solvent response is critical, then one could also infer that an important limitation of the Jortner and Bixon vibronic formulation⁴ is that to a single average response time, which can be far longer than that actually dominating the dynamics. It has in fact been argued that the regime of solvent response that is critical to the ET rate varies with the size of the activation barrier.²⁷ In contrast, Bixon and Jortner have presented clear theoretical arguments that activationless ET should, in fact, have only a weak dependence on the excess energy above the diabatic curve crossing.⁴¹ Since the contributing vibronic channels in the strongly inverted regime should correspond to nearly activationless transitions to vibrationally hot ground states, then, by analogy, they argue that rates in the strongly inverted regime also have only a very weak dependence on excess energy, and hence on solvent relaxation dynamics.

In fact, in alcohols,¹¹ the hybrid model noted above was only able to mimic experiment if the initial conditions for the solvent coordinate were relaxed by a significant fraction essentially instantaneously. These authors attributed this deviation from the original hybrid model to a fast reorganization of the solvent-solute hydrogen bonding, although they tentatively identified the effect on the electronic transition rate with a concomitant change in Franck-Condon factors associated with solute-solvent vibrations, rather than with ultrafast components of the solvation response per se.

Given the discussion above, it is clear that even in this relatively well studied case, important questions remain. The regime where solvent dynamics plays the dominant role is not clearly established, and the importance of alternative time scales for solvent relaxation is unclear. The role of intramolecular vibrations, particularly low-frequency vibrations, is uncertain, and the physical identity of such putative modes is not known. At the most basic level, there is a lack of detail about the potential energy surface on which the ground and excited-state electronic relaxation processes occur prior and after the ET event. Such details would be of great interest in making close and informative connections with recent resonance Raman studies of this system.⁴² Such Raman studies can reveal aspects of both solvent dynamics and intramolecular nuclear-electronic couplings. The models discussed above also use only one or two effective vibrational modes. This simplification makes implementation readily accessible, but the validity in describing ET dynamics quantitatively is unknown.

These issues can be addressed by detailed molecular level simulations that include the important quantum mechanical degrees of freedom explicitly and a suitable algorithm to treat nonadiabatic (NA) transitions between states. Here, we develop and implement a practical model and algorithm which includes all intramolecular and solvent degrees of freedom and an explicit treatment of solute electronic structure. The treatment of the electronic problem and its interface with the classical solvent and classical modes of the solute is described in more detail elsewhere;⁴³ the approach we use is very similar in spirit to that introduced long ago by Warshel and co-workers.^{44,45} For the electronic dynamics, we implement the surface hopping method of Tully (molecular dynamics with quantum transitions, MDQT),⁴⁶ where the system evolves on one electronic surface at any time and hops stochastically between surfaces based on the state-to-state transition amplitudes. The treatment of high-frequency intramolecular vibrations used here is quite simplified, but the extension to a more realistic treatment is described. The algorithm is applied to the $S_1 \rightarrow S_0$ ET dynamics in acetonitrile. We explore the roles of multiple time scale solvent response

and of the underlying solute potential surface and intramolecular modes in the dynamics. We also examine the character of the promoting modes responsible for stimulating the transition, including consideration of *all* solution degrees of freedom.

The paper is organized as follows. In section II, we describe the methodology developed for this study. The methodology represents one of the main contributions of this work. Section III reports and discusses the results derived from the excited-state trajectories of betaine-30. The conclusions are given in section IV. We include a set of appendices that give the details related to the algorithmic development.

II. Methodology

The computational expense of treating even a limited number of degrees of freedom quantum mechanically in a molecular dynamics (MD) simulation necessitates the use of approximate methods of electronic structure. Elsewhere, we have developed a MD model of betaine-30⁴³ which includes the π electron degrees of freedom of the molecule and treats the remaining electrons and nuclei as effective classical nuclear cores. The π system is treated with the semiempirical Pariser–Parr–Pople (PPP) SCF method^{47–49} with single excitation configuration interaction (CI). The intramolecular degrees of freedom are constrained to be rigid, with the exception of rotation around the six dihedral angles defining the relative orientation of the seven rings (see Figure 1). These angles and the solute center of mass and overall rotation are treated classically. The solvent molecules are also treated classically and modeled by the MD parametrization for acetonitrile of Edwards, Madden, and McDonald.⁵⁰ The electrostatic potential produced by the solvent molecules couples to the betaine-30 electronic degrees of freedom via a one electron contribution to the diagonal elements of the Fock matrix. The transition energies are calculated using single CI, which has proven to be very accurate in the PPP method in the calculation of transition energies of heteronuclear aromatic molecules.⁵¹ The model has proven to be accurate in calculating the wavelength, intensity, and bandwidth of the lowest energy transition of betaine-30 in acetonitrile, as well as the shift in these compared to a nonpolar medium.⁴³ In particular, the width and band shape of the lowest energy absorption (i.e., $S_0 \rightarrow S_1$) are well reproduced by the model when compared to that found from the experimental spectrum in acetonitrile after removal of the vibronic contribution to the band shape found from experiment. These facts indicate that the treatment of the wave function and solvent for the ground and lowest excited states of the molecule in solution are sufficiently accurate for an examination of excited-state relaxation processes.

Calculation of the Excited-State Forces. The reader is referred to ref 43 for complete details of the PPP Hamiltonian used for betaine-30. The derivation of adiabatic excited-state forces, required for the relevant dynamics, using this Hamiltonian is now discussed. The excited-state energies were calculated using single excitation configuration interaction. The single excitation configurational wave functions $|\psi_{i \rightarrow a}\rangle$ have matrix elements

$$\langle \psi_{i \rightarrow a} | (H_{el} - V_\pi) | \psi_{j \rightarrow b} \rangle = \delta_{ij} \delta_{ab} (\epsilon_a - \epsilon_i) + \sum_{\mu\nu} c_\mu^j c_\nu^a (2c_\mu^b c_\nu^i - c_\mu^i c_\nu^b) \gamma_{\mu\nu} \quad (1)$$

where H_{el} is the total *electronic* Hamiltonian, which includes the electron kinetic energy and electron–electron interactions as well as the electron–core and electron–solvent interactions,

and the term V_π is the SCF ground-state energy eigenvalue (see eq 2 of ref 43). The terms ϵ_i and $\{c^i\}$ are the molecular orbital (MO) energy and coefficients of the i th p-type orbital. The functional form of the two electron repulsion matrix element, $\gamma_{\mu\nu}$, is given by the Mataga–Nishimoto relationship⁵² in our calculations. The total energy of the system when the betaine-30 is in the l th CI state is given by

$$E_{TOT}^l = K + V_{TOT} + E_{CI}^l \quad (2)$$

where K is the total kinetic energy of the classical degrees of freedom of the system, V_{TOT} is the total ground-state potential, and E_{CI}^l is the l th eigenvalue of the CI matrix defined by eq 1. The total ground-state potential is given by

$$V_{TOT} = V_\pi + V_{C-C} + V_{S-S} + V_{C-S} \quad (3)$$

where the terms V_{C-C} , V_{S-S} , and V_{C-S} denote the core–core interactions of the betaine-30, the solvent–solvent, and core–solvent interactions, respectively. Complete details of the terms that make up eq 3 are given in ref 43. When the system is in the l th excited state, the force on a nuclear coordinate R (which can be either a solvent or betaine-30 atom) is given by

$$F_R = -\frac{\partial}{\partial R} (V_{TOT} + \sum_{mn} C_m^l C_n^l A_{nm}) \\ = -V_{TOT}^{(R)} - \sum_{mn} C_m^l C_n^l \frac{\partial}{\partial R} A_{nm} \quad (4)$$

where the CI energy has been rewritten in terms of its eigenvector coefficients $\{C^l\}$ and matrix elements given by eq 1, where an excitation involving promotion of an electron from an occupied orbital i to an unoccupied orbital a has been replaced by a single index n . Accordingly, the l th CI eigenvector vector is written as

$$|\Psi_l\rangle = \sum_n C_n^l |\psi_n\rangle \quad (5)$$

The symbol $X^{(R)}$ (e.g., $V_{TOT}^{(R)}$ in eq 4) denotes that the derivative is taken with respect to R while neglecting the coordinate dependence of the MO coefficients in X in evaluating the derivative. As noted elsewhere,^{53,54} the ground-state SCF energy is a variational minimum with respect to the MO coefficients; hence, no terms due to gradients of the molecular orbital expansion coefficients contribute to the ground-state nuclear forces (i.e., $\partial/\partial R V_{TOT} = V_{TOT}^{(R)}$). Likewise, the CI energy is a variational minimum with respect to the CI eigenvector coefficients; hence, their coordinate dependence can be neglected in eq 4. However, derivatives of the matrix elements A_{nm} require evaluation of gradients of the MO coefficients. These can be approached through the use of the coupled perturbed Hartree–Fock (CPHF) equations,⁵⁵ wherein a derivative of a MO coefficient is reexpressed in terms of derivatives of unitary transformation matrix elements:

$$\frac{\partial c_\mu^a}{\partial R} = \sum_l c_\mu^l u_{la}^R \quad (6)$$

The sum in the above equation extends over both real and virtual MOs. Using this relation, the final term of eq 4 can be shown to be^{53,56}

$$\sum_{mn} C_m^J C_n^J \frac{\partial}{\partial R} A_{nm} = \sum_{mn} C_m^J C_n^J A_{nm}^{(R)} + 2 \sum_{ks} u_{ks}^R \xi_{ks}^J \quad (7)$$

where the sum over m, n is over the space of one-electron excitations, the sum over k, s is over all occupied and unoccupied molecular orbitals, and ξ^J is the Lagrangian matrix where the changes of CI energy with respect to the MO coefficients are collected. Note that the matrix ξ^J is independent of which particular nuclear derivative is being calculated and need only be calculated once. It is, however, a function of the CI eigenvector coefficients $\{C^J\}$ and therefore must be calculated for each CI state. The first-order unitary transformation matrix derivatives are found through solving the CPHF equations, which for a closed-shell system are written as⁵⁵

$$(\epsilon_p - \epsilon_q) u_{qp}^R = B_{qp}^R + \sum_a \sum_i^{\text{virtual real}} A_{ai, qp} u_{qp}^R \quad (8)$$

where the vector B^R and matrix A are given in Appendix A. The efficient computation of the term $2 \sum_{ks} u_{ks}^R \xi_{ks}^J$ using the so-called Z vector method is also outlined in Appendix A.

Elements of the Nonadiabatic Dynamics Method. In this section, the details and algorithm for implementing the MDQT method⁴⁶ in the present context are described. We first outline how the method is implemented with the MD model for betaine-30 and the PPP semiempirical electronic structure approach used for the electronic degrees of freedom. In the MDQT method, or in adiabatic dynamics, the single state adiabatic force given by eq 4 is used to evolve the nuclear trajectory. The Schrödinger equation for the electronic degrees of freedom \mathbf{r} for a given configuration of nuclear coordinates \mathbf{R} is given by

$$H_{el}(\mathbf{R}; \mathbf{r}) |\Psi_I(\mathbf{R}; \mathbf{r})\rangle = (E_{CI}^I(\mathbf{R}) + V_\pi(\mathbf{R})) |\Psi_I(\mathbf{R}; \mathbf{r})\rangle \quad (9)$$

Here, the quantum mechanical state of the system is expanded in the adiabatic CI states

$$|\Phi(\mathbf{R}, \mathbf{r}, t)\rangle = \sum_I B_I(t) |\Psi_I\rangle \quad (10)$$

Using the time-dependent Schrödinger equation, equations of motion for the expansion coefficients, $B_I(t)$, can be derived

$$i\hbar \dot{B}_I = B_I (E_{CI}^I + V_\pi) - i\hbar \sum_J B_J \dot{\mathbf{R}} \cdot \mathbf{d}_{IJ} \quad (11)$$

where \mathbf{d}_{IJ} is the NA coupling vector given by

$$\mathbf{d}_{IJ} = \langle \Psi_I | \nabla_R \Psi_J \rangle \quad (12)$$

It should be noted that the ground state is included in the total expansion of the wave function in the above expansion. Since the ground-state Slater determinant does not couple to the single excitation configurations, we have, using the notation in eq 5,

$$|\Psi_0\rangle = \sum_n C_n^0 |\psi_n\rangle = C_0^0 |\psi_0\rangle = |\psi_0\rangle \quad (13)$$

where $|\psi_0\rangle$ is the ground-state Slater determinant.

For numerical convenience, one can define

$$\tilde{B}_I = B_I \exp\left(\frac{i}{\hbar} \int_0^t dt' V_\pi\right) \quad (14)$$

Equation 11 then becomes

$$i\hbar \dot{\tilde{B}}_I = \tilde{B}_I E_{CI}^I - i\hbar \sum_J \tilde{B}_J \dot{\mathbf{R}} \cdot \mathbf{d}_{IJ} \quad (15)$$

The NA coupling vector can be expressed in a form suitable for the semiempirical formulation used here by expanding the CI states in terms of their electronic configurations as given in eq 5

$$\begin{aligned} \mathbf{d}_{IJ} &= \sum_{nm} C_n^J \nabla_R C_m^J \langle \psi_n | \psi_m \rangle + \sum_{nm} C_n^J C_m^J \langle \psi_n | \nabla_R \psi_m \rangle \\ &= \sum_n C_n^J \nabla_R C_n^J + \sum_{nm} C_n^J C_m^J \langle \psi_n | \nabla_R \psi_m \rangle \end{aligned} \quad (16)$$

The first term of eq 16 can be further simplified by using the fact that the CI states diagonalize the Hamiltonian within the space of one-electron excitations, viz.,

$$\langle \Psi_I | (H_{el} - V_\pi) | \Psi_J \rangle = 0 \quad (17)$$

Taking the derivative of this expression, we have

$$\begin{aligned} \nabla_R \langle \Psi_I | (H_{el} - V_\pi) | \Psi_J \rangle &= \sum_{mn} \nabla_R C_n^J C_m^J A_{nm} + \sum_{mn} C_n^J \nabla_R C_m^J A_{nm} + \sum_{mn} C_n^J C_m^J \nabla_R A_{nm} \\ &= E_{CI}^J \sum_n C_n^J \nabla_R C_n^J + E_{CI}^I \sum_m C_m^J \nabla_R C_m^J + \sum_{mn} C_n^J C_m^J \nabla_R A_{nm} \end{aligned} \quad (18)$$

Then, using the orthonormality of the CI states, one can show that

$$\sum_n C_n^J \nabla_R C_n^J = - \sum_n C_n^J \nabla_R C_n^I \quad (19)$$

Substituting this relation into eq 18 and rearranging terms, it can be shown that the first term of eq 16 can be written as

$$\sum_n C_n^J \nabla_R C_n^J = \frac{\sum_{mn} C_n^J C_m^J \nabla_R A_{nm}}{(E_{CI}^I - E_{CI}^J)} \quad (20)$$

Simplification of the gradient terms $\langle \psi_n | \nabla_R \psi_m \rangle$ in the second term in eq 20 is done in Appendix B. The gradient terms $\langle \psi_n | \nabla_R \psi_m \rangle$ are zero if the wave functions differ by more than one spin-orbital. Hence, the only nonzero terms in the second term in eq 16 will be (see Appendix B)

$$\begin{aligned} \langle \psi_{i-a} | \nabla_R \psi_0 \rangle &= \sqrt{2} \sum_\mu c_\mu^i \nabla_R c_\mu^a \\ \langle \psi_{i-b} | \nabla_R \psi_{i-a} \rangle &= \sqrt{2} \sum_\mu c_\mu^b \nabla_R c_\mu^a \\ \langle \psi_{i-a} | \nabla_R \psi_{j-a} \rangle &= \sqrt{2} \sum_\mu c_\mu^j \nabla_R c_\mu^i \end{aligned} \quad (21)$$

As with the calculation of the adiabatic force, the derivatives in the above equation can be expanded in terms of the unitary transformation matrix elements. Combining these results the components of the NA coupling vector can be written

$$\begin{aligned}
\left\langle \Psi_I \left| \frac{\partial}{\partial R} \right| \Psi_J \right\rangle &= d_{IJ}^R \\
&= \sum_n C_n^I \frac{\partial}{\partial R} C_m^J + \sum_{nm} C_n^I C_m^J \left\langle \psi_n \left| \frac{\partial}{\partial R} \right| \psi_m \right\rangle \\
&= \frac{\sum_{mn} C_n^I C_m^J \frac{\partial}{\partial R} A_{nm}}{(E_{CI}^J - E_{CI}^I)} + \sum_{nm} C_n^I C_m^J \left\langle \psi_n \left| \frac{\partial}{\partial R} \right| \psi_m \right\rangle \quad (22) \\
&= \frac{\sum_{mn} C_n^I C_m^J A_{nm}^{(R)}}{(E_{CI}^J - E_{CI}^I)} + 2 \sum_{ks} u_{ks}^R \xi_{ks}^{IJ}
\end{aligned}$$

where the changes of the MO coefficients with respect to the nuclear coordinate in the NA coupling from the first and second terms of eq 16 have been collected in the vector ξ^{IJ} . The vector ξ^{IJ} is a function of the CI eigenfunction coefficients $\{C^I\}$ and $\{C^J\}$. The efficient calculation of the term $2 \sum_{ks} u_{ks}^R \xi_{ks}^{IJ}$ can be carried out using a modification of the Z vector method of Handy and Schaefer⁵⁶ and is outlined in Appendix A.

The high-frequency intramolecular degrees of freedom of betaine-30 play an important role in determining the absorption width of the S_0 to S_1 transition by giving rise to a vibronic progression which is manifest as a broadening of the absorption on the high-frequency side. An estimate of the corresponding inner sphere reorganization energy found from fits of the absorption spectrum is approximately 720 cm^{-1} with a single effective frequency of approximately 1600 cm^{-1} .²⁰ This effective quantum mechanical mode also appears to play a critical role in providing an efficient channel for the reverse electron transfer (i.e., $S_1 \rightarrow S_0$) in model calculations, as noted in the Introduction. Given the expectation that quantum intramolecular modes play an important role in the electron-transfer process that is being modeled here, an inclusion of quantum intramolecular modes of betaine-30 and how they couple the electronic states of the molecule is necessary. As noted earlier, the MD model that is used here explicitly includes only those intramolecular vibrations associated with relative rotational motions of the rings of the molecule. The remaining degrees of freedom are frozen out by the use of constraints.⁵⁷ Further, a quantum mechanical description of the remaining modes is evidently required, based on model calculations.^{4,24} A complete quantum mechanical description of the internal modes and their dynamics would require expanding the wave function in eq 10 in internal coordinates q , as

$$|\Phi(\mathbf{R}, \mathbf{r}, \mathbf{q}, t)\rangle = \sum_{I,\alpha} B_{I,\alpha}(t) |\Psi_I(\mathbf{R}, \mathbf{r}, \mathbf{q})\rangle |\xi_{I,\alpha}(\mathbf{q})\rangle \quad (23)$$

where the total wave function is expanded in internal vibrational state basis functions in addition to the electronic basis functions. The expressions that result from substitution into the time-dependent Schrödinger equation are given in ref 58. Such a scheme is complex because of the large number of coupled equations that result, and additional approximations are highly desirable to put the equations in a form tractable for the present purposes. Here, we focus on incorporation of the additional NA coupling that arises due to the intramolecular quantum degrees of freedom.

We begin with the NA coupling between two electronic state I and J given by the matrix element of the nuclear kinetic energy operator. Conventionally, in mixed quantum classical simula-

tions, the semiclassical expression for this matrix element is used, as given in eqs 11 and 15,

$$V_{IJ} = -i\hbar \dot{\mathbf{R}} \cdot \mathbf{d}_{IJ} \quad (24)$$

This form suffices for the coupling due to the solvent degrees of freedom and the internal relative ring rotations. Here, we add the remaining NA coupling due to the intramolecular degrees of freedom a posteriori to the equations of motion for the electronic basis state expansion such that for given vibronic states,

$$i\hbar \dot{\tilde{B}}_I = \tilde{B}_I E_{CI}^I - i\hbar \sum_J \tilde{B}_J \left(\dot{\mathbf{R}} \cdot \mathbf{d}_{IJ} - \frac{V_{IJ}^m}{i\hbar} \right) \quad (25)$$

where the additional coupling has the form

$$\begin{aligned}
V_{IJ}^m &= \left\langle \Psi_I \left| \left\langle \alpha_I \left| \sum_n^{3N-6} -\frac{\hbar^2}{2} \frac{\partial^2}{\partial q_n^2} \right| \beta_J \right\rangle \right| \Psi_J \right\rangle \\
&\approx \sum_n^{3N-6} -\hbar^2 \left\langle \Psi_I \left| \frac{\partial}{\partial q_n} \right| \Psi_J \right\rangle \left\langle \alpha_I \left| \frac{\partial}{\partial q_n} \right| \beta_J \right\rangle \quad (26)
\end{aligned}$$

where $|\beta_J\rangle$ and $|\alpha_I\rangle$ are the nuclear wave functions associated with the initial I th and final J th electronic state, respectively. The kinetic energy operator has been written here in terms of the $3N - 6$ normal modes of the betaine-30 molecule and the second derivative terms due to the nuclear degrees of freedom have been neglected in the second part of eq 26. We assume that the intramolecular nuclear wave function is a direct product of harmonic oscillator wave functions corresponding to the $3N - 6$ internal normal modes of the molecule; that is,

$$|\beta_J\rangle = |\beta_J^1\rangle |\beta_J^2\rangle |\beta_J^3\rangle \cdots |\beta_J^{3N-6}\rangle \quad (27)$$

$\langle \Psi_I | \partial / \partial q_n | \Psi_J \rangle$ is the electronic NA coupling associated with the n th normal mode and the nuclear coupling term $\langle \alpha_I | \partial / \partial q_n | \beta_J \rangle$ factors into

$$\left\langle \alpha_I \left| \frac{\partial}{\partial q_n} \right| \beta_J \right\rangle = \left\langle \alpha_I^n \left| \frac{\partial}{\partial q_n} \right| \beta_J^n \right\rangle \prod_{m \neq n}^{3N-6} \langle \alpha_I^m | \beta_J^m \rangle \quad (28)$$

In a full treatment, we should evaluate the evolution in eq 25 via a sum over all possible channels, with evaluation of the Franck-Condon factors (eq 28) and appropriate account of the energies of each channel through \tilde{B} (cf. eq 14). To do this in an effective manner requires a relatively thorough analysis, identifying the active vibrational modes and their appropriate parametrization in a harmonic model. Such an analysis, with connection to closely related experimental resonance Raman data,⁴² is not undertaken here. Rather, in the present work, we make a very rough approximation that allows us to carry out an initial exploration of the coupling due to the high-frequency modes. Here, we assume that the minima of the internal normal modes of the molecule have the same frequencies in the I th and J th electronic state, and are, further, *not* displaced. Under this approximation, the individual nuclear NA coupling matrix elements correspond only to single quanta changes and the Franck-Condon factors are either unity or zero so that

$$\left\langle \alpha_I \left| \frac{\partial}{\partial q_n} \right| \beta_J \right\rangle = \frac{1}{\hbar} \sqrt{\frac{\hbar \omega_n}{2}} \quad (29)$$

The electronic NA coupling associated with the j th normal mode can be found using the linear transformation coefficients $\{l\}$ between the Cartesian displacement coordinates and the normal modes:

$$\left\langle \Psi_I \left| \frac{\partial}{\partial q_j} \right| \Psi_J \right\rangle = \sum_i \frac{3N \langle l^{-1} \rangle_j^i}{\sqrt{m_i}} \left\langle \Psi_I \left| \frac{\partial}{\partial R_i} \right| \Psi_J \right\rangle \quad (30)$$

where the normal modes are given in terms of the Cartesian displacements of the atoms from their equilibrium positions in mass weighted coordinates,

$$q_i = \sum_j l_j \sqrt{m_j} \Delta R_j^0 \quad (31)$$

The inclusion of the quantum intramolecular contribution to the NA coupling necessitates a modification of the PPP model for betaine-30 in order to account for the distance dependence of the semiempirical π -electron overlap integral, β . The details of this modification are outlined in Appendix E.

The sets of eigenfrequencies $\{\omega\}$ and normal mode transformation coefficients $\{l\}$ for betaine-30 were calculated from an optimized ground-state geometry with MOPAC 6.0⁵⁹ using the AM1 Hamiltonian. The calculation of the displacements along the normal coordinates in eq 31 are made with respect to the minimum energy geometry of the molecule in the reference frame in which the normal modes were calculated:

$$\Delta \mathbf{R}_{B30}^0 = \mathbf{R}_{B30} - \mathbf{R}_{B30}^0 \quad (32)$$

where \mathbf{R}_{B30} is the vector of the betaine-30 atomic positions and \mathbf{R}_{B30}^0 is the minimum energy reference geometry at which the eigenvalues were calculated. The electronic NA coupling elements $\langle \Psi_I | \partial / \partial q_i | \Psi_J \rangle$ can be strongly dependent on the relative rotational orientation of the molecule with respect to the reference geometry of the molecule.⁶⁰ To remove this dependence of the electronic NA coupling elements on overall rotations, the positions, \mathbf{R}_{B30} , and Cartesian elements, $\langle \Psi_I | \partial / \partial R_i | \Psi_J \rangle$, must be expressed in a coordinate system that obeys the Eckart conditions.⁶⁰⁻⁶² This corresponds to applying an overall translation and rotation to the positions, \mathbf{R}_{B30} , and elements $\langle \Psi_I | \partial / \partial R_i | \Psi_J \rangle$ such that the displacements in the six normal modes corresponding to translation and overall rotation are zero. That is,

$$q_j = \sum_i l_i \sqrt{m_i} \Delta R_i^0 = 0 \quad \text{for } j = 3N - 5, 3N - 4, \dots, 3N \quad (33)$$

Details for this procedure are outlined in Appendix C.

Having established the details of the equations of motion for the expansion coefficients given by eq 25, we now outline the MDQT algorithm and modifications that must be made to it for the MD model of betaine-30. The equations of motion for the expansion coefficients $\{\tilde{B}\}$ must be integrated in tandem with the propagation of the MD trajectory for the nuclei. These were integrated from molecular dynamics time step t to the next time step $t + dt$ using a fourth-order Runge-Kutta scheme. Because of the highly oscillatory nature of the coefficients, a much smaller time step was used to integrate eq 25; we use $\delta t = dt/1000$. The computational expense of the calculation of the electronic NA coupling matrix elements precludes calculation of these elements at every one of the smaller time steps. As in

previous implementations,⁶³ these slowly varying coupling elements were linearly interpolated between MD time steps in the integration of the coefficients.

In the fewest switches algorithm,⁴⁶ the probability of a transition occurring between t and $t + dt$ from state K to I can be shown to be

$$P_{K \rightarrow I} = \frac{\int_t^{t+dt} dt b_{IK}(t)}{\tilde{B}_K^*(t) \tilde{B}_K(t)} \quad (34)$$

where

$$b_{IK}(t) = -2\text{Re}[\tilde{B}_I(t) \tilde{B}_K^*(t) \dot{\mathbf{R}} \cdot \mathbf{d}_{IK}(t)] + 2\hbar^{-1} \text{Im}[\tilde{B}_I(t) \tilde{B}_K^*(t) V_{IK}^m(t)] \quad (35)$$

The integration of $b_{IK}(t)$ was done numerically again using linear interpolation for $\dot{\mathbf{R}} \cdot \mathbf{d}_{IK}(t)$ and $V_{IK}^m(t)$. Transitions between states are determined stochastically, based on the state-to-state transition probabilities.

Although it turns out that it does not play an important role in the present results, we also discuss the algorithm for energy conservation when making a transition from one state to another. In this circumstance, the MDQT procedure is to adjust the velocities of the classical nuclei in order to maintain energy conservation. This is done by adjusting the velocity components of the nuclei along the NA coupling vector $\mathbf{d}_{IK}(t)$. However, the velocities are also subject to constraints forces which keep the betaine-30 and solvent molecules rigid. The additional forces that arise from an electronic transition must be adjusted to account for these constraints. Therefore, constraints must be applied to adapt the NA coupling vector so that the changes in velocities are orthogonal to the internal degrees of freedom that are constrained. The method for this is outlined in Appendix D. Once this is done, the velocities of the molecules can be adjusted as follows:

$$\dot{\mathbf{R}}_i = \dot{\mathbf{R}}_i' - \gamma_{KI} \tilde{\mathbf{d}}_{IK}^i / m_i \quad (36)$$

where $\dot{\mathbf{R}}_i'$ is the Cartesian velocity vector of the site i with mass m_i prior to the transition and $\tilde{\mathbf{d}}_{IK}^i$ is the adjusted NA coupling vector component for the site i . The scaling factor γ_{KI} is given by⁶³

$$\gamma_{IK} = \frac{b_{IK} \pm \sqrt{b_{IK}^2 + 4a_{IK}(E_{CI}^K - E_{CI}^I)}}{2a_{IK}} \quad (37)$$

where

$$a_{IK} = \sum_i \frac{|\tilde{\mathbf{d}}_{IK}^i|^2}{2m_i} \quad (38)$$

and

$$b_{IK} = \dot{\mathbf{R}} \cdot \tilde{\mathbf{d}}_{IK} \quad (39)$$

The positive root for γ_{IK} is used for $b_{IK} > 0$ and the negative for $b_{IK} < 0$. A transition can occur if γ_{IK} is real. If the particle velocities have insufficient velocity components along $\tilde{\mathbf{d}}_{IK}$, then the system does not make a switch and the velocity components of $\dot{\mathbf{R}}$ along $\tilde{\mathbf{d}}_{IK}$ are reversed using eq 36 and

$$\gamma_{IK} = \frac{b_{IK}}{a_{IK}} \quad (40)$$

Simulation Details. Simulation details of the MD model used here are described elsewhere⁴³ and will only be summarized. Simulations were run with a total of 1172 acetonitrile molecules at room temperature and a solvent density of 0.7867 g/cm³. To simulate the nonequilibrium process of photoexcitation and subsequent relaxation, the MD trajectories were run by placing the betaine-30 molecule in an excited state after the molecule and solvent had been equilibrated in the ground state. The subsequent excited state dynamics were generated with a time step of 2 fs. For computational efficiency, the dynamics was generated using only 50 single excitation configurations to generate the excited-state energies and forces. These 50 were chosen at every MD time step by selecting the 50 lowest energy diagonal elements of the CI matrix defined by eq 1. These 50 lowest energy single excitation states were then used in diagonalization to generate the excited-state energies and molecular forces. It was verified that the ground-state absorption spectrum for the three lowest energy transitions remained unchanged when compared to the spectrum generated using all possible single excitations. This indicated that the wave functions used for the three lowest energy states were well-described by the 50 lowest energy configurations within the space of single excitations. Two types of trajectories were generated. In the first type, of primary interest here, the betaine-30 was placed in the first excited state. In the second type, the betaine-30 was placed in the third excited state. The latter was done to explore the dynamics corresponding to photoexcitation experiments²² that use excitation wavelengths of both 800 and 400 nm which correspond to the $S_0 \rightarrow S_1$ and $S_0 \rightarrow S_3$ transitions in the experimental absorption spectrum.

III. Results

For this exploratory study, we have examined five trajectories initiated in the S_1 level of betaine-30. We have found that the insight obtained from alternative trajectories is equivalent, and therefore, below, we primarily discuss the results with reference to a particular representative trajectory. To gain an understanding of the details of the relaxation processes that occur after initial excitation of the betaine-30, we first examine the energetics and molecular details of individual trajectories.

The energies of the individual electronic states are shown in Figure 2 as a function of time after the betaine-30 has been placed in the first excited state. The electronic energies of the states are defined as (see section II)

$$E_{S_I} = E_{CI}^I + V_\pi + V_{C-C} + V_{C-S} \quad I = 1, 2, \dots \quad (41)$$

We note at the outset that evidence from comparison of experimental and calculated results⁴³ indicates that the ordering of the S_2 and S_3 states from the present electronic description are reversed, a result that can be seen from their polarities. As will be evident below, the S_2 and S_3 states are computed to be relatively close in energy, with the S_0 and S_1 states well separated from them. Therefore, we focus the present work on the S_0 and S_1 states.

As can be seen from Figure 2, the betaine-30 remains in the first excited state for the 25 ps of the trajectory shown, as discussed below. Examining Figure 2, it can be seen that, immediately after excitation, the S_0 state moves rapidly upward by approximately 1 eV in energy over the first 100 fs of the trajectory. The highest frequency fluctuations in the energy

levels are correlated with each other and have a small amplitude of approximately 0.2 eV. Superimposed on the highest frequency fluctuations is a larger amplitude variation of much lower frequency. The low-frequency motion is more pronounced in the S_0 ground-state level (amplitude ~ 1 eV). The same features can also be seen in the trajectory of the transition energies which are shown in Figure 3. The transition energies are the energy gaps between ground and excited states which are given by $\Delta E_{S_I} = E_{S_I} - E_{S_0} = E_{CI}^I$ where

$$E_{S_0} = V_\pi + V_{C-C} + V_{C-S} \quad (42)$$

To ascertain the connection between specific molecular degrees of freedom and the excitation energies of the betaine-30, we first examine how the torsional angles of the molecule change after excitation. The torsional ring angles as a function of time are plotted in Figure 4. Our previous *ground state* simulation results for betaine-30 in acetonitrile⁴³ have shown that, in that case, the torsional angles of the molecule only sample a narrow range of angles ($\pm 4-8^\circ$), indicating that the rings are confined to rotational potential energy wells by barriers much larger than thermal energies. Figure 4 shows the ring angle trajectories for the central ring angle (labeled θ in Figure 1), the two phenyl rings attached to the pyridinium (ϕ in Figure 1), the torsional angles subtended by the phenyl ring ortho to the nitrogen in the pyridinium (χ), and the remaining angle for the two phenyl rings attached to the phenolate group (ξ). As can be seen from Figure 4, the ring angles χ and ξ show no appreciable change from the range of angles that are sampled in the ground state. Further, it is clear that we need not distinguish between the individual angles in pairs of angles ϕ and ξ . However, the central ring angle θ and the two side ring angles ϕ do show considerable deviation from the distributions that they sample in the ground state⁴³ ($\langle \theta \rangle = 53^\circ \pm 4^\circ$ and $\langle \phi \rangle = 47^\circ \pm 4^\circ$, where the \pm denotes the distribution width at half-height).

After excitation, the central ring angle both increases and samples a larger range between 60° and 90° . In addition, the side ring angle motion is correlated with the central ring, and the side angles both increase as the central ring moves toward 90° . The motion of the central ring angle is readily determined to be strongly correlated with the low-frequency large-amplitude motion of the $S_0 \rightarrow S_1$ energy gap (cf. Figure 3 and Figure 4). As the central ring angle opens, the energy gap generally decreases in value, as can be seen by comparing the first 5 ps of the trajectory, shown as a separate frame in both Figures 3 and 4. The overall motion of the energy gaps is clearly correlated with the changes in the central ring angle, with the transition energies getting lower as the pyridinium and phenolate rings approach 90° with respect to each other.

This behavior can be explained by an examination of the calculated potential energy surfaces of the S_0 and S_1 states in the gas phase. The gas-phase surfaces shown in Figure 5 were generated as a function of the two ring angles ϕ and θ . These reduced surfaces were each found by first finding the minimum energy structure of the molecule in the gas phase via a simulated annealing MD calculation. The surfaces were then generated by varying only the two angles ϕ and θ and keeping the other angles constrained at their gas-phase minimum energy values; the two ϕ angles were kept equal to each other. In the ground state these two torsional angles have minimum energy values which are 52° and 49° , respectively. At a torsional angle of 0° , the π conjugation between the rings is maximized, but 90° minimizes the steric repulsion between the pendant rings. The $S_0 \rightarrow S_1$ excitation involves the promotion of an electron from

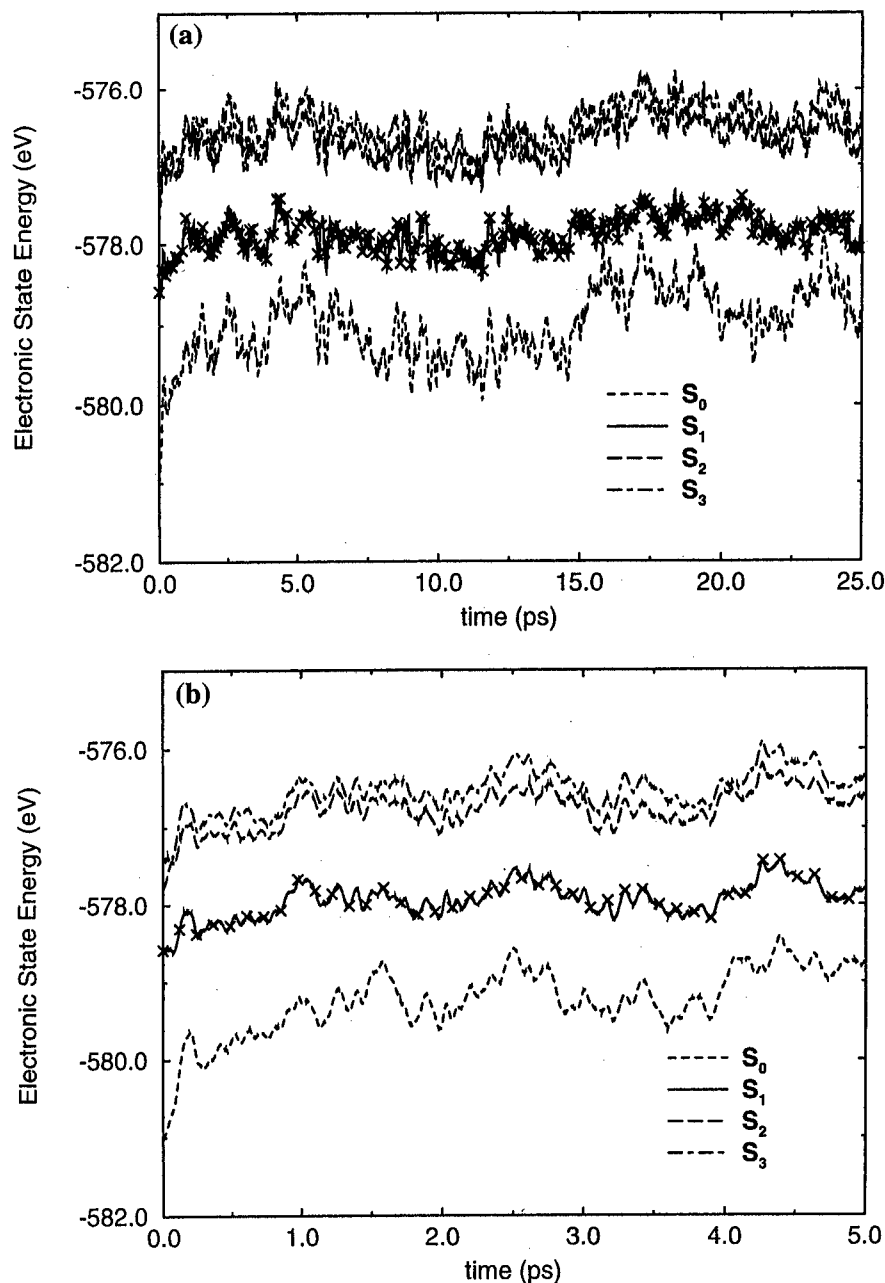


Figure 2. Time-dependent dynamics of the energy levels (see eqs 41 and 42) of betaine-30 after it has been placed in the first excited state S_1 for a typical trajectory. The occupied state is denoted by the crosses. The ground state, S_0 , is denoted by the dashed line. The excited states, S_1 , S_2 , and S_3 , are denoted by the solid, long dashed, and dot-dashed lines, respectively. The two frames differ only in the time scale.

a π orbital to a π^* antibonding orbital. This is found to decrease the amount of π conjugation energy in the molecule. For the central ring angle θ , this results in the potential energy minimum being shifted close to $\theta = 90^\circ$, where steric effects are minimized. It is interesting to note that, in the ring angle trajectories, large-amplitude motions occur in the ϕ angles when $\theta \approx 90^\circ$. This is due to the fact that S_1 potential surface is very flat along the ϕ coordinate along the $\theta \approx 90^\circ$ cut, as is evident from Figure 5. The decrease in the transition energies after excitation is also explained by Figure 5; the energy gap is considerably smaller when $\theta \approx 90^\circ$.

While the gas-phase surfaces can be used to interpret the solution state dynamics after excitation, it should be emphasized that there is considerable polarization of this surface by the electric field of the solvent. This is evidenced by the fact that the maximum in the $S_0 \rightarrow S_1$ transition energy in the gas phase is shifted from approximately 29 to 50 kcal/mol, with the solvent

increasing the separation of the surfaces shown in Figure 5. Furthermore, our previous simulation results of betaine-30 in the ground state⁴³ have shown that the solvent polarization substantially removes the θ torsional angle dependence of the $S_0 \rightarrow S_1$ transition energy in the vicinity of the ground state minimum, where the torsional ring angles only sample a very narrow distribution of angles. Conversely, the excited-state trajectories show a dependence of the transition energies on the central ring angle, a result that may be due in part to the much larger range of angles that are sampled in the excited-state trajectory and in part to the rather different solvent polarization present in that case.

We now consider the shorter time dynamics. In Figure 3, a rapid 1 eV drop in the $S_0 \rightarrow S_1$ transition energy is seen which takes place in the first 100–200 fs of the trajectory. This rapid drop in transition energy takes place on a time scale faster than any torsional motion in the betaine-30 molecule and is neces-

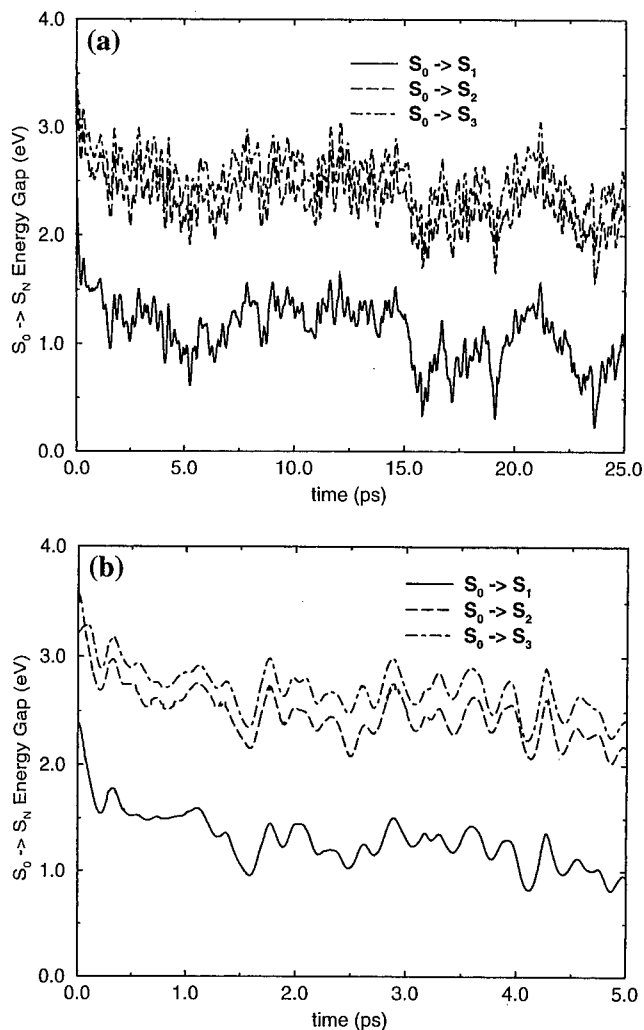


Figure 3. Time-dependent dynamics of the energy gaps $\Delta E_{S_i} = E_{S_i} - E_{S_0}$ of betaine-30 after it has been placed in the first excited state. The energy gaps ΔE_{S_1} , ΔE_{S_2} , and ΔE_{S_3} are denoted by the solid, long dashed, and dot-dashed lines. The trajectory is the same as that shown in Figure 2.

sarily due to solvent motion. This rapid drop immediately after excitation has been seen in many other contexts, both in MD simulations^{34–36} and in experiments.^{30–33} It occurs due to the rapid inertial motion of the solvent molecules, subject to the different forces present on the two electronic surfaces. The energy gap initially exhibits a Gaussian time dependence as has been shown by MD simulations³⁶ and molecular theories.^{37–40} Longer time solvent dynamics also occurs on a subpicosecond time scale, followed by relaxation dominated by intramolecular torsional motion. It is interesting to note here that the solvent contribution to the energy gap is associated *exclusively* with a rapid rise in the S_0 energy level. This is consistent with the fact that the S_0 state is a charge separated state with a large dipole moment while the S_1 has a much smaller dipole moment.

It is of considerable interest to examine the energy gap relaxation in more detail and to compare the dynamics exhibited in the present work to that inferred from recent modeling of resonance Raman spectra for the same system.⁴² In particular, it is evident from Figure 3 and our earlier discussion that, here, the energy gap relaxation exhibits (at least) three time scales. The first, of the order of 100 fs, corresponds to the inertial solvent time scale, and represents about 70% of the subpicosecond response in this trajectory. The second time scale, of the order of 0.5 ps, is the diffusive solvent time scale. After about 1 ps, the solvent is essentially completely relaxed. As

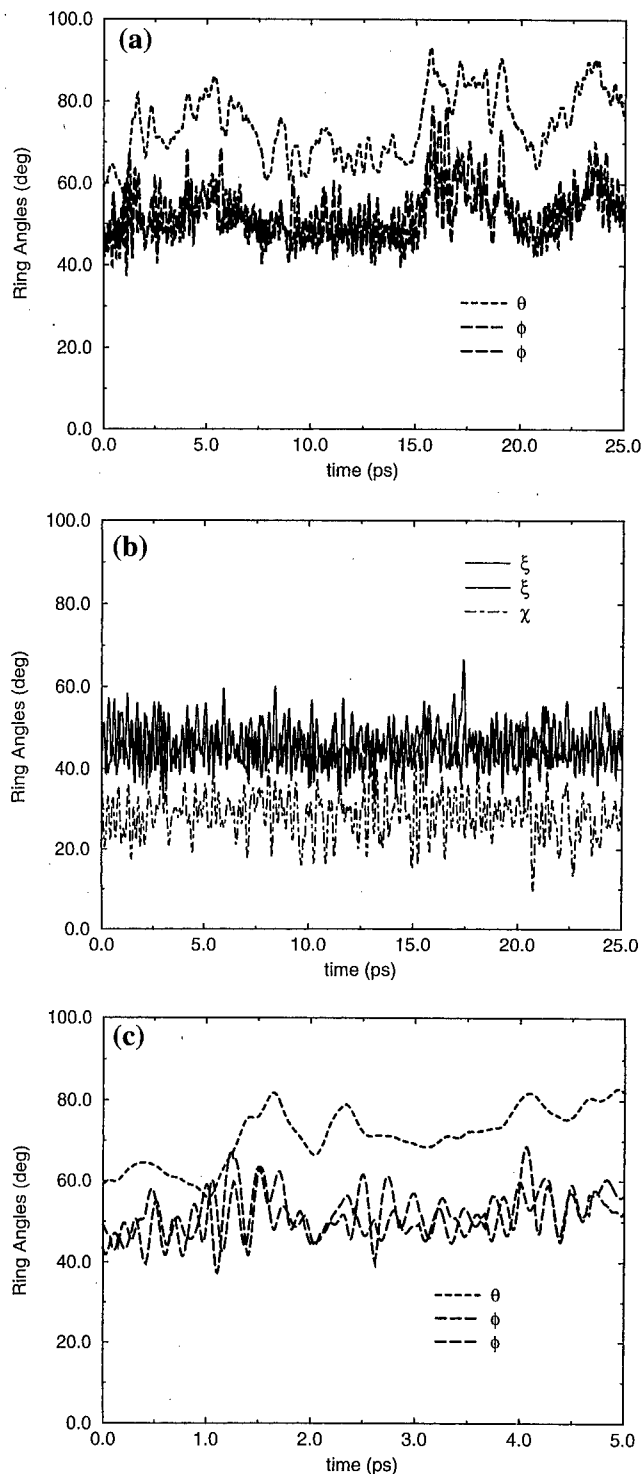


Figure 4. Dynamics of the torsional ring angles of betaine-30 after the system has been excited to the S_1 state at $t = 0$. The labeling of the various angles is given in Figure 1. The trajectory is the same as that shown in Figure 2.

noted above, however, there is the potential for considerable additional relaxation on a relatively much longer time scale, due to torsional relaxation around the solute's central dihedral angle. The solvent relaxation contributes about 0.8 eV by 1 ps after initial excitation to S_1 ; the assignment to solvent alone is evident from Figure 4. This energy relaxation would correspond to a Stokes shift of about 6400 cm^{-1} and an inferred solvent reorganization energy of about 3200 cm^{-1} . This value is comparable to the value of about 3600 cm^{-1} inferred by us for the same model by analysis of solvent contributions to *ground*

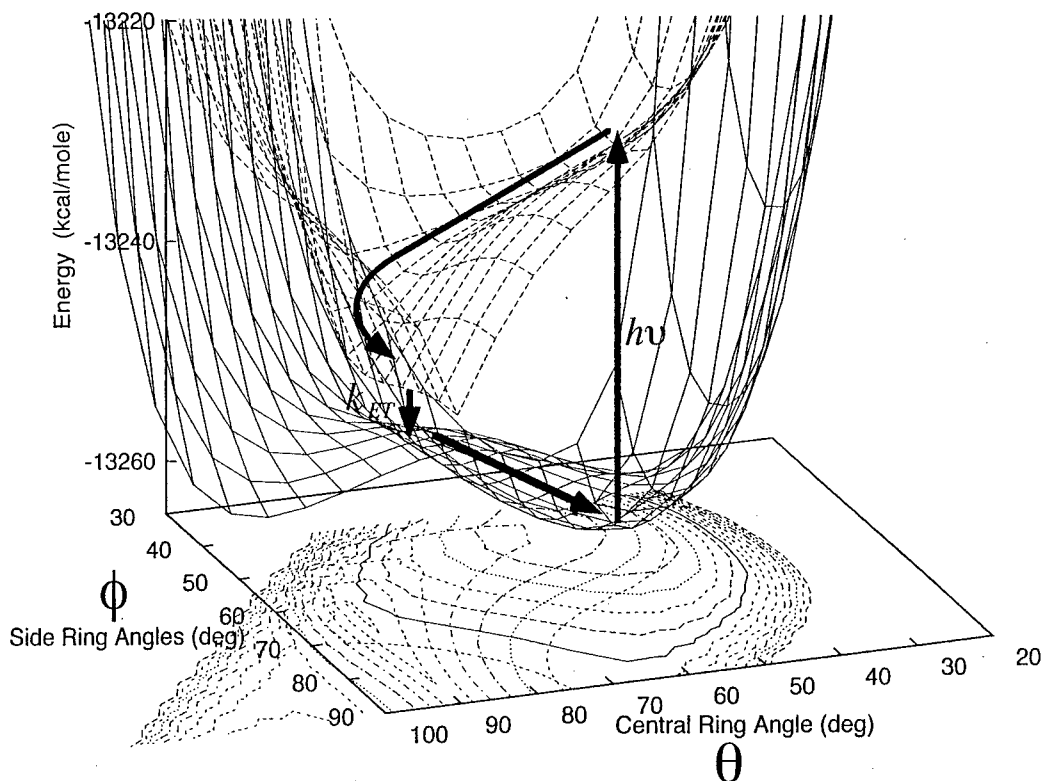


Figure 5. Gas-phase potential energy surfaces for the ground and first excited states as a function of the central phenolate–pyridinium torsion angle θ and the side ring angle ϕ . The minimum of the ground state surface is located at $\theta = 52^\circ$ and $\phi = 49^\circ$. The minimum in the first excited state is shifted to $\theta = 90^\circ$ and $\phi \approx 65^\circ$. The arrows denote the relaxation of the system in these two coordinates after excitation to the first excited state.

state absorption line broadening,⁴³ a result that also agrees with the corresponding analysis of experimental ground-state absorption spectra.²⁴ The total relaxation accessible including torsional relaxation (observed here due to the long S_1 lifetime of the model) is about $10\,000\text{ cm}^{-1}$.

In the cited resonance Raman spectral modeling, it was found that an ultrafast component of the solvation dynamics was needed to fit the measured results. In particular, McHale and co-workers⁴² found that, in addition to a solvation time for acetonitrile of about 0.6 ps, a time of 88 fs carrying an amplitude of about 60% of the solvation response was needed. This form for the solvent response is completely consistent with that seen in the present work. However, the corresponding solvent contribution to the reorganization energy inferred there, about 6000 cm^{-1} , is notably larger than our best estimate⁴³ of 3600 cm^{-1} . The present observations suggest that a possible factor in the comparison is the role of the slower torsional component observed here. The resonance Raman spectral analysis does not include a slower (classical) intramolecular component so that any effects arising from this would be included in the component attributed to the solvent. These authors⁴² have, in fact, suggested the possibility of coupled contributions of solvent with solute torsional degrees of freedom. We note that the torsional relaxation seen here is much slower than the acetonitrile solvent (and also much slower than the $\sim 300\text{ cm}^{-1}$ modes representing the lowest frequencies resolved in the Raman study⁴²). Thus, it is not clear without further detailed analysis whether the contribution of the present dihedral motion would be significant in describing the resonance Raman spectra.

As stated earlier, no transition back to the ground state in fact occurs in the present S_1 trajectories. The calculated transition probabilities were found to be extremely low, on the order of $P_{1\rightarrow 0} \approx 1 \times 10^{-4}$ per MD time step. A computational study of the estimated lifetime would require averaging over many

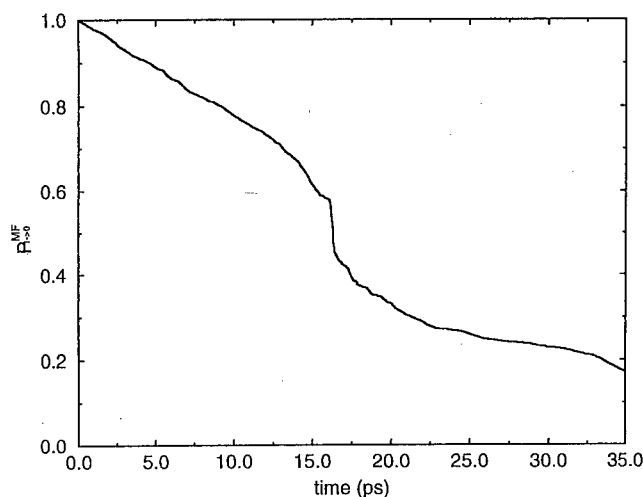


Figure 6. Graph of the accumulated transition probability as given in eq 43 for the trajectory shown in Figure 2.

nonequilibrium trajectories and is not warranted, since the experimental lifetime is known to be approximately 0.5 ps.²⁴ Alternatively, a first-order lifetime can be estimated from an accumulated transition probability expression

$$P_{1\rightarrow 0}^{MF} = \prod_i^{n_s} (1 - P_{1\rightarrow 0}^i) \quad (43)$$

where $P_{1\rightarrow 0}^i$ is the transition probability at every time MD step which is accumulated over n_s time steps. A graph of $P_{1\rightarrow 0}^{MF}$ as a function of trajectory length for the above trajectory is shown in Figure 6. A linear fit to $\ln[P_{1\rightarrow 0}^{MF}]$ gives an estimate of the excited-state lifetime. The slopes of five trajectories were

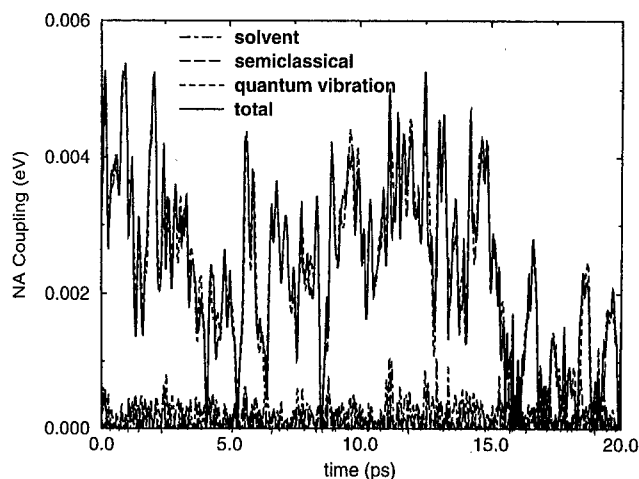


Figure 7. Time dependence of the various contributions to the NA coupling between the ground and first excited states of betaine-30. The solvent contribution to the NA coupling (the first term of eq 44) is given by the dot-dashed line. The semiclassical contribution from the betaine-30 degrees of freedom (the second term of eq 44) is given by the long dashed line. The contribution from the betaine-30 intramolecular vibrational degrees of freedom which has been estimated quantum mechanically (the final term of eq 44) is given by the dashed line. The trajectory is the same as that shown in Figure 2.

averaged to give an estimated lifetime of $\tau_{1-0} = 29 \pm 19$ ps. Clearly, this value is much larger than the experimentally inferred subpicosecond result. It is reasonable to attribute this difference to the relatively crude modeling of the intramolecular vibrational contribution to the transition amplitude used here, since all other aspects are treated much more completely. Among other things, this limits vibrational transitions to $\Delta v = 1$ so that the higher lying vibrational states of the product cannot be accessed from low lying vibrational states of S_1 . To explore this interpretation in more detail, we need to examine the separate contributions to the NA coupling from alternative sources, which we do below.

The total NA coupling between the electronic states is given by

$$V_{IJ} = -i\hbar(\dot{\mathbf{R}}^{\text{Sol}} \cdot \mathbf{d}_{IJ}^{\text{Sol}} + \dot{\mathbf{R}}^{\text{B30}} \cdot \mathbf{d}_{IJ}^{\text{B30}}) + V_{IJ}^{\text{qm}} \quad (44)$$

where, here, the semiclassical contribution to the NA coupling, $\dot{\mathbf{R}} \cdot \mathbf{d}_{IJ}$, has been subdivided into the portions coming from the solvent degrees of freedom and the betaine-30 nuclear degrees of freedom. Because of the fact that internal vibrations in the acetonitrile molecules are rigidly constrained, the only contribution from the solvent degrees of freedom to the NA coupling comes from the intermolecular rotational and translational degrees of freedom of the solvent molecules. Similarly constraints to the motion of the betaine-30 limit the semiclassical contribution to the coupling to that from internal torsional ring motion of the betaine-30. All the other intramolecular degrees of freedom of the betaine-30 contribute to the NA coupling quantum mechanically through the third term in the above equation. We note that the NA coupling from the torsional degrees of freedom is counted twice in the above formulation, but as will be seen below, the contribution from the torsional degrees of freedom is minimal and therefore correction for this is not warranted.

The magnitude of the total NA coupling between the ground and first excited state, $|V_{10}|$, and its three components are graphed as a function of time in Figure 7 for the trajectory considered in the other figures. As can be seen from the figure, the total NA coupling is determined almost completely by the

quantum intramolecular contribution. The semiclassical contributions from the betaine-30 and solvent degrees of freedom are both approximately an order of magnitude smaller than the quantum intramolecular part. The implication of this is that, within the context of the adiabatic reference point of the model presented here, the coupling between S_0 and S_1 that promotes the transition can be well approximated by the contribution due to intramolecular modes. Correspondingly, these modes are the primary recipients of the electronic energy during the NA transition, in accord with the prevailing view discussed in the Introduction. Of course, the observations made here do not imply that the dynamics of the other modes, including both solvent and ring motions, are not critical to the lifetime. The premise of several of the models discussed in the Introduction^{4,24,27,28} is that the time-dependent energy gap between electronic states determines the particular vibrational product channels that are potentially activationless and thus most active in the transition. Correspondingly, the rate is modulated by the Franck-Condon factors associated with these states. The present model is unable to address this aspect; this will require a more realistic description of mode displacements.

The contributions to the NA coupling between the various states was also further broken down by the contribution made from each normal mode. First, it was found that the majority (>80%) of the coupling was determined primarily by less than 10 distinct normal modes. Furthermore, the character of these normal modes was high frequency (>600 cm^{-1}), and, consistently, none of the modes included the low-frequency rotational ring torsional modes of the molecule. It is worth noting in this context that resonance Raman studies for the same system⁴² reveal a comparable number of active modes and that these cover a similar range of frequencies, although two lower frequency ($\sim 300 \text{ cm}^{-1}$) modes of relatively high displacement were also identified in the Raman context. Further analysis of the character of the active modes and how they contribute to the NA coupling is clearly a key subject for future analysis.

To examine the generality of the behaviors discussed above, we have also executed a trajectory initiated in the third excited state of our model. As noted earlier, this state appears to correspond electronically to the S_2 , rather than S_3 , state so that we do not focus on the details of the results here. However, ultrafast pump-probe experiments have been reported for the excitation of ground-state molecules at 400 nm, which corresponds to a $S_0 \rightarrow S_3$ excitation.²² One of the main experimental results from this study was that the spectral dynamics for excitation at 800 nm (which corresponds to $S_0 \rightarrow S_1$) were indistinguishable from those that resulted from excitation at 400 nm. The interpretation attached to this result was that internal conversion from $S_3 \rightarrow S_1$ was extremely rapid (<200 fs), followed by the $S_0 \rightarrow S_1$ transition process. For the third excited state in our simulations, with considerably smaller energy gaps between excited states, we do find that the system reaches the S_1 state in less than 500 fs. As for initiation on the S_1 state, the NA coupling is completely dominated by the intramolecular vibrational component. However, the coupling matrix elements are found to be 1–2 orders of magnitude larger than those for the $S_1 \rightarrow S_0$ transition. Thus, we find that these simulation results are consistent with the very short residence times in higher excited states that were inferred experimentally.

IV. Conclusions

The excited state dynamics of betaine-30 in acetonitrile at room temperature has been studied using combined quantum and classical MD simulations. The π electronic degrees of

freedom of the betaine-30 have been treated quantum mechanically using the semiempirical PPP electronic structure method,^{47–49,64} including perturbation by the solvent. Methods for carrying out time-dependent dynamics, including transitions between molecular electronic states of the molecule have been introduced using the MDQT algorithm⁴⁶ suitably modified for the PPP method and the internal geometric constraints of the solute molecule and solvent. An approximate quantum mechanical estimate of the nonadiabatic coupling between the electronic states due to the internal modes of betaine-30 has been used. This estimate does not take into account normal mode displacements between states.

Exploratory simulations reveal that excitation from S_0 to the first excited-state S_1 leads to energy level dynamics that are governed by both the solvent and internal torsional angles of the molecule. The initial response of the energy gap between S_0 and S_1 is governed by the motion of the solvent, with amplitudes and subpicosecond time scales that are consistent with many earlier studies of solvation dynamics in acetonitrile and with resonance Raman studies of betaine-30 in acetonitrile.⁴² However, a slower subsequent dynamics of the energy levels and gaps is governed by the internal central phenolate–pyridinium torsional angle of the molecule. This further energy gap relaxation in the first few picoseconds following excitation is substantial, amounting to about 50% of that due to the solvent response. In the S_1 state, the central rings of the molecule rotate toward a geometry where they are perpendicular to each other and sample a much wider distribution of angles than they do in the ground state. This is due both to steric effects and a decreased π conjugation energy in the excited state.

Although the possible role of torsional modes has been noted elsewhere,⁴² and fast intramolecular classical degrees of freedom have been invoked in modeling,²⁴ the inclusion of a relatively slow, but large-amplitude, component in the energy gap relaxation has not been addressed in ET modeling of this system. The identification of the specific mode here is also new. It is of considerable interest for future work to determine whether this internal rotation can be associated with those invoked in models and if inclusion of such a degree of freedom can be a benefit to the modeling of resonance Raman spectra. In any case, it would appear from these results that the a priori separation of solvent and intramolecular degrees of freedom from experimental data alone is, at best, very challenging.

While excitation gives rise to a response from the solvent and a change in the internal geometry of the molecule, the nonadiabatic couplings between the electronic states are found to be determined almost exclusively by a small number of high-frequency internal molecular modes of the betaine-30. Because of the very approximate model used for treating these high-frequency modes here, we have not been able to directly address the relative importance of the different solvent dynamical time scales on the back ET rate $S_1 \rightarrow S_0$. With improvements to this aspect of the model, and inclusion of multiple vibronic channels for relaxation, this question can be addressed and closer connection to resonance Raman experiments can be made. This will be the topic of future studies.

Appendix A: Evaluation of Nuclear Derivatives

The coupled perturbed Hartree–Fock (CPHF) equations are given by

$$(\epsilon_p - \epsilon_q)u_{qp}^R = F'_{qp} \quad (A1)$$

where F'_{qp} is given by

$$F'_{qp} = \sum_{\mu\nu} c_\mu^q \frac{\partial F_{\mu\nu}}{\partial R} c_\nu^p \quad (A2)$$

The matrix elements $F_{\mu\nu}$ are the Fock matrix elements in the atomic orbital representation. Using the definitions of the Fock matrix elements for the PPP Hamiltonian given by eq 4 in ref 43, the above equation becomes

$$(\epsilon_p - \epsilon_q)u_{qp}^R = B_{qp}^R + \sum_a \sum_i^{\text{virtual real}} A_{ai,qp} u_{qp}^R \quad (8)$$

where the matrix A can be shown to be

$$A_{ai,qp} = -\frac{1}{2} \sum_{\mu \neq \nu} X_{ai}^{\mu\nu} c_\mu^q c_\nu^p \gamma_{\mu\nu} + \frac{1}{2} \sum_{\mu} X_{ai}^{\mu\mu} c_\mu^q c_\mu^p \gamma_{\mu\mu} + \sum_{\mu \neq \rho} X_{ai}^{\rho\rho} c_\mu^q c_\mu^p \gamma_{\mu\rho} \quad (A3)$$

where

$$X_{ai}^{\mu\nu} = 2(c_\mu^i c_\nu^a + c_\mu^a c_\nu^i) \quad (A4)$$

The vector B is given by

$$B_{qp}^R = H'_{qp} - \frac{1}{2} \sum_{\mu \neq \nu} c_\mu^q c_\nu^p P_{\mu\nu} \gamma_{\mu\nu}^{(R)} + \frac{1}{2} \sum_{\mu} c_\mu^q c_\mu^p P_{\mu\mu} \gamma_{\mu\mu}^{(R)} + \sum_{\mu \neq \rho} c_\mu^q c_\mu^p P_{\rho\rho} \gamma_{\mu\rho}^{(R)} \quad (A5)$$

where

$$H'_{qp} = \sum_{\mu\nu} c_\mu^q \frac{\partial H_{\mu\nu}}{\partial R} c_\nu^p \quad (A6)$$

The matrix elements $H_{\mu\nu}$ are the one-electron Hamiltonian PPP matrix elements,⁶⁴ $P_{\mu\nu}$ is the density matrix defined by $P_{\mu\nu} = 2 \sum_i^{\text{real}} c_\mu^i c_\nu^i$.

To avoid explicitly solving the CPHF equations for each nuclear derivative we first rewrite eq 8 in matrix form

$$(\epsilon_p - \epsilon_q)u_{qp}^R - \sum_a \sum_i^{\text{virtual real}} A_{ai,qp} u_{qp}^R = B_{qp}^R$$

$$\mathbf{G}\mathbf{u}^R = \mathbf{B}^R \quad (A7)$$

which can be solved through matrix inversion

$$\mathbf{u}^R = \mathbf{G}^{-1}\mathbf{B}^R \quad (A8)$$

Rewriting eq 7 in matrix notation and substituting eq A8 into 7

$$\sum_{mn} C_m^I C_n^J \frac{\partial}{\partial R} A_{nm} = \sum_{mn} C_m^I C_n^J A_{nm}^{(R)} + 2\zeta^I \mathbf{u}^R$$

$$\sum_{mn} C_m^I C_n^J \frac{\partial}{\partial R} A_{nm} = \sum_{mn} C_m^I C_n^J A_{nm}^{(R)} + 2\zeta^I \mathbf{G}^{-1} \mathbf{B}^R$$

$$\sum_{mn} C_m^I C_n^J \frac{\partial}{\partial R} A_{nm} = \sum_{mn} C_m^I C_n^J A_{nm}^{(R)} + 2\mathbf{Z}_I \mathbf{B}^R \quad (A9)$$

The vector–matrix product $\zeta^I \mathbf{G}^{-1} = \mathbf{Z}_I$ need only be evaluated once per CI state, as opposed to $3N$ times (where N is the total

number of classical nuclei in the simulation) as it would be if the CPHF equations for \mathbf{u}^R were solved directly for each nuclear coordinate. Since \mathbf{u}^R is no longer solved for directly, the NA coupling vector from eq 22 must now be rewritten in terms of \mathbf{B}^R :

$$\begin{aligned} \left\langle \Psi_I \left| \frac{\partial}{\partial R} \right| \Psi_J \right\rangle &= d_{IJ}^R = \frac{\sum_{mn} C_n^I C_m^J A_{nm}^{(R)}}{(E_{CI}^J - E_{CI}^I)} + 2 \sum_{ks} u_{ks}^R \xi_{ks}^{IJ} \\ &= \frac{\sum_{mn} C_n^I C_m^J A_{nm}^{(R)}}{(E_{CI}^J - E_{CI}^I)} + 2 \xi^{IJ} \mathbf{G}^{-1} \mathbf{B}^R \\ &= \frac{\sum_{mn} C_n^I C_m^J A_{nm}^{(R)}}{(E_{CI}^J - E_{CI}^I)} + 2 \mathbf{Z}_{IJ} \mathbf{B}^R \end{aligned} \quad (\text{A10})$$

The vector-matrix product, $\xi^{IJ} \mathbf{G}^{-1} = \mathbf{Z}_{IJ}$, is evaluated once for every pair of CI states.

Appendix B: Simplification of Gradient Matrix Elements between Slater Determinants

The simplification of gradient terms of the form $\langle \psi_n | \nabla_R \psi_m \rangle$ can be carried out by recognizing that ∇_R acts as a one electron operator. Therefore, Slater determinants that differ by more than one spin-orbital will be zero, i.e.,

$$\langle \psi_{i \rightarrow a} | \nabla_R | \psi_{j \rightarrow b} \rangle = 0 \quad (\text{B1})$$

The remaining matrix elements for the one-electron excitations and ground-state Slater determinants will be

$$\langle \psi_0 | \nabla_R | \psi_0 \rangle = \sum_i^{\text{occupied}} \langle i | \nabla_R | i \rangle \quad (\text{B2a})$$

$$\langle \psi_{i \rightarrow a} | \nabla_R | \psi_{i \rightarrow a} \rangle = \sum_j^{\text{occupied}} \langle j | \nabla_R | j \rangle - \langle i | \nabla_R | i \rangle + \langle a | \nabla_R | a \rangle \quad (\text{B2b})$$

$$\langle \psi_{i \rightarrow a} | \nabla_R | \psi_0 \rangle = \sqrt{2} \langle a | \nabla_R | i \rangle \quad (\text{B2c})$$

$$\langle \psi_{i \rightarrow a} | \nabla_R | \psi_{j \rightarrow a} \rangle = \sqrt{2} \langle j | \nabla_R | i \rangle \quad (\text{B2d})$$

$$\langle \psi_{i \rightarrow a} | \nabla_R | \psi_{i \rightarrow b} \rangle = \sqrt{2} \langle a | \nabla_R | b \rangle \quad (\text{B2e})$$

The ket $|i\rangle$ is the state ket for the i th real space MO, which is expanded in terms of atomic orbital basis functions

$$|i\rangle = \sum_{\mu} c_{\mu}^i |\mu\rangle \quad (\text{B3})$$

There are two types of MO matrix elements in eqs B2a–e, diagonal elements of the type $\langle i | \partial/\partial R | i \rangle$ and off-diagonal elements of the form $\langle i | \partial/\partial R | a \rangle$. Expanding the diagonal elements using (B3), $\langle i | \partial/\partial R | i \rangle$ then become

$$\begin{aligned} \left\langle i \left| \frac{\partial}{\partial R} \right| i \right\rangle &= \sum_{\mu\nu} c_{\mu}^i c_{\nu}^i \left\langle \mu \left| \frac{\partial}{\partial R} \right| \nu \right\rangle + \sum_{\mu\nu} \langle \mu | \nu \rangle c_{\mu}^i \frac{\partial c_{\nu}^i}{\partial R} \\ &= \sum_{\mu\nu} c_{\mu}^i c_{\nu}^i \left\langle \mu \left| \frac{\partial}{\partial R} \right| \nu \right\rangle + \sum_{\mu} c_{\mu}^i \frac{\partial c_{\mu}^i}{\partial R} \end{aligned} \quad (\text{B4})$$

Focusing our attention on the first term of eq B4, off-diagonal elements, $\langle \mu | \partial/\partial R | \nu \rangle$, are approximated to be zero under the zero differential overlap approximation (i.e., the orthonormality of the atomic orbital basis functions) which was assumed in the implementation of the PPP method for betaine-30 as outlined in ref 43. Assuming that the atomic orbital basis functions are real, one can show that derivatives of the diagonal matrix elements are zero due to orthonormality, i.e.,

$$\frac{\partial}{\partial R} \langle \mu | \mu \rangle = 2 \left\langle \mu \left| \frac{\partial}{\partial R} \right| \mu \right\rangle = 0 \quad (\text{B5})$$

These two results demonstrate that the first term in eq B4 is zero. In a similar fashion, one can show using the orthonormality of the MOs that the second term is zero as well

$$\begin{aligned} \frac{\partial}{\partial R} \langle i | i \rangle &= \sum_{\mu\nu} \langle \mu | \nu \rangle c_{\mu}^i \frac{\partial c_{\nu}^i}{\partial R} + \langle \mu | \nu \rangle c_{\nu}^i \frac{\partial c_{\mu}^i}{\partial R} \\ &= 2 \sum_{\mu} c_{\mu}^i \frac{\partial c_{\mu}^i}{\partial R} = 0 \end{aligned} \quad (\text{B6})$$

It can be thus concluded that all diagonal elements of the form $\langle i | \partial/\partial R | i \rangle$ are zero and eqs B2a and B2b are both zero. Off-diagonal elements, however, are not zero and, using the previous results, are given by

$$\left\langle i \left| \frac{\partial}{\partial R} \right| a \right\rangle = \sum_{\mu} c_{\mu}^i \frac{\partial c_{\mu}^a}{\partial R} \quad (\text{B7})$$

Hence, one obtains the result shown in eq 21,

$$\begin{aligned} \langle \psi_{i \rightarrow a} | \nabla_R \psi_0 \rangle &= \sqrt{2} \sum_{\mu} c_{\mu}^i \nabla_R c_{\mu}^a \\ \langle \psi_{i \rightarrow b} | \nabla_R \psi_{i \rightarrow a} \rangle &= \sqrt{2} \sum_{\mu} c_{\mu}^b \nabla_R c_{\mu}^a \\ \langle \psi_{i \rightarrow a} | \nabla_R \psi_{j \rightarrow a} \rangle &= \sqrt{2} \sum_{\mu} c_{\mu}^j \nabla_R c_{\mu}^i \end{aligned} \quad (\text{B8})$$

Appendix C: Compliance with Eckart Conditions

The positions of the atoms of the betaine-30 molecule must be rotated and translated to a reference frame such that only $3N - 6$ of the normal modes of the molecule have finite displacements:

$$q_j = \sum_i^{3N} \sqrt{m_i} \Delta \mathbf{R}_i^0 = 0 \quad \text{for } j = 3N - 5, 3N - 4, \dots, 3N \quad (\text{C1})$$

The Cartesian displacement vector, $\Delta \mathbf{R}_{B30}^0$ (whose components are ΔR_i^0 in the above equation), is the difference between the betaine-30 coordinates in the MD simulation at a given time step *after* overall rotation and translation, \mathbf{R}_{B30} , and the coordinates of the molecule in its minimum energy gas-phase

configuration, $\mathbf{R}_{\text{B30}}^0$, i.e.,

$$\Delta \mathbf{R}_{\text{B30}}^0 = \mathbf{R}_{\text{B30}} - \mathbf{R}_{\text{B30}}^0 \quad (\text{C2})$$

The normal-mode frequencies and transformation coefficients are, of course, calculated at the configuration $\mathbf{R}_{\text{B30}}^0$. Equation C1 can only be satisfied by choosing the coordinate system such that the positions satisfy the Eckart conditions.⁶⁰⁻⁶² The first condition is trivially satisfied by making the center of masses coincident with the origin of the coordinate system:

$$\sum_i^N m_i \mathbf{R}_i = \sum_i^N m_i \mathbf{R}_i^0 = 0 \quad (\text{C3})$$

The vectors \mathbf{R}_i and \mathbf{R}_i^0 denote the coordinates of the i th betaine-30 atom position in the two respective geometries. The second Eckart conditions correspond to the static equivalent of the angular momentum between the two sets of coordinates being zero:

$$\sum_i^N m_i (\mathbf{R}_i \times \mathbf{R}_i^0) = 0 \quad (\text{C4})$$

This condition can be satisfied by applying a suitably chosen rotation matrix, \mathbf{T} , to the betaine-30 positions from the MD simulation. The procedure for finding such a rotation matrix is outlined in ref 65 and is not repeated here. With the rotation matrix in hand, the matrix element of the NA coupling in a normal mode coordinate system, $\langle \Psi_I | \partial / \partial q_j | \Psi_J \rangle$, can be found.

The notation of eq 30 is changed slightly to clarify the transformation of the Cartesian matrix elements using the rotation matrix

$$\left\langle \Psi_I \left| \frac{\partial}{\partial q_j} \right| \Psi_J \right\rangle = \sum_i^N \sum_k^3 \frac{(l^{-1})_j^{i,k}}{\sqrt{m_k}} \left\langle \Psi_I \left| \frac{\partial}{\partial R_{i,k}} \right| \Psi_J \right\rangle \quad (\text{C5})$$

The Cartesian elements of the NA coupling matrix, $\langle \Psi_I | \partial / \partial R_{i,k} | \Psi_J \rangle$, are calculated after application of the rotation to the betaine-30 positions. The rotation matrix transforms the positions, $\hat{\mathbf{R}}_i$, to ones that satisfy the Eckart conditions:

$$\mathbf{T} \hat{\mathbf{R}}_i = \mathbf{R}_i \quad (\text{C6})$$

Rewriting eq C6,

$$\tilde{\mathbf{T}} \mathbf{R}_i = \hat{\mathbf{R}}_i \quad (\text{C7})$$

one sees that the Cartesian derivatives in eq C5 may be rewritten as

$$\frac{\partial}{\partial R_{i,k}} = \sum_l^3 \frac{\partial \hat{R}_{i,l}}{\partial R_{i,k}} \frac{\partial}{\partial \hat{R}_{i,l}} \quad (\text{C8})$$

Using this relation, the elements, $\langle \Psi_I | \partial / \partial q_j | \Psi_J \rangle$, can now be expressed in terms of the Cartesian NA coupling matrix elements that are found in the MD simulation, $\langle \Psi_I | \partial / \partial \hat{R}_{i,l} | \Psi_J \rangle$:

$$\left\langle \Psi_I \left| \frac{\partial}{\partial q_j} \right| \Psi_J \right\rangle = \sum_i^N \sum_k^3 \sum_l^3 \frac{(l^{-1})_j^{i,k} \tilde{T}_{kl}}{\sqrt{m_k}} \left\langle \Psi_I \left| \frac{\partial}{\partial \hat{R}_{i,l}} \right| \Psi_J \right\rangle \quad (\text{C9})$$

Appendix D: Nuclear Velocity Adjustments with Molecular Constraints

Adjusting the nuclear velocities along components parallel to the NA coupling vector \mathbf{d}_{IJ}^i maintains energy conservation when a NA transition occurs. However, the presence of intramolecular constraints means that the NA coupling vector must be adjusted prior to adjusting the velocities by subtracting out the vector components along the derivative of the constraints. This is done by applying constraint conditions in form of Lagrange multipliers to the coupling vector itself. One considers \mathbf{d}_{IJ}^i / m_i for a site i to be a NA force to which a constraint may be applied. Following the method of Ciccotti, Ferrario, and Rychaert,⁶⁶ we subdivide the nuclear sites of a molecule into two sets. The first set consists of primary atoms between which distance constraints are applied. The second set is composed of atoms whose positions are expressed as linear combinations of the primary atom positions. There will be l_b primary constraints of the form

$$\sigma_p = d_p^2 - |\mathbf{R}_i - \mathbf{R}_j|^2 = 0 \quad (\text{D1})$$

where d_p is the distance between the sites \mathbf{R}_i and \mathbf{R}_j . In practice, these sites need not be primary nuclear positions themselves within the molecule, they can be linear combinations of primary nuclear site positions if an entire group of atoms within the molecule is being treated as a rigid whole, but for the sake of clarity it will be assumed that they represent the primary atomic positions themselves. The constraint conditions on the secondary atoms, of which there will be n_s , are given by

$$\boldsymbol{\tau}_\alpha = \sum_{i=1}^{n_b} C_{\alpha i} \mathbf{R}_i - \mathbf{r}_\alpha = 0 \quad (\text{D2})$$

where there are n_b primary sites. The NA force vectors are also divided into primary and secondary groups, to which the constraint conditions using the method of Lagrange multipliers are applied.

$$\frac{\tilde{\mathbf{d}}_{IK}^i}{m_i} = \frac{\mathbf{d}_{IK}^i}{m_i} - \sum_{p=1}^{l_b} \lambda_p \nabla_i \sigma_p - \sum_{\beta=1}^{n_s} \frac{\nabla_i (\boldsymbol{\mu}_\beta \cdot \boldsymbol{\tau}_\beta)}{m_i} \quad (\text{D3})$$

$$\frac{\tilde{\mathbf{d}}_{IK}^\alpha}{m_\alpha} = \frac{\mathbf{d}_{IK}^\alpha}{m_\alpha} - \sum_{\beta=1}^{n_s} \frac{\nabla_\alpha (\boldsymbol{\mu}_\beta \cdot \boldsymbol{\tau}_\beta)}{m_\alpha} \quad (\text{D4})$$

where λ_p and μ_β are the Lagrange multipliers for the primary and secondary constraint conditions. The adjusted NA coupling vectors $\tilde{\mathbf{d}}_{IK}^i$ and $\tilde{\mathbf{d}}_{IK}^\alpha$ will be used to adjust the velocities as per eq 36. Next, we use the fact that the adjusted NA force vectors for the secondary sites must obey eq D2:

$$\frac{\tilde{\mathbf{d}}_{IK}^\alpha}{m_\alpha} = \sum_{i=1}^{n_b} C_{\alpha i} \frac{\tilde{\mathbf{d}}_{IK}^i}{m_i} \quad (\text{D5})$$

Using this equation it is possible solve for the secondary Lagrange multipliers, μ_β , and show that

$$\tilde{\mathbf{d}}_{IK}^i = p_i - \sum_{p=1}^{l_b} \lambda_p \Delta_{ip} \quad (\text{D6})$$

where

$$\Delta_{iP} = \nabla_i \sigma_P - \sum_{j=1}^{n_b} \sum_{\alpha, \beta=1}^{n_s} C_{\alpha i} A_{\alpha \beta}^{-1} \frac{C_{\beta j}}{m_j} \nabla_j \sigma_P \quad (D7)$$

The matrix **A** is given by

$$A_{\alpha \beta} = \frac{\delta_{\alpha \beta}}{m_{\alpha}} + \sum_{i=1}^{n_b} \frac{C_{\alpha i} C_{\beta i}}{m_i} \quad (D8)$$

The first term of eq D6, p_i , is given by

$$p_i = \mathbf{d}_{IK}^i - \sum_{\alpha, \beta=1}^{n_s} C_{\alpha i} A_{\alpha \beta}^{-1} \mathbf{T}_{\beta} \quad (D9)$$

where

$$\mathbf{T}_{\beta} = \frac{\mathbf{d}_{IK}^{\beta}}{m_{\beta}} + \sum_{i=1}^{n_b} \frac{C_{\beta i} \mathbf{d}_{IK}^i}{m_i} \quad (D10)$$

Now all that remains to is to find the set Lagrange multipliers for the primary constraints. This can be done taking the equation for the scaled velocities (eq 36) and inserting eq D6 for $\tilde{\mathbf{d}}_{IK}^i$

$$\dot{\mathbf{R}}_i - \dot{\mathbf{R}}'_i = -\frac{\gamma_{IK}}{m_i} p_i + \frac{\gamma_{IK}}{m_i} \sum_{P=1}^{l_b} \lambda_P \Delta_{iP} \quad (D11)$$

We now subtract $(\dot{\mathbf{R}}_j - \dot{\mathbf{R}}'_j)$ from both sides of (D11) to obtain

$$\dot{\mathbf{R}}_{ij} - \dot{\mathbf{R}}'_{ij} = -\gamma_{IK} \left(\frac{p_i}{m_i} - \frac{p_j}{m_j} \right) + \gamma_{IK} \sum_{P=1}^{l_b} \lambda_P \left(\frac{\Delta_{iP}}{m_i} - \frac{\Delta_{jP}}{m_j} \right) \quad (D12)$$

If $\dot{\mathbf{R}}_{ij}$ is the difference in velocities between two sites that have a primary constraint between them, then the dot product of $\dot{\mathbf{R}}_{ij}$ with each term of the left-hand side of eq D12 will be zero, i.e.,

$$\dot{\mathbf{R}}_{ij} \cdot \mathbf{R}_{ij} = \dot{\mathbf{R}}'_{ij} \cdot \mathbf{R}_{ij} = 0 \quad (D13)$$

because the velocities along the derivative of the constraint should be zero both before and after they are adjusted for the NA transition. This implies that there are l_b equations of the form

$$\mathbf{R}_{ij} \cdot \left(\frac{p_i}{m_i} - \frac{p_j}{m_j} \right) = \sum_{P=1}^{l_b} \lambda_P \mathbf{R}_{ij} \cdot \left(\frac{\Delta_{iP}}{m_i} - \frac{\Delta_{jP}}{m_j} \right) \quad (D14)$$

These equations can be rewritten in matrix form

$$\tilde{\mathbf{B}} = \tilde{\mathbf{A}} \boldsymbol{\lambda} \quad (D15)$$

where the vector $\tilde{\mathbf{B}}$ is given by

$$\tilde{\mathbf{B}} = \begin{pmatrix} \mathbf{R}_{ij} \cdot \left(\frac{p_i}{m_i} - \frac{p_j}{m_j} \right) \\ \vdots \\ \mathbf{R}_{kn} \cdot \left(\frac{p_k}{m_k} - \frac{p_n}{m_n} \right) \end{pmatrix} \quad (D16)$$

The matrix $\tilde{\mathbf{A}}$ has elements

$$\tilde{A}_{mn} = \mathbf{R}_{ij} \cdot \left(\frac{\Delta_{in}}{m_i} - \frac{\Delta_{jn}}{m_j} \right) \quad (D17)$$

TABLE 1: Parameters for the Numerical Fit to the Lindberg⁶⁷ Equation for the Semiempirical Overlap Integral β_{CX}

site X	μ_{CX} (bohr ⁻¹)	β_1^{CX} (hartrees)	β_2^{CX} (hartrees bohr ⁻¹)
C	0.67931	-0.083032	0.031686
N	0.80659	-0.074106	0.029008
O	0.89987	-0.095542	0.035262

where the index m denotes a pair of sites (i, j) that make up the m th constraint. The matrix $\tilde{\mathbf{A}}$ can then be inverted to find the primary Lagrangian constraints. With the constraints in hand the adjusted primary NA coupling vectors $\tilde{\mathbf{d}}_{IK}^i$ can be found from eq D6 and the secondary NA coupling vectors $\tilde{\mathbf{d}}_{IK}^{\alpha}$ from eq D5.

Appendix E: Distance-Dependent β Parameter

In the implementation of the PPP method for betaine-30 in ref 43, the semiempirical π -electron overlap integral β was treated as a constant. This was appropriate since the relative motion between chemically bonded pairs of atoms was constrained. Furthermore, gradient terms of β need not be included in that case for the semiclassical NA coupling term $\mathbf{d}_P \cdot \dot{\mathbf{R}}$ in eq 25 because there are no nuclear velocities with components along the bonds of the molecule. However, the gradient of β terms must be included when evaluating the NA coupling matrix elements in eq 25 for the quantum intramolecular contribution to the NA coupling. The overlap integral in our previous implementation was evaluated using the Lindberg approximation:⁶⁷

$$\beta_{\mu\nu} = (\hbar^2/m_e) R_{\mu\nu}^{-1} \frac{dS_{\mu\nu}}{dR_{\mu\nu}} \quad (E1)$$

where \hbar is Planck's constant over 2π , m_e is the electron mass, and $S_{\mu\nu}$ is the overlap integral between atomic orbitals μ and ν which are separated by the distance $R_{\mu\nu}$. To evaluate eq E1 and its gradients in the calculations, we use a numerical fit to an evaluation of this a priori expression with standard Slater orbital parameters.⁶⁸ The fitting expression used is

$$\beta_{\mu\nu} = \exp(-\mu_{CX}(R_{\mu\nu} - R_{CX}^{\text{eq}})) [\beta_1^{CX} + \beta_2^{CX}(R_{\mu\nu} - R_{CX}^{\text{eq}})] \quad (E2)$$

The values of the parameters for eq E2 are listed in Table 1.

Acknowledgment. The authors are grateful for support of this research by a grant from the NSF. Partial support of this work by the Texas Advanced Research Program and the Institute for Theoretical Chemistry, University of Texas at Austin is also gratefully acknowledged. J.L. has been supported in part by a postdoctoral fellowship from the Natural Sciences and Engineering Research Council of Canada and by an NSF/CISE Postdoctoral grant (ASC-9704682).

References and Notes

- (1) Barbara, P. F.; Meyer, T. J.; Ratner, M. A. *J. Phys. Chem.* **1996**, *100*, 13148.
- (2) Sumi, H.; Marcus, R. A. *J. Chem. Phys.* **1986**, *84*, 4894.
- (3) Nadler, W.; Marcus, R. A. *J. Chem. Phys.* **1987**, *86*, 3906.
- (4) Jortner, J.; Bixon, M. *J. Chem. Phys.* **1988**, *88*, 167.
- (5) Alexandrov, I. V. *J. Chem. Phys.* **1980**, *51*, 449.
- (6) Calef, D. F.; Wolynes, P. G. *J. Phys. Chem.* **1983**, *87*, 3387.
- (7) Zwan, G. v. d.; Hynes, J. T. *J. Chem. Phys.* **1982**, *76*, 2993.
- (8) Zusman, L. D. *J. Chem. Phys.* **1980**, *49*, 295.
- (9) Tominaga, K.; Walker, G. C.; Kang, T. J.; Barbara, P. F. *J. Phys. Chem.* **1991**, *95*, 10485.
- (10) Reid, P. J.; Silva, C.; Barbara, P. F.; Karki, L.; Hupp, J. T. *J. Phys. Chem.* **1995**, *99*, 2609.

- (11) Reid, P.; Barbara, P. F. *J. Phys. Chem.* **1995**, *99*, 3554.
(12) Yoshihara, K.; Tominaga, K.; Nagasawa, Y. *Bull. Chem. Soc. Jpn.* **1995**, *68*, 696.
(13) Su, S.-G.; Simon, J. D. *J. Phys. Chem.* **1988**, *92*, 2395.
(14) Maroncelli, M.; MacInnis, J.; Fleming, G. R. *Science* **1989**, *243*, 1674.
(15) Reichardt, C. *Angew. Chem., Int. Ed. Engl.* **1979**, *18*, 98.
(16) Reichardt, C. *Solvents and Solvent Effects in Organic Chemistry*; Weinheim: New York, 1988.
(17) Plieninger, P.; Baumgärtel, H. *Ber. Bunsen-Ges. Phys. Chem.* **1982**, *86*, 161.
(18) Johnson, B. P.; Khaledi, M. G.; Dorsey, J. G. *J. Chromatogr.* **1987**, *384*, 221.
(19) Johnson, B. P.; Khaledi, M. G.; Dorsey, J. G. *Anal. Chem.* **1986**, *58*, 2354.
(20) Åkesson, E.; Walker, G. C.; Barbara, P. F. *J. Chem. Phys.* **1991**, *95*, 4188.
(21) Åkesson, E.; Johnson, A. E.; Levinger, N. E.; Gilbert, G. C.; DuBrail, T. P.; Barbara, P. F. *J. Chem. Phys.* **1992**, *96*, 7859.
(22) Levinger, N. E.; Johnson, A. E.; Walker, G. C.; Barbara, P. F. *Chem. Phys. Lett.* **1992**, *196*, 159.
(23) Walker, G. C. Ph.D. Thesis, University of Minnesota, 1991.
(24) Walker, G. C.; Åkesson, E.; Johnson, A. E.; Levinger, N. E.; Barbara, P. F. *J. Phys. Chem.* **1992**, *96*, 3728.
(25) Johnson, A. E.; Levinger, N. E.; Jarzeba, W.; Schlieff, R. E.; Kliner, D. A. V.; Barbara, P. F. *Chem. Phys.* **1993**, *176*, 555.
(26) Barbara, P. F.; Walker, G. C.; Smith, T. P. *Science* **1992**, *256*, 975.
(27) Zhu, J.; Rasaiah, J. C. *J. Chem. Phys.* **1994**, *101*, 9966.
(28) Gayathri, N.; Bagchi, B. *J. Chim. Phys.* **1996**, *93*, 1652.
(29) Maroncelli, M. *J. Mol. Liq.* **1993**, *57*, 1.
(30) Jimenez, R.; Fleming, G. R.; Kumar, P. V.; Maroncelli, M. *Nature* **1994**, *369*, 471.
(31) Rosenthal, S. J.; Xie, X.; Du, M.; Fleming, G. R. *J. Chem. Phys.* **1991**, *95*, 4715.
(32) Horng, M. L.; Gardecki, J. A.; Papazyan, A.; Maroncelli, M. *J. Phys. Chem.* **1995**, *99*, 17311.
(33) Gardecki, J.; Horng, M. L.; Papazyan, A.; Maroncelli, M. *J. Mol. Liq.* **1995**, *65*, 49.
(34) Maroncelli, M.; Fleming, G. R. *J. Chem. Phys.* **1988**, *89*, 5044.
(35) Maroncelli, M. *J. Chem. Phys.* **1991**, *94*, 2084.
(36) Carter, E. A.; Hynes, J. T. *J. Chem. Phys.* **1991**, *94*, 5961.
(37) Maroncelli, M.; Kumar, V. P.; Papazyan, A. *J. Phys. Chem.* **1993**, *97*, 13.
(38) Ladanyi, B. M.; Stratt, R. M. *J. Phys. Chem.* **1996**, *100*, 1266.
(39) Ladanyi, B. M.; Stratt, R. M. *J. Phys. Chem.* **1995**, *99*, 2502.
(40) Stratt, R. M.; Cho, M. *J. Chem. Phys.* **1994**, *100*, 6700.
(41) Bixon, M.; Jortner, J. *Chem. Phys.* **1993**, *176*, 467.
(42) Zong, Y.; McHale, J. L. *J. Chem. Phys.* **1997**, *106*, 4963.
(43) Lobaugh, J.; Rossky, P. J. *J. Phys. Chem.*, submitted.
(44) Warshel, A.; Karplus, M. *J. Am. Chem. Soc.* **1972**, *94*, 5612.
(45) Warshel, A.; Lippicirella, A. *J. Am. Chem. Soc.* **1981**, *103*, 4664.
Warshel, A.; *Nature* **1976**, *260*, 679. Warshel, A.; Chu, Z. T.; Hwang, J.-K. *Chem. Phys.* **1991**, *158*, 303.
(46) Tully, J. C. *J. Chem. Phys.* **1990**, *93*, 1061.
(47) Pariser, R.; Parr, R. G. *J. Chem. Phys.* **1953**, *21*, 466.
(48) Pariser, R.; Parr, R. G. *J. Chem. Phys.* **1953**, *21*, 767.
(49) Pople, J. A. *Trans. Faraday Soc.* **1953**, *49*, 1375.
(50) Edwards, D. M. F.; Madden, P. A.; McDonald, I. R. *Mol. Phys.* **1984**, *51*, 1141.
(51) Bailey, M. L. *Theor. Chim. Acta (Berlin)* **1969**, *13*, 56.
(52) Nishimoto, K.; Forster, L. S. *Theor. Chim. Acta* **1966**, *4*, 155.
(53) Yamaguchi, Y.; Osamura, Y.; Goddard, J. D.; Schaefer, H. F., III *A New Dimension to Quantum Chemistry: Analytic Derivative Methods in Ab Initio Molecular Electronic Structure Theory*; Oxford University Press: Oxford, 1994; p 471.
(54) Pulay, P. In *Ab initio Methods in Quantum Chemistry-II*; Lawley, K. P., Ed.; John Wiley & Sons Ltd.: New York, 1987; Vol. 69.
(55) Pople, J. A.; Krishnan, R.; Schlegel, H. B.; Binkley, J. S. *Int. J. Quantum Chem.: Quantum Chem. Symp.* **1979**, *13*, 225.
(56) Handy, N. C.; Schaefer, H. F., III *J. Chem. Phys.* **1984**, *81*, 5031.
(57) Hurley, M. M.; Hammes-Schiffer, S. *J. Phys. Chem.*, in press.
(58) Tully, J. C. In *Dynamics of Molecular Collisions, Part B*; Miller, W. H., Ed.; Plenum Press: New York, 1976; Vol. 2, p 217.
(59) Stewart, J. J. P.; Seiler, F. J. Quantum Chemistry Program Exchange, Indiana University, 1990.
(60) Hwang, J.-K.; Warshel, A. *J. Am. Chem. Soc.* **1987**, *109*, 715. Warshel, A. Calculations of Vibronic Transitions of Conjugated Molecules (unpublished).
(61) Eckart, C. *Phys. Rev.* **1935**, *47*, 552.
(62) Wilson, E. B.; Decius, J. C.; Cross, P. C. *Molecular Vibrations the Theory of Infrared and Raman Vibrational Spectra*; Dover Publications, Inc.: New York, 1980.
(63) Hammes-Schiffer, S.; Tully, J. C. *J. Chem. Phys.* **1994**, *100*, 4657.
(64) Murrell, J. N.; Harget, A. J. *Semiempirical Self-Consistent Molecular-Orbital Theory of Molecules*; Wiley-Interscience: London, 1972.
(65) Pickett, H. M.; Strauss, H. L. *J. Am. Chem. Soc.* **1970**, *92*, 7281.
(66) Ciccotti, G.; Ferrario, M.; Ryckaert, J.-P. *Mol. Phys.* **1982**, *47*, 1253.
(67) Linderberg, J. *Chem. Phys. Lett.* **1967**, *1*, 39.
(68) Atkins, P. W. *Molecular Quantum Mechanics*; Oxford University Press: Oxford, 1983.

Quantum Wave Packet Study of Nonadiabatic Effects in $\text{O}(^1\text{D}) + \text{H}_2 \rightarrow \text{OH} + \text{H}$

Stephen K. Gray*

Chemistry Division, Argonne National Laboratory, Argonne, Illinois 60439

Carlo Petrongolo

Department of Chemistry, University of Siena, Via Aldo Moro, I-53100 Siena, Italy

Karen Drukker and George C. Schatz

Chemistry Department, Northwestern University, 2145 Sheridan Road, Evanston, Illinois 60208-3113

Received: May 17, 1999; In Final Form: July 27, 1999

We develop a wave packet approach to treating the electronically nonadiabatic reaction dynamics of $\text{O}(^1\text{D}) + \text{H}_2 \rightarrow \text{OH} + \text{H}$, allowing for the $1^1\text{A}'$ and $2^1\text{A}'$ potential energy surfaces and couplings, as well as the three internal nuclear coordinates. Two different systems of coupled potential energy surfaces are considered, a semiempirical diatomics-in-molecules (DIM) system due to Kuntz, Niefer, and Sloan, and a recently developed *ab initio* system due to Dobbyn and Knowles (DK). Nonadiabatic quantum results, with total angular momentum $J = 0$, are obtained and discussed. Several single surface calculations are carried out for comparison with the nonadiabatic results. Comparisons with trajectory surface hopping (TSH) calculations, and with approximate quantum calculations, are also included. The electrostatic coupling produces strong interactions between the $1^1\text{A}'$ and $2^1\text{A}'$ states at short range (where these states have a conical intersection) and weak but, interestingly, nonnegligible interactions between these states at longer range. Our wave packet results show that if the initial state is chosen to be effectively the $1\text{A}'$ state (for which insertion to form products occurs on the adiabatic surface), then there is very little difference between the adiabatic and coupled surface results. In either case the reaction probability is a relatively flat function of energy, except for resonant oscillations. However, the $2\text{A}'$ reaction, dynamics (which involves a collinear transition state) is strongly perturbed by nonadiabatic effects in two distinct ways. At energies above the transition state barrier, the diabatic limit is dominant, and the $2\text{A}'$ reaction probability is similar to that for $1\text{A}''$, which has no coupling with the other surfaces. At energies below the barrier, we find a significant component of the reaction probability from long range electronic coupling that effectively allows the wave packet to avoid having to tunnel through the barrier. This effect, which is observed on both the DIM and DK surfaces, is estimated to cause a 10% contribution to the room temperature rate constant from nonadiabatic effects. Similar results are obtained from the TSH and approximate quantum calculations.

I. Introduction

The reaction



has long served as the prototypical insertion reaction. It is exoergic by almost 2 eV, and the lowest adiabatic potential surface ($1^1\text{A}'$) that correlates to both reactants and products includes a deep well associated with the ground electronic state of H_2O . (The zero-point energy of H_2O is ≈ 5 eV below the zero-point energy of the products.) Both products are easily detected, so there have been numerous experimental studies of thermal rate coefficients,^{1,2} isotope effects,^{3–6} product vibrational distributions,⁷ rotational distributions,^{8,9} integral cross sections,¹⁰ and angular and translational distributions.^{11–16} There have also been several theoretical studies of the ground singlet state potential surface^{17–21} and its reaction dynamics.^{22–28}

Recently there has been increasing interest in the reaction dynamics associated with excited states that also correlate to $\text{O}(^1\text{D}) + \text{H}_2$.^{29–35} Figure 1 shows a schematic diagram of the

key electronic states for collinear and nearly collinear OHH geometries. The bottom panel considers collinear OHH geometries. Actually, $\text{O}(^1\text{D})$ splits into a Σ , a doubly degenerate Π , and a doubly degenerate Δ component, so that the reactants in reaction 1 correlate with five electronic states. The Δ state is purely repulsive, and can only play a role in the reaction dynamics through its Coriolis interactions with the other states, which turns out not to be very important.³⁵ This state is not depicted. The Σ surface is the lowest energy surface while the reagents approach, with a very small barrier (< 0.5 kcal/mol or 0.02 eV), but it correlates to the excited $\text{A}^2\Sigma$ state of the OH product, and thus it cannot contribute to reaction. Only the Π state connects the reagent and product states, but there is a barrier to reaction of around 2 kcal/mol (0.09 eV). The top part shows how this picture changes for bent geometries. Here we show only the $1\text{A}'$ and $2\text{A}'$ components that come from the Σ and Π states. (For simplicity, we often omit the singlet spin labels on the various electronic states.) These have a conical intersection at the position of the Σ/Π crossing, making it possible for reaction to occur out of either state. Not shown in this panel is the $1\text{A}''$ state, which is the other component the Π

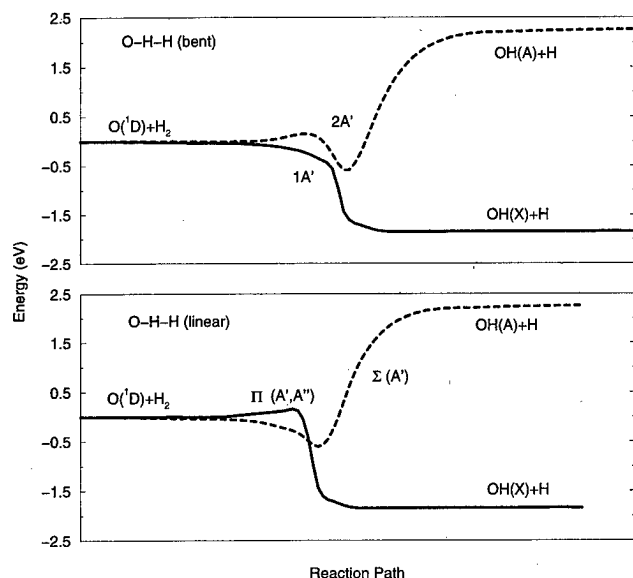


Figure 1. Schematic diagram of the two relevant electronic states for $O(^1D) + H_2$. As the reactants approach each other the initially degenerate surfaces split in energy. $OH(X)+H$ corresponds to products. Top part: Surfaces for bent OHH geometries. Bottom part: Surfaces for collinear OHH geometries.

state in the bottom panel. This has the same collinear barrier as $2A'$, but a lower bending frequency at the saddle point, so one expects that the reaction probability from this state will be larger than that from the $2A'$ state. Note, however, that the $2A'$ reaction probability would be zero if the dynamics were purely adiabatic, while the $1A''$ state is not coupled to the other states, and is reactive in the adiabatic limit.

Although the behavior of the potential surfaces in Figure 1 is now well established, the role of the excited states in the reaction dynamics of reaction 1 is still the subject of considerable confusion. Interest in excited state effects has arisen recently as a result of several experiments^{10,12,14-16} which show effects that are not consistent with a simple insertion reaction. In particular Che and Liu¹² measured differential cross sections for the $O(^1D) + HD$ at a collision energy of 4.55 kcal/mol (0.197 eV) and found substantial deviation from the forward-backward symmetry found for theoretical studies based on the ground state surface.²¹ In addition, similar measurements by other groups^{15,16} on $O(^1D) + H_2$, HD and D_2 at energies as low as 1 kcal/mol (0.04 eV) indicate asymmetry in the differential cross sections. In other studies¹⁴ the integral cross section was found to decrease with increasing energy for collision energies below 2 kcal/mol, as expected for an insertion reaction with no barrier, and to increase at higher energies, as expected for an abstraction reaction. This influences the $O(^1D) + H_2$ rate coefficients,⁴ and it is observed that the high temperature rate coefficient is substantially higher than at room temperature. This activated behavior is not expected for reaction on the ground state surface.

These experimental studies have stimulated theoretical studies of $O(^1D) + H_2$ that include excited states. In one of these studies, the excited states were included only as uncoupled adiabatic states in quasi-classical trajectory (QCT) calculations.³³ Other studies^{29-31,34} used trajectory surface hopping (TSH) methods^{36,37} and involved two coupled states ($1A'$ and $2A'$). The TSH studies included coupling due to electrostatic interactions that are important at short range (because of the conical intersection), but electronic Coriolis effects and long range electrostatic coupling were neglected. The conclusion of these studies is that the lowest state can account for most of the cross section at low collision energies ≤ 2 kcal/mol. The $2A'$ and

$1A''$ states become important at high energy once the barrier to reaction on these states is surmounted. This produces the increase in the cross section with energy observed above 2 kcal/mol.

Important discrepancies between theory and experiment remain that are unresolved at this point. In particular, several groups have noted³⁸⁻⁴⁰ that the agreement between the observed angular and translational energy distributions and those from TSH or adiabatic QCT calculations is worse when the excited states are included than when they are omitted. Also, Lee and Liu⁴¹ have recently demonstrated that the $1A''$ contribution to the cross section is larger for H_2 initial rotation state $j = 1$ compared to $j = 0$, the opposite of what was suggested by classical trajectory calculations.³³ In addition, the validity of the TSH method has been questioned in recent studies of other gas phase reactions,^{42,43} so these criticisms might also be valid for $O(^1D) + H_2$.

In this paper, we present a new study of nonadiabatic effects in $O(^1D) + H_2$, based on three dimensional (total angular momentum $J = 0$) wave packet calculations. These calculations are based on similar technology to what was used in recent wave packet calculations for the ground state surface,^{27,28} but in the present calculations we include for the coupled dynamics involving $1A'$ and $2A'$. We also present adiabatic results for the $1A''$ surface, so that the relative reactivity of $2A'$ and $1A''$ can be determined. Electronic Coriolis coupling effects will not be included; however, a recent quantum study has shown³⁵ that they play a relatively minor role in the overall reactivity for this system.

Our calculations consider two sets of coupled potential surfaces, one being the semiempirical diatomics-in-molecules (DIM) surfaces that were developed by Kuntz, Niefer, and Sloan^{30,31} and the other being the recently developed ab initio surfaces from Dobbyn and Knowles (DK).^{44,45} Included in our analysis are comparisons with the results of other methods for describing the reaction dynamics, including the TSH method noted above, and the recent vibrationally adiabatic quantum scattering method of Drukker and Schatz.³⁵ We also make estimates of the effect of nonadiabaticity on the thermal rate constant.

All of our quantum and our best TSH calculations are based on a diabatic representation where the electronic Hamiltonian is written as a 2×2 matrix that contains Σ -like and $\Pi(A')$ -like potentials along the diagonal, and an interaction potential $H_{\Sigma\Pi}$ that vanishes for linear geometries. We use the terms " Σ diabatic" and " Π -diabatic" to refer to these states (even for nonlinear geometries), and " $1A''$ " and " $2A''$ " to refer to the adiabats that are obtained by diagonalizing the 2×2 matrix. In Drukker and Schatz,³⁵ another diabatic representation was introduced in which the A' and A'' components of the Π state are rewritten in terms of complex exponentials so that they are also eigenfunctions of the electronic orbital angular momentum projection operator along the molecular axis. This alternative diabatic representation, in which the electronic Hamiltonian is 3×3 (or 5×5 if Δ states are included), is convenient for describing the Coriolis interactions. However if this interaction is left out, as in the present calculations, then the A' and A'' states are not coupled, and it is easier to use the 2×2 diabatic representation in terms of Σ and $\Pi(A')$ states.

This paper is organized as follows. In section II we describe the diabatic model, potential surfaces, and briefly outline essential aspects of the wave packet and other dynamical methods employed by us. Section III presents the application to $O(^1D) + H_2$. Section IV summarizes our conclusions.

II. Model and Methods

A. Diabatic Hamiltonian Model. Here we present the two-state electronic Hamiltonian used in the present calculations. A more rigorous five-state description of the $O(^1D) + H_2$ reaction dynamics is presented by Drukker and Schatz.³⁵ Reactant Jacobi coordinates R , r , and $\cos \gamma$ are employed, with R being the O to center of H_2 distance, r being the H_2 distance, and $\cos \gamma$ the cosine of the angle between the vectors associated with R and r .

In the two-state approximation, electronic orbital angular momentum is neglected, so that the Hamiltonian operator H is given by an expression that is very similar to the single surface result. This Hamiltonian is

$$H = \frac{p^2}{2\mu} + \frac{l^2}{2\mu R^2} + \frac{p^2}{2m} + \frac{j^2}{2mr^2} + H^{el} \quad (2)$$

where $\mu = 2m_H m_O / (2m_H + m_O)$, $m = m_H/2$, P and p are radial momentum operators associated with R and r , respectively, $l^2/2\mu R^2$ is the centrifugal term, $j^2/2mr^2$ is the rotational energy term, which involves derivatives associated with $\cos \gamma$, and H^{el} is the electronic Hamiltonian. Since electronic angular momentum is not included, the total angular momentum J is given by $J = j + l$, and the centrifugal term $l^2/2\mu R^2$ gives rise to (nuclear) Coriolis coupling effects when the wave function is expressed in body-fixed coordinates. In this work, only $J = 0$ will be considered in the wave packet calculations ($l^2 = j^2$), and \angle -shifting²⁸ or J -shifting⁴⁶ approximations are used in performing the partial wave sums to determine cross sections and rate constants.

The wave function (or wave packet) is expanded in terms of diabatic electronic states, which we call $|\Sigma\rangle$ and $|\Pi\rangle$. (For brevity we use $|\Pi\rangle$ to denote the state associated with the A' component, $\Pi(A')$, of the Π state.) These states depend not only on the electronic degrees of freedom, but on the nuclear degrees of freedom R , r , and $\cos \gamma$. However, it is assumed that these diabatic states have been suitably determined so that nuclear derivative terms associated with them, arising from the kinetic energy operators in eq 2, can be neglected. This, of course, is a key simplifying feature of a good diabatic representation since coupling matrix elements related to derivatives of the electronic states with respect to nuclear coordinates, which can be difficult to calculate (and sometimes divergent), do not occur. The Schrödinger equation then takes the form of a 2×2 matrix equation, with the nuclear kinetic energy terms in the Hamiltonian appearing along the diagonal, and the electronic Hamiltonian H^{el} appearing as a 2×2 matrix,

$$H^{el} = \begin{pmatrix} H_{\Sigma\Sigma} & H_{\Sigma\Pi} \\ H_{\Pi\Sigma} & H_{\Pi\Pi} \end{pmatrix} \quad (3)$$

where $H_{\Sigma\Sigma}$ is the Σ diabatic, $H_{\Pi\Pi}$ is the $\Pi(A')$ diabatic, and $H_{\Sigma\Pi} = H_{\Pi\Sigma}$ is the diabatic coupling potential. Note that the diabatic electronic matrix elements in the present treatment are real-valued functions, and are formally consistent with the use of real-valued electronic functions (e.g. cosines). This differs from the use of a complex exponential basis by Schatz and Drukker,³⁵ but is of course also a valid and equivalent representation. (See also the Introduction.)

Of course, all the matrix elements in eq 3 depend on the nuclear degrees of freedom, R , r , and $\cos \gamma$. If H^{el} is diagonalized, then the eigenvalues are the adiabatic potentials ($1A'$ and $2A'$), and the derivatives of the eigenvectors with

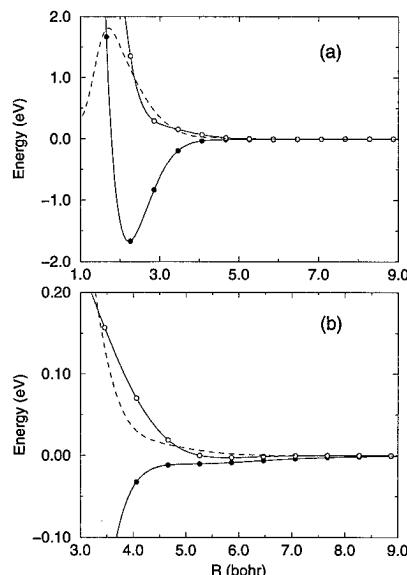


Figure 2. The DK diagonal diabatic energies, $H_{\Sigma\Sigma}$ (solid curve with filled circles), $H_{\Pi\Pi}$ (solid curve with open circles), and coupling $H_{\Sigma\Pi}$ (dashed curve), averaged over an asymptotic H_2 ground vibration-rotation state. (a) presents a broad view of these matrix elements and (b) is a blowup of the longer range portion.

respect to the nuclear variables define the usual nonadiabatic coupling matrix elements that couple the adiabatic states.

B. Potential Energy Surfaces. The Dobbryn-Knowles (DK) potential surface^{44,45} is based on high quality internally contracted multireference configuration interaction calculations. Although adiabatic states are produced in these calculations, a diabatic transformation was performed, so that the matrix elements $H_{\Sigma\Sigma}$, $H_{\Pi\Pi}$, and $H_{\Sigma\Pi}$ were directly provided. This diabaticization is based on calculating matrix elements associated with the component of the electronic orbital angular momentum operator and, in effect, constructing linear superpositions of the adiabatic states (i.e. diabatic states) that have significant Σ or Π character with respect to certain axes. The original theory of this approach was described by Rebentrost and Lester,⁴⁷ and a recent description that is more relevant to the present applications is given in Dobbryn et al.⁴⁸ Figure 2 illustrates the relevant diabatic energies and coupling for the DK surface. The $H_{\alpha,\alpha'}$ displayed in Figure 2 have been averaged over r and $\cos \gamma$, with weighting determined by the absolute square of an asymptotic H_2 ground vibration-rotation state. The top part, Figure 2a, gives a broad picture over a wide range of R values, whereas the lower part, Figure 2b, focuses on the diabats and coupling at longer range.

The DIM potential of Kuntz, Niefer, and Sloan^{30,31} has been developed in a slightly different way than the DK surface. This potential is available in the adiabatic representation, and it is not straightforward to transform it to a diabatic representation using the procedure just described. Another procedure is possible, however, because in addition to the $1A'$ and $2A'$ surfaces we also have the $1A''$ surface from the same DIM calculations.³⁴ This surface is similar to the Π diabatic, $H_{\Pi\Pi}$, so if we simply assume these are the same, it is possible to derive expressions for $H_{\Sigma\Sigma}$ and $H_{\Sigma\Pi}$ by inverting the following formulas, obtained from diagonalizing eq 3:

$$\begin{aligned} E(1A') &= \frac{1}{2}[(H_{\Sigma\Sigma} + H_{\Pi\Pi}) - ((H_{\Sigma\Sigma} - H_{\Pi\Pi})^2 - 4H_{\Sigma\Pi}^2)^{1/2}] \\ E(2A') &= \frac{1}{2}[(H_{\Sigma\Sigma} + H_{\Pi\Pi}) + ((H_{\Sigma\Sigma} - H_{\Pi\Pi})^2 - 4H_{\Sigma\Pi}^2)^{1/2}] \end{aligned} \quad (4)$$

We used the DIM diabats defined this way in all of our calculations.

The DK and DIM potential surfaces are qualitatively similar, but there are some important quantitative differences. Perhaps the most noticeable difference is in the (collinear) barrier height for reaction on the $1\text{A}'$ surface. This barrier is 2.3 kcal/mol on the DK surface and is located at $r_{\text{OH}} = 3.09 a_0$, $r_{\text{HH}} = 1.46 a_0$, with vibrational frequencies 3646, 271, and $661i \text{ cm}^{-1}$. On the DIM surface, the barrier is 3.7 kcal/mol, and is located at $r_{\text{OH}} = 3.17 a_0$, $r_{\text{HH}} = 1.43 a_0$, with frequencies of 4122, 174, $566i \text{ cm}^{-1}$. Another difference is in the long range part of the $1\text{A}'$ potential, which is more attractive on the DIM than on DK surface. These differences make the $1\text{A}'$ cross sections larger for the DIM surface, but the $1\text{A}''$ and $2\text{A}'$ cross sections (usually) larger on the DK surface.

C. Wave Packet Dynamics. The quantum dynamics calculations were carried out in a fashion similar to previous calculations for the $1\text{A}'$ adiabatic dynamics.^{27,28} The main difference, of course, is that the wave packet now also includes components associated with the two diabatic electronic states $\alpha = \Sigma$ and Π . The addition of the electronic degrees of freedom poses no difficulties with the $J = 0$ Hamiltonian being essentially the same as in refs 27 and 28 except that the adiabatic potential $V(R, r, \cos \gamma)$ is replaced by the 2×2 diabatic matrix, eq 3. We therefore only describe a few pertinent details.

The propagation scheme employed (see below) focuses on just the real part of the wave packet, which in terms of reactant Jacobi coordinates may be written

$$q^k(R, r, \cos \gamma) = \sum_{\alpha} \sum_j C_{j,\alpha}^k(R, r) \bar{P}_j(\cos \gamma) |\alpha\rangle \quad (5)$$

where \bar{P}_j are normalized Legendre polynomials, and $|\alpha\rangle$ formally represent the electronic states $\alpha = \Sigma$ and Π . The superscript k is used to denote iteration number or discrete time step. Evenly spaced grids are employed for R and r : with $x = R$ or r , $x_i = x_{\text{min}} + n\Delta x$, $n = 1, 2, \dots, N_x$, $\Delta x = (x_{\text{max}} - x_{\text{min}})/(N_x + 1)$. The introduction of finite sized grids, as well as a finite rotational basis in j , effectively implies q^k is approximated by a large vector \mathbf{q}^k and the Hamiltonian operator becomes a matrix \mathbf{H} .

The real wave packet propagation scheme⁴⁹ was employed, which features propagating the real vector \mathbf{q}^k according to Mandelshtam and Taylor's damped Chebyshev iterations.^{50,51} Introducing a linearly scaled Hamiltonian matrix $\mathbf{H}_s = a_s \mathbf{H} + b_s$, such that the eigenvalues of \mathbf{H}_s lie within $(-1, 1)$, the damped Chebyshev iteration is

$$\mathbf{q}^{k+1} = \mathbf{A} \cdot (-\mathbf{A} \cdot \mathbf{q}^{k-1} + 2\mathbf{H}_s \cdot \mathbf{q}^k) \quad (6)$$

here \mathbf{A} is some appropriate matrix which damps the wave packet amplitude as it approaches the R and r grid edges. We take \mathbf{A} to be a diagonal matrix with elements $a_R(R_i)a_r(r_j)$, where $a_x(x_i) = \exp[-c_x(x_i - x_a)^2]$ for $x_i \geq x_a$. In the real wave packet approach, the Chebyshev iterations above are identified with the real part of the *exact* Schrödinger time evolution, in discrete time steps $k\tau$, under an effective Hamiltonian matrix $f(\mathbf{H}) = -(\hbar/\tau) \cos^{-1} \mathbf{H}_s$, allowing standard time-dependent methods of analysis to be used in determining reaction probabilities.^{49,52} The effective Hamiltonian matrix differs from \mathbf{H} in a nonlinear fashion, so the "time" $k\tau$ is not physically meaningful. Indeed, τ is arbitrary and cancels in any formulas for observables. (This approach is also closely related to the "time-independent" wave packet approaches of Kouri and co-workers^{53,54} and can be viewed as a generalization to reactive scattering of approaches developed by Chen and Guo.⁵⁵) However, the magnitude of \mathbf{q}^k

is in fact a good approximation to the magnitude of the real part of an ordinary wave packet (evolving under \mathbf{H} and starting from the same initial condition) at a physically meaningful time t_{phys} given by $t_{\text{phys}} \approx ka_s \hbar / (1 - E_s^2)^{1/2}$, where E_s is the mean scaled energy of the wave packet.²⁷ This approximation, based on the linearization of $f(\mathbf{H})$ about E_s is usually quite accurate owing to the fact that, with typical initial conditions, the wave packet's energy is concentrated in a narrow range in comparison with the full energy range.

The initial conditions for our propagations are given by the discrete analogs of $q^0 = \text{Re}\psi$,

$$\psi(R, r, \cos \gamma) = \sqrt{\frac{1}{\sqrt{\pi}\omega}} \exp\left(\frac{-(R - R_0)^2}{2\omega^2}\right) \times \exp(-ik_0(R - R_0)) \chi_0(r) \bar{P}_0(\cos \gamma) |\alpha\rangle \quad (7)$$

which describes an incoming Gaussian wave packet in R with mean momentum $-\hbar k_0$, centered at $R = R_0$, and associated full width at half maximum of $2\omega \ln 2$. H_2 is initially in its ground vibration (χ_0) and rotation (\bar{P}_0) state, and the reactants are initially approaching on electronic state $|\alpha\rangle$. The recursion eq 6 requires \mathbf{q}^0 and \mathbf{q}^1 to be initiated. \mathbf{q}^1 , if the initial condition is complex as it is in the present case, is evaluated according to $\mathbf{q}^1 = \mathbf{H}_s \cdot \mathbf{q}^0 - (1 - \mathbf{H}_s^2)^{1/2} \cdot \mathbf{p}^0$, where \mathbf{p}^0 is the imaginary part of the initial condition.⁴⁹ The action of the square root operator is itself accomplished with a Chebyshev expansion.²⁷

Each iteration step eq 6 requires an evaluation of \mathbf{H} on a real vector. Fast sine Fourier transforms are used to evaluate the relevant kinetic energy terms associated with R and r . The wave packet is kept in the Legendre basis above, which is convenient for evaluation of the relevant centrifugal term associated with j^2 in eq 2. However, the potential terms are evaluated by transformation to a Gauss-Legendre quadrature grid associated with $\cos \gamma$, multiplication by the relevant potential terms on a full grid, and back transformation to the Legendre basis. This approach eliminates storage of large potential matrices. The calculations converge most favorably if the spectral range of the Hamiltonian is kept as small as possible without significantly altering accuracy. This is accomplished by introducing a cut-off energy V_{cut} , which is applied to all components of the diabatic electronic Hamiltonian as well as the centrifugal energy term.²⁷

We estimate total reaction probabilities with a flux approach,⁵² based on calculating the reactive flux on some surface separating reactants from products. In our case we define such a surface by $r = r^*$. (We should note that in the particular cases of the DIM propagation associated with $\alpha = \Sigma$, as well as adiabatic $1\text{A}'$ DIM propagation, there are much stronger long-range interactions relative to the DK surface, which lead to the underlying Σ or $1\text{A}'$ potentials still showing some variation even at $R_0 = 9.5 a_0$. The determination of the total reaction probabilities also requires knowledge of the asymptotic distribution of momenta or energies in the initial wave packet. Because of the potential variation, the analytical form consistent with an incoming Gaussian has some error in it, particularly at low and high energy. We compensate for this by carrying out a back propagation on an effective one-dimensional potential to determine a more correct asymptotic distribution, as discussed in ref 28.

Typical grid and basis set details are given in Table 1. We carry out propagations to typically 20000–30000 iterations of eq 6. A typical coupled electronic state calculation, with the parameters in Table 1, requires ≈ 2.3 days of computational time on an IBM RS/6000 workstation and requires ≈ 80 MB of

TABLE 1. Typical Grid/Basis Set and Initial Condition Details.

reactant scattering coordinate (R) range/ a_0	0–14.5
number of grid points in R	209
diatomic coordinate (r) range/ a_0	0.5–11.5
number of grid points in r	127
number of angular grid points	40 (using potential symmetry)
number of angular basis functions	40 ($j = 0, 2, \dots, 78$)
potential and centrifugal cut-off V_{cut}/eV	12
absorption in R starts at R_d/a_0	10.5
absorption strength in R , c_R/a_0^{-2}	0.005
absorption in r starts at r_d/a_0	7.5
absorption strength in r , c_r/a_0^{-2}	0.005
center of initial wave packet R_0/a_0	9.5
Gaussian width factor ω/a_0	0.4
initial translational kinetic energy/eV	0.15
flux analysis line r^\dagger/a_0	6.0

memory. The single surface calculations with the same parameters require just under a day of computational time.

D. Trajectory Surface Hopping and Vibrationally Adiabatic Coupled Channel Calculations. For comparison with the wave packet results, two more approximate dynamical calculations are carried out for the case corresponding to reactants being initially on the Π state, which has the most interesting electronic coupling effects.

The trajectory surface hopping (TSH) calculations were carried out using Tully's fewest switches approach³⁶ as described by Schatz et al.³⁴ This TSH method involves simultaneous integration of the nuclear coordinates according to the classical equations of motion and of the amplitudes for being on the two electronic states according to a time-dependent Schrödinger equation. The only departure from ref 34 is that with one exception we used a diabatic representation for the TSH calculations rather than an adiabatic representation. This means that the trajectories and coupled Schrödinger equation were integrated using the diabats, and the $H_{\Sigma,\Pi}$ coupling. Also, the direction perpendicular to the intersection surface (used in adjusting the momenta after a surface hop) was chosen to be the gradient of the difference potential ($H_{\Sigma,\Sigma} - H_{\Pi,\Pi}$) rather than the derivative coupling vector. The one exception that we considered was for the DIM surface, where we were also able to use the adiabatic representation of ref 34 with the derivative coupling vectors from the DIM function. We used this calculation to determine the dependence of the results on which representation was used. We found that while both representations give roughly similar results, the diabatic representation results were much more accurate. For example, at 0.2 eV collision energy, the TSH adiabatic representation probability is 0.08, while the corresponding TSH diabatic representation probability is 0.20, and the (DIM, initial Π state) quantum wave packet result is 0.22. Note that because of the conversion between adiabatic and diabatic representations was done approximately, as discussed in section IIB, even the quantum results for the two representations should be different. Although we have not done wave packet calculations in the adiabatic representation (this would be quite difficult), we have assessed the internal consistency of the two representations by determining the derivative couplings that are based on the diabatic representation defined above for the DIM surface, and the results agree reasonably for geometries close to the conical intersection with those in the original adiabatic representation that was used to define the DIM diabats in the first place. As a result, we expect the quantum results will be fairly close for the two representations. In contrast to this, the TSH method, being approximate, should give different results in different representations, even if they are rigorously equivalent in their quantum dynamics. In the present application it turns out that

the Π state dynamics is closer to being diabatic than adiabatic (this is discussed in detail later), so TSH in the diabatic representation is less sensitive to the accuracy of the hopping algorithm than in the adiabatic representation. In fact, the TSH probability in the adiabatic representation is zero in the absence of hopping, so all of the reaction probability of 0.08 comes from the hopping algorithm, whereas in the diabatic representation the probability at 0.2 eV is already 0.11 in the absence of hopping, which means that hopping changes the probability from 0.11 to 0.22. Thus we see that hopping is of lesser importance in the diabatic representation than in the adiabatic representation. Since the diabatic representation results are more accurate, we restrict the TSH results presented later to those based on the diabatic representation.

In the TSH calculations, we considered $J = 0$ and integrated 100 trajectories per energy. The uncertainties associated with the TSH probabilities are estimated to be within $\pm 5\%$. These calculations are quite time consuming for either the DK or DIM surfaces, requiring about a day of workstation time per energy. This is due to the DK and DIM surfaces being complicated functions that must be evaluated 10^4 – 10^5 times per trajectory, the small time steps needed to integrate the time-dependent Schrödinger equation accurately, and the fact that the trajectories can involve collision complexes. (Note the time-dependent Schrödinger equation referred to here is *not* the more rigorous one used in our wave packet calculations, but the one arising from the TSH model.) It would seem that the accurate quantum wave packet approach (which also generates information about all relevant energies at once) is more efficient! However, the effort needed to generate cross sections or rate constants with TSH is not much larger than the effort associated with the $J = 0$ TSH calculations, and the method scales much more favorably with dimensionality.

Approximate time-independent quantum results for the $\text{O} + \text{H}_2$ reaction were also obtained with a vibrationally adiabatic coupled channel method presented in more detail elsewhere.³⁵ In these studies the coupled channel equations were actually solved including all five electronic surfaces. The electronic states of the atom and the rotational states of the diatomic are included without any approximation to the vector coupling, or to the kinetic energy terms in the Hamiltonian. However, in order to keep the problem numerically tractable the diatomic vibration r is treated in an adiabatic fashion, and a limited rotational basis (most appropriate for relatively low collision energies) were employed. Also, the reactive flux is absorbed by using imaginary potentials in the interaction region before products have completely separated. The method was developed for the study of the effect of electronic Coriolis coupling on the reactive cross sections, but here results are presented for the Coriolis decoupled case for comparison with the wave packet calculations. Also, in these calculations we used the electronic Hamiltonian in eq 3 for the electrostatic coupling, rather than that in ref 35 that is based on a complex exponential basis. This leads to reaction probabilities that are consistent with the real-valued electronic functions employed in this paper. These scattering calculations involved using a basis of typically $j = 0, 2$, and 4 rotational states, along with all the appropriate projection states that are consistent with these values of j , for the five electronic states and a given value of J . For low J , this involves a small number of states (< 20), so the computational time per energy is on the order of tens of seconds on a workstation. In contrast to the wave packet and TSH calculations, these calculations are trivial in terms of computational effort. The approximations invoked, however, limit their reliability to low collision energies.

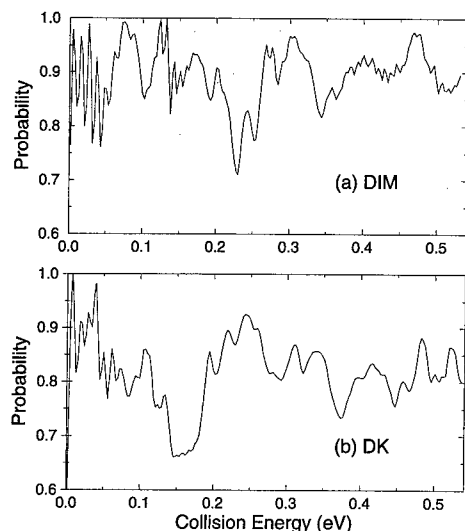


Figure 3. The total reaction probability for $\text{O}(^1\text{D}) + \text{H}_2(X; v=j=0) \rightarrow \text{OH}(X) + \text{H}$ with total angular momentum $J=0$ and assuming adiabatic dynamics on the ground $1\text{A}'$ electronic state. (a) corresponds to the DIM $1\text{A}'$ surface wave packet results, and (b) corresponds to the DK $1\text{A}'$ surface wave packet results.

III. Results and Discussion

A. Adiabatic and Diabatic Single Surface Reaction Dynamics. The ground $1\text{A}'$ adiabatic electronic state directly connects the reactants and products in reaction 1, and also correlates with the ground electronic state of H_2O . Adiabatic dynamics on this surface, is expected to be the most important contributor to the low energy reactive cross sections and moderate temperature rate constants. Figure 3 displays our quantum results for the total reaction probability associated with reaction 1, with the restrictions that the system have total angular momentum $J=0$ and that H_2 initially be in its ground vibration-rotation state, $v=j=0$. The total reaction probability reflects a sum over all energetically allowed $\text{OH}(X^2\Pi)$ vibration-rotation states, v' and j' . (We do not investigate any details concerning the product distributions.) Both the $1\text{A}'$ DIM surface result (Figure 3a) and the $1\text{A}'$ DK surface result (Figure 3b) show that the total reaction probability is, on average, quite high. Both surfaces exhibit significant reaction probability at very low collision energies, consistent with the $1\text{A}'$ surface having no barrier to reaction. While the DIM and DK reaction probabilities are roughly similar, the DIM surface is, on average, more reactive, than the DK surface. This reflects the fact that the DIM surface has stronger long range attraction than the ab initio DK surface. There is a lot of fine structure in Figure 3a and b, presumably because of the presence of numerous short-lived H_2O complexes and also due to the opening of various product v', j' channels. Similar behavior was seen in the adiabatic quantum dynamics of two other $1\text{A}'$ potential energy surfaces.^{26,27} Note also that the adiabatic $1\text{A}'$ DK surface result was also previously obtained²⁸ in relation to a capture model study of total angular momentum effects. The convergence details of the resonance features in Figure 3 are similar to those of this earlier study.²⁸ In particular, the highest frequency features in Figure 3 at low collision energies do show some sensitivity to grid and propagation time details. However, if one averages over a small collision energy window of, say, 0.04 eV, we estimate that our reaction probabilities are converged to ± 0.02 or 2%.

QCT studies^{28,56} have also been performed for the $1\text{A}'$ adiabatic dynamics. Using the surface of Ho et al.,²¹ which is similar to the present DK surface, Aoiz⁵⁶ presented $J=0$

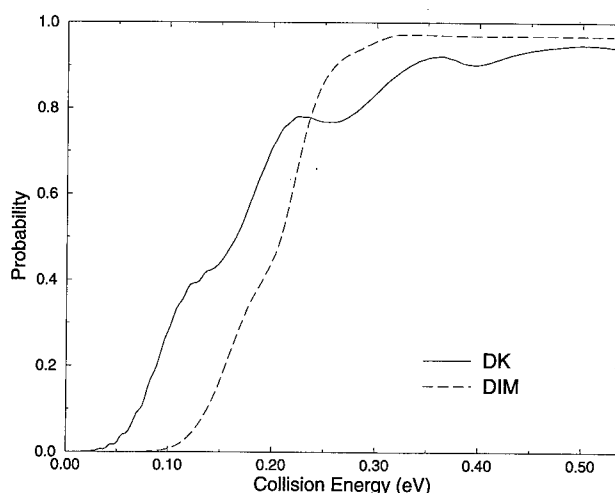


Figure 4. The total reaction probability for $\text{O}(^1\text{D}) + \text{H}_2(X; v=j=0) \rightarrow \text{OH}(X) + \text{H}$ with $J=0$, and assuming single surface dynamics on the Π diabatic state. The dashed curve corresponds to the DIM Π diabat wave packet results, and the solid curve corresponds to the DK Π diabat wave packet results.

reaction probabilities that were similar to but smoother than the corresponding quantum ones. These classical results were also generally upper bounds to the quantum ones. A $J=0$ QCT study at one energy on the $1\text{A}'$ DK surface also confirms this latter result.²⁸

As indicated by Figure 1, adiabatic dynamics on the $2\text{A}'$ surface cannot produce the desired $\text{OH}(X^2\Pi)$ products, since it correlates with electronically excited $\text{OH}(A^2\Sigma)$. Thus the reaction probability associated with reaction (1) is zero for this adiabatic surface. Similarly, in the diabatic representation discussed in sections I and II, the Σ diabat also correlates with $\text{OH}(A)$ and therefore has no reactivity. The Π diabat, however, correlates with $\text{OH}(X)$. Figure 4 shows the total reactivity associated with dynamics on the DIM (dashed curve) and DK (solid curve) Π diabats. These reaction probabilities are consistent with reaction being a direct and activated process on the Π diabat. The (collinear) barrier to reaction on the DIM Π diabat is ≈ 0.06 eV higher than the corresponding DK Π diabat (0.16 vs 0.10 eV), and this accounts for the DIM threshold for reaction being displaced to the right of the DK threshold in Figure 4. The DK Π diabat result in Figure 4 has more obvious step like structures than the DIM result. These structures are related to adiabatic thresholds associated with even excitations of the bending frequency (0.034 eV) at the collinear transition state. The associated DIM bending frequency (0.022 eV) is smaller, which brings the steps closer to one another so that they tend to a smoother structure.

As our final example of single surface dynamics, we consider the $1\text{A}''$ surface, which also correlates with $\text{OH}(X)$ products and has features similar to the Π diabat discussed above since for collinear geometries it is degenerate with this diabat. While the $1\text{A}''$ and Π diabat surfaces coincide at collinear geometries, some differences occur at bent geometries. For example, the DK $1\text{A}''$ surface exhibits a smaller bending frequency associated with motion away from the collinear saddle point. Figure 5 displays the DK $1\text{A}''$ reaction probability (solid curve) and contrasts it with the DK Π diabat result (dashed curve), confirming that the $1\text{A}''$ dynamics is similar to the Π diabat dynamics. However, as anticipated in the Introduction, the $1\text{A}''$ reaction probability is slightly higher than the corresponding uncoupled Π diabat result. Recall that in order to construct the DIM diabatic model (section II) we actually assumed that Π diabat was the same as the $1\text{A}''$ adiabat. The reasonably close

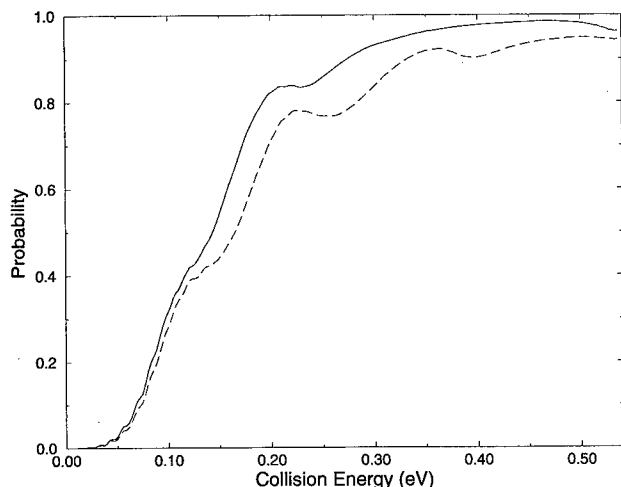


Figure 5. The solid curve corresponds to the total reaction probability for $\text{O}(^1\text{D}) + \text{H}_2(\text{X}; \nu = j = 0) \rightarrow \text{OH}(\text{X}) + \text{H}$ with $J = 0$, assuming adiabatic dynamics on the DK $1\text{A}''$ surface. The dashed curve is the corresponding Π diabat DK result for comparison.

correspondence of the curves in Figure 5 provides justification for this assumption.

B. Nonadiabatically Coupled Surfaces Reaction Dynamics.

In the asymptotic reactants limit, the Σ and Π diabats (sections I and II) are degenerate and one can determine all the relevant observable dynamics by considering initial conditions corresponding to any two linearly independent superpositions of Σ and Π . In particular, we consider an initial condition corresponding to reactants approaching initially on the pure Σ diabat, and another initial condition corresponding to reactants approaching on the pure Π diabat. What linear combinations of adiabatic ($1\text{A}'$ and $2\text{A}'$) states do these two particular pure diabatic initial conditions correspond to? One might naively anticipate simple symmetric and antisymmetric combinations of the $1\text{A}'$ and $2\text{A}'$ states but that is not the case. Consider the two-state mixing angle χ , given by $\tan(2\chi) = 2 H_{\Sigma\Pi} / (H_{\Sigma\Sigma} - H_{\Pi\Pi})$. In a simple two-state picture one can relate the $1\text{A}'$ and $2\text{A}'$ states to the corresponding diabatic states according to⁵⁷

$$\begin{aligned} |1\text{A}'\rangle &= \cos \chi |\Sigma\rangle + \sin \chi |\Pi\rangle \\ |2\text{A}'\rangle &= -\sin \chi |\Sigma\rangle + \cos \chi |\Pi\rangle \end{aligned} \quad (8)$$

As a function of R and $\cos \gamma$ with $r = 1.4 a_0$ one finds that for the R values of relevance to our initial conditions ($R \geq 9 a_0$), χ is relatively small for both the DK and DIM surfaces ($|\chi| \leq 0.1$ radians) which implies that the pure Σ diabat is, in fact, very close to a $1\text{A}'$ adiabatic state and, similarly, that the pure Π diabat is very close to a pure $2\text{A}'$ adiabatic state. This is convenient, since then the reaction probability for reaction 1 if we start in the $1\text{A}'$ ($2\text{A}'$) state is then essentially the same as the corresponding reaction probability if we start on the Σ (Π) state.

We first consider the case of $\text{O}(^1\text{D}) + \text{H}_2(\text{X}; \nu = j = 0)$ reactants initially approaching one another on the Σ diabat. In the absence of electronic coupling, as noted previously, this situation would lead to no products, i.e., zero reaction probability. Figure 6 displays as solid curves our calculated reaction probabilities. The nonadiabatic results on both the DIM (Figure 6a) and DK (Figure 6b) coupled surface systems indicate, in fact, a very high degree of reactivity occurs. These results, while not identical to the adiabatic $1\text{A}'$ results (indicated as dashed curves in Figure 6) are actually very similar to them, and exhibit many maxima and minima at approximately the same energies.

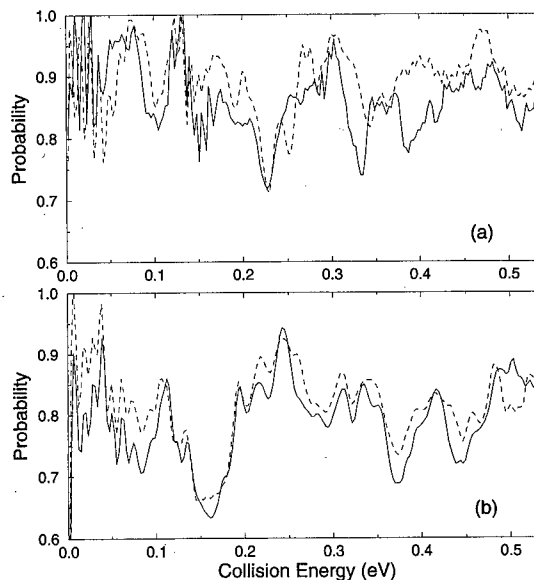


Figure 6. The solid curves correspond to the total reaction probability for $\text{O}(^1\text{D}) + \text{H}_2(\text{X}; \nu = j = 0)$ with $J = 0$, allowing for coupling of the Σ and Π diabats (or equivalently the $1\text{A}'$ and $2\text{A}'$ adiabatic states), with the initial reactant state being purely the Σ diabat, and the dashed curves correspond to the adiabatic results: (a) DIM surfaces, (b) DK surfaces.

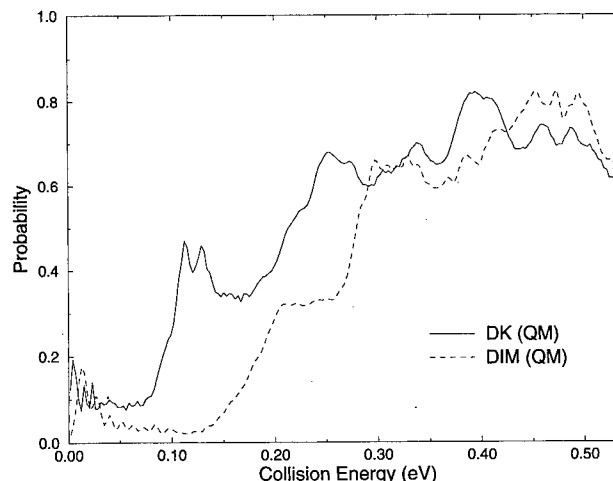


Figure 7. The total reaction probability for $\text{O}(^1\text{D}) + \text{H}_2(\text{X}; \nu = j = 0)$ with $J = 0$, allowing for coupling of the Σ and Π diabats, with the initial reactant state being purely the Π diabat: (a) DIM results, (b) DK results.

Electronic coupling in relation to the diabatic representation is very strong in this case, taking the pure Σ state into, effectively, a coherent superposition of Σ and Π states that corresponds to a good approximation of the $1\text{A}'$ adiabatic state. However, keeping the discussion of the above paragraph in mind, asymptotically the Σ and $1\text{A}'$ states are almost equivalent and so if we were to run our calculations in an adiabatic representation, starting from $1\text{A}'$, there would be very little coupling between the adiabatic states.

We next consider $\text{O}(^1\text{D}) + \text{H}_2(\text{X}; \nu = j = 0)$ initially approaching one another on the Π diabat. Recall that without electronic coupling the reaction probability was consistent with a direct, activated process and, at energies above the classical barrier was quite high (Figure 4). Figure 7 displays the resulting total reaction probabilities for the DIM (dashed curve) and DK (solid curve) surfaces, now allowing for coupling to the Σ surface to occur. There are at least two interesting features to note. First, the reaction probabilities at collision energies above

the collinear barrier can be significant, ranging between 0.4 and 0.8, which reflects a tendency towards an uncoupled diabatic mechanism, similar in spirit to that seen in our pure Π diabatic calculations of Figure 4. This represents the opposite of the near adiabatic limit noted above in relation to propagation of the Σ initial condition and can be interpreted as strong nonadiabatic coupling due to the conical intersection. However, the general magnitudes of the probabilities in Figure 7 can be 20% lower than the uncoupled results of Figure 4 at these higher collision energies and they also exhibit more structure, indicating that somewhat more complex dynamics is occurring. Note in particular that the steps in Figure 7 are more widely separated and more noticeable than in Figure 4. This suggests that the bottlenecks to reaction have moved from the saddle point region to shorter distances, such as near the conical intersection, where the bending frequency is higher.

The second interesting feature of the results in Figure 7 is at collision energies below the classical barrier to reaction. While these probabilities are small, on the order of magnitude of 0.1, they are non-zero even at very low energies close to the zero collision energy limit. Both the *ab initio* DK and the semiempirical DIM surfaces exhibit this behavior, although, interestingly, the *ab initio* surface shows a more significant low energy shoulder. These results are inconsistent with the barrier tunneling mechanism that is operative in the uncoupled Π diabatic results (Figure 4), which leads to much smaller reaction probabilities. We experimented with the coupling term $H_{\Sigma\Pi}$ and found that if it is exponentially damped for $R > 4.5 a_0$ then the low collision energy probabilities become much smaller and behave just as in Figure 4, while the higher energy probabilities are not significantly affected and remain similar to those in Figure 7. Thus we have an interesting mechanism wherein the necessity of tunneling through the Π barrier at close range is avoided by Π to Σ transitions at longer range. Once amplitude grows on the Σ state at these larger distances it behaves more like the Σ , propagation results discussed in the above paragraph, i.e., it behaves more like the $1A'$ adiabatic results, which exhibit nonzero reaction probabilities even at very low collision energies. (Notice also some fine resonance features that are apparent in Figure 7 at the low collision energies. These are similar to the resonance features in $1A'$ and Σ propagations presented in Figure 6.)

Figure 8 further solidifies the points noted above in relation to the DK surface. The solid curve corresponds to the initial Π state propagation result of Figure 7 that includes electronic coupling. The dashed curve is the corresponding adiabatic $1A''$ DK surface propagation result, which in turn is similar to the uncoupled Π diabatic result (see Figure 5). Filled circles correspond to our TSH results consistent with the Π state propagation (which should be compared to the solid curve quantum result), and the open circles correspond to ordinary quasiclassical trajectory results on the $1A''$ surface (which should be compared to the dashed curve quantum result). The dotted line with open diamonds corresponds to the vibrationally adiabatic scattering method of Drukker and Schatz,³⁵ which also should be compared with the solid curve quantum result. The TSH and $1A''$ trajectory results are in reasonably good qualitative agreement with the corresponding quantum results. In particular, note that the TSH calculations (filled circles) do predict a finite reaction probability for the coupled diabats at very low energies, and this contrasts with the trajectory results for the $1A''$ surface (open circles) at these energies. An examination of the TSH trajectories indicates that the hops that are responsible for this take place at relatively long range ($R >$

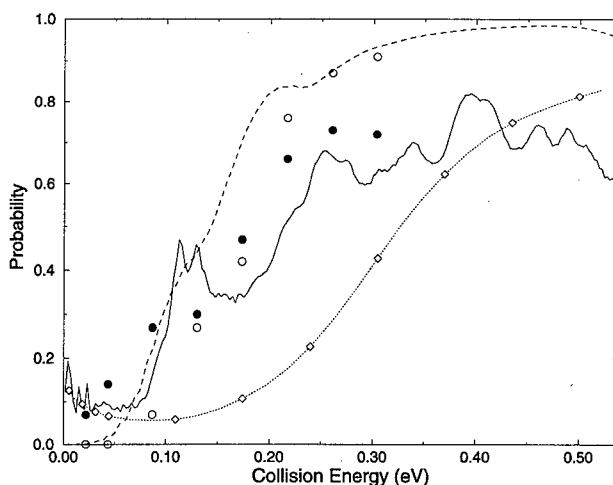


Figure 8. Various total reaction probability results for the DK surfaces are compared. The solid curve represents the nonadiabatically coupled quantum results with the reactant state being a pure Π state. The dashed curve corresponds to Π state dynamics with no nonadiabatic coupling allowed. The filled circles are trajectory surface hopping results. The open circles are adiabatic quasiclassical trajectory results for the $1A''$ surface. The dotted line with open diamonds corresponds to the vibrationally adiabatic scattering approximation. See text for further details.

$4 a_0$). At higher energy, the $1A''$ reaction probability rises up above the Π probability. Since the Π diabatic is very similar to the $1A''$ adiabatic, some of the difference between reaction probabilities at high energy is due to trajectories which start out on the Π diabatic, then transfer to the Σ diabatic after surmounting the barrier, and then get reflected from the repulsive Σ potential for linear geometry. Finally we note that the vibrationally adiabatic quantum scattering approach³⁵ yields behavior qualitatively similar to the Π state propagation (solid curve), including the presence of a noticeable shoulder at low collision energies. The reaction probabilities for this approach show much less structure than the Π wave packet propagation results, and in the middle collision energy region, are somewhat lower than the Π results. The adiabatic treatment of r and the use of optical potentials that absorb amplitude in the well region are partly responsible for these deviations. Also, the rotational basis used in these calculations, while adequate for the low collision energy region, was really too small to describe bending threshold effects accurately. While for brevity we do not display the results, a very similar figure to Figure 8 was determined with the DIM surfaces.

We close this section on the coupled diabatic state dynamics by examining the O_2H_2 angle γ averaged nuclear density contributions,

$$\rho_{\alpha}^k(R, r) = \sum_j |C_{j,\alpha}^k(R, r)|^2 \quad (9)$$

as the wave packets evolve, where α labels the diabatic electronic state and $C_{j,\alpha}^k(R, r)$ are the coefficients of the real wave packet of section II at iteration number k . Inspection of $\rho_{\alpha}^k(R, r)$ yields qualitative insights into the mechanism. Figure 9 displays ρ_{α}^k consistent with physical times $t_{\text{phys}} = 0, 75, 150$ and 225 fs for the DIM surfaces case with the initial wave packet on the Σ diabatic. (Similar results were obtained with the DK surface.) This corresponds to actual iteration numbers $k = 0, \approx 2600, \approx 5200$ and ≈ 7800 . Note that we carry out our calculations to much longer times or iteration numbers, e.g., iteration numbers on the order of 20,000 ($t_{\text{phys}} \approx 580$ fs), in

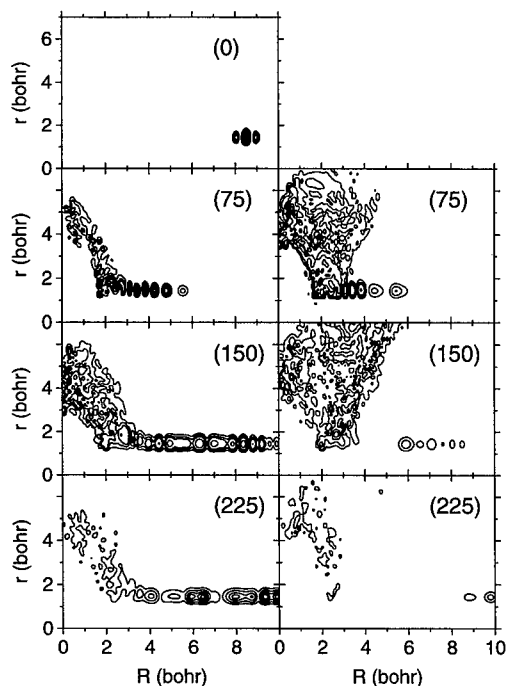


Figure 9. Contribution to the density from the real wave packet associated with the Σ and Π diabatic states for the case of the wave packet initially being on the Σ state. These results correspond to the DIM surface. The left column corresponds to the Σ state densities and the right column corresponds to the Π state densities. Approximate times t in femoseconds are indicated in brackets.

order to fine tune the reaction probability features. However most of the key dynamics is completed by much shorter times as is indicated by Figure 9. The left column of Figure 9 corresponds to the Σ state density and the right column of Figure 9 corresponds to the Π density. One sees the wave packet, initially localized on Σ approach the interaction region, spreading out also onto the Π state. Reaction can occur out of the Π state (right column) and that is most clearly indicated at $t_{\text{phys}} = 150$ fs in the figure with density streaming up to large r (and moderately large R). Notice also that significant density with R close to 0 au plays a role in the interaction region dynamics. This is the quantum equivalent of the insertion mechanism, which was also noted in an earlier $1A'$ adiabatic surface quantum study.²⁷

Figure 10 is similar to Figure 9 except it is the density for the case that we start on the DIM Π diabatic. The dynamics is much simpler, with a direct mechanism on the Π diabatic alone (right column) being evident. For example, at 75 fs one sees density streaming to the large r region consistent with products on the Π state. (The subsequent times 150 fs and 225 s are showing the nonreactive part of the wave packet going back down the reactant channel.) However, one also sees some nonadiabaticity at 75 fs: the Σ state showing significant density has grown in the interaction region. One also sees some of this density tending to much smaller R values than the Π state density.

C. Rate Constant Estimates. In this subsection we make some approximate estimates of the effect of the nonadiabatic features noted above on the thermal rate constant for reaction 1 using the ab initio DK surface results. A completely rigorous calculation of the rate constant requires much more information than we have. For example, we would need to know the reaction probabilities for a number of total angular momenta $J > 0$, and we would also need to know these reaction probabilities for thermally populated initial vibration-rotation states of H_2 , v, j .

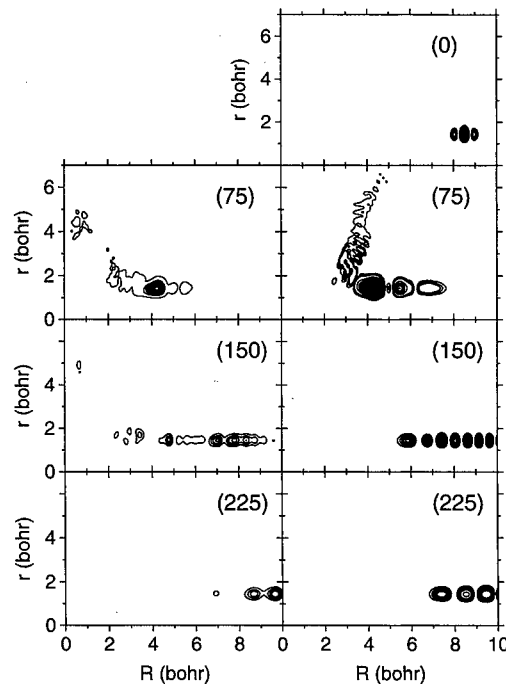


Figure 10. Density contribution associated with the Σ (left column) and Π (right column) diabatic states for the case of the wave packet initially being on the Π surface. Other details as those in Figure 9.

(More direct quantum approaches to obtaining $k(T)$ are also possible and can involve less work than calculating all the individual state-to-state information.⁵⁸) The rigorous calculation of $k(T)$ for reaction (1) is clearly a formidable task. We have at our disposal here only $J = 0$ reaction probabilities out of H_2 in its ground vibration-rotation state, $v = j = 0$. We must make two approximations. First, we assume that the reaction probabilities (as a function of collision energy) are independent of v, j and equal to the $v = j = 0$ ones. As a consequence of this approximation, in what follows no thermal averages over v and j occur and it is always assumed that reaction probabilities or cross sections are those from $v = j = 0$. Second, we estimate the required $J > 0$ reaction probabilities from our $J = 0$ ones by employing either capture model ideas as previously invoked in a study of the $1A'$ surface,²⁸ or J -shifting ideas.⁴⁶

An earlier, more detailed study²⁸ of the J -dependence of the reaction probabilities on the $1A'$ surface showed that J (or J -shifting based on $J = 0$ reaction probabilities can lead to errors in the rate constant on the order of 15–20%. The assumption that cross sections are independent of the initial v, j state of H_2 and equal to the $v = j = 0$ ones is probably good for the $1A'$ dynamics because, over the temperature range of interest (300–1000 K), $v = 0$ is the dominant contribution to the rate constant and it has also been shown that there is relatively little j dependence in the reaction probabilities.^{21,26} The excited state ($2A'$ or Π and $1A''$) dynamics is more sensitive to initial j ,³³ and it is difficult to quantify the associated uncertainties introduced. However, the excited state contributions are in general relatively small and we expect these uncertainties to not be severe, i.e., less than the uncertainties introduced by J -shifting.

The rate constant for reaction 1 can be written as

$$k(T) = k_{\Sigma}(T) + k_{\Pi}(T) + k_{1A''}(T) \quad (10)$$

where $k_{\alpha}(T)$ represents the contribution from initial electronic state $\alpha = \Sigma, \Pi$, or $1A''$. In turn we can write each $k_{\alpha}(T)$ as an appropriate Boltzmann average of the corresponding reactive

cross section form state α , σ_α ,

$$k_\alpha(T) = \frac{1}{5} \sqrt{\frac{8}{\pi \mu (k_B T)^3}} \int_0^\infty E_{\text{col}} \sigma_\alpha(E_{\text{col}}) \exp(-E_{\text{col}}/k_B T) dE_{\text{col}} \quad (11)$$

where we have included the electronic degeneracy factor of 1/5 appropriate to reaction 1 in the prefactor. (An alternative would be to include the electronic degeneracy in the definition of σ_α . However, we are following the convention previously employed.^{28,33}) The cross sections that enter into eq. 11 may be written in two ways. One way is

$$\sigma_\alpha(E_{\text{col}}) = \frac{\pi}{k_{\text{col}}^2} \sum_{J=0}^\infty (2J+1) P'_\alpha(E_{\text{col}}) \quad (12)$$

where $k_{\text{col}} = \sqrt{2\mu E_{\text{col}}}/\hbar$. J -shifting approximations⁴⁶ can then be employed to approximate reaction probability P'_α . Such approximations are most appropriate to direct reactions with barriers. In the case of a collinear transition state, the simplest J -shifting approximation is that the reaction probability $P'_\alpha(E_{\text{col}}) = P_{\alpha}^{J=0}(\epsilon = E_{\text{col}} - J(J+1)B)$, where B is the rotational constant associated with the linear transition state ($B \approx 2 \text{ cm}^{-1}$ for the $1\text{A}''$ state).

The second relevant form for σ_α is a sum over orbital angular momenta associated with the O, H_2 motion⁴⁸

$$\sigma_\alpha(E_{\text{col}}) = \frac{\pi}{k_{\text{col}}^2} \sum_{\ell=0}^\infty (2\ell+1) P'_\alpha(E_{\text{col}}) \quad (13)$$

The ℓ -shifting approximation,²⁸ which is most appropriate when reaction occurs via a capture process without any significant (bare) potential barrier, can then be invoked. This approximation is a quantum generalization of the classical capture or optical model that assumes the reaction probability is unity if a centrifugal barrier height is exceeded and zero otherwise. A simple ℓ -shifting approximation is $P'_\alpha(E_{\text{col}}) \approx P_{\alpha}^{J=0}(\epsilon = E_{\text{col}} - V^*)$. Here, V^* represents the centrifugal barrier height of an appropriate effective potential along R that includes the centrifugal term $\ell(\ell+1)/2\mu R^2$. (See ref 28 for more details.) Note that in the present case, with $j=0$ initial state for H_2 , $\ell=0$ corresponds to $J=0$ and so, as with the J -shifting approximation, only $J=0$ information is needed.

In our calculations we have estimated the relevant cross sections and then rate constants for the DK surfaces using the formulae above. We employed the $J=0$ reaction probabilities for the coupled electronic state Σ and Π initial states, as well as the $J=0$ adiabatic reaction probabilities for the $1\text{A}''$ state. It is clear that the J -shifting model outlined above is appropriate to the case $\alpha = 1\text{A}''$ which, as discussed in the text, is an adiabatic reaction with a collinear transition state and direct dynamics. It is also reasonably clear that the ℓ -shifting approximation is appropriate to estimate the Σ state cross sections, since we showed in the previous subsection that the Σ dynamics was very similar to the insertion and capture dominated $1\text{A}'$ dynamics. The relevant centrifugal barriers were determined just as in ref 28, employing the $1\text{A}'$ adiabatic potential. (The Σ diabatic potential also leads to very similar results.) Which model is most appropriate to the Π propagation results is less clear since the low collision energy region is dominated by the long-range coupling mechanism (which would suggest an ℓ -shifting approximation based on the $1\text{A}'$ adiabatic potential, would also be appropriate), and the higher collision energies

are dominated by a more direct diabatic mechanism that would suggest that the J -shifting approximation, based on the transition state for the Π diabat (which is the same as the $1\text{A}''$ transition state) would be most appropriate. We discuss two results, a relatively low temperature ($T = 300 \text{ K}$) for which the ℓ -shifting model was used for the Π rate constant estimate, and a high temperature result ($T = 1000 \text{ K}$) for which the J -shifting approximation was used for σ_Π .

At $T = 300 \text{ K}$ we find, on the basis of the approximations above, that $k(T) = 1.0 \times 10^{-10} \text{ cm}^3 \text{ s}^{-1}$. The experimental range is $1.0\text{--}1.4 \times 10^{-10} \text{ cm}^3 \text{ s}^{-1}$.²¹ The most significant contribution to this rate constant comes from k_Σ , which contributes 86% to the total. However, 13% of $k(T)$ is due to k_Π and the long range mechanism discussed in the previous subsection, and 1% is due to $k_{1\text{A}''}$. If J -shifting (instead of ℓ -shifting) were used to estimate k_Π , $k(T)$ would be lowered by 8% to $0.90 \times 10^{-10} \text{ cm}^3 \text{ s}^{-1}$, and the contribution to this from k_Π would be 7%, which is still a reasonable contribution. It is also of interest to contrast our $T = 300 \text{ K}$ estimate of the rate constant including nonadiabatic effects, $1.0 \times 10^{-10} \text{ cm}^3 \text{ s}^{-1}$, with the result based on purely adiabatic dynamics on the $1\text{A}'$ surface, which we calculate to be $0.9 \times 10^{-10} \text{ cm}^3 \text{ s}^{-1}$. The purely adiabatic result is thus 10% lower than the nonadiabatic result. (The $1\text{A}'$ adiabatic reaction probability, at low energies, includes some aspects of both the Σ and Π reaction probabilities, and so the purely adiabatic $1\text{A}'$ result is a little higher and closer to the nonadiabatic result than might be expected.) At the higher temperature of $T = 1000 \text{ K}$ we find $k(T) = 1.5 \times 10^{-10} \text{ cm}^3 \text{ s}^{-1}$, with $\approx 13\%$ contributions from each of k_Π and $k_{1\text{A}''}$. Effects due to nonadiabatic dynamics are clearly largest here, with the purely adiabatic $1\text{A}'$ estimate being just $1.2 \times 10^{-10} \text{ cm}^3 \text{ s}^{-1}$, i.e., 20% lower.

IV. Concluding Remarks

A variety of calculations were carried out in order to assess the role of electronic nonadiabaticity in the reaction of $\text{O}(^1\text{D})$ with H_2 . We focused mostly on the coupled nuclear/electronic dynamics associated with two key electronic states. These states are the $1\text{A}'$ and $2\text{A}'$ adiabatic electronic states or, equivalently, certain Σ -like and $\Pi(\text{A}')$ -like diabatic electronic states. A conical intersection occurs between these states at collinear OHH geometries, and previous more approximate TSH studies,³⁴ and vibrationally adiabatic coupled channel studies,³⁵ have pointed to the possibility of interesting nonadiabatic effects.

Most of our calculations were quantum wave packet calculations based on the real wave packet methodology.^{49,52} Our largest calculations corresponded to total angular momentum $J = 0$ wave packet propagations, including all three internal nuclear coordinates and the two electronic states within a diabatic representation. Several single surface wave packet propagations, and some TSH and vibrationally adiabatic coupled channel calculations were also carried out for comparison. We studied two different systems of coupled potential surfaces, a semiempirical DIM system due to Kuntz, Niefer, and Sloan,^{30,31} and a recent ab initio system due to Dobbyn and Knowles.^{44,45}

We confirmed that nonadiabaticity is not an important issue if one starts effectively on the $1\text{A}'$ potential energy surface. This is the surface that correlates with the ground electronic state of water and the reaction dynamics involves insertion coupled with some brief dynamics that can be associated with short-lived water complexes. No barrier exists for reaction on this surface, and significant reaction probabilities are seen for all collision energies examined, including very low collision energies. The dynamics of a wave packet initiated on, effectively, the $2\text{A}'$ electronic state is much more interesting. In terms of the Σ and

$\Pi(A')$ diabatic representation we employed, an initial $2A'$ state correlates with the $\Pi(A')$ state, which has a simple barrier to reaction at collinear geometries. One might expect strong nonadiabatic coupling (due to the conical intersection noted above) such that in a diabatic representation the system would remain on the Π diabat throughout (i.e., very little "nonadiabatic coupling"). We do see evidence of this, particularly at collision energies above the collinear barrier. However, at low collision energies a new mechanism for reaction emerges—electronic transitions at long range that allow amplitude to avoid having to tunnel through the Π barrier. This leads to small but noticeable reaction probabilities even as the collision energy approaches zero. The TSH and vibrationally adiabatic coupled channel calculations also exhibit this behavior, further solidifying our conclusions. It is also noteworthy that the TSH results for the Π initial state case agreed reasonably well with the wave packet results, as just the opposite behavior has been found in studies of other reactions.^{42,43} One significant difference associated with the present work is that the TSH calculations have been done in a diabatic representation, rather than the usual adiabatic representation, and the uncoupled diabats provide a better zero order description of the Π state dynamics.

We made estimates of the thermal rate constant for reaction at two temperatures, 300 K and 1000 K. These calculations were rather approximate, owing in part to the necessity of using J -shifting⁴⁶ and L -shifting²⁸ techniques to infer $J > 0$ reaction probabilities from $J = 0$ ones. We showed that at 300 K nonadiabatic effects, especially the low collision energy mechanism noted above, could contribute 10% or more to the rate constant. At 1000 K nonadiabatic effects, as well as the contribution from the adiabatic $1A''$ surface, are much more important and the rate constant is 20% larger than the single surface result based on the $1A'$ adiabatic surface.

In view of the uncertainties introduced in our estimates of the rate constants (see section IIID), it is possible we are overestimating the relative contribution of nonadiabatic and excited state dynamics to the rate constants. It is therefore important to carry out much more detailed studies. Future work includes making better $J > 0$ estimates of the reaction probabilities, as well as an examination of the effect of H_2 initial vibration-rotation state.⁵⁹ It should be possible, for example, to carry out helicity decoupled calculations in the spirit of ref 28. Theoretical estimates of the differential cross sections, and how they are influenced by nonadiabatic effects, would also be very welcome, owing to the interesting experimental data that is becoming available.³⁹ Finally, we note that there are many other reactions with electronic states that behave as those in Figure 1, so the present results provide significant motivation for studying the role of excited electronic states more generally.

Acknowledgment. SKG was supported by the Office of Basic Energy Science, Division of Chemical Sciences, U.S. Department of Energy, under Contract W-31-109-ENG-38. C.P. acknowledges the CNR for a short-term visit grant and MURST for financial support. K.D. and G.C.S. were supported by NSF Grant CHE-9873892. We thank A. J. Dobbyn and P. J. Knowles for providing us with their potential energy surface which was computed under Grant GR/K41656 of the EPSRC. We also thank G. G. Balint-Kurti for valuable comments.

References and Notes

- (1) Davidson, J. A.; Sadowski, C. M.; Schiff, H. I.; Streit, G. E.; Howard, C. J.; Jennings, D. A.; Schmeltekopf, A. L. *J. Chem. Phys.* **1976**, *64*, 57.
- (2) DeMore, W. B.; Sander, S. P.; Golden, D. M.; Hampson, R. F.; Kurylo, M. J.; Howard, C. J.; Ravishankara, A. R.; Kolb, C. E.; Molina, M. Chemical kinetics and photochemical data for use in stratospheric modeling. JPL publication 94-26; Jet Propulsion Laboratory, Pasadena, 1994.
- (3) Talukdar, R. K.; Ravishankara, A. R. *Chem. Phys. Lett.* **1996**, *253*, 177.
- (4) Laurent, T.; Naik, P. D.; Volpp, H. R.; Wolfrum, J.; Arusi-Parpar, T.; Bar, I.; Rosenwaks, S. *Chem. Phys. Lett.* **1995**, *236*, 343.
- (5) Matsumi, Y.; Tonokura, K.; Kawasaki, M.; Kim, H. L. *J. Phys. Chem.* **1992**, *96*, 10622.
- (6) Tsukiyama, K.; Katz, B.; Bersohn, R. *J. Chem. Phys.* **1985**, *83*, 2889.
- (7) Butler, J. E.; MacDonald, R. G.; Donaldson, D. J.; Sloan, J. J. *Chem. Phys. Lett.* **1983**, *95*, 183.
- (8) Jursich, G. M.; Wiesenfeld, J. R. *Chem. Phys. Lett.* **1985**, *119*, 511.
- (9) Butler, J. E.; Jursich, G. M.; Watson, I. A.; Wiesenfeld, J. R. *J. Chem. Phys.* **1986**, *84*, 5365.
- (10) Hsu, Y. T.; Wang, J. H.; Liu, K. J. *J. Chem. Phys.* **1997**, *107*, 2351.
- (11) Buss, R. J.; Casavecchia, P.; Hirooka, T.; Sibener, S. J.; Lee, Y. T. *Chem. Phys. Lett.* **1981**, *82*, 386.
- (12) Che, D. C.; Liu, K. J. *J. Chem. Phys.* **1995**, *103*, 5164.
- (13) Alexander, A. J.; Aoiz, F. J.; Brouard, M.; Burak, I.; Fujimura, Y.; Short, J.; Simons, J. P. *Chem. Phys. Lett.* **1996**, *262*, 589.
- (14) Hsu, Y. T.; Liu, K. J. *J. Chem. Phys.* **1997**, *107*, 1664.
- (15) Casavecchia, P. Private communication.
- (16) Ahmed, M.; Peterka, D. S.; Suits, A. G. *Chem. Phys. Lett.* **1999**, *301*, 372.
- (17) Sorbie, K. S.; Murrell, J. N. *Mol. Phys.* **1976**, *31*, 905.
- (18) Howard, R. E.; McLean, A. D.; Lester, W. A., Jr. *J. Chem. Phys.* **1979**, *71*, 2492.
- (19) Schinke, R.; Lester, W. A., Jr. *J. Chem. Phys.* **1980**, *72*, 3754.
- (20) Murrell, J. N.; Carter, S. J. *J. Phys. Chem.* **1984**, *88*, 4887.
- (21) Ho, T. S.; Hollebeek, T.; Rabitz, H.; Harding, L. B.; Schatz, G. C. *J. Chem. Phys.* **1996**, *105*, 10472.
- (22) Dunne, L. J. *Chem. Phys. Lett.* **1989**, *158*, 535.
- (23) Aker, P. M.; Sloan, J. J.; Wright, J. S. *Chem. Phys.* **1986**, *110*, 275.
- (24) Fitzcharles, M. S.; Schatz, G. C. *J. Phys. Chem.* **1986**, *90*, 3634.
- (25) Aoiz, F. J.; Brouard, M.; Enriquez, P. A. *J. Chem. Phys.* **1996**, *105*, 4964.
- (26) Peng, T.; Zhang, D. H.; Zhang, J. Z. H.; Schinke, R. *Chem. Phys. Lett.* **1996**, *248*, 37.
- (27) Balint-Kurti, G. G.; Gonzalez, A. I.; Goldfield, E. M.; Gray, S. K. *Faraday Discuss.* **1998**, *110*, 169.
- (28) Gray, S. K.; Goldfield, E. M.; Schatz, G. C.; Balint-Kurti, G. G. *Phys. Chem. Chem. Phys.* **1999**, *1*, 1141.
- (29) Whitlock, P. A.; Muckerman, J. T.; Fisher, E. R. *J. Chem. Phys.* **1982**, *76*, 4468.
- (30) Kuntz, P. J.; Niefer, B. I.; Sloan, J. J. *J. Chem. Phys.* **1988**, *88*, 3629.
- (31) Kuntz, P. J.; Niefer, B. I.; Sloan, J. J. *J. Chem. Phys.* **1991**, *151*, 77.
- (32) Walch, S. P.; Harding, L. B. *J. Chem. Phys.* **1988**, *88*, 7653.
- (33) Schatz, G. C.; Papaioannou, A.; Pederson, L. A.; Harding, L. B.; Hollebeek, T.; Ho, T. S.; Rabitz, H. *J. Chem. Phys.* **1997**, *107*, 2340.
- (34) Schatz, G. C.; Pederson, L. A.; Kuntz, P. J. *Faraday Discuss.* **1997**, *108*, 357.
- (35) Drukker, K.; Schatz, G. C. *J. Chem. Phys.* **1999**, *111*, 2451.
- (36) Tully, J. C. *J. Chem. Phys.* **1990**, *93*, 161.
- (37) Hammes-Schiffer, S.; Tully, J. C. *J. Chem. Phys.* **1994**, *101*, 4657.
- (38) Alexander, A. J.; Blunt, D. A.; Brouard, M.; Simons, J. P.; Aoiz, F. J.; Banares, L.; Fujimura, Y.; Tsubouchi, M. *Faraday Discuss.* **1997**, *108*, 375.
- (39) Alagia, M.; Balucani, N.; Cartechini, L.; Casavecchia, P.; van Kleef, E. H.; Volpi, G. G.; Kuntz, P. J.; Sloan, J. J. *J. Chem. Phys.* **1998**, *108*, 6698.
- (40) Hsu, Y. T.; Liu, K.; Pederson, L. A.; Schatz, G. C. *J. Chem. Phys.* In press.
- (41) Lee, S.-H.; Liu, K. J. *J. Chem. Phys.* **1999**, *0000*, 0000.
- (42) Topaler, M. S.; Hack, M. D.; Allison, T. C.; Liu, Y. P.; Mielke, S. L.; Schwenke, D. W.; Truhlar, D. G. *J. Chem. Phys.* **1997**, *106*, 8699.
- (43) Allison, T. C.; Mielke, S. L.; Schwenke, D. W.; Truhlar, D. G. *J. Chem. Soc. Faraday Trans.* **1997**, *93*, 825.
- (44) Dobbyn, A. J.; Knowles, P. J. *Mol. Phys.* **1997**, *91*, 1107.
- (45) Dobbyn, A. J.; Knowles, P. J. *Faraday Discuss.* **1998**, *110*, 247.
- (46) Bowman, J. M. *J. Phys. Chem.* **1991**, *95*, 4960.
- (47) Rebentrost, F.; Lester, W. A., Jr. *J. Chem. Phys.* **1975**, *63*, 3737.
- (48) Dobbyn, A. J.; Connor, J. N. L.; Besley, N. A.; Schatz, G. C.; Knowles, P. J. *J. Phys. Chem. Chem. Phys.* **1999**, *1*, 957.
- (49) Gray, S. K.; Balint-Kurti, G. G. *J. Chem. Phys.* **1998**, *108*, 950.
- (50) Mandelshtam, V. A.; Taylor, H. S. *J. Chem. Phys.* **1995**, *102*, 7390.
- (51) Mandelshtam, V. A.; Taylor, H. S. *J. Chem. Phys.* **1995**, *103*, 2903.

(52) Meijer, A. J. H. M.; Goldfield, E.; Gray, S. K.; Balint-Kurti, G. G. *Chem. Phys. Lett.* **1998**, 293, 270.

(53) Huang, Y.; Kouri, D. J.; Hoffman, D. K. *J. Chem. Phys.* **1994**, 101, 10493.

(54) Huang, Y.; Iyengar, S. S.; Kouri, D. J.; Hoffman, D. K. *J. Chem. Phys.* **1996**, 105, 927.

(55) Chen, R.; Guo, H. *J. Chem. Phys.* **1996**, 105, 3569.

(56) Aoiz, F. J. *Faraday Discuss.* **1998**, 110, 245.

(57) Rebentrost, F. *Theoretical Chemistry: Advances and Perspectives*; Henderson, D., Ed.; Academic: New York, 1981; Vol. 6B, p 1.

(58) Miller, W. H. *Acc. Chem. Res.* **1993**, 26, 174.

(59) Balint-Kurti, G. G.; Gray, S. K.; Schatz, G. C. To be submitted.

Electronic Coherence in Mixed-Valence Systems: Spectral Analysis

Yoonjoon Jung, Robert J. Silbey, and Jianshu Cao*

Department of Chemistry, Massachusetts Institute of Technology, Cambridge, Massachusetts 01239

Received: June 1, 1999; In Final Form: August 24, 1999

The electron transfer kinetics of mixed-valence systems is studied via solving the eigenstructure of the two-state nonadiabatic diffusion operator for a wide range of electronic coupling constants and energy bias constants. The calculated spectral structure consists of three branches in the eigendiagram: a real branch corresponding to exponential or multiexponential decay, and two symmetric branches corresponding to population oscillations between donor and acceptor states. The observed electronic coherence is shown as a result of underdamped Rabi oscillations in an overdamped solvent environment. The time evolution of electron population is calculated by applying the propagator constructed from the eigensolution to the nonequilibrium initial preparation, and it agrees perfectly with the result of a direct numerical propagation of the density matrix. The resulting population dynamics confirms that increasing the energy bias destroys electronic coherence.

I. Introduction

Quantum coherence in the dynamics of condensed phase systems has become a subject of recent experimental and theoretical studies. A central issue is the observability of electronic coherence in electron transfer systems given the fast dephasing time in many-body quantum systems. Experimentally, with the advance in ultrafast laser technology, oscillations in electronic dynamics have been observed in photosynthetic reaction centers and other electron transfer systems and are believed to arise from vibrational and/or electronic coherence.^{1–3} Accurate measurements on photoinduced electron transfer in mixed-valence compounds have demonstrated oscillations in electronic populations on the femtosecond time scale.⁴ Theoretically, detailed path-integral simulations suggest that such oscillations take place in electron transfer systems with large electronic coupling constants and are sensitive to the initial preparation of the bath modes associated with the transfer processes. Lucke et al.⁵ extended the noninteracting blip approximation to incorporate the nonequilibrium initial preparation and carried out extensive path-integral quantum dynamics simulations for electron transfer reactions. According to their findings, large-amplitude oscillations are most likely to be observed in symmetric mixed-valence systems that are nearly adiabatic and with initial configurations that are centered in the Landau–Zener crossing region. Using the transfer matrix technique,⁶ Evans, Nitzan, and Ratner⁷ calculated short-time evolution for the photoinduced electron transfer reaction in $(\text{NH}_3)_5\text{Fe}^{\text{II}}(\text{CN})\text{Ru}^{\text{III}}(\text{CN})_5$. Their results show fast oscillations in the electronic population on the short time scale (20 fs) followed by a slower population relaxation on the long time scale (100 fs). They pointed out that these fast oscillations arise as the wave function oscillates coherently between the donor and acceptor states. The calculated long-time decay rate is considerably smaller than the prediction by the golden-rule formulas,^{8,9} confirming the inadequacy of nonadiabatic rate theory in studying mixed-valence systems.

In fact, a simple classical argument helps understand the nature of the observed oscillations. As a function of the ratio between λ (the bath reorganization energy) and V (the electronic

coupling constant), there is a thermodynamic transition from the localized electronic state in a double-well potential to the delocalized electronic state in a single-well potential.^{10–14} (i) In the localized regime ($\lambda \gg V$), the large reorganization energy destroys electronic coherence; hence, electron transfer is an incoherent rate process, which can be described by the noninteracting blip approximation or golden-rule rate in the nonadiabatic limit and by transition state theory in the adiabatic limit.^{15–17} (ii) In the delocalized regime ($\lambda \leq V$), the electronic wave function extends to both the donor and acceptor states and electronic coherence persists over several oscillations.¹⁰ For mixed-valence compounds, the electronic coupling constant is estimated to be in the range of 10^3 cm^{-1} , which is in the same order as the reorganization energy.^{1,7} Therefore, the observed oscillations and relaxation in mixed-valence systems are the consequence of a highly nonequilibrium coherence transfer process.

Due to the delocalization nature of electronic states, an adiabatic picture¹⁸ is more useful than the diabatic representation for analyzing the short-time dynamics in strongly-coupled systems. In this picture, electronic coherence arises from Rabi oscillations between two adiabatic surfaces and decays because of electronic dephasing. Further, initial preparation and wavepacket dynamics can modulate Rabi oscillations and the overall electronic dynamics. Thus, the adiabatic representation provides a simple picture for mixed-valence systems as well as a simple analytical method to model fast electron dynamics initiated by laser pulses.

As a general approach to describe condensed phase dynamics, we recently proposed a spectral analysis method,¹⁹ which is based on eigenstructures of dissipative systems instead of dynamic trajectories. An important application of the approach is to analyze a set of two-state diffusion equations, which was first used by Zusman to treat solvent effects on electron transfer in the nonadiabatic limit. The analysis allows us to characterize multiple time scales in electron transfer processes including vibrational relaxation, electronic coherence, activated curve crossing, or barrier crossing. With this unified approach, the observed rate behavior, biexponential and multiexponential decay, and population oscillations are different components of the same kinetic spectrum. Thus, several existing theoretical

* Corresponding author. E-mail: jianshu@mit.edu.

models, developed for limited cases of electron transfer, can be analyzed, tested, and extended. In particular, rate constants extracted from the analysis bridge smoothly between the adiabatic and nonadiabatic limits, and the kinetic spectrum in the large coupling regime reveals the nature of the localization–delocalization transition as the consequence of two competing mechanisms.

In this paper, the spectral analysis approach developed in ref 19 is employed to study the electron transfer dynamics in mixed-valence systems. We invoke the nonadiabatic diffusion equation proposed by Zusman to describe the electron transfer process in the over-damped solvent regime. As discussed earlier, electron transfer in mixed-valence systems takes place in a different kinetic regime from the thermal activated regime described by Marcus theory. Thus, the time-scale separation is not satisfied, and multiexponential decay and oscillations are intrinsic nature of electron transfer kinetics. As a result, the kinetic spectra exhibit bifurcation, coalescence, and other complicated patterns. Careful examination of these patterns reveals the underlying mechanisms in mixed-valence systems.

The rest of the paper is organized as follows: The spectral structure of the nonadiabatic diffusion equation is formulated in section II. Numerical examples of the spectral structure of strongly mixed electron transfer systems are presented and discussed in section III, and concluding remarks are given in section IV.

II. Theory

There have been extensive studies of the solvent effect on electron transfer dynamics in literature with various approaches.^{20–24} One of the most extensively studied models for quantum dissipation is the spin–boson Hamiltonian,^{14,23}

$$H_{\text{SB}} = \frac{\epsilon}{2} \sigma_z + V \sigma_x + \sum_{\alpha} \frac{p_{\alpha}^2}{2m_{\alpha}} + \sum_{\alpha} \frac{1}{2} m_{\alpha} \omega_{\alpha}^2 \left(x_{\alpha} - \sigma_z \frac{c_{\alpha}}{m_{\alpha} \omega_{\alpha}^2} \right)^2 \quad (1)$$

where ϵ is the energy bias between the two electronic states, V is the electronic coupling constant, σ_z and σ_x are the usual Pauli matrices, and $\{x_{\alpha}, p_{\alpha}\}$ represents the bath degree of freedom with mass m_{α} , frequency ω_{α} , and the coupling constant c_{α} . In this model effects of the bath modes on the dynamics of the system can be described via the spectral density defined by

$$J(\omega) = \frac{\pi}{2} \sum_{\alpha} \frac{c_{\alpha}^2}{m_{\alpha} \omega_{\alpha}} \delta(\omega - \omega_{\alpha}) \quad (2)$$

Equivalently, the spin–boson Hamiltonian in eq 1 can be separated into the electronic two-level part H_{TLS} and the nuclear bath part H_{B} ,

$$H_{\text{SB}} = H_{\text{TLS}} + H_{\text{B}} \quad (3)$$

The two-level part of the Hamiltonian can be explicitly written as

$$H_{\text{TLS}}(E) = U_1(E)|1\rangle\langle 1| + U_2(E)|2\rangle\langle 2| + V(|1\rangle\langle 2| + |2\rangle\langle 1|) \quad (4)$$

where the diabatic energy surfaces $U_1(E)$ and $U_2(E)$ are functions of the stochastic variable E , which represents the polarization energy for a given solvent configuration.²⁰ The transformation from the spin–boson Hamiltonian to the two-level system

Hamiltonian has been shown in the literature^{23,25} by the identity

$$E(\{x_{\alpha}\}) = \sum_{\alpha} c_{\alpha} x_{\alpha} \quad (5)$$

It is worthwhile to mention that the polarization energy E was recognized as the reaction coordinate by Marcus in formulating nonadiabatic electron transfer theory.¹⁵ Since the electron transfer process involves the collective motion of a large number of solvent degrees of freedom and the two-level system is linearly coupled to the harmonic bath modes in the spin–boson Hamiltonian in eq 1, the functional form for the free energy surface is harmonic,²⁶ thus giving

$$U_1(E) = \frac{(E + \lambda)^2}{4\lambda} \quad (6)$$

$$U_2(E) = \frac{(E - \lambda)^2}{4\lambda} + \epsilon \quad (7)$$

where λ is the reorganization energy, which is related to the parameters in eq 1

$$\lambda = \sum_{\alpha} \frac{c_{\alpha}^2}{2m_{\alpha}\omega_{\alpha}^2} = \frac{1}{\pi} \int d\omega \frac{J(\omega)}{\omega} \quad (8)$$

Considering the fact that electron transfer processes are usually probed at room temperature in polar solvents, we can treat the bath degrees of freedom in H_{B} classically. Then, the spin–boson Hamiltonian in eq 3 can be used to derive a two-level classical equation of motion

$$i\frac{\partial}{\partial t}\rho(t) = \mathcal{L}\rho(t) + (\mathcal{L}_{\text{B}} + \mathcal{L}_{\text{TLS}})\rho(t) \quad (9)$$

where $i\mathcal{L}_{\text{B}} = \{, H_{\text{B}}\}$ is the Poisson operator for the classical bath and $\mathcal{L}_{\text{TLS}} = [H_{\text{TLS}},]/\hbar$ is the Liouville operator for the two-level system. Explicitly, we express eq 9 in terms of the density matrix elements

$$\dot{\rho}_1 = \mathcal{L}_1\rho_1 + iV(\rho_{12} - \rho_{21}) \quad (10a)$$

$$\dot{\rho}_2 = \mathcal{L}_2\rho_2 - iV(\rho_{12} - \rho_{21}) \quad (10b)$$

$$\dot{\rho}_{12} = \mathcal{L}_{12}\rho_{12} - i\omega_{12}\rho_{12} + iV(\rho_1 - \rho_2) \quad (10c)$$

$$\dot{\rho}_{21} = \mathcal{L}_{21}\rho_{21} + i\omega_{12}\rho_{21} - iV(\rho_1 - \rho_2) \quad (10d)$$

where the Planck constant \hbar is set to unity for simplicity, ρ_i is the diagonal matrix element for electronic population, and ρ_{ij} is the off-diagonal matrix element for electronic coherence. Here, \mathcal{L} describes the relaxation process of classical bath, with \mathcal{L}_i defined on the free energy surface for the i th electronic state, and with \mathcal{L}_{12} and \mathcal{L}_{21} defined on the averaged free energy surface. This set of semiclassical two-state equations has been previously derived in different context by several authors.^{20,23,27} It should be mentioned that the mapping from the spin–boson Hamiltonian into the Zusman model requires the Lorentzian form of the spectral density

$$J(\omega) = 2\lambda \frac{\omega\omega_c}{\omega^2 + \omega_c^2} \quad (11)$$

Furthermore, we note that many chemically and biologically important electron transfer processes take place in the over-

damped solvent environment. Therefore, to describe the density matrix evolution in the electron transfer kinetics in the mixed-valence system, we invoke the nonadiabatic diffusion equation proposed by Zusman.²⁰ Then, the bath relaxation operators in eq 9 are one-dimensional Fokker–Planck operators \mathcal{L}_{ij}

$$\mathcal{L}_i = D_E \frac{\partial}{\partial E} \left(\frac{\partial}{\partial E} + \beta \frac{\partial U_i(E)}{\partial E} \right) \quad (12)$$

$$\mathcal{L}_{12} = \mathcal{L}_{21} = \frac{\mathcal{L}_{11} + \mathcal{L}_{22}}{2} = D_E \frac{\partial}{\partial E} \left(\frac{\partial}{\partial E} + \beta \frac{\partial \bar{U}(E)}{\partial E} \right) \quad (13)$$

where $\beta = 1/k_B T$, \bar{U} and ω_{12} are the average and the difference of the two free energy surfaces, respectively

$$\bar{U}(E) = \frac{U_1(E) + U_2(E)}{2} \quad (14)$$

$$\omega_{12}(E) = U_1(E) - U_2(E) \quad (15)$$

The energy diffusion constant D_E is defined as

$$D_E = \Omega \Delta_E^2 \quad (16)$$

where Δ_E^2 is the mean square fluctuation of the solvent polarization energy

$$\Delta_E^2 = \langle E^2 \rangle = 2\lambda k_B T$$

and $\tau_D = 1/\Omega$ is the characteristic timescale of the Debye solvent. The correlation function of the solvent polarization energy is given by

$$C(t) = \langle E(t) E(0) \rangle = \Delta_E^2 \exp(-\Omega t) \quad (17)$$

Note that since the nuclear dynamics is modeled by the Fokker–Planck operator, the possibility of the vibrational coherence is excluded in this model of electron transfer dynamics. It is worthwhile to mention that one can obtain the nonadiabatic diffusion equation starting from the spin–boson Hamiltonian by first deriving the evolution equation for the quantum dissipative dynamics, and then taking the semiclassical limit using the Wigner distribution functions, and finally assuming the overdamped diffusion limit.²³

We investigate the spectral structure of the nonadiabatic diffusion operator by calculating the eigenvalues $\{-Z_v\}$ and the corresponding eigenfunctions $\{|\psi_v\rangle\}$. Hereafter we use Greek indices to denote the eigenstates and Latin indices to denote the basis states of the nonadiabatic diffusion operator. Because the nonadiabatic Liouville operator is non-Hermitian, the eigenvalues are generally given by complex values, and the right and left eigenfunctions corresponding to the same eigenvalue are not simply the Hermitian conjugate to each other.²⁸ For a given eigenvalue Z_v , the right and left eigenfunctions of the nonadiabatic diffusion operator are obtained from

$$\mathcal{L}|\psi_v^R\rangle = -Z_v|\psi_v^R\rangle \quad (18)$$

$$\langle\psi_v^L|\mathcal{L} = -Z_v\langle\psi_v^L| \quad (19)$$

The method of eigenfunction solution is well-known for the diffusion process on the harmonic potential energy surface.²⁹ For a single quadratic potential $U(x) = \frac{1}{2}m\omega^2 x^2$, the one-dimensional Fokker–Planck operator $\mathcal{L}_{FP} = D((\partial^2/\partial x^2) + \beta \partial U/\partial x)$ can be transformed into the quantum mechanical Hamilto-

nian in imaginary time

$$H_s = -e^{\beta U(x)/2} \mathcal{L}_{FP} e^{-\beta U(x)/2} = -\frac{1}{2\mu} \frac{\partial^2}{\partial x^2} + V_s(x) \quad (20)$$

where $\mu^{-1} = 2D$, and the quadratic potential is

$$V_s(x) = D \left[\frac{1}{4}(\beta U'(x))^2 - \frac{1}{2}\beta U''(x) \right] = \frac{1}{2}\mu\gamma^2 x^2 - \frac{\gamma}{2} \quad (21)$$

with $\gamma = Dm\omega^2/k_B T$. Since the transformed potential in eq 21 is just the same form as for a simple harmonic oscillator with zero-point energy compensation, the eigenvalues and the eigenfunctions for the original Fokker–Planck operator can be constructed immediately from the eigensolutions of the harmonic oscillator Hamiltonian. Unlike the diffusion problem on the single potential energy surface, there have been limited studies on the nonadiabatic diffusion problem involving more than one potential energy surface. In this aspect, Cukier and co-workers have calculated the electron transfer rate by calculating the lowest eigenvalue of the nonadiabatic diffusion equation; however, their calculation was limited to the weak-coupling regime where the Zusman rate is applicable.²⁷

An important issue in solving the nonadiabatic diffusion equation for electron transfer is the choice of the basis functions since three different free energy surfaces are involved in eq 9: two diabatic surfaces for the population density matrix elements and one averaged surface for the coherence density matrix element. In this paper, the eigenfunctions of \mathcal{L}_{12} are used as our basis set to represent the nonadiabatic diffusion equation. In principle, one could have chosen the eigenfunctions of \mathcal{L}_1 or \mathcal{L}_2 as basis functions; however, in that case one has to evaluate appropriate Franck–Condon factors when calculating the coupling matrix elements even with the Condon approximation. The Fokker–Planck operator \mathcal{L}_{12} is defined on the averaged harmonic potential centered at $E = 0$, and its eigensolutions are

$$\mathcal{L}_{12}|\phi_n^R\rangle = -n\Omega|\phi_n^R\rangle \quad (22)$$

$$\langle\phi_n^L|\mathcal{L}_{12} = -n\Omega\langle\phi_n^L| \quad (23)$$

where the right and left eigenfunctions are

$$\phi_n^R(E) = \frac{1}{(2^n n!)^{1/2} (2\pi \Delta_E^2)^{1/4}} \exp\left(-\frac{E^2}{2\Delta_E^2}\right) H_n\left(\frac{E}{\sqrt{2}\Delta_E}\right) \quad (24)$$

$$\phi_n^L(E) = \frac{1}{(2^n n!)^{1/2} (2\pi \Delta_E^2)^{1/4}} H_n\left(\frac{E}{\sqrt{2}\Delta_E}\right) \quad (25)$$

where H_n is the n th-order Hermite polynomial. As shown below, this choice of the basis set is convenient for our purpose.

To be consistent with the \mathcal{L}_{12} basis set, we separate the real and imaginary parts of the coherence density matrix, namely, $u = \text{Re}\rho_{12}$ and $v = \text{Im}\rho_{12}$, and rewrite eq 9 as

$$\dot{\rho}_1 = (\mathcal{L}_{12} + \delta\mathcal{L})\rho_1 - 2Vv \quad (26a)$$

$$\dot{\rho}_2 = (\mathcal{L}_{12} - \delta\mathcal{L})\rho_2 + 2Vv \quad (26b)$$

$$\dot{u} = \mathcal{L}_{12}u + \omega_{12}v \quad (26c)$$

$$\dot{v} = \mathcal{L}_{12}v - \omega_{12}u + V(\rho_1 - \rho_2) \quad (26d)$$

where we have defined $\delta\mathcal{L}$ as

$$\delta\mathcal{L} = \frac{\mathcal{L}_{11} - \mathcal{L}_{22}}{2} \quad (27)$$

Then, all the relevant operators in eqs 26a–26d can be evaluated in terms of the right and left eigenfunctions of \mathcal{L}_{12} , giving

$$\langle\phi_n^L|\mathcal{L}_{12}|\phi_m^R\rangle = -n\Omega\delta_{nm} \quad (28)$$

$$\langle\phi_n^L|\delta\mathcal{L}|\phi_m^R\rangle = -\Omega\sqrt{\frac{\lambda}{2k_B T}}\sqrt{m+1}\delta_{n,m+1} \quad (29)$$

$$\langle\phi_n^L|\omega_{12}|\phi_m^R\rangle = \sqrt{2\lambda k_B T}(\sqrt{m}\delta_{n,m-1} + \sqrt{m+1}\delta_{n,m+1}) - \epsilon\delta_{nm} \quad (30)$$

$$\langle\phi_n^L|V|\phi_m^R\rangle = V\delta_{nm} \quad (31)$$

where we assume the Condon approximation; i.e., the electronic coupling matrix element is independent of the solvent degrees of freedom. With the basis set, we can expand the density matrix elements as

$$\rho_1(E,t) = \sum_{n=0}^{\infty} a_n(t)\phi_n^R(E) \quad (32a)$$

$$\rho_2(E,t) = \sum_{n=0}^{\infty} b_n(t)\phi_n^R(E) \quad (32b)$$

$$u(E,t) = \sum_{n=0}^{\infty} c_n(t)\phi_n^R(E) \quad (32c)$$

$$v(E,t) = \sum_{n=0}^{\infty} d_n(t)\phi_n^R(E) \quad (32d)$$

Substituting eqs 32a–32d into the eigenvalue equation eq 18, we have the following coupled linear equations

$$-Z_v a_n = -n\Omega a_n - \Omega\sqrt{\frac{\lambda}{2k_B T}}\sqrt{n}a_{n-1} - 2Vd_n \quad (33a)$$

$$-Z_v b_n = -n\Omega b_n + \Omega\sqrt{\frac{\lambda}{2k_B T}}\sqrt{n}b_{n-1} + 2Vd_n \quad (33b)$$

$$-Z_v c_n = -n\Omega c_n + \sqrt{2\lambda k_B T}(\sqrt{n+1}d_{n+1} + \sqrt{n}d_{n-1}) - \epsilon d_n \quad (33c)$$

$$-Z_v d_n = -n\Omega d_n - \sqrt{2\lambda k_B T}(\sqrt{n+1}c_{n+1} + \sqrt{n}c_{n-1}) + \epsilon c_n + V(a_n - b_n) \quad (33d)$$

which is an explicit basis set representation for the two-state diffusion operator in eq 9. The linear equations for the left eigensolution as defined by eq 19 can be written by the transpose of eqs 33a–33d. Diagonalizing the $4N \times 4N$ matrix (N = number of basis functions) defined in eqs 33a–33d, we obtain

the eigenvalues $-Z_v$ and the corresponding eigenvectors of the nonadiabatic diffusion operator

$$|\psi_v^R\rangle = \sum_n R_{nv}|\phi_n^R\rangle \quad (34)$$

$$\langle\psi_v^L| = \sum_n L_{vn}\langle\phi_n^L| \quad (35)$$

where R_{nv} and L_{vn} are elements of the transformation matrices.

In general, due to the non-Hermitian nature of the nonadiabatic diffusion operator, the right and left eigenfunctions do not form an orthogonal set by themselves. However, when the eigenvalues are all nondegenerate, the left and right eigenfunctions form an orthogonal and complete set in dual Hilbert space.³⁰ Explicitly, we have

$$\sum_{n=0}^{\infty} L_{vn}R_{nv'} = \delta_{vv'} \quad (36)$$

for the orthogonality and

$$\sum_v R_{nv}L_{vn} = \delta_{nn} \quad (37)$$

for the completeness. Using these properties, we can construct the real time propagator for the operator \mathcal{L} as

$$G(t) = \sum_v |\psi_v^R\rangle\langle\psi_v^L|e^{-Z_v t} \quad (38)$$

and express the time evolution of the density matrix by projecting a given initial distribution onto the eigenstates, giving

$$|\rho(t)\rangle = G(t)|\rho(0)\rangle = \sum_v |\psi_v^R\rangle\langle\psi_v^L|\rho(0)\rangle e^{-Z_v t} \quad (39)$$

Hence, the eigensolution to the two-state nonadiabatic diffusion equation leads to a complete description of electron transfer dynamics.

III. Results and Discussion

In the section, we present the spectral structure of the nonadiabatic diffusion operator by diagonalizing its matrix representation in eqs 33a–33d. In principle, we need infinite number of basis functions to diagonalize the nonadiabatic diffusion operator; however, in practice, we have to truncate our basis set at some finite number. In all the calculations below, we have used $N = 50$ – 200 to diagonalize the $4N \times 4N$ matrix and the effect of finite number basis on the spectral structure has been carefully examined.

A. Spectral Structure. 1. Mixed-Valence Systems. In the mixed-valence compounds, the electronic coupling constant has the same order of magnitude as the reorganization energy and the electron transfer dynamics is usually probed experimentally at room temperature in polar solvents. To study this process, Evans, Nitzan, and Ratner⁷ carried out real time path-integral simulations for the photoinduced electron transfer reaction in $(\text{NH}_3)_5\text{Fe}^{\text{II}}(\text{CN})\text{Ru}^{\text{III}}(\text{CN})_5$. On the basis of their model, we chose the parameters for the calculation shown in Figure 1 as $\beta\Omega = 0.6716$, $\beta\lambda = 18.225$, $\beta V = 11.99$, and $\beta\epsilon = 18.705$. As mentioned in the Introduction, the mapping between the spin-boson Hamiltonian and the semiclassical Zusman equation is not rigorously defined. For example, for the nonadiabatic diffusion equation, the solvation energy correlation function takes an exponential form with the rate Ω , whereas for the spin-boson model Hamiltonian, it depends on the functional form

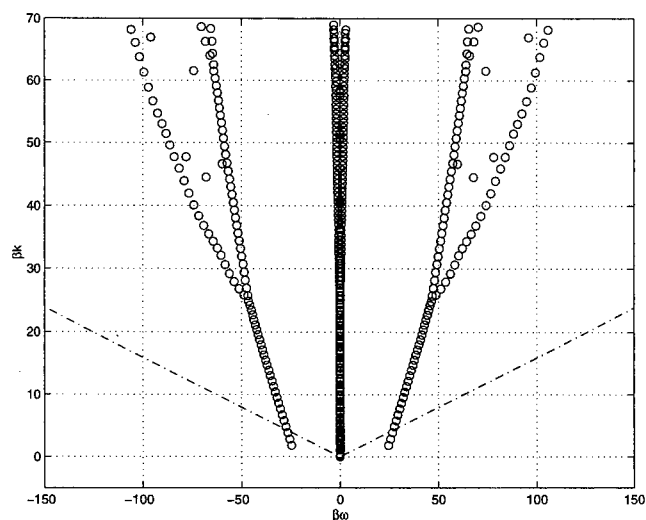


Figure 1. A plot of the lowest 400 eigenvalues for the nonadiabatic operator in a mixed-valence system. The parameters are $\beta\Omega = 0.6716$, $\beta\lambda = 18.225$, $\beta V = 11.99$, and $\beta\epsilon = 18.705$. The dot-dashed line is for the case $k = \omega/2\pi$.

of the spectral density. It can be shown that the Ohmic spectral density with an exponential cutoff ω_c

$$J(\omega) = \eta\omega \exp(-\omega/\omega_c) \quad (40)$$

used in the calculation of Evans et al. leads to an energy correlation function with a Lorentzian form at high temperature²³

$$C_{SB}(t) \approx \frac{2\eta\omega_c k_B T}{\pi} \frac{1}{1 + (\omega_c t)^2} \quad (41)$$

Then, the relaxation rate Ω used in our calculation is taken as the inverse of the mean survival time of $C_{SB}(t)$, which is $\Omega = 2\omega_c/\pi$.

In Figure 1 the spectral structure of the nonadiabatic operator is shown in complex space. We have used $N = 200$ ($4N = 800$) basis functions to calculate the eigenvalues. To remove the effect of finite basis set from the resulting spectral structure, we only show the first 400 eigenvalues in the complex plane. Since the nonadiabatic diffusion operator is non-Hermitian, the resulting spectrum shows complex conjugate paired eigenvalues as well as real eigenvalues, giving rise to the tree structure with three major branches (which we will call the *eigentree*). In Figure 1, we separate the real and imaginary parts of eigenvalue by

$$-Z_\nu = -k_\nu - i\omega_\nu \quad (42)$$

Obviously, the real part, $-k_\nu$, is always negative as all nonequilibrium physical quantities decay to zero at time infinity, and it scales linearly with the index ν since the relaxation rate corresponding to the n th basis state ϕ_n is proportional to n . In general, the relative magnitudes of real and imaginary parts of eigenvalues determine the time evolution of the density matrix: the real eigenvalues correspond to the simple exponential decay components and the complex conjugate paired eigenvalues correspond to the damped oscillation components.

To classify the eigenvalues quantitatively according to their dynamic behavior, we introduce the dimensionless quantity θ_ν

$$\theta_\nu \equiv \frac{2\pi k_\nu}{|\omega_\nu|} \quad (43)$$

where k_ν is the decay rate and $2\pi/\omega_\nu$ is the oscillation period. The time evolution of the density matrix component associated with the eigenvalue Z_ν is an exponential decay if $\theta_\nu = \infty$, an underdamped oscillation if $\theta_\nu \leq 1$, and a damped oscillation if $\theta_\nu > 1$. The relative amplitude of each component depends on the overlap matrix element between the initial density matrix and the eigenstate. As an approximate criterion for the classification of the eigenvalues, the slope corresponding to $\theta_\nu = 1$ is shown in the eigentree diagram in Figure 1. There are a few eigenstates around and below the $\theta_\nu = 1$ line, with a typical rate of $\beta k_\nu \approx 5$. For the parameters used in the calculation, β corresponds to ~ 170 fs in real time, and, therefore, these eigenstates exhibit underdamped oscillations with a period and a decay time in the femtosecond regime. In their real-time path integral simulations, Evans et al. showed that the population in the acceptor state oscillates with a few femtosecond period and these oscillations decay within 20 fs. Thus, qualitative features of the electron transfer dynamics can be predicted and understood from a careful examination of the spectral structure. Since the spectral analysis presented here is based on the semiclassical diffusion equation while the path-integral study is based on the quantum mechanical spin-boson Hamiltonian, the comparison between the two approaches is expected to be qualitative. In the following subsection, further analysis reveals the nature of these oscillations.

2. Dependence on the Coupling Constant V . To examine the underlying spectral structure in more detail, eigenvalues of the nonadiabatic diffusion operator are plotted as functions of the electronic coupling constant in Figure 2. All the parameters except for the electronic coupling constant are the same as used in Figure 1.

In Figure 2a, the real parts of the first 20 eigenvalues are shown as functions of the electronic coupling constant. Note that eigenvalues corresponding to complex conjugate pairs have the same real part, and thus they coalesce in the real eigenvalue diagram. When the coupling constant is very small ($\beta V \ll 1$), the real part of the first nonzero eigenvalue is very well separated from the eigenvalues of excited states, so the dynamics of electron transfer can be considered as a incoherent rate process with a well-defined rate constant, k_1 . When the coupling constant is larger ($\beta V \approx 1$), the first excited state becomes close to the second excited state, and they start to merge into a complex conjugate pair. If the coupling constant increases further, eigenvalues show a bifurcation behavior at $\beta V \approx 10$. Therefore, in this regime, the electron transfer kinetics show multiple time scale relaxation as well as coherent oscillation. The complicated behavior of coalescence and bifurcation in the real eigenvalue appears more frequently at higher states.

Another interesting feature of the real eigenvalue diagram is that a set of real eigenvalues decreases consistently as the coupling constant increases from zero. It turns out that these eigenstates take on large imaginary parts, which are responsible for the onset of the imaginary branches of the eigentree. In Figure 2b, the imaginary parts of the lowest 30 eigenvalues are plotted as functions of the coupling constant. Interestingly, the imaginary part of the eigenvalue increases approximately linearly with the coupling constant at large coupling regime. In fact, the dependence on the coupling constant is similar to that of the Rabi frequency for the two-level system

$$\Omega_R = \sqrt{\epsilon^2 + 4V^2} \quad (44)$$

which is shown in Figure 2b. As pointed out in a recent paper,¹⁸ electronic coherence in mixed-valence systems arises from Rabi

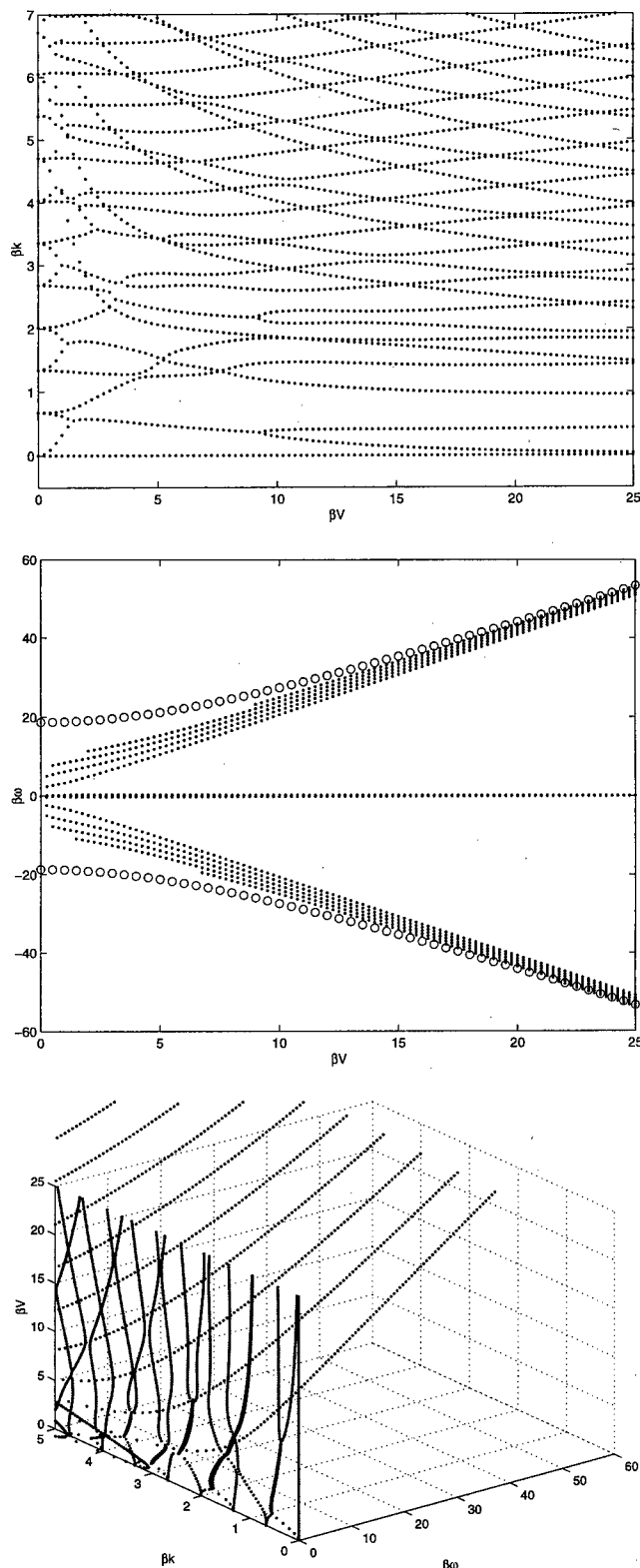


Figure 2. Plots of (a, top) real and (b, middle) imaginary parts of the lowest 30 eigenvalues as a function of the coupling constant, V . Except for the coupling constant, all the other parameters are set equal to those used in Figure 1. In (b), open circles correspond to the Rabi frequency $\Omega_R = (\epsilon^2 + 4V^2)^{1/2}$. (c, bottom) Three-dimensional plot of eigenvalues as a function of the coupling constant.

oscillations between two adiabatic surfaces and decays because of dephasing.

To demonstrate the correlation of the real and imaginary parts of the eigenvalues as functions of the coupling constant, we present a three-dimensional plot of the spectral structure in

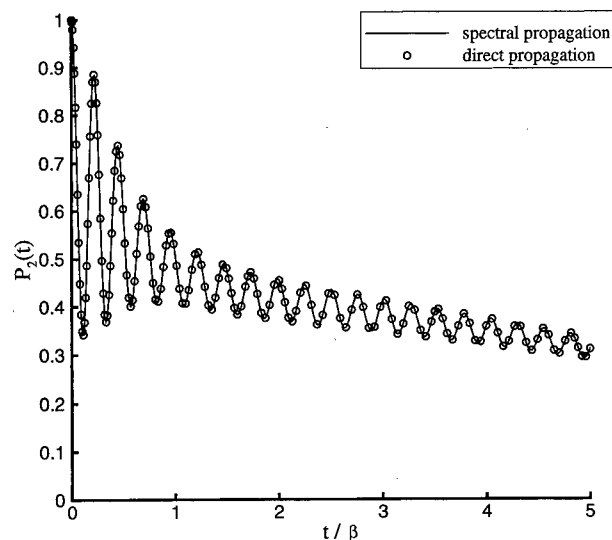


Figure 3. Comparison between the result of direct numerical propagation and spectral propagation. The parameters are chosen as $\beta\Omega = 1$, $\beta\lambda = 15$, $\beta V = 12$, and $\beta\epsilon = 3$.

Figure 2c. For clarity, only the positive branches of the imaginary eigenvalues are shown. If we compare Figure 2c with Figure 2a, the very rapidly decaying states shown in Figure 2a take on large imaginary parts corresponding to the Rabi oscillations as the coupling constant increases, and these states are responsible for the onset of the imaginary branches in the eigentree for the mixed-valence system shown in Figure 1.

B. Density Matrix Propagation. To check the validity of the spectral analysis as a density matrix propagation scheme, we calculated the time evolution of the density matrix by applying the propagator defined by eq 38 to the initial density matrix for various energy biases. Although it may seem straightforward to use the spectral method as a propagation scheme, the case for a non-Hermitian operator is not trivial and has not been explored. The main reason is that though the left and right eigenfunctions of a non-Hermitian operator can be shown to form a biorthogonal set for the nondegenerate eigenvalue case, numerically these eigenfunctions may not be stable enough to be used as a complete orthonormal basis for the density matrix propagation, especially in the nearly degenerate eigenvalue case. We can understand the situation as follows: When the two nearly degenerate eigenvalues Z_1 and Z_2 are obtained from a non-Hermitian operator, the orthogonality implies that $\langle L_2 |$ and $|R_1\rangle$ are orthogonal to each other as well as $\langle L_1 |$ and $|R_2\rangle$. When two eigenvalues become very close to each other, unlike the Hermitian operator case, $\langle L_1 |$ and $\langle L_2 |$ almost coincide and so do $|R_1\rangle$ and $|R_2\rangle$, so that $\langle L_1 |$ and $|R_1\rangle$ become almost orthogonal to each other. To still satisfy the normalization condition $\langle L_n | R_n \rangle$ in this case, the eigenfunction should be scaled up, thus making the spectral structure very sensitive to the numerical error involved in the calculation of eigenfunctions. For an interesting discussion on this point, one may refer to the work by Nelson and co-workers.³⁰ Due to this numerical instability, the use of the spectral method as a density matrix propagation scheme is not without limitation.

Figure 3a shows the spectral structure and the time evolution of the density matrix propagation for the case of $\beta\Omega = 1$, $\beta\lambda = 15$, $\beta V = 12$, and $\beta\epsilon = 5$. Generally, when the energy bias is small ($\beta\epsilon \leq 5$), the left and right eigenfunctions can form a complete orthonormal basis set, so the spectral method is stable and can be used as a numerical propagation method for the density matrix. With a large energy bias, however, the calculated eigenfunctions may not form a complete orthonormal basis. To

model for the photoinduced back electron transfer experiment in the mixed-valence compounds the initial density matrix is chosen as a thermal equilibrium distribution of the donor state (i.e., 1-state) pumped to the acceptor state (i.e., 2-state),^{4,5,7}

$$\rho_i(E,0) = \frac{1}{\sqrt{2\pi}\Delta_E} \exp\left(-\frac{(E+\lambda)^2}{2\Delta_E^2}\right) \delta_{i2} \quad (45a)$$

$$\rho_{12}(E,0) = \rho_{21}(E,0) = 0 \quad (45b)$$

It would be straightforward to calculate the spatial distribution of the density matrix in time $\rho(E,t)$ by applying the propagator in eq 38 to the above initial density matrix; however, to demonstrate the overall temporal behavior only the time evolution of the total population in the acceptor state is calculated

$$P_2(t) = \int dE \rho_2(E,t) \quad (46)$$

In order to check the validity of the spectral method as a propagation scheme in this case, we also calculated the time evolution of the density matrix by directly solving the $4N$ differential equations for the expansion coefficients of the density matrix using the Bulirsch–Stoer algorithm,³¹ and the comparison in Figure 3a shows a perfect agreement. If only the transient behavior is concerned with, the direct propagation method would be preferred over the spectral method; however, the spectral propagation has the advantage when calculating the long-time behavior once the complete spectrum is known. Overall, the computational costs for the two methods are comparable to each other. As expected from the spectral structure shown in the previous section, the population in the acceptor state shows an underdamped coherent oscillation behavior at initial times followed by a damped oscillation behavior at later times.

Further, we have also studied the density matrix propagation for different energy biases to examine the electronic dephasing effect. As seen from Figure 4a, the increase in energy bias destroys the electronic coherence dramatically. Another interesting observation is the phase shift in the population dynamics as the energy bias is varied, and it is because the Rabi oscillation frequency increases with energy bias. We can confirm the temporal behavior of the density matrix propagation by examining the spectral structure shown in Figure 4b. The period of the initial coherence is estimated to be $\tau_{\text{osc}} \approx 0.25\beta$ from Figure 4a. In comparison, the Rabi frequency for the corresponding adiabatic two-level system is given by $\Omega_R = (\epsilon^2 + 4V^2)^{1/2} \approx 25\beta^{-1}$, which can also be obtained from the onset of imaginary branches in the eigentree shown in Figure 4b, and the estimation is consistent with the oscillation period observed in the dynamics since $\tau_{\text{osc}} \approx 2\pi/\Omega_R$. The real eigenvalues of the lowest excited states in the imaginary branches are estimated to be $\beta k \approx 1-2$, and they agree with the decay time of the oscillation amplitude in Figure 4a, confirming the validity of the spectral method as a density matrix propagation scheme. Even though it has been well-known in the literature that the damping of population is enhanced with increased energy asymmetry,¹⁴ we have also confirmed this through the spectral analysis method.

As an example of the eigenfunction responsible for the coherent oscillation behavior observed in Figure 4b, we show the left and right eigenfunctions corresponding to a complex eigenvalue $\beta Z = 2.6228 \pm i26.394$ for a symmetric case ($\beta\epsilon = 0$) and $\beta Z = 2.8057 \pm i26.466$ for an asymmetric case ($\beta\epsilon = 5$) in Figures 5 and 6. The eigenfunctions corresponding to a

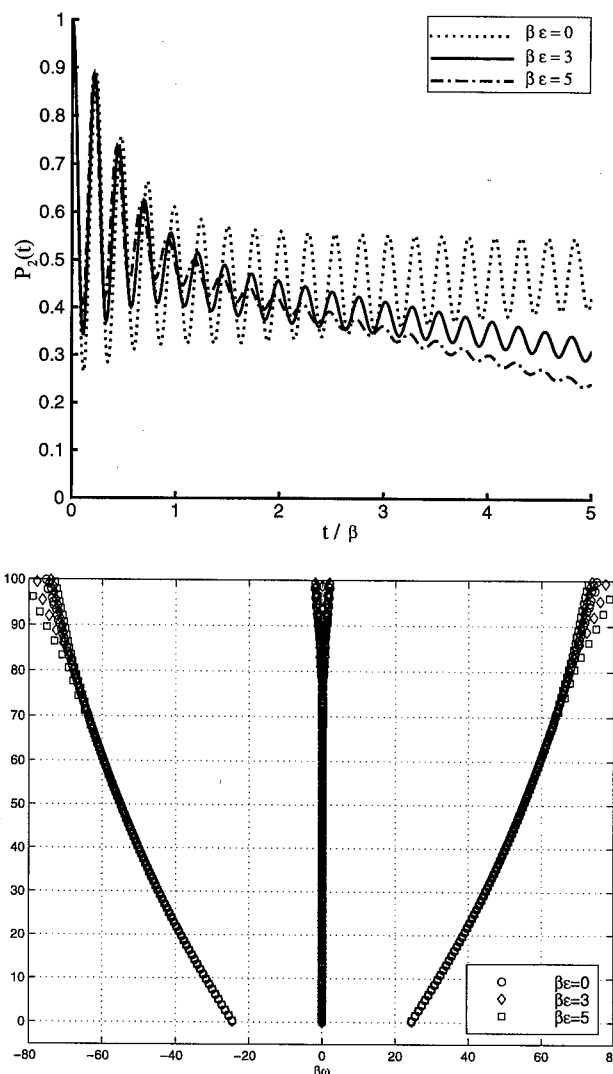


Figure 4. Comparison of (a, top) the dynamics and (b, bottom) the spectra in the mixed-valence system for three different energy biases. Except for the energy bias, all the other parameters are set equal to those used in Figure 3. Agreements between the results of numerical and spectral propagation have been checked in these cases.

complex conjugate pair of eigenvalues are also complex conjugate to each other; therefore, the frequency spectrum of the density matrix evolution is proportional to the norm of wave function. We note that the left eigenfunction is more extended than the right eigenfunction. Although the population distribution in the donor and acceptor states corresponding to coherent oscillation is inverted with respect to the Boltzmann distribution, it does not contribute to the steady-state population distribution due to the transient nature.

IV. Concluding Remarks

In this paper we have applied the spectral analysis method to the nonadiabatic two-state diffusion equation that describes electron transfer dynamics in Debye solvents. In particular, we have examined electronic coherence in mixed-valence compounds and demonstrated that underdamped Rabi oscillations are observed in an overdamped solvent environment. Detailed study of the spectral structure of the nonadiabatic operator for various energy biases and coupling constants allows us to determine the underlying mechanisms of electron transfer kinetics. Eigenvalues form three branches in the eigendiagram: a single branch of real eigenvalues and two symmetric branches

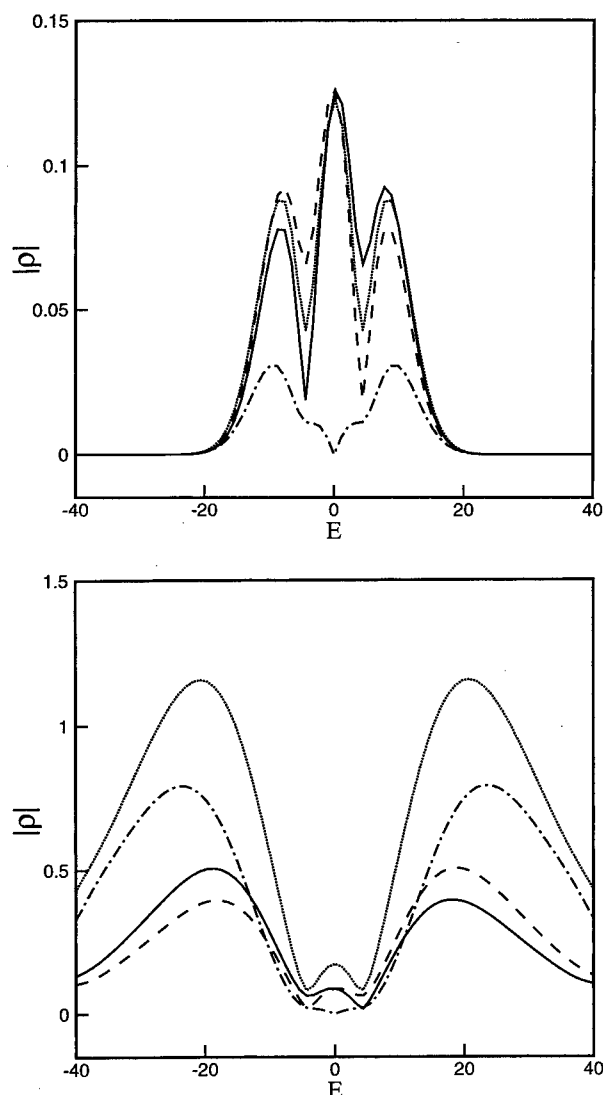


Figure 5. (a, top) Right and (b, bottom) left eigenfunctions with an eigenvalue $\beta Z = 2.6228 \pm i26.394$ for a symmetric bias case ($\beta\epsilon = 0$). All the other parameters are set equal to those used in Figure 3 except for the energy bias. Each line corresponds to ρ_1 (solid), ρ_2 (dashed), u (dot-dashed), and v (dotted), respectively.

of complex conjugate eigenvalues. In strongly coupled systems, all three branches have a similar order of magnitude, indicating that both multiple-exponential decay and coherent oscillations can be observed experimentally.

We have investigated the dependence of the spectral structure on the coupling constant. In the very weak coupling regime, the lowest excited state is well separated from higher states, which makes the electron transfer dynamics a well-defined rate process. In the strong coupling regime, however, the eigenvalue diagram shows coalescence/bifurcation behavior in the complex plane. We have used the spectral method to calculate the time evolution of the density matrix, and indeed, observed electronic coherence in the temporal behavior of population in the acceptor state for nonequilibrium initial distributions. We also found a good agreement between results of the spectral propagation method and the numerical propagation method for small energy bias cases. Due to non-Hermiticity of the nonadiabatic operator, the spectral propagation method was not numerically stable for large energy bias cases.

For an isolated quantum system, the eigensolution to the Schrödinger equation completely determines its dynamics. In a similar fashion, the eigensolution to the nonadiabatic diffusion

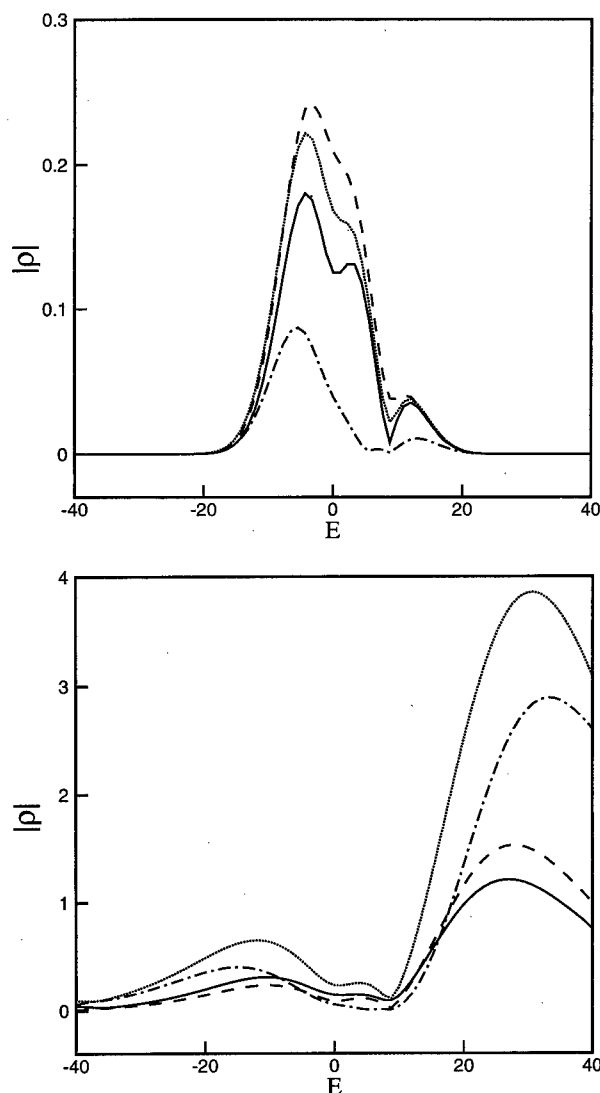


Figure 6. (a, top) Right and (b, bottom) left eigenfunctions with an eigenvalue $\beta Z = 2.8057 \pm i26.466$ for an asymmetric bias case ($\beta\epsilon = 5$). All the other parameters are set equal to those used in Figure 3 except for the energy bias. Each line corresponds to ρ_1 (solid), ρ_2 (dashed), u (dot-dashed), and v (dotted), respectively.

operator completely characterizes the dynamics of a dissipative system and thus provides a powerful tool to analyze dissipative dynamics. It is well-known that quantum dynamics comes from the underlying spectra, especially in gas-phase chemical systems;³² however, the spectral aspect of condensed phase dissipative systems has not been well recognized yet and deserves further investigation. Though the analysis presented here is restricted to semiclassical dissipative systems, it may also be applied to quantum dissipative dynamics. In principle, we can derive the evolution equation for quantum dissipative systems either from first principles or through numerical reduction, and then pose the quantum dissipative equation of motion as an eigenvalue problem. Along this line, the dissipative dynamics of the spin-boson Hamiltonian, which has been studied mostly as a dynamic problem,^{6,33} can also be explored as a spectral problem in the future.

Acknowledgment. The authors thank the NSF for financial support. J.C. thanks the MIT start-up fund and the Petroleum Research Fund for financial support. Y.J. thanks the Korean Foundations for Advanced Studies for financial support.

References and Notes

- (1) Vos, M. H.; Rappaport, F.; Lambry, J.-C.; Breton, J.; Martin, J.-L. *Nature* **1993**, 363, 320.
- (2) Jonas, D.; Bradford, S.; Passino, S.; Fleming, G. *J. Chem. Phys.* **1995**, 99, 2554.
- (3) Arnett, D. C.; Vohringer, P.; Scherer, N. F. *J. Am. Chem. Soc.* **1995**, 117, 12262.
- (4) Reid, P. J.; Silva, C.; Barbara, P. F.; Karki, L.; Hupp, J. T. *J. Phys. Chem.* **1995**, 99, 2609.
- (5) Lucke, A.; Mak, C. H.; Egger, R.; Ankerhold, J.; Stockburger, J.; Grabert, H. *J. Chem. Phys.* **1997**, 107, 8397.
- (6) Makarov, D.; Makri, N. *Chem. Phys. Lett.* **1994**, 221, 482.
- (7) Evans, D. G.; Nitzan, A.; Ratner, M. A. *J. Chem. Phys.* **1998**, 108, 6387.
- (8) Coalson, R. D.; Evans, D. G.; Nitzan, A. *J. Chem. Phys.* **1994**, 101, 486.
- (9) Cho, M.; Silbey, R. J. *J. Chem. Phys.* **1995**, 103, 595.
- (10) Harris, R. A.; Silbey, R. *J. Chem. Phys.* **1983**, 78, 7330.
- (11) Silbey, R.; Harris, R. A. *J. Chem. Phys.* **1984**, 80, 2615.
- (12) Carmeli, B.; Chandler, D. *J. Chem. Phys.* **1985**, 82, 3401.
- (13) Chandler, D. In *Liquides, Cristallisation et Transition Vitreuse, Les Houches, Session LI*; Levesque, D., Hansen, J., Zinn-Justin, J., Eds.; Elsevier: New York, 1991.
- (14) Leggett, A. J.; Chakravarty, S.; Dorsey, A. T.; Fisher, M. P. A.; Garg, A.; Zwerger, W. *Rev. Mod. Phys.* **1987**, 59, 1.
- (15) Marcus, R. A.; Sutin, N. *Biochim. Biophys. Acta.* **1985**, 811, 265.
- (16) Newton, M. D.; Sutin, N. *Annu. Rev. Phys. Chem.* **1984**, 35, 437.
- (17) Bader, J. S.; Kuharski, R. A.; Chandler, D. *J. Chem. Phys.* **1990**, 93, 230.
- (18) Cao, J. *Chem. Phys. Lett.*, in press.
- (19) Cao, J. *J. Chem. Phys.*, in press.
- (20) Zusman, L. D. *Chem. Phys.* **1980**, 49, 295.
- (21) Calef, D. F.; Wolynes, P. G. *J. Phys. Chem.* **1983**, 87, 3387.
- (22) Hynes, J. T. *J. Phys. Chem.* **1986**, 90, 3701.
- (23) Garg, A.; Onuchic, J. N.; Ambegaokar, V. *J. Chem. Phys.* **1985**, 83, 4491.
- (24) Sparpaglione, M.; Mukamel, S. *J. Chem. Phys.* **1988**, 88, 3263.
- (25) Cao, J.; Voth, G. A. *J. Chem. Phys.* **1997**, 106, 1769.
- (26) Onuchic, J. N.; Wolynes, P. G. *J. Chem. Phys.* **1993**, 98, 2218.
- (27) Yang, D. Y.; Cukier, R. I. *J. Chem. Phys.* **1989**, 91, 281.
- (28) Simons, J. *Chem. Phys.* **1973**, 2, 27.
- (29) Risken, H. *The Fokker-Planck Equation*; Springer-Verlag: New York, 1984.
- (30) Dahmen, K. A.; Nelson, D. R.; Shnerb, N. M. *cond-mat/9903276* **1999**.
- (31) Press, W. H.; Teukolsky, S. A.; Vetterling, W. T.; Flannery, B. P. *Numerical Recipes in FORTRAN*, 2nd ed.; Cambridge University Press: Cambridge, U.K., 1992.
- (32) Field, R. W.; O'Brien, J. P.; Jacobson, M. P.; Solina, S. A. B.; Pollik, W. F.; Ishikawa, H. *Adv. Chem. Phys.* **1997**, 101, 463-490.
- (33) Wang, H.; Song, X.; Chandler, D.; Miller, W. H. *J. Chem. Phys.* **1999**, 110(10), 4828.

Semiclassical Wave Packet Dynamics with Electronic Structure Computed on the Fly: Application to Photophysics of Electronic Excited States in Condensed Phase

Alfredo E. Cárdenas, Roman Krems, and Rob D. Coalson*

Department of Chemistry, University of Pittsburgh, Pittsburgh, Pennsylvania 15260

Received: June 1, 1999; In Final Form: July 28, 1999

Many semiclassical wave packet propagation methods require only local potential energy surface information in order to update a Gaussian wave packet over a short time interval. These data, which include the evaluation of the potential energy at the instantaneous configuration space center of the wave packet, plus the gradient vector and Hessian (second derivative) matrix at the same configuration, can be generated efficiently by extant electronic structure packages. This leads to an algorithm for propagating semiclassical Gaussian wave packets using electronic structure data computed "on the fly" in the course of the propagation. The feasibility of such a strategy for condensed phase systems is demonstrated by using it (with an appropriate approximate level of electronic structure theory) to calculate Franck–Condon absorption and emission spectra of *all-trans* 1,3,5,7-octatetraene in the gas phase, and in both chloroform and methanol solvents. Good agreement with the corresponding experimentally measured spectra is obtained.

1. Introduction

The problem of computing reliable dynamical signatures (spectra, scattering cross sections, reaction rate constants, etc.) of condensed phase quantum systems remains challenging for two basic reasons. First, there are severe practical difficulties in propagating wave packets¹ that describe the quantum motion of the nuclear coordinates. Second, a quantum dynamics calculation is ultimately only as good as the potential energy surfaces upon which it is based, yet high-level *ab initio* electronic structure calculations¹ can only be carried out for small isolated molecule systems. The task of generating such surfaces for large molecules or for probe molecules that interact with a condensed phase environment is a daunting one. The situation is particularly bleak when the relevant quantum dynamics occurs on electronically excited potential energy surfaces (e.g., in many photoinduced processes), since it is much more difficult to compute accurate excited electronic potential surfaces than ground state properties.

For systems with only a few degrees of freedom (ca. 5 or less), it is possible to calculate and store global potential energy surfaces, i.e., ones which span the full relevant range of each nuclear coordinate, via *ab initio* electronic structure theory. Once the relevant potential energy surface (PES) is stored, nuclear coordinate wave packets can be propagated on it using exact numerical grid and/or basis set technology. For systems much larger than this, construction of a global PES is not feasible. Of course, in many situations a global potential surface is not strictly required. For example, if the nuclear coordinates can be treated classically, one needs only to determine the gradient of the potential surface at the *instantaneous* configuration of the nuclear coordinates in order to update this configuration by a small time step. The gradient has to be recomputed at each time step, but for a system with many nuclear coordinates (e.g. a condensed phase system), this is vastly preferable to attempting to construct a global multidimensional potential surface. Indeed, this strategy, namely, using electronic structure methodology to determine the potential energy gradient at the instantaneous

nuclear coordinate configuration coupled with Newton's equations of classical mechanics, has proven extremely useful in recent years.² The central issue we wish to consider here is to what extent the concept of on the fly determination of potential energy surfaces can be extended to enable *quantum mechanical* propagation of the nuclear coordinates.

A nuclear coordinate wave packet is localized in some region of space at a particular time, and it is only necessary to know the potential energy surface in that region (i.e., where the wave packet has nonzero amplitude) to update it by a small time step according to the time-dependent Schrödinger equation. This property does not necessarily provide any practical advantage: one would still need to map out (by quadrature) the potential energy surface in the appropriate region of multidimensional coordinate space, and then update the wave packet on the corresponding multidimensional coordinate grid. However, if the wave packet is well localized, several features conspire to make the prospect of wave packet dynamics with potential surfaces computed on the fly much more attractive. A narrow Gaussian wave packet remains Gaussian in time (until it broadens to a critical width; cf. below). This allows the utilization of Heller's Gaussian wave packet dynamics (GWD) algorithm to propagate *multidimensional* wave packets.³ GWD requires at most a quadratic Taylor series expansion of the potential energy surface around the instantaneous center of the wave packet (the "thawed Gaussian approximation").⁴ Thus, a call to the electronic structure (ES) part of the algorithm need only provide at each step the value of the potential energy at the current nuclear coordinate configuration, plus the gradient and Hessian (second derivative matrix) at that configuration. These quantities are readily produced by standard electronic structure programs/software packages. With this minimal amount of "local" potential energy information it is possible to update the Gaussian wave packet representing the nuclear coordinate wave packet state by a small time step, and then repeat the process again. Indeed, we note that in certain situations (e.g., if the width of the nuclear coordinate wave packet is *very small*) a simpler approximation to the nuclear coordinate wave packet

motion, namely the frozen Gaussian approximation,⁵ suffices. In this case second derivative (Hessian) ES data is not required, and the strategy reduces to the one used to propagate the nuclear coordinates classically (vide supra).⁶

Of course, the condition that the nuclear coordinate wave packet remains narrow imposes restrictions on the range of dynamical processes that can be treated by the strategy proposed above. For the general case of anharmonic potential energy surfaces, an initially narrow wave packet will eventually spread until the potential surface cannot be represented by a quadratic form in the entire spatial region where the wave packet is nonzero.⁸ How long it takes to reach this point depends on the details of the shape of the potential surfaces, mass of the atoms, initial conditions, etc. A variety of applications of the technique indicate that many dynamical processes on a subpicosecond time scale can be successfully treated using the Gaussian approximation of the nuclear coordinate wave packet states.^{9–13} It is this class of processes which we focus on here.¹⁴

In the present work we combine Gaussian wave packet dynamics with potential energy surfaces computed on the fly to study the electronic absorption and emission spectra of *all-trans* octatetraene, both as an isolated molecule and immersed in a liquid solvent. Octatetraene is the shortest polyene that shows clear emission spectra.^{19–21} It is composed of 18 atoms, and hence 48 vibrational coordinates. We treat their quantum dynamical evolution motion via Gaussian wave packet dynamics, while the relevant 48-dimensional PES's are computed on the fly using Warshel's semiempirical QCFF/PI electronic structure code.^{22,23} We are able to reproduce well-resolved experimental gas phase Franck–Condon spectra using this procedure. We then model the analogous spectra for octatetraene in room temperature polar solvents, specifically chloroform and methanol. Because solvent relaxation takes place on a multipicosecond time scale while the relevant nuclear wave packet dynamics contributing to Franck–Condon absorption/emission spectra lasts less than 100 fs, we employ a static solvent model; i.e., the solute (octatetraene) motion takes place in the potential field generated by a static solvent configuration. (This external potential is added to the internal Coulombic interactions of the nuclei and electrons of the octatetraene molecule in the computation of potential energy surfaces using QCFF/PI). We average over solvent configurations selected from a classical equilibrium molecular dynamics simulation to obtain a prediction for the observed condensed phase octatetraene spectrum. Good agreement is found with experimental measurements. Not only are solvent-induced shifts of the absorption and emission bands successfully accounted for, but so are the shapes of the bands. The latter are altered by solvent broadening, but nevertheless retain some vibrational structure. The ability of the methodology utilized here to account for vibronic structure justifies the effort of propagating nuclear coordinate wave packets, and the accuracy of the results compared to experiment demonstrates the utility of performing detailed electronic structure calculations to obtain the required potential energy surfaces.

The outline of the paper is as follows. In section 2 we present methodological details. Section 2.1 briefly reviews the QCFF/PI electronic structure method, and the modifications needed to treat the influence of an external potential energy field (to be provided by electrostatic and nonbonded interactions of the solute molecule with surrounding solvent molecules). In section 2.2 we discuss the classical MD simulations used to generate solvent configurations. In section 2.3 we summarize the GWD method for quantum mechanical propagation of the vibrational

coordinates of the solute molecules, and the procedure used to extract Franck–Condon spectra from this wave packet dynamics. In section 3 we present results for calculated electronic absorption and emission spectra of gas phase octatetraene and the analogues of these spectra for an octatetraene molecule in chloroform and methanol solvents. Direct comparison with experiment is made. Section 4 contains concluding remarks.

2. Methodological Details

2.1. Semiempirical Electronic Structure USING QCFF/PI. Consider a single solute molecule immersed in a liquid solvent. For a given configuration of solute nuclei and solvent atoms, the Hamiltonian for the electrons of the solute is

$$\hat{H} = \hat{H}_{\text{mol}} + \hat{H}_{\text{sol}} + \hat{H}_{\text{mol/sol}} \quad (1)$$

where \hat{H}_{mol} is the quantum mechanical Hamiltonian of the solute (in atomic units):

$$\hat{H}_{\text{mol}} = -\frac{1}{2} \sum_i^n \nabla_i^2 + \sum_{i,j>i}^n \frac{e^2}{r_{ij}} - \sum_i^n \sum_{\alpha}^N \frac{eZ_{\alpha}}{r_{i\alpha}} + \sum_{\alpha}^N \sum_{\beta>\alpha}^N \frac{Z_{\alpha}Z_{\beta}}{R_{\alpha\beta}} \quad (2)$$

Here i labels the solute electrons (n in all) and α the solute nuclei (N in all); r_{ij} is the distance between electrons i and j and $R_{\alpha\beta}$ the distance between nuclei α and β . Z_{α} is the atomic number of nucleus α and e the magnitude of the electron charge. Of the other terms in eq 1, \hat{H}_{sol} is the classical Hamiltonian for the solvent (specified in section 2.2) and $\hat{H}_{\text{mol/sol}}$ is the interaction Hamiltonian that describes the interaction between the solute and the solvent, namely:

$$\hat{H}_{\text{mol/sol}} = - \sum_i^n \sum_k^M \frac{eq_k}{r_{ik}} + \sum_{\alpha}^N \sum_k^M \frac{Z_{\alpha}q_k}{R_{\alpha k}} + \sum_{\alpha}^N \sum_k^M \epsilon_{\alpha k} \left(\frac{\sigma_{\alpha k}^{12}}{R_{\alpha k}^{12}} - \frac{\sigma_{\alpha k}^6}{R_{\alpha k}^6} \right) \quad (3)$$

In this equation the solvent atoms are labeled by k (M atoms in all), q_k is the charge on solvent atom k , r_{ik} is the distance between solute electron i and solvent atom k , $R_{\alpha k}$ is the distance between solute nucleus α and solvent atom k , and $\epsilon_{\alpha k}$ and $\sigma_{\alpha k}$ are Lennard-Jones parameters. Clearly, the first two terms in eq 3 account for electrostatic interactions between the (partial) charges on the solvent atoms and the electrons and nuclei of the solute molecule, while the third term accounts for short-range van der Waals forces between solute and solvent atoms.

To calculate the electronic absorption and emission spectra of octatetraene, we require equilibrium geometries and potential energy surfaces for the ground and the first two excited states. Simple MO theories can be used to describe the ground state 1^1A_g and the second excited state 1^1B_u . This corresponds to the $|\text{HOMO}\rangle \rightarrow |\text{LUMO}\rangle$ transition. To describe the first excited state 2^1A_g it is necessary to use configuration interaction with double excitations, since this state is a mixture of single ($|\text{HOMO} - 1\rangle \rightarrow |\text{LUMO}\rangle$ and $|\text{HOMO}\rangle \rightarrow |\text{LUMO} + 1\rangle$) and double (mainly, $|\text{HOMO}, \text{HOMO}\rangle \rightarrow |\text{LUMO}, \text{LUMO}\rangle$) excitations. It is possible to perform ab initio calculations for the octatetraene molecule, but our “structure on the fly” method requires many of these calculations to evaluate the potential energy surfaces at the center of the wave packet during its time propagation. For this reason, we have chosen to employ a semiempirical technique to determine the electronic structure of the molecule, specifically the QCFF/PI method developed by Warshel and others with single plus double excited configurations included.^{22,23} This model describes the σ electrons with

an empirical potential and the π electrons via a semiempirical quantum-mechanical calculation comprising of self-consistent field plus configuration interaction components. The QCFF/PI program has proven reliable for computing ground and excited states of gas phase polyenes and their associated optical/UV spectra,²³ and has the additional advantage that from a single electronic eigenfunction (obtained by solving the electronic Schrödinger equation at a particular nuclear coordinate configuration) the first and second derivatives with respect to the Cartesian positions of the atoms at that nuclear configuration can be calculated analytically (hence rapidly). These derivatives are needed in order to evolve the nuclear coordinate dynamics using GWD techniques. As noted above (and discussed further below), the QCFF/PI program has been modified to include an additional term in the diagonal elements of the Fock matrix to take into account the electrostatic influence of the partial charges of the solvent molecules on the electronic structure of the solute molecule. Specifically, the Fock matrix under the influence of the solvent can be written as^{24,25}

$$F_{ii} = F_{ii}^0 - \sum_k \sum_l \left\langle \varphi_i \left| \frac{eq_l}{r_{kl}} \right| \varphi_i \right\rangle$$

$$F_{ij} = F_{ij}^0 \quad (4)$$

Here F^0 is the Fock matrix of the isolated solute, expressed in a basis of orthogonalized atomic orbitals φ_i . The diagonal Fock matrix elements are modified by the indicated correction terms which reflect electrostatic interactions of the solute electrons with the charges on the solvent atoms according to the first term in $\hat{H}_{\text{mol/sol}}$. (The second and third terms in $\hat{H}_{\text{mol/sol}}$ do not depend on solute electronic coordinates and can be treated as an external field and added directly to the total energy.) The one-electron integrals associated with the interaction Hamiltonian are evaluated analytically using the appropriate expressions for Slater orbitals.²⁶ The van der Waals parameters used in this calculation are the same ones used in the molecular dynamics calculation detailed below.

2.2. Classical MD of the Solvent. For an isolated octatetraene molecule, the QCFF/PI program can be used to evaluate the PES at any atomic configuration. However, when this molecule is immersed in a condensed phase environment, the relevant PES is modified by the presence of the surrounding molecules of the bath. In particular, if the solvent molecules are polar, the electrostatic interaction of the partial charges of these molecules will significantly affect the electronic structure of the polyatomic molecule. This effect can be accounted for by calculating the Coulombic potential in the region of the solute atoms generated by the partial charges present in the solvent. The electric potential field generated by the solvent charges modifies the diagonal elements of the Fock matrix of the molecule (cf. eq 4), and this modification perturbs the potential energy surfaces of the molecule. To incorporate such perturbations we take advantage of the fact that the dynamical time scale for the absorption correlation function is <100 fs, while the typical time scale for rotational relaxation of polyatomic molecules in a liquid phase can be several picoseconds. Therefore, the effects of the solvent can be treated in the "static limit", i.e., the configuration of the solvent is frozen, nuclear wave packet dynamics on the molecular potential energy surface perturbed by that solvent configuration is computed (details are given in section 2.3), and an average is taken over configurations selected from a thermal equilibrium ensemble to get the condensed phase spectrum. For a liquid solute-solvent system at room temper-

ature, the equilibrium configurations of the (room temperature) solvent can be sampled via classical molecular dynamics (MD) simulations.

We performed MD simulations using the AMBER²⁷ force field, according to which the total potential energy function for the ensemble of solvent molecules has the form

$$E_{\text{total}} = \sum_{\text{bonds}} K_r (r - r_{\text{eq}})^2 + \sum_{\text{angles}} K_\theta (\theta - \theta_{\text{eq}})^2 + \sum_{\text{dihedrals}} \frac{V_n}{2} [1 + \cos(n\phi - \gamma)] + \sum_{i < j} \left[\frac{A_{ij}}{R_{ij}^{12}} - \frac{B_{ij}}{R_{ij}^6} + \frac{q_i q_j}{\epsilon R_{ij}} \right] \quad (5)$$

(The definitions of the various force field parameters can be found elsewhere.²⁷) For the solvents studied, chloroform and methanol, a rectangular box of solvent molecules was generated (containing 787 and 633 solvent molecules in the cases of chloroform and methanol, respectively). We employed a flexible all-atom model for the molecules using force fields parameters developed as part of the AMBER package.^{28,29} The molecular dynamics simulations were performed using explicit image periodic boundary conditions with a time step of 0.5 fs and a temperature of 300 K. We first calculated molecular dynamics of the solvent alone to ensure that solvent properties such as the bulk density were reproduced for the force field parameters chosen for the simulations. Then one molecule of octatetraene was introduced into the solvent box and an MD simulation was performed on the solvent/solute system, keeping the solute rigid (freezing internal vibrations) for the purposes of the simulation. After equilibrating at 1 atm, constant volume dynamics was carried out and we generated multiple sets of solvent configurations separated by 1 ps. For absorption spectrum calculations, the equilibrium geometry and partial charges of octatetraene in the ground electronic state were used in the molecular dynamics simulations. For emission spectrum calculations, the geometry and charges for the 2^1A_g state were used.

2.3. Nuclear Coordinate Wave Packet Evolution via Gaussian Nuclear Wave Packet Dynamics and the Extraction of Vibronic Spectra. As discussed above, to calculate quantum nuclear coordinate evolution on general multidimensional potential energy surfaces it is necessary to use approximate techniques. One such technique is Gaussian wave packet dynamics (GWD), which has been extensively utilized in the past to produce rapid and reliable results for nuclear dynamics on the scale of a picosecond or shorter.⁹⁻¹³ The general Gaussian wave function for a D -dimensional system at time t with spatial coordinate \vec{x} is

$$\phi(\vec{x}, t) = \exp[i[(\vec{x} - \vec{x}_t) \cdot A_t (\vec{x} - \vec{x}_t) + \vec{p}_t \cdot (\vec{x} - \vec{x}_t) + \gamma_t]] \quad (6)$$

where A_t is a $D \times D$ complex symmetric matrix, \vec{x}_t and \vec{p}_t are real D -dimensional vectors specifying the position and momentum of the center of the wave packet, and γ_t is a complex phase/normalization parameter.

The equations of motion governing the time evolution of the parameters in this Gaussian wave packet depend only on local information about the potential energy surface near the center of the wave packet. Specifically, frozen Gaussian approximation (FGA) wave packet dynamics requires only the gradient of the potential surface at the position space center of the wave packet.⁵ Thawed Gaussian approximation (TGA) dynamics also requires second derivative information as input.⁴

Covalently bound molecules usually occupy the ground vibrational state of the ground electronic PES prior to photoexcitation, because typically the vibrational quantum is much larger than $k_B T$ (k_B is Boltzmann's constant, T the absolute temperature) for all Franck–Condon active normal modes. The initial wave packet $\phi^{(0)}(\bar{x})$ is then Gaussian in shape. After the photoexcitation event, this initial wave packet evolves on an excited electronic surface. The evolution of this wave packet $\phi(\bar{x}, t)$ can be computed by solving the equations of motion for the Gaussian parameters,^{3–5} using as input excited state PES data. The electronic absorption spectrum is calculated using the well-known prescription³

$$\sigma(\omega_L) = \frac{Re}{\pi} \int_0^\infty dt \exp[i(\omega_L + E^{(0)})t] \langle \phi^{(0)} | \phi(t) \rangle \quad (7)$$

where ω_L is the frequency of the laser beam and $E^{(0)}$ is the vibrational energy eigenvalue corresponding to $\phi^{(0)}$. The equation for the emission spectrum is similar with reversal of the roles played by ground and excited electronic states and the change $\omega_L \rightarrow -\omega_L$.

We use the GWD technique to propagate the nuclear wave packets associated with the octatetraene molecule. These wave packets evolve on the anharmonic potential surfaces generated by QCFF/PI. For the absorption spectrum the initial wave packet is written as a product of the ground vibrational eigenfunctions associated with the normal modes of the ground electronic state of the molecule. For the emission spectrum, the ground vibrational eigenfunctions for the first excited state, 2^1A_g , are used. At $t = 0$ this initial wave packet is placed on the second excited state (absorption) or the ground state (emission) and evolved there. At every time step, the potential energy and appropriate derivatives of the PES at the center of the wave packet are evaluated via QCFF/PI (on the fly dynamics). For the systems studied in this paper, the FGA and TGA produced essentially identical results. Time evolution was carried out for 100 fs for each solvent configuration and the spectra were collected and averaged for the different configurations. We obtained converged static averages for the condensed phase spectra using 150–200 solvent configurations.

We executed the programs on a DEC α workstation. It took several days to get the set of solvent configurations using AMBER, and 1 h to compute the nuclear wave packet evolution using QCFF/PI.

3. Results

The electronic spectroscopy of all-*trans*-1,3,5,7-octatetraene has been studied theoretically²³ and experimentally.^{19–21} The absorption spectrum of this molecule involves an electronic transition from a ground state with A_g symmetry to the second lowest excited singlet state with B_u symmetry. The emission spectrum in the gas phase involves a transition between the same two states, and hence appears as a mirror image of the corresponding absorption spectrum. However, in the condensed phase the observed emission spectrum is due to a forbidden transition from the lowest excited singlet state with A_g symmetry. The energy gap between these first excited states of octatetraene is 6400 cm^{-1} .

The absorption and emission spectra of all-*trans*-1,3,5,7-octatetraene in the gas phase shows Franck–Condon structure arising from single and double bond C–C stretches (at 1645 and 1235 cm^{-1} , respectively).²⁰ Gavin et al.²⁰ also obtained experimental absorption and emission spectra of octatetraene in 10 different solvents. They observed that the absorption and emission spectra in solution are broad and some vibrational

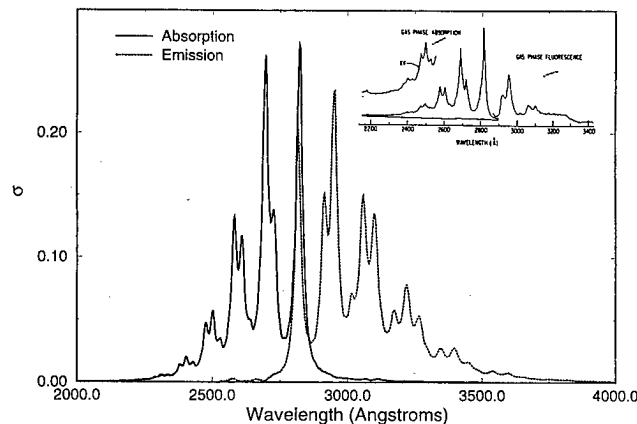


Figure 1. Calculated absorption and emission spectra of all-*trans*-octatetraene in the gas phase computed via Gaussian wave packet dynamics and QCFF/PI electronic structure is shown in the main panel. The inset shows both experimental spectra.²⁰

structure is apparent in the absorption spectrum. They noted that these spectra do not change in shape from solvent to solvent but the overall spectral band shifts in frequency. They also noticed a large energy gap that separates the absorption and emission spectra for a given solvent due to the different electronic states involved in the two processes.

We have chosen two solvents (chloroform and methanol) to test the sensitivity of our method. Experimentally,²⁰ the 0–0 absorption band of octatetraene in chloroform and methanol is red-shifted with respect to the gas phase band (by 2973 and 2333 cm^{-1} , respectively).

Figure 1 shows the absorption and emission spectra of octatetraene in the gas phase calculated using QCFF/PI plus GWD techniques. (In order to mimic instrumental broadening in the experimental gas phase measurements, we invoked an additional exponential damping factor in the integrand of eq 7. That is, in eq 7, $E^{(0)} \rightarrow E^{(0)} + i\Gamma$. A numerical value of $\Gamma = 160 \text{ cm}^{-1}$ was employed.) The similarity between the calculated absorption spectrum and the experimental result²⁰ (shown in the inset of the figure) indicates that the combination of QCFF/PI electronic structure and GWD wave packet propagation is accurate enough to compute vibrationally resolved Franck–Condon spectra for this system. The calculated emission spectrum is almost a mirror image of the calculated absorption spectrum, consistent with the experimental situation. (The presence of resonance fluorescence prevented an accurate emission spectrum near the 0–0 region from being measured experimentally.) In Figure 2 we show the absorption spectrum calculated for octatetraene in the gas phase and in liquid chloroform at room temperature. (For the condensed phase spectra shown in Figures 2–4, no artificial correlation function damping was imposed.) Both are similar to the corresponding experimental spectra²⁰ (cf. insets of Figures 1 and 3). Interaction with the solvent broadens the spectrum of the solute molecule and shifts the calculated spectrum to the red by about 2500 cm^{-1} , in reasonable agreement with the experimental result of 2973 cm^{-1} . In Figure 3 we show the absorption and emission spectra of octatetraene in chloroform. The excited states involved in these two spectroscopic signatures are different, as noted above. This explains the energy gap between the origins of the two spectra. The calculated energy gap is about 1200 cm^{-1} higher than the experimental one. This difference may be caused in part by the different level of electronic structure theory used in QCFF/PI to calculate the electronic states involved in the two transitions. A comparison of these spectra with the corresponding experimental results (see inset to Figure 3) reveals good

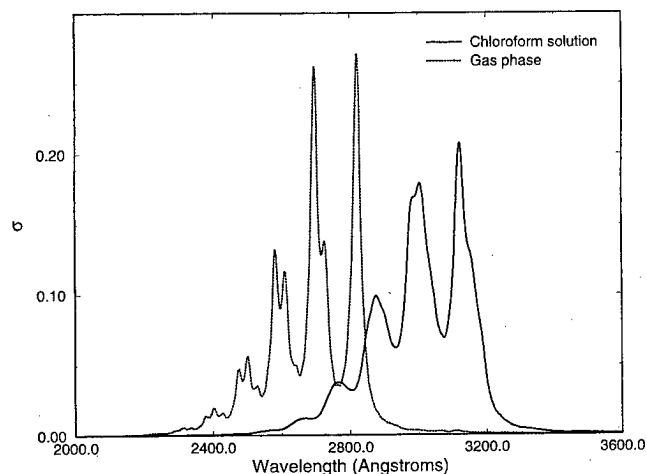


Figure 2. Calculated absorption spectra of all *trans*-octatetraene in chloroform solution at room temperature and in the gas phase. (The corresponding experimental spectra are presented in the insets to Figures 1 and 3.)

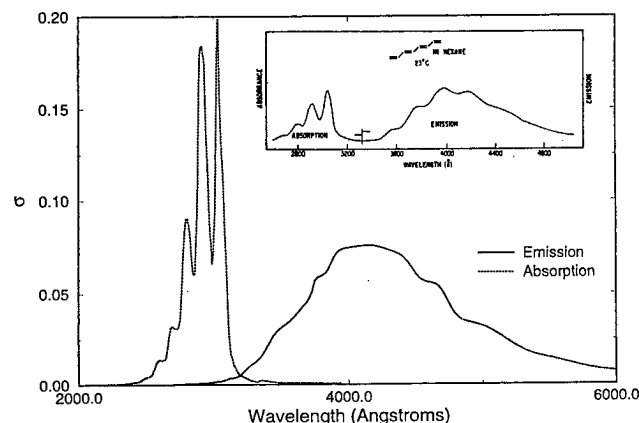


Figure 3. Calculated emission and absorption spectra of *trans*-octatetraene in chloroform solution at room temperature. The inset shows the corresponding experimental spectra in a hexane solution.²⁰ The experimental spectra in both solvents have a similar shape but the 0–0 absorption band in chloroform is shifted 550 cm^{-1} to the red compared with the one for hexane and the fluorescence maximum in chloroform is shifted 190 cm^{-1} to the red compared with the maximum for hexane.²⁰

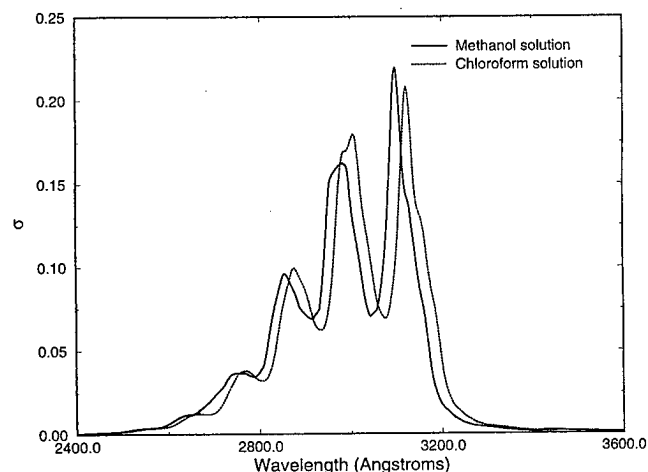


Figure 4. Calculated absorption spectra of *trans*-octatetraene in methanol and chloroform solutions at room temperature.

general agreement. Our emission spectrum is about 180 Å broader than the experimental one but it clearly reproduces the

loss of vibrational structure compared to the corresponding absorption spectrum.

To test the sensitivity of our method to changes in solvent environments, we show in Figure 4 the calculated absorption spectra of octatetraene in methanol and in chloroform at room temperature. It has been observed experimentally that the absorption spectrum of octatetraene does not change much in shape from solvent to solvent, but the overall absorption band shifts in frequency.²⁰ The absorption spectra we obtain indeed have similar shape and they are shifted to the red compared with the gas phase spectrum. The absorption spectrum in methanol is shifted to the blue compared with the spectrum in chloroform by about 450 cm^{-1} . The experimental shift is 640 cm^{-1} , in reasonable agreement with the result obtained in our computation. This provides evidence that the technique utilized here can be used to study a wide range of solvent–solute systems that show vibrational signatures in their Franck–Condon spectra. The quality of the results can vary depending on such factors as the accuracy of the electronic structure program that calculates the potential energy surfaces associated with the solute molecule and the degree of anharmonicity of the potential energy surfaces. However, due to the short-time nature of the associated dynamics (the condensed phase wave packet correlation functions calculated in the present work decayed irreversibly to zero in <60 fs), the method described in this paper should yield accurate results for many systems of chemical interest. The use of fast GWD techniques to propagate nuclear wave packets using potential surfaces evaluated on the fly via semiempirical electronic structure calculations (utilizing a spectroscopically calibrated ES program) will allow the use of this technique to study spectroscopic signatures for solutes with higher dimensionality than octatetraene (e.g., organic dyes that are commonly used in laser devices³⁰).

4. Concluding Remarks

We have developed a methodology that uses Gaussian wave packet techniques to propagate the nuclear coordinate wave packets associated with a polyatomic molecular system on instantaneous potential energy surfaces generated on the fly by an appropriate electronic structure program. These potential surfaces can incorporate interactions between the molecule and the surrounding environment. We have applied this algorithm to study the one-photon absorption and emission spectra of *all-trans*-1,3,5,7-octatetraene in the gas phase and in polar liquid solvents (specifically, chloroform and methanol). Comparison with experimental results shows that the technique is accurate enough to reproduce the main solvent-induced perturbations in the spectroscopic signals studied. The relatively small deviations of our computations compared to the experimental results can be attributed to the approximations inherent in the semiempirical QCFF/PI procedure and the force fields determining solvent–solute and solute–solvent interactions, and the use of the “static limit” approximation for the effect of the solvent on the nuclear wave packet dynamics. Our results suggest that the methodology can be applied to other problems involving short-time quantum dynamics of condensed phase systems. These systems are not limited to solutes immersed in liquid solvents, but include, for example, molecular adsorbates on solid surfaces³¹ and photodissociation dynamics of small molecules bound to biomolecules.³²

We note in concluding that there has been a recent resurgence of interest in computing nuclear coordinate wave packet evolution via methods founded upon the initial value representation (IVR) of the van Vleck time-dependent semiclassical (SC)

propagator.^{33,34} The intrinsic accuracy of the SC propagator appears to be very high.¹⁵ Its evaluation for high-dimensional systems is not completely straightforward and is still under investigation.^{16–18} Nevertheless, all IVR methods for evaluating the SC propagator use the same elementary ingredient found in simple Gaussian wave packet dynamics (GWD), namely a classical trajectory is propagated (based on specified initial values of position and momentum) and the second derivative matrix of the potential energy function (the Hessian matrix) is evaluated along the trajectory. In GWD this needs to be done only once to propagate an initially Gaussian wave packet, whereas in IVR-SC propagator methods, many trajectories (and the associated Hessian matrices) have to be propagated. The method developed here can thus be employed without essential modification in IVR-SC schemes in situations where the simple GWD approximation is inadequate. Since each classical trajectory is independent of all the others, it should be possible to employ parallel processing computer platforms to relieve the burden of having to evolve many trajectories in order to propagate one nuclear coordinate wave packet.

Acknowledgment. This work was supported by NSF grant CHE9529674. A.E.C. thanks the Andrew D. Mellon Committee for support through a Mellon Predoctoral Fellowship at the University of Pittsburgh. We also thank Profs. P. R. Callis and F. Zerbetto for providing us with updated versions of the QCFF/PI program and for helpful discussions.

References and Notes

- (1) For a cross section of recent developments in methods for quantum wave packet dynamics and molecular electronic structure, consult: *Encyclopedia of Computational Chemistry*; Schleyer, P. v. R., Allinger, N. L., Clark, T., Gasteiger, J., Kollman, P. A., Schaefer III, H. F., Schreiner, P. R., Eds.; John Wiley & Sons: Chichester, UK, 1998.
- (2) Carr, R.; Parrinello, M. *Phys. Rev. Lett.* **1985**, *55*, 2471.
- (3) Heller, E. J. *Acc. Chem. Res.* **1981**, *14*, 368.
- (4) Heller, E. J. *J. Chem. Phys.* **1975**, *62*, 1544.
- (5) Heller, E. J. *J. Chem. Phys.* **1981**, *75*, 2923.
- (6) Martinez et al. have propagated frozen Gaussian wave packets based on force fields obtained from ab initio electronic structure calculations performed on the fly,⁷ but not for excited state spectroscopy and not for condensed phase systems.
- (7) Martinez, T. J.; Levine, R. D. *Chem. Phys. Lett.* **1996**, *259*, 252. Martinez, T. J.; Levine, R. D. *J. Chem. Phys.* **1996**, *105*, 6334. Martinez, T. J. *Chem. Phys. Lett.* **1997**, *272*, 139. Ben-Nun, M.; Martinez, T. J. *Chem. Phys. Lett.* **1998**, *298*, 57. Thompson, K.; Martinez, T. J. *J. Chem. Phys.* **1999**, *110*, 1376.
- (8) If the potential energy surface is at most quadratic in the nuclear coordinates, then Gaussian wave packet dynamics is exact for all times.
- (9) Neria, E.; Nitzan, A. *J. Chem. Phys.* **1993**, *99*, 1109; *Chem. Phys.* **1994**, *183*, 351.
- (10) Kulander, K.; Heller, E. J. *J. Chem. Phys.* **1978**, *69*, 2439. Drolshagen, G.; Heller, E. J. *J. Chem. Phys.* **1983**, *79*, 4005. Drolshagen, G.; Heller, E. J. *Surf. Sci.* **1984**, *139*, 260.
- (11) Coalson, R. D.; Karplus, M. *J. Chem. Phys.* **1990**, *93*, 3919.
- (12) Messina, M.; Coalson, R. D. *J. Chem. Phys.* **1990**, *92*, 5712. Messina, M.; Coalson, R. D. *J. Chem. Phys.* **1991**, *95*, 5364. Messina, M.; Coalson, R. D. *J. Chem. Phys.* **1991**, *95*, 8977.
- (13) Braun M.; Metiu, H.; Engel, V. *J. Chem. Phys.* **1998**, *108*, 8983.
- (14) Gaussian wave packet dynamics is a simple example of a time-dependent semiclassical wave packet propagation technique. More sophisticated semiclassical propagation schemes have been developed which yield longer-time accuracy on anharmonic potential surfaces.^{15–18} The "cost" of this improved performance is the need to independently propagate a large set of Gaussians instead of a single one as required by GWD. Thus the method proposed in this work for propagating a single Gaussian wave packet can be used to propagate swarms of Gaussians as required in the more sophisticated schemes. This point is discussed further in the Concluding Remarks.
- (15) Heller, E. J. *J. Chem. Phys.* **1991**, *94*, 2723.
- (16) Sun, X.; Miller, W. H. *J. Chem. Phys.* **1997**, *106*, 6346; **1998**, *108*, 8870.
- (17) Herman, M. F.; Kluk, E. *Chem. Phys.* **1984**, *91*, 27. Kluk, E.; Herman, M. F.; Davis, H. L. *J. Chem. Phys.* **1986**, *84*, 326.
- (18) Ovchinnikov, M.; Apkarian, V. A. *J. Chem. Phys.* **1998**, *105*, 10312.
- (19) Kohler, B. E.; Spiglanin, T. A.; Hemley, R. J.; Karplus, M. *J. Chem. Phys.* **1984**, *80*, 23.
- (20) Gavin Jr., R. M.; Weisman, C.; McVey, J. K.; Rice, S. A. *J. Chem. Phys.* **1978**, *68*, 522.
- (21) Heimbrook, L. A.; Kenny, J. E.; Kohler, B. E.; Scott, G. W. *J. Chem. Phys.* **1981**, *75*, 4338.
- (22) Warshel, A.; Karplus, M. *J. Am. Chem. Soc.* **1972**, *94*, 5612; Warshel, A. *Isr. J. Chem.* **1973**, *11*, 709.
- (23) Orlandi, G.; Zerbetto, F.; Zgierski, M. Z. *Chem. Rev.* **1991**, *91*, 867. Zerbetto, F.; Zgierski, M. Z.; Negri, F.; Orlandi, G. *J. Chem. Phys.* **1988**, *89*, 3681.
- (24) Muino, P. L.; Callis, P. R. *J. Chem. Phys.* **1994**, *100*, 4093.
- (25) Broo, A.; Pearl, G.; Zerner, M. C. *J. Phys. Chem. A* **1997**, *101*, 2478.
- (26) Roothaan, C. C. J. *J. Chem. Phys.* **1951**, *19*, 1445.
- (27) Pearlman, D. A.; Case, D. A.; Caldwell, J. W.; Ross, W. S.; Cheatham III, T. E.; Ferguson, D. M.; Seibel, G. L.; Chandra Singh, U.; Weiner, P. K.; Kollman, P. A. *AMBER 4.1*, University of California, San Francisco, 1995.
- (28) Cornell, W. D.; Cieplak, P.; Bayly, C. I.; Gould, I. R.; Merz Jr., K. M.; Ferguson, D. M.; Spellmeyer, D. C.; Fox, T.; Caldwell, J. W.; Kollman, P. A. *J. Am. Chem. Soc.* **1995**, *117*, 5179.
- (29) Eksterowicz, J. E.; Miller, J. L.; Kollman, P. A. *J. Phys. Chem. B* **1997**, *101*, 10971.
- (30) Grofcsik, A.; Kubinyi, M.; Jones, W. J. *J. Mol. Struct.* **1995**, *348*, 197. Hasche, T.; Ashworth, S. H.; Riedle, E.; Woerner, M.; Elsaesser, T. *Chem. Phys. Lett.* **1995**, *244*, 164. Ashworth, S. H.; Hasche, T.; Woerner, M.; Riedle, E.; Elsaesser, T. *J. Chem. Phys.* **1996**, *104*, 5761.
- (31) Harrison, I.; Polanyi, J. C.; Young, P. A. *J. Chem. Phys.* **1988**, *89*, 1475.
- (32) Mohny, B. K.; Wang, C.; Walker, G. C. *Abstr. Pap. Am. Chem. Soc.* **1998**, *216*, U779.
- (33) Van Vleck, J. H. *Proc. Nat. Acad. Sci.* **1928**, *14*, 178.
- (34) Miller, W. H. *Adv. Chem. Phys.* **1974**, *25*, 69.

Propagation Matrices from the Finite Element Method

Bjørn R. Jensen[†] and Jan Linderberg^{*,‡}

Henry Eyring Center for Theoretical Chemistry, Department of Chemistry, University of Utah, 315 South 1400 East Rm Dock, Salt Lake City, Utah 84112-0850, and Department of Chemistry, Aarhus University, DK-8000 Aarhus, Denmark

Received: June 7, 1999; In Final Form: August 24, 1999

Optimization of action integrals is suggested as an alternative to initial value algorithms for the study of time-evolving quantum systems. The finite element method provides a convenient and rapidly convergent scheme for some simple cases where analytical solutions are available. Two level systems are given particular attention.

Introduction

Examination of the options offered by the finite element method, as a means of estimating the evolution of quantum mechanical systems, is the subject of this article. An action integral is defined and its optimization provides an alternative to time-stepping algorithms and provides a quadratic convergence toward the accurate result. Thus, inaccuracies in a state vector affect the propagator only in second order.

Molecular change, which is the essence of chemistry, derives from quantum mechanics in the time domain. Approximate solutions to Schrödinger's and Liouville's equations are desired, and a rich literature has evolved on different algorithms. Kosloff reviewed the field well in 1988¹ and later developments are represented in this issue, so no attempt is made here to create a survey of the methods favored at this time. An algorithm based on the time-integrated Lagrangian formulation² was suggested in 1992³ as a means of effective application of the finite element method and is reconsidered here in further detail and with additional results on convergence properties and computational feasibility.

The action integral and the basics of the finite element method representation are presented in the next section. There follows a section with a few elementary results and a fourth section with application to a two-level problem as in a spin resonance situation. Conclusions are given in the last section.

Action Integral

Schrödinger's picture with a time-dependent state vector, $|\Psi(t)\rangle$, will be used and the symmetrized Lagrangian is formed as

$$L(t) = \frac{i\hbar}{2} \left(\langle \Psi(t) | \frac{\partial \Psi(t)}{\partial t} \rangle - \frac{i\hbar}{2} \left(\frac{\partial \langle \Psi(t) |}{\partial t} \right) | \Psi(t) \right) - \langle \Psi(t) | H(t) | \Psi(t) \rangle \quad (1)$$

so that the action integral S , with the boundary terms will be

$$S(\Psi, \Lambda) = \int_0^T dt L(t) + \frac{i\hbar}{2} \{ \langle \Psi(T) | \Lambda_T \rangle - \langle \Lambda_T | \Psi(T) \rangle - \langle \Psi(0) | \Lambda_0 \rangle + \langle \Lambda_0 | \Psi(0) \rangle + \langle \Lambda_T | U | \Lambda_0 \rangle - \langle \Lambda_0 | U^\dagger | \Lambda_T \rangle \} \quad (2)$$

Auxiliary vectors $|\Lambda\rangle$ serve to define the evolution operator U . The variations of the action S and conditions of stationarity imply the equations

$$\begin{aligned} i\hbar \frac{\partial}{\partial t} |\Psi(t)\rangle - H |\Psi(t)\rangle &= 0 \\ |\Psi(0)\rangle &= |\Lambda_0\rangle \quad |\Psi(T)\rangle = |\Lambda_T\rangle \\ |\Psi(T)\rangle &= U |\Lambda_0\rangle \quad |\Psi(0)\rangle = U^\dagger |\Lambda_T\rangle \end{aligned} \quad (3)$$

that are the standard ones.

It will be assumed that an approximate state vector is defined in terms of parameters, which are functions of time. A common form is the linear one where a fixed basis in the relevant Hilbert space is used

$$|\Psi(t)\rangle = \sum_j |j\rangle a_j(t) \quad (4)$$

More involved are the forms where the state vector depends on general parameters

$$|\Psi[t; \alpha_1(t), \alpha_2(t), \dots]\rangle \quad (5)$$

such as the coherent state representations used by Öhrn and collaborators.⁴

We consider first the linear case and introduce a finite element representation for the time dependence of the amplitudes $a_j(t)$ in terms of their values at a discrete set of times:

$$a_j(t) = \sum_k a_j(t_k) f_k(t) \quad f_k(t_k) = \delta_{kk} \quad 0 = t_0 < t_1 < \dots < t_n = T \quad (6)$$

where the form functions⁵ are localized on a few intervals which may have varying lengths. The set of amplitudes $\{a_j(t_k)\}$ are the variational parameters of the problem together with amplitudes of the auxiliary states at the beginning and end of the time interval

$$|\Lambda_\tau\rangle = \sum_j |j\rangle b_{j\tau} \quad \tau = 0, T \quad (7)$$

The action S becomes a sesquilinear form

[†] E-mail: bjorn@kemi.aau.dk

[‡] E-mail: jan@kemi.aau.dk

$$S = \sum_{jkj'k'} a_j^*(t_k) A_{jkj'k'} a_{j'}(t_k) + \frac{i\hbar}{2} \sum_j [a_j^*(T) b_{jT} - b_{jT}^* a_j(T) - a_j^*(0) b_{j0} + b_{j0}^* a_j(0)] + \frac{i\hbar}{2} \sum_{jj'} [b_{jT}^* U_{jj'} b_{j'0} - b_{j0}^* U_{jj'}^{\dagger} b_{j'T}] \quad (8)$$

and optimization results in a matrix problem. The detailed equations are

$$\sum_{j'k} A_{jkj'k'} a_{j'}(t_k) = \begin{cases} \frac{i\hbar}{2} b_{j0}, & t_k = 0, \\ 0, & 0 < t_k < T, \\ -\frac{i\hbar}{2} b_{jT}, & t_k = T \end{cases} \quad (9)$$

$$a_j(0) = \sum_{j'} U_{jj'}^{\dagger} b_{j'} T$$

$$a_j(T) = \sum_{j'} U_{jj'} b_{j'} 0$$

Matrix elements $A_{jkj'k'}$ and $U_{jj'}$ are complex and the matrices \mathbf{A} and \mathbf{U} are hermitian and unitary, respectively. It has been implicit that the basis is orthonormal.

Elimination of the amplitudes at intermediate times from eq 9 reduces the system to a form that, in matrix notation, reads as

$$\tilde{\mathbf{A}}_{00} \mathbf{a}_0 + \tilde{\mathbf{A}}_{0n} \mathbf{a}_n = \frac{i\hbar}{2} \mathbf{b}_0; \quad \tilde{\mathbf{A}}_{n0} \mathbf{a}_0 + \tilde{\mathbf{A}}_{nn} \mathbf{a}_n = -\frac{i\hbar}{2} \mathbf{b}_n; \quad (10)$$

$$\mathbf{a}_0 = \mathbf{U}^{\dagger} \mathbf{b}_n; \quad \mathbf{a}_n = \mathbf{U} \mathbf{b}_0;$$

where the reduced matrices refer only to the initial and final times. A satisfactory, partial solution to this problem is obtained by looking for eigenvectors of the unitary transformation

$$\mathbf{U} \mathbf{b}_0 = \mathbf{b}_0 z \quad \mathbf{U}^{\dagger} \mathbf{b}_n = \mathbf{b}_n z^* = \mathbf{b}_n \left(\frac{1}{z} \right) \quad (11)$$

so that

$$\tilde{\mathbf{A}}_{00} \mathbf{a}_0 + \tilde{\mathbf{A}}_{0n} \mathbf{b}_0 z = \frac{i\hbar}{2} \mathbf{b}_0 \quad \tilde{\mathbf{A}}_{n0} \mathbf{a}_0 + \tilde{\mathbf{A}}_{nn} \mathbf{b}_0 z = -\frac{i\hbar}{2} \mathbf{a}_0 z \quad (12)$$

which implies the eigenvalue equation

$$\begin{bmatrix} \frac{2i}{\hbar} \tilde{\mathbf{A}}_{n0} & 0 \\ \frac{2i}{\hbar} \tilde{\mathbf{A}}_{00} & 1 \end{bmatrix} \begin{bmatrix} \mathbf{a}_0 \\ \mathbf{b}_0 \end{bmatrix} = \begin{bmatrix} 1 & -\frac{2i}{\hbar} \tilde{\mathbf{A}}_{nn} \\ 0 & -\frac{2i}{\hbar} \tilde{\mathbf{A}}_{0n} \end{bmatrix} \begin{bmatrix} \mathbf{a}_0 \\ \mathbf{b}_0 \end{bmatrix} z \quad (13)$$

The reduced matrix $\tilde{\mathbf{A}}$ is hermitian and its off-diagonal block $\tilde{\mathbf{A}}_{0n}$ is assumed to have an inverse; a singularity would indicate a linear dependence in the basis.

Eigenvalues of the matrix⁶

$$\mathbf{T} = \begin{bmatrix} 1 & -\frac{2i}{\hbar} \tilde{\mathbf{A}}_{nn} \\ 0 & -\frac{2i}{\hbar} \tilde{\mathbf{A}}_{0n} \end{bmatrix}^{-1} \begin{bmatrix} \frac{2i}{\hbar} \tilde{\mathbf{A}}_{n0} & 0 \\ \frac{2i}{\hbar} \tilde{\mathbf{A}}_{00} & 1 \end{bmatrix} = \begin{bmatrix} 1 & \frac{2i}{\hbar} \tilde{\mathbf{A}}_{nn} \\ 0 & 1 \end{bmatrix} \begin{bmatrix} \frac{2i}{\hbar} \tilde{\mathbf{A}}_{n0} & 0 \\ 0 & \frac{i\hbar}{2} \tilde{\mathbf{A}}_{0n}^{-1} \end{bmatrix} \begin{bmatrix} 1 & 0 \\ \frac{2i}{\hbar} \tilde{\mathbf{A}}_{00} & 1 \end{bmatrix} \quad (14)$$

have unit modulus, $|z_j| = 1$, or come in pairs, $z_j^* = z_k^{-1}$, since the inverse of \mathbf{T} is related to its adjoint through a similarity transformation

$$\mathbf{T}^{\dagger} = \begin{bmatrix} 0 & 1 \\ 1 & 0 \end{bmatrix} \mathbf{T}^{-1} \begin{bmatrix} 0 & 1 \\ 1 & 0 \end{bmatrix} \quad (15)$$

This implies that for a solution to eq 13

$$\mathbf{T} \begin{bmatrix} \mathbf{a}_0 \\ \mathbf{b}_0 \end{bmatrix} = \begin{bmatrix} \mathbf{a}_0 \\ \mathbf{b}_0 \end{bmatrix} z \quad (16)$$

it holds that

$$\mathbf{T}^{\dagger} \begin{bmatrix} \mathbf{b}_0 \\ \mathbf{a}_0 \end{bmatrix} = \begin{bmatrix} 0 & 1 \\ 1 & 0 \end{bmatrix} \mathbf{T}^{-1} \begin{bmatrix} \mathbf{a}_0 \\ \mathbf{b}_0 \end{bmatrix} = \begin{bmatrix} \mathbf{b}_0 \\ \mathbf{a}_0 \end{bmatrix} \frac{1}{z}$$

or, equivalently

$$[\mathbf{b}_0^{\dagger} \quad \mathbf{a}_0^{\dagger}] \mathbf{T} = \frac{1}{z^*} [\mathbf{b}_0^{\dagger} \quad \mathbf{a}_0^{\dagger}] \quad (18)$$

Two possibilities arise from this relation: (i) $z_j^* = z_j^{-1}$ where a "normalization" can be chosen so that

$$\mathbf{b}_{0j}^{\dagger} \mathbf{a}_{0j} + \mathbf{a}_{0j}^{\dagger} \mathbf{b}_{0j} = \pm 2 \quad (19)$$

and (ii) $z_j^* = z_{pj}^{-1}$ where pj indicates a permutation of the set of indices and where we choose the "normalization" such that

$$\mathbf{b}_{0j}^{\dagger} \mathbf{a}_{0pj} + \mathbf{a}_{0j}^{\dagger} \mathbf{b}_{0pj} = \mathbf{b}_{0pj}^{\dagger} \mathbf{a}_{0j} + \mathbf{a}_{0pj}^{\dagger} \mathbf{b}_{0j} = 2 \quad (20)$$

It is recognized that these eigenvalues are spurious in the sense that their magnitude differs from unity and cannot correspond to proper values of a unitary matrix. Their occurrence is related to large time steps in the finite element discretization. A form of orthogonality holds for eigenvalues that are unrelated

$$\mathbf{b}_{0j}^{\dagger} \mathbf{a}_{0k} + \mathbf{a}_{0j}^{\dagger} \mathbf{b}_{0k} = 0 \quad z_k^* \neq z_j^{-1} \quad (21)$$

The case of degenerate eigenvalues offers the possibility that there are two or more linearly independent vectors in the subspace, but there will be a linear transformation among them which brings them to the fulfill the conditions of eqs 19–21.

There are twice as many eigenvalues of \mathbf{T} as there are of the unitary transformation \mathbf{U} . Vectors $\mathbf{a}_0, \mathbf{b}_0$ represent approximations to an initial state and should be close to parallel, thus we choose those solutions which have a positive "normalization" value in relation (eq 19) as being the ones giving the appropriate representation for \mathbf{U} . Solutions of the type considered in eq 20 require a reconsideration of the procedure from the start. We will first establish the relation between the vectors $\{\mathbf{a}_{0j}, \mathbf{b}_{0j} | j = 1, 2, \dots\}$ and conclude, from the set of eq 10 that

$$\tilde{\mathbf{A}}_{00} \mathbf{a}_{0j} + \tilde{\mathbf{A}}_{0n} \mathbf{b}_{0j} z_j = \frac{i\hbar}{2} \mathbf{b}_{0j} \quad \tilde{\mathbf{A}}_{n0} \mathbf{a}_{0j} + \tilde{\mathbf{A}}_{nn} \mathbf{b}_{0j} z_j = -\frac{i\hbar}{2} \mathbf{a}_{0j} z_j \quad (22)$$

and that

$$\mathbf{a}_{0k}^{\dagger} \tilde{\mathbf{A}}_{00} + z_k^* \mathbf{b}_{0k}^{\dagger} \tilde{\mathbf{A}}_{n0} = -\frac{i\hbar}{2} \mathbf{b}_{0k}^{\dagger} \quad \mathbf{a}_{0k}^{\dagger} \tilde{\mathbf{A}}_{0n} + z_k^* \mathbf{b}_{0k}^{\dagger} \tilde{\mathbf{A}}_{nn} = \frac{i\hbar}{2} z_k^* \mathbf{a}_{0k}^{\dagger} \quad (23)$$

which provides the relations

$$\mathbf{a}_{0k}^{\dagger} \tilde{\mathbf{A}}_{00} \mathbf{a}_{0j} + z_k^* \mathbf{b}_{0k}^{\dagger} \tilde{\mathbf{A}}_{n0} \mathbf{a}_{0j} + \mathbf{a}_{0k}^{\dagger} \tilde{\mathbf{A}}_{0n} \mathbf{b}_{0j} z_j + z_k^* \mathbf{b}_{0k}^{\dagger} \tilde{\mathbf{A}}_{nn} \mathbf{b}_{0j} z_j = i\hbar \delta_{kj} - \frac{i\hbar}{2} \mathbf{b}_{0k}^{\dagger} \mathbf{a}_{0j} (1 + z_k^* z_j) \quad (24)$$

and the conclusion

$$\mathbf{b}_{0k}^\dagger \mathbf{a}_{0j} = \delta_{kj} + iL_{kj}, \quad L_{kj} = L_{jk}^* \quad (25)$$

where the new, hermitian matrix \mathbf{L} is a transformation of the hermitian matrix \mathbf{A} . Neither set of vectors, $\{\mathbf{a}_{0j}|j = 1, 2, \dots\}$ nor $\{\mathbf{b}_{0j}|j = 1, 2, \dots\}$, is an orthogonal basis set for the unitary transformation nor are they normalized.

A constrained optimization is required in order to arrive at an acceptable representation of the propagation matrix \mathbf{U} . It is necessary to make the vectors \mathbf{a}_0 and \mathbf{b}_0 of eq 13 proportional to a common one

$$\mathbf{a}_0 = \mathbf{c}_0 \kappa \quad \mathbf{b}_0 = \mathbf{c}_0 \lambda \quad (26)$$

and use the consistency of the two components of the equation to determine the ratio of κ to λ . The constraints (eq 26) lead in the system (eq 10), with substitutions (eq 11), to the forms

$$(\tilde{\mathbf{A}}_{00}\kappa + \tilde{\mathbf{A}}_{0n}\lambda z)\mathbf{c}_0 = \frac{i\hbar}{2}\lambda\mathbf{c}_0 \quad (\tilde{\mathbf{A}}_{n0}\kappa + \tilde{\mathbf{A}}_{nn}\lambda z)\mathbf{c}_0 = -\frac{i\hbar}{2}\kappa z\mathbf{c}_0 \quad (27)$$

which are combined to the hermitian eigenvalue relation

$$(\kappa^* \tilde{\mathbf{A}}_{00} \kappa + \kappa^* \tilde{\mathbf{A}}_{0n} \lambda z + z^* \lambda^* \tilde{\mathbf{A}}_{n0} \kappa + z^* \lambda^* \tilde{\mathbf{A}}_{nn} \lambda z) \mathbf{c}_0 = \frac{i\hbar}{2} (\kappa^* \lambda - z^* \lambda^* \kappa z) \mathbf{c}_0 \quad (28)$$

Only the ratio κ/λ is relevant, and we replace λ with μ according to

$$\lambda z = \mu \quad (29)$$

to obtain

$$(\kappa^* \tilde{\mathbf{A}}_{00} \kappa + \kappa^* \tilde{\mathbf{A}}_{0n} \mu + \mu^* \tilde{\mathbf{A}}_{n0} \kappa + \mu^* \tilde{\mathbf{A}}_{nn} \mu) \mathbf{c}_0 = \frac{i\hbar}{2} (\kappa^* \mu z^* - \mu^* \kappa z) \mathbf{c}_0 \quad (30)$$

which exhibits the relation between the phase of the unitary matrix eigenvalue and an eigenvalue of a suitably time-integrated Lagrangian. It is seen that only the phase of the product $\kappa^* \mu$ and one of the magnitudes $|\kappa|$ or $|\mu|$ are numerically relevant. Thus it is convenient to choose

$$|\kappa^* \mu| = |\kappa| |\mu| = 1 \quad (31)$$

Eigenvalues of the matrix on the left-hand side in eq 30 will be functions of the two real parameters and are denoted as $s_j(\kappa, \mu)$ and it follows that

$$z_j = \frac{\kappa^* \mu}{\hbar} (\sqrt{\hbar^2 - s_j^2(\kappa, \mu)} + i s_j(\kappa, \mu)) \quad (32)$$

and, with properly normalized eigenvectors, the propagation matrix is

$$\mathbf{U} = \sum_j \mathbf{c}_{0j} z_j \mathbf{c}_{0j}^\dagger \quad (33)$$

while there remains to resolve the appropriate values of the parameters κ and μ .

Optimal choices of the parameters will be studied further as more numerical experience is acquired.

Integrable Examples

Two cases are examined with the view of showing the numerical stability and accuracy of the variational formulation in the finite element implementation. The evolution of a single

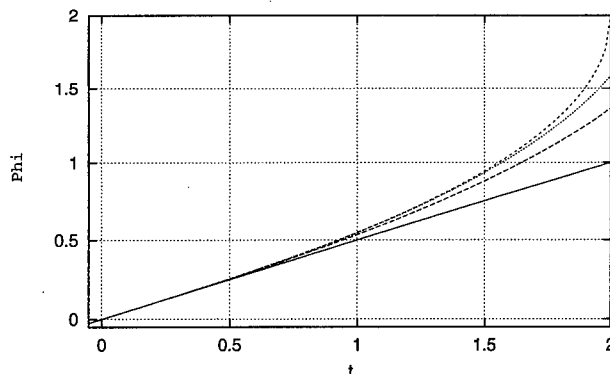


Figure 1. Approximations to the evolution operator phase from finite element method calculations for a constant energy case. The normal line represents the correct result where φ is proportional to the time elapsed. Variational results are, from the top, for two pieces of linear interpolation, parabolic interpolation, and the linear wave function choice on the interval.

state under a constant or periodic Hamiltonian is governed by the energy function

$$E(t) = E(0) \cos(\omega t) \quad (34)$$

so that the evolution operator is

$$U(t) = U(0) \exp\left[-\frac{iE(0)}{\hbar\omega} \sin(\omega t)\right] \quad (35)$$

The static case is the limit at zero frequency ω . All integrals in the action integral are elementary, and the matrix problem for the wave function amplitudes is tridiagonal and readily solvable.

We show in Figure 1 a comparison of three approximations to the phase of the evolution matrix for a constant energy state and the accurate result: a linear interpolant over the interval, two pieces of linear, and a parabolic interpolant. All are quite accurate as long as $\varphi \equiv |E(0)t|/\hbar < 0.5$ and there is no advantage to the more elaborate approximations for larger intervals even though an error analysis shows that for small φ errors occur in third, fifth, and seventh order, respectively. One pays for the accuracy at small intervals by decreasing the range of applicability of the formulation; the analytical solutions have branch points for smaller parameter values for the higher order forms.

Numerical calculations have been carried out for the oscillatory form (eq 34) and the results are given in Figure 2. Parameters and units are chosen so that $E(0) = \hbar\omega$ and integrations are for the interval where $0 \leq \omega t \leq 5$. Piecewise linear approximations are used on equidistant intervals. Rapid convergence is observed with the number of time steps. These findings hold for longer time lapses, and there is no propagation of errors as might be the case in finite difference stepping of an initial value; the variational formulation optimizes the propagator and not the wave function.

A Matrix Propagator

Additional complications arise in a system with several states as is evident from the formal development. An examination of a two-state system is facilitated by the use of the Pauli spin matrix basis and we express the Hamiltonian as

$$H(t) = \alpha(t)\sigma_0 + \beta_x(t)\sigma_x + \beta_y(t)\sigma_y + \beta_z(t)\sigma_z = \begin{bmatrix} \alpha(t) + \beta_z(t) & \beta_x(t) - i\beta_y(t) \\ \beta_x(t) + i\beta_y(t) & \alpha(t) - \beta_z(t) \end{bmatrix} \quad (36)$$

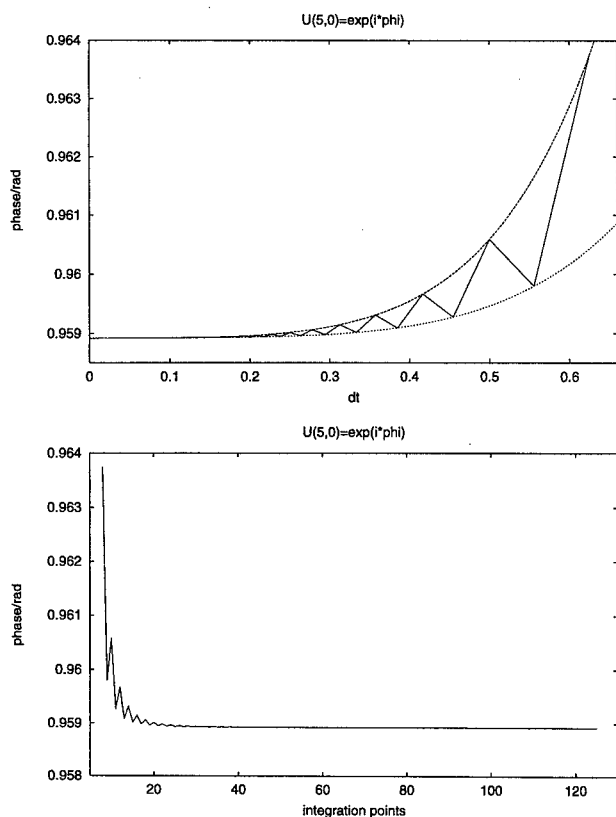


Figure 2. Display of approach to the accurate evolution operator phase value for the function (eq 35) with finite element method equidistant interval length, upper panel, and number of intervals, lower panel for total interval $0 \leq \omega t \leq 5$.

in terms of real functions of time. For simplicity we consider only one interval with linear interpolants for the state vector

$$\Psi(t) = \begin{bmatrix} a_{10}\left(1 - \frac{t}{T}\right) + a_{11}\frac{t}{T} \\ a_{20}\left(1 - \frac{t}{T}\right) + a_{21}\frac{t}{T} \end{bmatrix} \quad (37)$$

Time integration over the Hamiltonian results in the forms

$$\int_0^T dt \alpha(t) \left(1 - \frac{t}{T}\right)^{2-n} \left(\frac{t}{T}\right)^n \equiv \alpha(n) \quad n = 0, 1, 2 \quad (38)$$

where an additional notation is introduced. The relevant matrices in eq 10 and the following are then

$$\begin{aligned} \mathbf{A}_{00} &= \alpha(0)\sigma_0 + \beta_x(0)\sigma_x + \beta_y(0)\sigma_y + \beta_z(0)\sigma_z \\ \mathbf{A}_{01} &= \left[\alpha(1) + \frac{i\hbar}{2}\right]\sigma_0 + \beta_x(1)\sigma_x + \beta_y(1)\sigma_y + \beta_z(1)\sigma_z \\ \mathbf{A}_{11} &= \alpha(2)\sigma_0 + \beta_x(2)\sigma_x + \beta_y(2)\sigma_y + \beta_z(2)\sigma_z \end{aligned} \quad (39)$$

It cannot be assumed that the vectors $\{\beta(0), \beta(1), \beta(2)\}$ are parallel and thus there is no basis which diagonalizes all three matrices (eq 39). The average action matrix, see eq 30, appears

as

$$\begin{aligned} \mathbf{A} &= [\bar{\alpha} + \hbar \sin(\phi)]\sigma_0 + \bar{\beta}_x\sigma_x + \bar{\beta}_y\sigma_y + \bar{\beta}_z\sigma_z \\ \bar{\alpha} &= \alpha(0)|\kappa|^2 + 2\alpha(1)\cos(\phi) + \alpha(0)|\kappa|^{-2} \\ \kappa\mu^* &= \cos(\phi) + i\sin(\phi) \end{aligned} \quad (40)$$

where the average notation applies to all parameters. It follows that the eigenvalues are

$$s_{\pm}(\kappa, \mu) = \bar{\alpha} + \hbar \sin(\phi) \pm |\bar{\beta}| \quad (41)$$

and the unitary transformation comes as

$$\mathbf{U} = \frac{z_+}{2|\bar{\beta}|} [|\bar{\beta}| \sigma_0 + \bar{\beta} \cdot \sigma] + \frac{z_-}{2|\bar{\beta}|} [|\bar{\beta}| \sigma_0 - \bar{\beta} \cdot \sigma] \quad (42)$$

which can be reduced in the case of a constant Hamiltonian to be of the similar form as the one state problem dealt with in the previous section.

Conclusions

Development of variational methods in the time domain of quantum mechanics promises effective numerical algorithms when implemented in the finite element method framework. The rather simple examples given in this article demonstrate the feasibility of the approach and will be further exploited in the context of control mechanisms as employed in magnetic resonance experiments.⁷ Greater challenges are provided by the chemical reactions where the single potential surface picture breaks down and multistate propagation is required. Such problems are on our agenda.

Acknowledgment. Generous hospitality has been extended to us at the Henry Eyring Center for Theoretical Chemistry at the University of Utah. We are grateful to Professor Jack Simons for scientific and economic stimulus during our extended stay at Salt Lake City. He and the other organizers of the workshop at Brian Head receive our thanks for the support for participation and for the creation of a congenial atmosphere. Professor Greg Voth, the director of the Henry Eyring Center, and Professor Thanh Truong maintain with Simons the excellent working environment. Travel support was obtained by one of us (B.R.J.) from the Faculty of Natural Science, Aarhus University under the graduate student program.

References and Notes

- (1) Kosloff, R. *J. Phys. Chem.* **1988**, 92, 2087.
- (2) Kramer, P.; Saraceno, M. *Geometry of the Time-Dependent Variational Principle in Quantum Mechanics*, Springer: Berlin, 1981.
- (3) Linderberg, J. In *Time-Dependent Quantum Molecular Dynamics*; Broeckhove, J., Lathouwers, L., Eds.; Plenum: New York, 1992; p 201.
- (4) Deumens, E.; Diz, A.; Longo, R.; Öhrn, N. *Y. Rev. Mod. Phys.* **1994**, 66, 917.
- (5) Ciarlet, P. G. *The finite element method for elliptic problems*; North-Holland: Amsterdam, 1978.
- (6) Löwdin, P. O. *Linear Algebra for Quantum Theory*, John Wiley & Sons: New York, 1998; p 111 ff.
- (7) Glaser, S. J.; Schulte-Herbrüggen, T.; Sieveking, M.; Schedletsky, O.; Nielsen, N. C.; Sørensen, O.; Griesinger, C. *Science* **1998**, 280, 421.

Forward–Backward Semiclassical Dynamics with Linear Scaling

Jiushu Shao

School of Chemical Sciences, University of Illinois, 601 S. Goodwin Avenue, Urbana, Illinois 61801

Nancy Makri*

*School of Chemical Sciences, University of Illinois, 601 S. Goodwin Avenue, Urbana, Illinois 61801,
and Theoretical & Physical Chemistry Institute, National Hellenic Research Foundation,
48 Vassileos Constantinou Avenue, Athens, Greece 11635*

Received: June 7, 1999; In Final Form: July 23, 1999

A forward–backward semiclassical method is presented for calculating correlation functions of polyatomic systems. Unlike conventional semiclassical theories, this formulation does not require evaluation of the prefactor that contains a determinant with elements defined by the stability matrix. It is shown rigorously that the contribution of the semiclassical prefactor in the present formulation can be absorbed in the semiclassical phase and initial density if the momentum jump at the end of the forward propagation is chosen to be one-half of that dictated by the classical equations of motion. As a consequence, the number of equations of motion to be solved in its implementation is linearly proportional to the number of degrees of freedom. The method is applied to the dynamics of water clusters which involve strongly anharmonic interactions.

1. Introduction

Although large-scale computer simulations of many-body systems by means of classical molecular dynamics have become extremely common, fully quantum mechanical calculations on such systems remain far beyond the reach of current computational capability because their cost scales exponentially with the size of the system. An attractive compromise is the time-dependent semiclassical method in which Planck's constant is treated as a small parameter compared to the classical action. While the semiclassical propagator results from asymptotic analysis, it offers an accurate description of quantum evolution for short or intermediate times without requiring storage of multidimensional functions or diagonalization of large matrices. Since this time domain is relevant in many molecular dynamical processes, the semiclassical method is appealing as a numerical tool in theoretical chemistry.

The traditional analysis of semiclassical dynamics is based on the Van Vleck propagator.^{1,2} The accuracy of the semiclassical expression has been demonstrated in several calculations,^{3–6} including systems exhibiting quantum chaotic behavior.^{7,8} There are two main difficulties in implementing the Van Vleck propagator. First, one has to perform a root search in order to identify classical trajectories satisfying double-ended boundary conditions; and second, the expression diverges at caustics (see, for example, refs 9 and 10). Several insightful techniques have been devised to overcome these problems in the calculation of correlation functions. Initial value representations,⁴ which replace the integral over final coordinate to one involving the initial momentum of a trajectory, and coarse graining schemes based on cellular dynamics¹¹ or coherent state representations¹² are proven free of these difficulties. The semiclassical propagator involves a prefactor, a determinant whose elements are defined by the stability (monodromy) matrix. This means that in addition

to the $2n$ classical equations of motion in phase space for an n -dimensional system, one must also solve $(2n)^2$ differential equations determining the stability matrix, while evaluation of the determinant requires effort proportional to n^3 .

Because of the linear superposition principle inherent in quantum mechanics, both the quantum and the semiclassical propagators are oscillatory. This behavior results in the so-called sign problem when applied to the evaluation of physical observables or correlation functions. A solution toward this problem is offered by the introduction by our group of forward–backward semiclassical dynamics (FBS).¹³ A physical quantity can in general be cast into a form of an ensemble average which involves propagators in the forward and backward time directions. By combining the forward and backward propagations into a single semiclassical time evolution, the oscillations associated with these opposite in time motions can be canceled to a large extent and the resulting integrand is sufficiently smooth for treatment by Monte Carlo integration. The original formulation of FBS for the evaluation of influence functionals in the context of a path integral description of the observable system^{13,14} has been extended to schemes which treat all degrees of freedom semiclassically.^{15–17} The FBS representation of the influence functional arises if the integration connecting the forward and backward semiclassical propagators is evaluated by the stationary phase method and is thus completely consistent with the spirit of the semiclassical approximation. If the observable system is also treated semiclassically, the expression to which one should apply the final stationary phase procedure is not unique, leading to several versions of FBS. A number of studies to date have shown that the FBS scheme is sufficiently accurate for many situations of interest in chemical dynamics and feasible for systems of several atoms.^{13,14,16–19}

In a recent letter¹⁷ we described a new formulation of FBS for calculating semiclassical correlation functions. In this scheme, the prefactor is compensated for by the semiclassical phase and the expensive evaluation of the stability matrix and

* Address correspondence to School of Chemical Sciences, University of Illinois, 601 S. Goodwin Avenue, Urbana, Illinois 61801.

the corresponding determinant is no longer required. Compared to the full semiclassical treatment which deals with the forward and backward propagators separately, the new version of FBSD reduces by a factor of 2 the number of integration variables, guarantees a smooth integrand, and eliminates the calculation of the prefactor. For this reason, this FBSD scheme is practical for simulations on polyatomic systems. At the same time, owing to the partial neglect of interference between the forward and backward propagations (which seems to be more serious than the corresponding neglect inherent in the semiclassical propagator within a given time direction), one can expect FBSD to be less accurate than the fully semiclassical method. Nevertheless, model studies¹⁷ on multidimensional anharmonic systems have shown that FBSD gives very reasonable results over several oscillation periods, a time length often sufficient for important chemistry to take place. The loss of accuracy in FBSD may be roughly understood as follows: The semiclassical method is an asymptotic theory in which the absolute value of the classical action is assumed to be much larger than Planck's constant. In FBSD, the relevant quantity is the sum of actions along the forward and backward time contours, which are partially canceled out with each other. As a consequence, the effective action is not so large and the phase varies less rapidly than in the individual propagators.

This paper presents a more detailed derivation of the new FBSD for multidimensional systems and the results of its application to the dynamics of water clusters. As in ref 17, we focus on correlation functions of the type

$$C(t) = \text{Tr}(\rho(0)Ae^{iHt/\hbar}Be^{-iHt/\hbar}) \quad (1.1)$$

where H is the Hamiltonian of the n -dimensional system

$$H = \frac{1}{2}\mathbf{p}^T \cdot \mathbf{m}^{-1} \cdot \mathbf{p} + V(\mathbf{q}) \quad (1.2)$$

with \mathbf{m} being the mass matrix and the ordinary potential energy, A and B are two (scalar) Hermitian operators, and $\rho(0)$ is the initial density matrix. (The superscript denotes the transpose of a matrix or of a vector.) For simplicity we assume that B is a function of the position operator corresponding to the observable dynamical variable(s). It is straightforward to extend the following discussion to an arbitrary operator that is a general function of all phase space variables. Section II gives the rigorous derivation of the prefactor-free FBSD in the coherent state representation. In section III we discuss the implementation of FBSD to study the vibrational motion of a water molecule or cluster. Finally, section IV summarizes the present work.

II. Theory

The dynamical part in the correlation function of eq 1.1 is the Heisenberg representation of the operator second operator, $B_H = e^{iHt/\hbar}Be^{-iHt/\hbar}$. For later use we rewrite B_H as a derivative of an operator with respect to a parameter μ , namely

$$B_H = -i \lim_{\mu \rightarrow 0} \frac{\partial}{\partial \mu} U(t; \mu) \quad (2.1)$$

where

$$U(t; \mu) = e^{iHt/\hbar} e^{i\mu B} e^{-iHt/\hbar} \quad (2.2)$$

is unitary and can be regarded as the evolution operator along a forward-backward time contour $0 \rightarrow t \rightarrow 0$ for the time-dependent Hamiltonian

$$H(t') = H - \hbar\mu\delta(t' - t)B \quad (2.3)$$

which includes an instantaneous "kick" at time t . In the semiclassical coherent state representation,¹² $U(t; \mu)$ takes the form

$$U(t; \mu) = (2\pi\hbar)^{-n} \int d\mathbf{q}_0 \int d\mathbf{p}_0 D(\mathbf{q}_0, \mathbf{p}_0; \mathbf{q}_f, \mathbf{p}_f) \times \exp\left(\frac{i}{\hbar} S(\mathbf{q}_0, \mathbf{p}_0; \mu)\right) |g(\mathbf{q}_f, \mathbf{p}_f)\rangle \langle g(\mathbf{q}_0, \mathbf{p}_0)| \quad (2.4)$$

Here $\mathbf{q}_f, \mathbf{p}_f$ denote the coordinates and momenta at the end of the forward-backward propagation, S is the corresponding classical action, and g is a coherent state described by the wave function

$$\langle g | g(\mathbf{q}_0, \mathbf{p}_0) \rangle = \left(\frac{2}{\pi}\right)^{n/4} (\det \Gamma)^{1/4} \exp\left[-(\mathbf{q}^T - \mathbf{q}_0^T) \cdot \Gamma \cdot (\mathbf{q} - \mathbf{q}_0) + \frac{i}{\hbar} \mathbf{p}_0^T \cdot (\mathbf{q} - \mathbf{q}_0)\right] \quad (2.5)$$

where the elements of Γ (a diagonal matrix) are arbitrary parameters representing the widths of the Gaussians. The prefactor D in eq 2.4 assumes the form

$$D(\mathbf{q}_0, \mathbf{p}_0; \mathbf{q}_f, \mathbf{p}_f) = 2^{-n/2} \left[\det \left(\frac{\partial \mathbf{q}_f}{\partial \mathbf{q}_0} + \Gamma^{-1} \cdot \frac{\partial \mathbf{p}_f}{\partial \mathbf{p}_0} \cdot \Gamma - 2i\hbar \frac{\partial \mathbf{q}_f}{\partial \mathbf{p}_0} \cdot \Gamma - \frac{1}{2i\hbar} \Gamma^{-1} \cdot \frac{\partial \mathbf{p}_f}{\partial \mathbf{q}_0} \right) \right]^{1/2} \quad (2.6)$$

The elements entering this determinant are determined from the stability matrix

$$\mathbf{M}(t') = \begin{pmatrix} \frac{\partial \mathbf{q}(t')}{\partial \mathbf{q}_0} & \frac{\partial \mathbf{q}(t')}{\partial \mathbf{p}_0} \\ \frac{\partial \mathbf{p}(t')}{\partial \mathbf{q}_0} & \frac{\partial \mathbf{p}(t')}{\partial \mathbf{p}_0} \end{pmatrix} \quad (2.7)$$

which obeys the differential equation

$$\frac{d}{dt'} \mathbf{M}(t') + \mathbf{F}(t') \cdot \mathbf{M}(t') = 0 \quad (2.8a)$$

with the initial condition

$$\mathbf{M}(0) = \begin{pmatrix} 1 & 0 \\ 0 & 1 \end{pmatrix} \quad (2.8b)$$

where the matrix \mathbf{F} has the form

$$\mathbf{F}(t') = \begin{pmatrix} 0 & -\mathbf{m}^{-1} \\ \left. \frac{\partial^2 V}{\partial \mathbf{q}^2} \right|_{t'} & 0 \end{pmatrix} \quad (2.9)$$

The stability matrix is thus given from the solution of $(2n)^2$ coupled first-order differential equations. Furthermore, the numerical effort required for evaluation of the determinant is proportional to n^3 . For these reasons computation of the prefactor is prohibitive if the number of coupled degrees of freedom is large. It is argued in ref 17 that when FBSD is formulated in the above derivative form, one can arrange for the contribution of the prefactor to be compensated for by other terms. In the following we present a detailed analysis of this result, which eliminates the need for calculating the semiclassical determinant.

Note that the propagator $U(t; \mu)$ contains contributions from all classical trajectories in phase space. The classical dynamics is governed by Hamilton's equations, namely

$$\frac{d\mathbf{q}}{dt'} = \frac{\partial H(t')}{\partial \mathbf{p}} = \mathbf{m}^{-1} \cdot \mathbf{p} \quad (2.10a)$$

$$\begin{aligned} \frac{d\mathbf{p}}{dt'} &= -\frac{\partial H(t')}{\partial \mathbf{q}} \\ &= -\frac{\partial V(\mathbf{q})}{\partial \mathbf{q}} + \hbar\mu\delta(t' - t)\frac{\partial B(\mathbf{q})}{\partial \mathbf{q}} \end{aligned} \quad (2.10b)$$

and the equation of motion for the classical action is

$$\frac{dS}{dt'} = \frac{1}{2}\mathbf{p}^T \cdot \mathbf{m}^{-1} \cdot \mathbf{p} - V(\mathbf{q}) \quad (2.10c)$$

The classical forward-backward motion in phase space is simple. Starting from $(\mathbf{q}_0, \mathbf{p}_0)$ at time 0, the trajectory lands at $(\mathbf{q}_t, \mathbf{p}_t^F)$ at the time t and then evolves from $(\mathbf{q}_t, \mathbf{p}_t)$ backward to reach the phase point $(\mathbf{q}_t, \mathbf{p}_t)$ when the total time returns to zero. The essential physics lies in the dynamics in an infinitesimal time domain around the intermediate time t . According to the equations of motion, all coordinates and momenta evolve continuously except at time t . At that instant the momentum undergoes a jump equal to the amount

$$\delta\mathbf{p} = \hbar\mu\mathbf{B}_t' \quad (2.11)$$

where $\mathbf{B}_t' \equiv \partial B(\mathbf{q}_t)/\partial \mathbf{q}_t$. Finally, the action at the time t increments by the amount

$$\delta S = \hbar\mu B_t \quad (2.12)$$

where $B_t \equiv B(\mathbf{q}_t)$. If the operator B is a constant equal to B_0 , all trajectories return to their original point at the final time. In that case $U(t; \mu) = \exp(i\mu B_0)$, namely, the propagator is a multiplier independent of time.

At this point we return to eq 2.1, the derivative expression of the Heisenberg operator B_H . Because the final phase space variables as well as the action in eq 2.4 depend on the parameter μ , we may divide B_H into three parts corresponding to the derivatives of the prefactor $D(\mathbf{q}_0, \mathbf{p}_0; \mathbf{q}_t, \mathbf{p}_t)$, the action $S(\mathbf{q}_0, \mathbf{p}_0; \mu)$, and the final coherent state $|g(\mathbf{q}_t, \mathbf{p}_t)\rangle$, respectively. The correlation function eq 1.1 can also be partitioned into three terms accordingly

$$C(t) = C_1(t) + C_2(t) + C_3(t) \quad (2.13)$$

Using the fact that as μ approaches zero the trajectories become continuous at the midpoint, i.e., $(\mathbf{q}_t, \mathbf{p}_t) \rightarrow (\mathbf{q}_0, \mathbf{p}_0)$, $S \rightarrow 0$, and $D \rightarrow 1$, we readily obtain

$$\begin{aligned} C_1(t) &= -i(2\pi\hbar)^{-n} \int d\mathbf{q}_0 \int d\mathbf{p}_0 \frac{\partial}{\partial \mu} D(\mathbf{q}_0, \mathbf{p}_0; \mathbf{q}_t, \mathbf{p}_t) \Big|_{\mu=0} \\ &\times \langle g(\mathbf{q}_0, \mathbf{p}_0) | \rho(0) A | g(\mathbf{q}_0, \mathbf{p}_0) \rangle \end{aligned} \quad (2.14a)$$

$$\begin{aligned} C_2(t) &= \frac{1}{\hbar} (2\pi\hbar)^{-n} \int d\mathbf{q}_0 \int d\mathbf{p}_0 \frac{\partial}{\partial \mu} S(\mathbf{q}_0, \mathbf{p}_0; \mu) \Big|_{\mu=0} \\ &\times \langle g(\mathbf{q}_0, \mathbf{p}_0) | \rho(0) A | g(\mathbf{q}_0, \mathbf{p}_0) \rangle \end{aligned} \quad (2.14b)$$

and

$$\begin{aligned} C_3(t) &= -i(2\pi\hbar)^{-n} \int d\mathbf{q}_0 \int d\mathbf{p}_0 \\ &\frac{\partial}{\partial \mu} \langle g(\mathbf{q}_0, \mathbf{p}_0) | \rho(0) A | g(\mathbf{q}_t, \mathbf{p}_t) \rangle \Big|_{\mu=0} \end{aligned} \quad (2.14c)$$

To proceed, we examine the stability matrix in the neighborhood of $\mu = 0$. Expanding through linear terms, one finds

$$\frac{\partial \mathbf{q}_f}{\partial \mathbf{q}_0} = \mathbf{1} + \mu \frac{\partial}{\partial \mathbf{q}_0} \left(\frac{\partial \mathbf{q}_f}{\partial \mathbf{p}_t} \cdot \frac{\partial \mathbf{p}_t}{\partial \mu} \right) \quad \frac{\partial \mathbf{q}_f}{\partial \mathbf{p}_0} = \mu \frac{\partial}{\partial \mathbf{p}_0} \left(\frac{\partial \mathbf{q}_f}{\partial \mathbf{p}_t} \cdot \frac{\partial \mathbf{p}_t}{\partial \mu} \right) \quad (2.15)$$

$$\frac{\partial \mathbf{p}_f}{\partial \mathbf{q}_0} = \mu \frac{\partial}{\partial \mathbf{q}_0} \left(\frac{\partial \mathbf{p}_f}{\partial \mathbf{p}_t} \cdot \frac{\partial \mathbf{p}_t}{\partial \mu} \right) \quad \frac{\partial \mathbf{p}_f}{\partial \mathbf{p}_0} = \mathbf{1} + \mu \frac{\partial}{\partial \mathbf{p}_0} \left(\frac{\partial \mathbf{p}_f}{\partial \mathbf{p}_t} \cdot \frac{\partial \mathbf{p}_t}{\partial \mu} \right) \quad (2.16)$$

where $\mathbf{1}$ is the $n \times n$ identity matrix. The derivatives $\partial \mathbf{q}_f / \partial \mathbf{p}_t$, etc. are elements of the stability matrix that corresponds to the backward evolution, i.e., the final point $(\mathbf{q}_t, \mathbf{p}_t)$ depends on the initial condition $(\mathbf{q}_0, \mathbf{p}_0)$ of the backward trajectory. At this stage we do not evaluate the derivative $\partial \mathbf{p}_t / \partial \mu$ explicitly, as we wish to allow an arbitrary momentum jump. By inserting these expressions into eq 2.6 and using the following relation

$$\det(\mathbf{R} + \delta \mathbf{R}) = \det \mathbf{R} (1 + \text{Tr}(\mathbf{R}^{-1} \cdot \delta \mathbf{R})) \quad (2.17)$$

which holds for any matrix \mathbf{R} and an infinitesimal variation $\delta \mathbf{R}$, the derivative of the prefactor takes the following form:

$$\begin{aligned} \frac{\partial}{\partial \mu} D(\mathbf{q}_0, \mathbf{p}_0; \mathbf{q}_t, \mathbf{p}_t) &= \frac{1}{4} \text{Tr} \left\{ \frac{\partial}{\partial \mathbf{q}_0} \left(\frac{\partial \mathbf{q}_f}{\partial \mathbf{p}_t} - \frac{1}{2i\hbar} \Gamma^{-1} \cdot \frac{\partial \mathbf{p}_f}{\partial \mathbf{p}_t} \right) \cdot \frac{\partial \mathbf{p}_t}{\partial \mu} \right. \\ &\quad \left. + \frac{\partial}{\partial \mathbf{p}_0} \left(\frac{\partial \mathbf{p}_f}{\partial \mathbf{p}_t} - 2i\hbar \frac{\partial \mathbf{q}_f}{\partial \mathbf{p}_t} \cdot \Gamma \right) \cdot \frac{\partial \mathbf{p}_t}{\partial \mu} \right\} \end{aligned} \quad (2.18)$$

Inserting this expression in eq 2.14a and integrating by parts, we obtain

$$\begin{aligned} C_1(t) &= \frac{i}{4} (2\pi\hbar)^{-n} \int d\mathbf{q}_0 \int d\mathbf{p}_0 \frac{\partial \mathbf{p}_t^T}{\partial \mu} \Big|_{\mu=0} \\ &\times \left[\left(\frac{\partial \mathbf{q}_f^T}{\partial \mathbf{p}_t} - \frac{1}{2i\hbar} \frac{\partial \mathbf{p}_f^T}{\partial \mathbf{p}_t} \cdot \Gamma^{-1} \right) \cdot \frac{\partial}{\partial \mathbf{q}_0} + \left(\frac{\partial \mathbf{p}_f^T}{\partial \mathbf{p}_t} - 2i\hbar \frac{\partial \mathbf{q}_f^T}{\partial \mathbf{p}_t} \cdot \Gamma \right) \cdot \frac{\partial}{\partial \mathbf{p}_0} \right] \\ &\langle g(\mathbf{q}_0, \mathbf{p}_0) | \rho(0) A | g(\mathbf{q}_0, \mathbf{p}_0) \rangle \end{aligned} \quad (2.19)$$

where it is assumed that $\langle g(\mathbf{q}_0, \mathbf{p}_0) | \rho(0) A | g(\mathbf{q}_0, \mathbf{p}_0) \rangle \rightarrow 0$ as one component of the coordinates or the momenta go to $\pm\infty$. Through some algebra one can show

$$\begin{aligned} \frac{\partial}{\partial \mathbf{q}_0} \langle g(\mathbf{q}_0, \mathbf{p}_0) | \rho(0) A | g(\mathbf{q}_0, \mathbf{p}_0) \rangle &= \\ -4\Gamma \cdot \mathbf{q}_0 \langle g(\mathbf{q}_0, \mathbf{p}_0) | \rho(0) A | g(\mathbf{q}_0, \mathbf{p}_0) \rangle &+ 2\Gamma \cdot \langle g(\mathbf{q}_0, \mathbf{p}_0) | \\ [\rho(0) A + \rho(0) A \mathbf{q}] g(\mathbf{q}_0, \mathbf{p}_0) \rangle \end{aligned} \quad (2.20)$$

and

$$\begin{aligned} \frac{\partial}{\partial \mathbf{p}_0} \langle g(\mathbf{q}_0, \mathbf{p}_0) | \rho(0) A | g(\mathbf{q}_0, \mathbf{p}_0) \rangle &= \\ \frac{i}{\hbar} \langle g(\mathbf{q}_0, \mathbf{p}_0) | [\rho(0) A \mathbf{q} - \mathbf{q} \rho(0) A] | g(\mathbf{q}_0, \mathbf{p}_0) \rangle \end{aligned} \quad (2.21)$$

Combining these results we may write $C_1(t)$ in the compact form

$$\begin{aligned} C_1(t) &= -i(2\pi\hbar)^{-n} \int d\mathbf{q}_0 \int d\mathbf{p}_0 \langle g(\mathbf{q}_0, \mathbf{p}_0) | \rho(0) A | \\ &| g(\mathbf{q}_0, \mathbf{p}_0) \rangle \mathbf{q}_0^T - \langle g(\mathbf{q}_0, \mathbf{p}_0) | \rho(0) A \mathbf{q}^T | g(\mathbf{q}_0, \mathbf{p}_0) \rangle \\ &\times \frac{\partial}{\partial \mathbf{p}_t} \left(\Gamma \cdot \mathbf{q}_f - \frac{1}{2i\hbar} \mathbf{p}_f \right) \cdot \frac{\partial \mathbf{p}_t}{\partial \mu} \Big|_{\mu=0} \end{aligned} \quad (2.22)$$

Thus, the term in the correlation function arising from the prefactor takes the form

$$C_1(t) = \int d\mathbf{q}_0 \int d\mathbf{p}_0 \mathbf{f}_1(\mathbf{q}_0, \mathbf{p}_0) \cdot \frac{\partial \mathbf{p}_t}{\partial \mu} \Big|_{\mu=0} \quad (2.23)$$

The derivative of the total action with respect to the parameter μ can be evaluated straightforwardly:

$$\frac{\partial S}{\partial \mu} \Big|_{\mu=0} = \hbar \frac{\partial \mathbf{p}_t}{\partial \mu} \Big|_{\mu=0} \cdot \frac{\partial \mathbf{q}_f}{\partial \mu} \cdot \mathbf{p}_0 + \hbar B_t \quad (2.24)$$

which yields

$$\begin{aligned} C_2(t) &= (2\pi\hbar)^{-n} \int d\mathbf{q}_0 \int d\mathbf{p}_0 \left(\frac{\partial \mathbf{p}_t}{\partial \mu} \Big|_{\mu=0} \cdot \frac{\partial \mathbf{q}_f}{\partial \mu} \cdot \mathbf{p}_0 + \hbar B_t \right) \\ &\times \langle g(\mathbf{q}_0, \mathbf{p}_0) | \rho(0) A | g(\mathbf{q}_0, \mathbf{p}_0) \rangle \\ &\equiv \int d\mathbf{q}_0 \int d\mathbf{p}_0 \mathbf{f}_2(\mathbf{q}_0, \mathbf{p}_0) \cdot \frac{\partial \mathbf{p}_t}{\partial \mu} \Big|_{\mu=0} + C_{qc}(t) \end{aligned} \quad (2.25)$$

where the contribution $C_{qc}(t)$ due to the delta pulse in the effective Hamiltonian can be viewed as a quasiclassical correlation function, namely, the Heisenberg operator B_H is replaced by the classical counterpart $B(t)$ in the definition of $C(t)$ eq 1.1. The first term in eq 2.25 is proportional to the momentum jump, while the second quasiclassical term arises from the net increment of the action. In a similar manner we obtain an explicit formula for $C_3(t)$:

$$\begin{aligned} C_3(t) &= 2i\hbar(2\pi\hbar)^{-n} \int d\mathbf{q}_0 \int d\mathbf{p}_0 \left\{ [\langle g(\mathbf{q}_0, \mathbf{p}_0) | \rho(0) A | g(\mathbf{q}_0, \mathbf{p}_0) \rangle \mathbf{q}_0^T - \langle g(\mathbf{q}_0, \mathbf{p}_0) | \rho(0) A \mathbf{q}^T | g(\mathbf{q}_0, \mathbf{p}_0) \rangle] \right. \\ &\times \frac{\partial}{\partial \mathbf{p}_t} \left(\Gamma \mathbf{q}_f - \frac{1}{2i\hbar} \mathbf{p}_f \right) - \frac{1}{2i\hbar} \mathbf{p}_0^T \cdot \frac{\partial \mathbf{q}_f}{\partial \mathbf{p}_t} \\ &\left. \langle g(\mathbf{q}_0, \mathbf{p}_0) | \rho(0) A | g(\mathbf{q}_0, \mathbf{p}_0) \rangle \right\} \cdot \frac{\partial \mathbf{p}_t}{\partial \mu} \Big|_{\mu=0} \end{aligned} \quad (2.26)$$

Again, the integrand is seen to be proportional to the derivative of the momentum jump, i.e.,

$$C_3(t) = \int d\mathbf{q}_0 \int d\mathbf{p}_0 \mathbf{f}_3(\mathbf{q}_0, \mathbf{p}_0) \cdot \frac{\partial \mathbf{p}_t}{\partial \mu} \Big|_{\mu=0} \quad (2.27)$$

Adding eqs 2.23, 2.25, and 2.27 one sees that

$$\begin{aligned} C(t) &= \int d\mathbf{q}_0 \int d\mathbf{p}_0 [\mathbf{f}_1(\mathbf{q}_0, \mathbf{p}_0) + \mathbf{f}_2(\mathbf{q}_0, \mathbf{p}_0) + \mathbf{f}_3(\mathbf{q}_0, \mathbf{p}_0)] \\ &\times \frac{\partial \mathbf{p}_t}{\partial \mu} \Big|_{\mu=0} + C_{qc}(t) \end{aligned} \quad (2.28)$$

Furthermore, comparison of the above results reveals that

$$-\frac{1}{2}[\mathbf{f}_2(\mathbf{q}_0, \mathbf{p}_0) + \mathbf{f}_3(\mathbf{q}_0, \mathbf{p}_0)] = \mathbf{f}_1(\mathbf{q}_0, \mathbf{p}_0) \quad (2.29)$$

from which it follows that

$$\begin{aligned} C(t) &= \frac{1}{2} \int d\mathbf{q}_0 \int d\mathbf{p}_0 [\mathbf{f}_2(\mathbf{q}_0, \mathbf{p}_0) + \mathbf{f}_3(\mathbf{q}_0, \mathbf{p}_0)] \\ &\times \frac{\partial \mathbf{p}_t}{\partial \mu} \Big|_{\mu=0} + C_{qc}(t) \end{aligned} \quad (2.30)$$

It is thus possible to eliminate the contribution of the prefactor from the correlation function. To compensate for this omission, the part of the correlation function that arises from the momentum increment at the time t must be multiplied by 1/2.

As that part cannot be separated from the one arising from the quasiclassical contribution associated with the change in the action, this must be achieved by multiplying the momentum increment by a factor of 1/2.

Equation 2.30 is the main result outlined in ref 17. The correlation function is given by the expression

$$\begin{aligned} C(t) &= -i(2\pi\hbar)^{-n} \frac{\partial}{\partial \mu} \int d\mathbf{q}_0 \int d\mathbf{p}_0 \exp\left(\frac{i}{\hbar} S(\mathbf{q}_0, \mathbf{p}_0; \mu)\right) \\ &\times \langle g(\mathbf{q}_0, \mathbf{p}_0) | \rho(0) A | g(\mathbf{q}_f, \mathbf{p}_f) \rangle \Big|_{\mu=0} \end{aligned} \quad (2.31)$$

The trajectories follow the classical equations of motion with the Hamiltonian H up to the time t , at which point the momentum component jumps by the amount

$$\delta \mathbf{p}_{\text{opt}} = \frac{1}{2} \hbar \mu \mathbf{B}'_t \quad (2.32)$$

for a small value of the finite difference parameter μ . At the same time, the action increments by the full amount given by eq 2.12. Subsequent evolution takes place in the negative time direction, and the integrand is evaluated when the time parameter reaches zero once again.

Equation 2.31 (along with the momentum and action jumps given by eqs 2.32 and 2.12, respectively) is a rigorous semiclassical formulation of correlation functions that uses trajectories in combined forward-backward time for all degrees of freedom. Its main advantage is that the contribution from the prefactor is eliminated. As a consequence, the number of equations to be solved scale linearly with the number of degrees of freedom in the Hamiltonian. Note that the elimination of the prefactor is achieved via an *exact* transformation of the derivative form of the correlation function, resulting in an expression where *the momentum jump is one-half of that dictated by the classical equations of motion*. This transformation was feasible because the derivative formulation in terms of a small parameter allows linearization of the equations. It should be noted that the prefactor is equal to the negative of the total contribution from terms arising directly from the momentum jump; these terms are extremely important, as the remaining term is merely a quasiclassical contribution.

The combined forward-backward treatment of the correlation function amounts to a stationary phase evaluation of the full semiclassical expression, in which the individual forward and backward time-evolution operators are treated via the Van Vleck propagator. That full semiclassical formulation takes the form

$$\begin{aligned} C(t) &= (2\pi\hbar)^{-2n} \int d\mathbf{q}_F \int d\mathbf{p}_F \int d\mathbf{q}_B \int d\mathbf{p}_B D_F(\mathbf{q}_F, \mathbf{p}_F) \\ &\times D_B(\mathbf{q}_B, \mathbf{p}_B) \exp\left(\frac{i}{\hbar} S(\mathbf{q}_F, \mathbf{p}_F; \mathbf{q}_B, \mathbf{p}_B)\right) \langle g(\mathbf{q}_F, \mathbf{p}_F) | \rho(0) A | g(\mathbf{q}_B, \mathbf{p}_B) \rangle \langle g(\mathbf{q}_B, \mathbf{p}_B) | B | g(\mathbf{q}_F, \mathbf{p}_F) \rangle \end{aligned} \quad (2.33)$$

where $\mathbf{q}_F, \mathbf{p}_F$ and $\mathbf{q}_B, \mathbf{p}_B$ are the endpoints of the forward and backward trajectories. Often A and B are operators that depend on only a few observable degrees of freedom (the "system") while the remaining coordinates constitute the environment (or "bath"). Treating the intermediate integrations associated with the bath components of $\mathbf{q}_B, \mathbf{p}_B$ via the stationary phase method leads¹⁶ to an FBSD expression where the trajectories evolve continuously in the space of the bath, while their system component jumps at the intermediate time t . That procedure amounts to an enormous simplification, as the cancellation between the forward and the backward parts corresponding to the dynamics of the solvent gives rise to small actions and thus

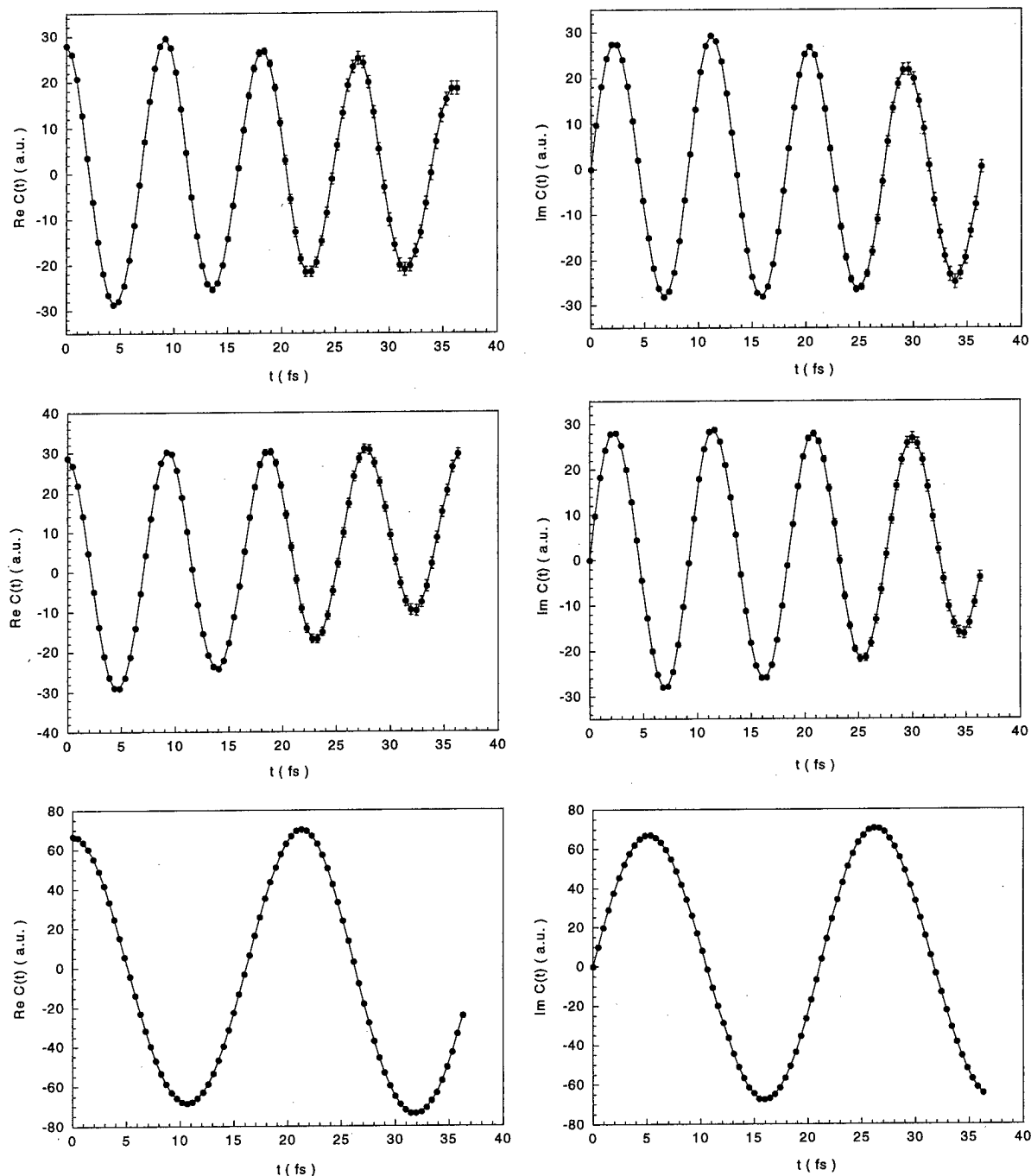


Figure 1. (a) Real and imaginary parts of the correlation function of the O-H asymmetric stretch as obtained from the FBSD calculations. Error bars indicate one standard deviation. Solid lines are guides to the eye only. (b) Real and imaginary parts of the correlation function of the O-H symmetric stretch. (c) Real and imaginary parts of the correlation function of the H-O-H bend.

smooth integrands; at the same time, the integrand is more oscillatory along the direction of the variables associated with the probed system, and thus these integration variables must be treated via a combination of Monte Carlo and quadrature methods. Replacing the exact integration by the stationary phase result wipes out the interference between multiple bounce contributions across the forward and backward parts of the dynamics and thus may degrade the accuracy if the potential of the bath degrees of freedom is very anharmonic. However, important interference between system trajectories is fully accounted for in that scheme. Another way of arriving at FBSD expressions where the system component of the momentum jumps at the intermediate time while the trajectories remain continuous in the space of the bath involves¹⁵ expressing the operator B in exponential form by invoking the Wigner-Weyl

representation^{20,21} and implementing FBSD for all degrees of freedom. While the system components of $\mathbf{q}_B, \mathbf{p}_B$ are also treated within the stationary phase method in that approach, the finite-size momentum jumps permitted in the space of the system allow for some interference between multiple bounce trajectories. The present formulation, which uses a derivative method to exponentiate the operators, is simpler than all of the above in that no additional integrations are introduced and, most importantly, there is no prefactor to be computed. At the same time, the prefactor-free FBSD described here cannot account for interference between distinct trajectories of the forward and reverse time propagators as the momentum jump performed at the time t is infinitesimal in magnitude. As a consequence, the present method is similar in spirit to the linearization approximation of Miller and co-workers,^{22,23} although the math-

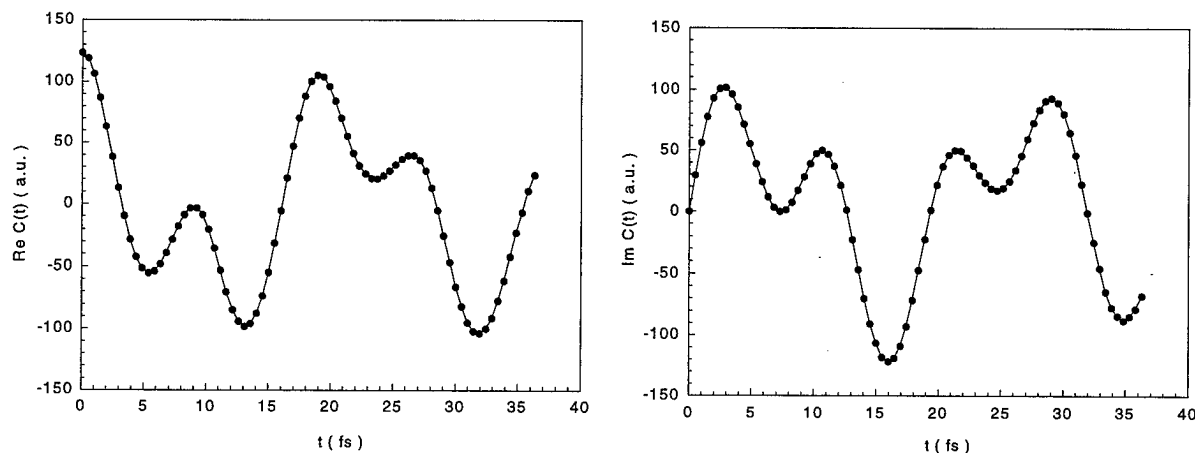


Figure 2. Real and imaginary parts of the sum of the three correlation functions.

ematical details differ and the present prefactor-free FBSD was obtained via a rigorous semiclassical procedure. Sun et al.²⁴ have found that their linearization approximation, which also neglects similar interference terms, captures the short time, transition-state-like features of thermal rate constants correctly but fails to describe nonclassical aspects of the recrossing dynamics resulting from quantum interference on the time scale of two or more vibrational periods. Our tests¹⁷ have demonstrated that the prefactor-free FBSD leads to reasonably accurate results for correlation functions in multidimensional potentials where relaxation and dissipative effects tend to weaken interference phenomena.

III. Application: Vibrational Dynamics of Water

The FBSD developed above is a general technique for investigating dynamical properties of a system. In addition to correlation functions, the quantum average at time t of any observable corresponding to the operator B can be evaluated via eq 1.1 in which A is set equal to the identity operator. In the following we consider molecular vibrations of a molecule or small cluster at low temperatures. Because vibrations are collective motions, we focus on the numerical implementation of the FBSD for calculating correlation functions of the type

$$C(t) = \text{Tr}(\rho(0)Q_k e^{iHt/\hbar} Q_k e^{-iHt/\hbar}) \quad (3.1)$$

where Q_k is one of the normal modes of the system with respect to the global potential minimum. It is a straightforward matter to extend the procedure to the calculation of the dipole correlation function if the functional form of the dipole moment operator is available.

The initial density is constructed in terms of the ground vibrational state, $\rho(0) = |\Psi_0\rangle\langle\Psi_0|$, which factorizes in the normal mode representation

$$\langle Q|\Psi_0\rangle = \prod_{j=1}^n \left(\frac{\omega_j}{\pi}\right)^{1/4} \exp\left(-\frac{\omega_j}{2\hbar} Q_j^2\right) \quad (3.2)$$

where $n = 3N - 6$, N being the total number of atoms and ω_j the normal-mode frequencies. We take Γ as a diagonal matrix with elements equal to $\omega_j/2\hbar$. Carrying out the Gaussian integrals, one readily obtains

$$\begin{aligned} \langle g(\mathbf{Q}_0, \mathbf{P}_0) | \rho(0) Q_k | g(\mathbf{Q}_f, \mathbf{P}_f) \rangle &= \frac{1}{2} \left(Q_{k,f} + i \frac{P_{k,f}}{\omega_k} \right) \prod_{j=1}^n \\ &\times \exp \left[-\frac{\omega_j}{4\hbar} (Q_{j,0}^2 + Q_{j,f}^2) - \frac{1}{4\hbar\omega_j} (P_{j,0}^2 + P_{j,f}^2) \right. \\ &\left. - \frac{1}{2i\hbar} (Q_{j,0}P_{j,0} - Q_{j,f}P_{j,f}) \right] \end{aligned} \quad (3.3)$$

and

$$\begin{aligned} \langle g(\mathbf{Q}_0, \mathbf{P}_0) | \rho(0) Q_k | g(\mathbf{Q}_0, \mathbf{P}_0) \rangle &= \frac{1}{2} \left(Q_{k,0} + i \frac{P_{k,0}}{\omega_k} \right) \prod_{j=1}^n \\ &\times \exp \left(-\frac{\omega_j}{2\hbar} Q_{j,0}^2 - \frac{1}{2\hbar\omega_j} P_{j,0}^2 \right) \end{aligned} \quad (3.4)$$

These expressions are inserted into eq 2.28 in numerical calculations.

It is convenient to retain the normal mode coordinates for the representation of the FBSD correlation function. The RWK2 potential²⁵ which has been designed for calculating vibrational spectra of water clusters is adopted in our work. That potential consists of the Morse oscillator potential from the intramolecular interaction plus atom-atom interactions and Coulomb terms between point charges from the intermolecular interaction. The classical equations of motion are solved in normal mode coordinates. Our previous work¹⁷ showed that it is feasible to sample the initial conditions via a Metropolis procedure with the absolute value of eq 3.4 being the weight function. Here for fast convergence we invoke the Genz-Monahan algorithm developed specifically for higher dimensional integrals over unbounded regions with Gaussian weight.²⁶ Their approach is based on the stochastic spherical-radial rules for integrations. We report the results of the method described in the previous section for a single water molecule as well as two- and four-molecule clusters using 2500 trajectories for each degree of freedom. The largest of these systems has 30 active degrees of freedom and thus the calculation involves a 60-dimensional integral which is evaluated with a total of 150 000 trajectories.

Figure 1 shows the correlation functions of the three vibrational modes of a water molecule, namely the O-H asymmetric stretch, O-H symmetric stretch, and H-O-H bend, obtained via the prefactor-free FBSD scheme described in section II. Figure 2 shows the sum of the three correlation functions. Since rotational degrees of freedom evolve on a

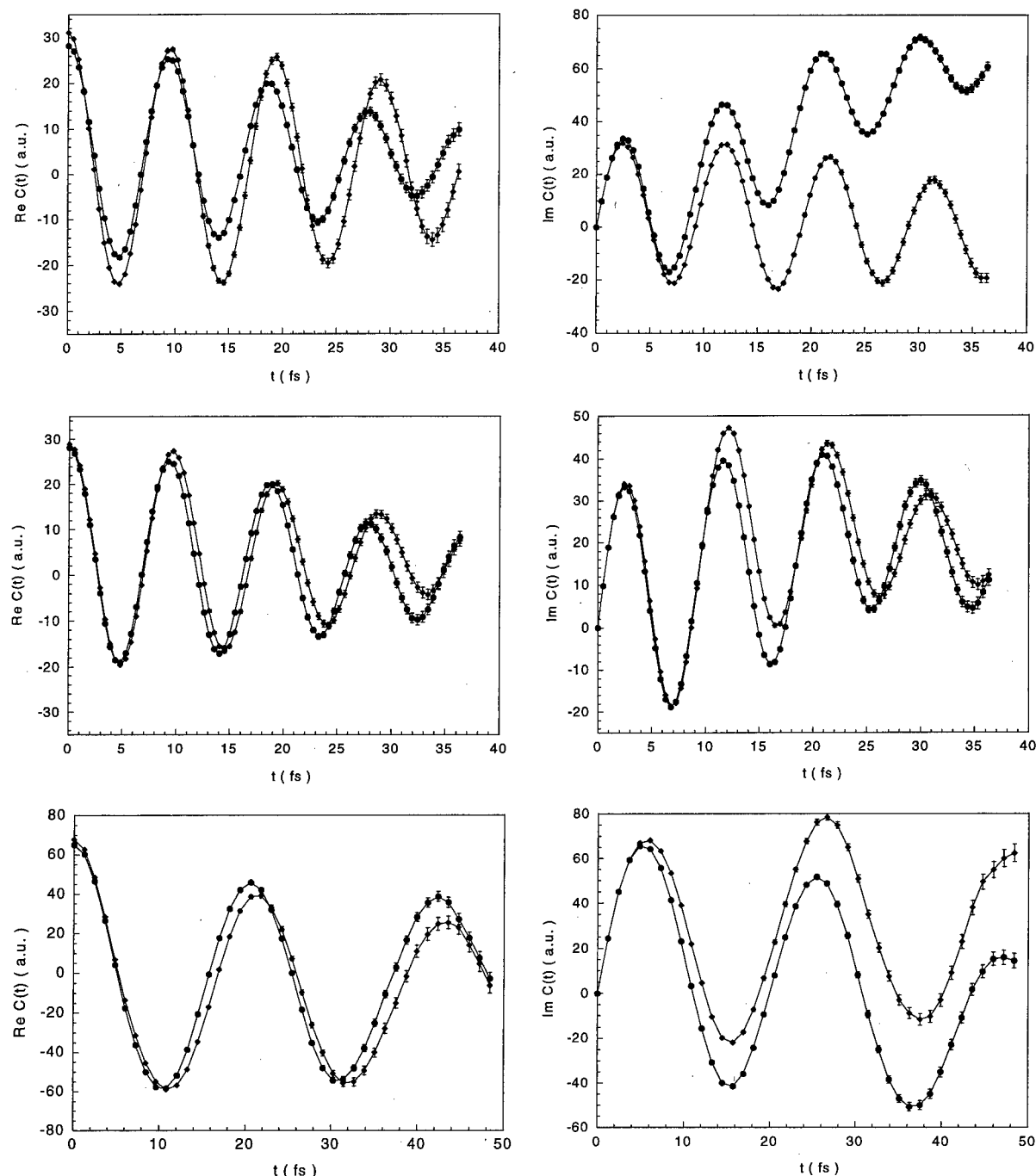


Figure 3. (a) Real and imaginary parts of the correlation functions: the two O—H stretches of the donor in the water dimer. (b) Real and imaginary parts of the correlation functions: the two O—H stretches of the acceptor in the water dimer. (c) Real and imaginary parts of the correlation functions of the two H—O—H bends in the water dimer.

slower time scale, this sum represents a good approximation to the correlation function for the normal mode vector of water.

The fundamental frequencies of vibrations can be estimated from these figures. The frequencies for the O—H asymmetric stretch, O—H symmetric stretch, and H—O—H bend are about 3658, 3573, and 1576 cm^{-1} , respectively. Comparing with the results of the normal-mode analysis, which are 3922, 3817, and 1639 cm^{-1} , respectively, we see strong red shifts due to the anharmonicity of the system. It is clearly shown in these figures that anharmonic interactions affect the dynamics within about 10 fs. In addition, one observes energy transfer from the O—H asymmetric stretch to the nearly resonant O—H symmetric stretch during the initial 40 fs. This time is still short for the H—O—H bend to be involved in the process of energy redistribution in the molecule.

Figures 3 and 4 show similar results for the water dimer and tetramer, respectively. The stable configuration of the tetramer is cyclic. We also find red shifts (mainly due to intramolecular vibrations) for the studied normal modes. This observation is in agreement with the results from the self-consistent field calculations by Jung and Gerber.²⁷ In the dimer, the hydrogen bond induces an increment of the amplitude and a decrement of the frequency for one of the OH stretches in the donor. In general, the larger number of degrees of freedom leads to stronger mixing among the normal modes during evolution. All figures exhibit imaginary parts comparable in size to the real parts of the correlation functions. This behavior is a manifestation of the quantum mechanical aspect of the dynamics at zero temperature. It is remarkable that the error bars are small in all cases, even though the number of samples per integration

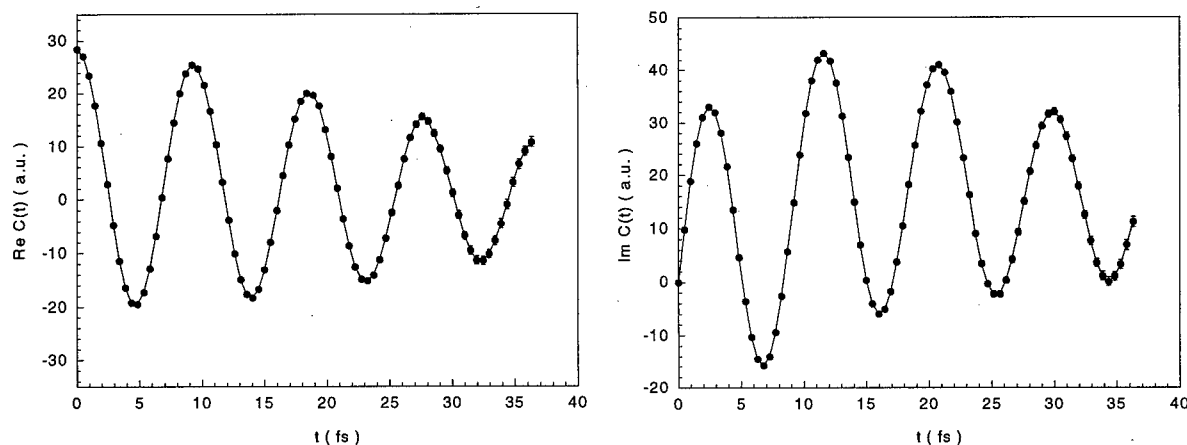


Figure 4. Real and imaginary parts of the correlation function of the O-H stretch with the highest frequency in the water tetramer.

variable is rather small. Most importantly, the size of the error bars is seen to be a slowly varying function of cluster size. This is very encouraging for performing FBSD calculations with truly large systems.

IV. Concluding Remarks

We have presented a rigorous, yet practical methodology for calculating semiclassical correlation functions or expectation values. The key features of this approach are (a) the combined treatment of the forward and backward time evolution operators, which guarantee a smooth integrand amenable to Monte Carlo sampling, and (b) the absence of a semiclassical prefactor which leads to linear scaling. Starting from a derivative formulation of the correlation function, it was shown that the prefactor amounts to *exactly one-half* of the combined semiclassical phase and initial density terms proportional to the momentum jump at the end of the forward evolution. As a consequence, using momentum increments of half the magnitude dictated from the classical equations of motion cancels the contribution from the semiclassical determinant. Given the near elimination of the sign problem and the linear scaling with system size, the prefactor-free FBSD opens the way to large-scale simulations in real time.

Implementation of the prefactor-free methodology is straightforward. If the coherent state matrix element involving the initial density is known, one uses its absolute value as a sampling function to carry out a stochastic procedure for the integrals, say, selecting initial conditions via a Metropolis random walk. After integrating to the desired propagation time t , trajectories incur an instantaneous discontinuity and subsequently continue in the backward time direction until the time origin is reached. Evaluation of the required derivative by a two-point finite difference formula requires a single calculation. As the finite difference parameter is infinitesimal, the corresponding momentum jump and resulting forward-backward action are small. These facts ensure excellent Monte Carlo statistics with modest numbers of samples.

Application to the vibrational dynamics of a water molecule was employed to illustrate the practicality of the scheme. The correlation functions of the normal modes were computed for several oscillation periods. The calculations give rise to a large imaginary component of the correlation functions. Such imagi-

nary components are of purely quantum mechanical origin, as classical correlation functions are always real-valued. If the dipole moment operator is known to a reasonable approximation, the real part of correlation function can be used to extract spectral line shapes. Future work in our group will deal with similar investigations in molecular clusters.

Acknowledgment. This work has been supported by the David and Lucile Packard Foundation through a Packard Fellowship for Science and Engineering and the National Science Foundation. N.M. thanks the researchers of the National Hellenic Research Foundation for their hospitality during her sabbatical leave from the University of Illinois.

References and Notes

- (1) Van Vleck, J. H. *Proc. Nat. Acad. Sci. U.S.A.* **1928**, *14*, 178.
- (2) Morette, C. *Phys. Rev.* **1952**, *81*, 848.
- (3) Miller, W. H. *J. Chem. Phys.* **1970**, *53*, 3578.
- (4) Miller, W. H. *Adv. Chem. Phys.* **1974**, *25*, 69.
- (5) Eu, B. C. *Semiclassical theory of molecular scattering*; Springer-Verlag: Berlin, 1984.
- (6) Child, M. S. *Semiclassical mechanics with molecular applications*; Clarendon: Oxford, 1991.
- (7) Tomsovic, S.; Heller, E. J. *Phys. Rev. Lett.* **1991**, *67*, 664.
- (8) Sepulveda, M. A.; Tomsovic, S.; Heller, E. J. *Phys. Rev. Lett.* **1992**, *69*, 402.
- (9) Gutzwiller, M. C. *Chaos in classical and quantum mechanics*; Springer-Verlag: New York, 1990.
- (10) Schulman, L. S. *Techniques and applications of path integration*; John Wiley and Sons: New York, 1981.
- (11) Heller, E. J. *J. Chem. Phys.* **1991**, *94*, 2723.
- (12) Herman, M. F.; Kluk, E. *Chem. Phys.* **1984**, *91*, 27.
- (13) Makri, N.; Thompson, K. *Chem. Phys. Lett.* **1998**, *291*, 101–109.
- (14) Thompson, K.; Makri, N. *J. Chem. Phys.* **1999**, *110*, 1343.
- (15) Miller, W. H. *Faraday Discuss.* **1998**, *110*, 1.
- (16) Thompson, K.; Makri, N. *Phys. Rev.* **1999**, *E 59*, R4729.
- (17) Shao, J.; Makri, N. *J. Phys. Chem.* **1999**, in press.
- (18) Batista, V.; Zanni, M. T.; Greenblatt, J.; Neumark, D. M.; Miller, W. H. *J. Chem. Phys.* **1999**, *110*, 3736–3747.
- (19) Kühn, O.; Makri, N. *J. Phys. Chem.*, submitted.
- (20) Wigner, E. J. *J. Chem. Phys.* **1937**, *5*, 720.
- (21) Weyl, H. Z. *Phys.* **1927**, *46*, 1.
- (22) Wang, H.; Sun, X.; Miller, W. H. *J. Chem. Phys.* **1998**, *108*, 9726.
- (23) Sun, X.; Wang, H.; Miller, W. H. *J. Chem. Phys.* **1998**, *109*, 7064.
- (24) Sun, X.; Wang, H.; Miller, W. H. *J. Chem. Phys.* **1998**, *109*, 4190.
- (25) Coker, D. F.; Watts, R. O. *J. Phys. Chem.* **1987**, *91*, 2513.
- (26) Genz, A.; Monahan, J. *J. Comput. Appl. Math.*, to be published. We thank Prof. Genz for providing his program RANRTH.
- (27) Jung, J. O.; Gerber, R. B. *J. Chem. Phys.* **1996**, *105*, 10332.

Forward–Backward Semiclassical Calculation of Spectral Line Shapes: I₂ in a Rare Gas Cluster

Oliver Kühn

*Institut für Chemie, Physikalische und Theoretische Chemie, Freie Universität Berlin,
Takustr. 3, 14195 Berlin, Germany*

Nancy Makri*

*School of Chemical Sciences, University of Illinois, 601 S. Goodwin Avenue, Urbana, Illinois 61801, and
Theoretical and Physical Chemistry Institute, National Hellenic Research Foundation,
48 Vassileos Constantinou Avenue, Athens, Greece 11635*

Received: June 7, 1999; In Final Form: July 19, 1999

The forward–backward semiclassical representation introduced by Makri and Thompson (*Chem. Phys. Lett.* **1998**, 291, 101–109.) is employed to evaluate dipole correlation functions for electronic transitions of molecules in clusters or the condensed phase. The method is applied to the $X \rightarrow B$ transition of an iodine molecule in a host of argon atoms. In this case, where the spectrum is dominated by the short-time dynamics of the system, a factorization of the stability matrix entering the semiclassical expression of the propagator provides an excellent approximation, substantially reducing the computational cost.

1. Introduction

The microscopic description of condensed phase dynamics has provided a challenge over the past two decades. An exact quantum mechanical description of such processes as photoinduced reactive (photodissociation) and nonreactive (solvation) dynamics remains out of reach, as the numerical effort for solving the multidimensional Schrödinger equation grows exponentially with the number of coupled degrees of freedom. The alternative very appealing path integral description is plagued by the so-called sign problem which amounts to the inability of stochastic sampling methods to handle the integration of oscillatory functions.

In view of these difficulties inherent in quantum mechanical treatments of complicated many-body Hamiltonians, simplified models of the environment provide an attractive alternative. A popular description of many condensed phase processes is based on system–bath models. Here, the molecular system, i.e., a molecule in solution or in a solid state matrix, is mapped onto a low (one- or two-) dimensional system interacting with a bath which consists of uncoupled harmonic oscillators (see, for example, ref 1). The microscopic information about the bath and its interaction with the system is replaced by the spectral density function, a quantity which is often approximated by means of classical molecular dynamics simulations. Given the simplified system–bath Hamiltonian, the ensuing dynamics can be obtained either perturbatively^{2–4} or exactly using numerical path integral methods.^{5–12} Recent work has analyzed the conditions for validity of the system–bath description.¹³ Clearly, the drawback in these formulations is the loss of microscopic information as a consequence of the mapping procedure. This has motivated efforts toward methods for dealing with large systems in full dimensionality, the most popular of which involve time-dependent mean field approximations,^{14–16} mixed

quantum-classical^{17–19} and surface hopping schemes,^{20–25} Gaussian wavepacket ideas,^{26,27} and semiclassical approximations.^{28–49} In addition, significant progress has been made in the direction of using the results of equilibrium path integral calculations via analytic continuation^{50–53} and maximum entropy methods^{54,55} or centroid density ideas^{56–61} to deduce dynamical information. For recent reviews the reader is referred to refs 62 and 63.

In close analogy with the path integral situation,⁶⁴ Monte Carlo integration of the semiclassical propagator suffers from a phase cancellation problem due to its oscillatory character. A number of elegant methods for dealing with the semiclassical sign problem based on filtering procedures^{38,39} or linearized approximations^{41–43} have met with considerable success. An alternative, more rigorous approach^{44–49} is based on the combined treatment of the forward and backward time evolution operators entering the influence functional or a correlation function. The forward–backward semiclassical dynamics (FBSD) method has the advantage that most of the rapid oscillations cancel and one is left with a smooth integrand.

In the present contribution we employ the FBSD scheme in the context of the spectroscopy of electronic transitions in the condensed phase. In section II we give a brief account of the theoretical apparatus. As phase cancellation is minimal in FBSD calculations, the most severe obstacle toward applying the method to large systems appears to be the computation of the prefactor, which scales as the third power of the number of atoms involved. We thus explore a simple factorization which substantially reduces the required computational effort associated with integrating the stability matrix. The specifics of the line-shape calculation are discussed in section III along with the numerical results that we obtained. The paper is finally summarized in section IV.

II. Theory

We focus on spectroscopic experiments described in terms of two electronic states, labeled g and e , which are coupled by

* Address correspondence to this author at the School of Chemical Sciences, University of Illinois, 601 S. Goodwin Avenue, Urbana, IL 61801.

the electromagnetic radiation field. Adopting the conventional classical treatment of the radiation field and the dipole approximation, the total Hamiltonian is written as

$$H(\mathbf{p}, \mathbf{q}) = H_g(\mathbf{p}, \mathbf{q})|g\rangle\langle g| + H_e(\mathbf{p}, \mathbf{q})|e\rangle\langle e| - \mathbf{E}(t) \cdot (\boldsymbol{\mu}_{eg}(\mathbf{q})|e\rangle\langle g| + \boldsymbol{\mu}_{ge}(\mathbf{q})|g\rangle\langle e|) \quad (2.1)$$

Here \mathbf{q} and \mathbf{p} are Cartesian coordinates and momenta for the multidimensional system of interest, $\mathbf{E}(t)$ is the external electric field, and $\boldsymbol{\mu}_{ge}(\mathbf{q})$ is the dipole operator. Optical spectroscopy in weak external fields is conveniently described by employing a perturbation expansion of the time evolution operator with respect to the field (see, for example, ref 65). This results in expressions for the linear and nonlinear optical response functions in terms of dipole-dipole correlation functions. For instance, the linear absorption line shape normalized to unit area is given by the Fourier transform

$$\alpha(\omega) = \frac{1}{\pi} \text{Re} \int_0^\infty dt e^{i\omega t} C(t) \quad (2.2)$$

where the dipole-dipole correlation function is

$$C(t) = \text{Tr}[U_e(t)\boldsymbol{\mu}_{eg}(\mathbf{q})\rho_g U_g^{-1}(t)\boldsymbol{\mu}_{ge}(\mathbf{q})] \quad (2.3)$$

Here U_g and U_e are the time evolution operators of the ground and excited potential surfaces, respectively, ρ_g is the initial density operator prior to excitation, and the trace is taken with respect to the nuclear degrees of freedom. Assuming a thermal distribution of the molecular system of interest, the initial density is given by the Boltzmann operator,

$$\rho_g = Z^{-1} \exp(-\beta H_g) \quad (2.4)$$

where Z is the canonical partition function and $\beta = 1/k_B T$. Invoking the Condon approximation and setting $\boldsymbol{\mu}_{ge} = 1$, the correlation function takes the form

$$C(t) = \text{Tr}(U_e(t)\rho_g U_g^{-1}(t)) \quad (2.5)$$

In the condensed phase the calculation of correlation functions of the type shown in eq 2.3 poses severe numerical difficulties unless one can resort to simple system-bath descriptions like the Brownian oscillator model which allows for an exact evaluation of (2.3) by using a cumulant expansion.¹³ Although such mappings are justified in condensed phase situations under conditions that favor the validity of the linear response approximation, they are clearly inadequate for describing processes involving a few strongly interacting degrees of freedom such as those encountered in medium size clusters. The present article aims at describing a rigorous semiclassical methodology for dealing with the spectroscopy of such systems, treating the potential interactions in full dimensionality.

The semiclassical propagator in the coordinate representation can be obtained by applying the stationary phase approximation to the path integral.^{66,67} The result, first obtained by Van Vleck²⁸ by a different method, involves a phase equal to the action along classical trajectories connecting the initial and final points and a prefactor which amounts to contributions from quadratic fluctuations about a classical path. The endpoint representation is not useful for the purpose of performing numerical calculations as the determination of the relevant trajectories requires the solution of a double ended boundary value problem. This numerical difficulty is overcome in initial value representations of time correlation functions which replace the integration over

final coordinates by one involving initial momenta³⁰ or invoke cellular discretizations³⁴ or coherent state representations.³² In these formulations, the classical trajectories are specified by their initial conditions in phase space. A number of successful applications to small model^{35,36} and chemical systems^{39,49,68} have demonstrated the high accuracy of the semiclassical approximation as well as some of its limitations. In addition, semiclassical ideas have been successfully combined with quantum-classical approaches to treat polyatomic systems.⁶⁹⁻⁷¹ Multidimensional calculations require integration by Monte Carlo methods which (because of the oscillatory phase present in the semiclassical integrand) are plagued by a sign problem very similar to that encountered in real-time path integration. Even though a few successful calculations employing filtering procedures^{38,39} or linearization approximations^{41,42} have been reported, rigorous semiclassical calculations in large systems have in the past been considered unfeasible.

In previous attempts to develop a semiclassical representation of (2.5) and its obvious generalization to nonlinear spectroscopies the forward and backward propagation has been treated separately while the integrals associated with switching between electronic states that appear in higher order terms were performed within the stationary phase approximation.⁷²⁻⁷⁵

In ref 72 this procedure was combined with a harmonic expansion around the center of the classical orbits of the forward and backward trajectories in the spirit of Gaussian wave packet and cellular dynamics³⁴ with application to an electronic two-level system coupled to a single nuclear coordinate. Spencer and Loring⁷⁴ treated a solute in a Lennard-Jones solvent semiclassically, simplifying matters by neglecting the amplitude of the semiclassical propagator. They also discussed the shortcomings of semiclassical approaches which reduce the correlation function to the ground or excited state dynamics of the instantaneous energy gap.

To circumvent the difficulty associated with the oscillatory nature of the semiclassical propagator, Makri and Thompson formulated a FBSD scheme for ensemble-averaged quantities.^{44,46,47} The main idea is to apply the semiclassical approximation to the combined forward and reverse time evolution operators. After reaching the desired propagation time, trajectories are subsequently propagated back to time zero, such that the net accumulated action is generally small. This fact implies that the semiclassical integrand is now only mildly oscillatory, allowing Monte Carlo sampling. Batista et al.⁴⁹ have used this scheme to simulate the photoelectron spectrum of I_2^- in the gas phase.

References 44 and 46 present in detail the FBSD scheme for the influence functional arising from coupling of a multidimensional medium to a time-dependent system. Equation 2.5 for the correlation function pertinent to the photoabsorption spectrum has exactly the same structure, the forward and backward evolution operators now involving the forces on the ground and excited potential surfaces. For this purpose, we simply rewrite the result of refs 44 and 46 in the present notation:

$$C(t) = (2\pi\hbar)^{-n} \int d\mathbf{p}_0 \int d\mathbf{q}_0 D(\mathbf{q}_0, \mathbf{p}_0) \times \exp\left(\frac{i}{\hbar} S(\mathbf{q}_0, \mathbf{p}_0)\right) \langle G(\mathbf{q}_0, \mathbf{p}_0) | \rho_g | G(\mathbf{q}_f, \mathbf{p}_f) \rangle \quad (2.6)$$

Here

$$G(\mathbf{q}_0, \mathbf{p}_0) = \left(\frac{2}{\pi}\right)^{n/4} (\det \gamma)^{1/4} \times \exp\left(-(\mathbf{q} - \mathbf{q}_0) \cdot \gamma \cdot (\mathbf{q} - \mathbf{q}_0) + \frac{i}{\hbar} \mathbf{p}_0 \cdot (\mathbf{q} - \mathbf{q}_0)\right) \quad (2.7)$$

where γ is a diagonal matrix, defines a multidimensional coherent state. According to eq 2.6, trajectories are chosen with initial conditions $\mathbf{q}_0, \mathbf{p}_0$ based on weights given by the coherent state transform of the initial density operator. These trajectories are first propagated to time t according to the ground state Hamiltonian and subsequently return to zero time following the forces in the excited electronic state. Finally, S is the net action during this forward-backward evolution, i.e.

$$S(\mathbf{q}_0, \mathbf{p}_0) = \int_0^t (\mathbf{p}(t') \cdot \dot{\mathbf{q}}(t') - H_g) dt' + \int_t^0 (\mathbf{p}(t') \cdot \dot{\mathbf{q}}(t') - H_g) dt' \quad (2.8)$$

The main advantage of the FBSD formulation in the context of propagation in a single electronic state^{12,13} is that the combined forward-backward action tends to be small on the scale of Planck's constant and thus the integrand is only mildly oscillatory. In the present context, the extent of forward-backward cancellation depends on how different the ground and excited state Hamiltonians are. In the limit $H_g = H_e$, the forward and backward propagation steps cancel exactly and the corresponding action is identically equal to zero. The prefactor in (2.6) is given by $D(\mathbf{q}_0, \mathbf{p}_0) = \sqrt{\det \mathbf{M}}$ with the matrix \mathbf{M} defined in terms of the elements of the stability matrix

$$M_{ij} = \frac{1}{2} \left(\frac{\partial q_{j,f}}{\partial q_{i,0}} + \frac{\gamma_i}{\gamma_j} \frac{\partial p_{j,f}}{\partial p_{i,0}} - 2i\hbar \gamma_i \frac{\partial q_{j,f}}{\partial p_{i,0}} + \frac{i}{2\hbar \gamma_j} \frac{\partial p_{j,f}}{\partial q_{i,0}} \right) \quad (2.9)$$

To calculate the determinant, one needs to solve the $(2n)^2$ differential equations for these elements. Having in mind applications to large systems, the quadratic scaling of this procedure becomes the bottleneck. For this reason we will also explore the validity of the simplest approximation in which the correlations between initial and final phase space points of different degrees of freedom are neglected, i.e. $M_{ij} \approx \delta_{ij} M_{ii}$. In this approximation, the prefactor D is replaced by $D_{\text{fact}} = [\prod_i M_{ii}]^{1/2}$.

Finally, we mention how the FBSD treatment described in this section can be used to evaluate the dipole correlation function without invoking the Condon approximation. For this purpose, eq 2.5 is written in the form

$$C(t) = -i \frac{\partial}{\partial \mathbf{z}} \cdot \text{Tr}(\boldsymbol{\mu}_{\text{eg}}(\mathbf{q}) \rho_g U_g^{-1}(t) e^{i\mathbf{z} \cdot \boldsymbol{\mu}_{\text{ge}}(\mathbf{q})} U_e(t))|_{\mathbf{z}=0} \quad (2.10)$$

The product of the three last operators in this expression can be interpreted as propagation with the following time-dependent Hamiltonian:^{45,48}

$$\tilde{H}(t') \equiv H - \hbar \mathbf{z} \cdot \boldsymbol{\mu} \delta(t' - t) \quad (2.11)$$

The classical dynamics generated by this effective Hamiltonian are described by Hamilton's equations,

$$\dot{\mathbf{q}}(t') = \frac{\partial \tilde{H}}{\partial \mathbf{p}} = \frac{\partial H}{\partial \mathbf{p}}, \quad \dot{\mathbf{p}}(t') = -\frac{\partial \tilde{H}}{\partial \mathbf{q}} = -\frac{\partial H}{\partial \mathbf{q}} + \hbar \frac{\partial \boldsymbol{\mu}}{\partial \mathbf{q}} \cdot \mathbf{z} \delta(t - t') \quad (2.12)$$

According to these, the momentum of each trajectory must jump

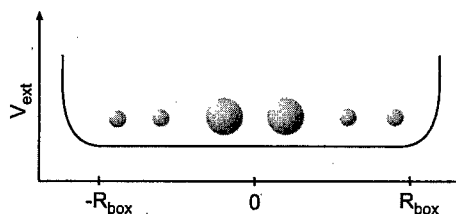


Figure 1. Linear chain configuration of I_2 (large spheres) in an Ar (small spheres) environment. The system is placed in a box introduced via the external potential $V_{\text{ext}}(\mathbf{q})$. The latter is taken as the repulsive part of the Ar-Ar Lennard-Jones potential thus modeling the presence of further Ar atoms.

at time t by the amount

$$\delta \mathbf{p} = \hbar \frac{\partial \boldsymbol{\mu}}{\partial \mathbf{q}} \cdot \mathbf{z} \quad (2.13)$$

The action generated by the Hamiltonian of eq 2.11 also increments discontinuously at the time t by the amount

$$\delta S = \hbar \boldsymbol{\mu}(t) \cdot \mathbf{z} \quad (2.14)$$

Application of the semiclassical approximation to the effective Hamiltonian in the coherent state representation brings the correlation function to the form

$$C(t) = -i(2\pi\hbar)^{-1} \frac{\partial}{\partial \mathbf{z}} \cdot \int d\mathbf{q}_0 \int d\mathbf{p}_0 D(\mathbf{q}_0, \mathbf{p}_0) \times \exp\left(\frac{i}{\hbar} S(\mathbf{q}_0, \mathbf{p}_0)\right) \langle G(\mathbf{q}_0, \mathbf{p}_0) | \rho_g \boldsymbol{\mu} | G(\mathbf{q}_f, \mathbf{p}_f) \rangle|_{\mathbf{z}=0} \quad (2.15)$$

III. Application to I_2 in an Ar cluster

The photodissociation of I_2 in a cluster environment has been an active testing ground for new theoretical propagation methods. Gerber and co-workers applied their classical separable potential based approach to this system calculating absorption and resonance Raman spectra.^{76,77} A so-called mixed-order semiclassical approach combining zeroth- and second-order approximations to the propagator has been used by Ovchinnikov et al. to obtain the absorption, emission, and resonance Raman profiles for I_2 in solid Kr.^{70,78}

Much effort has also been invested in the theoretical simulation of pump-probe spectra which show a pronounced pressure dependence.^{79,80} Purely classical molecular dynamics simulations,^{79,81} and quantum/classical hybrid methods,^{82,83} as well as the combination of quantum propagation for the early time dynamics with classical simulations for later times⁸⁴ have added much to the understanding of the relaxation/recombination dynamics in this system.

In this section we apply the FBSD expression for the linear absorption correlation function to the spectroscopy of the $X \rightarrow B$ electronic transition of an iodine molecule embedded in a cluster of argon atoms at finite temperature. In the absence of detailed information for the dipole moment function we restrict ourselves to the Condon approximation. Nonadiabatic transitions within the I_2 excited electronic state manifold do not play a significant role for the linear absorption profile⁷⁷ and therefore will be neglected. Further, to keep the matter simple we restrict ourselves to a linear chain configuration (see Figure 1) as has been done for the present system in^{82,83} and for the I_2 anion in Ar and Xe in refs 82 and 83.

The Cartesian coordinates and momenta of the two iodine atoms are denoted \mathbf{r}_i and \mathbf{p}_i ($i = 1, 2$), respectively, while those of the n Ar atoms are written as \mathbf{R}_j , \mathbf{P}_j ($j = 1, \dots, n$). In the actual calculation we will describe the solute by its relative (bond

TABLE 1: Parameters of the Morse Potential Describing the Ground and Excited States of I₂ (from Ref 79)

	D (cm ⁻¹)	λ (Å ⁻¹)	b (Å)	d (cm ⁻¹)
ground state	12547.2	1.875	2.656	0
excited state	4382.8	1.75	3.03	7605

distance) and center of mass coordinates $\tilde{\mathbf{r}}$ and \mathbf{R}_0 , respectively. The respective conjugate momenta are $\tilde{\mathbf{p}}$ and \mathbf{P}_0 . Employing a pairwise additive potential, the Hamiltonian takes the form

$$H = H_{I_2} + H_{\text{sol}} \quad (3.1)$$

where

$$H_{I_2} = \frac{\tilde{p}^2}{2\mu_{I_2}} + V_{I_2}(\tilde{r}) \quad (3.2)$$

describes the internal vibration of the iodine molecule and

$$H_{\text{sol}} = \sum_{i=1}^n \frac{\mathbf{P}_i^2}{2m_{\text{Ar}}} + \sum_{i>j}^n V_{\text{Ar-Ar}}(|\mathbf{R}_i - \mathbf{R}_j|) + \sum_{i=1}^n V_{\text{I-Ar}}(|\mathbf{r}_i - \mathbf{R}_i|) + \sum_{i=1}^n V_{\text{I-Ar}}(|\mathbf{r}_2 - \mathbf{R}_i|) + \frac{\mathbf{P}_0^2}{4m_1} + V_{\text{ext}}(\mathbf{R}_0 \dots \mathbf{R}_n) \quad (3.3)$$

is the Hamiltonian of the argon atoms and their interactions with the iodine molecule as well as the overall translation of the latter. The ground and excited-state potentials for I₂, Ar–Ar, and the I–Ar interaction are taken from ref 79. Specifically, the vibrational motion of I₂ is described by a Morse potential of the form

$$V_{I_2}(\tilde{r}) = D[\exp(-2\lambda(\tilde{r} - b)) - 2\exp(-\lambda(\tilde{r} - b))] + d$$

and the Ar–Ar and I–Ar interaction potentials are of the Lennard-Jones type:

$$V_{\text{LJ}}(\delta R) = 4\epsilon \left[\left(\frac{\sigma}{\delta R} \right)^{12} - \left(\frac{\sigma}{\delta R} \right)^6 \right]$$

with no distinction made for the ground and excited state of I₂. The parameters of these potentials are given in Tables 1 and 2. To mimic the effect of additional solvent atoms the system is placed in a box of length $2R_{\text{box}}$ (see Figure 1). For the external box potential entering eq 3.3, we chose the repulsive part of the Lennard-Jones potential with the parameters for the Ar–Ar interaction.

The initial density operator is approximated by the product

$$\rho(0) \approx \exp(-\beta H_{\text{sol}}) |\psi_{I_2}\rangle \langle \psi_{I_2}| \quad (3.4)$$

where $\psi_{I_2}(\tilde{r})$ is the wave function of the iodine molecule in the vibrational ground state of the ground electronic state. Note that H_{sol} is evaluated in eq 3.4 with the iodines fixed at their ground state equilibrium position. For simplicity, the ground state wave function for the solute is approximated by a Gaussian form,

$$\psi_{I_2}(\tilde{r}) = \left(\frac{2\alpha}{\pi} \right)^{1/4} \exp\{-\alpha(\tilde{r} - \tilde{r}_{\text{eq}})^2\} \quad (3.5)$$

where \tilde{r}_{eq} is the equilibrium bond length.

Since the Ar atoms are fairly heavy, we use the high-temperature approximation to calculate the solvent part of the Boltzmann matrix element. The density matrix elements in the

coherent state representation have been given in refs 12 and 13. With these assumptions the correlation function becomes

$$C(t) = 2^{3(n+2)} \prod_{k=1}^n \int d\mathbf{R}_{k,0} \int d\mathbf{P}_{k,0} \int d\mathbf{Q}_k \int d\mathbf{r}_{1,0} \int d\mathbf{p}_{1,0} \int d\mathbf{r}_{2,0} \int d\mathbf{p}_{2,0} D(\mathbf{r}_{1,0}, \mathbf{p}_{1,0}, \mathbf{r}_{2,0}, \mathbf{p}_{2,0}, \mathbf{R}_{k,0}, \mathbf{P}_{k,0}) \times f_{\text{norm}}(\mathbf{r}_{1,0}, \mathbf{p}_{1,0}, \mathbf{r}_{2,0}, \mathbf{p}_{2,0}, \mathbf{R}_{k,0}, \mathbf{P}_{k,0}, \mathbf{Q}_k) \times \exp\left(\frac{i}{\hbar} S(\mathbf{r}_{1,0}, \mathbf{p}_{1,0}, \mathbf{r}_{2,0}, \mathbf{p}_{2,0}, \mathbf{R}_{k,0}, \mathbf{P}_{k,0})\right) \times \exp\left(-\sum_{k=1}^n \frac{m_k}{m_k + \hbar^2 \beta \gamma_k} \left(\frac{\beta}{4m_k} \mathbf{P}_{k,f}^2 + \gamma_k |\mathbf{Q}_k - \mathbf{R}_{k,f}|^2 + \frac{i}{\hbar} \mathbf{Q}_k \cdot (\mathbf{P}_{k,0} - \mathbf{P}_{k,f}) - \frac{i}{\hbar} (\mathbf{P}_{k,0} \cdot \mathbf{R}_{k,0} - \mathbf{P}_{k,f} \cdot \mathbf{R}_{k,f}) \right)\right) \times \exp\left(-\frac{\alpha \gamma_0}{\alpha + \gamma_0} |\tilde{\mathbf{r}}_f - \tilde{\mathbf{r}}_{\text{eq}}|^2 - \frac{\tilde{p}_f^2}{4(\alpha + \gamma_0)} - \frac{i}{\hbar} \frac{\alpha}{\alpha + \gamma_0} (\tilde{\mathbf{p}}_0 \cdot (\tilde{\mathbf{r}}_0 - \tilde{\mathbf{r}}_{\text{eq}}) - \tilde{\mathbf{p}}_f \cdot (\tilde{\mathbf{r}}_f - \tilde{\mathbf{r}}_{\text{eq}}))\right) \quad (3.6)$$

In the above equation, \mathbf{Q}_k are auxiliary integration variables arising from the coherent state transform of the Boltzmann operator in the high-temperature approximation, and the normalized sampling function is given by the expression

$$f_{\text{norm}}(\mathbf{r}_{1,0}, \mathbf{p}_{1,0}, \mathbf{r}_{2,0}, \mathbf{p}_{2,0}, \mathbf{R}_{k,0}, \mathbf{P}_{k,0}, \mathbf{Q}_k) = \exp\left(-\sum_{k=1}^n \frac{m_k}{m_k + \hbar^2 \beta \gamma_k} \left(\frac{\beta}{4m_k} \mathbf{P}_{k,0}^2 + \gamma_k |\mathbf{Q}_k - \mathbf{R}_{k,0}|^2 - \frac{\alpha \gamma_0}{\alpha + \gamma_0} |\tilde{\mathbf{r}}_0 - \tilde{\mathbf{r}}_{\text{eq}}|^2 - \frac{\tilde{p}_0^2}{4(\alpha + \gamma_0)} \right)\right) \quad (3.7)$$

Details of the Monte Carlo procedure are discussed in ref 46.

We start our discussion by assessing the importance of correlations in the calculation of the determinant prefactor D in eq 3.6. In Figure 2 we plot a set of trajectories for the case of four Ar atoms. The initial conditions have been taken from a Monte Carlo sampling step at $T = 300$ K. The solute is in the excited state; i.e., the trajectories correspond to the forward propagation. The elements of the stability matrix entering eq 2.9 have been calculated by running for each selected set of initial conditions concurrent trajectories with slightly modified initial values such as to allow for a finite difference approximation to the derivatives in (2.9). The integration of the classical equations of motion was performed using the velocity Verlet algorithm.⁸⁵

Apparently, on the time scale covered in Figure 2 the factorized approximation is very accurate for these trajectories. As can be seen from the upper panel the deviation is only about 4% within the first 700 fs. Note that initially the I₂ is compressed to an extent that the energy on the excited state is above the dissociation threshold for this bond. The initial momenta are zero for all particles.

In Figure 3 we show a situation where the factorization approximation completely breaks down at longer times. From the forward trajectories propagated on the excited solute state the reason for this break down does not become obvious.

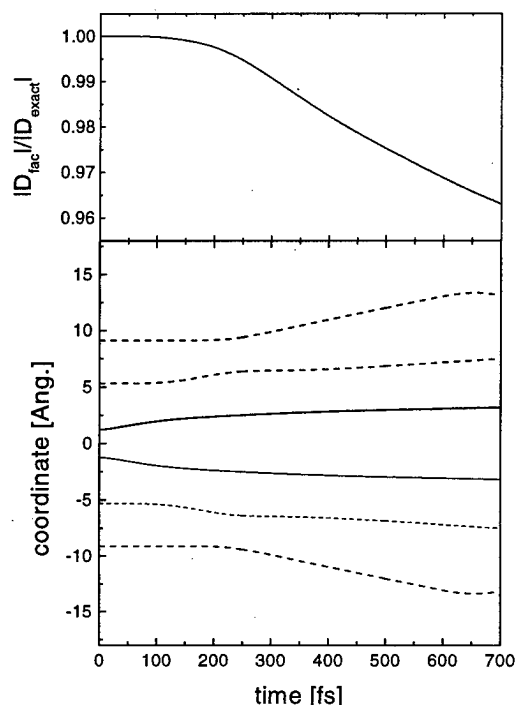


Figure 2. Classical trajectories and semiclassical prefactor for a linear chain of I_2 plus four Ar atoms. The solute dynamics is on the excited state (forward propagation). The external confining potential starts at $R_{\text{box}} = 14.6 \text{ \AA}$. This corresponds to the situation where for I_2 in the ground state the equilibrium I–Ar and Ar–Ar distances are equal to the Lennard-Jones minimum $2^{1/6}\sigma$. The initial conditions for the trajectories are taken from an arbitrary step in the Monte Carlo sampling of the integrals in eq 3.6. With this initial condition the forward and backward parts of the trajectories are nearly indistinguishable. The lower panel shows the coordinates of the I atoms (solid lines) and those of the Ar atoms (dashed lines). The upper panel shows the ratio between the absolute values of the factorized and the exact determinant.

TABLE 2: Parameters of the Lennard-Jones Potentials Describing the I–Ar and Ar–Ar Interactions (from Ref 79)

	$\epsilon \text{ (cm}^{-1}\text{)}$	$\sigma \text{ (\AA)}$
I–Ar	209.7	3.59
Ar–Ar	84.0	3.40

However, if one inspects the complete forward–backward trajectory as is done for the final time (700 fs) in the lower panel of Figure 3, the reason for the failure of the factorization approximation becomes transparent. Tracing their backward motion on the I_2 ground state, one observes an intramolecular I_2 collision and the attraction between an iodine and a neighboring Ar atom. These cause the final phase space points of the involved particles to become correlated, in contrast to the case shown in Figure 2 where the backward ground state trajectory traced the forward trajectory almost exactly for a final time of 700 fs. Figure 3 also suggests that one can improve the factorization approximation by including correlations between neighboring particles, for instance, those in the first solvation shell surrounding the solute. In this case the matrix (2.9) would take a block-diagonal form; the resulting ratio $|D_{\text{approx}}|/|D_{\text{exact}}|$ is shown as the dashed line in the upper panel of Figure 3. Including also the next-nearest-neighbor interaction with the Argon atom whose trajectory starts at about -8 \AA accounts for most of the correlations in the time interval examined (thin solid line in upper panel of Figure 3).

The broad absorption spectrum of I_2 is dominated by the short-time dynamics of the system. As shown, for example, in ref 39, the ground state wave packet once promoted to the

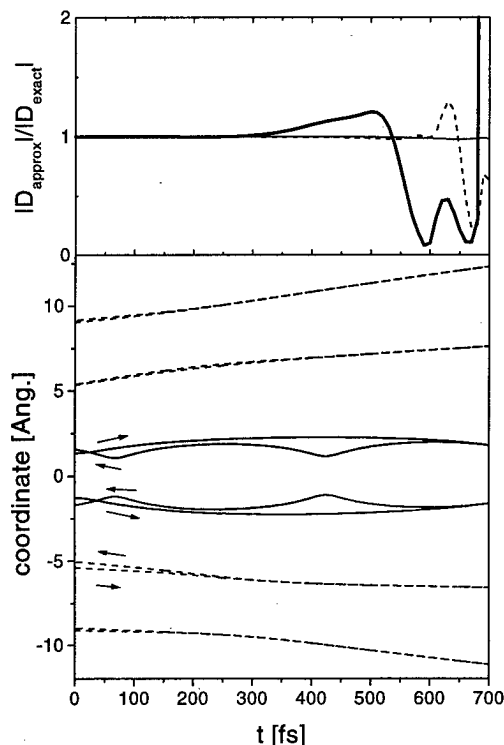


Figure 3. Same as in Figure 2 but for a different set of initial conditions. In addition to the forward trajectories on the I_2 excited state, the backward parts of the trajectories on the ground states are shown for the longest forward propagation time. The respective directions are indicated by arrows. In the upper panel the determinant for the full factorization (thick solid line) and block diagonal approximation (dashed: only first solvation shell; thin solid: additional inclusion of the argon whose trajectory starts at about -8 \AA) is compared to the exact determinant according to eq 2.9.

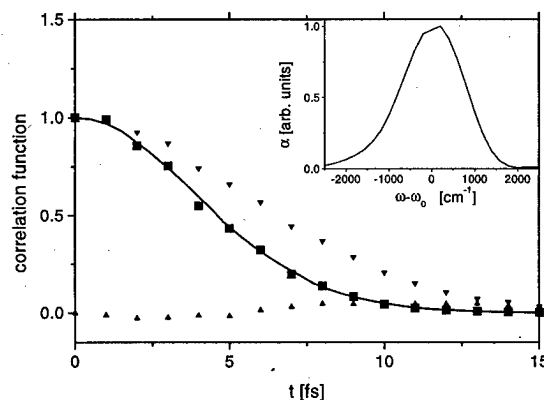


Figure 4. Comparison between the exact gas phase (solid line) and the FBSD condensed phase results (markers) for the correlation function of the $X \rightarrow B$ state Franck–Condon transition at room temperature. The triangles show the real and imaginary parts of the correlation function. The inset shows the spectrum taken with respect to the vertical transition frequency ω_0 .

excited state leaves the Franck–Condon region in about 15 fs. On this time scale the factorization approximation should perform rather well, judging from the two extreme cases shown in Figures 2 and 3. In Figure 4 we plot the correlation function for the I_2 plus four Ar atoms system using the factorized determinant. For each integration variable in eq 3.6 35 000 Monte Carlo points have been sampled with a rejection ratio for the Metropolis random walk of 50%. It turns out that the correlation function is nearly identical to the gas phase result which has been obtained by calculating the overlap $\langle \psi_{I_2} | \exp(-iH_{\text{et}}/\hbar) | \psi_{I_2} \rangle$ using the standard split-operator technique in

conjunction with a fast Fourier transform scheme for calculating the action of the kinetic energy operator.⁸⁶ This finding is in line with the fact that the spectrum is determined by the short-time dynamics in the Franck–Condon region where the gas phase potentials are not substantially altered by the interaction with the rare gas environment.

IV. Summary

The FBSD scheme for calculating correlation functions offers a straightforward and practical methodology for studying the dynamics and spectroscopy of polyatomic molecules and clusters. In the Condon approximation, the correlation function for the linear absorption spectrum involves a time evolution on the excited potential surface followed by reverse propagation on the ground state Hamiltonian. Combining both steps into a single semiclassical evolution eliminates the most severe oscillations of each separate semiclassical propagator, giving rise to a smooth integrand that invites the use of Monte Carlo methods. We have also discussed how the scheme can be formulated without reference to the Condon approximation. Furthermore, combination of the FBSD idea a stationary phase state switching procedure^{72–75} will lead to a powerful methodology for simulating nonlinear spectroscopies.

In the present paper we applied the FBSD procedure to calculate the absorption spectrum for the $X \rightarrow B$ transition of iodine embedded in a cluster of four argon atoms in a linear arrangement. In this case the spectrum is dominated by the short time dynamics of I_2 , which dissociates very rapidly once promoted to the excited B surface. As a consequence, the interaction with the Ar environment plays a minor role in determining the spectrum. Nevertheless, the present results obtained via the full semiclassical method are useful as benchmarks since the present system continues to serve as a testing ground for less rigorous approximations. It will be challenging to apply the FBSD methodology to other situations where persisting recurrences in the correlation function give rise to vibrational structure, while interaction with the medium results in line-shape broadening.

As the FBSD methodology reduces dramatically the severity of the Monte Carlo sign problem encountered in path integral or single-direction semiclassical treatments, the major computational overhead of the method is associated with the determinant prefactor. The latter requires costly propagation of the stability matrix as well as the evaluation of a determinant that scales as the third power of the number of degrees of freedom. In the present work we explored a few ways of simplifying this procedure. Full factorization of the determinant leads to an extremely efficient algorithm that reproduces the short-time dynamics rather faithfully. At longer times binary collisions become important and the factorization scheme breaks down. We found that following the full stability matrix of the solute plus one solvation shell leads to significant improvement while resulting in an economical block-diagonal form. Finally, we expect that inclusion of off-diagonal terms between neighboring atoms only will offer further increase in accuracy at little additional cost, as the resulting stability matrix will be tridiagonal. These procedures offer a promising starting point but further tests will be needed to establish the most fruitful approach to the semiclassical dynamics of polyatomic systems.

Acknowledgment. O.K. gratefully acknowledges financial support by the Deutsche Forschungsgemeinschaft (project Ku952/2-1). N.M. thanks the Packard Foundation and the National Science Foundation for supporting this work and the

Faculty of the National Hellenic Research Foundation for their hospitality during her sabbatical stay. We also thank Dr. Keiran Thompson for an early version of the code and useful discussions.

References and Notes

- (1) May, V.; Kühn, O. *Theory of charge and energy transfer in molecular systems*; Wiley: New York, 1999.
- (2) Jean, J.; Friesner, R. A.; Fleming, G. R. *J. Chem. Phys.* **1992**, *96*, 5827.
- (3) Kohen, D.; Marston, C. C.; Tannor, D. J. *J. Chem. Phys.* **1997**, *107*, 5236–5253.
- (4) Pollard, W. T.; Felts, A. K.; Friesner, R. A. *Adv. Chem. Phys.* **1996**, *XCIII*, 77.
- (5) Makri, N. *Chem. Phys. Lett.* **1992**, *193*, 435–444.
- (6) Makri, N.; Makarov, D. E. *J. Chem. Phys.* **1995**, *102*, 4600–4610.
- (7) Makri, N.; Makarov, D. E. *J. Chem. Phys.* **1995**, *102*, 4611–4618.
- (8) Sim, E.; Makri, N. *Comput. Phys. Commun.* **1997**, *99*, 335–354.
- (9) Makri, J. *Phys. Chem.* **1998**, *102*, 4414–4427.
- (10) Mak, C. H. *Phys. Rev. Lett.* **1992**, *68*, 899–902.
- (11) Mak, C. H.; Egger, R. *Phys. Rev. E* **1994**, *49*, 1997–2008.
- (12) Mak, C. H.; Egger, R. *Adv. Chem. Phys.* **1996**, *XCIII*, 39–76.
- (13) Makri, N. *J. Phys. Chem.* **1999**, *103*, 2823–2829.
- (14) Dirac, P. A. *Proc. Cambridge Philos. Soc.* **1930**, *26*.
- (15) Heller, E. J. *J. Chem. Phys.* **1976**, *64*, 63–73.
- (16) Harris, R. *J. Chem. Phys.* **1980**, *72*, 1776.
- (17) Mittleman, M. H. *Phys. Rev.* **1961**, *122*, 499.
- (18) Gerber, R. B.; Buch, V.; Ratner, M. A. *J. Chem. Phys.* **1982**, *77*, 3022–3030.
- (19) Wahnstrom, G.; Carmeli, B.; Metiu, H. *J. Chem. Phys.* **1988**, *88*, 2478–2491.
- (20) Tully, J. C.; Preston, R. K. *J. Chem. Phys.* **1971**, *55*, 562–572.
- (21) Tully, J. C. *J. Chem. Phys.* **1990**, *93*, 1061–1071.
- (22) Hammes-Schiffer, S.; Tully, J. C. *J. Chem. Phys.* **1994**, *101*, 4657–4667.
- (23) Hammes-Schiffer, S. *J. Chem. Phys.* **1996**, *105*, 2236.
- (24) Space, B.; Coker, D. F. *J. Chem. Phys.* **1992**, *96*, 652–663.
- (25) Coker, D. F.; Xiao, L. *J. Chem. Phys.* **1995**, *102*, 496–510.
- (26) Heller, E. J. *J. Chem. Phys.* **1975**, *62*, 1544–1555.
- (27) Heller, E. J. *J. Chem. Phys.* **1981**, *75*, 2923–2930.
- (28) Van Vleck, J. H. *Proc. Nat. Acad. Sci. U.S.A.* **1928**, *14*, 178.
- (29) Morette, C. *Phys. Rev.* **1952**, *81*, 848.
- (30) Miller, W. H. *Adv. Chem. Phys.* **1974**, *25*, 69.
- (31) Miller, W. H. *Adv. Chem. Phys.* **1975**, *30*, 77.
- (32) Herman, M. F.; Kluk, E. *Chem. Phys.* **1984**, *91*, 27–34.
- (33) Kluk, E.; Herman, M. F.; Davis, H. L. *J. Chem. Phys.* **1986**, *84*, 326–334.
- (34) Heller, E. J. *J. Chem. Phys.* **1991**, *94*, 2723.
- (35) Tomsovic, S.; Heller, E. J. *Phys. Rev. Lett.* **1991**, *67*, 664–667.
- (36) Sepulveda, M. A.; Tomsovic, S.; Heller, E. J. *Phys. Rev. Lett.* **1992**, *69*, 402–405.
- (37) Herman, M. F. *Annu. Rev. Phys. Chem.* **1994**, *45*, 83.
- (38) Walton, A. R.; Manolopoulos, D. E. *Mol. Phys.* **1996**, *84*, 961.
- (39) Brewer, M. L.; Hulme, J. S.; Manolopoulos, D. E. *J. Chem. Phys.* **1997**, *106*, 4832–4839.
- (40) Sun, X.; Miller, W. H. *J. Chem. Phys.* **1997**, *106*, 6346–6353.
- (41) Wang, H.; Sun, X.; Miller, W. H. *J. Chem. Phys.* **1998**, *108*, 9726–9736.
- (42) Sun, X.; Wang, H.; Miller, W. H. *J. Chem. Phys.* **1998**, *109*, 4190–4200.
- (43) Sun, X.; Wang, H.; Miller, W. H. *J. Chem. Phys.* **1998**, *109*, 7064–7074.
- (44) Makri, N.; Thompson, K. *Chem. Phys. Lett.* **1998**, *291*, 101–109.
- (45) Miller, W. H. *Faraday Discuss.* **1998**, *110*, 1–21.
- (46) Thompson, K.; Makri, N. *J. Chem. Phys.* **1999**, *110*, 1343–1353.
- (47) Thompson, K.; Makri, N. *Phys. Rev. E* **1999**, *59*, R4729–R4732.
- (48) Shao, J.; Makri, N. *J. Phys. Chem.* submitted for publication.
- (49) Batista, V.; Zanni, M. T.; Greenblatt, J.; Neumark, D. M.; Miller, W. H. *J. Chem. Phys.* **1999**, *110*, 3736–3747.
- (50) Thirumalai, D.; Berne, B. J. *J. Chem. Phys.* **1984**, *81*, 2512–2513.
- (51) Thirumalai, D.; Berne, B. J. *Comput. Phys. Commun.* **1991**, *63*, 415–426.
- (52) Behrman, E. C.; Jongeward, G. A.; Wolynes, P. G. *J. Chem. Phys.* **1983**, *79*, 6277–6281.
- (53) Cline, R. E.; Wolynes, P. G. *J. Chem. Phys.* **1987**, *86*, 3836.
- (54) Jarrell, M.; Gubernatis, J. E. *Phys. Rep.* **1996**, *269*, 133.
- (55) Galliccio, E.; Berne, B. J. *J. Chem. Phys.* **1996**, *105*, 7064–7078.
- (56) Gillan, M. J. *J. Phys. C* **1987**, *20*, 3621–3641.
- (57) Voth, G. A.; Chandler, D.; Miller, W. H. *J. Chem. Phys.* **1989**, *91*, 7749–7760.
- (58) Sun, Y.-C.; Voth, G. A. *J. Chem. Phys.* **1993**, *98*, 7451–7458.

- (59) Cao, J.; Voth, G. A. *J. Chem. Phys.* **1994**, *100*, 5106.
(60) Cao, J.; Voth, G. A. *J. Chem. Phys.* **1994**, *101*, 6157.
(61) Voth, G. A. *Adv. Chem. Phys.* **1996**, *XCIII*, 135.
(62) Gerber, R. B. *Chem. Rev.* **1999**, *99*, 1583–1606.
(63) Makri, N. *Adv. Chem. Phys.* **1999**.
(64) Makri, N. *Comput. Phys. Commun.* **1991**, *63*, 389–414.
(65) Mukamel, S. *Principles of nonlinear optical spectroscopy*; Oxford University Press: New York, 1995.
(66) Feynman, R. P.; Hibbs, A. R. *Quantum Mechanics and Path Integrals*; McGraw-Hill: New York, 1965.
(67) Schulman, L. S. *Techniques and applications of path integration*; John Wiley and Sons: New York, 1981.
(68) Batista, V. S.; Miller, W. H. *J. Chem. Phys.* **1998**, *108*, 498–510.
(69) Sun, X.; Miller, W. H. *J. Chem. Phys.* **1997**, *106*, 916–927.
(70) Ovchinnikov, M.; Apkarian, V. A. *J. Chem. Phys.* **1997**, *105*, 10312.
(71) Ovchinnikov, M.; Apkarian, V. A. *J. Chem. Phys.* **1998**, *108*, 2277–2284.
(72) Sepulveda, M. A.; Mukamel, S. *J. Chem. Phys.* **1995**, *102*, 9327–9344.
(73) Sepulveda, M. A.; Grossmann, F. *Adv. Chem. Phys.* **1996**, *XCVI*, 191.
(74) Spencer, C. F.; Loring, R. F. *J. Chem. Phys.* **1996**, *105*, 6596.
(75) Pentidis, S. A.; Loring, R. F. *Chem. Phys. Lett.* **1998**, *287*, 217.
(76) Jungwirth, P.; Fredj, E.; Gerber, R. B. *J. Chem. Phys.* **1996**, *104*, 9332–9339.
(77) Jungwirth, P.; Fredj, E.; Gerber, R. B. *J. Chem. Phys.* **1997**, *107*, 8963.
(78) Ovchinnikov, M.; Apkarian, V. A. *J. Chem. Phys.* **1997**, *106*, 5775–5778.
(79) Potter, E. D.; Liu, Q.; Zewail, A. H. *Chem. Phys. Lett.* **1992**, *200*, 605.
(80) Wan, C.; Gupta, M.; Baskin, J. S.; Kim, Z. H.; Zewail, A. H. *J. Chem. Phys.* **1997**, *106*, 4353–4356.
(81) Whitnell, R. M.; Wilson, K. R.; Yan, Y.; Zewail, A. H. *J. Mol. Liq.* **1994**, *61*, 153–165.
(82) Liu, L.; Guo, H. *J. Chem. Phys.* **1995**, *103*, 7851.
(83) Ka, J.; Shin, S. *Chem. Phys. Lett.* **1997**, *269*, 227.
(84) Yan, Y.; Whitnell, R. M.; Wilson, K. R. *Chem. Phys. Lett.* **1992**, *193*, 402–412.
(85) Swope, W. C.; Andersen, H. C.; Berens, P. H.; Wilson, K. R. *J. Chem. Phys.* **1982**, *76*, 637.
(86) Feit, M. D.; Fleck, J. A.; Steiger, A. *J. Comput. Phys.* **1982**, *47*, 412.

Quantum Dynamics and Vibrational Relaxation

S. A. Egorov,[†] K. F. Everitt, and J. L. Skinner*

Theoretical Chemistry Institute and Department of Chemistry, University of Wisconsin, Madison, Wisconsin 53706

Received: June 11, 1999; In Final Form: July 19, 1999

The accurate numerical calculation of general quantum time correlation functions for many-body systems is not possible at present. We discuss several schemes for obtaining approximate quantum time correlation functions using as input only the corresponding classical results, and assess the merits of each scheme by considering three exactly solvable model problems. We then turn to the problem of the vibrational energy relaxation of a high-frequency oscillator in a liquid, where the relaxation rate constant can be related to a certain quantum force–force time correlation function. Focusing specifically on the case of liquid oxygen, we calculate the classical force–force time correlation function using a molecular dynamics simulation and then determine various approximations to the relaxation rate constant by applying the schemes considered earlier. The Egelstaff scheme is found to lead to reasonable agreement with experiment.

I. Introduction

It is well-known that for condensed phase systems many experimental observables can be related theoretically to time correlation functions (TCFs) of appropriate dynamical variables. And in many cases it is essential that these TCFs be calculated quantum mechanically, since thermal energies can be small compared to the relevant energy splittings. While there is much interest, and has been much progress, in the numerical calculation of quantum TCFs for many-body interacting systems, a general, tractable, and reliable method is not yet at our disposal.

On the other hand, the calculation of classical TCFs for many-body interacting systems is commonplace, either by analytic methods or by molecular dynamics simulation. It would be very useful, therefore, if there was some reliable method by which one could obtain an approximate quantum TCF from its classical analogue. While a general solution to this problem seems unlikely, to say the least, several such approximation schemes have been discussed over the last 40 years.^{1,2} One of the purposes of this paper is to examine critically these approximation schemes by considering three exactly solvable model problems.

The other purpose of this paper is to apply these various approximation schemes to a problem of current theoretical and experimental interest, namely, condensed phase vibrational energy relaxation.^{3–6} A simple golden rule calculation shows that the state-to-state relaxation rate constant is related to the Fourier transform, at the oscillator frequency, of a certain quantum force–force TCF.⁷ If \hbar times the oscillator frequency is smaller than thermal energies, then it may be possible to approximate the quantum TCF simply by its classical analogue. If, however, the oscillator energy is much higher than thermal energies, the classical approximation is quite poor, and it becomes essential to use better approximations. As an example of this latter situation, we consider specifically the vibrational relaxation of neat liquid oxygen at 70 K.^{8,9}

II. Exact and Approximate Quantum Dynamics

Consider the quantum TCF for a general non-Hermitian operator A :

$$G(t) = (\langle A(t) A^\dagger(0) \rangle + \langle A^\dagger(t) A(0) \rangle)/2, \quad (1)$$

where the time dependence of any operator O is given by the Heisenberg expression

$$O(t) = e^{iHt/\hbar} O e^{-iHt/\hbar}, \quad (2)$$

H is the Hamiltonian of the system, and the ensemble average of operator O is

$$\langle O \rangle = \text{Tr}[e^{-\beta H} O] / \text{Tr}[e^{-\beta H}], \quad (3)$$

with $\beta = 1/kT$. This TCF is a complex function of t , but it is easy to show that it has the following time symmetries:¹⁰

$$G(-t) = G(t)^* = G(t - i\beta\hbar). \quad (4)$$

We will also be interested in the Fourier transform of the quantum TCF, defined by

$$\hat{G}(\omega) = \int_{-\infty}^{\infty} dt e^{i\omega t} G(t). \quad (5)$$

From the first of the time symmetries it follows that $\hat{G}(\omega)$ is real. It is also straightforward to show that $\hat{G}(\omega) \geq 0$. From the second time symmetry follows the detailed balance condition:¹⁰

$$\hat{G}(-\omega) = e^{-\beta\hbar\omega} \hat{G}(\omega). \quad (6)$$

Decomposing $G(t)$ into its real and imaginary parts:

$$G(t) = G_R(t) + i G_I(t), \quad (7)$$

[†] Present address: Department of Chemistry, University of Virginia, Charlottesville, VA 22901.

one can define the Fourier transforms

$$\hat{G}_S(\omega) = \int_{-\infty}^{\infty} dt e^{i\omega t} G_R(t), \quad (8)$$

$$\hat{G}_A(\omega) = i \int_{-\infty}^{\infty} dt e^{i\omega t} G_I(t), \quad (9)$$

so that of course

$$\hat{G}(\omega) = \hat{G}_S(\omega) + \hat{G}_A(\omega). \quad (10)$$

Since $G_R(t)$ and $G_I(t)$ are both real and are symmetric and antisymmetric functions of t , respectively, it is straightforward to show that $\hat{G}_S(\omega)$ and $\hat{G}_A(\omega)$ are both real and are symmetric and antisymmetric functions of ω , respectively.

The detailed balance condition shows that $\hat{G}_S(\omega)$ and $\hat{G}_A(\omega)$ are not independent, but in fact are related by¹

$$\hat{G}_A(\omega) = \hat{G}_S(\omega) \tanh(\beta\hbar\omega/2). \quad (11)$$

That means that $\hat{G}(\omega)$ can be related to either $\hat{G}_S(\omega)$ by

$$\hat{G}(\omega) = \frac{2}{1 + e^{-\beta\hbar\omega}} \hat{G}_S(\omega), \quad (12)$$

or to $\hat{G}_A(\omega)$ by

$$\hat{G}(\omega) = \frac{2}{1 - e^{-\beta\hbar\omega}} \hat{G}_A(\omega). \quad (13)$$

It is also clear that $G_R(t)$ and $G_I(t)$ are not independent; by expanding the hyperbolic tangent in eq 11 in powers of ω , performing the inverse Fourier transform term by term, and resumming, one sees that¹¹

$$G_I(t) = \tan\left(\frac{\beta\hbar}{2} \frac{d}{dt}\right) G_R(t). \quad (14)$$

The classical limit is defined by $\hbar \rightarrow 0$, and so we can define $G_{cl}(t)$ by $G_{cl}(t) = \lim_{\hbar \rightarrow 0} G(t)$. From eq 14 it is clear that in the classical limit $G_I(t) \rightarrow 0$, and since $G_R(t)$ is a symmetric function of time, so is $G_{cl}(t)$ (as is well-known). Furthermore, one sees from taking the classical limit of eq 6 that $\hat{G}_{cl}(\omega) = \hat{G}_{cl}(-\omega)$. Of particular interest is some sort of semiclassical approximation to $G(t)$, which will be approximately valid when $\hbar \neq 0$, and which does satisfy detailed balance. Below we will discuss four such schemes; for an excellent general discussion of these schemes the reader is referred to the book by Frommhold.¹

The first scheme, associated with the names of Litovitz,¹² Berne,¹⁰ and Oxtoby,⁷ which has also been discussed by Frommhold¹ (and probably by many others), and which we denote as the "standard" approximation, comes about as follows. In the classical limit by definition $G_R(t) = G_{cl}(t)$, and one can in fact expand $G_R(t)$ in powers of \hbar^2 ,¹³ $G_{cl}(t)$ being the zeroth-order term. The standard approximation is equivalent to simply taking $G_R(t) \approx G_{cl}(t)$, even when $\hbar \neq 0$, which at least ensures that $G_R(t)$ is a symmetric function of time. Defining

$$\hat{G}_{cl}(\omega) = \int_{-\infty}^{\infty} dt e^{i\omega t} G_{cl}(t), \quad (15)$$

eq 8 shows that within this approximation $\hat{G}_S(\omega) = \hat{G}_{cl}(\omega)$, and then one uses the exact equation 12 to determine $\hat{G}(\omega)$:

$$\hat{G}(\omega) = \frac{2}{1 + e^{-\beta\hbar\omega}} \hat{G}_{cl}(\omega). \quad (16)$$

As a result, $\hat{G}(\omega)$ does indeed satisfy detailed balance, and from it $G(t)$ can be obtained by inverse Fourier transformation.

The second approximation scheme, associated with the names of Wilson,¹⁴ Frommhold,¹ and Berne,¹⁵ which for reasons to become clear below we denote the "harmonic" approximation, can be obtained by expanding the tangent in eq 14 to lowest order in \hbar :

$$G_I(t) \approx \frac{\beta\hbar}{2} \frac{d}{dt} G_R(t). \quad (17)$$

Next, expanding (as above) $G_R(t)$ in powers of \hbar^2 and keeping only the zeroth-order term yields

$$G_I(t) \approx \frac{\beta\hbar}{2} \frac{d}{dt} G_{cl}(t). \quad (18)$$

Upon Fourier transformation we then obtain

$$\hat{G}_A(\omega) \approx \frac{\beta\hbar\omega}{2} \hat{G}_{cl}(\omega). \quad (19)$$

Finally, one then uses the exact eq 13 to obtain the approximation

$$\hat{G}(\omega) = \frac{\beta\hbar\omega}{1 - e^{-\beta\hbar\omega}} \hat{G}_{cl}(\omega). \quad (20)$$

Note that within this approximation $\hat{G}(\omega)$ also satisfies detailed balance, but, for example, is distinctly different from the standard approximation in eq 16.

The third approximation scheme, originally due to Schofield,¹⁶ can be obtained by combining ideas from the first two schemes (that is, to expand $G_R(t)$ to zeroth order in \hbar , and $G_I(t)$ to first order in \hbar), to arrive at the exact equation

$$G(t) = G_{cl}(t) + \frac{i\beta\hbar}{2} \frac{d}{dt} G_{cl}(t) + O(\hbar^2). \quad (21)$$

Now suppose that in fact $G(t) = G_{cl}(t + i\beta\hbar/2)$. Expansion to first order in \hbar gives precisely the above equation, and furthermore this approximation satisfies the required time symmetries for $G(t)$, which means, for example, that detailed balance is obeyed. In the frequency domain one obtains

$$\hat{G}(\omega) = e^{\beta\hbar\omega/2} \hat{G}_{cl}(\omega). \quad (22)$$

This simple and seemingly attractive approximation, again distinctly different from the first two, is called the "Schofield" approximation.

The fourth scheme, first discussed by Egelstaff,¹⁷ is closely related to the Schofield approximation. There is another form for $G(t)$ that also yields eq 21 when expanded to first order in \hbar , and also satisfies the required time symmetries, which is $G(t) = G_{cl}((t + i\beta\hbar)/2)$. This, the "Egelstaff" approximation, in the frequency domain gives¹⁸

$$\hat{G}(\omega) = e^{\beta\hbar\omega/2} \int_{-\infty}^{\infty} dt e^{i\omega t} G_{cl}(\sqrt{t^2 + (\beta\hbar/2)^2}). \quad (23)$$

One feature common to the first three schemes is that $\hat{G}(0) = \hat{G}_{cl}(0)$ (see eqs 16, 20, and 22), a result that is sometimes, but not generally, correct. The Egelstaff scheme, on the other hand, does not lead to this equality. The first three schemes also all give $\hat{G}(\omega) \geq 0$ (which, as discussed earlier, is always true for the exact quantum TCF), since $\hat{G}_{cl}(\omega) \geq 0$ (for example, from the Wiener-Khinchine theorem) and the multiplicative correction factors in eqs 16, 20, and 22 are all positive. The

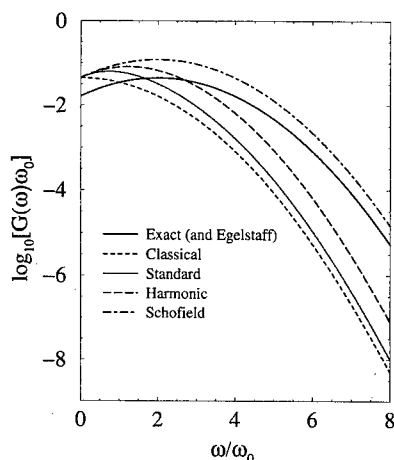


Figure 1. Exact and approximate $\hat{G}(\omega)$ for the free particle dynamic structure factor. $kT/\hbar\omega_0 = 1/2$.

Egelstaff scheme does not share this felicitous feature and can in fact sometimes lead to a negative $\hat{G}(\omega)$ (see below).

In summary, then, we have described four different semiclassical schemes for obtaining an approximation to the quantum TCF, each of which satisfies detailed balance, and each of which requires only the classical TCF as input. Our next step is to evaluate the merits and demerits of these four schemes by comparing results for three exactly solvable model problems.

III. Results for Exactly Solvable Model Problems

The first model involves the dynamic structure factor for a free particle in three dimensions. Thus $H = \vec{p} \cdot \vec{p}/2m$, where \vec{p} is the momentum and m is the mass of the particle, and $A = e^{i\vec{k} \cdot \vec{r}}$, where \vec{r} is the particle's position and \vec{k} is a wave vector. $G(t)$ as defined in eq 1 is then

$$G(t) = (F_s(\vec{k}, t) + F_s(-\vec{k}, t))/2, \quad (24)$$

where $F_s(\vec{k}, t)$ (the dynamic structure factor) is given by

$$F_s(\vec{k}, t) = \langle e^{i\vec{k} \cdot \vec{r}(t)} e^{-i\vec{k} \cdot \vec{r}(0)} \rangle. \quad (25)$$

$G(t)$ can be calculated exactly, with the result that¹⁹

$$G(t) = e^{-\omega_0^2 t(t + i\beta\hbar)}, \quad (26)$$

where $\omega_0^2 = k^2/2\beta m$. The classical limit is of course $G_{cl}(t) = e^{-\omega_0^2 t^2}$. One notices immediately that since in this case $G(t) = G_{cl}((t(t + i\beta\hbar))^{1/2})$ the Egelstaff scheme is exact! (This fact has been appreciated for some time.¹)

In this work we will be particularly interested in the frequency-domain comparison of the various approximation schemes. To this end we note that for this free-particle problem one can obtain simple analytic results for both $\hat{G}(\omega)$ and $\hat{G}_{cl}(\omega)$.

In Figure 1 we compare the exact results for $\hat{G}(\omega)$, with the various approximations to $\hat{G}(\omega)$ discussed earlier, as well as with $\hat{G}_{cl}(\omega)$, for $kT/\hbar\omega_0 = 1/2$. One sees that in this case the Schofield scheme provides the best approximation to the exact result, differing from it by a constant factor. (Recall again that the Egelstaff scheme is exact in this case.) The harmonic and standard approximations (as well as the classical result) all fall off significantly too fast as frequency increases.

The next exactly solvable problem involves a collection of harmonic oscillators with Hamiltonian $H = \sum_k \hbar \omega_k (b_k^\dagger b_k + 1/2)$, where ω_k are the mode frequencies and b_k^\dagger and b_k are the

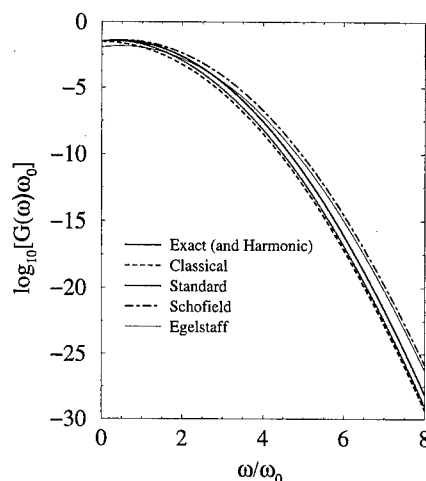


Figure 2. Exact and approximate $\hat{G}(\omega)$ for the harmonic/linear model. $kT/\hbar\omega_0 = 1/2$, $\lambda = 0.2$, and $\alpha = 1$.

creation and annihilation operators. We next define a collective coordinate by $q = \sum_k c_k (b_k^\dagger + b_k)$ (c_k are real expansion coefficients), and the TCF $C(t)$ by $C(t) = \langle q(t)q(0) \rangle$. Now taking A in eq 1 to be q , in this case we have $G(t) = C(t)$. (In the third model problem, discussed below, $C(t)$ will be defined as above but $G(t)$ will be different.)

The exact solution for $C(t)$ can be represented conveniently in terms of the spectral density $\Gamma(\omega) = \sum_k c_k^2 \delta(\omega - \omega_k)$ and thermal occupation number $n(\omega) = (e^{\beta\hbar\omega} - 1)^{-1}$ by²

$$C(t) = \int_0^\infty d\omega \Gamma(\omega) ([n(\omega) + 1] e^{-i\omega t} + n(\omega) e^{i\omega t}). \quad (27)$$

Note that the classical limit can be obtained easily from this expression to give

$$C_{cl}(t) = \frac{2}{\beta\hbar} \int_0^\infty d\omega \frac{\Gamma(\omega)}{\omega} \cos(\omega t). \quad (28)$$

(c_k are implicitly proportional to $\hbar^{1/2}$, and so $\Gamma(\omega)$ is implicitly proportional to \hbar^2 .) Note also that in this case these two equations lead to the exact equality

$$G_1(t) = \frac{\beta\hbar}{2} \frac{d}{dt} G_{cl}(t). \quad (29)$$

Recall that for a general TCF this equation is only correct to first order in \hbar , and so the previously discussed "harmonic" scheme derived from this equation is (in general) only an approximation. But since for this harmonic model this equation is exact, it means that the "harmonic" approximation scheme is exact for this model, hence the name.

To present explicit calculations for this model we must specify the form of the spectral density, for which we choose (see also Egorov and Berne²⁰):

$$\Gamma(\omega) = 2\lambda \frac{\omega^\alpha}{\omega_0^{\alpha+1}} e^{-\omega^2/\omega_0^2}, \quad (30)$$

with α equal to 1 or 3. For either value of α , $\Gamma(\omega)$ is normalized according to

$$\int_0^\infty d\omega \Gamma(\omega) = \lambda. \quad (31)$$

In Figure 2 we show our calculations for $\hat{G}(\omega)$ for this model, taking $\alpha = 1$ ("Ohmic dissipation"), $\lambda = 0.2$, and $kT/\hbar\omega_0 = 1/2$. As in the previous case all results can be obtained

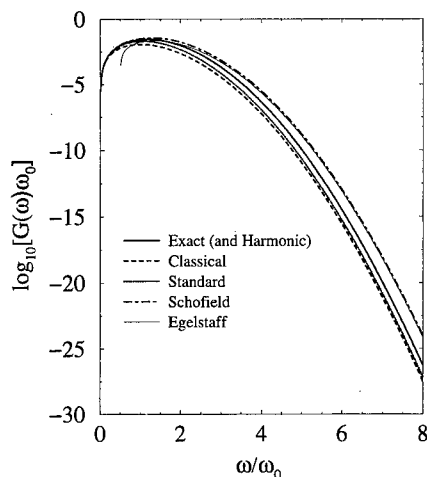


Figure 3. Exact and approximate $\hat{G}(\omega)$ for the harmonic/linear model. $kT/\hbar\omega_0 = 1/2$, $\lambda = 0.2$, and $\alpha = 3$.

analytically. One sees that (except for small frequencies) both Schofield and Egelstaff overestimate the value of $\hat{G}(\omega)$, while the standard approximation (and the purely classical result) are underestimates. (Recall again that in this case the harmonic approximation is exact.) Note the scale on the ordinate! Even when the value of $\hat{G}(\omega)$ has decreased by 20 orders of magnitude, the worst approximation scheme is only off by 2 orders of magnitude.

In Figure 3 we show results for the same parameters except now $\alpha = 3$. As in the case for $\alpha = 1$ all approximate and exact results can be obtained analytically. The Egelstaff scheme actually goes negative for $\omega/\omega_0 < 1/2$! For higher frequencies the Schofield and Egelstaff approximations overestimate, and the standard and classical approximations underestimate, the exact (and harmonic) result. Note again, however, that none of the approximation schemes is too bad at high frequency, even when the value of $\hat{G}(\omega)$ has dropped dramatically.

Our final exactly solvable model is closely related to the above.² The Hamiltonian is harmonic (as above), and q is defined identically as above, but now $A = e^q - \langle e^q \rangle$. In this case the TCF is

$$G(t) = \langle e^{q(t)} e^{q(0)} \rangle - \langle e^q \rangle^2. \quad (32)$$

The exact solution to this TCF is given by²¹

$$G(t) = e^{C(t)} (e^{C(t)} - 1), \quad (33)$$

where $C(t)$ is given by eq 27. As before, the time domain results can all be obtained analytically, but now the Fourier transforms must be performed numerically.

Our numerical results for the same parameters as in Figure 2 are shown in Figure 4. One sees that for this model at high frequencies the different approximations are quite different. The Egelstaff result, while clearly an overestimate, is the closest to the exact result. Results for the same parameters as in Figure 3 are shown in Figure 5. In this case the Egelstaff result again becomes negative for low frequencies, while at high frequencies it is the best approximation.

To summarize this section, for the dynamic structure factor for the free particle the Egelstaff result is exact, and the Schofield result is off by a constant factor. The harmonic result can easily be off by several orders of magnitude, especially at high frequencies and low temperatures. For the harmonic model the harmonic result is exact, and the Egelstaff and other

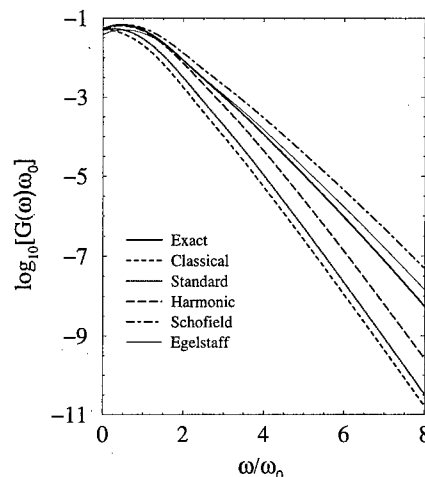


Figure 4. Exact and approximate $\hat{G}(\omega)$ for the harmonic/exponential model. $kT/\hbar\omega_0 = 1/2$, $\lambda = 0.2$, and $\alpha = 1$.

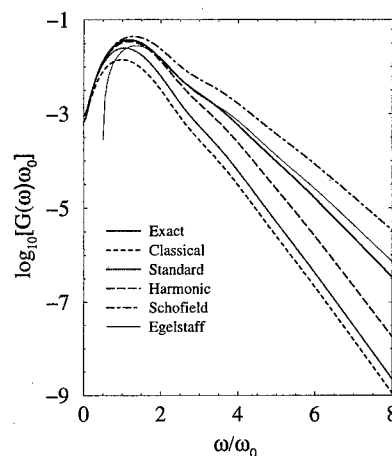


Figure 5. Exact and approximate $\hat{G}(\omega)$ for the harmonic/exponential model: $kT/\hbar\omega_0 = 1/2$, $\lambda = 0.2$, and $\alpha = 3$.

approximations can be off by several orders of magnitude. For the model involving an exponential function of harmonic coordinates, none of the approximation schemes is exact, but the Egelstaff approximation generally performs significantly better than the other schemes. The Egelstaff scheme does, however, suffer from the unfortunate drawback that it can lead to negative (unphysical) results at low frequencies.

So we clearly do not yet have a satisfactory solution to this problem. Indeed, it would not be reasonable to expect one of these simple schemes, involving only the classical TCF, to be able to reproduce the quantum TCF for all physical situations. Nonetheless, under certain circumstances, one or more of these schemes may provide reasonable approximations to the quantum TCF.

IV. Applications to Vibrational Relaxation in Liquid Oxygen

In this section we apply the ideas discussed above to the physical problem of vibrational energy relaxation (VER) in liquids. To be specific, consider the VER of neat liquid oxygen, for which experimental measurements of the vibrational state-to-state ($\nu = 1$ to $\nu = 0$) relaxation rate constant have been performed.⁸ While vibration-vibration (excitonic) energy transfer is surely rampant in liquid oxygen, the experiments measure only the total population of the $\nu = 1$ state, independent of whether it has transferred from molecule to molecule during the course of the experiment. The relaxation mechanism must

therefore be due solely to vibration–translation and vibration–rotation channels.⁹

The simplest way to approach this problem divides the Hamiltonian into system, bath, and interaction components. The system is the harmonic oscillator for a single oxygen molecule, the bath consists of the translations and rotations of all the oxygen molecules (including the “tagged” one), and the interaction involves the force exerted by the neighboring molecules on the bond of the tagged one. Within this picture the VER state-to-state rate constant can be calculated using Fermi’s golden rule. Translated into the TCF language one finds that^{9,22}

$$k_{1-0} = \frac{\hat{G}(\omega_0)}{2\mu\hbar\omega_0} \quad (34)$$

where $G(t) = \langle \delta F(t) \delta F(0) \rangle$ is the quantum TCF of the force fluctuations on the tagged molecule’s bond, and μ and ω_0 are the reduced mass and frequency of the oscillator. Such a quantum TCF, for say 500 interacting oxygen molecules, is not possible to calculate at present. And so in order to proceed one is forced to consider the approximation schemes discussed herein.

Of course, the big question is which (if any) of the approximation schemes is appropriate for this problem? There are several issues to consider. The first involves simply the ratio of the oscillator frequency (1552.5 cm^{-1} for oxygen) compared to kT (about 50 cm^{-1}) at 70 K. The large size of this ratio indicates that quantum effects are likely to be important (that is, the purely classical approximation to calculating $\hat{G}(\omega)$ will fail).

One way to think about the VER process in this system is similar to multiphonon relaxation in crystals.^{23,24} That is, one considers the translations and rotations of the oxygen molecules in the liquid to be more or less harmonic, with characteristic frequencies on the order of 50 or 100 cm^{-1} (above which, for example, the Fourier transforms of the velocity or angular velocity TCFs decay considerably). Since the energy gap of the system is much larger than that, to emit one quantum of oxygen vibration one must create many quanta of translations and rotations.^{9,20,22,25,26} This is possible since the force is a strongly nonlinear function of the (nearly) harmonic coordinates. This picture is reminiscent of the third model discussed in the previous section—that of a harmonic bath, but the TCF involves an exponential function of the coordinates. In that case for the high-frequency Fourier transform of the TCF we found that the Egelstaff approximation was the best, implying to us that it might also be the most appropriate approximation scheme for the oxygen problem.

An alternative picture is that, presumably because of central limit theorem arguments, the (classical) force on a given molecule describes a Gaussian random process. As such, this force can be thought of as a “coordinate” of an effective harmonic bath, which because of nonlinear couplings within the bath has a spectral density that extends well past the characteristic frequencies described in the preceding paragraph. In this view, then, the VER process corresponds to the creation of only one quantum of a very high frequency effective “mode” of the bath. This picture is equivalent to the purely harmonic model discussed in the previous section (the bath is harmonic and the TCF involves a linear function of the coordinates). To the extent that this scenario is valid, then, the harmonic approximation discussed above might be the most appropriate scheme for the oxygen problem. To assess the validity of this picture, one can consider, for example, a special case of the

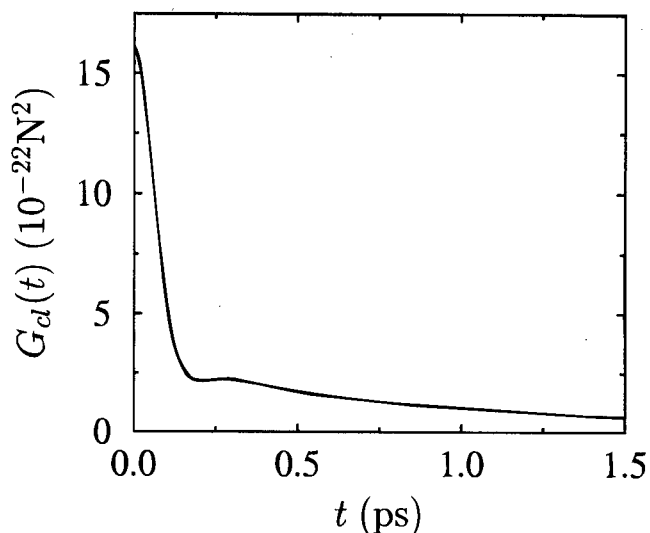


Figure 6. Classical force–force TCF for liquid oxygen at 70 K.

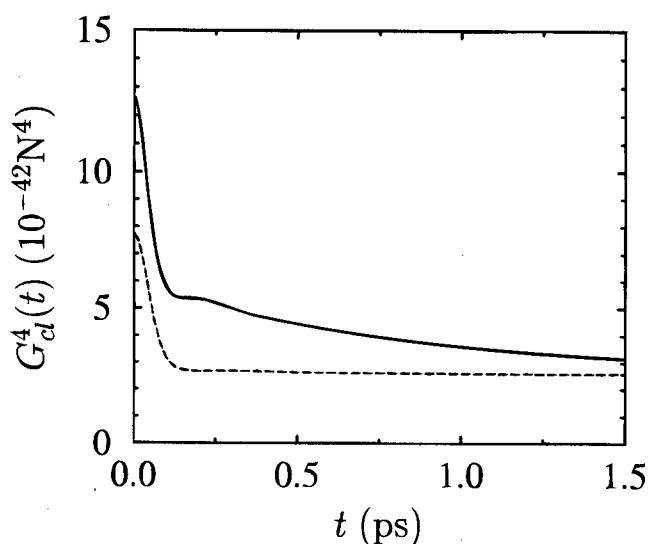


Figure 7. Comparison of $\langle \delta F(t)^2 \delta F(0)^2 \rangle_{\text{cl}}$ (solid line) and $\langle \delta F^2 \rangle_{\text{cl}}^2 + 2G_{\text{cl}}(t)^2$ (dashed line).

four-point TCF: $G_{\text{cl}}^4(t) = \langle \delta F(t)^2 \delta F(0)^2 \rangle_{\text{cl}}$, which if the force is “Gaussian” should be equal to $\langle \delta F^2 \rangle_{\text{cl}}^2 + 2G_{\text{cl}}(t)^2$.

We have performed a classical molecular dynamics simulation of neat rigid oxygen at 70 K,^{9,27} and from the simulation we have obtained the fluctuating force on the bond of a tagged oxygen molecule. Our result for $G_{\text{cl}}(t)$ is shown in Figure 6. In Figure 7 we show the comparison of the four-point TCF discussed above and its Gaussian decomposition. We see in fact that the force does not appear to be very Gaussian. This is really not surprising: since the intermolecular force is such a quickly varying function of distance, essentially only a few neighboring molecules contribute to the total force on a given molecule at any given time,²⁶ whereas for the central limit theorem to apply one needs many independent and roughly equal magnitude contributions. This observed non-Gaussian behavior of the fluctuating force would seem to indicate that the harmonic approximation scheme would not be appropriate for oxygen.

The Fourier transform of $G_{\text{cl}}(t)$ is shown in Figure 8. Also shown is the Egelstaff approximation to $\hat{G}(\omega)$, obtained from eq 23 numerically. It is seen that the Fourier transforms are only reliable up to about 500 or 600 cm^{-1} , whereas according to eq 34 they need to be evaluated at 1552.5 cm^{-1} . We have discussed several approaches toward extending the frequency

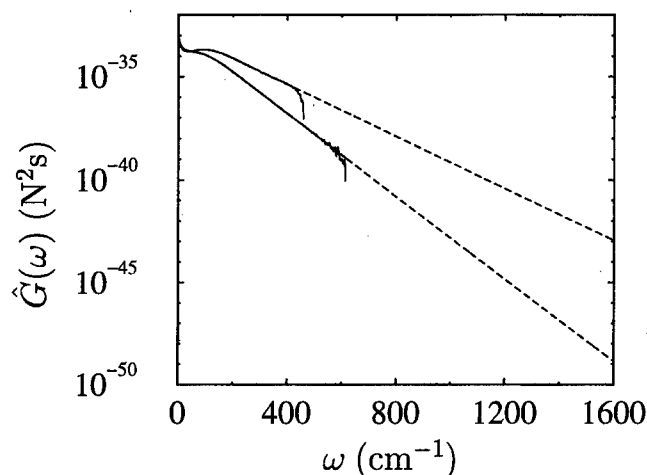


Figure 8. Classical (lower) and Egelstaff (upper) approximations to $\hat{G}(\omega)$ for liquid oxygen. The solid lines are directly calculated from $G_{cl}(t)$, while the dashed lines are their extrapolations to high frequency.

TABLE 1: $k_{1 \rightarrow 0}$ at 70 K for Liquid Oxygen, Theory and Experiment^a

experiment ⁸	360	harmonic	0.015
classical	0.00047	Egelstaff	270
standard	0.00095	Schofield	4030

^a All numbers in units of s^{-1} .

range, using the Wiener–Khinchine theorem, or using an analytical ansatz for $G_{cl}(t)$ whose parameters can be determined from a short-time expansion.⁹ Here we simply perform a linear (on a log plot) extrapolation of the displayed Fourier transforms, which is essentially equivalent to assuming that the VER rate exhibits an exponential energy gap law.^{22,28}

Using these results, eq 34, and the expressions in section II, we can then compare the predictions of the various approximation schemes to the VER rate for the oxygen problem. The different results, together with the experimental rate, are shown in Table 1. One sees that the different approximation schemes give wildly different results, that the classical result is off by orders of magnitude (as anticipated), that the harmonic approximation is not in good agreement with experiment (also as anticipated), and that the Egelstaff approximation is in surprisingly good agreement with experiment.

Of course the success of the Egelstaff result could be fortuitous, arising from a cancellation of errors due to (1) the approximation scheme, (2) the extrapolation to high frequencies, and (3) the intermolecular potential. While we cannot rule out any of these possibilities, regarding the third one we do note that this same system has been studied using a potential function with quite different parameters, and the result for the VER rate is similar (differing by about a factor of 5).²⁹

V. Conclusion

The accurate numerical calculation of quantum time correlation functions for many-body systems is not yet at hand. We have discussed several schemes for obtaining approximate quantum TCFs using as input only the corresponding classical TCFs and have tried to assess the merits of each scheme by comparing the results for exactly solvable model problems. It

is clear that no scheme will work well for all physical problems. We then considered the difficult theoretical problem of the energy relaxation of a high-frequency vibration in a simple liquid. Our calculations indicate that for liquid oxygen at 70 K the Egelstaff scheme may provide a reasonable approximation to the required quantum force–force TCF.

Note Added in Proof. From Figures 4 and 5 one can see that for the harmonic/exponential model the logarithmic average of the harmonic and Schofield approximations would agree quite well with the exact results. Such an average produces the approximation

$$\hat{G}(\omega) = e^{\beta \hbar \omega / 4} \left(\frac{\beta \hbar \omega}{1 - e^{-\beta \hbar \omega}} \right)^{1/2} \hat{G}_{cl}(\omega).$$

This new suggestion does not have strong theoretical justification, and may or may not be a good approximation for specific systems (for example, for the liquid oxygen problem at 70 K it gives $k_{1 \rightarrow 0} \approx 8 \text{ s}^{-1}$). But it does satisfy the basic symmetry requirements of a quantum TCF, and does not suffer from the low-frequency problems of the Egelstaff approximation.

Acknowledgment. The authors thank Branka Ladanyi, Bruce Berne, and Rich Stratt for helpful discussions. The authors are grateful for support from the National Science Foundation (grant no. CHE-9816235).

References and Notes

- Frommhold, L. *Collision-induced absorption in gases*, 1st ed.; Cambridge Monographs on Atomic, Molecular, and Chemical Physics, Vol. 2; Cambridge University Press: London, 1993.
- Egorov, S. A.; Skinner, J. L. *Chem. Phys. Lett.* **1998**, 293, 469.
- Stratt, R. M.; Maroncelli, M. *J. Phys. Chem.* **1996**, 100, 12981.
- Owrutsky, J. C.; Raftery, D.; Hochstrasser, R. M. *Annu. Rev. Phys. Chem.* **1994**, 45, 519.
- Harris, C. B.; Smith, D. E.; Russell, D. J. *Chem. Rev.* **1990**, 90, 481.
- Oxtoby, D. W. *J. Phys. Chem.* **1983**, 87, 3028.
- Oxtoby, D. W. *Adv. Chem. Phys.* **1981**, 47 (Part 2), 487.
- Faltermeier, B.; Protz, R.; Maier, M. *Chem. Phys.* **1981**, 62, 377.
- Everitt, K. F.; Egorov, S. A.; Skinner, J. L. *Chem. Phys.* **1998**, 235, 115.
- Berne, B. J.; Harp, G. D. *Adv. Chem. Phys.* **1970**, 17, 63.
- Barocchi, F.; Moraldi, M.; Zoppi, M. *Phys. Rev. A* **1982**, 26, 2168.
- An, S. C.; Montrose, C. J.; Litovitz, T. A. *J. Chem. Phys.* **1976**, 64, 3717.
- Bafle, U.; Ulivi, L.; Zoppi, M.; Pestelli, S. *Mol. Phys.* **1993**, 79(1), 179.
- Berens, P. H.; White, S. R.; Wilson, K. R. *J. Chem. Phys.* **1981**, 75, 515.
- Bader, J. S.; Berne, B. J. *J. Chem. Phys.* **1994**, 100(11), 8359.
- Schofield, P. *Phys. Rev. Lett.* **1960**, 4, 239.
- Egelstaff, P. A. *Adv. Phys.* **1962**, 11, 203.
- Berne, B. J.; Jortner, J.; Gordon, R. *J. Chem. Phys.* **1967**, 47(5), 1600.
- Kneller, G. R. *Mol. Phys.* **1994**, 83, 63.
- Egorov, S. A.; Berne, B. J. *J. Chem. Phys.* **1997**, 107, 6050.
- Nitzan, A.; Mukamel, S.; Jortner, J. *J. Chem. Phys.* **1975**, 63, 200.
- Egorov, S. A.; Skinner, J. L. *J. Chem. Phys.* **1996**, 105(16), 7047–58.
- Egorov, S. A.; Skinner, J. L. *J. Chem. Phys.* **1995**, 103, 1533.
- Egorov, S. A.; Skinner, J. L. *J. Chem. Phys.* **1996**, 105, 10153.
- Kenkre, V. M.; Tokmakoff, A.; Fayer, M. D. *J. Chem. Phys.* **1994**, 101, 10618.
- Larsen, R. E.; Stratt, R. M. *J. Chem. Phys.* **1999**, 110, 1036.
- Everitt, K. F.; Skinner, J. L. *J. Chem. Phys.* **1999**, 110, 4467.
- Rostkier-Edelstein, D.; Graf, P.; Nitzan, A. *J. Chem. Phys.* **1997**, 107, 10470.
- Ladanyi, B. M., private communication.

On Obtaining Reactive Potential Energy Surfaces from Transition State Photodetachment Spectra. I. Sensitivity Analysis

Ward H. Thompson[†]

Department of Chemistry, University of California, Berkeley, California 94720, and Department of Chemistry and Biochemistry, University of Colorado, Boulder, Colorado 80309-0215

Received: June 17, 1999; In Final Form: October 1, 1999

We investigate the possibility of obtaining potential energy surfaces for chemical reactions from experimental photodetachment spectra by carrying out a sensitivity analysis. Specifically, the variations of the theoretical photodetachment spectrum with respect to the values of the potential on a grid of points (the “derivatives” of the spectrum) are calculated. We show how these derivatives can be obtained at no extra cost beyond that required to obtain the spectrum. Sensitivity analysis is performed on one- and two-degrees-of-freedom model photodetachment systems. The results are discussed in the context of the prospects for the “inversion” of transition state spectra to obtain potential surfaces in reactive systems.

1. Introduction

For a chemical reaction, the barrier region is the most difficult part of the potential energy surface to obtain by electronic structure calculations, yet it is the most important in determining reactivity. A method for extracting this information from experimental measurements would thus be very useful. It is well established that transition state (photodetachment) spectroscopy experiments can directly probe the barrier region of a reactive potential energy surface.^{1–4} In these experiments a bound anion (e.g., ABC^-) is formed, the excess electron is detached by a photon of fixed energy to form the unstable neutral species (ABC^*), and the kinetic energy of the detached electron is measured. The resulting electron kinetic energy spectrum contains information about the reactive neutral potential energy surface (governing the $A + BC \rightarrow AB + C$ reaction). In particular, if the geometry of the anion is similar to that of the “activated complex” on the neutral surface, the spectrum contains detailed information about the neutral transition state. In this case, the spectrum will consist of peaks at the vibrational energy levels of the neutral activated complex (with intensities governed by the Franck–Condon overlap of the anion bound state and neutral scattering wave functions) with widths determined by the lifetimes of these states.

These experiments possess a number of advantages over conventional scattering experiments. For example, in reactive scattering experiments the measured cross sections include effects due to the entrance and exit valleys of the potential surface. However, the information about the barrier region contained in transition state spectra is not obscured in this way. Also, the information contained in the spectra is not averaged over many partial waves, which clouds the details of the reaction dynamics. This is actually a two-fold advantage as the corresponding theoretical calculations are more easily performed.

A straightforward method for obtaining a potential energy surface from a spectrum is a perturbative approach. That is, one calculates how the spectrum is affected (to first order) by changes in the neutral reactive potential, i.e., the “derivatives” of the spectrum. Given an experimental spectrum, these deriva-

tives can be used to obtain the potential surface giving the theoretical spectrum in best agreement with the experimental one. This can be accomplished by an iterative scheme in which, at each step, the potential is modified, using the derivatives, to minimize the “error” (i.e., the deviation of the theoretical spectrum from the experimental one) until convergence is reached. The following paper in this issue describes and applies such an approach.⁵

However, it is important to first understand what information is contained in transition state spectra before attempting to invert experimental spectra to obtain potential energy surfaces. Sensitivity analysis is a useful tool in determining an appropriate approach for inverting experimental spectra. For example, it can be used to decide if a “point-by-point” representation can be obtained from the spectra, if information about the barrier can be extracted when the Franck–Condon region does not overlap the transition state, and if spectra from vibrationally excited states of the anion can provide additional information. In this paper we address the question—To what part of the neutral potential energy surface are the photodetachment spectra sensitive? This question can be answered by examining the derivatives of the spectrum discussed above.

The theoretical approach for calculating photodetachment spectra and their derivatives with respect to potential parameters is described in Section 2. Particularly, we show how these derivatives can be obtained with no extra computational effort beyond that needed to calculate the photodetachment spectrum itself. To illustrate the basic features of the sensitivity of the photodetachment spectra to the neutral potentials, this method is implemented for two model transition state spectroscopy systems in Section 3. The results are discussed in terms of the prospects for inverting spectra to obtain potential energy surfaces. Finally, concluding remarks are given in Section 4.

2. Theory

In this section we review the theoretical methodology developed previously^{6,7} for efficiently calculating anion photodetachment intensities. We also show how this approach can be extended to calculate the derivatives of the photodetachment intensities with respect to parameters of the neutral potential surface with no extra computational cost.

[†] Current address. University of Colorado.

Consider a potential energy surface for a chemical reaction defined by a set of M parameters $\alpha = \{\alpha_j\}_{j=1,\dots,M}$. For example, the set α could be the values of the potential on a grid of points or the parameters in an analytical representation. The derivative $\partial I(E)/\partial \alpha_j$ indicates the first order dependence of the spectrum $I(E)$ on one of the parameters, α_j , and is thus a measure of the sensitivity of the spectrum to α_j . For example, if $\partial I(E)/\partial \alpha_j \approx 0$ then a small change in α_j will not change the spectrum. However, if $\partial I(E)/\partial \alpha_j$ has significant magnitude, varying α_j will modify the photodetachment intensity at energy E . Naturally, the derivative will depend on the value of α_j and the energy E at which this derivative is evaluated.

The photodetachment intensity is given within the Franck–Condon approximation as

$$I(E) = \rho(E) \sum_{\mathbf{n}} |\langle \Psi_{\mathbf{n}}^+(E) | \phi_b \rangle|^2, \quad (1)$$

where $\Psi_{\mathbf{n}}^+(E)$ is the scattering wave function on the neutral surface at energy E with outgoing wave boundary conditions and asymptotic quantum numbers \mathbf{n} , $\rho(E)$ is the neutral density of states, and ϕ_b is the bound state wavefunction of the anion. As shown previously,⁶ the photodetachment spectrum can be obtained using a discrete variable representation^{8–10} (DVR) Green's function with absorbing boundary conditions^{11–15} (ABC). In this formulation, the photodetachment intensity is given by⁶

$$I(E) = -\frac{1}{\pi} \text{Im} \phi_b^T \cdot \mathbf{G}^+(E) \cdot \phi_b \quad (2)$$

where ϕ_b is the anion bound state wavefunction vector in the DVR basis and $\mathbf{G}^+(E)$ is the DVR-ABC Green's function,¹⁶

$$\mathbf{G}^+(E) = (E\mathbf{I} - \mathbf{H} + i\epsilon)^{-1} \quad (3)$$

with outgoing wave boundary conditions (as indicated by the superscript +). Here, $\mathbf{H} = \mathbf{T} + \mathbf{V}$ is the Hamiltonian matrix for the neutral species in the DVR basis and \mathbf{T} , \mathbf{V} , and ϵ are the kinetic energy, potential, and absorbing potential DVR matrices, respectively.

A prime advantage of this approach is that, in principle, the entire photodetachment spectrum can be obtained in a single calculation using the multiply shifted quasi-minimal residual (QMRES) method¹⁷ for acting the Green's function on the anion bound state.⁷ This is possible because the state upon which the Green's function is acted, ϕ_b , does not depend on the scattering energy. The reader is referred to ref 7 for a detailed description of this approach; here we concentrate only on the features relevant to the problem of calculating the sensitivity of photodetachment spectra.

In the expression for the photodetachment intensity in eq 2, the neutral potential energy surface appears only in the Green's function. Thus, taking the derivative of the photodetachment intensity with respect to a potential parameter α_j gives

$$\frac{\partial I(E)}{\partial \alpha_j} = -\frac{1}{\pi} \text{Im} \phi_b^T \cdot \mathbf{G}^+(E) \cdot \frac{\partial \mathbf{V}}{\partial \alpha_j} \cdot \mathbf{G}^+(E) \cdot \phi_b \quad (4)$$

Note that, in the DVR, the potential operator, which is only a function of position, is approximated as a diagonal matrix with each diagonal element equal to the potential evaluated at the corresponding DVR grid point. If we define the scattering wavefunction,

$$\Phi_b^+(E) = \mathbf{G}^+(E) \cdot \phi_b \quad (5)$$

then

$$\Phi_b^+(E)^T = \phi_b^T \cdot \mathbf{G}^+(E) \quad (6)$$

(Note the absence of complex conjugation.) Then, eq 4 can be compactly written as

$$\frac{\partial I(E)}{\partial \alpha_j} = -\frac{1}{\pi} \text{Im} \Phi_b^{+T}(E) \cdot \frac{\partial \mathbf{V}}{\partial \alpha_j} \cdot \Phi_b^+(E) \quad (7)$$

Analogous equations for this derivative have previously been derived in a time-dependent framework by Baer and Kosloff¹⁸ and in a time-independent formulation by Wu and Zhang.¹⁹ These workers have demonstrated their approaches by inverting absorption spectra (where the excitation is to a dissociative state).^{18,20}

The formulation of the derivative in terms of the DVR-ABC Green's function is new, however. Note that the major computational effort in calculating such a derivative via eq 7 is the same as that in obtaining $I(E)$: the action of the Green's function on the anion wavefunction. Thus, the derivative information can be generated with essentially no more effort than that required to calculate the photodetachment spectrum. In addition, this means that both the spectrum and all desired derivatives of the spectrum can be obtained at all energies in a single calculation using the QMRES method.

As an example, consider the potential as expressed in a discrete variable representation basis:

$$\hat{V} = \sum_{j=1}^{N_{\text{DVR}}} |j\rangle V_j \langle j| \quad (8)$$

Here, $|j\rangle$ is the j th DVR basis function localized about the grid point \mathbf{r}_j and V_j is the value of the potential at \mathbf{r}_j . The values of the potential at the DVR grid points can then be regarded as the parameters defining the potential. In this case, the derivatives have the particularly simple form

$$\frac{\partial I(E)}{\partial V_j} = -\frac{1}{\pi} \text{Im} [\Phi_b^+(E)]_j^2 \quad (9)$$

and thus reflect the form of the scattering wavefunction obtained from the action of the Green's function on the anion bound state. Equation 9 is the crucial formula for the purposes of this paper. In the following section, we use this equation to calculate these derivatives for two model systems to investigate the sensitivity of photodetachment spectra to the neutral potential energy surface.

3. Applications

A. Eckart Barrier. The one-dimensional Eckart barrier provides a simple, but quite useful, test problem for examining the basic properties of the sensitivity of the photodetachment spectrum to the neutral potential. In this model,²¹ the neutral potential is given by

$$V(q) = V_0 \text{sech}^2(q/a) \quad (10)$$

and the anion potential by

$$v_{\text{anion}}(q) = \frac{1}{2} m \omega^2 (q - q_0)^2 \quad (11)$$

In what follows, we take $V_0 = 0.425$ eV, $a = 1$ au, $m = 1060$ au, $\omega = 3000$ cm⁻¹, and different values of q_0 . The potentials

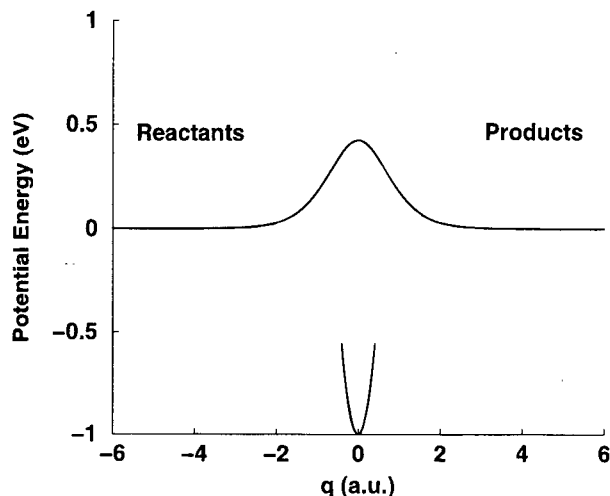


Figure 1. Depiction of the neutral and anion potential surfaces for the model one-dimensional Eckart barrier photodetachment system.

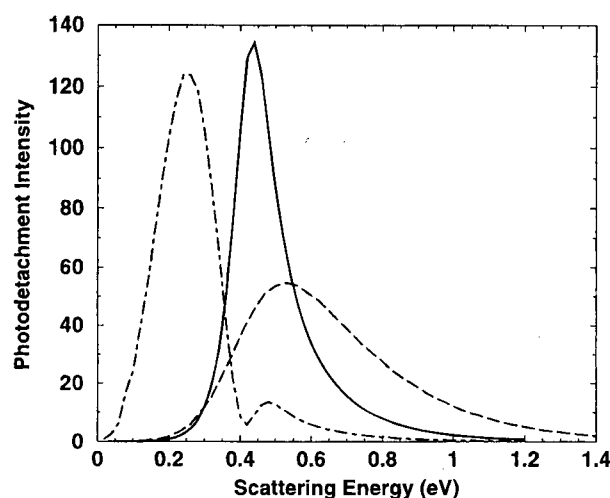


Figure 2. Photodetachment spectra for the one-dimensional model Eckart barrier system with $V_0 = 0.425$ eV, $a = 1$ au, $m = 1060$ au, and $\omega = 3000$ cm^{-1} . The photodetachment spectrum from the anion ground state ($\nu = 0$) with $q_0 = 0$ is shown as the solid line, the spectrum from the $\nu = 1$ anion state with $q_0 = 0$ as the dashed line, and the $\nu = 0$ spectrum with $q_0 = 1$ au as the dot-dashed line.

are shown in Figure 1 for $q_0 = 0$. For the purposes of discussion we define the reactants on the neutral surface as $q < 0$ and products as $q > 0$.

Figure 2 shows the photodetachment spectra calculated for the model Eckart barrier system in three different cases. The spectra are shown versus the scattering energy on the neutral surface for photodetachment from the $\nu = 0$ anion bound state with $q_0 = 0$, the $\nu = 1$ state with $q_0 = 0$, and the $\nu = 0$ state with $q_0 = 1$ au. The $\nu = 0$, $q_0 = 0$ spectrum consists of a single asymmetric peak centered around $E \approx 0.43$ eV $\approx V_0$. The anion wave function in this case is largest in the region of the barrier, leading to small intensities at energies below the barrier height where the neutral scattering wave function is decaying exponentially. The $\nu = 1$, $q_0 = 0$ spectrum has a similar structure but is peaked at ≈ 0.5 eV and has a tail at higher energies. Both differences reflect the better overlap of the $\nu = 1$ anion state with the more oscillatory neutral scattering wave functions at higher energies. The $\nu = 0$, $q_0 = 1$ au is peaked at ≈ 0.25 eV with a smaller peak around 0.48 eV. The displaced anion wave function is largest outside the barrier region leading to larger intensities at lower scattering energies.

Figure 3a shows the derivatives, at three different scattering

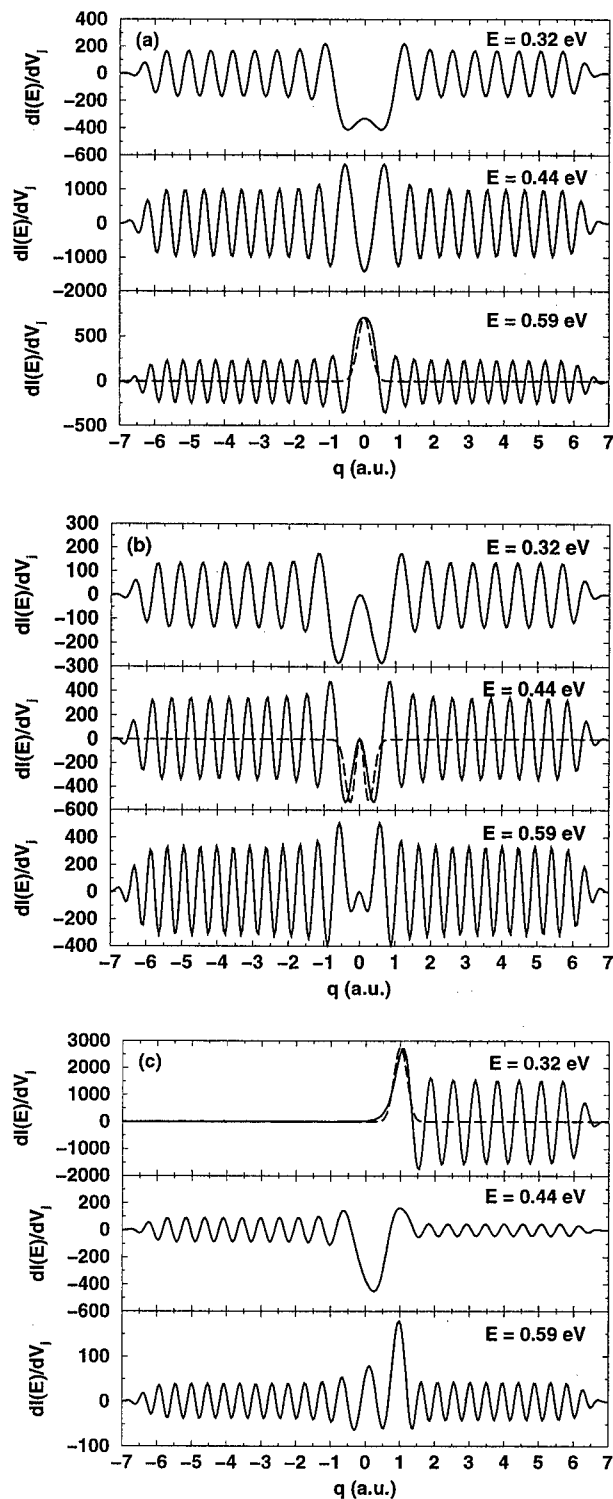


Figure 3. Sensitivity of the photodetachment spectrum to the neutral potential (in units of hartrees⁻²) as represented on a DVR grid at three different values of the scattering energy. The absolute square of the anion wave function is indicated by a dotted line, scaled to be of the same magnitude as the sensitivity. Results are shown for (a) the $\nu = 0$ anion bound state with $q_0 = 0$, (b) the $\nu = 1$ anion bound state with $q_0 = 0$, and (c) the $\nu = 0$ anion bound state with $q_0 = 1$ au.

energies, of the photodetachment spectrum from the anion ground state with respect to the value of the neutral Eckart barrier potential at the DVR grid points, (cf. eq 8). Briefly, we use a sinc-function DVR basis¹⁰ to represent the Green's function and anion bound state. In this basis the DVR grid points are evenly spaced. For these calculations a significantly higher DVR grid density (Δq , the spacing between grid points ≈ 0.04

au) is used than is required to converge the photodetachment spectra in order to better observe the structure in the derivatives. The basic structure of the "sensitivity" is the same for all the energies. Namely, the derivatives of the spectrum with respect to the potential are (not surprisingly) largest in the Franck-Condon region and oscillate on both sides of this region.

It can be immediately seen that the frequency of these oscillations vary with the scattering energy. In fact, the wavelength of the oscillations at a given energy is precisely half the de Broglie wavelength corresponding to that scattering energy. That this should be so can be seen from eq 9, which shows that the derivative is proportional to the square of the scattering wave function. At large values of $|q|$, where the potential is flat, the scattering wavefunction has the form for $|q| \rightarrow \infty$

$$\Phi_b^+(E) \sim e^{ik|q|} \quad (12)$$

where $k = \sqrt{2mE}/\hbar$, so asymptotically

$$[\Phi_b^+(E)]^2 \sim e^{2ik|q|} \quad (13)$$

Thus, the presence of the square gives oscillations at a frequency twice that corresponding to the scattering energy. Note that the wave function decays to zero at the largest values of $|q|$ due to the absorbing boundary conditions.

The correspondence of the largest derivatives with the Franck-Condon region is particularly striking for energies significantly above the barrier. This can be seen in the bottom panel of Figure 3a ($E = 0.59$ eV) where the derivative of the spectrum with respect to the potential is superimposed with the absolute square of the anion wave function (suitably scaled).

This direct relationship is not observed for the two lower energies shown. The lowest energy, $E = 0.32$ eV, shown in the top panel of Figure 3a, is more than 0.1 eV below the barrier height and the magnitude of the derivative is peaked to either side of the barrier, where the anion bound state has greatest overlap with the scattering wave function at this energy. A similar pattern is observed for the derivative at $E = 0.44$ eV which is close to the barrier height. At this energy the derivative has positive peaks on either side of the center of the anion wave function and a negative peak at the center.

Figure 3b shows the derivatives of the photodetachment spectrum for the $\nu = 1$ anion bound state with $q_0 = 0$ with respect to the values of the neutral potential at the DVR grid points. There are some interesting differences between the structure seen here and that observed for the $\nu = 0$ ground state in Figure 3a. An important point to note is that for photodetachment from the $\nu = 1$ anion state the sensitivity is always zero at $q = 0$ (the center of the barrier) since the anion wave function has a node at that point.

The derivatives $\partial I(E)/\partial V_j$ at $E = 0.32$ eV are similar to that in Figure 3a for the $\nu = 0$ anion bound state. The primary difference is the node at $q = 0$ for the $\nu = 1$ spectrum. In both cases the spectrum is most sensitive to the sides of the neutral barrier. However, in the $\nu = 0$ case the derivative is nonzero near $q = 0$ due to the overlap between the exponentially decaying scattering wave function and the anion bound state which is largest in that region (cf. eq 1).

At all the energies, oscillations are again observed at a wavelength half of that corresponding to the scattering energy for large $|q|$. However, the $\nu = 1$ spectrum is somewhat more sensitive to the potential at larger values of $|q|$ than the $\nu = 0$ spectrum. This is not surprising since the $\nu = 1$ anion state is greater in extent than the ground state. However, it indicates

that additional information about the neutral potential, above that in the $\nu = 0$ spectrum, is contained in the spectra for vibrationally excited anion bound states.

The sensitivity of the photodetachment spectra from the $\nu = 0$ anion bound state with $q_0 = 1$ au in the anion potential, eq 11, is shown in Figure 3c for three different scattering energies. The case where the anion bound state does not sit directly under the neutral transition state is often the situation in realistic systems and is thus important to investigate.

The most striking difference between the $q_0 = 0$ (Figure 3a) and $q_0 = 1$ au sensitivities is at $E = 0.32$ eV where for $q_0 = 1$ au the derivative $\partial I(E)/\partial V_j$ is zero for $q < 0$. At this energy the transmission probability for the Eckart barrier is less than ~ 0.01 so photodetachment from this state yields only products.²¹ Thus, the spectrum is not sensitive to the reactant side of the potential.

At the scattering energy $E = 0.44$ eV the absolute value of the derivative peaks around $q \approx 0.24$ au and has significant magnitude in the barrier region. This is an important result as it indicates that information about the barrier may be obtained even when the Franck-Condon region for the photodetachment does not coincide with the transition state. The same is true for the sensitivity at $E = 0.59$ eV which consists of two large peaks and the usual oscillations at greater q . The dominant peak is at the position of the anion bound state, $q = 1$ au, while the smaller peak is centered at slightly positive values of q near $q = 0$. Thus, at this energy there is also sensitivity to the barrier region.

Recently, Skodje and co-workers²² have proposed a scheme for controlling the anion bound state in photodetachment systems. Their goal was to assign photodetachment spectra by changing the character of the anion state to accentuate, for example, resonance or direct scattering contributions. The large sensitivity of the spectrum to the neutral potential in the Franck-Condon region suggests that such a scheme could instead be used to map out the neutral potential energy surface.

B. Photodetachment of Collinear H_3^- . As a second application we consider a two-degrees-of-freedom model system in which the neutral potential energy surface is that for the collinear $H + H_2$ system²³ (as given by the LSTH surface²⁴). The anion potential is a separable harmonic oscillator potential in the Jacobi coordinates of the reactant arrangement:

$$v_{\text{anion}}(r, R) = \frac{1}{2} \mu_r \omega_r^2 (r - r_0)^2 + \frac{1}{2} \mu_R \omega_R^2 (R - R_0)^2. \quad (14)$$

Here, r is the diatomic H_2 distance in the reactants and R is the distance from the center of mass of H_2 to the colliding H atom; μ_r and μ_R are the reduced masses associated with these coordinates and ω_r and ω_R are the harmonic frequencies of the anion potential in these coordinates. The classical barrier to reaction is 0.425 eV for the LSTH surface.

We examine two different parameter sets for the anion potential which we will refer to as Sets A and B. In Set A the anion equilibrium geometry lies directly under the neutral transition state with $\omega_r = 2500$ cm^{-1} , $r_0 = 1.757$ au, $\omega_R = 2000$ cm^{-1} , and $R_0 = 2.6355$ au. The frequencies are kept the same but the anion equilibrium geometry is displaced into the reactant valley in parameter Set B for which $r_0 = 1.6$ au and $R_0 = 3.2$ au.

The photodetachment spectra for this model collinear H_3^- photodetachment system are shown in Figure 4 for the two parameter sets. Figure 5 shows a contour plot of the neutral $H + H_2$ (LSTH) potential superimposed with the anion bound states for parameter Sets A and B. The spectrum with parameter Set A is peaked around a scattering energy of $E \approx 0.56$ eV,

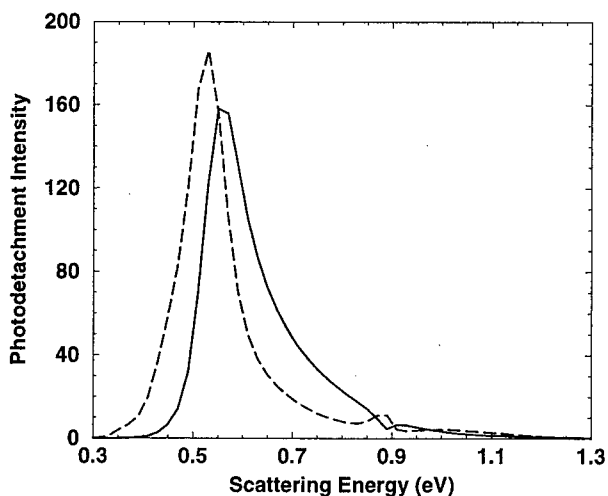


Figure 4. Photodetachment spectra for the model collinear H_3^- system. The spectrum obtained using parameter Set A for the anion potential is given by the solid line, while the spectrum for Set B is shown as the dashed line.

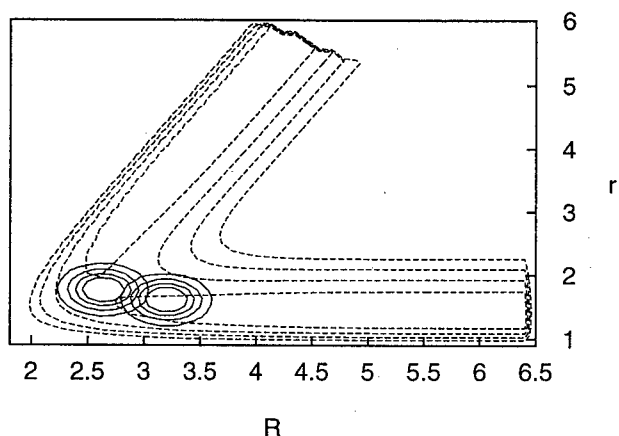


Figure 5. Contour plot of the LSTH potential energy surface and the absolute square of the anion bound state wave functions for the model collinear H_3^- photodetachment model system. The wave function for the anion potential parameter Set A appears to the left of that for Set B. The contours for the potential surface are spaced 0.4 eV apart from 0.4 to 2.4 eV; for the wave functions the contours range from 0.008 to 0.032 in increments of 0.008. The distances R and r are in atomic units.

corresponding to the threshold for reaction in the collinear $\text{H} + \text{H}_2$ system. In analogy with the Eckart barrier model considered above, the displaced anion potential of parameter Set B leads to a spectrum peaking at somewhat lower energies. Both spectra have structure around $E = 0.9$ eV relating to the threshold for production of H_2 ($\nu = 1$). The threshold for reaction into (or out of) the $\nu = 1$ state of H_2 for collinear $\text{H} + \text{H}_2$ occurs at ~ 0.88 eV.²⁵

Figure 6 shows some illustrative examples of the sensitivity of the photodetachment spectra to the neutral potential for the model H_3^- system. Many of the general features of the sensitivities in this system are the same as in the one-dimensional Eckart barrier model considered above. Specifically, the magnitude of the derivative, $\partial I(E)/\partial V_j$, peaks in the vicinity of the Franck–Condon region and the derivative exhibits oscillatory structure in the reactant and product asymptotic valleys with a wavelength dependent on the scattering energy. However, there are some noteworthy differences as well as further similarities which we now discuss.

In Figure 6a contour plots of the derivative $\partial I(E)/\partial V_j$ and the neutral potential are shown for parameter Set A at a scattering

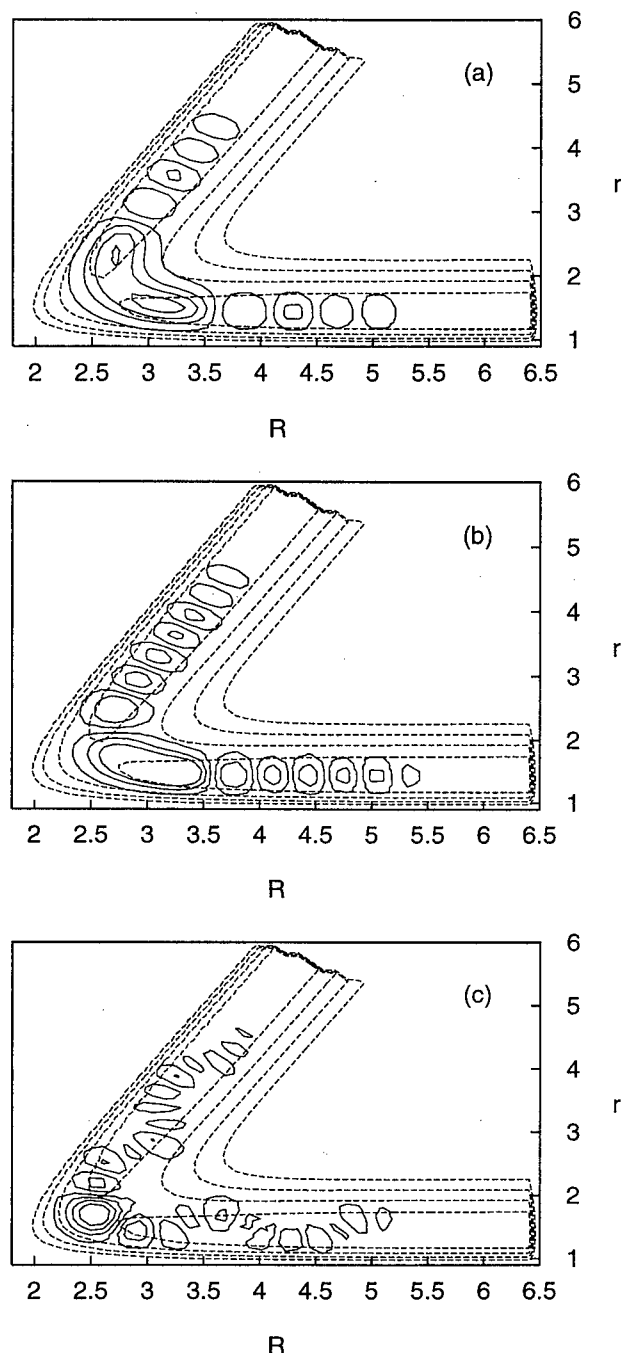


Figure 6. The sensitivity of the photodetachment spectrum for the collinear H_3^- model system is shown. (a) Results using anion potential parameter Set A and a scattering energy of $E = 0.49$ eV; the contours for the sensitivity range from -600 to 100 in increments of 175 in units of hartrees^{-2} . (b) Results using anion potential parameter Set B and a scattering energy of $E = 0.59$ eV; the contours for the sensitivity range from -350 to 650 in increments of 250 in units of hartrees^{-2} . (c) Results using anion potential parameter Set A and a scattering energy of $E = 0.95$ eV; the contours for the sensitivity range from -40 to 85 in increments of 25 in units of hartrees^{-2} . The distances R and r are in atomic units.

energy of $E = 0.49$ eV. The sensitivity has a large negative doubly peaked maximum encompassing much of the transition state region and extending significantly into the reactant and product valleys. This energy is below the threshold for reaction in the collinear $\text{H} + \text{H}_2$ system and reaction occurs only through tunneling. Thus, as observed for the Eckart barrier model (cf. $E = 0.32$ eV in Figure 3a), the spectrum at this energy is most sensitive to the sides of the barrier. A more subtle detail of this

plot is that the magnitude of the sensitivity is largest somewhat away from the transition state where the anion bound state is largest. In fact, the sensitivity here is somewhat suggestive of the "corner-cutting" nature of tunneling.²⁶

An analogous contour plot is shown in Figure 6b but for parameter Set B and at a scattering energy of $E = 0.59$ eV. In this case the sensitivity peaks in a broad area extending from the Franck-Condon region (recall that here the anion bound state is displaced toward the reactant valley) to the transition state. This is a very interesting result in that it shows that for this system the photodetachment spectrum is sensitive to the barrier region even when the anion wave function is small or zero there. This is encouraging from the point of view of using spectra to obtain information about potential surfaces, particularly in the transition state region.

Figure 6c shows the derivative $\partial I(E)/\partial V_j$ and the neutral potential for parameter Set A at a scattering energy of $E = 0.95$ eV. The most striking feature of the sensitivity at this energy is the nodal structure in the vibrational H_2 coordinate in the asymptotic valleys. This is present because photodetachment is now leading to the production of H_2 ($v = 1$) in both the reactants and products. Another interesting difference from Figure 6, parts a and b, is that the derivative is largest near the repulsive wall occurring for smaller values of H-H distances in the transition state.

4. Concluding Remarks

We have shown how the derivatives of photodetachment intensities with respect to parameters of the neutral potential energy surface can be calculated within the DVR-ABC Green's function formulation. These derivatives can be obtained with no extra computational effort beyond that required to calculate the photodetachment spectrum itself. In addition, using the quasi-minimal residual method for applying the Green's function onto the anion bound state, both the spectrum and any desired derivatives can be obtained at all energies in a single calculation.

We have examined the sensitivity of the photodetachment spectra to the neutral potential energy surfaces for two model systems to illustrate the general features in transition state spectroscopy systems. In general, the spectrum is most sensitive to the neutral potential in the Franck-Condon region where the anion wave function is largest and in the area around the transition state. The spectra do not appear to be sensitive to the global potential surface. This is discouraging from the point of view of inverting a transition state spectrum to obtain the potential in a "point-by-point" representation. However, the results are quite encouraging if the goal is extracting information about the potential in the region of the barrier. This is, after all, the most difficult part of the potential to obtain by other means, e.g., ab initio calculations.

Acknowledgment. I gratefully acknowledge Prof. William H. Miller for his generous support and encouragement as well as for many productive conversations and Prof. James T. Hynes for his support during the completion of this work. I also thank Prof. Daniel M. Neumark for useful discussions.

References and Notes

- (1) Neumark, D. M. *Acc. Chem. Res.* **1993**, 26, 33; Metz, R. B.; Bradforth, S. E.; Neumark, D. M. *Adv. Chem. Phys.* **1992**, 81, 1.
- (2) Weaver, A.; Metz, R. B.; Bradforth, S. E.; Neumark, D. M. *J. Chem. Phys.* **1990**, 93, 5352; Weaver, A.; Neumark, D. M. *Faraday Discuss. Chem. Soc.* **1991**, 91, 5; Bradforth, S. E.; Arnold, D. W.; Neumark, D. M.; Manolopoulos, D. E. *J. Chem. Phys.* **1993**, 99, 6345.
- (3) Manolopoulos, D. E.; Stark, K.; Werner, H. J.; Arnold, D. W.; Bradforth, S. E.; Neumark, D. M. *Science* **1993**, 262, 1852.
- (4) Schatz, G. C. *J. Chem. Phys.* **1989**, 90, 3582; Schatz, G. C. *J. Chem. Phys.* **1989**, 90, 4847; Schatz, G. C. *J. Phys. Chem.* **1990**, 94, 6157.
- (5) Thompson, W. H. *J. Phys. Chem. A* **1999**, 103, 9506.
- (6) Thompson, W. H.; Miller, W. H. *J. Chem. Phys.* **1994**, 101, 8620.
- (7) Thompson, W. H.; Karlsson, H. O.; Miller, W. H. *J. Chem. Phys.* **1996**, 105, 5387.
- (8) Dickinson, A. S.; Certain, P. R. *J. Chem. Phys.* **1963**, 49, 4209; Harris, D. O.; Engerholm, G. G.; Gwinn, W. D. *J. Chem. Phys.* **1965**, 43, 1515.
- (9) Lill, J. V.; Parker, G. A.; Light, J. C. *Chem. Phys. Lett.* **1982**, 89, 483; Light, J. C.; Hamilton, I. P.; Lill, J. V. *J. Chem. Phys.* **1985**, 82, 1400; Bačić, Z.; Light, J. C. *J. Chem. Phys.* **1986**, 85, 4594; Whitnell, R. M.; Light, J. C. *J. Chem. Phys.* **1988**, 89, 3674; Choi, S. E.; Light, J. C. *J. Chem. Phys.* **1990**, 92, 2129.
- (10) Colbert, D. T.; Miller, W. H. *J. Chem. Phys.* **1992**, 96, 1982.
- (11) Goldberg, A.; Shore, B. W. *J. Phys. B* **1978**, 11, 3339.
- (12) Leforestier, C.; Wyatt, R. E. *J. Chem. Phys.* **1983**, 78, 2334.
- (13) Jolicard, G.; Austin, E. J. *Chem. Phys. Lett.* **1985**, 121, 106; Jolicard, G.; Austin, E. J. *Chem. Phys.* **1986**, 103, 295; Jolicard, G.; Perrin, M. Y. *Chem. Phys.* **1987**, 116, 1; Jolicard, G.; Leforestier, C.; Austin, E. J. *J. Chem. Phys.* **1988**, 88, 1026.
- (14) Kosloff, R.; Kosloff, D. *J. Comput. Phys.* **1986**, 63, 363.
- (15) Neuhauser, D.; Baer, M. *J. Chem. Phys.* **1989**, 90, 4351; Neuhauser, D.; Baer, M. *J. Chem. Phys.* **1989**, 91, 4651; Neuhauser, D.; Baer, M.; Kouri, D. J. *J. Chem. Phys.* **1990**, 93, 2499.
- (16) Seideman, T.; Miller, W. H. *J. Chem. Phys.* **1992**, 96, 4412; Seideman, T.; Miller, W. H. *J. Chem. Phys.* **1992**, 97, 2499; Miller, W. H.; Seideman, T. In *Time Dependent Quantum Molecular Dynamics: Experiment and Theory*; Broeckhove, J., Ed.; NATO ARW 1992; Thompson, W. H.; Miller, W. H. *Chem. Phys. Lett.* **1993**, 206, 123.
- (17) Freund, R. W.; Nachtigal, N. M. *Numer. Math.* **1991**, 60, 315; Freund, R. W. In *Numerical Linear Algebra*; Reichel, L.; Rutman, A.; Varga, R., Eds.; de Gruyter: Berlin, 1993.
- (18) Baer, R.; Kosloff, R. *Chem. Phys. Lett.* **1992**, 200, 183.
- (19) Wu, Q.; Zhang, J. Z. H. *Spectrochim. Acta A* **1997**, 53, 1189.
- (20) Wang, D.; Zhang, J. Z. H. *J. Chem. Phys.* **1998**, 108, 10027.
- (21) Thompson, W. H. Ph.D. Thesis, Lawrence Berkeley Laboratory, University of California, 1996.
- (22) Sadeghi, R.; Skodje, R. T. *J. Chem. Phys.* **1996**, 105, 7504; Skodje, R. T.; Sadeghi, R.; Krause, J. L. *Trans. Faraday Soc.* **1997**, 93, 765; Skodje, R. T.; Sadeghi, R.; Krause, J. L. *Chem. Phys.* **1999**, 240, 129.
- (23) Spath, B. W.; Miller, W. H. *Chem. Phys. Lett.* **1996**, 262, 486.
- (24) Liu, B.; Siegbahn, P. J. *Chem. Phys.* **1978**, 68, 2457; Truhlar, D. G.; Horowitz, C. *J. Chem. Phys.* **1978**, 68, 2566; *J. Chem. Phys.* **1979**, 71, 1514.
- (25) Bondi, D. K.; Connor, J. N. L. *J. Chem. Phys.* **1985**, 82, 4383.
- (26) See, for example, George, T. F.; Miller, W. H. *J. Chem. Phys.* **1972**, 56, 5722.

On Obtaining Reactive Potential Energy Surfaces from Transition State Photodetachment Spectra. II. Inversion of Spectra in Model Systems

Ward H. Thompson[†]

Department of Chemistry, University of California, Berkeley, California 94720,

and Department of Chemistry and Biochemistry, University of Colorado, Boulder, Colorado 80309-0215

Received: June 17, 1999; In Final Form: October 1, 1999

We present a method for determining reactive potential energy surfaces from experimental photodetachment spectra. The variations of the theoretical photodetachment spectrum with respect to potential parameters (the “derivatives” of the spectrum) are calculated. These derivatives are used in an iterative Levenberg–Marquardt-based algorithm to find the optimal values of the potential parameters, i.e., those yielding the theoretical spectrum that best matches the experimental one. Applications of the method to one- and two-degrees-of-freedom model systems are presented, and accurate results are obtained with a small number of iterations. Prospects for treating realistic systems are discussed.

1. Introduction

In the preceding paper¹ in this issue (hereafter referred to as Paper I) we carried out a sensitivity analysis of transition state (photodetachment) spectra. Specifically, for two model systems, we determined the regions of the neutral potential energy surface to which the spectra are sensitive. One of the primary conclusions drawn from that analysis is that the spectra are sensitive to the barrier region in a wide number of cases, including those where the Franck–Condon region (i.e., the location of the anion bound state) does not coincide with the transition state. This result suggests that it should be possible to use transition state spectra to obtain information about the barrier on the neutral potential surface. In this paper we present an iterative method for “inverting” a transition state spectrum to obtain an accurate representation of the neutral surface in the barrier region.

2. Methodology

In Paper I, we showed how the derivative of a photodetachment spectrum with respect to a parameter of the neutral potential energy surface can be obtained for no extra cost beyond that required to calculate the spectrum itself. In this section, we review the relevant formulas for completeness and then describe the methodology for “inverting” transition state spectra.

As in Paper I, we consider a potential surface for a chemical reaction defined by a set of M parameters $\alpha = \{\alpha_j\}_{j=1,\dots,M}$. For the purposes of this paper the set α will represent the parameters in an analytical representation of the potential energy surface. The derivative $\partial I(E)/\partial \alpha_j$ can be used to optimize the values of the potential parameters for which $\partial I(E)/\partial \alpha_j \neq 0$. Specifically, given an experimentally measured spectrum, $I_{\text{ex}}(E)$, at a set of N_E energies $\{E_i\}$ we can define a measure of the “error” in the trial spectrum as

$$\chi^2 = \sum_{i=1}^{N_E} [I(E_i; \alpha) - I_{\text{ex}}(E_i)]^2 \quad (1)$$

The optimum potential is then the one that minimizes χ^2 .

The derivative of χ^2 with respect to a potential parameter α_j indicates how the error changes as α_j is varied and is then given by

$$\frac{\partial \chi^2}{\partial \alpha_j} = 2 \sum_{i=1}^{N_E} \frac{\partial I(E_i; \alpha)}{\partial \alpha_j} [I(E_i; \alpha) - I_{\text{ex}}(E_i)] \quad (2)$$

Thus, the key to this approach is the calculation of the derivatives $\partial I(E)/\partial \alpha_j$.

In Paper I, we showed how these derivatives can be obtained using a Green’s function in a discrete variable representation^{2–4} (DVR) with absorbing boundary conditions^{5–9} (ABC). This approach allows the calculation of the derivatives with no additional effort beyond that required to calculate the spectrum itself. Briefly, the photodetachment intensity in the DVR-ABC formulation is given within the Franck–Condon approximation by^{10,11}

$$I(E) = -\frac{1}{\pi} \text{Im} \phi_b^T \Phi_b^+(E) \quad (3)$$

And, as shown in Paper I, the derivative of the intensity at energy E with respect to a potential parameter α_j is

$$\frac{\partial I(E)}{\partial \alpha_j} = -\frac{1}{\pi} \text{Im} \Phi_b^{+T}(E) \cdot \frac{\partial \mathbf{V}}{\partial \alpha_j} \cdot \Phi_b^+(E) \quad (4)$$

The scattering wavefunction $\Phi_b^+(E)$ is defined as

$$\Phi_b^+(E) = \mathbf{G}^+(E) \cdot \phi_b \quad (5)$$

where ϕ_b is the anion bound state wavefunction vector in the DVR and $\mathbf{G}^+(E)$ is the DVR-ABC Green’s function:¹²

$$\mathbf{G}^+(E) = (\mathbf{E}\mathbf{I} - \mathbf{H} + i\epsilon)^{-1} \quad (6)$$

with outgoing wave boundary conditions. Here, \mathbf{H} and ϵ are the DVR matrices of the Hamiltonian and the absorbing potential.

As can be seen from eqs 3–5 the primary effort in calculating the photodetachment intensity, $I(E)$, and its derivative with respect to a potential parameter, $\partial I(E)/\partial \alpha_j$, is the same: the action of the Green’s function onto the anion bound state. Thus,

[†] Current address. University of Colorado.

any and all derivatives of the spectrum can be obtained with no extra effort beyond that required to compute $I(E)$ itself. In addition, we note that, in principle, the entire photodetachment spectrum can be obtained in a single calculation using the quasi-minimal residual (QMRES) method¹³ for acting the Green's function on the anion bound state.¹¹

A generic iterative scheme for obtaining the neutral potential energy surface from an experimental photodetachment spectrum is as follows:

- (1) Make an initial guess for the potential, \tilde{V} .
- (2) Calculate the photodetachment spectrum (and its derivatives) associated with \tilde{V} using eqs 3–5.
- (3) Calculate the “error” of the theoretical spectrum relative to the experimental one using eq 1.
- (4) Use the derivatives $\partial I(E)/\partial \alpha_j$ to obtain a new \tilde{V} .
- (5) Return to 2, iterating until χ^2 is minimized.

A variety of schemes of this sort can be conceived, particularly several that differ only in the method used in Step 4. In this paper we use a Levenberg–Marquardt algorithm¹⁴ for implementing this scheme. This algorithm uses a combination of the inverse-Hessian and steepest descent methods to update the parameters to be optimized, $\{\alpha_j\}_{j=1,\dots,M}$.

On the basis of sensitivity analysis in Paper I, it seems unlikely that, in general, an accurate “point-by-point” representation of the potential surface can be obtained by inverting transition state spectra. An extreme example is the case where the Franck–Condon region is in the reactant valley. If photodetachment of the anion does not lead to formation of the neutral products then the spectrum contains no information about the product side of the potential. Nevertheless, as seen in Paper I, the photodetachment spectrum can still provide information about the barrier region in this case. Thus, here we consider the optimization of parameters in an analytical representation of the neutral surface. The goal is to establish the viability and properties of the present approach by treating model systems. Thus, the “experimental” spectrum is generated by a theoretical calculation using one potential (what we will call the exact potential). Then the “experimental” spectrum is used to optimize the parameters of a trial potential with a different functional form by minimizing the error of the theoretical spectrum (obtained using the trial potential) relative to the “experimental” one.

3. Model Systems

A. One-Dimensional Barrier. As a first test of the method proposed in Section 2, we consider a one-dimensional model problem in which the exact (i.e., “experimental”) spectra are those for the Eckart barrier model considered in Paper I.^{1,15} The exact, or target, neutral potential is given by

$$V_{\text{ex}}(q) = V_0^{\text{ex}} \text{sech}^2(q/a) \quad (7)$$

with $V_0^{\text{ex}} = 0.425$ eV and $a = 1$ au and the anion potential is a harmonic oscillator of frequency $\omega = 3000$ cm^{-1} centered at q_0 . The mass is taken to be 1060 au and in what follows we consider both $q_0 = 0$ and $q_0 = 1$ au. The trial potential has a different functional form and is a Gaussian,

$$\tilde{V}(q) = V_0 e^{-bq^2} \quad (8)$$

where V_0 and b are the parameters to be optimized using the “experimental” spectrum.

The test of the method is as follows. The “experimental” photodetachment spectrum, $I_{\text{ex}}(E)$, is first calculated at 60 values

of the scattering energy using the exact potential, eq 7. Initial guesses are made for the parameters V_0 and b in the trial potential. The Levenberg–Marquardt-based scheme described in Section 2 is then used to minimize the error χ^2 (eq 1) of the theoretical spectrum $I(E)$ obtained with the trial potential, eq 8, relative to $I_{\text{ex}}(E)$.

Figure 1a shows the initial, optimized, and “experimental” photodetachment spectra resulting from this exercise for the case where $q_0 = 0$ and initially $V_0 = 0.7$ eV and $b = 1.4$ au. Here the spectra are for photodetachment from the anion ground state ($v = 0$). The initial trial potential gives a spectrum peaking at significantly higher energy than the exact spectrum due to the greater barrier height. However, the spectrum obtained from the optimized trial potential is in excellent agreement with the exact spectrum. Figure 2a shows the error χ^2 (on a semilog plot) and the values of V_0 and b at each iteration of the optimization. Convergence is achieved in 15 iterations yielding excellent agreement in the barrier height with optimized values of $V_0 = 0.424$ eV and $b = 0.977$ au. Note that while there is a plateau in the value of χ^2 it decreases monotonically with the number of iterations. It is interesting that the value of b initially increases by an order of magnitude from its initial value before converging to its optimum value. On the other hand, the route of the barrier height to its final value is much more direct.

Figure 1b shows the initial, optimized, and “experimental” photodetachment spectra from the $v = 1$ anion state with $q_0 = 0$. The initial parameters in the trial potential are taken as $V_0 = 1.0$ eV and $b = 0.6$ au. These result in a spectrum peaked at very high energies (in fact the intensity is nonzero outside the range of energies considered in the optimization). Despite the initial barrier height being more than twice the exact value, the optimization is completed in 16 iterations giving a spectrum in excellent agreement with the “experimental” one.

The error in the theoretical spectrum and the values of the trial potential parameters are shown in Figure 2b as a function of the number of iterations. As in Figure 2a, χ^2 decreases monotonically while b initially increases by an order of magnitude before converging (to 0.948 au). Here the value of V_0 first increases to ~ 1.4 eV before decreasing to its optimized value of 0.422 eV, in excellent agreement with the barrier height of the exact potential.

The initial, optimized, and “experimental” photodetachment spectra from the anion ground state with $q_0 = 1$ au are shown in Figure 1c. The initial values of V_0 and b are taken to be 0.2 eV and 0.6 au, respectively. The initial spectrum is quite different from the “experimental” one; it is peaked at a significantly lower energy and consists of a narrow peak with a shoulder at higher energy whereas the exact spectrum consists of two distinct broad peaks with the second having much less intensity. The optimized spectrum is in excellent agreement with the exact spectrum reproducing both the position and width of the peaks.

The convergence of the error in the theoretical spectrum and the trial potential parameters is shown for this case in Figure 2c. The behavior observed here is notably different from that in Figure 2, parts a and b. First, convergence is achieved in significantly fewer iterations, 9 vs ~ 15 . Second, both V_0 and b rise almost monotonically to their optimized values of 0.404 eV and 0.81 au, respectively. As before, χ^2 decreases monotonically. The final barrier height is slightly lower than that obtained in the previous cases with $q_0 = 0$, but is still in excellent agreement within 0.5 kcal/mol of the exact value.

Note that the different choices for the anion bound state used to obtain the spectrum (i.e., the values of v and q_0) do not lead

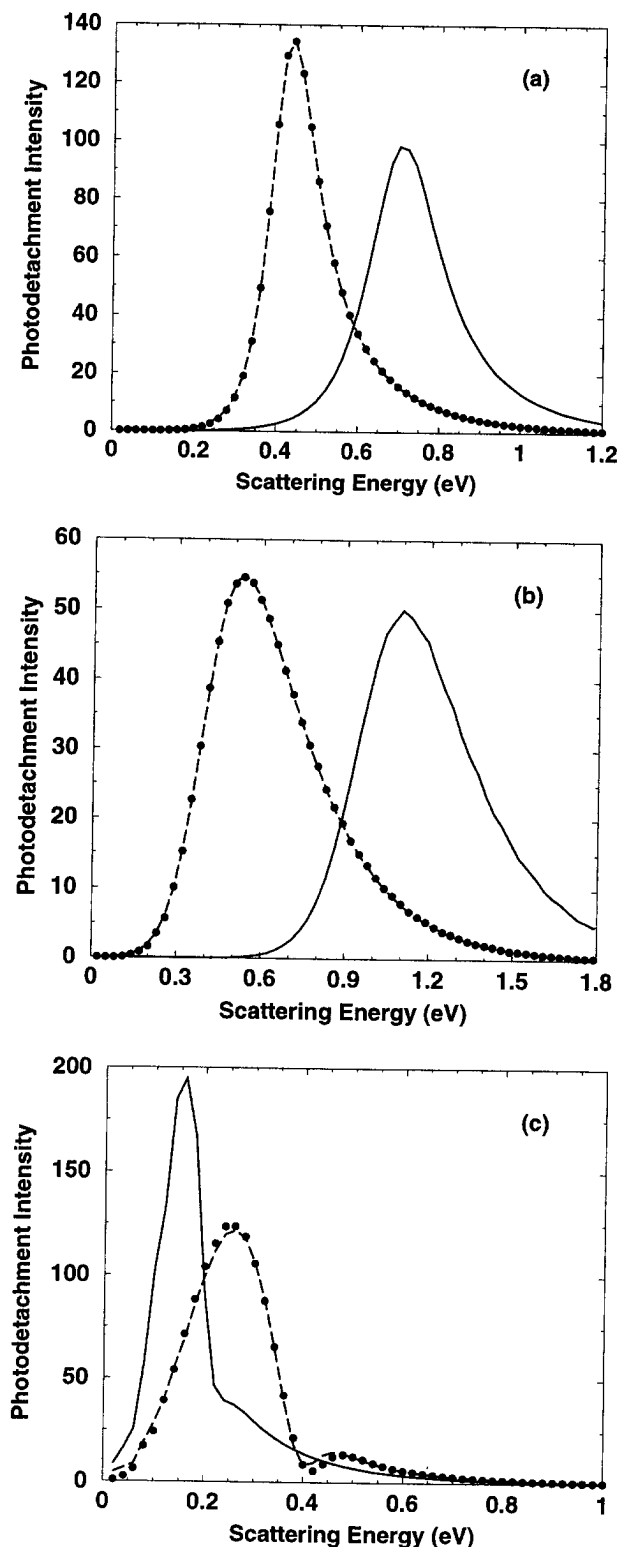


Figure 1. The initial, optimized, and “experimental” photodetachment spectra for the one-dimensional model are plotted. In each case, the initial spectrum is shown as the solid line, the optimized spectrum as the dashed line, and the “experimental” spectrum ($V_0 = 0.425$ eV, $a = 1.0$ au) as the solid circles. Results are shown for photodetachment from (a) the $\nu = 0$ anion state with $q_0 = 0$, (b) the $\nu = 1$ anion state with $q_0 = 0$, and (c) the $\nu = 0$ anion state with $q_0 = 1$ au. The initial and optimized potential parameters are given in the text.

to the same optimized V_0 and b . This is a consequence of using a different functional form for the exact and trial potentials. Each anion state probes somewhat different regions of the

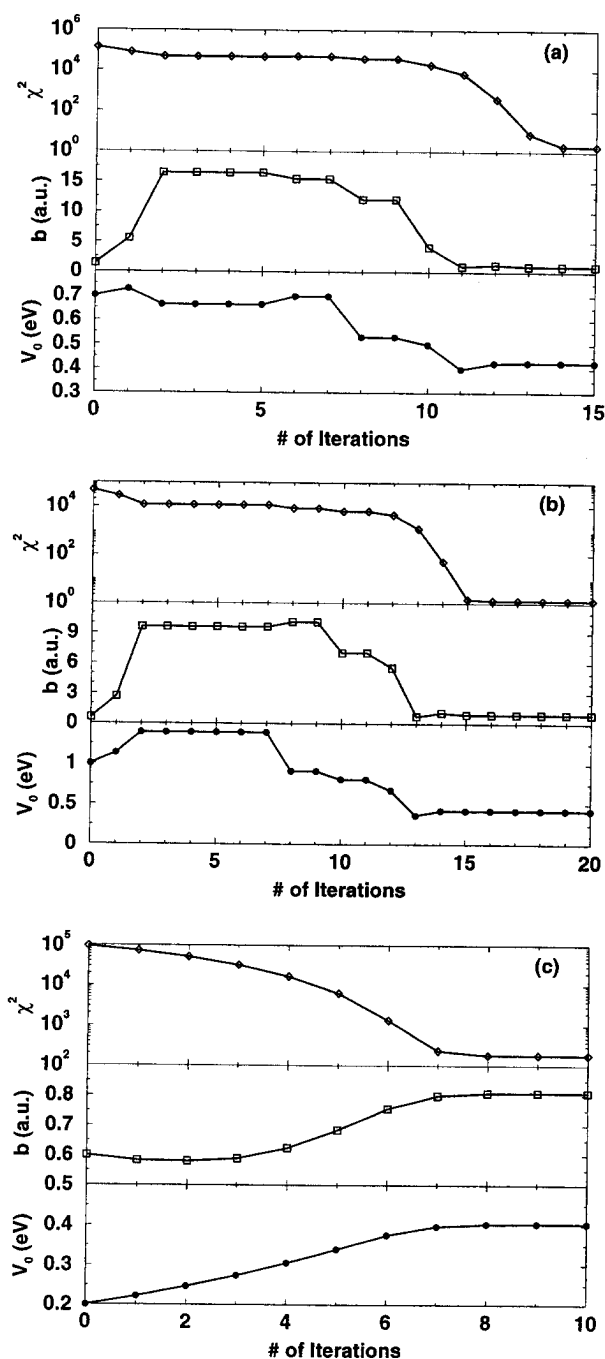


Figure 2. The error χ^2 and potential parameters V_0 and b for the optimization of the potential, corresponding to the cases shown in Figures 1a–c, are plotted as a function of the number of iterations in the optimization. Again, results are shown for photodetachment from (a) the $\nu = 0$ anion state with $q_0 = 0$, (b) the $\nu = 1$ anion state with $q_0 = 0$, and (c) the $\nu = 0$ anion state with $q_0 = 1$ au.

neutral potential and the optimized values of the trial potential parameters are those that best match the trial and exact potentials in those regions. Note that in all cases the optimized photodetachment spectra are in excellent agreement with the “experimental” spectra. However, we saw that for $q_0 = 0$ the $\nu = 0$ and $\nu = 1$ anion states yield slightly different optimized values of V_0 and b . And, for the $\nu = 0$, $q_0 = 1$ au anion state we obtained an optimum value of b that is $\sim 15\%$ lower and a slightly lower value for V_0 . The initial, optimized, and exact neutral potentials for this case are shown in Figure 3. Note that the optimum potential is indistinguishable from the exact potential on the sides of the barrier. Also, while the final barrier

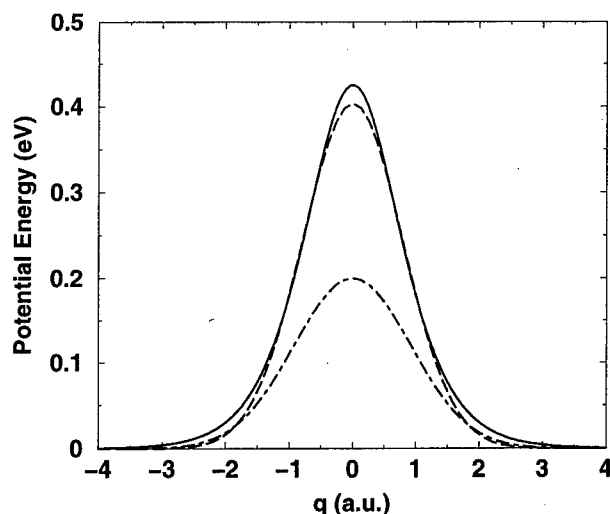


Figure 3. The initial, optimized, and exact potentials for the one-dimensional model problem are plotted. The results shown are from the optimization carried out using the photodetachment spectrum from the $\nu = 0$ anion state with $q_0 = 1$ au. The exact (Eckart barrier) potential is shown as the solid line while the initial and optimized (Gaussian) potentials are indicated by the dot-dashed and dashed lines, respectively.

height is somewhat low, it is still in excellent agreement with the exact value.

B. Collinear $H + H_2$. As a second example we consider a two-degrees-of-freedom model system in which the neutral potential energy surface is that for the collinear $H + H_2$ reaction. In this case, the exact neutral potential is given by the LSTH surface¹⁶ which has a barrier height of 0.425 eV.^{1,17} The "experimental" photodetachment spectrum is obtained using this potential with a separable harmonic oscillator anion potential in the Jacobi coordinates of the reactant arrangement,

$$v_{\text{anion}}(r, R) = \frac{1}{2}\mu_r\omega_r^2(r - r_0)^2 + \frac{1}{2}\mu_R\omega_R^2(R - R_0)^2 \quad (9)$$

Here r and R are the vibrational and translational Jacobi coordinates, respectively, with associated reduced masses μ_r and μ_R . As in Paper I, we consider two sets of parameters for the anion potential with $\omega_r = 2500 \text{ cm}^{-1}$ and $\omega_R = 2000 \text{ cm}^{-1}$ in both cases. Set A has an equilibrium geometry identical to that of the neutral transition state with $r_0 = 1.757$ au and $R_0 = 2.6355$ au. For Set B the equilibrium geometry is displaced into the reactant valley with $r_0 = 1.6$ au and $R_0 = 3.2$ au.

The trial potential to be optimized is of the London-Eyring-Polanyi-Sato (LEPS) form,

$$\tilde{V}(r, R) = Q_{ab} + Q_{ac} + Q_{bc} - \frac{\sqrt{J_{ab}^2 + J_{ac}^2 + J_{bc}^2 - J_{ab}J_{ac} - J_{ab}J_{bc} - J_{ac}J_{bc}}}{(1 + S^2)} \quad (10)$$

where a, b, and c label the three atoms and, e.g.,

$$Q_{ab} = \frac{1}{4}D[(3 + S^2)e^{-2\beta(r_{ab}-r_0)} - (2 + 6S^2)e^{-\beta(r_{ab}-r_0)}]/(1 + S^2) \quad (11)$$

and

$$J_{ab} = \frac{1}{4}D[(1 + 3S^2)e^{-2\beta(r_{ab}-r_0)} - (6 + 2S^2)e^{-\beta(r_{ab}-r_0)}]/(1 + S^2) \quad (12)$$

Here D , β , and r_0 are the Morse parameters for the diatomic

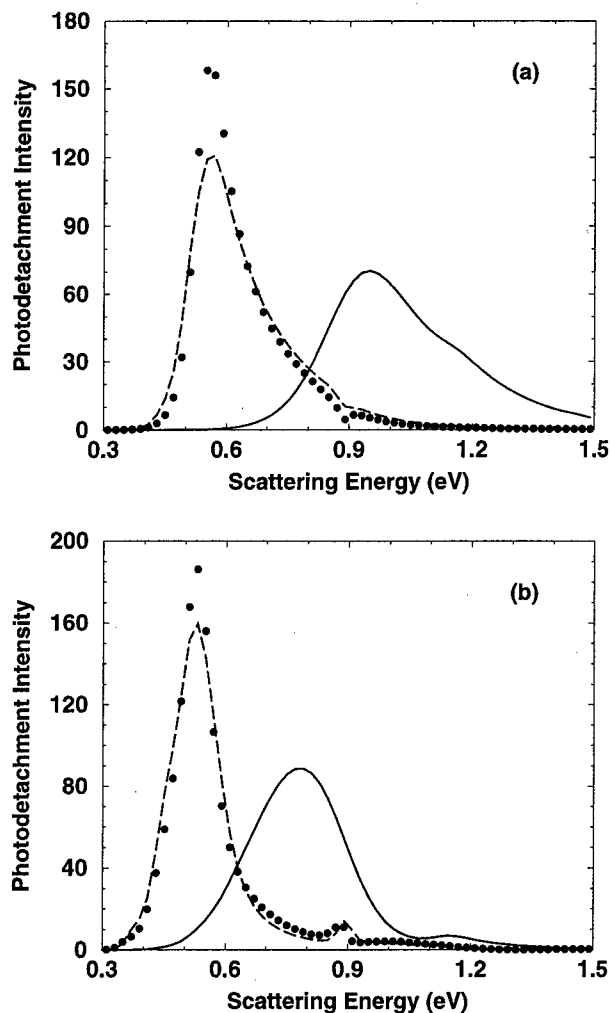


Figure 4. The "experimental", initial, and optimized photodetachment spectra for the collinear H_3^- model are plotted. Results using the anion potential parameter (a) Set A and (b) Set B are shown. The initial spectra ($S = 0.2$ corresponding to $V_0 = 0.828$ eV) are plotted as solid lines, the optimized spectrum ($S = 0.355$ corresponding to $V_0 = 0.439$ eV for Set A and $S = 0.347$ corresponding to $V_0 = 0.464$ eV for Set B) as dashed lines, and the "experimental" spectra ($V_0 = 0.425$ eV) as the solid circles.

fragment; by symmetry these parameters are the same for each pair and can be obtained from the well-known diatomic H_2 potential. The values are taken to be $D = 4.75$ eV, $\beta = 1.044$ au, and $r_0 = 1.42$ au. The Sato parameter, S , is here the parameter to be optimized by minimizing the error of the theoretical photodetachment spectrum relative to the "experimental" one.

For parameter Set A, Figure 4a shows the "experimental" spectrum calculated using the LSTH potential and the initial and optimized spectra from the LEPS surface. The initial value of S is taken as 0.2 corresponding to a barrier height of 0.828 eV. Due to the larger barrier height the initial spectrum is shifted to higher energy and broadened relative to the exact one. The optimized spectrum obtained after 15 iterations is in very good agreement with the "experimental" one, the primary difference being that the peak maximum has a lower value. Note that the sharp dip at ~ 0.9 eV due to the production of H_2 ($\nu = 1$)¹ is well reproduced. Plots of the analogous photodetachment spectra for parameter Set B are shown in Figure 4b for the same initial S . The results are much the same for this displaced anion geometry as observed for Set A. The initial spectrum peaks at a higher energy and is broadened while the optimized spectrum

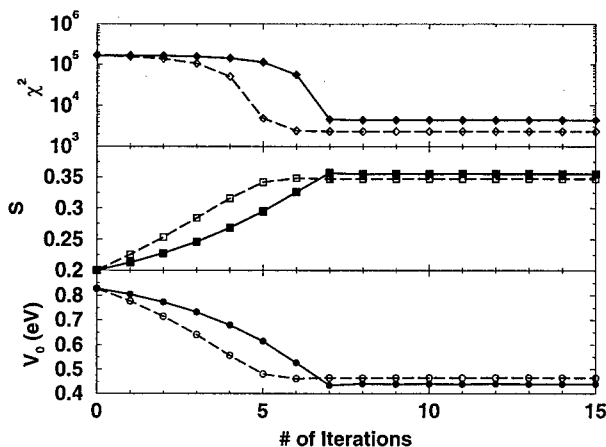


Figure 5. The error χ^2 , Sato parameter S , and corresponding barrier height V_0 for the optimizations of the LEPS potential corresponding to Figure 4 are plotted as a function of the number of iterations. The results are shown for anion potential parameter Set A as the solid lines with filled symbols and for Set B as the dashed lines with open symbols.

is in quite good agreement with a minor difference in the peak maximum. This is true even though the anion bound state wave function for Set B has little overlap with the barrier region of the neutral potential.

Figure 5 shows the error in the theoretical spectrum, χ^2 , the value of the Sato parameter, and the corresponding barrier height at each iteration for both the Set A and Set B cases. As seen for the one-dimensional example above, the different anion states lead to slightly different values of the optimized parameter. Using Set A the optimum value of S is found to be 0.355 while Set B yields 0.347. This difference naturally leads to different barrier heights in the optimized potentials, giving values of 0.439 and 0.464 eV for Sets A and B, respectively. It is worth noting that these are within <1 kcal/mol of the exact barrier height. In both cases the convergence of the Sato parameter is smooth and rapid, being completed in 10 iterations.

One factor that can limit the effectiveness of an inversion procedure is finite experimental resolution. This can be reasonably represented by Gaussian convolution of the theoretical spectrum. That is, in making a comparison with an experimental spectrum the theoretical spectrum to be used is given by

$$I_c(E) = N \int I(E') e^{-(E-E')^2/\eta^2} dE' \quad (13)$$

where N is a normalization constant determined, e.g., by scaling to match the maximum value of the experimental spectrum. We can examine the effect on the inversion of the transition state spectra by generating an "experimental" spectrum by convoluting the calculated spectrum for the exact potential.

To this end, we have optimized the LEPS potential using the H_3^- spectrum calculated using the LSTH potential (with anion potential parameter Set B) and convoluted with $\eta = 0.01$ eV, a reasonable experimental value. Since the exact resolution may not always be known, we convolute the trial spectra with a different value, $\tilde{\eta} = 0.008$ eV. The initial, optimized, and exact (convoluted) spectra are shown in Figure 6 for this case. Note that the optimized spectrum is in very good agreement with the "experimental" spectrum. The optimized value of the Sato parameter is 0.347, corresponding to a barrier height of 0.466 eV. The convergence is smooth, similar to that in Figure 5, and is completed in 15 iterations. Thus, excellent agreement with the exact barrier height is obtained despite the convolution and the use of different values of η for the exact and trial spectra.

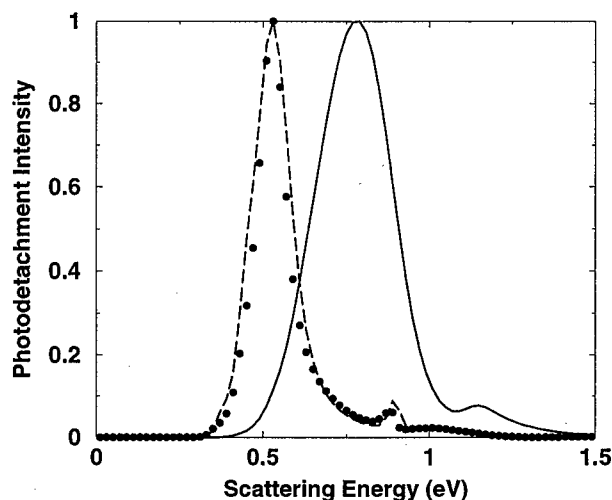


Figure 6. Same as Figure 4b but the "experimental" spectrum has been convoluted with $\eta = 0.01$ eV (cf. eq 13) and the trial spectra with $\tilde{\eta} = 0.008$ eV (see the text). Here the optimized spectrum has $S = 0.347$ corresponding to $V_0 = 0.466$ eV.

In fact, while a somewhat larger number of iterations is required, the final values of the Sato parameter is almost identical (within 0.001) to the unconvoluted case.

4. Concluding Remarks

We have presented a method for determining reactive potential energy surfaces from transition state photodetachment spectra. The method makes use of the derivatives of the photodetachment spectra with respect to parameters of the neutral potential energy surface. As shown previously,¹ these derivatives can be obtained at no additional cost above that required to calculate the spectrum itself. An iterative Levenberg–Marquardt-based scheme is used to optimize the potential parameters by minimizing the differences between the theoretical and experimental photodetachment spectra.

The viability of this approach has been demonstrated by its application to two model systems. Excellent agreement is obtained with the barrier height on the neutral potential energy surfaces in all cases. The method converges rapidly and thus requires only a small number of calculations of the photodetachment spectrum (and its derivatives). In addition, the finite resolution of experimental spectra can be dealt with by convolution of the theoretical spectrum and does not hinder the determination of the potential surface even if the resolution is not known exactly.

It is worth noting that multiple spectra for the same system obtained with different initial anion bound states can be used to advantage in this method. The measure of the error in eq 1 (which is minimized) can be simply extended to include more than one spectrum. The development of experimental techniques for varying the anion wave function would thus improve the ability to accurately determine the neutral potential surface.

There are a number of systems that would be interesting to treat with this method. These include the XHY^- systems (the $X + HY$ reactions), where X and Y are halides. The photodetachment spectra of these anions have been the subject of extensive experimental studies.¹⁸ In addition, larger molecules are such as cyclooctatetraene¹⁹ are of interest which, while not amenable to a full-dimensional quantum mechanical description, can be accurately treated in reduced dimensionality. In the case of cyclooctatetraene the photodetachment spectrum probes the barrier to isomerization of the molecule.

Acknowledgment. I gratefully acknowledge Prof. William H. Miller for his support and encouragement as well as for productive conversations, and Prof. James T. Hynes for his support during the completion of this work. I also thank Profs. Daniel M. Neumark and W. Carl Lineberger for useful discussions.

References and Notes

- (1) Thompson, W. H. *J. Phys. Chem. A* **1999**, *103*, 9500.
- (2) Dickinson, A. S.; Certain, P. R. *J. Chem. Phys.* **1963**, *49*, 4209; Harris, D. O.; Engerholm, G. G.; Gwinn, W. D. *J. Chem. Phys.* **1965**, *43*, 1515.
- (3) Lill, J. V.; Parker, G. A.; Light, J. C. *Chem. Phys. Lett.* **1982**, *89*, 483; Light, J. C.; Hamilton, I. P.; Lill, J. V. *J. Chem. Phys.* **1985**, *82*, 1400; Bačić, Z.; Light, J. C. *J. Chem. Phys.* **1986**, *85*, 4594; Whitnell, R. M.; Light, J. C. *J. Chem. Phys.* **1988**, *89*, 3674; Choi, S. E.; Light, J. C. *J. Chem. Phys.* **1990**, *92*, 2129.
- (4) Colbert, D. T.; Miller, W. H. *J. Chem. Phys.* **1992**, *96*, 1982.
- (5) Goldberg, A.; Shore, B. W. *J. Phys. B* **1978**, *11*, 3339.
- (6) Leforestier, C.; Wyatt, R. E. *J. Chem. Phys.* **1983**, *78*, 2334.
- (7) Jolicard, G.; Austin, E. J. *Chem. Phys. Lett.* **1985**, *121*, 106; Jolicard, G.; Austin, E. J. *Chem. Phys.* **1986**, *103*, 295; Jolicard, G.; Perrin, M. Y. *Chem. Phys.* **1987**, *116*, 1; Jolicard, G.; Leforestier, C.; Austin, E. J. *J. Chem. Phys.* **1988**, *88*, 1026.
- (8) Kosloff, R.; Kosloff, D. *J. Comput. Phys.* **1986**, *63*, 363.
- (9) Neuhauser, D.; Baer, M. *J. Chem. Phys.* **1989**, *90*, 4351; Neuhauser, D.; Baer, M. *J. Chem. Phys.* **1989**, *91*, 4651; Neuhauser, D.; Baer, M.; Kouri, D. J. *J. Chem. Phys.* **1990**, *93*, 2499.
- (10) Thompson, W. H.; Miller, W. H. *J. Chem. Phys.* **1994**, *101*, 8620.
- (11) Thompson, W. H.; Karlsson, H. O.; Miller, W. H. *J. Chem. Phys.* **1996**, *105*, 5387.
- (12) Seideman, T.; Miller, W. H. *J. Chem. Phys.* **1992**, *96*, 4412; Seideman, T.; Miller, W. H. *J. Chem. Phys.* **1992**, *97*, 2499; Miller, W. H.; Seideman, T. In *Time Dependent Quantum Molecular Dynamics: Experiment and Theory*; Broeckhove, J., Ed.; NATO ARW 1992; Thompson, W. H.; Miller, W. H. *Chem. Phys. Lett.* **1993**, *206*, 123.
- (13) Freund, R. W.; Nachtigal, N. M. *Numer. Math.* **1991**, *60*, 315; Freund, R. W. In *Numerical Linear Algebra*; Reichel, L.; Rutan, A.; Varga, R., Eds.; de Gruyter: Berlin, 1993.
- (14) Press, W. H.; Flannery, B. P.; Teukolsky, S. A.; Vetterling, W. T. *Numerical Recipes, The Art of Scientific Computing*; Cambridge University Press: Cambridge, UK, 1992.
- (15) Thompson, W. H. Ph.D. Thesis, Lawrence Berkeley Laboratory, University of California, 1996.
- (16) Liu, B.; Siegbahn, P. *J. Chem. Phys.* **1978**, *68*, 2457; Truhlar, D. G.; Horowitz, C. *J. Chem. Phys.* **1978**, *68*, 2566; *J. Chem. Phys.* **1979**, *71*, 1514.
- (17) Spath, B. W.; Miller, W. H. *Chem. Phys. Lett.* **1996**, *262*, 486.
- (18) See, for example, Neumark, D. M. *Acc. Chem. Res.* **1993**, *26*, 33; Metz, R. B.; Bradforth, S. E.; Neumark, D. M. *Adv. Chem. Phys.* **1992**, *81*, 1; Bradforth, S. E.; Weaver, A.; Arnold, D. W.; Metz, R. B.; Neumark, D. M. *J. Chem. Phys.* **1990**, *92*, 7205; Waller, I. M.; Kitsopoulos, T. N.; Neumark, D. M. *J. Phys. Chem.* **1990**, *94*, 2240; Metz, R. B.; Weaver, A.; Bradforth, S. E.; Kitsopoulos, T. N.; Neumark, D. M. *J. Phys. Chem.* **1990**, *94*, 1377; Weaver, A.; Metz, R. B.; Bradforth, S. E.; Neumark, D. M. *J. Phys. Chem.* **1988**, *92*, 5558; Metz, R. B.; Kitsopoulos, T.; Weaver, A.; Neumark, D. M. *J. Chem. Phys.* **1988**, *88*, 1463.
- (19) Wenthold, P. G.; Hrovat, D. A.; Borden, W. T.; Lineberger, W. C. *Science* **1996**, *272*, 1456.

Quantum Molecular Dynamics Simulations of Low-Temperature High Energy Density Matter: Solid p-H₂/Li and p-H₂/B

Soonmin Jang, Seogjoo Jang, and Gregory A. Voth*

Department of Chemistry and Henry Eyring Center for Theoretical Chemistry, University of Utah,
315 S. 1400 E. Rm Dock, Salt Lake City, Utah 84112-0850

Received: June 23, 1999; In Final Form: September 8, 1999

The metastability of atomic impurities, Li and B, trapped in solid parahydrogen is studied by employing path integral molecular dynamics (PIMD) and centroid molecular dynamics (CMD) simulations at 4 K and zero external pressure. Starting from pure solid hydrogen consisting of 1440 particles, doped systems are prepared by substituting impurity atoms for hydrogen molecules at substitutional defect sites. For various concentrations, thermodynamic quantities are then calculated and the stability of the systems is monitored. For the case of lithium, systems containing 2.5 mol % dopants remain metastable with convergent thermodynamic quantities, but systems with 3.3 mol % or more dopants become unstable. For the case of boron, systems containing as high as 15 mol % dopants remain metastable on the time scale of the simulation, while systems with 25 mol % dopants do not. These results provide evidence of the transition from metastability to global instability and a rough estimate of the maximum doping density of the two atomic species. The calculations show that boron-doped systems have the potential to achieve a higher impurity concentration than lithium-doped systems. The intrinsic boron reaction rate at longer times was calculated for 6.25 mol % of boron impurities. The quantum centroid potential of mean force (PMF) was calculated and then the recombination reaction rate was estimated using path integral quantum transition state theory (PI-QTST). The PI-QTST calculation suggests that the transition state for boron dimer recombination at this concentration occurs at 5.39 Å separation and its free energy barrier is 360 ± 36 K. The calculated intrinsic recombination reaction rate is approximately $8 \times 10^{-27} \text{ s}^{-1}$. This result suggests that the overall reaction rate of boron recombination reaction may be limited by the intrinsic recombination rate rather than by self-diffusion of the impurities. It is also found that the initial reaction of boron induces only local recombination of other boron impurities at this concentration and not a global instability. The dynamical effect of a single boron pair reaction on the rest of the system has also been studied by CMD simulations. These simulations show that the energy release from the dimer recombination does not lead to global melting of the solid.

1. Introduction

Solid parahydrogen is one of the simplest quantum solids and has been the subject of many theoretical and experimental studies. Experimental evidence shows that impurity atoms such as Li, B, and F can be metastably trapped in the solid hydrogen matrix, suggesting its potential usage as high energy density matter (HEDM).^{1–3} Classical molecular dynamics (MD) simulation is not suitable for these systems because of the substantial quantum behavior of the host and guest molecules. To date, various quantum simulations have been performed, but they have been mostly confined to pure solid parahydrogen or hydrogen systems containing at most two lithium impurities.^{4–8} For boron atoms with parahydrogen, there have been simulation studies on the stability of small B(H₂)_n clusters,^{9,10} and it is suggested that the clusters are stable from these studies.

For the doped solid hydrogen to be useful as HEDM, the impurity atoms must remain metastably trapped for a substantial lifetime. In addition, the concentration of the metastable impurity should be as high as possible. However, each system will have some maximal possible impurity concentration. This concentration, in principle, can be determined through a series of experiments, but uncontrollable experimental factors make it very difficult to correlate microscopic details of a system with its metastability in a quantitative and systematic way, so complementary simulation studies are useful.

A complete simulation study of the metastability of a quantum many-body system is a daunting problem. One must identify quantum metastable states in multidimensional space and adapt a suitable quantum dynamical simulation method or quantum rate theory. Only one model system is not enough to study as the information for various concentrations of the dopant are required.

The purpose of the present work is as follows: First, a qualitative global stability analysis of Li doped p-H₂ and B doped p-H₂ is carried out and an identification of metastable states with converging thermodynamic quantities will be made. For large scale model systems with varying concentration of the dopants, path integral molecular dynamics (PIMD)¹¹ simulations, an equilibrium finite temperature quantum simulation technique, are performed. The stability of the system is monitored along with the convergence of the thermodynamic quantities. Since PIMD is a fictitious time molecular dynamics simulation method, the lifetime determined by this method does not have a genuine physical meaning in real time. However, it can give an upper bound for the maximum metastable concentration and the qualitative estimation of the relevant thermodynamic quantities. This information is useful for the guidance of future experimental efforts to prepare samples and for more quantitative simulation studies.

Second, the pairwise reactivity of boron impurities in a solid

p-H₂ matrix will be studied. An earlier study on the recombination of Li impurities was carried out by two of us, and it was found that the Li atom shows significant quantum tunneling behavior and that the recombination reaction is estimated to be diffusion limited.⁸ The boron counterpart of this study is performed here by constructing a quantum centroid potential of mean force (CPMF) at a globally stable impurity concentration.

Finally, the structural and dynamical effects of the pairwise boron impurity recombination on the rest of the system are studied. The pairwise reaction of two impurities may induce a structural change in the lattice and can release significant amounts of energy into the surrounding environment, both of which could in turn induce other impurity recombination reactions. Since the energy release process is a quantum dynamical process rather than an equilibrium process, the centroid molecular dynamics (CMD) method¹²⁻¹⁵ will be used for this purpose. There have been previous CMD studies on pure solid p-hydrogen in our group¹⁶ which showed that the calculated phonon spectrum is in good agreement with the experimentally observed spectrum, while the classical calculation resulted in very different results. Also, the self-diffusion constant of liquid p-hydrogen was calculated using CMD,¹⁷ showing good agreement with experimental data. Recently, Kinugawa reported a CMD study on the dynamic structure factor of liquid p-hydrogen.¹⁸

The present paper is organized as follows: In section II a brief description is given of PIMD and CMD. The potential energies and calculation methods used in this study will also be presented in this section. Section III contains the simulation results and discussion, while concluding remarks are presented in section IV.

II. Methods

A. Path Integral Molecular Dynamics. The quantum canonical partition function Z has the following form

$$Z = \text{Tr}[e^{-\beta H}] \quad (1)$$

$$= \int d\mathbf{q} \langle \mathbf{q} | e^{-\beta H} | \mathbf{q} \rangle \quad (2)$$

where $\beta = 1/k_B T$ and H is the system Hamiltonian. Using indexed complete sets of coordinate and $e^{-\beta H} = (e^{-\epsilon H})^P$ with $\epsilon = \beta/P$, the partition function can be reexpressed as

$$Z = \prod_{i=1}^P \int d\mathbf{q}_i \langle \mathbf{q}_i | e^{-\epsilon H} | \mathbf{q}_{i+1} \rangle \quad (3)$$

Feynman showed that for a large enough number of discretizations P , this partition function can be described analytically in terms of quantum paths, i.e.

$$Z = (m/2\pi\hbar^2\epsilon)^{P/2} \prod_{i=1}^P \int d\mathbf{q}_i \exp[-\beta V_{\text{eff}}(\mathbf{q}_i)] \quad (4)$$

where the effective potential $V_{\text{eff}}(\mathbf{q})$ is given by

$$V_{\text{eff}}(\mathbf{q}_i) = \sum_{i=1}^P \left[\frac{mP}{2\hbar^2\beta^2} (q_i - q_{i+1})^2 + \frac{1}{P} V(q_i) \right] \quad (5)$$

In the limit $P \rightarrow \infty$, one obtains

$$Z = \int \cdots \int D\mathbf{q}(\tau) \exp\{-S[\mathbf{q}(\tau)]/\hbar\} \quad (6)$$

with

$$S[\mathbf{q}(\tau)] = \int_0^{\beta\hbar} d\tau \left\{ \frac{m}{2} \dot{\mathbf{q}}(\tau)^2 + V[\mathbf{q}(\tau)] \right\} \quad (7)$$

One can use PIMD generated by the effective potential in eq 5 to calculate the quantum equilibrium ensemble-averaged properties of the system.¹¹

B. Centroid Molecular Dynamics. In CMD,¹²⁻¹⁵ dynamical properties are calculated by classical-like equations of motion for the system path centroids, i.e.

$$m \frac{d^2 \mathbf{q}_c}{dt^2} = -\nabla V_c[\mathbf{q}_c(t)] \quad (8)$$

where $\mathbf{q}_c(t)$ is centroid coordinate of the system. The effective centroid potential $V_c(\mathbf{q}_c)$ is given by

$$V_c(\mathbf{q}_c) = -(1/\beta) \ln \left[\frac{\rho_c(\mathbf{q}_c)}{\rho_c^0(\mathbf{q}_c)} \right] \quad (9)$$

where $\rho_c^0(\mathbf{q}_c)$ is free particle centroid density, and $\rho_c(\mathbf{q}_c)$ is the centroid density for a given potential. The centroid density $\rho_c(\mathbf{q}_c)$ is given by

$$\rho_c(\mathbf{q}_c) = \int \cdots \int D\mathbf{q}(\tau) \delta(\mathbf{q}_c - \mathbf{q}_0) \exp\{-S[\mathbf{q}(\tau)]/\hbar\} \quad (10)$$

where \mathbf{q}_0 is particle centroid variable, defined as

$$\mathbf{q}_0 = \frac{1}{\hbar\beta} \int_0^{\hbar\beta} d\tau \mathbf{q}(\tau) \quad (11)$$

Since the harmonic spring term of eq 5 gives poor sampling efficiency (especially if the number of discretization P is large), one can use the normal-mode transformation to diagonalize this term.^{15,19} This can be done by Fourier expansion of the path, which is given by

$$\mathbf{q}_j = \sum_{n=1}^P \alpha_n \exp[2\pi i(j-1)(n-1)/P] \quad (12)$$

with normal mode α_n .¹⁹ The normal modes α_n are complex with the following properties

$$\alpha_1 = \mathcal{R}(\alpha_1) \quad (13)$$

$$\alpha_{P/2+1} = \mathcal{R}(\alpha_{P/2+1}) \quad (14)$$

$$\alpha_n = \alpha_{P+2-n}^* \quad (n = 2, \dots, P/2) \quad (15)$$

where \mathcal{R} here stands for the "real part of" and \mathcal{I} stands for the "imaginary part of" below. Redefining the normal-mode coordinates as (with P even)

$$\mathbf{a}_1 = \alpha_1 \quad (16)$$

$$\mathbf{a}_P = \alpha_{P/2+1} \quad (17)$$

$$\mathbf{a}_{2n-2} = \sqrt{2} \mathcal{R}[\alpha_n] \quad (n = 2, \dots, P/2) \quad (18)$$

$$\mathbf{a}_{2n-1} = \sqrt{2} \mathcal{I}[\alpha_n] \quad (n = 2, \dots, P/2) \quad (19)$$

The final expression for the harmonic spring potential in terms of the normal-mode coordinate α_j is given by

$$\sum_{i=1}^P \frac{mP}{2\hbar\beta} (\mathbf{q}_{i+1} - \mathbf{q}_i)^2 = \frac{mP}{2\hbar\beta} \sum_{n=1}^P \lambda_n \mathbf{a}_j^2 \quad (20)$$

where $\lambda_1 = 0$, $\lambda_P = 4P$ and

$$\lambda_{2n-1} = \lambda_{2n-2} = 2P[1 - \cos(2\pi[n-1]/P)] \quad (21)$$

It should also be noted that once the effective centroid potential in eq 9 is associated with a reaction coordinate and all other centroids of the system are integrated over, the reaction rate can be estimated by path integral quantum transition state theory (PI-QTST)^{20–24} which is based on the centroid potential of mean force (CPMF) for the reaction coordinate. The calculation of the CPMF as a function of the reaction coordinate involves the direct calculation of its derivative and then the integration of this quantity over the reaction coordinate values of interest. Such a procedure for lithium impurity recombination is described in a previous paper,⁸ and the same procedure is used here for boron impurities.

C. Potential Energy Functions. The Silvera–Goldman potential²⁵ was used for the H₂–H₂ interaction as in previous studies.^{4–7} For the p-H₂/Li studies, the H₂–Li and Li–Li interactions were represented by Cheng and Whaley's⁶ and Jang and Voth's⁸ potentials, respectively. For the p-H₂/B studies, Alexander and Wang²⁶ calculated the H₂–B potential energies and generated an analytical expression by averaging over three different orientations of the 2p orbitals of the boron atom with respect to the p-H₂ molecule. The resulting potential has the fitted form

$$v(r) = c_1 \exp(-\lambda_1 r) + (c_2 + c_3 r) \exp(-\lambda_2 r) - \frac{c_4}{2r^6} [\tanh\{1.2(r - \lambda_3)\} + 1] \quad (22)$$

where $c_1 = -7.7200 \times 10^3 \text{ cm}^{-1}$, $c_2 = -5.0553 \times 10^6 \text{ cm}^{-1}$, $c_3 = 2.4887 \times 10^6 \text{ cm}^{-1}/\text{\AA}^{-1}$, $c_4 = -5.5570 \times 10^5 \text{ cm}^{-1}/\text{\AA}^{-6}$, and $\lambda_1 = 6.7219 \times 10^{-1} \text{ \AA}^{-1}$, $\lambda_2 = 1.7967 \text{ \AA}^{-1}$, $\lambda_3 = 7.3479 \text{ \AA}$. The interactions of the boron impurities with the hydrogen lattice were approximated by pairwise summation over these isotropic model potentials.

There have been several studies on the B–B potential energy surfaces by both experiment and theory.^{27–30} The ground state electronic potential is $X^3\Sigma_g^-$ and the next high-lying electronic state is $I^5\Sigma_u^-$.²⁹ The potential energy difference between these two states is several orders of $k_B T$ at the potential minimum (1.590 16 Å) and the difference increases dramatically as the dimer distance is increased. There is curve crossing around 1.46 Å, but once the boron pair undergoes recombination reactions, the sampling of the potential energy contribution from the boron–boron distances less than equilibrium dimer distance should be ignorable. Recently, there has been new ground state ab initio calculations by Peterson et al.³¹ at the val-CAS-ICMRCI (complete active space–internally contracted multi-reference configuration interaction)/cc-pCV5Z all-electron correlated level, which are the most recent and accurate results. The data is available only near the potential minimum. Their results were used to construct an analytical boron–boron potential using a Morse-like potential form, the Varshni function. The fitted potential is given by

$$v(r) = D_0[1 - (r_0/r) \exp\{-\alpha(r^2 - r_0^2)\}]^2 - D_0 \quad (23)$$

where $D_0 = 23\,475.49 \text{ cm}^{-1}$, $r_0 = 1.590\,16 \text{ \AA}$, and $\alpha = 3.304 \times 10^{-2} \text{ \AA}^{-2}$. Another ab initio calculation by Dupuis and Liu²⁷

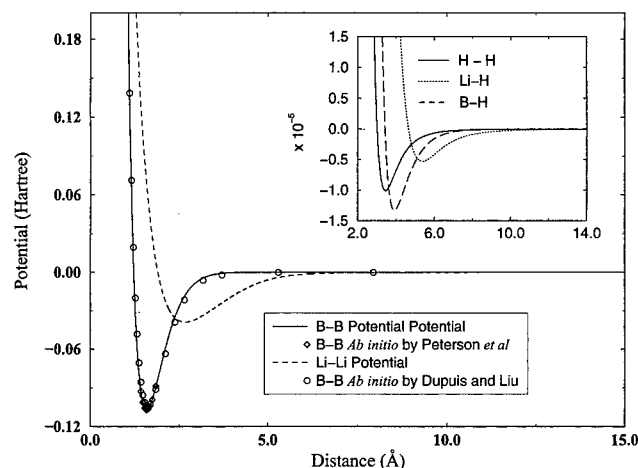


Figure 1. Various potential energy functions. The analytical boron–boron interaction potential is compared with ab initio data.

shows almost the same behavior as our fitted potential. Figure 1 shows the fitted analytical potential for the boron–boron interaction against the ab initio data of both Peterson et al. and Dupuis and Liu. The Li–Li and H₂–B interaction potentials are also shown for comparison.

D. Simulation Details. The velocity Verlet (VV-I)³² algorithm was used as an integrator of the thermostated dynamical equations of motion. The number of quantum discretizations P (“pseudo particles”) was set at 48.^{4–8} Nosé–Hoover chain dynamics^{19,33–35} were used to keep the system at a constant temperature. Nosé–Hoover chains of length 4 were attached to each normal mode in each Cartesian direction of the pseudoparticles.^{32,36–38} The simulation temperature was 4 K throughout the simulation.

This study required simulations of systems of large size with numerous initial trials under varying conditions, which proved to be computationally demanding. Especially the calculation of the CPMF and the CMD simulations required large amounts of averaging. To help overcome these difficulties, extensive parallel computations were used in all the calculations.

1. Global Stability Simulations for Lithium and Boron Impurities in Solid Hydrogen. To perform a stability analysis and to obtain an estimate of the maximum impurity doping densities for lithium and boron in solid hydrogen, it was necessary that the system be large enough to contain a reasonable number of impurities in the solid parahydrogen matrix. Large PIMD simulations with 1440 total particles were therefore used for this purpose.

Since solid parahydrogen has a large compressibility, there will be some global volume change after the dopants are trapped. Conventional constant pressure MD^{39,40} was employed to treat this situation properly. Nosé–Hoover chains were implemented with a constant pressure simulation box wall. Pure solid parahydrogen has a hexagonal cubic packing structure (hcp). Independent scaling of the three orthogonal directions was allowed to accommodate the anisotropic nature of this lattice structure. The external pressure was then set to zero. The simulation parameters were adjusted to maximize the speed of convergence. If they are within reasonable range, the simulation parameters do not affect the simulation results. Table 1 lists the simulation parameters used.

The initial equilibrium configuration of the pure parahydrogen was generated starting from the hcp lattice structure with simulation box lengths of 38.20, 39.70, and 37.43 Å in the three orthogonal directions, respectively. This corresponds to the experimental density of pure solid parahydrogen of 23.1 cm³/

TABLE 1: Simulation Parameters

system	time step (t_s) ^a	Nosé–Hoover mass ^b	wall mass ^b	Nosé–Hoover mass of wall ^b
H ₂ /Li	0.02	5.0	50.0	50.0
H ₂ /B	0.007	20.0	200.0	200.0

^a The time step is given by $t_s = \hbar\beta/(4P)^{1/2}$, where P is number of PIMD pseudoparticles. ^b Masses are in units of $t_s^2/(2\pi^2\beta)$ (see Appendix).

mol. It took about 4.0 ps of PIMD time, which is about 5000 iterations, to reach equilibrium. The average box size of pure solid parahydrogen after it has reached equilibrium was 37.94, 39.45, and 37.19 Å. The configuration of the impurity-doped parahydrogen was then generated by replacing selected hydrogen molecules in the equilibrated pure solid hydrogen with the same number of impurities. Starting from this configuration, parahydrogen with impurities then evolved under further isothermal and isobaric PIMD simulation for a long enough time to reach “equilibrium”, even though this metastable state could be valid only within the simulation time. A series of different impurity concentrations was then studied by changing the amount of trapped impurities systematically.

2. Intrinsic Recombination Rate Calculations for Boron Impurities in Solid Hydrogen. It is possible that recombination reactions might occur in the p-H₂/B system on a time scale much longer than that of the global stability simulations, and that such recombinations could trigger global instabilities in the lattice. Therefore, two B impurities were forced to recombine in a 6.25 mol % p-H₂/B system to study this possibility. PI-QTST simulations were^{20–24} used for this purpose.

The reaction coordinate for the recombination of boron impurities in solid p-hydrogen matrix was defined as the boron–boron separation, and the CPMF was calculated as a function of this distance. The same method was followed as in previous work⁸ on lithium impurity recombination except that the normal-mode transformation¹⁵ was used to speed up the convergence of the path integral simulations.

In these simulations, the system consisted of 1152 particles in total. Starting from a perfect hcp lattice structure, the PIMD simulations were first performed under constant temperature and pressure as described above. The equilibrium structure of the pure solid p-H₂ was generated after 10 000 PIMD iterations (about 9.7 ps of PIMD time).

Instead of placing just two reacting impurities in the hydrogen simulation cell as in ref 8, in these simulations 72 hydrogen molecules were replaced with the same number of boron impurity atoms. The concentration of this system was 6.25 mol % boron, which is a stable concentration according to a large scale PIMD stability study similar to those described in the previous section. The box length after reaching equilibrium with 5000 PIMD iteration was 58.75, 75.40, and 71.21 Å. A pair of boron atoms in the direction of the longest box length was then chosen for the PMF calculation at this equilibrium configuration. Constant temperature and constant volume normal mode PIMD (NMPIMD)^{11,32,39,40} was used for the calculations.

The equilibrium configurations of the system at different recombining boron pair distances (reaction coordinate) were quasistatically generated by increasing/decreasing the pair distance followed by 2500 NMPIMD iterations. The distance change was 0.0529 Å and the NMPIMD iterations were performed with a centroid distance constraint between the selected boron atoms during this procedure. All other boron atoms were free to move during the simulations. The mean force was calculated with a separation interval of 0.397 Å or less if

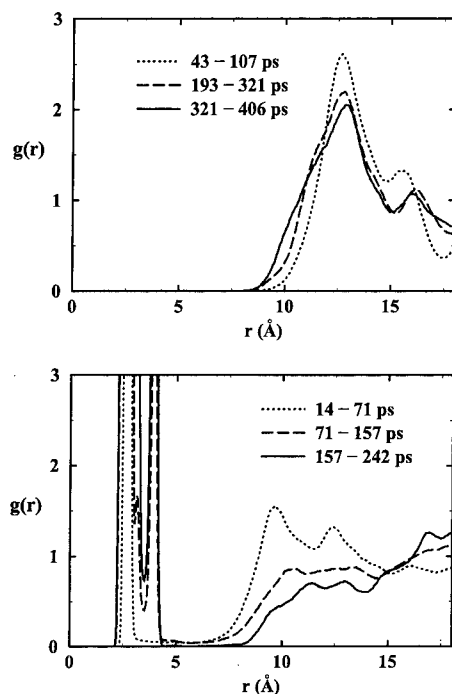


Figure 2. Time-dependent Li–Li pair distribution functions for 2.5 mol % (upper panel) and 3.3 mol % (lower panel) impurity concentrations.

necessary. A total of 25 000 normal-mode PIMD samplings were performed at each reaction coordinate for the PMF calculation. The number of sampling steps was increased to up to 75 000, depending on the reaction coordinate value, to ensure good convergence of the calculated PMF.

3. Energy Disposal Calculations for Boron Impurities in Solid Hydrogen. The energy disposal dynamics during boron recombination was studied using CMD at 6.25 mol %, i.e., the same concentration as in the PI-QTST intrinsic recombination rate calculations. Due to the computational cost, the system was reduced to 432 particles in total of which 27 were boron impurities. The equilibrium configuration was generated by the same method as described in the previous section except for a different system size. The simulation box size after equilibration was 22.92, 19.85, and 37.43 Å.

The initial CMD configuration was prepared by quasistatically reducing the distance of a selected boron pair until it reached 5.39 Å, which is the barrier top for the recombination reaction as determined from the PI-QTST study. Then, CMD simulations were performed by starting the boron pair slightly to the product side from the top of the CPMF barrier. The boron pair distance was reduced by 0.01 Å from the barrier top to accomplish this.

The PIMD time step for solid hydrogen with boron impurities is about 0.25 fs. The CMD time step was correspondingly 0.0125 fs and the number of centroid force samplings was 10 at every CMD time step. A single CMD trajectory was calculated and the energies and structure of the system were monitored as a function of the CMD simulation time.

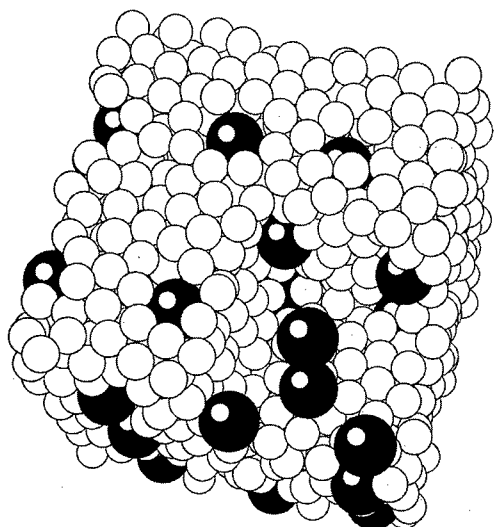
III. Results and Discussion

A. Global Stability Calculations for Lithium and Boron Impurities in Solid Hydrogen. In the simulations of the p-H₂/Li system, it was found that 36 Li atoms (2.5 mol %) with 1404 hydrogen molecules remain stable on the time scale of the simulation. The upper panel of Figure 2 shows the Li–Li pair distribution function sampled at different PIMD time intervals. The minimum distance that has a nonzero value in the pair

TABLE 2: Thermodynamic Quantities of the 2.5 mol % p-H₂/Li System^a

simulation time (ps)	T_h/N_h	T_l/N_l	V_{hh}/N_h	V_{hl}/N_l	V_{ll}/N_l	E_l/N_l	vol/vol ₀
43–107	53	31	-124	-413	-12	-394	1.21
107–192	54	31	-125	-428	-12	-410	1.21
107–320	54	31	-125	-436	-13	-419	1.21

^a Energies are in K. T_h is the average kinetic energy of H₂; T_l is average kinetic energy of Li; V_{hh} , V_{hl} , and V_{ll} are the average interaction energies of H₂–H₂, H₂–Li, and Li–Li, respectively; N_h and N_l are number of H₂ and Li, respectively; E_l/N_l gives the total released energy per Li atom; vol/vol₀ is the ratio of the final system volume to the pure hydrogen volume.

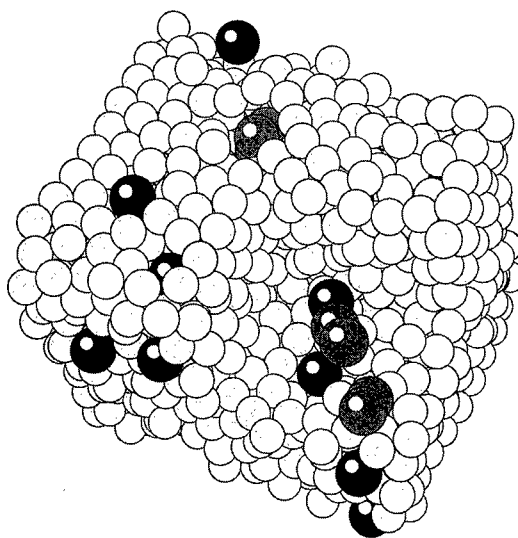
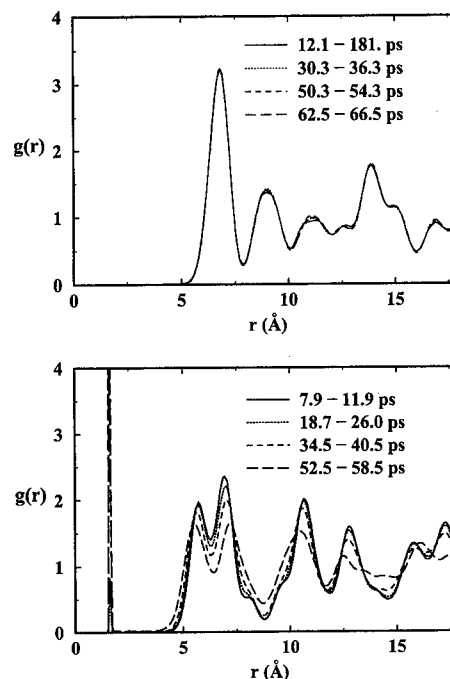
**Figure 3.** Snapshot of 34 Li atoms (2.5 mol %) in 1406 hydrogen molecules after 406 ps PIMD simulation time.**TABLE 3: Thermodynamic Quantities for the 3.3 mol % p-H₂/Li System^a**

simulation time (ps)	T_h/N_h	T_l/N_l	V_{hh}/N_h	V_{hl}/N_l	V_{ll}/N_l	E_l/N_l	vol/vol ₀
0–14	49	30	-116	-342	-35	-347	1.28
14–71	53	39	-120	-374	-3249	-3584	1.25

^a Definitions are the same as in Table 2.

distribution function is 7.8 Å. Table 2 lists various thermodynamic quantities calculated at this concentration. Both the upper panel of Figure 2 and Table 2 indicate that there is no Li–Li recombination reaction and it has reached equilibrium; i.e., the trapped Li atoms remain in a metastable state during the tested interval of time. Figure 3 shows a configuration of the 2.5 mol % system from near the end of the simulation.

The same calculation with 48 Li atoms (3.3 mol %) showed that the system is not stable and Li–Li recombination reactions begin to occur on a short time scale. The lower panel of Figure 2 is the Li–Li pair distribution function at different times of PIMD simulation. As the recombination reaction progresses, energy begins to be released mainly due to the strong Li–Li interaction potential. The amount of energy released during the two time intervals is listed in Table 3 along with other thermodynamic quantities. The large peaks in the pair distribution function at distances less than 8.0 Å in the lower panel of Figure 2 clearly show the degree of recombination reactions at this concentration, which begins a cascade process. The potential of mean force calculation by Jang and Voth⁸ shows that the Li–Li recombination barrier top is at impurity distances of about 8.28 Å. Even though their calculation was performed at a much lower concentration, the present study is in qualitative agreement

**Figure 4.** Snapshot of 48 Li atoms (3.3 mol %) in 1392 hydrogen molecules after 242 ps PIMD simulation time. The recombined lithium atoms are shaded in gray.**Figure 5.** Time-dependent boron–boron pair distribution functions for 15.0 mol % (upper panel) and 25.0 mol % (lower panel) impurity concentrations.

with their results. Figure 4 shows a configuration of the 3.3 mol % system near the end of the simulation. Note the recombined lithium impurities.

The boron–boron pair potential is much shorter ranged and more attractive than the Li–Li interaction potential, while the H₂–B interaction is shorter ranged and deeper than that of H₂–Li (cf. Figure 1). As a result, more boron atoms are expected to be metastably trapped than Li atoms. The simulations indeed show that 216 boron atoms (15.0 mol %) in 1224 p-H₂ molecules remain stable on the time scale of the simulation, while 360 boron atoms (25.0 mol %) in 1080 p-H₂ molecules do not. The time-dependent boron–boron pair distribution functions at these concentrations are shown in Figure 5.

The long-range region of the model boron–boron potential might influence the results of the present calculations, but the boron–boron potential is a fairly short-ranged interaction, which

TABLE 4: Thermodynamic Quantities for the 15 mol % p-H₂/B System^a

simulation time (ps)	T_h/N_h	T_b/N_b	V_{hh}/N_h	V_{hb}/N_b	V_{bb}/N_b	E_b/N_b	vol/vol ₀
18.1–24.1	64	19	–116	–480	–0.12	–461	1.10
30.2–36.3	64	25	–116	–480	–0.16	–455	1.10
50.4–54.4	64	24	–116	–480	–0.16	–456	1.09
62.5–66.5	64	23	–112	–452	–0.20	–388	1.09

^a Definitions are the same as in Table 2.**TABLE 5: Thermodynamic Quantities of the 25 mol % p-H₂/B System^a**

simulation time (ps)	T_h/N_h	T_b/N_b	V_{hh}/N_h	V_{hb}/N_b	V_{bb}/N_b	E_b/N_b	vol/vol ₀
3.0–7.9	64	25	–92	–416	–0.60	–391	1.19
26.0–32.2	64	20	–92	–420	–544	–940	1.17
46.5–52.5	64	29	–92	–420	–2360	–2743	1.15

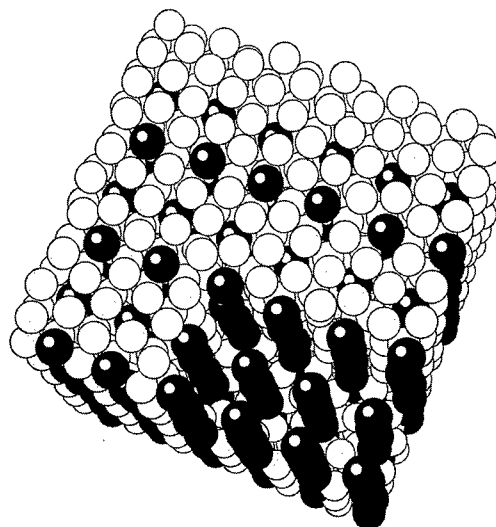
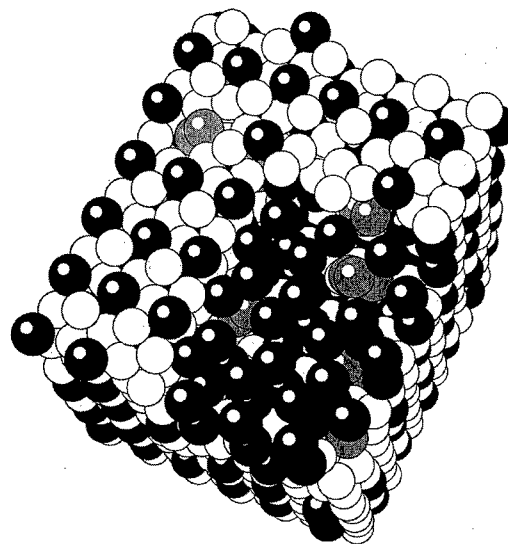
^a Definitions are the same as in Table 2.

is well characterized by our fitted potential. It is therefore expected that there would be no qualitative change due to errors in the long-range tail. There might be another more serious error caused by using a model H₂–B potential which is isotropic and does not have the dependence on the orientation of the 2p boron orbitals. However, considering the condensed phase environment and dynamic fluctuations of the hydrogen matrix which average the interaction around each boron, the use of the isotropic potential may be justified.

It should also be pointed out that the present simulations do not consider vacancy sites which might play an additional role in the stability issue. The impurities are initially arranged such that they make a uniform distribution at a given concentration. During the actual experimental deposition of impurities, there might be an irregular distribution of impurities and some reacted species which may induce local or global reactions. It is important that the number of impurities in the present case be understood as an upper bound for the stability of the system. The 216 boron atoms (15.0 mol %) case is certainly only a threshold density. For more highly concentrated systems, the time-dependent pair distribution function shows boron pairs with less than 4.3 Å separation readily undergo recombination reactions. The minimum distance between boron impurities in the 15.0 mol % system is 4.59 Å. Considering the lattice constant of pure solid p-H₂ is about 3.5 Å, this is a rather short distance. The thermodynamic data for the two p-H₂/B calculations with 216 B atoms and 360 B atoms are listed in Tables 4 and 5, respectively. Also shown in Figures 6 and 7 are snapshots of the p-H₂/B simulations at the final states showing their stability and/or instability.

The p-H₂/B systems have a considerably higher impurity concentration than p-H₂/Li in its metastable state. It is therefore likely that B is potentially more useful than Li for creating high energy density matter. The small size of the B atom contributes to this extra stability, causing less distortion of the solid p-H₂ matrix than the Li atom. This can be seen from Tables 2 and 3. The total volume of the system changes slightly for the 15 mol % p-H₂/B system even though its impurity concentration was 6 times greater than that for the 2.6 mol % p-H₂/Li system. The B–H₂ interaction potential is also much more attractive than the Li–H₂ potential (cf. inset in Figure 1) and not much different than the H₂–H₂ potential. This suggests that B atoms may go into substitutional defects in the p-H₂ lattice readily.

In the present work, chemical reactions of the impurity atoms with the hydrogen molecules were not considered. Recent experimental results show that a boron atom can undergo an

**Figure 6.** Snapshot of 216 B atoms (15 mol %) in 1224 hydrogen molecules after 78 ps PIMD simulation time.**Figure 7.** Snapshot of 360 B atoms (25 mol %) in 1080 hydrogen molecules after 59 ps PIMD simulation time. The recombined boron atoms are shaded in gray.

insertion reaction.^{1–3} According to ab initio calculations for cluster systems,^{41,42} the activation energy barrier for such a reaction is about 80 kJ/mol, which is much higher than the thermal energy at 4 K. It should also be noted that only single initial configurations of the impurity systems were studied due to the computationally demanding nature of the simulations. A more systematic study will be the subject of future research.

B. Intrinsic Recombination Rate Calculations for Boron Impurities in Solid Hydrogen. Figures 8 and 9 show the computed centroid mean force and centroid potential of mean force, respectively, for the recombination reaction of two boron impurities. The overall statistical error of the calculated potential of mean force is about 10%. The transition state is at 5.39 Å and there is an abrupt change of the centroid force (and thus the CPMF) toward the impurity recombination after the transition state. This is because there is a significant onset of quantum tunneling of the borons as pointed out in previous work on impurity recombination.⁸ The calculated barrier height is 350 ± 35 K. As can be seen in Figure 1, the B–H₂ well depth is 3 times deeper than the Li–H₂ potential, and the latter has more repulsive energy within the H₂ lattice owing to its large size. Therefore, it may not be surprising that the barrier for intrinsic

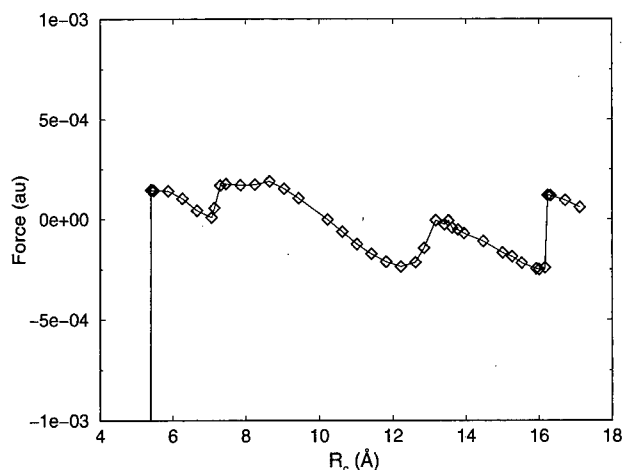


Figure 8. Centroid mean force as a function of centroid distance R_c between two boron impurities at 6.25 mol %. Note that force at 5.36 Å is not shown here which is -1.09×10^{-2} .

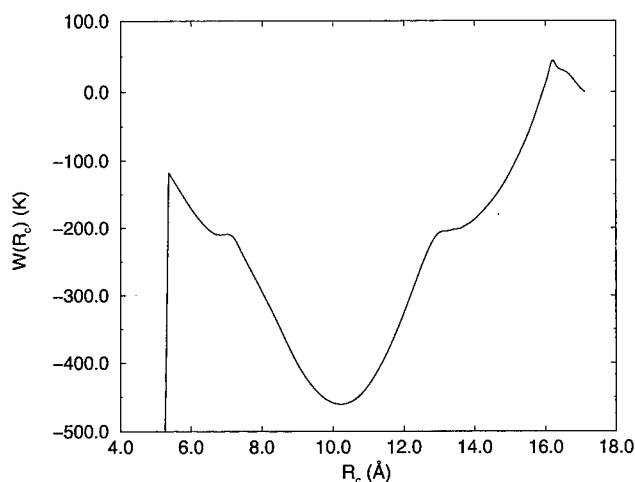


Figure 9. Centroid potential of mean force (CPMF) from integration of Figure 8.

recombination of Li in solid H_2 is 4 times less (80 K) than that for boron.⁸ The other abrupt changes in the CPMF away from the barrier region are due to lattice rearrangements in the vicinity of the recombining impurities.

Using the same analysis as in a previous study,⁸ the quantum intrinsic reaction rate is estimated to be $8 \times 10^{-27} \text{ s}^{-1}$. Considering the error in the calculated CPMF, the intrinsic rate range is 1×10^{-30} to $7 \times 10^{-24} \text{ s}^{-1}$. The rate of impurity recombination can then be described in terms of the intrinsic recombination rate and the diffusion rate.^{43–45} Following the same analysis as for the Li reaction rate,⁸ the intrinsic recombination rate is estimated from the intrinsic reaction rate to be $2 \times 10^{-46} \text{ cm}^3 \text{ s}^{-1}$. This extremely slow intrinsic reaction rate can be compared with the estimated self-diffusion rate which is $2 \times 10^{-30} \text{ cm}^3 \text{ s}^{-1}$ if boron has the same self-diffusion rate as pure solid hydrogen. Based on the above qualitative arguments, it can be suggested that in a perfect solid the overall boron recombination reaction rate is limited by the intrinsic recombination step (unlike lithium which was estimated to be a diffusion-limited reaction⁸). The forced recombination of two boron impurities at the 6.25 mol % concentration results in only local recombination of three boron atoms, not global instability, as will be further discussed at the end of the next section.

Of course, in a real solid there will be defects, grain boundaries, etc., which may influence the intrinsic recombination rates. The effects of these will be the subject of future research.

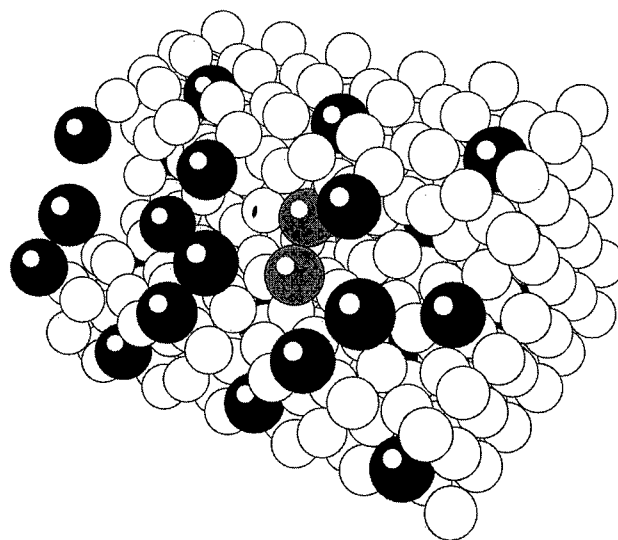


Figure 10. Snapshot of 405 hydrogen molecules and 27 boron atoms (6.25 mol %) before the CMD simulation.

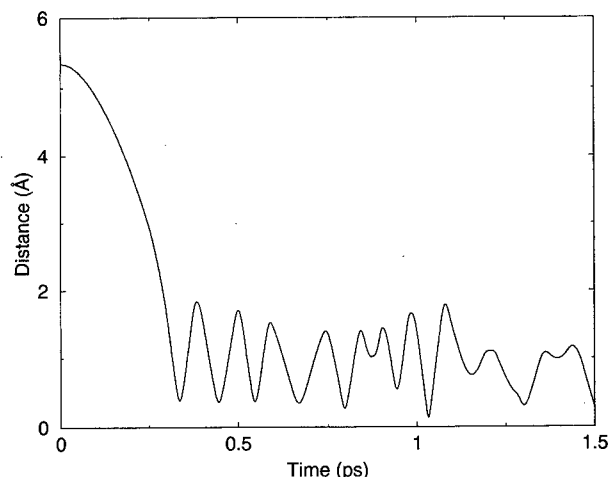


Figure 11. Centroid distance of the selected recombining boron pair as a function of time. Plotted is the distance as a function of the equilibrium B–B distance from Figure 1.

It should also be noted that the current calculation was at only one particular boron concentration. Furthermore, the selected boron pair represents only one possible reacting configuration in the ordered solid hydrogen matrix at the specified concentration.

C. Energy Disposal Calculations for Boron Impurities in Solid Hydrogen. As can be seen from the B–B potential energy function in Figure 1, a boron pair recombination will release a significant amount of energy during the recombination event. It was therefore important to study the dynamical effects of the boron recombination on the overall system stability using a CMD simulation. The released energy may trigger other nonequilibrium recombination reactions of adjacent boron atoms which could produce a cascade effect of recombination reactions. This is certainly true at higher impurity concentrations as seen from the global stability simulations at 25 mol %.

Figure 10 shows the system configuration before the CMD simulation was started. The change of centroid distance between the selected recombination pair of boron atoms (gray atoms in Figure 10) is shown in Figure 11 as a function of time. Plotted is the interpair B–B distance. The distance change is large at the early stage of the CMD simulation as the pair rapidly releases its energy to the environment (hydrogen and other

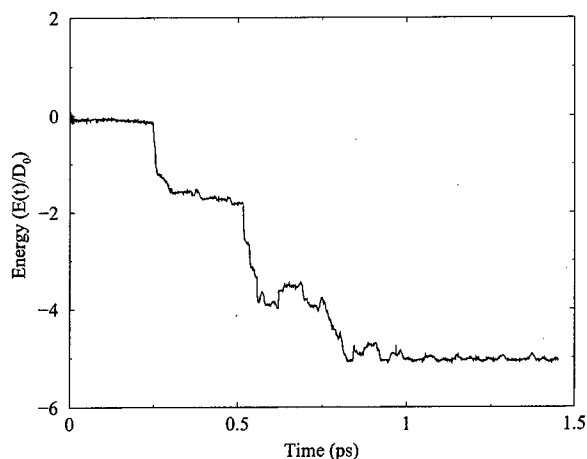


Figure 12. Released energy as a function of time for the recombining B-B pair. Plotted is the released energy as a function of the B-B well depth from Figure 1.

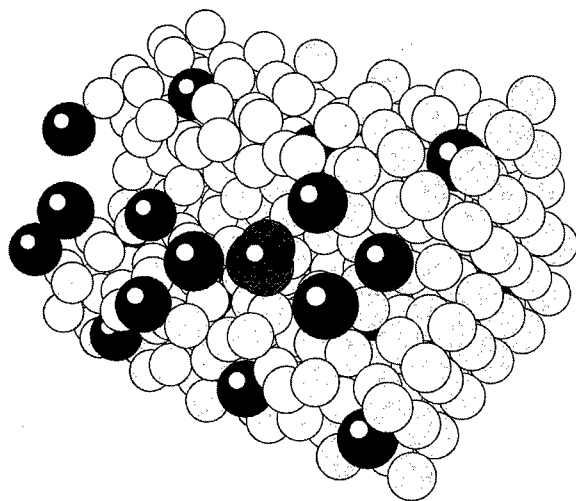


Figure 13. Snapshot of 405 hydrogen and 27 boron atoms (6.25 mol %) after 1.6 ps of CMD simulation. The locally recombined boron atoms are shown.

borons). Figure 12 shows the total energy of the boron impurities in the system as a function of time (as a fraction of a single B-B well depth). As one can see both from the boron pair distance change and from the energy release plots, the time scale by which the boron pair releases a significant amount of energy to the environment is around 0.25 ps at this impurity concentration. The released energy from the first recombination helps to trigger further local recombination reactions with other nearby boron impurities within the simulation time scale and thereby changes the local solid structure. The "stair step" nature of the boron impurity energy as a function of time in Figure 12 shows the recombination of other local impurities with the initially recombining pair to form a more stable cluster of five borons at larger time scales (greater than 1 ps). It is interesting to note the very short time scale of each additional recombination event in Figure 12. Figure 13 shows a snapshot of the system after 1.75 ps. The five boron impurities shaded in gray are seen to have undergone a local recombination process, but the global structure of the system is unchanged at this concentration. These results are consistent with those from the PI-QTST simulations described in the last section. The actual number of borons included in the local cluster may differ due to the approximate nature of the pair potential that we have used (i.e., we have ignored the many-body effects) but the qualitative picture should remain the same.

Finally, it should be mentioned that the forced recombination of a boron pair is a nonequilibrium process and that CMD is clearly approximate in this situation.

IV. Concluding Remarks

In this paper, solid parahydrogen systems doped with lithium and boron impurities have been studied. Both the global stability simulations and the computed thermodynamic properties show that boron is a more effective impurity than lithium in a solid hydrogen matrix for HEDM purposes since the concentration stability threshold for boron is estimated to be at least twice that of lithium. These results also suggest that a realistic concentration of boron impurities cannot likely exceed 10 mol %. It was found that the boron recombination reaction rate may be limited by the intrinsic recombination reaction rather than the impurity self-diffusion process. The dynamical CMD simulations and PI-QTST calculations at 6.25 mol % show that the reaction of a single boron pair induces only local boron recombinations and may not induce a global instability. The present results therefore support the concept that the p-H₂/B system may eventually represent a useful form of HEDM.

Acknowledgment. This research was supported by the Air Force Office of Scientific Research. We thank Kirk Peterson for providing his *ab initio* results, Youngshang Pak for helping in the construction of the potential energy surface, and Millard Alexander for providing the H₂-B interaction potential. The calculations were carried out through a DOD Challenge Grant at the Maui High Performance Computing Center on the IBM SP2, and on the SGI Origin 2000 at NCSA and IBM SP2 and Cray T3E at The San Diego Supercomputing Center through an NSF MetaCenter computing grant. Parts of the calculation were also performed on the IBM SP2 at the Center for High Performance Computing (CHPC) at the University of Utah. The SP2 was partially funded by an NSF grant CDA 9601580 and a Shared University Research (SUR) grant from IBM.

Appendix: Constant Pressure MD with a Nosé-Hoover Chain Thermostat

In Andersen's constant-pressure MD method, the volume of the simulation box is allowed to fluctuate by introducing an extended Lagrangian. In this view, the volume of the system is changed by a piston (wall) with a fictitious mass. The Nosé-Hoover chain is then attached both to the atomic particles and to the fictitious wall.⁴⁶

After the atomic particle coordinate r_i is replaced with scaled coordinate $\rho_i = Q^{-1/3}r_i$, where Q is volume, the extended Lagrangian of the system is given by

$$L = \sum_{i=1}^N \frac{1}{2} m_i Q^{2/3} \dot{\eta}_{1(i)}^2 - V(\rho_i Q^{1/3}, i = 1, \dots, N) + \frac{1}{2} M_Q \dot{Q}^2 - P_{\text{ext}} Q + \sum_{j=1}^K \frac{1}{2} M_{\zeta_j} \dot{\zeta}_j^2 - g k_B T \zeta_1 - \sum_{j=2}^K k_B T \zeta_j + \sum_{i=1}^N \left(\sum_{j=1}^K \frac{1}{2} M_{\eta_{j(i)}} \dot{\eta}_{j(i)}^2 - g k_B T \eta_{1(i)} - \sum_{j=2}^K k_B T \eta_{j(i)} \right) \quad (\text{A1})$$

where m_i is the mass of the atomic particle, N is total number of particles, V is potential of the system, M_Q is mass of the fictitious wall, P_{ext} is the external pressure, ζ_j is the position of the j th Nosé-Hoover chain attached to wall, M_{ζ_j} is the mass of the j th Nosé-Hoover chain attached to wall, K is the number of Nosé-Hoover chains, g is the degree of freedom of the

Nosé—Hoover chain attached to a given object, $\eta_{j(i)}$ is the position of the j th Nosé—Hoover chain attached to the i th atomic particle, and $M_{\eta_{j(i)}}$ is the mass of the j th Nosé—Hoover chain attached to the i th atomic particle.

One can then derive the equations of motion of the system. In the resulting expression, the Nosé—Hoover chain attached to the atomic particles is different from the Nosé—Hoover chain attached to the fictitious wall, and each atomic particle has its own Nosé—Hoover chain.

References and Notes

- (1) Fajardo, M. E.; Carrick, P. G.; Kenney III, J. W. *J. Chem. Phys.* **1991**, 5812, 94.
- (2) Fajardo, M. E. *J. Chem. Phys.* **1993**, 110, 98.
- (3) Fajardo, M. E.; Tam, S.; Thompson, T. L.; Cordonnier, M. E. *Chem. Phys.* **1994**, 351, 189.
- (4) Li, D.; Voth, G. A. *J. Chem. Phys.* **1992**, 5340, 96.
- (5) Li, D.; Voth, G. A. *J. Chem. Phys.* **1993**, 5734, 98.
- (6) Cheng, E.; Whaley, K. B. *J. Chem. Phys.* **1996**, 3155, 104.
- (7) Scharf, D.; Martyna, G. J.; Li, D.; Voth, G. A.; Klein, M. L. *J. Chem. Phys.* **1993**, 99, 9013.
- (8) Jang, S.; Voth, G. A. *J. Chem. Phys.* **1998**, 4098, 108.
- (9) Gerber, R. B.; Li, Z.; McCoy, A. B. In *Proceedings of the High Energy Density Matter (HEDM) Contractors' Meeting*, 6–8 June 1993, Woods Hole, MA; Thompson, T. L. Ed.; USAF Phillips Laboratory: Edwards AFB, CA, 1993; PL-TR-93-3041.
- (10) Vegiri, A.; Alexander, M. H.; Gregurick, S.; McCoy, A. B.; Gerber, R. B. *J. Chem. Phys.* **1994**, 101, 2577.
- (11) For reviews, see: (a) Berne, B. J.; Thirumalai, D. *Annu. Rev. Phys. Chem.* **1986**, 37, 401. (b) Freeman, D. L.; Doll, J. D. *Adv. Chem. Phys. B* **1988** 70, 139. (c) Doll, J. D.; Freeman, D. L. *Adv. Chem. Phys. B* **1989** 73, 289. (d) Doll, J. D.; Gubernatis, J. E., Eds. *Quantum Simulation of Condensed Matter Phenomena*; World Scientific: Singapore, 1990. (e) Chandler, D. In *Liquides, Cristallisation et Transition Virtueuse, Les Houches, Session LI*; Levesque, D., Hansen, J. P., ZinnJustin, J., Eds.; Elsevier: New York, 1991.
- (12) Cao, J.; Voth, G. A. *J. Chem. Phys.* **1993**, 10070, 99.
- (13) Cao, J.; Voth, G. A. *J. Chem. Phys.* **1994**, 5106, 100.
- (14) Cao, J.; Voth, G. A. *J. Chem. Phys.* **1994**, 6157, 101.
- (15) Cao, J.; Voth, G. A. *J. Chem. Phys.* **1994**, 6168, 101.
- (16) Calhoun, A.; Pavese, M.; Voth, G. A. Unpublished results.
- (17) Calhoun, A.; Pavese, M.; Voth, G. A. *Chem. Phys. Lett.* **1996**, 415, 262.
- (18) Kinugawa, K. *Chem. Phys. Lett.* **1998**, 454, 292.
- (19) Martyna, G. J.; Klein, M. L.; Tuckerman, M. *J. Chem. Phys.* **1992**, 2635, 97.
- (20) Voth, G. A.; Chandler, D.; Miller, W. H. *J. Chem. Phys.* **1989**, 7749, 91.
- (21) Voth, G. A. *Chem. Phys. Lett.* **1990**, 289, 270.
- (22) Voth, G. A. *J. Phys. Chem.* **1993**, 8365, 97.
- (23) Gillan, M. J. *J. Phys. C* **1987**, 3621, 20.
- (24) Cao, J.; Voth, G. A. *J. Chem. Phys.* **1996**, 6856, 105.
- (25) Silvera, I. F.; Goldman, V. V. *J. Chem. Phys.* **1978**, 4209, 69.
- (26) Alexander, M. H.; Yang, M. *J. Chem. Phys.* **1995**, 9756, 103.
- (27) Dupuis, M.; Liu, B. *J. Chem. Phys.* **1978**, 2902, 68.
- (28) Deutsch, P. W.; Curtiss, L. A.; Pople, J. A. *Chem. Phys. Lett.* **1990**, 33, 174.
- (29) Hachey, M.; Karna, S. P.; Grein, F. *J. Phys. B: At. Mol. Opt. Phys.* **1992**, 1119, 25.
- (30) Martin, J. M. L.; Francois, J. P.; Gijbels, R. *Chem. Phys. Lett.* **1992**, 529, 189.
- (31) Peterson, K. A.; Wilson, A. K.; Woon, D. E.; Dunning, T. H., Jr. *Theor. Chem. Acc.* **1997**, 97, 251.
- (32) Jang, S.; Voth, G. A. *J. Chem. Phys.* **1997**, 9514, 107.
- (33) Nosé, S. *J. Chem. Phys.* **1984**, 511, 81.
- (34) Nosé, S. *Mol. Phys.* **1984**, 255, 52.
- (35) Hoover, W. G. *Phys. Rev. A* **1985**, 1695, 31.
- (36) Tuckerman, M. E.; Berne, B. J.; Martyna, G. J.; Klein, M. L. *J. Chem. Phys.* **1993**, 2796, 99.
- (37) Tuckerman, M. E.; Parrinello, M. *J. Chem. Phys.* **1994**, 1302, 101.
- (38) Tuckerman, M. E.; Marx, D.; Klein, M. L.; Parrinello, M. *J. Chem. Phys.* **1996**, 5579, 104.
- (39) Andersen, H. C. *J. Chem. Phys.* **1980**, 2384, 72.
- (40) Parrinello, M.; Rahman, A. *Phys. Rev. Lett.* **1980**, 1196, 45.
- (41) Alexander, M. H. *J. Chem. Phys.* **1993**, 6014, 99.
- (42) Alexander, M. H.; Vegiri, A. In *Proceedings of the High Energy Density Matter (HEDM) Contractors Conference*, 6–8 June 1993, Woods Hole, MA; Thompson, T. L., Ed.; USAF Phillips Laboratory: Edwards AFB, CA, 93524-5000, 1993; PL-TR-93-3041.
- (43) Smoluchowski, M. *Z. Phys. Chem.* **1918**, 129, 92.
- (44) Collins, F. C.; Kimball, G. E. *Science* **1949**, 425, 4.
- (45) Noyes, R. M. *Prog. React. Kinet.* **1961**, 129, 1.
- (46) Ferrario, M. In *Computer Simulation in Chemical Physics*; Allen, M. P., Tildesley, D. J., Eds.; NATO ASI Series C.; Kluwer Academic Publishers: New York, 1993; Vol. 397.

Dimensional Strategies and the Minimization Problem: Barrier-Avoiding Algorithms

Daniel B. Faken,[†] A. F. Voter,[‡] David L. Freeman,[§] and J. D. Doll^{*,†}

Department of Chemistry, Brown University, Providence, Rhode Island 02912, Theoretical Division, Los Alamos National Laboratory, Mail Stop B268 Los Alamos, NM 87545, and Department of Chemistry, University of Rhode Island, Kingston, Rhode Island 02881

Received: June 23, 1999; In Final Form: August 10, 1999

In the present paper we examine the role of dimensionality in the minimization problem. Since it has such a powerful influence on the topology of the associated potential energy landscape, we argue that it may prove useful to alter the dimensionality of the space of the original minimization problem. We explore this general idea in the context of finding the minimum energy geometries of Lennard-Jones clusters. We show that it is possible to locate barrier-free, high-dimensional pathways that connect local, three-dimensional cluster minima. The performance of the resulting, "barrier-avoiding minimization" algorithm is examined for clusters containing as many as 55 atoms.

I. Introduction

Perhaps because we instinctively sense that our tools at any moment are, in truth, relatively primitive, we tend to display a reluctance to confront certain issues. Random processes are a case in point. Historically, our view of "noise" was basically that it was "bad". As a consequence, in the past we sought to eradicate, avoid, or minimize it whenever possible. As our abilities to deal with noise have advanced, our views of it have also fundamentally changed. Far from universally avoiding stochastic elements, today we often intentionally introduce them into purely deterministic problems for reasons of "convenience". Random walk treatments of electronic structure⁴ and simulated annealing strategies^{12,19} for minimization are important examples of this changing perspective.

Years of low-dimensional pedagogy have left an unfortunate legacy. The tendency is to view larger dimensional problems as automatically more difficult than their smaller dimensional counterparts. There are obvious counter examples. Laplace's "two-dimensional" evaluation of the one-dimensional Gaussian integral is a particularly striking one.¹³ More recently, advances in formal and computational tools for higher-dimensional systems³ have contributed to a growing awareness that dimensionality can be transformed from "foe" to "friend".

Dimensionality exerts a powerful influence on phenomenology. The absence of phase transitions in one-dimension⁵ and the formal divergence of diffusion coefficients for two-dimensional fluids^{1,2} are familiar examples. Because it has such a fundamental influence on the topology of potential energy "landscapes", it is, as suggested by Purisima and Scheraga,^{20,21} useful to consider dimensional modification as a tool within the context of the minimization problem.

The present paper examines a particular class of dimensional modification strategies. As a prototype application, we consider the problem of finding the minimum energy geometry of Lennard-Jones clusters. We show that there exist barrierless,

higher dimensional pathways that connect three-dimensional, local cluster minima. On the basis of our findings we suggest that dimensional modification may prove to be a useful strategy for certain classes of minimization problems.

The remainder of this paper is organized as follows: Section II introduces the basic idea of dimensional expansion. Results of the application of these methods to Lennard-Jones clusters are presented in Section III. Section IV contains a discussion and summary of the results as well as a comparison with currently available methods.

II. Formal Developments

Minimization problems are arguably among the most ubiquitous in science and engineering. They are also among the most frustrating. What appears to be a relatively simple task for a few variables rapidly becomes quite challenging as the number of degrees of freedom increases. This rise in complexity mirrors the rapid increase of the number of local minima in the associated potential energy landscape with increasing numbers of degrees of freedom. For example, the number of stable local minima increases roughly exponentially with the number of particles for relatively simple Lennard-Jones cluster systems.^{22,26} At heart, therefore, the minimization problem is effectively the local minimum problem.

In the present section we explore the potential of dimensionality for use as a tool in the treatment of minimization problems. We examine whether the increase in the complexity of the minimization problem with system size is inevitable or whether it is an example of allowing the potential "solution" to become the "problem". We consider conventional minimization techniques only briefly, referring the reader to existing reviews of those methods for more detailed treatments.¹⁹ To provide an explicit framework for our discussion, we adopt the viewpoint throughout the following that the objective function we seek to minimize is a generalized potential energy surface for a realizable physical system whose natural coordinates are continuously variable quantities.

For the present discussion, it is convenient to divide minimization techniques into two broad classes—those that modify the underlying potential energy surface and those that

* Corresponding author: (Tel.) 401-863-3443; (fax) 401-863-2594; (e-mail) doll@ken.chem.brown.edu.

[†] Brown University.

[‡] Los Alamos National Laboratory.

[§] University of Rhode Island.

do not. Standard conjugate gradient methods as well as various "annealing" approaches¹⁹ fall into the latter category. On the basis of a variety of physically motivated analogies, annealing methods leave the underlying potential energy surface itself unchanged. The most common of these methods, simulated annealing,^{12,19} adopts a classical statistical-mechanical point of view. Specifically, the strategy is to locate the potential minimum by following the associated classical probability density as the "temperature" of the system is reduced. If the "cooling schedule" is sufficiently conservative (i.e., if care is taken to ensure that the thermal fluctuations are sufficient to defeat the local minimum problem), the density will ultimately condense onto the global potential minimum in the limit of zero temperature. Unfortunately, however, this procedure can fail in practice. Situations in which differences between the energies of major potential basins are small relative to the barriers that separate them can, for example, prove particularly difficult. By the time it becomes apparent that one is headed toward a local minimum, the scale of the relevant thermal fluctuations can, for computationally feasible cooling schedules, be too small to have any practical chance of overcoming the energy barrier.

Rather than viewing the original objective function as a potential surface for a finite temperature *classical* system, "quantum annealing" methods^{6,11} employ a finite temperature, *quantum-mechanical* model. The global minimum of the specified potential is again located by following the density (or ground state wave function) toward the zero-temperature, classical limit. If we perform the limits by first turning off the quantum mechanics and then reducing the temperature, we recover conventional simulated annealing. We are free, however, to reverse the order of the limits, first taking temperature to zero and then turning down the quantum mechanics. There is practical merit to this second approach. Specifically, ground state diffusion Monte Carlo methods⁴ provide a general (stochastic!) means for performing the zero-temperature limit not available in purely classical approaches. Once the ground state is reached, the quantum mechanics of the problem can be turned off by, for example, gradually increasing the masses of the particles of the system. In quantum annealing, tunneling, as opposed to thermal fluctuations, provides the mechanism for avoiding local minima. Quantum-mechanical optimization approaches based on a dynamical model have been proposed by Straub et al.¹⁴

As indicated earlier, annealing methods do not alter the underlying potential energy surface. Quantum annealing does, however, change the way in which information concerning the potential is processed during intermediate stages of the minimization process. While the classical density at a point depends on the potential energy at that specific location, the quantum-mechanical density is influenced by the values of the potential energy throughout a surrounding neighborhood.

A second broad strategy for the design of minimization algorithms involves purposefully modifying the original potential energy surface. That is, rather than simply modifying the way in which potential energy information is processed, we seek to distort the potential in such a way that we obtain an algorithmic advantage while leaving the global minimum essentially intact. Early work by Stillinger and Stillinger²³ is an example of this type of approach. They sought to reduce the number of local minima by altering the long-range form of simple pair potentials. Strategies based on "smoothing" techniques have also been proposed.^{18,23} More recently, Wales et al.^{10,27} have devised an approach based on a "basin hopping" methodology in which the original potential energy at each point is replaced by the energy of its corresponding local minimum or "inherent

TABLE 1: Number of Stable Isomers Found for a 13 Atom Lennard-Jones Cluster in Various Dimensions

dimension	no. of isomers
1	1
2	345
3	1505
4	363
5	88
6	27
7	16
8	5
9	4
10	2
11	1
12	1

structure".^{22,24,25} By construction, the basin hopping method, unlike some distortion strategies, is guaranteed to leave the energetics of the various potential minima unaltered. By eliminating or lessening barriers between neighboring inherent structures, however, the approach promotes transitions between various local minima. The procedure is simple to implement and has proved effective in a variety of applications.^{7,9,15,16,28}

The present work explores another class of minimization strategies. Broadly speaking, the approach is a potential modification technique that combines elements of both basin-hopping and dimensional-relaxation strategies. A simple analogy will suffice to convey the essential idea. As anyone who has ever hiked in the mountains knows, it is often easier to "contour" around a local "barrier" than to climb over it. Rather than blindly restricting ourselves to lower dimensional ridge routes that go over barriers, we seek instead higher dimensional, barrier-free routes that bypass them. In a similar spirit, the present method attempts to defeat the local minimum problem by constructing barrier-free, high-dimensional pathways that connect the various three-dimensional inherent structures.

Why do we have any hope that such high-dimensional pathways either exist or that they will be helpful for the general minimization problem? To answer this basic question, it is useful to first pose another: How many three-dimensional isomers exist for a four-atom Lennard-Jones cluster? A bit of reflection will reveal that the answer to the latter question is one. In three dimensions each of the four atoms can be a nearest neighbor of all of the remaining particles by forming a tetrahedron. Using similar arguments, it is simple to see that an N -particle Lennard-Jones cluster will have a single isomer in $N - 1$ dimensions. Because all atoms can be nearest neighbors of every other atom, it is also simple to see that the energy of this $N - 1$ dimensional, minimum energy structure is less than the energy of any other inherent structure in any number of dimensions.

To make the connection between dimensionality and the number of local minima more explicit, we list in Table 1 the number of energetically distinct isomers found for the 13 atom Lennard-Jones cluster as a function of the number of spatial dimensions. We assume the potential energy of these clusters to be of the pairwise form

$$V(R) = \sum_{i < j} V_{LJ}(|\mathbf{r}_i - \mathbf{r}_j|) \quad (2.1)$$

where \mathbf{r}_i is a D -dimensional vector whose components $(x_{i,1}, x_{i,2}, \dots, x_{i,D})$ specify the position of atom "i". The Lennard-Jones interaction, $V_{LJ}(r)$, specified in terms of the usual well-depth, ϵ , and length scale, σ , parameters by

$$V_{LJ}(r) = 4\epsilon \left[\left(\frac{\sigma}{r} \right)^{12} - \left(\frac{\sigma}{r} \right)^6 \right] \quad (2.2)$$

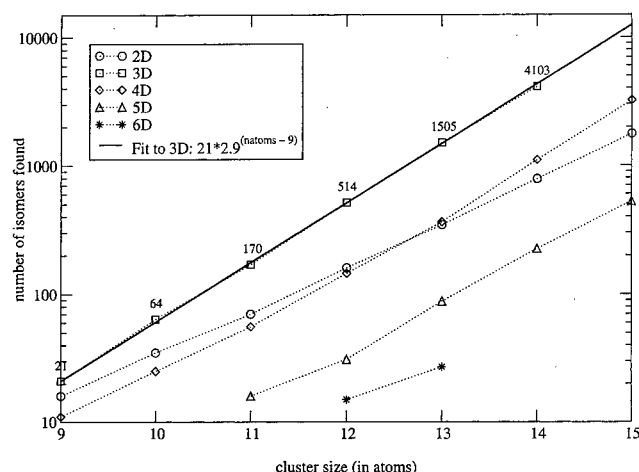


Figure 1. The number of stable isomers found for Lennard-Jones clusters of various sizes in different numbers of dimensions. As discussed in the text, the results are intended to convey the effects of cluster size and dimensionality on the inherent structure topology. Given the uncertainty inherent in attempts to locate all local minima, the numbers shown should be regarded as lower bounds to the exact values. A fit to the number of stable isomers for an N -atom cluster in three dimensions, $I(N) = I(N_0)\Gamma^{N-N_0}$, shows essentially exponential growth relative to a baseline value for 21 isomers for $N_0 = 9$. The fitted value of Γ indicates that the number of stable isomers grows (on average) by roughly a factor of 2.9 with the addition of each new particle. The corresponding two-dimensional value is 2.22.

is a function of the D -dimensional interparticle Euclidian distance, $|\mathbf{r}_i - \mathbf{r}_j|$,

$$|\mathbf{r}_i - \mathbf{r}_j| = \left(\sum_{n=1}^D (x_{i,n} - x_{j,n})^2 \right)^{1/2} \quad (2.3)$$

These results in Table 1 were established by quenching initial configurations produced by a D -dimensional, basin-hopping random walk with standard gradient methods. The resulting structures were tested to ensure they indeed corresponded to stable minima. The number of quenches used is sufficient to identify the general trend with respect to dimensionality (i.e., that the number of stable isomers is a decreasing function of dimensionality above three dimensions). Although we do find slightly more three-dimensional isomers for the 13 atom system than were reported by Tsai and Jordan²⁶ or by Doye, Miller, and Wales,⁸ the results of Table 1 should not in general be taken as definitive with respect to the exact number of stable isomers for any particular cluster and dimension.

Figure 1 charts the growth of the number of isomers of Lennard-Jones clusters from 9 to 15 atoms for various numbers of dimensions. The growth appears roughly exponential in this cluster size range. It is interesting to note that the number of stable isomers for these clusters appears to be a maximum for three-dimensions.

How can we exploit the apparent "simplifying" effect of dimensionality on the cluster's inherent structure topology? One possibility, suggested by Purisima and Scheraga,^{20,21} is to start with what we know a priori to be the unique global minimum in $N - 1$ dimensions and attempt to compress that structure back to three dimensions. While appealing, we have not found this approach to be a generally successful one for our applications. The essential difficulty is that dimensional quenches do not appear to link high and low-dimensional global minima in a direct, "adiabatic" fashion.

We have, however, found another, and apparently more general, way to exploit dimensional expansion. From Table 1

and Figure 1, we see that the number of local cluster minima tends to decrease as the dimensionality of the system is increased above three dimensions. In fact, as discussed previously, when the dimensionality is sufficiently large, we know that the number of high-dimensional minima ultimately shrinks to unity. We further know that the energy of this unique, high-dimensional minimum lies below that of any other minimum (local or global) in any number of dimensions. Although these results do not specify how to find it, they guarantee the existence of a barrier-free, $N - 1$ dimensional pathway between any three-dimensional local minimum and the three-dimensional global minimum for an N -particle cluster. To see this result, it is sufficient to note that the three-dimensional local and global minima both are points on a single, $N - 1$ dimensional potential basin. By construction, therefore, there is an $N - 1$ dimensional, barrier-free pathway that connects the designated local and global minima. It is straightforward to generalize this argument to show that any two local, three-dimensional minima are connected by a barrier-free, $N - 1$ dimensional pathway. How large does the dimensionality have to be in practice in order that a barrier-free pathway exist? How general is the simplifying effect of dimensionality on the topology of the high-dimensional inherent structure surface? The answer to the second question awaits further study. On the basis of results presented in the following section, however, it appears that the answer to the first question is, for Lennard-Jones clusters, only slightly greater than three.

III. Numerical Method and Examples

We now describe our implementation of barrier-avoiding minimization and examine its performance for small ($N < 55$ atoms) Lennard-Jones clusters. In part, we have chosen this system for our initial applications because resources like the Cambridge Cluster Database (<http://brian.ch.cam.ac.uk>) greatly simplify the process of validating the cluster structures and energies that are encountered.

The function we are trying to minimize, $V(\mathbf{R})$, is assumed to depend only on the distances between the particles. The class of such functions includes the pairwise additive potentials of the present study, as well as other forms which will be discussed below. In this way, the function is defined for configurations in any dimension; only the definition of the distance changes.

Let D be the dimension (usually 3) in which the original N -particle cluster configuration resides, and H the number of "extra" dimensions to be used in the search. H is useful from 1 to $(N - 1 - D)$. Above this value of H , the $(D + H)$ dimensional atoms only see an $(N - 1)$ dimensional subspace. Given this configuration, we denote the new $(D + H)$ dimensional coordinates by $\mathbf{R} = (\mathbf{r}_1, \mathbf{r}_2, \dots, \mathbf{r}_N)$, where $\mathbf{r}_i = (x_{i,1}, x_{i,2}, \dots, x_{i,D}, x_{i,(D+1)}, \dots, x_{i,(D+H)})$ and where $x_{i,j}$ is the j th component of the Cartesian coordinates of particle i . We call \mathbf{R} D -dimensional (but embedded in a $(D + H)$ dimensional space) if $x_{i,(D+1)} = x_{i,(D+2)} = \dots = x_{i,(D+H)} = 0$ for all i .

In the algorithm discussed below it is necessary both to expand and compress the cluster between D and $D + H$ dimensions. To execute such expansions and compressions it is essential that we have available a suitable "signature" of the dimensionality of the space. We assume in the following that we have available some suitable "width" function, $W_D(\mathbf{R})$, that is continuous in \mathbf{R} , equal to zero when \mathbf{R} is D -dimensional, and otherwise positive. One choice for the width function, the

one used in the present study, is

$$W_D(\mathbf{R}) = \sum_{i=1}^N \sum_{n=D+1}^{D+H} x_{i,n}^2 \quad (3.1)$$

The basic idea behind the present algorithm is that, given a local minimum in three dimensions, we can find another, three-dimensional structure via a random walk *at constant potential energy* in a higher dimension. That is, we can move from a three-dimensional energy minimum to another energy "basin" using higher dimensional pathways. The new structure is either another local minimum at the same energy as the starting configuration, or it is a new structure that is not a local minimum. If the new structure is energetically degenerate with the starting configuration, we simply continue the search. If, as is much more likely, the new structure is not a local minimum, then we are assured that it can be relaxed to a new local minimum *with a lower energy*. In this way, we produce a sequence of three-dimensional inherent structures of decreasing potential energies leading to the lowest energy three-dimensional structure.

The steps performed by the algorithm are as follows: given an arbitrary starting configuration, \mathbf{R} ;

1. Find the "inherent structure" for \mathbf{R} . We minimize $V(\mathbf{R})$ for \mathbf{R} constrained to stay in D dimensions (i.e., the H higher components are zero). Any minimization technique¹⁹ that decreases V is acceptable for this step (e.g., steepest descent, conjugate-gradient, etc.). More formally, given an initial configuration \mathbf{R}_0 , we find \mathbf{R} such that:

$$\begin{aligned} \text{(a)} \quad & \frac{dV(\mathbf{R})}{dr_i} = 0 \text{ for all } r_i \\ \text{(b)} \quad & \frac{d^2V(\mathbf{R})}{dr_i dr_j} > 0 \text{ for all } r_i, r_j \\ \text{(c)} \quad & V(\mathbf{R}) \leq V(\mathbf{R}_0) \end{aligned}$$

In part (b) we exclude the directions equivalent to overall translation and rotation of the system. We denote the energy of the (local) minimum produced by steps (a–c) E_{LM} and the associated configuration \mathbf{R}_{LM} .

2. Perform a constant-energy random walk. This walk consists of $nsteps$ constrained random displacements of \mathbf{R} in $(D+H)$ dimensions, the constraint being $V(\mathbf{R}) = E_{LM}$. In the present paper, we generate trial displacements, $\Delta\mathbf{R}$, by uniformly translating all particles within a "box" of about 0.1σ . The value of $nsteps$ was 100 for the smaller clusters, 50 for the 38 atom cluster, and 30 for the 55 atom cluster. The constraint was imposed (to first order) by removing the component of $\Delta\mathbf{R}$ parallel to the gradient of $V(\mathbf{R})$. For large translations, this is not sufficient, and one must either use a higher order correction (involving the Hessian) or, as was done in the present paper, readjust $\Delta\mathbf{R}$ by moving parallel to the energy gradient until the constraint is met (rejecting the "trial" $\Delta\mathbf{R}$ if the constraint cannot be met this way).

3. Minimize $W_D(\mathbf{R})$ while keeping $V(\mathbf{R}) = E_{LM}$. Techniques for such minimizations are widely available in the "nonlinear programming" literature.¹⁷ Our technique is to use the strategy outlined in Step (2), but setting $\Delta\mathbf{R} = -c \nabla W_D(\mathbf{R})$, where c adjusts the step size at each step so that the gradient is followed downhill (with respect to $W_D(\mathbf{R})$) to a (constrained) local minimum.

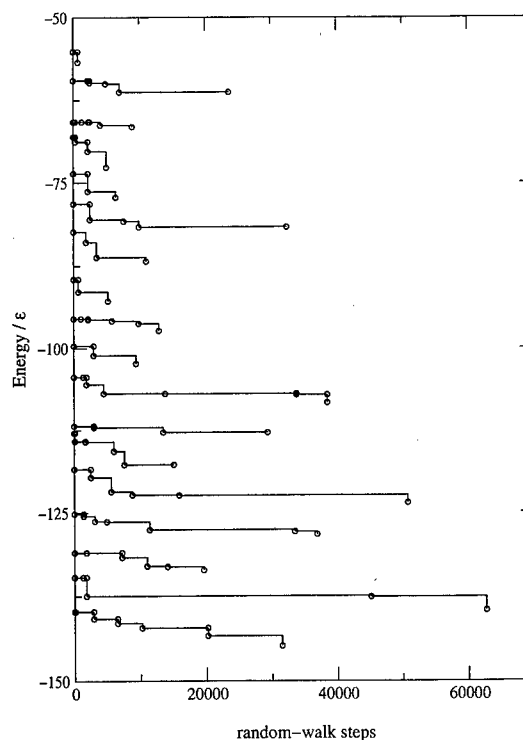


Figure 2. Barrier-avoiding minimization histories for Lennard-Jones clusters containing from 16 to 33 atoms. Starting from a different, randomly chosen configuration for each cluster size, the minimization proceeds, via high-dimensional, barrier-free pathways, through a series of local minima (plateaus in the figure) to the minimum energy configuration. Traces correspond, in order from top to bottom, to results for 16–33 atoms.

4. If the minimization in (3) results in \mathbf{R} being D -dimensional (i.e., $W_D(\mathbf{R}) = 0$), and $\mathbf{R} \neq \mathbf{R}_{LM}$, then we may have succeeded in finding a configuration that will quench to a lower energy, D -dimensional inherent structure. In this instance, we start again at Step (1) with the new configuration. By proceeding through a sequence of inherent structures of successively lower energies, we are removing large numbers of local minima from the search as it proceeds.

5. On the other hand, the constrained minimization in (3) can fail in its attempt to "compress" the $(D+H)$ dimensional configuration in Step (2) completely back to D -dimensions. In such cases, we resume our high-dimensional search by resetting \mathbf{R} to the last, high-dimensional configuration generated by the random walk in Step (2) and continuing the expanded dimensional walk from that point until Step (4) is satisfied.

We have implemented this "barrier avoiding minimization" procedure and have examined its efficacy for finding the global minima of clusters whose atoms interact via the Lennard-Jones pair-potential. All calculations reported here were done with $H = 1$; that is, the random walk was performed in four dimensions. Although four dimensions proved to be sufficient to produce barrier-free minimization pathways for all examples considered in the present work, it may be necessary to revisit this issue for other applications. We first discuss the cases of 16–33 atoms and then do a more detailed examination of the 38 atom case.

Figure 2 shows the results of a typical set of applications of the barrier avoiding minimization procedure (Steps 1–5) above) for clusters ranging from 16 to 33 atoms. This figure is presented both to convey a sense of the sequence of inherent structure energies visited by the clusters enroute to their global potential energy minima and to illustrate (crudely) the scaling of effort with respect to cluster size. In Figure 2, the minimizations for

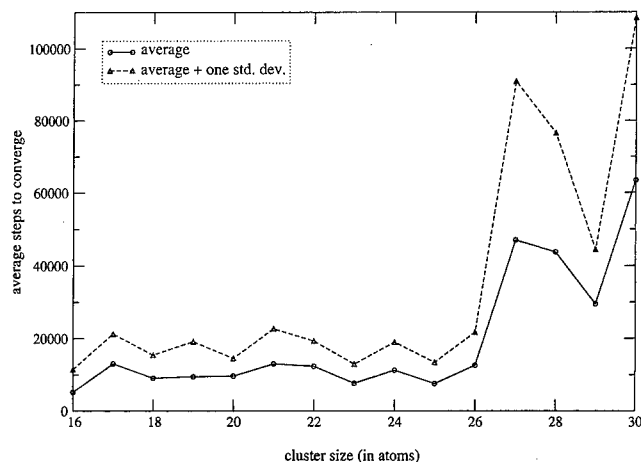


Figure 3. Average number of steps required to reach global minimum for Lennard-Jones clusters of various sizes. The solid (dotted) line represents the average (average plus one standard deviation) of the number of steps required to find the ground state structure for 20 randomly chosen initial configurations for each cluster size.

each cluster size have each been initiated from a single, randomly chosen initial configuration. Figure 3 elaborates upon the issue of the scaling of effort. There we show the average number of steps required to achieve the global potential minima for 20 randomly generated initial configurations for each cluster size. It is first important to note that the present procedure successfully locates the global minima for *all* random initial configurations for *all* cluster sizes. It is also important to note that the level of effort required to find the global minimum energy structure in the range of 16–26 atoms is relatively constant. In particular, over the size range shown in Figure 2, the number of local minima grows (based on exponential fits to the results of Figure 1) by roughly 3×10^6 (from approximately 3.6×10^4 (16 atoms) to 1×10^{11} (30 atoms)). Beyond 26 atoms, the effort required increases, although not prohibitively, as evidenced by our success (see below) with both the 38 and 55 atom clusters. The reasons for this increase in effort are, at present, unclear. It may, however, be an indication that higher dimensional ($H > 1$) minimization pathways could prove useful for studies of larger clusters.

As a somewhat more demanding test of the procedure, we examine its performance for the 38 atom Lennard-Jones cluster. As discussed by Doye, Miller, and Wales,⁷ this cluster presents significant challenges in optimization and simulation studies. Its *fcc*-like global minimum is separated from a low-lying, icosahedral local minimum by an appreciable barrier. Figure 4 displays the results of applying the barrier-avoiding minimization method to this system. As illustrated in Figure 4, starting from a randomly generated configuration, the method successfully locates the global minima. It is important to note that the minimization trace shown in Figure 4 actually proceeds through the 38 atom icosahedral local minimum. This is significant in that it confirms that the method did, in fact, locate a barrier-free, four-dimensional pathway “around” what is otherwise a significant, three-dimensional barrier. From Figure 4 we see that in this case roughly 400 000 high-dimensional steps (8000 dimensional quenches) are required to locate the global minimum. The number of quenches for this single minimization is not wildly out of line with the mean first-encounter time of 2000 conjugate-gradient quenches reported for the basin-hopping treatment of the same system.⁷

Finally, although it is a somewhat less challenging example than the 38 atom case, we note that we have also had success

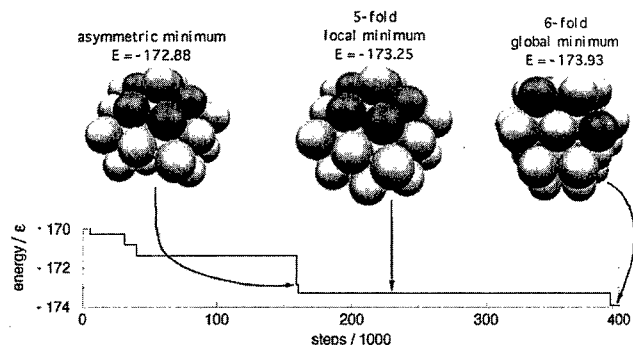


Figure 4. A barrier-avoiding minimization history for the 38 atom Lennard-Jones cluster. The trace shows the results for a single, randomly chosen configuration. It is important to note that the global minimum is reached by way of the icosahedral local minimum. This confirms that the minimization strategy successfully located a barrier-free, high-dimensional pathway from the *fcc* local minimum to the ground-state configuration.

in locating the minimum energy structure for the 55 atom cluster. Systematic studies of larger clusters are planned.

IV. Discussion & Summary

In the present paper, we have explored the use of dimensional strategies for minimization problems. We have presented a particular method that exploits the simplifying influence of dimensionality on inherent structure topology. For one class of systems, Lennard-Jones clusters, we have shown the resulting approach represents a practical minimization method. Using this method, we have succeeded in locating high-dimensional, barrier-free pathways between three-dimensional local minima and the corresponding global minimum-energy structures for clusters containing up to 55 atoms. We are encouraged by the present results, particularly by the method's performance in locating the global minimum for the 38 atom cluster.

In order for the current approach to be of general significance, it will be necessary to establish its utility for a broader range of applications. Although we are cautiously optimistic, the final decision concerning the ultimate fate of the present method must, therefore, await the outcome of ongoing studies.

If dimensional approaches are to be of general merit, two basic conditions must be satisfied. First, it is necessary that dimensionality exert a simplifying effect on the inherent structure topology for the problem of interest. Second, one must find a way to translate this simplification into a practical minimization algorithm. In the present work, both conditions have been met. As discussed in Section II, increasing cluster dimensionality reduces the number of local minima. We have shown, using the barrier-avoiding methods discussed in Section III, how to transform this dimensional simplification into a viable minimization procedure. Although the particular strategy described by Purisima and Scheraga^{20,21} for exploiting it does not appear to be general, their work illustrates the important point that the simplifying effects of dimensionality on the minimization problem extend to classes of potentials of chemical interest. Leaving aside the particulars for the moment, the “take-home” message of the present investigation is that whether it is the barrier-avoiding methodology of Section III or some other, yet to be discovered, implementation, dimensional strategies appear to represent a potentially valuable tool for the construction of new classes of minimization algorithms.

Acknowledgment. J.D.D. and D.L.F. would like to thank the National Science Foundation for support of the present

research through Grant CHE-9714970. In addition, J.D.D. would like to acknowledge support through the NSF Grant CDA-9724347. Work at Los Alamos National Laboratory was performed under the Department of Energy contract W-7405-ENG-36.

References and Notes

- (1) Alder, B. J.; Wainwright, T. E. *J. Phys. Soc. Jpn.* **1969**, 26, 267–269.
- (2) Alder, B. J.; Wainwright, T. E. *Phys. Rev. A: At., Mol., Opt. Phys.* **1970**, 1, 18–21.
- (3) Berne, B. J.; Ciccotti, G.; Coker, D. F., Eds. *Classical and Quantum Dynamics in Condensed Phase Simulations*; World Scientific: River Edge, NJ, 1998.
- (4) Ceperley, D.; Alder, B. *Science (Washington, D.C.)* **1986**, 231, 555–560.
- (5) Chandler, D. *Introduction to Modern Statistical Mechanics*; Oxford University Press: New York, 1987.
- (6) Doll, J. D.; Freeman, D. L. *IEEE Comput. Sci. Eng.* **1994**, 1, 22.
- (7) Doye, J. P. K.; Miller, M. A.; Wales, D. J. *J. Chem. Phys.* **1999**, 110, 6896.
- (8) Doye, J. P. K.; Miller, M. A.; Wales, D. J. Los Alamos Preprint: cond-mat/9903305, 1999.
- (9) Doye, J. P. K.; Wales, D. J. *Phys. Rev. B: Condens. Matter* **1999**, 59, 2292.
- (10) Doye, J. P. K.; Wales, D. J.; Miller, M. A. *J. Chem. Phys.* **1998**, 109, 8143–8153.
- (11) Finnila, A. B.; Gomez, M. A.; Sebenik, C.; Stenson, C.; Doll, J. D. *Chem. Phys. Lett.* **1994**, 219, 343.
- (12) Kirkpatrick, S.; Gelatt, C. D.; Vecchi, M. P. *Science (Washington, D.C.)* **1983**, 220.
- (13) Laplace, P. S. *Oeuvres completes de Laplace*; Gauthier-Villars: Paris, 1878; Vol. 10.
- (14) Ma, J.; Hsu, D.; Straub, J. E. *J. Chem. Phys.* **1993**, 99, 4024.
- (15) Naumkin, F. Y.; Wales, D. J. *Mol. Phys.* **1998**, 93, 633.
- (16) Naumkin, F. Y.; Wales, D. J. *Mol. Phys.* **1999**, 96, 1295.
- (17) G. L.; Kan, A. H. G. R.; Todd, M. J., Eds.; *Optimization*; Nemhauser, North-Holland: Amsterdam, 1989.
- (18) Piela, L.; Olszewski, K. A.; Cherayil, B. J.; Scheraga, H. A. *J. Mol. Struct.: THEOCHEM* **1994**, 308, 229.
- (19) Press, W. H.; Teukolsky, S. A.; Vetterling, W. T.; Flannery, B. P. *Numerical Recipes in Fortran 77*, 2nd ed.; Cambridge University Press: Cambridge, 1996.
- (20) Purisima, E. O.; Scheraga, H. A. *Proc. Natl. Acad. Sci. U.S.A.* **1986**, 83, 2782–2786.
- (21) Purisima, E. O.; Scheraga, H. A. *J. Mol. Biol.* **1987**, 196, 697–709.
- (22) Stillinger, F. H. *Phys. Rev. E: Stat. Phys., Plasmas, Fluids, Relat. Interdiscip. Top.* **1999**, 59, 48.
- (23) Stillinger, F. H.; Stillinger, D. K. *J. Chem. Phys.* **1990**, 93, 6106.
- (24) Stillinger, F. H.; Weber, T. A. *Phys. Rev. A: At., M.I., Opt. Phys.* **1983**, 28, 2408.
- (25) Stillinger, F. H.; Weber, T. A. *Science (Washington, D.C.)* **1984**, 225, 983.
- (26) Tsai, C. J.; Jordan, K. D. *J. Phys. Chem.* **1993**, 97, 11227–11237.
- (27) Wales, D. J.; Doye, J. P. K. *J. Phys. Chem. A* **1997**, 101, 5111–5116.
- (28) Wales, D. J.; Hodges, M. P. *Chem. Phys. Lett.* **1998**, 286, 65.

A Modification of Path Integral Quantum Transition State Theory for Asymmetric and Metastable Potentials

Seogjoo Jang, Charles D. Schwieters,[†] and Gregory A. Voth*

Department of Chemistry and Henry Eyring Center for Theoretical Chemistry, University of Utah,
315 S. 1400 E. Rm Dock, Salt Lake City, Utah 84112-0850

Received: June 28, 1999; In Final Form: August 18, 1999

Path integral quantum transition state theory (PI-QTST) and its modified versions are studied for an asymmetric Eckart barrier and a metastable potential. For low temperatures, it is confirmed that the PI-QTST overestimates the reaction rate, as do other quantum activated rate theories. A simple correction method which modifies the product part of the potential such that it is bounded by the potential reactant well bottom energy is then implemented. The resulting tests for the asymmetric Eckart barrier and a cubic metastable potential demonstrate that this method gives a reliable estimate of the reaction rate for the model systems considered. For an understanding of the source of the error in the usual PI-QTST method and of the underlying mechanism of the correction, a detailed semiclassical analysis is then performed. This analysis demonstrates that the modified PI-QTST of Cao and Voth [Cao, J.; Voth, G. A. *J. Chem. Phys.* **1996**, *105*, 6856] becomes equivalent to the semiclassical bounce theory at low temperature only if a certain subset of classical paths is used. It is therefore concluded that the errors originate from the inappropriate mixing-in of paths associated with the product bound states in numerical path integral evaluations. These product paths are eliminated by the suggested correction method, thus rendering PI-QTST much more accurate for strongly asymmetric or metastable systems at low temperatures.

I. Introduction

From a molecular viewpoint, activated reaction events^{1–9} are rare phenomena, and the probability that the system will visit the reactive zone, as determined by the free energy barrier, accounts for the dominant contribution to the reaction rate. Transition state theory (TST),¹⁰ in this sense, amounts to the simplest approximation. It plays an important practical role in estimating the reaction rates in various systems and is indeed amenable to further improvement.^{8,9} In generalizing TST to the quantum case,^{1–7,11–13} however, one is confronted with some conceptual difficulties due to quantum dispersion and tunneling even in the simplest generic case of a single adiabatic barrier crossing.

Only in the two limiting cases of high and low temperature does the quantum description become simplified. In the former case, one can proceed in close analogy with classical picture by including a small amount of quantum dispersion and barrier top tunneling only.^{14,15} In the zero temperature limit, within the path integral formalism,^{16–19} one can identify with the reactant state those paths localized near the bottom of the reactant potential well. Barrier-crossing events are associated with paths which traverse from the reactant region to the product. Within the semiclassical approximation, the resulting rate can be expressed in terms of the properties of one (or more) periodic orbits on the inverted potential.^{20–27}

The approaches used in the two limiting situations above are rather different, though the two results can be formally unified in a single mathematical expression.^{24,25} In this context, Gillan's observation²⁸ and the ensuing work of Voth, Chandler, and

Miller (VCM)²⁹ provided an important contribution. Gillan found that known reaction rate expressions for a symmetric double well potential coupled to a harmonic bath can be recast into classical-like forms employing the path centroid defined within the imaginary time path integral formalism.^{16–19} Later, VCM carried out a more rigorous analysis, the outcomes of which are the path integral quantum TST (PI-QTST), a rigorous derivation of some of Gillan's results, and the idea of supplementing the approximate reaction rate with additional exact quantum dynamics calculations.

Subsequent tests and analyses^{7,30–35} have shown that PI-QTST is very accurate in the high temperature limit and near the so called crossover temperature in which the dynamics begins to be dominated by tunneling. Below the crossover, it reproduces the dominant exponential term for symmetric or weakly asymmetric potentials, and it can be improved with a modification of the preexponential factor.^{36,37} Recent work has focused on finding a more universal expression for this factor and also on the extension of the theory to nonadiabatic cases.^{36,38–40} On the other hand, applications of the PI-QTST to strongly exothermic or metastable potentials at low temperature can be problematic. The reaction rate appears to be overestimated by orders of magnitude or, in fact, may not be defined in some cases.^{33,41,42} The reason for this has been explained in a way analogous to classical multidimensional TST. In the general function space of cyclic paths, the centroid used in PI-QTST, the zeroth mode of the path, belongs to a specific class of dividing surfaces. For the case of asymmetric potentials, the optimal dividing surface seems to be rotated⁴² in a direction different from any of the surfaces corresponding to a fixed centroid and the use of the centroid coordinate results in overestimation of the reaction rate. On the basis of this idea, Cao and Voth (CV)³⁶ and Mills et al.⁴² independently developed

* Corresponding author.

[†] Present address: Computational Bioscience and Engineering Laboratory, NIH, Bethesda, MA 20892.

schemes for identifying the optimum surface in the general function space of paths, one of which has been applied to some systems.⁴² However, this approach may limit the application of the theory to small systems, so a more practical solution that does not abandon the practical merits of PI-QTST is still desirable.

Recently, two new approaches to a QTST have also appeared.^{43–45} These start from an expression for the flux-side correlation function⁴⁶ and then invoke mathematically or physically motivated approximations. These new QTSTs produce results comparable to those of PI-QTST when tested for the symmetric Eckart barrier. For the case of asymmetric Eckart barrier, a detailed comparison has not been made, although the new theories have also been reported to perform unsatisfactorily.

The present paper was thus motivated by the incomplete understanding of the performance of PI-QTST for the cases of asymmetric and metastable potentials at low temperature. The first objective is to calculate the reaction rates based on PI-QTST for the asymmetric Eckart barrier and to compare these with published results for a collection of different QTSTs. The results presented show that, although the PI-QTST performs worse than the semiclassical bounce theory^{20–27} below the crossover temperature, it is somewhat better than other simple QTSTs. However, these data again confirm that one should be cautious in applying the theory to asymmetric or metastable potentials at low temperature. The second objective is then to provide a simple, mathematically motivated, correction procedure to PI-QTST to render it again quantitatively accurate for such systems.

This paper is organized as follows: In section II, the PI-QTST and its improved versions using different preexponential factors are summarized and the results of their application to the asymmetric Eckart barrier are presented. In section III, a practical remedy is suggested for the strongly asymmetric barrier problem and then tested for the asymmetric Eckart barrier and for a cubic metastable potential. In section IV, a semiclassical analysis is made of the centroid density, which illuminates its relation with the semiclassical bounce theory and the sources of the errors involved in PI-QTST for strongly asymmetric system at low temperature. Section V provides concluding remarks.

II. Path Integral Transition State Theory Applied to An Asymmetric Eckart Barrier

A. Formal Expressions. The quantum partition function in the path integral formalism can be recast into the following classical-like form:^{16,47,48}

$$Z \equiv \text{Tr} \{e^{-\beta \hat{H}}\} = \sqrt{\frac{m}{2\pi\hbar^2\beta}} \int dx_c \rho_c(x_c) \quad (1)$$

where β is the inverse temperature in units of the Boltzmann constant, m is the mass, and the “excess” centroid density beyond the free particle limit along the reaction coordinate is given by the path integration over all constrained cyclic paths such that

$$\rho_c(x_c) \equiv e^{-\beta V_c(x_c)} = \sqrt{\frac{2\pi\hbar^2\beta}{m}} \int \cdots \int D[x(\tau)] \delta(x_c - x_0) \exp \{-S[x(\tau)]/\hbar\} \quad (2)$$

with $x_0 = \int_0^{\beta\hbar} d\tau x(\tau)/(\beta\hbar)$. In eq 2, $D[x(\tau)]$ is the usual path measure^{16–19} and $S[x(\tau)]$ is the Euclidean action functional,^{16–19}

defined as

$$S[x(\tau)] = \int_0^{\beta\hbar} d\tau \left\{ \frac{m}{2} \dot{x}(\tau)^2 + V(x(\tau)) \right\} \quad (3)$$

where $\dot{x}(\tau)$ is the derivative of $x(\tau)$ with respect to τ . A one-dimensional notation is used throughout for simplicity. Note that, as opposed to some of our earlier papers, the centroid potential of mean force $V_c(x_c)$ is defined here to be the excess centroid free energy over the free particle limit. The notation “ $\rho_c(x_c)$ ” in this paper will also refer to the excess centroid density beyond the free particle limit, which is the important contribution to the rate constant.

The rate expression in PI-QTST,^{7,29} expressed as $k_{\text{PI-QTST}}$ hereafter, has the following classical form:

$$k_{\text{PI-QTST}} = \frac{1}{2\pi\beta\hbar} \frac{e^{-\beta V_c(x_c^*)}}{Z_R} = \frac{(2\pi m\beta)^{-1/2}}{\int_{-\infty}^{x_c^*} dx_c e^{-\beta V_c(x_c)}} e^{-\beta V_c(x_c^*)} \quad (4)$$

where x_c^* corresponds to the barrier position of V_c and Z_R is the reactant state partition function. This rate expression is, in fact, the variational version of PI-QTST. At high temperature and for the inverted harmonic barrier, this expression has been shown to yield the exact high temperature result. Near or below the crossover temperature, however, eq 4 begins to underestimate the reaction rate for the symmetric Eckart barrier. Cao and Voth (CV)³⁶ have provided a unified expression for the preexponential factor which improves on this feature of the theory. They used Affleck’s well-known correction factor²⁴ in a way consistent with the known high temperature result, and based on the assumption that the free energy saddle point in the general space of paths can be well represented by the centroid coordinate alone. The resulting expression is given by

$$k_{\text{CV}} = \min \left(\frac{\omega_b}{\omega_{c,b}}, \frac{2\pi}{\omega_{c,b}\beta\hbar} \right) k_{\text{PI-QTST}} \quad (5)$$

where ω_b is the frequency of the inverted harmonic function fitting the barrier top of $V(x)$ and $\omega_{c,b}$ is that fitting the barrier top of $V_c(x_c)$.

More recently, Ramirez³⁷ suggested a different uniform expression for the preexponential factor based on an empirical relation which seems to work well for the symmetric Eckart barrier. It is given by

$$k_R = \left(\frac{V_c(x_c^*)}{E_c(x_c^*)} \right)^{1/2} k_{\text{PI-QTST}} \quad (6)$$

where x_c^* is again understood as the position of the barrier top of V_c and $E_c(x_c)$ corresponds to an average energy for a fixed centroid minus $1/(2\beta)$, the Virial form^{49,50} of which is given by

$$E_c(x_c) = \left\langle \frac{1}{2} (x(\tau) - x_c) V'(x(\tau)) + V(x(\tau)) \right\rangle_c \quad (7)$$

where $\langle \cdots \rangle_c$ means average over the centroid constrained path integral of eq 2.

B. Results. The reaction rates were calculated for the following asymmetric Eckart barrier:

$$V(x) = \frac{A}{1 + e^{-ax}} + \frac{B}{4 \cosh^2(ax/2)} \quad (8)$$

with $V(-\infty) = 0$, $V(\infty) = A = -18/\pi$, $B = 54/\pi$, and $a =$

$\sqrt{3\pi}/4$. Natural units have been chosen such that $\hbar = \omega_b = m = 1$. These choices of parameters and units result in a classical barrier height of $V^* = 6/\pi$ and a classical barrier location of $q^* = -\ln 2/a$. The quantity to be compared is Γ , the ratio of the quantum rate to the classical rate. Thus, calculation of the reaction rates requires the determination of $V_c(x_c)$ defined by eq 2, and the average centroid energy function given by eq 7 if Ramirez's expression for the rate is used. These calculations can be performed using any path integral simulation method, along with the imposition of the centroid constraint.

The method of staging path integral molecular dynamics (SPIMD) was chosen in the present work.⁵¹ The number of quasiparticles, $P = 25\beta$, gave converged thermodynamic data for all the values of β tested. The number of primary quasiparticles used was 10 for all temperatures, and each intervening segment consisting of $P/10 - 1$ quasiparticles was transformed into staging coordinate. To ensure canonical sampling, a Nosé-Hoover chain⁵² of length 4 was attached to each transformed degree of freedom. The use of this thermostat in the presence of the centroid constraint was made possible using modified NHC equations of motion,⁵³ which account for the constrained degree of freedom correctly, and by employing one of the corresponding simple reversible velocity Verlet type algorithms, VV-3.⁵³ The mass of the primary quasiparticle was chosen to be $P/10$, the mass of the k th ($k = 1, \dots, P/10 - 1$) staging transformed coordinate was chosen to be $P^2(k+1)/(100k)$, and the Nosé mass was set to $0.012P$. A time step of $6.32 \times 10^{-4}P$ was used in the simulation.

The centroid mean force was calculated using

$$F_c(x_c) = \langle F(x(\tau)) \rangle_c = -\frac{d}{dx_c} V_c(x_c) \quad (9)$$

while eq 7 was used for the average centroid energy. These quantities were calculated at successive centroid positions from -12 to 12 , in increments of 0.2 . At each given value of x_c , the system was equilibrated for 10^5 steps and then sampled for 2×10^6 steps. The centroid potential of mean force $V_c(x_c)$ was then calculated by the integration of the centroid mean force, using cubic interpolation and quadratic extrapolation where necessary.

Figure 1 shows the calculated centroid potentials of mean force and the average centroid energies for six different values of β . As β increases (temperature decreases), the maximum value of V_c decreases and its position shifts toward the reactant side. Table 1 presents the ratio Γ for various versions of PI-QTST, identified by subscript. In calculating the reaction rate, significant figures were kept to three and all the calculated V_c 's were rounded off up to the second decimal point. The results of other QTSTs are also shown, along with the results due to the semiclassical bounce method calculated using the standard procedure.^{20,24,54} In this table, Γ_{HA} represents the QTST2 results by Hansen and Andersen,⁴⁴ Γ_{PL} represents the QTST results by Pollak and Liao,⁴⁵ and Γ_{SPL} is the best perturbation expansion results taken from Table 3 of the paper by Shao et al.⁵⁵ The table shows that PI-QTST gives results comparable to Γ_{SPL} , a complicated variational perturbation theory, thus implying that the PI-QTST includes a substantial part of the nontrivial anharmonic contributions. The expression of CV improves these results further, remaining quite close to the exact ones. On the other hand, the expression of Ramirez seems to worsen the estimation of the PI-QTST, which indicates that his present empirical relation may not have much generality beyond the symmetric limit.

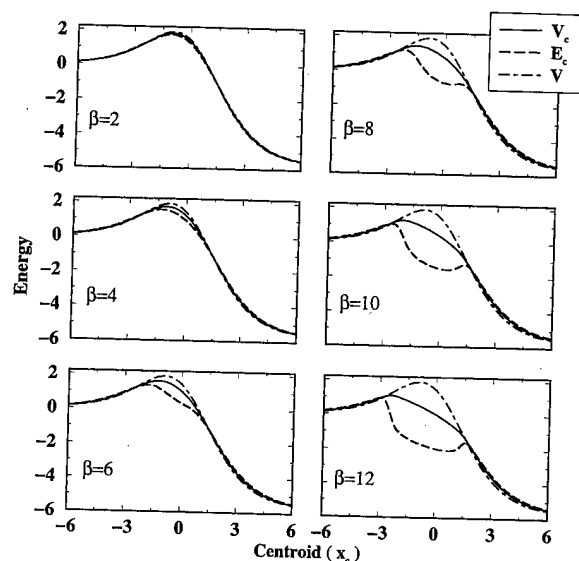


Figure 1. Centroid potential of mean force (V_c) and average energy function (E_c) as a function of the centroid x_c compared with the classical potential, for the asymmetric Eckart barrier given by eq 8, at six different values of β .

TABLE 1: Ratio of QTSTs to the Classical TST, Denoted as Γ , for the Asymmetric Eckart Barrier of eq 8

β	$\Gamma_{PI-QTST}^a$	Γ_{CV}^b	Γ_R^c	Γ_{HA}^d	Γ_{PL}^e	Γ_{SPL}^f	Γ_{sc}^g	Γ_{ex}^h
2	1.17	1.23	1.20	1.2	1.2	1.2		1.2
4	1.97	2.16	2.09	2.0	2.0	2.0		2.0
6	5.69	6.35	6.58	5.2	5.6	5.4		5.3
8	36.6	30.6	50.9	38	44	31	28.1	26
10	544	335	925	1100	1100	655	233	250
12	16600	7620	65000	87000	28000	13100	3710	4100

^a Path integral quantum transition state theory (PI-QTST). ^b Cao and Voth modification of PI-QTST. ^c Ramirez modification of PI-QTST. ^d QTST2 by Hansen and Andersen. ^e QTST by Pollak and Liao. ^f The best perturbation expansion result calculated by Shao, Liao, and Pollak. ^g Semiclassical bounce theory. ^h Exact result.

It is seen that PI-QTST overestimates the rate at lower temperature, while the CV modification is most successful. However, it is still in error by almost a factor of two at $\beta = 12$. These results are in contrast to those of the semiclassical bounce theory which somewhat underestimates the exact rate, but achieves agreement to within a few percent. This situation seems to contradict the analysis by VCM,²⁹ which showed that the semiclassical limit of PI-QTST can be made equivalent to the bounce theory by a modification of the preexponential factor only. Indeed PI-QTST performs quite well for the case of the symmetric Eckart barrier, but not as well for the asymmetric case.

III. Simple Correction Method

The data calculated in section II are consistent with the previous findings regarding the performance of PI-QTSTs for asymmetric or metastable potentials.^{41,42} Makarov and Topaler⁴¹ provided an insightful analysis and suggested a simple correction method where the underlying potential energy $V(x)$ in the calculation is modified to be $\max\{V(x), V_{cut}\}$ with V_{cut} chosen to be an arbitrary number smaller than the potential reactant well bottom energy. They tested this method for a cubic metastable potential.⁴¹ Above the cross-over temperature, the results were in close agreement with the exact one irrespective of the choice of V_{cut} . However, below the crossover, they found the results become sensitive to the value of V_{cut} and are not as reliable as those calculated by the semiclassical bounce theory.⁵⁶

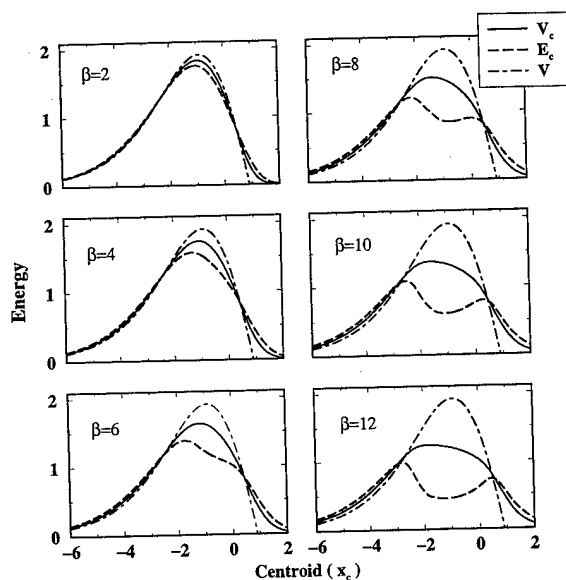


Figure 2. Centroid potential of mean force (V_c) and average energy function (E_c) as a function of the centroid x_c compared with the classical potential, for the asymmetric Eckart barrier given by eq 8 modified in the way of eq 10, at six different values of β .

TABLE 2: Ratio of PI-QTSTs to the Classical TST for the Asymmetric Eckart Barrier of Equation 8 Modified by the Way of Equation 10^a

β	$\Gamma_{\text{PI-QTST}}$	Γ_{CV}	Γ_{R}	Γ_{sc}	Γ_{ex}
2	1.17	1.23	1.20		1.2
4	1.97	2.19	2.09		2.0
6	5.36	6.65	6.07		5.3
8	26.5	30.7	33.1	28.1	26
10	244	287	346	233	250
12	3490	4140	5560	3710	4100

^a The symbols are as described in Table 1. The semiclassical bounce theory and the exact results for the original potential are provided for reference.

In the present paper, we suggest and more clearly justify the use of a similar correction method, but with the value of V_{cut} always fixed to be that of the potential reactant well bottom energy. That is, given a potential, the reaction rates are calculated by applying PI-QTST and its modifications to the following potential:

$$V(x) = \begin{cases} V(x), & V(x) \geq V_r \\ V_r, & V(x) < V_r \end{cases} \quad (10)$$

with V_r being the reactant well bottom energy.

First, the asymmetric Eckart barrier considered in the previous section was tested, where $V_r = 0$. The potential used in the simulation was the original potential for $x \leq 0.9$ and a Gaussian tail joined at $x = 0.9$ such that the potential and the first derivative change continuously. Since the value of the potential at the joining point is very small (about 0.006) and the Gaussian tail decays to zero rapidly, this method of modification is practically the same as the one suggested by eq 10. Numerical calculation of the centroid potential of mean force V_c was then performed as described in section II.B. Figure 2 shows the potentials for six different values of β . Table 2 shows the calculated values of Γ , using the three PI-QTST based approaches with the modified potential. The semiclassical and exact results given in Table 1 are shown again for reference. As can be seen in Table 2, the modified PI-QTST results all show much better agreement with the exact ones.

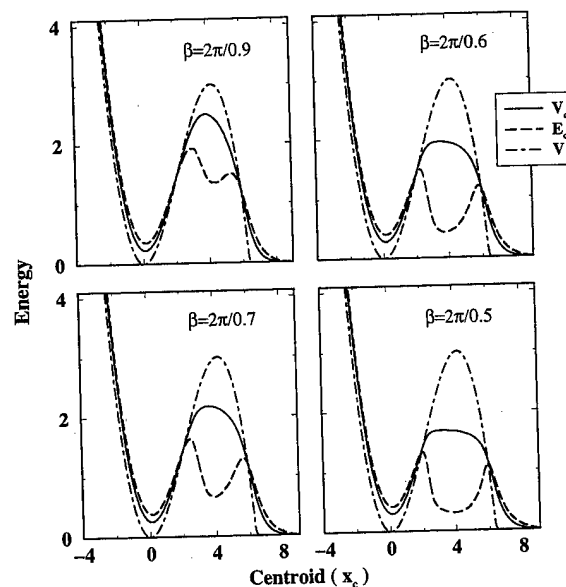


Figure 3. Centroid potential of mean force (V_c) and average energy function (E_c) as a function of the centroid x_c compared with the classical potential, for the metastable cubic potential of eq 11 modified in the way of eq 10, at four different values of β below the crossover temperature.

In this case, the PI-QTST underestimates the reaction rate, a trend similar to the case of the symmetric Eckart barrier.^{29,36,37} The CV reaction rate expression corrects the PI-QTST results in the right direction and provides the best estimates for the reaction rates below the crossover temperature. The rates calculated by Ramirez's expression also differ from the PI-QTST results in the proper direction, but below the crossover temperature, it results in a much larger overestimation of the rate than the CV result.

As an additional test case, the same approach was implemented for a cubic metastable potential that was previously treated by Makarov and Topaler.⁴¹ The explicit form of the model potential is given by

$$V(x) = \frac{1}{2}x^2 - \frac{1}{9\sqrt{2}}x^3 \quad (11)$$

with the same natural units as before. For this potential, $x_b = 3/\sqrt{2}$ and $V_b = 3$. Since $\omega_b = 1$, the crossover value of β is equal to 2π . For the present case also, $V_r = 0$. The potential was modified in a similar way as before by joining the original potential with a Gaussian tail at $x = 6.3$. Four different values of β below the cross-over temperature were considered. For a given value of β , the number of path integral quasiparticles was chosen to be $180\beta/(2\pi)$, and the number of primary quasiparticles was set to 10. The staging transformation was made for each intervening segment as before. The centroid mean force was calculated in the same way as before by varying the centroid with the interval of 0.2 in the range from -3 to 12 . Figure 3 shows the centroid potential of mean force, and Table 3 compares the calculated reaction rates with the exact ones.⁵⁶ The rates based on the semiclassical bounce theory have again been calculated according to the standard method.^{20,24,54} For this case also, the CV theory gives quite accurate results and becomes comparable to the semiclassical approximations in the low temperature limit, except for the case of $\beta = 2\pi/0.5$, where the deviation seems simply originate from the breakdown of the stationary phase integration approximation in the centroid variable space. As can be seen from Figure 3, the centroid

TABLE 3: Reaction Rate Calculated by PI-QTSTs Modified in the Way of Equation 10 for the Cubic Metastable Potential of Equation 11^a

β	$k_{\text{PI-QTST}}$	k_{CV}	k_{sc}	k_{ex}
$2\pi/0.9$	1.90	2.16	2.45	$1.92 (\times 10^{-8})$
$2\pi/0.7$	4.63	6.47	7.26	$6.77 (\times 10^{-9})$
$2\pi/0.6$	3.91	6.24	6.26	$5.83 (\times 10^{-9})$
$2\pi/0.5$	3.97	7.61	6.02	$5.60 (\times 10^{-9})$

^a The reaction rates are denoted as k with the subscripts having the same meaning as in Table 1. The semiclassical bounce theory and the exact results are for the original potential. For the units, refer to the main text.

potential of mean force cannot be well approximated by a quadratic function down to the energy comparable to $k_B T$. Therefore, the result could be improved by using an effective curvature rather than the one at the barrier top.

The results of the two test cases show that the CV theory applied to the modified potential of eq 10 predicts reaction rates comparable to those based on the semiclassical bounce theory below the cross-over temperature. This implies that when the choice of $V_{\text{cut}} = V_r$ is made, the centroid coordinate recovers its role as the proper reaction coordinate and the action for this modified potential at the local maximum in the centroid variable space is very close to the action for the original potential at the saddle point in the general space of paths. In the following section, a detailed semiclassical analysis of the centroid density is provided, which illuminates the source of the error involved in the original applications of PI-QTST and CV theory to strongly asymmetric and metastable potentials, as well as the mechanism of the correction made by the simple remedy suggested here.

IV. Semiclassical Centroid Density

A. General Expressions. In the present section, a semiclassical expression for the excess centroid density is provided. For this purpose, eq 2 is rewritten as

$$\rho_c(x_c) = \sqrt{\frac{2\pi\hbar^2\beta}{m}} \int_{-\infty}^{\infty} \frac{d\xi}{2\pi} \int_{-\infty}^{\infty} dx \int \cdots \int_x D'[x(\tau)] \times \exp\{-S[x(\tau)]/\hbar + i\xi(x_0 - x_c)\} \quad (12)$$

where the delta function in the integrand of eq 2 has been replaced with its Fourier integral expression. The path integration is over those paths with $x(0) = x(\beta\hbar) = x$ as indicated by the subscript of the path integral, and the prime in the path measure indicates that the integration over x has been singled out. In the semiclassical limit, the dominant contribution of this integral comes from paths close to the classical paths on the inverted potential. These paths can be decomposed into

$$x(\tau) = x_{\text{cl}}(\tau) + \delta x(\tau) \quad (13)$$

where $x_{\text{cl}}(\tau)$ is a classical path on the inverted potential satisfying the boundary condition $x_{\text{cl}}(0) = x_{\text{cl}}(\beta\hbar) = x$, and $\delta x(\tau)$ is an arbitrary fluctuation away from the classical path with the restriction $\delta x(0) = \delta x(\beta\hbar) = 0$. Including up to the second order variation of the action with respect to $\delta x(\tau)$, the semiclassical approximation for the centroid density of eq 12 is given by

$$\rho_c^{\text{sc}}(x_c) = \int dx \sum_{Cl(x)} e^{-S[Cl(x)]/\hbar} I[x_c, Cl(x)] \quad (14)$$

where $Cl(x)$ is a classical trajectory starting at x and ending at the same point after an interval $\tau = \beta\hbar$, and the summation

implies that there can be more than one such trajectory. The quantity $I[x_c, Cl(x)]$ is a centroid-constrained quadratic path integral, which depends on x_c , x , and on the specific classical orbit chosen. This quantity is defined as

$$I[x_c, Cl(x)] = \sqrt{\frac{\hbar^2\beta}{2\pi m}} \int_{-\infty}^{\infty} d\xi \exp\{i\xi(x_{\text{cl},0} - x_c)\} \times \int \cdots \int_0^{\beta\hbar} D'[\delta x(\tau)] \exp\left\{-\frac{m}{2\hbar} \int_0^{\beta\hbar} d\tau \int_0^{\beta\hbar} d\tau' \delta x(\tau) \times L(\tau, \tau') \delta x(\tau') + \frac{i\xi}{\beta\hbar} \int_0^{\beta\hbar} d\tau \delta x(\tau)\right\} \quad (15)$$

with $x_{\text{cl},0} = \int_0^{\beta\hbar} x_{\text{cl}}(\tau)/(\beta\hbar)$ and

$$L(\tau, \tau') = \left\{ -\frac{\partial^2}{\partial \tau^2} + \frac{1}{m} V''(x_{\text{cl}}(\tau)) \right\} \delta(\tau - \tau') \quad (16)$$

Note that these latter objects also implicitly depend on the value of x and on the specific classical orbit chosen. The subscript of 0 in the path integral of eq 15 indicates that $\delta x(\tau)$ starts and ends at zero. For the differential operator of eq 16, the zero eigenvalue Green function^{19,57,58} can be defined by the following relation:

$$\int_0^{\beta\hbar} d\tau' L(\tau, \tau') G(\tau', \tau'') = \int_0^{\beta\hbar} d\tau' G(\tau, \tau') L(\tau', \tau'') = \delta(\tau - \tau'') \quad (17)$$

which satisfies the same boundary condition as $\delta x(\tau)$ stated above. It will be shown later that the explicit expression for the semiclassical centroid density involves this Green function. For the time being, it is assumed that the operator of eq 16 does not have a zero eigenvalue so that the Green function defined by eq 17 is not singular. Later, it will be shown that the case with zero eigenvalue can be included as a limiting case in performing the final integration.

Equation 15 can be transformed into an expression involving a solution of the differential equation of eq 16 and an integration over the Green function defined by eq 17. The detailed method of evaluation and the final expression depend on whether or not the differential operator of eq 16 has a negative eigenvalue. Appendix A starts with the discretized approximation for eq 15 and then provides a general expression which allows explicit Gaussian integrations. For the case where all the eigenvalues are positive, the Gaussian integrations over all the fluctuation modes can be performed without any ambiguity, and this is described in Appendix B. The case where there is a single negative eigenvalue and no zero eigenvalue is treated in Appendix C. Here greater care must be taken with the order of integration, and the existence of the result is seen to depend on the shape of the potential.

The expression in eq 14 shows that a given semiclassical centroid density, whether it is convergent or divergent, can be formally decomposed into disjoint components, which we characterize by the specific classical orbits. All of the nonstationary classical trajectories must have at least one turning point because of the boundary condition $x_{\text{cl}}(0) = x_{\text{cl}}(\beta\hbar)$. Since a given classical trajectory spends a substantial part of its time near the turning point(s), the characteristics of each component of the semiclassical centroid density given by eq 14 can be related to the nature of the turning points. Thus it is reasonable to decompose the semiclassical centroid density into components

associated with the location of the turning points of their underlying classical trajectories, as follows:

$$\rho_c^{\text{sc}}(x_c) = \rho_{c,r}^{\text{sc}}(x_c) + \rho_{c,b}^{\text{sc}}(x_c) + \rho_{c,p}^{\text{sc}}(x_c) \quad (18)$$

where the subscripts *r*, *b*, and *p* respectively represent the reactant, the barrier, and the product parts of the centroid density. For more quantitative statement, we temporarily introduce dividing surfaces: d_{rb} , which lies between the reactant bottom and the barrier top, and d_{bp} , which lies between the barrier top and the product bottom. In most situations where the reaction rate can be defined, although somewhat arbitrary, these dividing surfaces can always be found such that, in the classical limit, the reactant region of the configuration space corresponds to the lefthand side of d_{rb} and the product region of the configuration space corresponds to the righthand side of d_{bp} . Within the semiclassical approximation, the turning points of the underlying classical trajectories can play such roles. That is, the reactant centroid density, $\rho_{c,r}^{\text{sc}}(x_c)$, is the centroid density around the classical trajectories with all of their turning points at the left hand side of d_{rb} ; and vice-versa for the product centroid density. The barrier centroid density is the centroid density around those classical trajectories with the turning points in between d_{rb} and d_{bp} , and around those classical trajectories with turning points on both the lefthand side of d_{rb} and the righthand side of d_{bp} . In the high temperature limit, only the former contributes to the barrier centroid density, and the latter appears only below some temperature in most cases and becomes more dominant as the temperature goes down. The details of the decomposition depend on the topology of the potential and the temperature. In the following, the simple generic case is considered where the regions near the reactant bottom and the barrier top can be well approximated by quadratic functions and where the potential changes in a smooth and continuous fashion between these regions.

B. Reactant Centroid Density. Due to the generic shape of the potential assumed in the analysis, the reactant centroid density consists of those classical trajectories which have only one turning point on the reactant side hill of the inverted potential. Such trajectories, denoted as $\text{Cl}(x; r)$, start at x , approach (from either side) the top of the reactant side hill of the inverted potential without crossing it, and then after a time $\beta\hbar$, return to their original position x , with momentum at $\tau = \beta\hbar$ equal in magnitude and opposite in sign to that at $\tau = 0$. Note that there is only one such trajectory for given x and $\beta\hbar$. The stationary trajectory sitting at the top of the hill can be included as a limiting situation of these trajectories. The general expression is given by

$$\rho_{c,r}^{\text{sc}}(x_c) = \int_r dx e^{-S[\text{Cl}(x;r)]/\hbar} I[x_c, \text{Cl}(x; r)] \quad (19)$$

where $I[x_c, \text{Cl}(x; r)]$ is the centroid constrained quadratic path integration defined by eq 15 around the classical trajectory of $\text{Cl}(x; r)$. The subscript of *r* denotes that the integration is performed only for x satisfying the condition of $x_{c1}(\beta\hbar/2) < d_{rb}$. At high enough temperature, $\beta\hbar$ is small and the starting point x should be close to the turning point. Thus, the dominant contribution to eq 19 is from the reactant bottom region of the original potential, which can be approximated by the following harmonic potential:

$$V(x) \approx V_r + \frac{m\omega_r^2}{2} (x - x_r)^2 \quad (20)$$

Then, the classical trajectory on the inverted potential satisfying the boundary condition is given by

$$x_{c1}(\tau) = x_r + (x - x_r) \frac{\cosh(\omega_r(\beta\hbar/2 - \tau))}{\cosh(\omega_r\beta\hbar/2)} \quad (21)$$

The center of this trajectory, the time average, is given by

$$x_{c1,0} = x_r + (x - x_r) \frac{2}{\omega_r\beta\hbar} \tanh(\omega_r\beta\hbar/2) \quad (22)$$

and the action along the given trajectory is given by

$$S_{c1} = \beta\hbar V_r + m\omega_r(x - x_r)^2 \tanh(\omega_r\beta\hbar/2) \quad (23)$$

For the given trajectory, the second derivative of the potential is constant and the differential operator defined by eq 16 simplifies to

$$L(\tau, \tau') = \left(-\frac{\partial^2}{\partial \tau^2} + \omega_r^2 \right) \delta(\tau - \tau') \quad (24)$$

which is independent of x . This operator does not have any negative or zero eigenvalues and the centroid-constrained path integral of $I[x_c, \text{Cl}(x; r)]$ in eq 19 can be calculated as described in Appendix B. For the present case, the explicit expressions for eqs B3 and B5 can be shown to be

$$f(\beta\hbar) = \frac{1}{\omega_r} \sinh(\omega_r\beta\hbar) \quad (25)$$

$$\gamma = \left(\frac{b\hbar}{\omega_r} \right)^2 \left(1 - \frac{2}{\omega_r\beta\hbar} \tanh\left(\frac{\omega_r\beta\hbar}{2}\right) \right) \quad (26)$$

Inserting eqs 22, 25, and 26 into eq B6, and then using the resulting expression in eq 19 along with eq 23 one can obtain an expression for the reactant centroid density which involves Gaussian integration over x . Performing this integration, the following high temperature expression is obtained:

$$\rho_{c,r}^{\text{sc}}(x_c) \approx \frac{(\omega_r\beta\hbar/2)}{\sinh(\omega_r\beta\hbar/2)} \exp \left\{ -\beta V_r - \frac{\beta m \omega_r^2}{2} (x_c - x_r)^2 \right\} \quad (27)$$

As the temperature is reduced, the imaginary time $\beta\hbar$ becomes larger and the important classical trajectories sample a larger region of the potential, away from the reactant minimum. Eventually, the harmonic approximation for the potential will break down. However, as long as the curvature of the original potential increases as the trajectories approach the turning point, all the eigenvalues of the differential operator of eq 16 remain positive and the semiclassical centroid density can be evaluated in the same manner of Appendix B. Although it is not in general possible to find the explicit expressions for the eigenvalue spectrum and the Green function, one can usually make an effective harmonic approximation and the final expression can be brought into the form of eq 27 with the frequency ω_r replaced with the x_c dependent effective frequency $\Omega_r(x_c)$. Note that the value of $\rho_{c,r}^{\text{sc}}(x_c)$ decreases in a Gaussian fashion as the centroid x_c is moved away from the reactant minimum x_r toward the barrier top. This feature will be revisited later in the analysis of the simple correction scheme.

C. Barrier Centroid Density. The barrier centroid density consists of those classical trajectories which connect the reactant

and the product sides of the potential. At high enough temperature (small $\beta\hbar$), the only possible trajectories of this kind are those concentrated near the barrier region. On the other hand, at temperatures low enough that $\beta\hbar$ is larger than the period of the small harmonic oscillation near the barrier region, periodic orbits with much lower action exist and the paths near these orbits represent the dominant contribution to barrier crossing.

1. High Temperature Limit. In this case there is no periodic orbit crossing the barrier top of the original potential, and the only possible trajectories are those which start near the local minimum of the inverted potential, climb up toward either the reactant or the product side slightly, and then return to their original position. The constant trajectory sitting at the local minimum of the inverted potential is included as a limiting case of these trajectories. The expression for the barrier region centroid density, therefore, can be written as

$$\rho_{c,b}^{sc}(x_c) = \int_b dx e^{-S[Cl(x)]/\hbar} I[x_c, Cl(x; b)] \quad (28)$$

where the subscript b implies that the integration is done only for x satisfying $d_{tb} < x_{cl}(\beta\hbar/2) < d_{bp}$ and $I[x_c, Cl(x; b)]$ is the centroid constrained quadratic path integration defined by eq 15 around the barrier region classical trajectory of $Cl(x; b)$. Again, it is assumed that the potential in this region can be well approximated by the inverted parabolic form

$$V(x) \approx V_b - \frac{m\omega_b^2}{2} (x - x_b)^2 \quad (29)$$

Then, for a given x , there exists a unique classical trajectory on the inverted potential satisfying the boundary condition as follows:

$$x_{cl}(\tau) = x_b + (x - x_b) \frac{\cos(\omega_b(\tau - \beta\hbar/2))}{\cos(\omega_b\beta\hbar/2)} \quad (30)$$

This expression becomes singular when $\beta\hbar = \pi/\omega_b$. For the moment, it is assumed that $\beta\hbar < \pi/\omega_b$. The time average of this trajectory, its centroid, is given by

$$x_{cl,0} = x_b + (x - x_b) \frac{\tan(\omega_b\beta\hbar/2)}{(\omega_b\beta\hbar/2)} \quad (31)$$

and the action along the trajectory is given by

$$S_{cl} = \beta\hbar V_b - m\omega_b(x - x_b)^2 \tan(\omega_b\beta\hbar/2) \quad (32)$$

For the trajectory of eq 30, the differential operator defined by eq 16 simplifies to

$$L(\tau, \tau') = \left(-\frac{\partial^2}{\partial \tau^2} - \omega_b^2 \right) \delta(\tau - \tau') \quad (33)$$

The eigenvalues of this operator are all positive under the limitation of $\beta\hbar < \pi/\omega_b$ as stated above, and the centroid constrained path integration $I[x_c, Cl(x)]$ in eq 28, can be calculated in the manner of Appendix B. The explicit expressions for eqs B3 and B5 can be calculated to be

$$f(\beta\hbar) = \frac{1}{\omega_b} \sin(\omega_b\beta\hbar) \quad (34)$$

$$\gamma = \left(\frac{\beta\hbar}{\omega_b} \right)^2 \left(\frac{2}{\omega_b\beta\hbar} \tan \left(\frac{\omega_b\beta\hbar}{2} \right) - 1 \right) \quad (35)$$

Inserting eqs 31, 34, and 35 into eq B6, and then using the resulting expression in eq 28 along with eq 32, one can obtain the following expression for the barrier centroid density:

$$\rho_{c,b}^{sc}(x_c) \approx \sqrt{\frac{\omega_b\beta\hbar}{\sin(\omega_b\beta\hbar)}} \sqrt{\frac{m\beta^3\hbar^2}{2\pi\gamma}} e^{-\beta V_b + \beta m\omega_b^2(x_c - x_b)^2/2} \int_{-\infty}^{\infty} dx \times \exp \left\{ -\frac{m\beta^2\hbar}{\omega_b\gamma} \tan(\omega_b\beta\hbar/2) (x - x_c)^2 \right\} \quad (36)$$

Since γ is positive, the Gaussian integration over x is defined and the resulting centroid density can be written as

$$\rho_{c,b}^{sc}(x_c) \approx \frac{(\omega_b\beta\hbar/2)}{\sin(\omega_b\beta\hbar/2)} \exp \left\{ -\beta V_b + \frac{\beta m\omega_b^2}{2} (x_c - x_b)^2 \right\} \quad (37)$$

This is equal to the exact centroid density for the inverted harmonic oscillator with frequency ω_b .

As has been stated, the derivation of eq 37 is valid only when $\beta\hbar < \pi/\omega_b$. For the case where $\pi/\omega_b \leq \beta\hbar < 2\pi/\omega_b$, two difficulties are encountered in its derivation even though the final expression of eq 37 can still be used. First, the classical equation of motion, eq 30 becomes singular at $\beta\hbar = \pi/\omega_b$. The reason is that, at this temperature, the classical trajectory starting at x always ends up at $2x_b - x$ after half the period time, within the harmonic approximation, and the only solutions satisfying the given boundary condition are those trajectories starting at $x = x_b$. For values of $\beta\hbar$ slightly larger than that corresponding to the half-period, the classical solution of eq 30 can be used again. Second, when $\pi/\omega_b < \beta\hbar < 2\pi/\omega_b$, there appears a negative eigenvalue, and one cannot perform the path integral as described in Appendix B; nor can the approach of Appendix C be used because α_1 of the unstable mode appearing in eq C1 vanishes, making the resulting centroid density undefined. In fact, there exists an anharmonic contribution which was not considered above but resolves the difficulties stated here. That is, a small participation of the anharmonicity removes the singularity at $\beta\hbar = \pi/\omega_b$ and allows α_1 of the unstable mode to survive. Therefore, the centroid density changes continuously at the singularity and the method of Appendix C can be used in the range of $\pi/\omega_b < \beta\hbar < 2\pi/\omega_b$ as long as other criteria are satisfied. Thus, while anharmonic contributions from a realistic potential become crucial to the definition of the centroid density in this parameter regime, the qualitative behavior of the solution seems to remain the same as that for higher temperatures. That is, the final expression for the centroid density is expected to be well approximated by the form given by eq 37, with the barrier frequency ω_b replaced with an x_c -dependent effective harmonic barrier frequency, $\Omega_b(x_c)$.²⁹

2. Low Temperature Limit. Below the temperature defined by $\beta\hbar = 2\pi/\omega_b$, there appear one or more periodic orbit(s) which bridge the reactant and the product regions. A feature of these trajectories is that the action along the trajectory does not depend on the choice of the initial position. The dominant contribution comes from the periodic orbit with period $\beta\hbar$, and the semiclassical barrier centroid density is approximated to be

$$\rho_{c,b}^{sc}(x_c) \approx e^{-S_{po}/\hbar} \int_{po} dx I[x_c, Cl(x; po)] \quad (38)$$

where S_{po} is the action along the periodic orbit and $I[x_c, Cl(x; po)]$ is the centroid-constrained path integral defined by eq 15

along the periodic orbit. The integration subscript of ρ implies that integration over x are performed along the points in the given periodic orbit.

For the special case where x corresponds to a turning point, $\dot{x}_{po}(\tau)$, becomes the zero eigenvalue solution of the differential operator of eq 16 satisfying the given boundary condition of $\dot{x}_{po}(0) = \dot{x}_{po}(\beta\hbar) = 0$. Otherwise, $\dot{x}_{po}(\tau)$ does not vanish at the boundary and the true solution should be obtained through a perturbative correction. This correction forces the solution to vanish at the boundary and the resulting eigenvalue becomes slightly larger than zero in a way analogous to a free particle confined to a one dimensional box with an infinite wall.¹⁹ On the other hand, this (almost) zero eigenvalue mode has one node, which implies that there should be a solution without any node which has a negative eigenvalue.

Given the qualitative feature above, the calculation of $I[x_c, Cl(x; p)]$ can be made as described in Appendix C, except for the case where $\dot{x}_{po}(0) = \dot{x}_{po}(\beta\hbar) = 0$, which will be included as a limiting case later. Since $\dot{x}_{po}(0) = \dot{x}_{po}(\beta\hbar)$ and the period of the orbit is independent of the initial point x , eq C8 simplifies to⁵⁹

$$f(\beta\hbar) = m\dot{x}_{po}(0)^2 \frac{d(\beta\hbar)}{dE} \quad (39)$$

where E is the negative of the energy of the periodic orbit on the inverted potential. In the present case, the existence of a negative eigenvalue is equivalent to the condition that $d(\beta\hbar)/dE < 0$. Inserting the expression of eq 39 into eq C6 and then using the resulting expression in eq 37, the barrier centroid density can be written as

$$\rho_{c,b}^{sc}(x_c) \approx e^{-S_{po}/\hbar} \int d\dot{x}_{po}(0) \frac{1}{|\dot{x}_{po}(0)|} \sqrt{\frac{dE}{d(\beta\hbar)} \frac{\beta^2\hbar}{2\pi\gamma}} \times \exp\left\{-\frac{m\beta(x_{po,0} - x_c)^2}{2\gamma}\right\} \quad (40)$$

with γ defined by eq C14 having the following form for the present case:

$$\gamma = \frac{m}{\beta\hbar} \frac{d(\beta\hbar)}{dE} \left\{ \frac{\partial}{\partial(\beta\hbar)} \int_0^{\beta\hbar} d\tau x_{po}(\tau; \beta\hbar)^2 - \left(\frac{\partial}{\partial(\beta\hbar)} \int_0^{\beta\hbar} d\tau x_{po}(\tau; \beta\hbar) \right)^2 \right\} \quad (41)$$

Since $d(\beta\hbar)/dE$ is negative, the condition of $\gamma < 0$, a necessary condition for the existence of the semiclassical barrier centroid density, is equivalent to the condition that the quantity within the curly bracket of eq 41 is positive, which seems to be satisfied in most cases.²⁹

Equation 40 can be simplified further.⁵⁹ The differential of $d\dot{x}_{po}(0)/|\dot{x}_{po}(0)|$ can be replaced with $d\tau$, thereby also including the limiting case of $\dot{x}_{po}(0) = 0$. The rest of the integrand is independent of τ . Therefore, after the integration over τ , the final expression for the barrier centroid density is given by

$$\rho_{c,b}^{sc}(x_c) \approx \beta\hbar e^{-S_{po}/\hbar} \sqrt{\frac{dE}{d(\beta\hbar)} \frac{\beta^2\hbar}{2\pi\gamma}} \exp\left\{-\frac{m\beta(x_{po,0} - x_c)^2}{2\gamma}\right\} \quad (42)$$

where both $dE/d(\beta\hbar)$ and γ are negative.

D. Product Centroid Density. The product centroid density consists of the classical trajectories which have all the turning points on the product side hill of the inverted potential. Representing these trajectories as $Cl(x; p)$, the centroid density can be expressed as

$$\rho_{c,p}^{sc}(x_c) = \int_p dx \sum_{Cl(x;p)} e^{-S[Cl(x;p)]/\hbar} I[x_c, Cl(x; p)] \quad (43)$$

where all the symbols have meanings analogous to those in the reactant centroid density of eq 19 and a general situation is considered such that the product region can have an arbitrary shape allowing multiple classical trajectories and the product side of the original potential can be either bounded or unbounded. While a formal definition of this product centroid density has been possible, there is no guarantee that it can always have a convergent value for the case of an unbounded product state. If the potential decrease is steep, either the path integration or the final integration over x in eq 43 can be divergent. On the other hand, if the product side of the original potential is bounded or it decreases less steeply than a quadratic function, it always has a convergent value.

For the purpose of the analysis to be made in the following section, an approximate explicit form for the product centroid density (when it converges) is useful. Again an effective harmonic expression is used for this purpose. In analogy with the reactant centroid expression of eq 27, the final result is given by

$$\rho_{c,p}^{sc}(x_c) \approx \frac{(\Omega_p(x_c)\beta\hbar/2)}{\sinh(\Omega_p(x_c)\beta\hbar/2)} \times \exp\left\{-\beta V_p - \frac{\beta m \Omega_p(x_c)^2}{2} (x_c - x_p)^2\right\} \quad (44)$$

If the value of $\Omega_p(x_c)$ is real, the centroid density of eq 44 represents a bound state case. An imaginary value of $\Omega_p(x_c)$ with its absolute value being smaller than $2\pi/\beta\hbar$ can represent the moderately steep unbound state where the centroid density is still defined. On the basis of the above expression and the similar expression for the reactant centroid density in eq 27, the primary factor determining the relative values of these two terms is the difference $V_r - V_p$. If this is much different than zero and positive, the product centroid density will be significantly larger than the reactant contribution for any value of the centroid constraint x_c near the location of the barrier top.

E. Analysis. One of the assumptions involved in the PI-QTST and its improved versions is that the path centroid is a natural variable that can differentiate the reactant, the barrier, and the product parts of the partition function. As we shall see, this assumption is at the heart of the problem when applying PI-QTST to strongly asymmetric or metastable potentials at low temperatures using numerical path integral methods to compute the centroid density. Indeed, in the semiclassical approximation, such an assumption is not necessary if one decomposes the centroid density into its constituent components as in the preceding sections. One can then apply the unified theory of CV using the semiclassical expressions for the centroid densities from the previous subsections. Defining the reactant partition function as

$$Z_{c,r}^{sc} = \sqrt{\frac{m}{2\pi\beta\hbar^2}} \int_{-\infty}^{x_c^*} dx_c \rho_{c,r}^{sc}(x_c) \quad (45)$$

with $\rho_{c,r}^{sc}(x_c)$ the reactant centroid density defined in section

III.B, the rate expression is given by

$$k_{CV}^{sc} = \min \left(\frac{\omega_b}{\omega_{c,b}}, \frac{2\pi}{\omega_{c,b}\beta\hbar} \right) \frac{1}{2\pi\beta\hbar} \frac{\rho_{c,b}^{sc}(x_c^*)}{Z_{c,r}^{sc}} \quad (46)$$

where $\rho_{c,b}^{sc}(x_c^*)$ is the value of the barrier centroid density defined in section III.C evaluated at its minimum value.

At high temperatures, the barrier centroid density can be expressed as eq 37 or its variational version with ω_b replaced with $\Omega_b(x_c)$. Therefore,

$$k_{CV}^{sc} = \frac{1}{2\pi\beta\hbar} \frac{(\omega_b\beta\hbar/2)}{\sin(\Omega_b(x_c^*)\beta\hbar/2)} \frac{e^{-\beta V_b}}{Z_{c,r}^{sc}}, \quad \beta\hbar < 2\pi/\omega_b \quad (47)$$

where $\Omega_b(x_c^*)$ is the frequency of the effective inverted harmonic function fitting the maximum of the effective barrier centroid potential $V_c(x_c)$ and is seen to be equal to $\omega_{c,b}$, defined in section II. In the low temperature limit where there appears a periodic orbit, the barrier centroid density of eq 42 can be used. The resulting expression is

$$k_{CV}^{sc} = \frac{1}{\sqrt{2\pi\hbar}} \left| \frac{dE}{d(\beta\hbar)} \right|^{1/2} \frac{e^{-S_{po}/\hbar}}{Z_{c,r}^{sc}}, \quad \beta\hbar \geq 2\pi/\omega_b \quad (48)$$

This is of the same form as the Affleck's rate expression below the crossover temperature.^{24,25} That is, within the semiclassical approximation, the unified theory of CV is equivalent to the bounce theory below the crossover temperature, *as long as the correct barrier part of the centroid density is used.*

In actual numerical path integral simulations, different parts of the centroid density cannot be separated and the calculated numerical value at a given centroid is the summation from all the contributions. To better understand this issue, eq 18 can be rewritten as

$$\rho_c^{sc}(x_c^*) = \rho_{c,b}^{sc}(x_c^*) \left[\frac{\rho_{c,r}^{sc}(x_c^*)}{\rho_{c,b}^{sc}(x_c^*)} + \frac{\rho_{c,p}^{sc}(x_c^*)}{\rho_{c,b}^{sc}(x_c^*)} + 1 \right] \quad (49)$$

Note that this expression in this case is to be evaluated at or near the barrier ($x_c = x_c^*$). On the basis of the analysis of this section, one would clearly wish to have the term in brackets as close to unity as possible in order for any centroid-based approach such as PI-QTST or CV theory to be accurate for the rate constant. The first term inside of the bracket should always be quite small, essentially because this is what defines an activated rate process. Even in the classical limit, the intrinsic nonlinearity of the potential in the barrier region causes $\rho_{c,p}^{sc}(x_c^*)$ to be much larger than $\rho_{c,r}^{sc}(x_c^*)$ which, according to eq 27, effectively corresponds to the density from a cusped barrier at $x = x_c^*$. By contrast, the second term in the bracket in eq 49 is larger than the first term by a factor of $e^{\beta(V_r - V_p)}$, though it will still be quite small in the classical, or nearly classical, limit. On the other hand, for strongly exothermic systems at low temperature, the second term begins to be much larger and creates the situation $\rho_c^{sc}(x_c^*) \gg \rho_{c,p}^{sc}(x_c^*)$, thus leading to the serious overestimation of the rate when PI-QTST is used with a numerically determined centroid density. A similar situation occurs if $\Omega_p(x_c^*)^2$ in eq 44 becomes effectively negative, as can be the case for metastable potentials.

The analysis presented above is only valid within the semiclassical approximation. For the more general situation where one should go beyond the semiclassical limit, the separation of the centroid density into different parts is not

possible and the analysis becomes unclear. However, such a semiclassical perspective provides a framework in which to understand the simple correction method presented in section III. That is, within this simple scheme, the lower bound of V_r in eq 10 seems to be an optimal choice because it does not change the barrier contribution to the centroid density but minimizes the spurious product contribution to this quantity described in the preceding paragraph. Thus a numerically determined path integral centroid density for the modified potential becomes much closer to the barrier part of this quantity as identified semiclassically. The modification procedure therefore results in an improvement in the estimation of the reaction rate using PI-QTST or CV theory in conjunction with numerical path integral methods. This approach also allows for the computational benefits of PI-QTST to be preserved in a straightforward manner. It should be noted that all of the analysis presented until now assumed that the product state potential bottom lies lower than that of the reactant state, which corresponds to an exothermic reaction. In the opposite situation of an endothermic reaction, similar analysis and conclusion are possible by reversing the role of the reactant and the product states. This is discussed in Appendix D.

V. Concluding Remarks

The PI-QTST and its variants^{29,36,37} were tested in this paper for an asymmetric Eckart barrier and compared with other recent QTSTs.^{43-45,55} The results show that all the theories overestimate the reaction rate as has been reported before.^{41,42} The CV theory³⁶ is shown to be better than the other approaches in the low temperature limit. On the other hand, the CV theory is worse than the semiclassical bounce theory.^{20,24,54} This is in contrast to the case of symmetric Eckart barrier, where the CV theory gives results comparable to the bounce theory.³⁶ When a simple correction method is employed which modifies the potential such that the product part of the potential never lies lower than the reactant well bottom potential energy, both PI-QTST and CV theory again are seen to give results comparable to those based on the bounce theory.

The present semiclassical analysis of the centroid density has provided two important findings. First, if only the barrier part of the centroid density is used, which is possible within the semiclassical approximation, the CV theory becomes equivalent to the bounce theory in the low temperature limit. Second, the effect of the simple correction mechanism to PI-QTST and CV theory presented in section III can be understood. The correction does not change the barrier part of the centroid density, but it reduces the spurious product contribution to the centroid density which arises in numerical path integral calculations. In this regard, the choice of V_r as the cutoff value seems to be the optimal choice because it is the value that makes the contribution from the product part minimal without affecting the barrier part [cf. eq 49 and the subsequent discussion].

For multidimensional cases, the correction method and the semiclassical analysis can be generalized in a straightforward way as long as the additional nonreactive degrees of freedom are coupled linearly. If there is nonlinear coupling, the semiclassical analysis becomes more complicated. Although the correction method of section III may become less straightforward in this case, the reaction rate calculated by such a method is still expected to be much closer to the exact one. Further analysis is needed and this will be the topic of future research. From the practical perspective, the correction method of section III seems not to have any difficulty associated with multidimensional situations. However, only applications of this approach to realistic situations can shed the appropriate light on this issue.

Acknowledgment. This research was supported by the National Science Foundation (Grant CHE-9712884). The authors thank Profs. David Reichman and Jianshu Cao for valuable comments. Seogjoo Jang is a graduate student in the Department of Chemistry, University of Pennsylvania.

Appendix A

Centroid Constrained Quadratic Path Integration. In the discretized path approximation, eq 15 can be written as

$$I[x_c, Cl(x)] \approx \sqrt{\frac{\hbar^2 \beta}{2\pi m}} \int_{-\infty}^{\infty} d\zeta \exp\{i\zeta(x_{cl,0} - x_c)\} \times \left(\frac{m}{2\pi\epsilon\hbar}\right)^{P/2} \int dy_1 \cdots \int dy_{P-1} \exp\left\{-\frac{m}{2\epsilon\hbar} \mathbf{y}^T \mathbf{D}_{P-1} \mathbf{y} + \frac{i\zeta}{P} (y_1 + \cdots + y_{P-1})\right\} \quad (\text{A1})$$

with

$$\mathbf{y}^T = (y_1, \cdots, y_{P-1}) \quad (\text{A2})$$

and

$$\mathbf{D}_{P-1} = \begin{pmatrix} 2 + \frac{\epsilon^2}{m} V_1'' - 1 & 0 & \cdots & 0 \\ -1 & 2 + \frac{\epsilon^2}{m} V_2'' - 1 & \cdots & 0 \\ \vdots & \vdots & \ddots & \vdots \\ 0 & 0 & 0 & \cdots & -1 \\ 0 & 0 & 0 & \cdots & 2 + \frac{\epsilon^2}{m} V_{P-2}'' \end{pmatrix} \quad (\text{A3})$$

There are $P - 1$ eigenvalues and eigenvectors which satisfy

$$\mathbf{D}_{P-1} \cdot \mathbf{u}^{(k)} = \lambda_k \mathbf{u}^{(k)}, \quad k = 1, \cdots, P - 1 \quad (\text{A4})$$

along with the normalization condition

$$\sum_{j=1}^{P-1} u_j^{(k)} u_j^{(l)} = \delta_{kl} \quad (\text{A5})$$

Then, introducing the following unitary matrix,

$$\mathbf{U} = (\mathbf{u}^{(1)}, \cdots, \mathbf{u}^{(P-1)}) \quad (\text{A6})$$

and the relevant coordinate transformation

$$\mathbf{z} = \mathbf{U}^T \mathbf{y} \quad (\text{A7})$$

Equation A1 can be simplified to

$$I[x_c, Cl(x)] \approx \sqrt{\frac{\hbar^2 \beta}{2\pi m}} \left(\frac{m}{2\pi\epsilon\hbar}\right)^{P/2} \int_{-\infty}^{\infty} d\zeta \exp\{i\zeta(x_{cl,0} - x_c)\} \int dz_1 \cdots \int dz_{P-1} \exp\left\{-\frac{m}{2\epsilon\hbar} (\lambda_1 z_1^2 + \cdots + \lambda_{P-1} z_{P-1}^2) + i\zeta (\alpha_1 z_1 + \cdots + \alpha_{P-1} z_{P-1})\right\} \quad (\text{A8})$$

where

$$\alpha_k = \frac{1}{P} \sum_{j=1}^{P-1} U_{jk} = \frac{1}{P} \sum_{j=1}^{P-1} u_j^{(k)} \quad (\text{A9})$$

In this expression, each λ_k and α_k depends on x and the classical trajectory $Cl(x)$.

By completing the square with respect to each z_k in the exponent of eq A8, one can reduce the discretized path integral into independent Gaussian integrations. However, if there is a negative eigenvalue, the integration over the unstable mode diverges and the centroid constrained path integration may not be defined. In this case, in fact, the centroid constraint should be imposed before integrating over the unstable mode. With some restrictions, this makes the originally unstable mode stable and a convergent expression for the centroid density can be obtained. The case where all the eigenvalues are positive is treated in Appendix B, and the case where there is one negative eigenvalue is considered in Appendix C.

Appendix B

All Positive Eigenvalues. In this case, the integrations over each z_k in eq A8 can be made by completing the squares. The resulting expression contains an exponential of a quadratic expression in terms of ζ , which can again be integrated over, leading to

$$I[x_c, Cl(x)] \approx \sqrt{\frac{\beta\hbar}{\epsilon}} \prod_{k=1}^{P-1} \lambda_k^{-1/2} \sqrt{\frac{m\beta}{2\pi\gamma_P}} \times \exp\left\{-\frac{m\beta(x_{cl,0} - x_c)^2}{2\gamma_P}\right\} \quad (\text{B1})$$

where

$$\gamma_P = \frac{(\beta\hbar)^2}{P} \left(\frac{\alpha_1^2}{\lambda_1} + \cdots + \frac{\alpha_{P-1}^2}{\lambda_{P-1}} \right) \quad (\text{B2})$$

The exact value of $I[x_c, Cl(x)]$ is obtained in the limit $P \rightarrow \infty$. In this limit, according to the theorem of Gel'fand and Yaglom,^{18,19,60}

$$\lim_{P \rightarrow \infty} \epsilon \prod_{k=1}^{P-1} \lambda_k = f(\beta\hbar) \quad (\text{B3})$$

where $f(\tau)$ is the homogeneous solution of the differential operator of eq 16

$$\int_0^{\beta\hbar} d\tau' L(\tau, \tau') f(\tau') = 0 \quad (\text{B4})$$

satisfying the boundary condition of $f(0) = 0$ and $f'(\beta\hbar) = 1$. On the other hand, in the same continuum limit, the quantity of eq B2 becomes the following integration of the Green function^{57,58} defined by eq 17:

$$\gamma \equiv \lim_{P \rightarrow \infty} \gamma_P = \frac{1}{\beta\hbar} \int_0^{\beta\hbar} d\tau \int_0^{\beta\hbar} d\tau' G(\tau, \tau') \quad (\text{B5})$$

which is positive for the present case. Then, the exact expression of the centroid constrained path integral of eq B1 is given by

$$I[x_c, Cl(x)] = \sqrt{\frac{m\beta^2\hbar}{2\pi\gamma f(\beta\hbar)}} \exp\left\{-\frac{m\beta(x_{cl,0} - x_c)^2}{2\gamma}\right\} \quad (\text{B6})$$

Appendix C:

One Negative Eigenvalue. The case where there is one negative eigenvalue and all other eigenvalues are positive is considered here. Let the negative eigenvalue be λ_1 . The Gaussian

integrations over other modes with positive eigenvalues can be made first in eq A8. The resulting expression is

$$I[x_c, Cl(x)] \approx \frac{1}{2\pi} \sqrt{\frac{\beta\hbar}{\epsilon}} \sqrt{\frac{m}{2\pi\epsilon\hbar}} \left(\prod_{k=2}^{P-1} \lambda_k^{-1/2} \right) \int_{-\infty}^{\infty} d\zeta \int_{-\infty}^{\infty} dz_1 \exp \left\{ -\frac{\gamma'_P \zeta^2}{2m\beta} + i\zeta(x_{cl,0} - x_c + \alpha_1 z_1) - \frac{m\lambda_1}{2\epsilon\hbar} z_1^2 \right\} \quad (C1)$$

where

$$\gamma'_P = \frac{(\beta\hbar)^2}{P} \left(\frac{\alpha_2^2}{\lambda_2} + \dots + \frac{\alpha_{P-1}^2}{\lambda_{P-1}} \right) \quad (C2)$$

In eq C1, the integration over ζ should be performed first, which is equivalent to imposing the centroid constraint first. The resulting expression is

$$I[x_c, Cl(x)] \approx \sqrt{\frac{\beta\hbar}{\epsilon}} \sqrt{\frac{m}{2\pi\epsilon\hbar}} \left(\prod_{k=2}^{P-1} \lambda_k^{-1/2} \right) \times e^{-m\beta(x_{cl,0} - x_c)^2/(2\gamma_P)} \int_{-\infty}^{\infty} dz_1 \left(\frac{m\beta}{2\pi\gamma'_P} \right)^{1/2} \times \exp \left\{ -\frac{m\lambda_1\gamma_P}{2\epsilon\hbar\gamma'_P} \left(z_1 + \frac{\alpha_1(\beta\hbar)^2(x_{cl,0} - x_c)}{P\lambda_1\gamma_P} \right)^2 \right\} \quad (C3)$$

where it has been assumed that α_1 is nonzero and $\gamma_P = \gamma'_P + (\beta\hbar)^2\alpha_1/(P\lambda_1)$ is the same quantity previously defined by eq B2. Since λ_1 is negative and γ'_P defined by eq C2 is positive, the integration over z_1 in eq C3 can be performed only when the following condition is satisfied:

$$\gamma_P < 0 \quad (C4)$$

Performing integration over z_1 in eq C3 assuming the condition of eq C4,

$$I[x_c, Cl(x)] \approx \left\{ \frac{\beta\hbar}{\epsilon} \left(\prod_{k=1}^{P-1} \lambda_k^{-1} \right) \frac{m\beta}{2\pi\gamma_P} \right\}^{1/2} \times \exp \left\{ -\frac{m\beta(x_{cl,0} - x_c)^2}{2\lambda_P} \right\} \quad (C5)$$

where the quantity within the square root of the preexponential factor is positive. In the limit $P \rightarrow \infty$, as is the case of Appendix B, this becomes

$$I[x_c, Cl(x)] = \sqrt{\frac{m\beta^2\hbar}{2\pi f(\beta\hbar)\gamma}} \exp \left\{ -\frac{m\beta(x_{cl,0} - x_c)^2}{2\gamma} \right\} \quad (C6)$$

which has the same form as eq B6 with the same definitions of $f(\beta\hbar)$ and γ given by eqs B3 and B5. The difference here is that both $f(\beta\hbar)$ and γ are negative.

It is important to clarify the conditions of existence of eq C6 again. The derivation of eq C3 required that both γ'_P and α_1 are nonzero. In fact, as long as α_1 is nonzero, the integration over z_1 can be made even if γ'_P is zero, which has the same form as eq C5. Therefore, the only required conditions are that (i) $\alpha_1 \neq$

0 and that (ii) $\gamma < 0$. Note that $f(\beta\hbar)$ is negative due to the condition that there is only one negative eigenvalue and no zero eigenvalue. The condition of (i) implies that motion along the unstable mode should accompany a change in the centroid position.

The quantities of $f(\beta\hbar)$ and γ appearing in eq C6 can be expressed in terms of the underlying classical trajectory. First, $f(\beta\hbar)$ is considered. One can show that the differential operator of eq 16, along the given classical trajectory $x_{cl}(\tau)$, has $\dot{x}_{cl}(\tau)$ as its homogeneous solution, although this may not satisfy the given boundary condition. In terms of the linear combination of this solution and the second independent solution generated from this, one can construct the following homogeneous solution:^{18,19,57-59}

$$f(\tau) = \dot{x}_{cl}(0)\dot{x}_{cl}(\tau) \int_0^\tau \frac{d\tau'}{\dot{x}_{cl}(\tau')^2} \quad (C7)$$

One can show that this is the solution of the differential operator of eq 16 satisfying the boundary condition^{18,19,60} of $f(0) = 0$ and $f(0) = 1$. Special care should be taken in performing the integration over τ' in eq C7. When $\tau = \tau_0$ with $\dot{x}_{cl}(\tau_0) = 0$, the quantity of eq C7 can be defined as the limiting situation. When $\tau > \tau_0$, the integration can be defined only on a contour which goes around the singularity at τ_0 by gaining a small imaginary term. Due to this nature of the integration contour, the integral in eq C7 can have a negative value. With this point being clarified,

$$f(\beta\hbar) = \dot{x}_{cl}(0)\dot{x}_{cl}(\beta\hbar) \int_0^{\beta\hbar} \frac{d\tau'}{\dot{x}_{cl}(\tau')^2} = m\dot{x}_{cl}(0)\dot{x}_{cl}(\beta\hbar) \frac{\partial T_{cl}(E, x)}{\partial E} \quad (C8)$$

where the second equality is the special case ($k = 0$) of the following general identity:

$$\int_0^{\beta\hbar} d\tau \frac{x_{cl}(\tau)^k}{\dot{x}_{cl}(\tau)^2} = m \frac{\partial}{\partial E} \int_0^{T_{cl}(E, x)} d\tau x_{cl}(\tau; E, x)^k \quad (C9)$$

with $T_{cl}(E, x) = \beta\hbar$ and E being the negative of the classical energy for the motion on the inverted potential satisfying the following relation:

$$\frac{m}{2} \dot{x}_{cl}(\tau)^2 - V(x_{cl}(\tau)) = -E \quad (C10)$$

The verification of eq C9 can be made through a change of integration variable from τ into x and then performing a partial integration. Care should be taken in taking the limit such that the divergent quantities cancel out.

Second, the quantity of γ can be expressed in a similar way. For this purpose, the Green function defined by eq 17 should be obtained first. Through the Wronski construction,^{19,57-59} one can show that

$$G(\tau, \tau') = \dot{x}_{cl}(\tau)\dot{x}_{cl}(\tau') \int_0^{\tau <} \frac{d\tau_1}{\dot{x}_{cl}(\tau_1)^2} \int_{\tau >}^{\beta\hbar} \frac{d\tau_2}{\dot{x}_{cl}(\tau_2)^2} \int_0^{\beta\hbar} \frac{d\tau_3}{\dot{x}_{cl}(\tau_3)^2} \quad (C11)$$

where $\tau < = \min(\tau, \tau')$ and $\tau > = \max(\tau, \tau')$. The integration of

this Green function given by eq C11 over τ and τ' leads to

$$\int_0^{\beta\hbar} d\tau \int_0^{\beta\hbar} d\tau' G(\tau, \tau') = \int_0^{\beta\hbar} d\tau \frac{x_{cl}(\tau)^2}{\dot{x}_{cl}(\tau)^2} - \left(\int_0^{\beta\hbar} d\tau \frac{x_{cl}(\tau)}{\dot{x}_{cl}(\tau)^2} \right) \left(\int_0^{\beta\hbar} \frac{d\tau}{\dot{x}_{cl}(\tau)^2} \right) \quad (C12)$$

Using eq C9 with $k = 1, 2$, one can show that eq C12 can be written as

$$\int_0^{\beta\hbar} d\tau \int_0^{\beta\hbar} d\tau' G(\tau, \tau') = m \frac{\partial T_{cl}(E, x)}{\partial E} \left\{ \frac{\partial}{\partial T_{cl}} \int_0^{T_{cl}} \times d\tau x_{cl}(\tau; T_{cl}, x)^2 - \left(\frac{\partial}{\partial T_{cl}} \int_0^{T_{cl}} d\tau x_{cl}(\tau; T_{cl}, x) \right)^2 \right\} \quad (C13)$$

Therefore, γ defined by eq B5 is given by

$$\gamma = \frac{m}{\beta\hbar} \frac{\partial T_{cl}(E, x)}{\partial E} \left\{ \frac{\partial}{\partial T_{cl}} \int_0^{T_{cl}} d\tau x_{cl}(\tau; T_{cl}, x)^2 - \left(\frac{\partial}{\partial T_{cl}} \int_0^{T_{cl}} d\tau x_{cl}(\tau; T_{cl}, x) \right)^2 \right\} \quad (C14)$$

Appendix D

Case of an Endothermic Reaction. In this case, a similar analysis can be made by reversing the roles of the reactant and the product states in the semiclassical analysis of section IV. Then, in the strongly endothermic case, the following situation can occur:

$$\rho_{c,r}^{sc}(x_c^*) \gg \rho_{c,b}^{sc}(x_c^*) \quad (D1)$$

so that $\rho_c^{sc}(x_c^*) \gg \rho_{c,b}^{sc}(x_c^*)$ according to eq 49. That is, the mixing-in of the reactant part and the barrier part of the centroid density can lower the effective barrier, which can result in the overestimation of the reaction rate when using numerical path integral methods to calculate the overall centroid density in the barrier region. This error can be corrected in the following way. For the calculation of the reactant partition function, the centroid potential of mean force for the original potential would be used. For the calculation of the centroid density in the barrier region, however, the simulation would be performed for the following modified potential:

$$V(x) = \begin{cases} V(x), & V(x) \geq V_p \\ V_p, & V(x) < V_p \end{cases} \quad (D2)$$

where V_p is the bottom value of the product part of the potential. The PI-QTST or CV theory given by eq 5 can then be applied using the reactant partition function calculated from the original potential with the centroid potential of mean force for the barrier contribution to the formula calculated with the modified potential of eq D2. This procedure will result in a reaction rate which satisfies detailed balance and becomes comparable to the semiclassical results in the low temperature limit.

References and Notes

- (1) Pechukas, P. In *Dynamics of Molecular Collisions, Part B*; Miller, W. H., Ed.; Plenum: New York, 1976.
- (2) Truhlar, D. G.; Hase, W. L.; Hynes, J. T. *J. Phys. Chem.* **1983**, *2664*, 87.
- (3) Hynes, J. T. In *Theory of Chemical Reaction Dynamics*; Baer, M., Ed.; CRC Press: Boca Raton, 1985.
- (4) Chandler, D. *J. Stat. Phys.* **1986**, *49*, 42.
- (5) Onuchic, J. N.; Wolynes, P. G. *J. Phys. Chem.* **1988**, *6495*, 92.
- (6) Hänggi, P.; Talkner, P.; Borkovec, M. *Rev. Mod. Phys.* **1990**, *251*, 62.
- (7) Voth, G. A. *J. Phys. Chem.* **1993**, *8365*, 97.
- (8) Anderson, J. B. *Adv. Chem. Phys.* **1995**, *381*, 91.
- (9) Pollak, E. In *Dynamics of Molecules and Chemical Reactions*; Wyatt, R. E., Zhang, J. Z. H., Eds.; Marcel Dekker: New York, 1996.
- (10) Refer to refs 1–9 and the references cited therein.
- (11) Yamamoto, T. *J. Chem. Phys.* **1960**, *281*, 33.
- (12) Miller, W. H. In *Dynamics of Molecules and Chemical Reactions*; Wyatt, R. E., Zhang, J. Z. H., Eds.; Marcel Dekker: New York, 1996.
- (13) Miller, W. H. *J. Phys. Chem. A* **1998**, *793*, 102.
- (14) Wigner, E. P. *Z. Phys. Chem. Abt. B* **1932**, *203*, 19.
- (15) Wolynes, P. G. *Phys. Rev. Lett.* **1981**, *968*, 47.
- (16) Feynman, R. P.; Hibbs, A. R. *Quantum Mechanics and Path Integrals*; McGraw-Hill Book Company: New York, 1965.
- (17) Feynman, R. P. *Statistical Mechanics*, Addison-Wesley Publishing Company: New York, 1972.
- (18) Schulman, L. S. *Techniques and Applications of Path Integration*; Wiley-Interscience: New York, 1981.
- (19) Kleinert, H. *Path Integrals in Quantum Mechanics, Statistics, and Polymer Physics*; World Scientific: Singapore, 1995.
- (20) Miller, W. H. *J. Chem. Phys.* **1975**, *1899*, 62.
- (21) Callan, J. C. G.; Coleman, S. *Phys. Rev. D* **1977**, *1762*, 16.
- (22) Coleman, S. *Phys. Rev. D* **1977**, *2929*, 15.
- (23) Coleman, S. In *The Why's of Subnuclear Physics*; Zichichi, A., Ed.; Plenum: New York, 1979.
- (24) Affleck, I. *Phys. Rev. Lett.* **1981**, *388*, 46.
- (25) Hänggi, P.; Hontscha, W. *J. Chem. Phys.* **1988**, *4094*, 88.
- (26) Benderskii, V. A.; Goldanskii, V. I.; Makarov, D. E. *Phys. Rep.* **1993**, *195*, 233.
- (27) Nakamura, T.; Ottewill, A.; Takagi, S. *Ann. Phys.* **1997**, *9*, 87.
- (28) Gillan, M. J. *J. Phys. C* **1987**, *3621*, 20.
- (29) Voth, G. A.; Chandler, D.; Miller, W. H. *J. Chem. Phys.* **1989**, *7749*, 91.
- (30) McRae, R. P.; Schenter, G. K.; Garrett, B. C.; Haynes, G. R.; Voth, G. A.; Schatz, G. C. *J. Chem. Phys.* **1992**, *7392*, 97.
- (31) Toapler, M.; Makri, N. *J. Chem. Phys.* **1994**, *7500*, 101.
- (32) Voth, G. A. *Adv. Chem. Phys.* **1996**, *135*, 93.
- (33) Stuchebrukhov, A. A. *J. Chem. Phys.* **1991**, *4258*, 95.
- (34) Messina, M.; Schenter, G. K.; Garrett, B. C. *J. Chem. Phys.* **1993**, *8525*, 98.
- (35) Messina, M.; Schenter, G. K.; Garrett, B. C. *J. Chem. Phys.* **1993**, *8644*, 99.
- (36) Cao, J.; Voth, G. A. *J. Chem. Phys.* **1996**, *6856*, 105.
- (37) Ramirez, R. *J. Chem. Phys.* **1997**, *3550*, 107.
- (38) Cao, J.; Voth, G. A. *J. Chem. Phys.* **1997**, *1769*, 106.
- (39) Schwieters, C. D.; Voth, G. A. *J. Chem. Phys.* **1998**, *1055*, 108.
- (40) Schwieters, C. D.; Voth, G. A. *J. Chem. Phys.* **1999**, In press.
- (41) Makarov, D. E.; Topaler, M. *Phys. Rev. E* **1995**, *178*, 52.
- (42) Mills, G.; Schenter, G. K.; Makarov, D. E.; Jónsson, H. *Chem. Phys. Lett.* **1998**, *91*, 278.
- (43) Hansen, N. F.; Andersen, H. C. *J. Chem. Phys.* **1994**, *6032*, 101.
- (44) Hansen, N. F.; Andersen, H. C. *J. Phys. Chem.* **1996**, *1137*, 100.
- (45) Pollak, E.; Liao, J.-L. *J. Chem. Phys.* **1998**, *2733*, 108.
- (46) Miller, W. H.; Schwartz, S. D.; Tromp, J. W. *J. Chem. Phys.* **1993**, *4889*, 79.
- (47) Giachetti, R.; Tognetti, V. *Phys. Rev. Lett.* **1985**, *912*, 55.
- (48) Feynman, R. P.; Kleinert, H. *Phys. Rev. A* **1986**, *5080*, 34.
- (49) Parrinello, M.; Rahman, A. *J. Chem. Phys.* **1984**, *861*, 80.
- (50) Cao, J.; Berne, B. J. *J. Chem. Phys.* **1989**, *6359*, 91.
- (51) Tuckerman, M. E.; Berne, B. J.; Martyna, G. J.; Klein, M. L. *J. Chem. Phys.* **1993**, *2796*, 99.
- (52) Martyna, G. J.; Klein, M. L.; Tuckerman, M. *J. Chem. Phys.* **1992**, *2635*, 97.
- (53) Jang, S.; Voth, G. A. *J. Chem. Phys.* **1997**, *9514*, 107.
- (54) Hänggi, P.; Hontscha, W. *Ber. Bunsen-Ges. Phys. Chem.* **1991**, *379*, 95.
- (55) Shao, J.; Liao, J.; Pollak, E. *J. Chem. Phys.* **1998**, *9711*, 108.
- (56) Hontscha, W.; Hänggi, P.; Riseborough, P. *Phys. Rev. B* **1990**, *2210*, 41.
- (57) Courant, R.; Hilbert, D. *Methods of Mathematical Physics*; Interscience Publishers, Inc.: New York, 1953; Vol. 1.
- (58) Mathews, J.; Walker, R. L. *Mathematical Methods of Physics*; W. A. Benjamin, Inc.: Menlo Park, California, 1969.
- (59) Dashen, R.; Hasslacher, B.; Neveu, A. *Phys. Rev. D* **1974**, *4114*, 10.
- (60) Gel'fand, I. M.; Yaglom, A. M. *J. Math. Phys.* **1960**, *48*, 1.

Classical Approximation to Nonradiative Electronic Relaxation in Condensed Phase Systems

Eran Rabani,[†] S. A. Egorov,^{‡,§} and B. J. Berne*

Department of Chemistry, Columbia University, 3000 Broadway, New York, New York 10027

Received: June 28, 1999; In Final Form: August 26, 1999

We present a study of the classical limit of nonradiative electronic relaxation in condensed phase systems. The discrete Hamiltonian representing an impurity in a condensed phase environment is mapped onto a continuous form using the Meyer–Miller approach. The classical electronic relaxation rate is obtained within the framework of the reactive flux formalism and is compared to the fully quantum mechanical result, and to a mixed quantum–classical approximation. Similar to the case of vibrational relaxation, we find that the fully classical treatment is closer to the fully quantum mechanical rate than the mixed quantum–classical treatment. We provide a time domain analysis of the results.

I. Introduction

Nonradiative relaxation in condensed phases plays an important role in many processes of scientific and technological interest, including the operation of lasers and chemical reactions in solutions.^{1–3} Radiationless decay is most conveniently introduced by contrasting it to radiative relaxation, where the system goes from the excited state to the ground state by emitting a photon of the same energy as the gap between the two states involved in the transition. In radiationless relaxation, the excitation energy of the system is not transferred to the electromagnetic field, but instead is dissipated into other forms of motion, such as heat. Particular examples of nonradiative decay include electronic relaxation of ionic impurity centers in solids, vibrational relaxation of molecules in crystals and in solutions, intramolecular vibrational energy redistribution in large polyatomic molecules, energy transfer processes, etc. It is often the case that the amount of energy transferred from the impurity to the host exceeds by many times the typical energy associated with the thermal motion of the solvent. Clearly, in contrast to radiative decay, many quanta of bath excitations need to be created in this process, which is generally referred to as multiphonon relaxation (MPR).

Most theoretical treatments of MPR are based on the time-dependent perturbation theory, where the relaxation rate is expressed in terms of the appropriate time correlation function. A fully quantum mechanical evaluation of this time correlation function is a daunting task that is achievable only for highly simplified models, such as the harmonic bath model. The latter model would be appropriate for treating radiationless decay in a low-temperature solid, but is inadequate for problems involving liquid hosts.^{4–6} Given the extreme difficulty of calculating quantum time correlation functions in liquids, a common approach is to obtain the relaxation rates from mixed quantum–classical simulations, where the two discrete states of the impurity are treated quantum mechanically, while the solvent degrees of freedom are treated classically.^{7,8} In our recent

work,^{9,10} we have highlighted the problems associated with such mixed treatment by considering an exactly solvable model Hamiltonian. It was shown that for large energy gaps of the impurity, that are typical for the electronic energy relaxation, the rates obtained within the mixed quantum–classical treatment can differ by several orders of magnitude from the exact quantum results.^{9,10}

The mixed quantum–classical approximation was also discussed in the context of vibrational energy relaxation,^{11,12} and vibronic absorption spectra.^{13,14} For the vibrational energy relaxation it was found that in certain cases the mixed quantum–classical approximation can underestimate the vibrational relaxation rate by several orders of magnitude.^{11,12} One important difference between the treatments of electronic and vibrational energy relaxation processes concerns the model Hamiltonian for the solute itself. In the former case, due to the large electronic energy gaps, it is usually sufficient to consider only two states of the impurity (ground and excited), while in the latter case the whole vibrational manifold can be involved in the process. It is straightforward to formulate the problem of vibrational energy relaxation *fully classically*, *provided* one calculates the overall energy relaxation rate for the whole vibrational manifold of the solute, rather than state-to-state transition rates. In fact, it has been found that such a fully classical treatment provides consistently more accurate results for overall vibrational relaxation rates compared to the mixed quantum–classical approach.^{11,12}

In view of the above finding, we became interested in performing a fully classical treatment of the electronic relaxation problem. Since a typical model for the electronic relaxation involves two discrete solute electronic states (with two distinct solvent PES associated with them), it is more difficult to formulate a fully classical treatment of this model than in the vibrational relaxation case. One possibility is to employ the method of Meyer and Miller,^{15–17} which provides a classical analogue for a system involving discrete quantum states. To study the classical limit of the nonradiative electronic relaxation we will treat the electronic degrees of freedom and the bath degrees of freedom in the Meyer–Miller Hamiltonian classically.

The most convenient way to obtain the rate in this approach is to use the reactive–flux method,^{18–22} which was generalized

[†] Permanent address: School of Chemistry, The Sackler Faculty of Science, Tel Aviv University, Tel Aviv 69978, Israel.

[‡] Present address: Theoretical Chemistry Institute and Department of Chemistry, University of Wisconsin, Madison, WI 53706.

[§] Permanent address: Department of Chemistry, University of Virginia, McCormick Road, Charlottesville, VA 22901.

to the quantum mechanical case by Miller, Schwartz, and Tromp.²³ This approach has recently been applied to the unbiased spin-boson problem by Miller and coworkers.^{24,25} As will become clear in the next Section, our Hamiltonian is more general, but the model we employ is still exactly solvable quantum mechanically (within the lowest order perturbation theory), which will allow us to compare the fully quantum and fully classical results for the electronic relaxation rates. Since the quantum mechanical rates are obtained within the lowest order perturbation theory while the fully classical rates are obtained from the non-perturbative reactive flux approach, we limit the magnitude of the nonadiabatic coupling terms to the range where the Fermi golden rule is valid.

We consider two routes for computing the classical limit of the electronic relaxation rates. In both cases the propagation of all degrees of freedom is done classically. The two classical limits differ with respect to choice of the mapping of the quantum mechanical operators that appear in the reactive flux formalism. In the fully classical approximation we follow the quasi-classical mapping and sampling of initial conditions,¹⁵ while in the other approach we perform a Wigner-Weyl^{26,27} transform of the relevant operators. In semiclassical language, the latter approach is often referred to as the Wigner phase space method,²⁸ or the linearized semiclassical initial value representation (linearized SC-IVR or LSC-IVR).²⁹

The organization of the paper is as follows: in Section II we introduce our model Hamiltonian and provide a summary of the quantum mechanical reactive flux method.²³ In Section III we describe the mapping of the discrete model Hamiltonian onto the continuous Meyer-Miller form.^{15,17} We also outline the details of the implementation of the LSC-IVR and the fully classical approximation to the reactive flux formalism. The results of our calculations using this formalism are given in Section IV, where the classical electronic relaxation rates are compared with the exact quantum rates. In Section V we conclude.

II. Model Hamiltonian and Nonradiative Relaxation Rate

The model Hamiltonian used in this work is identical to the one we used in our previous study of mixed quantum-classical approximations to nonadiabatic electronic relaxation.⁹ We consider an impurity embedded in a condensed phase environment, which we model as a harmonic bath. The impurity has two relevant quantum levels which we label as $|0\rangle$ and $|1\rangle$ for the ground and excited states with energies E_0 and E_1 , respectively. The most convenient, yet completely general, form of the Hamiltonian is given by⁹

$$H = (H_b + \Delta + E_0)|0\rangle\langle 0| + (H_b + E_1)|1\rangle\langle 1| + V_{01}|0\rangle\langle 1| + V_{10}|1\rangle\langle 0| \quad (1)$$

where H_b is the bath Hamiltonian which we take to be a sum over harmonic mass-weighted normal modes Q_α with frequencies ω_α and conjugate momenta P_α :

$$H_b = \frac{1}{2} \sum_{\alpha} (P_{\alpha}^2 + \omega_{\alpha}^2 Q_{\alpha}^2) \quad (2)$$

The diagonal coupling term, Δ , is taken to be a quadratic function of the bath degrees of freedom³⁰⁻³²

$$\Delta = \sum_{\alpha} \omega_{\alpha}^2 \delta_{\alpha} Q_{\alpha} + \frac{1}{2} \sum_{\alpha} \omega_{\alpha}^2 \delta_{\alpha}^2 + \sum_{\alpha\alpha'} g_{\alpha\alpha'} Q_{\alpha} Q_{\alpha'} \quad (3)$$

This form of diagonal coupling would arise when the two potential energy surfaces corresponding to the two electronic states can be described by two multidimensional harmonic surfaces with different equilibrium positions and different frequencies with the additional possibility of mode mixing between the two states. It reduces to the form used by Miller and coworkers^{24,25} when Δ is taken to be a linear function of the bath modes and E_0 is taken to be equal to E_1 . The procedure of obtaining the coupling constant δ_{α} and $g_{\alpha\alpha'}$ was described in our recent work.⁹

For simplicity we limit the discussion here to the static-coupling (crude Born-Oppenheimer) approach in which the off-diagonal coupling matrix elements, V_{01} and V_{10} , are taken to be real constants, i.e., they are independent of the bath degrees of freedom,⁹ $V_{01} = V_{10} = V_c$. In our previous work we have also considered a more general form of the off-diagonal coupling matrix elements.⁹

As mentioned in the Introduction, we obtain the nonradiative relaxation rate using the reactive flux formalism.¹⁸⁻²¹ The quantum mechanical rate is given in terms of the time integral over the symmetrized flux-flux correlation function²³

$$k_{0 \rightarrow 1} = \frac{1}{Z_r} \int_0^{\infty} dt C_f(t) \quad (4)$$

where Z_r is the partition function of the reactants, and the flux-flux correlation function is given by

$$C_f(t) = \text{Tr} F_{\beta} F(t) \quad (5)$$

In the above, F_{β} is the Boltzmannized flux operator ($\beta = 1/k_B T$ is the inverse temperature)

$$F_{\beta} = e^{-\beta H/2} F e^{-\beta H/2} \quad (6)$$

and the symmetrized flux operator, F , can be expressed in terms of a commutator between the Hamiltonian (H) and a projection operator on the products ($P_0 = |0\rangle\langle 0|$)²³

$$F = \frac{i}{\hbar} [H, P_0] = \frac{i}{\hbar} (V_{10}|1\rangle\langle 0| - V_{01}|0\rangle\langle 1|) \quad (7)$$

The fully quantum mechanical calculation of the flux-flux time correlation function is not feasible for most many-body systems. Recently, Miller and coworkers^{24,25,29,33} have introduced a semiclassical method based on a linear approximation to the Van Vleck propagator.^{34,35} In the following section we will provide a brief description of their semiclassical method and make the connection to our model.

III. The Classical Approximation

A. Meyer-Miller Hamiltonian. To obtain a consistent classical description of the nonradiative relaxation rate we need to represent the Hamiltonian in eq 1 with a set of continuous degrees of freedom. One convenient approach to reduce the discrete representation of the Hamiltonian to a continuous one is based on the early work of Meyer and Miller (sometimes referred to as the Meyer-Miller Hamiltonian).¹⁵ Recently, Stock and Thoss¹⁷ have shown that the Meyer-Miller Hamiltonian can be obtained by extending the formulation due to Schwinger. In their derivation, the mapping relation between the basis set and the harmonic oscillator creation and annihilation operators, a_n and a_m^{\dagger} , with commutation relations $[a_n, a_m^{\dagger}] = \delta_{nm}$, is given by

$$|n\rangle\langle m| \rightarrow a_n^\dagger a_m \quad (8)$$

Using the identity $|0\rangle\langle 0| + |1\rangle\langle 1| = 1$ along with the above specified map (cf. eq 8), the Hamiltonian in the continuous representation reads

$$H = E_0 a_0^\dagger a_0 + E_1 a_1^\dagger a_1 + H_b + \Delta a_0^\dagger a_0 + V_{01} a_0^\dagger a_1 + V_{10} a_1^\dagger a_0 \quad (9)$$

with H_b and Δ given by eqs 2 and 3, respectively. Introducing the position

$$q_n = \frac{1}{\sqrt{2}}(a_n^\dagger + a_n)$$

and momentum

$$p_n = \frac{i}{\sqrt{2}}(a_n^\dagger - a_n)$$

operators, the corresponding Hamiltonian takes the form

$$H = \frac{1}{4}\hbar\omega_{el}(p_1^2 + q_1^2 - 1) - \frac{1}{4}\hbar\omega_{el}(p_0^2 + q_0^2 - 1) + H_b + \frac{1}{2}\Delta(p_0^2 + q_0^2 - 1) + \frac{1}{2}(V_{01} + V_{10})(q_0 q_1 + p_0 p_1) \quad (10)$$

where $\hbar\omega_{el} = E_1 - E_0$, and we have set the zero of energy to be halfway between the two states. The fully quantum mechanical dynamics generated by the Hamiltonian in eq 10 is exactly the same as those generated by the Hamiltonian in eq 1. The advantage of eq 10 is that it can be used as a starting point for a rigorous classical as well as semiclassical approximations.

B. Classical Nonradiative Relaxation Rate. We discuss two classical approximations to the electronic relaxation rates. The first is based on a linearized approximation to the SC-IVR propagator³⁶⁻⁴³ introduced by Miller and coworkers,²⁹ which is referred to as the linearized SC-IVR approach (LSC-IVR). In many ways this approach is identical to the Wigner phase space method due to Heller.²⁸ It is not a pure classical limit in the sense that the relevant operators are replaced with the corresponding Wigner–Weyl transforms.^{26,27} However, both the electronic and the bath degrees of freedom are propagated classically in this approach, i.e., $q_n(t)$, $p_n(t)$, $Q_\alpha(t)$, and $P_\alpha(t)$ are classical dynamic variables. The LSC-IVR flux–flux correlation function is given by²⁹

$$C_f(t) = \frac{1}{(2\pi\hbar)^f} \int d\mathbf{q} d\mathbf{p} d\mathbf{Q} d\mathbf{P} F_{w\beta}(\mathbf{q}, \mathbf{p}, \mathbf{Q}, \mathbf{P}) F_w(\mathbf{q}(t), \mathbf{p}(t)) \quad (11)$$

where \mathbf{q} and \mathbf{p} label the electronic phase space variables, \mathbf{Q} and \mathbf{P} label the bath phase space variables, and f is the total number of degrees of freedom. We approximate F_β in eq 6 by $F_\beta = Fe^{-\beta H_b}$ which is equivalent to neglecting the diagonal coupling term, Δ , for the initial distribution,²⁵ an approximation not always justified. The Wigner–Weyl form of F_β is then given by

$$F_{\beta}^w(\mathbf{q}, \mathbf{p}, \mathbf{Q}, \mathbf{P}) = F^w(\mathbf{q}, \mathbf{p}) \rho_{\beta}^w(\mathbf{Q}, \mathbf{P}) \quad (12)$$

where

$$F^w(\mathbf{q}, \mathbf{p}) = 16V_c(p_1 q_0 - p_0 q_1) e^{-(q_0^2 + p_0^2 + q_1^2 + p_1^2)} \quad (13)$$

and

$$\rho_b^w(\mathbf{Q}, \mathbf{P}) = \prod_{\alpha} \frac{1}{\cosh(\beta \hbar \omega_{\alpha}/2)} \exp \left\{ -\frac{2 \tanh(\beta \hbar \omega_{\alpha}/2)}{\hbar \omega_{\alpha}} \left[\frac{P_{\alpha}^2}{2} + \frac{\omega_{\alpha}^2 Q_{\alpha}^2}{2} \right] \right\} \quad (14)$$

In the other classical approach, the Wigner–Weyl form of the operators is replaced with the purely classical form, and the quantum mechanical partition function, Z_r , needed to obtain the electronic relaxation rate is also replaced with its classical counterpart. The flux–flux correlation function is obtained in a similar way to the LSC-IVR with

$$F^w(\mathbf{q}, \mathbf{p}) = V_c(p_1 q_0 - p_0 q_1) \quad (15)$$

and ρ_b^w is replaced by the classical distribution function, i.e., by taking the limit $\hbar \rightarrow 0$ in eq 14.

One technical point we would like to make before we discuss the results is related to the sampling of the initial distribution of the electronic degrees of freedom. In the LSC-IVR, the Wigner form of the Boltzmannized flux operator suggests a Gaussian sampling of the electronic phase space variables, according to eq 13, and each trajectory carries a weight of $p_1 q_0 - p_0 q_1$. On the other hand, the classical form of the flux operator is given only in terms of the weight $p_1 q_0 - p_0 q_1$. Thus, in the fully classical approach we adopt the quasiclassical prescription,¹⁵ where the population of the two states ($N_n = (q_n^2 + p_n^2 - 1)/2$) is sampled randomly in the interval 0–1 such that the total population is unity, and the conjugate angle, $\phi_n = \tan^{-1}(-p_n/q_n)$, is sampled randomly between the interval 0– 2π . As before, each trajectory carries a weight of $p_1 q_0 - p_0 q_1$.

IV. Results

To demonstrate the limitations of the classical approximations we consider a simple model studied by Stock and Thoss,¹⁷ which is the well known spin–boson model⁴⁴ with only one vibrational mode. Specifically, the model consists of two coupled electronic states with a Hamiltonian $H_{sb} = (Q^2 + P^2)/20 + (q_1^2 + p_1^2)/2 + (p_0 p_1 + q_0 q_1)/5 + Q(q_0^2 + p_0^2 - q_1^2 - p_1^2)/40$. In Figure 1 we show the time dependence of the ground state population. The full-blown SC-IVR for this model is in very good agreement with the fully quantum mechanical result (not shown).¹⁷ It captures both the period of the oscillations as well as the dephasing and rephasing of the ground state population. The LSC-IVR and the classical approximation are in good agreement with the SC-IVR for short times; however, they fail to capture the rephasing of the ground state population.¹⁷ The LSC-IVR does a somewhat better job compared to the classical approximation. We note that in the classical approximation shown, we have used a Wigner form for the initial distribution, i.e., the electronic and nuclear degrees of freedom were sampled from a Wigner distribution. However, the Wigner–Weyl transform of the population operator was employed only for the LSC-IVR approach and not for the classical approximation. To be more specific, the classical ground state population was given by

$$P_{\text{classical}} = \frac{1}{2}(q_0^2 + p_0^2 - 1) \quad (16)$$

and in the LSC-IVR the ground state population was given by

$$P_{\text{LSC-IVR}} = 8(q_0^2 + p_0^2 - 1/2) e^{q_0^2 + p_0^2 + q_1^2 + p_1^2} \quad (17)$$

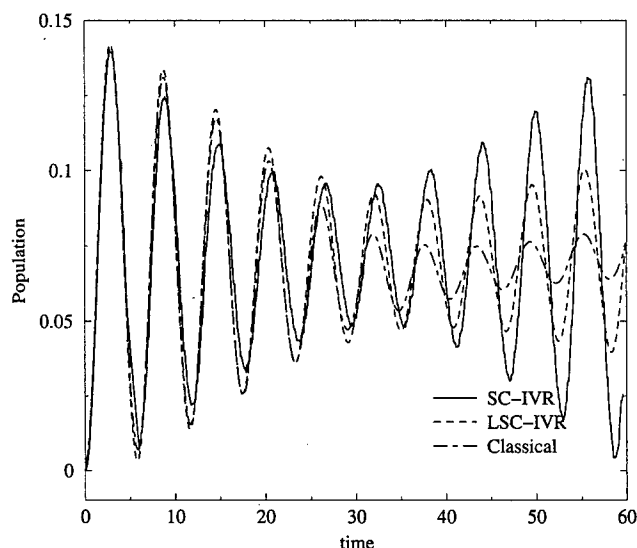


Figure 1. Plot of the time dependence of the ground state population for a spin-boson model with only one vibrational mode. The solid, dashed, and dashed-dotted lines are the SC-IVR, LSC-IVR, and classical approximations, respectively. The SC-IVR is in very good agreement with the fully quantum mechanical result (not shown).

The lesson to be learned from the above model is that the LSC-IVR and the classical approximation are reliable only for relatively short times, and they fail to capture the rephasing phenomena.³³ Moreover, the Wigner–Weyl transform of the relevant operators improves the agreement at long times, but is still not sufficient to capture the full SC-IVR rephasing. Thus, the success of these classical approximations in condensed phase systems depends mainly on the time scale of the decay of the correlation function associated with the relevant observable. In the case that the correlation function decays on a short time scale, and rephasing is not important, they are expected to provide reasonable results.^{24,25} Such a situation is likely to occur in condensed phase problems.

In view of the above, we have performed a test of the classical and LSC-IVR approaches for a non-trivial many-body problem defined by the Hamiltonian given in eq 10. The above model is completely specified by the two spectral densities— $J_0(\omega)$ and $J_1(\omega)$ —corresponding to the ground and excited states of the impurity, respectively. The procedure for obtaining the coefficients δ_α and $g_{\alpha\alpha'}$ in eq 3 from these spectral densities is outlined in ref 9. Since we are primarily interested in the electronic nonradiative relaxation processes characterized by large energy gaps, we assume that the dominant contribution to the relaxation rate comes from the high-frequency optical phonons. In order to model the corresponding spectral density, we have chosen a Gaussian form centered at ω_{op} with the width parameter σ and the normalization constant λ^{30}

$$J_{0,1}(\omega) = \frac{\lambda_{0,1}}{(2\pi\sigma^2)^{1/2}} \exp[-(\omega - \omega_{op}^{0,1})^2/2\sigma^2] \quad (18)$$

where the labels 0 and 1 refer to the ground and excited state of the impurity, respectively. Since optical phonons are characterized by a narrow dispersion, we have limited ourselves to the case $\sigma/\omega_{op}^{0,1} \ll 1$ (from now on we employ atomic units), which, in addition, allows us to avoid the nonphysical contributions arising from the tail of the Gaussian function extending to negative frequencies. Specifically, we have chosen the following values of the parameters: $\sigma = 0.1$, $\omega_{op}^0 = 1.1$, $\omega_{op}^1 = 1.0$, $\lambda_0 = 0.05$, and $\lambda_1 = 0.125$. With the above spectral densities,

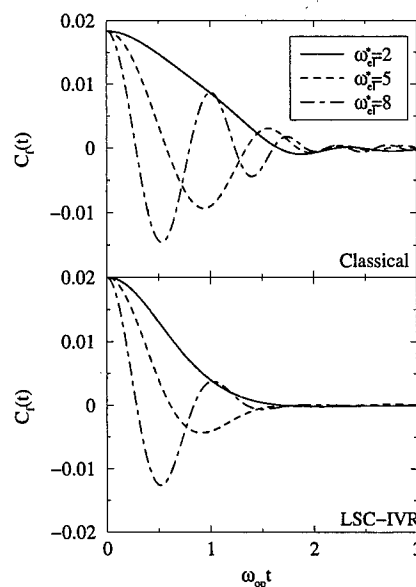


Figure 2. Plots of the flux–flux correlation function for the LSC-IVR (lower panel) and the classical approximation (upper panel) versus time. Note that as the electronic gap increases, the flux–flux correlation function becomes oscillatory, reflecting the recrossing of the dividing surface.

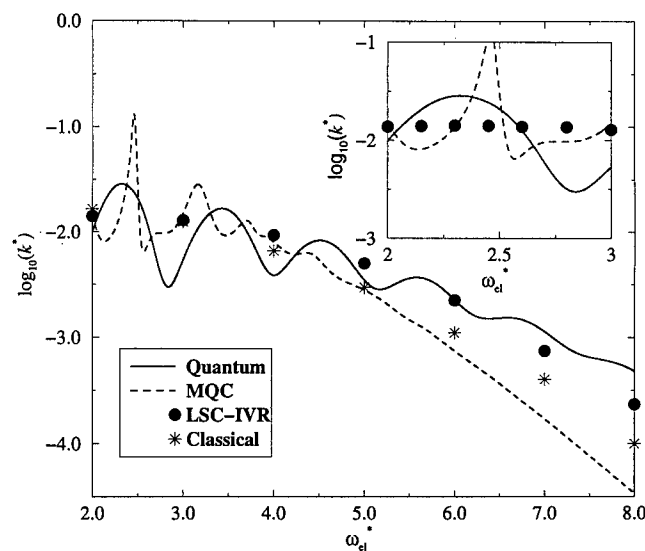


Figure 3. Semilog plot of the electronic relaxation rate as a function of the reduced electronic gap. The fully quantum mechanical (solid line) and the mixed quantum–classical (dashed line) results were obtained using the Fermi golden rule. The LSC-IVR (●) and the fully classical (*) results were obtained using the reactive flux formalism. The LSC-IVR provides the best overall agreement, but fails to reproduce the oscillation (see the inset).

we have calculated the flux–flux correlation function using the LSC-IVR method and the classical approach, as discussed in the previous section. The results of our calculations are shown in Figure 2 for three values of the dimensionless electronic energy gap $\omega_{el}^* = \omega_{el}/\omega_{op}$. One sees that with increasing energy gap the flux–flux correlation function in both methods becomes more oscillatory and is therefore likely to become less accurate. Note also that for a given energy gap the oscillations are less pronounced in the LSC-IVR result compared to the fully classical method.

The results for the electronic relaxation rates are shown in Figure 3 on a semilog plot versus the dimensionless electronic energy gap. Also shown are the fully quantum mechanical and mixed quantum–classical (the so called dynamic classical limit

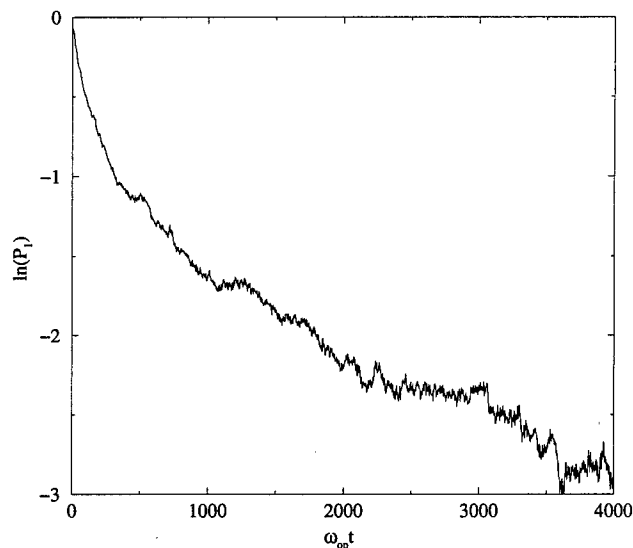


Figure 4. Semilog plot of the time dependence of the excited state population ($P_1(t) = 1/2(q_1^2 + p_1^2 - 1)$) for the classical approximation. The LSC-IVR is identical to the classical result within the noise level of the computation, and thus is not shown.

(DCL) which was described in detail in ref 9) results, both obtained within the low order perturbation theory.⁹ One sees that for small electronic energy gaps the LSC-IVR approach does not capture the oscillations present in the quantum result, which is reminiscent of the static classical method.⁴⁵ These oscillations are absent even when the Wigner–Weyl transform of the flux operator is used (LSC-IVR). Thus, it is the classical treatment of the *dynamics* of the electronic degrees of freedom which fails to reproduce the resonances.³³

For large energy gaps, the performance of the classical methods is better compared to the mixed quantum–classical approximation, similar to the situation for vibrational energy relaxation.^{11,12} The LSC-IVR provides the best overall agreement among the approximations considered in this work. We would like to emphasize that going from the classical to LSC-IVR treatment involves the Wigner–Weyl transform not only of the initial distribution, but also of the flux operators, and the transformation of the flux operator turns out to be important for the calculation of the electronic relaxation rate.

An alternative approach to obtain the electronic relaxation rates is based on a nonequilibrium approach, where the system is initiated in the excited state, and the rate is obtained from the long time decay of the excited state population. The fully quantum mechanical rate obtained using this approach should be in agreement with the rate obtained via the fully quantum mechanical reactive flux formalism. The strength of the reactive flux approach is that the rate is obtained from relatively short time information, while the approach based on the time dependent population requires a consideration of much longer times. As we have shown, the classical limit of the reactive flux approach is a good approximation of the quantum result. It might be thought that one could equally well determine the rate by using the Meyer–Miller dynamics to generate the long time decay of the population. Unfortunately, this is not the case, as is illustrated in Figure 4, where we show a semilog plot of the classical excited state population for an inverse temperature $\beta = 2$. From the long decay of the excited state population one would determine a rate constant much smaller than that found from the reactive flux approach. The reason for this is that the classical approach presented in this work was derived from a

semiclassical approximation, which is known to deviate from the exact quantum dynamics at long times.

V. Conclusions

Motivated by recent work on vibrational energy relaxation in condensed phases, which has shown that a fully classical treatment of the problem is superior to the mixed quantum–classical approach,^{11,12} we have performed a fully classical calculation of the electronic energy relaxation rates. We have employed the reactive flux formalism combined with the method of mapping of discrete quantum degrees of freedom onto the classical ones proposed two decades ago by Meyer and Miller¹⁵ and recently modified by Stock and Thoss.¹⁷ We have considered two implementations of the method: a fully classical approximation and a linearized semiclassical initial value representation, that involves a Wigner–Weyl transform of the initial distribution and the flux operator.

In calculating the electronic relaxation rates for an impurity coupled to a condensed phase environment, we have employed a model studied previously by us,⁹ where an impurity is represented by a two-level system, and all the nuclear (bath) degrees of freedom are treated in the harmonic approximation. In the earlier study of this model, we have treated it both quantum mechanically and in the mixed quantum–classical approximation. The results of the present work have demonstrated that, similarly to the case of vibrational relaxation, a fully classical treatment produces better agreement with the fully quantum mechanical rates than the mixed quantum–classical approach. Furthermore, the rates obtained within LSC-IVR method are closer to the exact quantum rates than the fully classical results. However, the LSC-IVR approach requires performing Wigner–Weyl transformations which are difficult to obtain for a general system, and even for the present application several approximation were introduced. In addition, both classical methods performed rather poorly for small electronic energy gaps, where they failed to reproduce the resonances present in the exact quantum rates.

In more general terms, one can mention the following feature that makes a fully classical approach more robust compared to the mixed quantum–classical approximation. Namely, the time propagation of the classical degrees of freedom in the fully classical approach is unique, while the mixed quantum–classical propagation approach suffers from nonuniqueness,^{9,10} i.e., there is freedom in the choice of the Hamiltonian used to propagate the classical degrees of freedom in the mixed quantum classical approach. This nonuniqueness can be actually turned into an advantage: one can improve the results of mixed quantum–classical treatment by choosing the optimal propagation scheme. However, the criteria for choosing the optimal propagation scheme must be established for a general system where the bath is not taken in the harmonic approximation.

Both the classical treatment and the mixed quantum classical approximation lend themselves to a systematic improvement, that would involve going from classical to a full-blown semiclassical approximation for the degrees of freedom that were treated classically. It seems to be imperative to use the fully SC-IVR in order to reproduce the resonances mentioned earlier. However, the latter approach is not yet practical for the many-body system.^{46,47}

Finally, we can draw one more conclusion from the present study, namely, that it is always advantageous to employ the framework where the required time-correlation functions are characterized by a fast decay. We have illustrated this point by showing that the classical results obtained from the flux–flux

correlation function were far superior to those obtained from the analysis of the population decay.

Acknowledgment. This work was supported by a grant to B.J.B. from the National Science Foundation.

References and Notes

- (1) Englman, R. *Non-Radiative Decay of Ions and Molecules in Solids*; North Holland: Amsterdam, The Netherlands, 1979.
- (2) Fong, F. K., Ed. *Radiationless Processes in Molecules and Condensed Phases*; Springer: Berlin, 1976.
- (3) Lin, S. H., Ed.; *Radiationless Transitions*; Academic: New York, 1980.
- (4) Neria, E.; Nitzan, A. *J. Chem. Phys.* **1993**, *99*, 1109.
- (5) Staib, A.; Borgis, D. *J. Chem. Phys.* **1995**, *103*, 2642.
- (6) Prezhdo, O. V.; Rossky, P. J. *J. Phys. Chem.* **1996**, *100*, 17094.
- (7) Tully, J. C. *J. Chem. Phys.* **1990**, *93*, 1061.
- (8) Webster, F. J.; Schnitker, J.; Friedrichs, M. S.; Friesner, R. A.; Rossky, P. J. *Phys. Rev. Lett.* **1991**, *66*, 3172.
- (9) Egorov, S. A.; Rabani, E.; Berne, B. J. *J. Chem. Phys.* **1999**, *110*, 5238.
- (10) Egorov, S. A.; Rabani, E.; Berne, B. J. Submitted to *J. Phys. Chem.*, 1999.
- (11) Bader, J. S.; Berne, B. J. *J. Chem. Phys.* **1994**, *100*, 8359.
- (12) Egorov, S. A.; Berne, B. J. *J. Chem. Phys.* **1997**, *107*, 6050.
- (13) Egorov, S. A.; Rabani, E.; Berne, B. J. *J. Chem. Phys.* **1998**, *108*, 1407.
- (14) Rabani, E.; Egorov, S. A.; Berne, B. J. *J. Chem. Phys.* **1998**, *109*, 6376.
- (15) Meyer, H. D.; Miller, W. H. *J. Chem. Phys.* **1979**, *70*, 3214.
- (16) Sun, X.; Miller, W. H. *J. Chem. Phys.* **1997**, *106*, 6346.
- (17) Stock, G.; Thoss, M. *Phys. Rev. Lett.* **1997**, *78*, 578.
- (18) Anderson, J. B. *J. Chem. Phys.* **1973**, *58*, 4684.
- (19) Bennett, C. H. *Molecular Dynamics and Transition State Theory: The Simulation of Infrequent Events*. In *Algorithms for Chemical Computations*; Christofferson, R. E., Ed.; American Chemical Society: Washington, DC, 1977.
- (20) Chandler, D. *J. Chem. Phys.* **1978**, *68*, 2959.
- (21) Montgomery, J. A., Jr.; Chandler, D.; Berne, B. J. *J. Chem. Phys.* **1979**, *70*, 4056.
- (22) Berne, B. J. *Molecular Dynamics and Monte Carlo Simulation of Rare Events*. In *Multiple Time Scales*; Brackbill, J. U., Cohen, B. I., Eds.; Academic Press: New York, 1985.
- (23) Miller, W. H.; Schwartz, S. D.; Tromp, J. W. *J. Chem. Phys.* **1983**, *79*, 4889.
- (24) Sun, X.; Wang, H. B.; Miller, W. H. *J. Chem. Phys.* **1998**, *109*, 7064.
- (25) Wang, H.; Song, X. Y.; Chandler, D.; Miller, W. H. *J. Chem. Phys.* **1999**, *110*, 4828.
- (26) Weyl, H. Z. *Phys.* **1927**, *46*, 1.
- (27) Wigner, E. *Phys. Rev.* **1932**, *40*, 749.
- (28) Heller, E. J. *J. Chem. Phys.* **1976**, *65*, 1289.
- (29) Wang, H.; Sun, X.; Miller, W. H. *J. Chem. Phys.* **1998**, *108*, 9726.
- (30) Weissman, Y.; Nitzan, A.; Jortner, J. *J. Chem. Phys.* **1977**, *26*, 413.
- (31) Tang, J. *J. Chem. Phys.* **1994**, *188*, 143.
- (32) Tang, J. *J. Chem. Phys. Lett.* **1994**, *227*, 170.
- (33) Sun, X.; Wang, H. B.; Miller, W. H. *J. Chem. Phys.* **1998**, *109*, 4190.
- (34) Van Vleck, J. H. *Proc. Natl. Acad. Sci. U.S.A.* **1928**, *14*, 178.
- (35) Gutzwiller, M. C. *J. Math. Phys.* **1967**, *8*, 1979.
- (36) Miller, W. H. *J. Chem. Phys.* **1970**, *53*, 3578.
- (37) Miller, W. H. *J. Chem. Phys.* **1991**, *95*, 9428.
- (38) Herman, M. F.; Kluk, E. *J. Chem. Phys.* **1984**, *91*, 27.
- (39) Heller, E. J. *Phys. Rev. Lett.* **1991**, *67*, 664.
- (40) Heller, E. J. *J. Chem. Phys.* **1991**, *94*, 2723.
- (41) Kay, K. G. *J. Chem. Phys.* **1994**, *100*, 4377.
- (42) Kay, K. G. *J. Chem. Phys.* **1994**, *100*, 4432.
- (43) Provost, D.; Brumer, P. *Phys. Rev. Lett.* **1995**, *74*, 250.
- (44) Leggett, A. J.; Chakravarty, S.; Dorsey, A. T.; Fisher, M.; Garg, A.; Zwirger, W. *Rev. Mod. Phys.* **1987**, *59*, 1.
- (45) Lax, M. *J. Chem. Phys.* **1952**, *20*, 1752.
- (46) Makri, N.; Thompson, K. *J. Chem. Phys. Lett.* **1998**, *291*, 101.
- (47) Thompson, K.; Makri, N. *J. Chem. Phys.* **1999**, *110*, 1343.

Toward an ab Initio Treatment of the Time-Dependent Schrödinger Equation of Molecular Systems

Yngve Öhrn* and Erik Deumens

Quantum Theory Project, Departments of Chemistry and Physics, University of Florida,
Gainesville, Florida 32611-8435

Received: July 15, 1999; In Final Form: August 27, 1999

The time-dependent variational principle (TDVP) is employed to produce equations of motion that approximate the time-dependent Schrödinger equation. Choices of wave function and basis sets are discussed. The use of electron translation factors and the electronic and nuclear parts of the molecular wavefunction are put in the context of the electron nuclear dynamics (END) theory. The role of wave function parameters as dynamical variables is discussed, and the use of coherent state parametrization is explored.

1. Introduction

Application of the time-dependent Schrödinger equation as is done for instance in the theory of molecular reaction dynamics has traditionally sought a description of molecular events in terms of a basis of stationary molecular electronic states and their associated potential energy surfaces. This approach often leads to attractive pictures and seeks an understanding of microscopic processes in terms of the properties of potential energy surfaces. Such descriptions of e.g. elementary chemical reactions in terms of preconstructed potential energy surfaces are omnipresent in molecular reaction dynamics. An example is the popular and widely applied transition state theory. In general, when one or more potential energy surfaces of acceptable accuracy together with the nonadiabatic coupling terms are known, the nuclear dynamics can be done classically, semiclassically, or quantum mechanically.

In spite of the many successes, this approach is undoubtedly being hindered by the lack of generally available accurate potential energy surfaces and the associated nonadiabatic coupling terms. Ab initio electronic structure theory, which generates the "best" potential energy surfaces, solves the electronic Schrödinger equation for stationary nuclei in a large number of discrete points and can similarly generate nonadiabatic coupling terms. Application of this data in molecular reaction dynamics requires some interpolation (often in many dimensions), a far from trivial task, when accurate energy values and gradients are required. The difficulties in generating full, accurate, ab initio, potential energy surfaces for general polyatomic systems have caused many dynamics treatments to rely on semiempirical surfaces, such as those obtained via the method of diatomics in molecules (DIM).

In recent years, a new set of dynamics methods have appeared that proceed without precalculated potential energy surfaces. These methods use one of three approaches: (1) the potential energy surface and its gradient is calculated on demand using conventional electronic structure methods such as self-consistent field (SCF) or Kohn–Sham density functional theory (DFT); or (2) a dynamical system in parallel with the nuclear dynamics is set up for artificial electronic degrees of freedom such that the parallel dynamics produces the state and gradient that is

the same as or close to what the electronic structure methods would produce for the same geometry; or (3) a coupled dynamical system involving both the nuclear and the physical electronic degrees of freedom is constructed and solved. The first approach is now available in almost all electronic structure software. The method of Car and Parinello¹ is an implementation of the second approach and has received some notoriety in the current literature. The electron–nuclear dynamics (END) theory, which is discussed here, follows the third approach. END uses a basis different from that of stationary electronic states for solution of the dynamical equations but routinely employs stationary electronic states in the analysis of the evolving state. Even the END dynamics often follows closely one potential energy surface. This is particularly true at very low collision energies and for part of the dynamics where the stationary electronic states are well separated. In this way, END provides support for using the Born–Oppenheimer approximation in such processes. When admixtures of other states are required, the END automatically provides the correct couplings through the dynamical equations.

END is a general approach to find approximate solutions to the time-dependent Schrödinger equation. It has been described in the literature in considerable detail.^{2,3} The END theory offers a hierarchy or natural progression of approximations from the simplest model of classical nuclei and a single determinantal representation of the electrons all the way to a full multiconfigurational quantum description of both electrons and nuclei.

Applications of the basic END approach have been made to a number of ion–atom and ion–molecule reactive collisions of small species in order to test the sensitivity to the choice of basis set and the overall performance in order to reach predictive accuracy. Proton collisions with atoms of hydrogen, helium, and oxygen,^{3–6} and α particles with Ne atoms,⁷ at energies ranging from a fraction of an eV to tens of keV (depending on the system) have been studied with calculated transition probabilities and cross sections for electron transfer and excitation in agreement with experimental results.

Ion–molecule reactive collisions have been studied with equally promising results. This includes proton collisions with H₂ molecules^{4,8} at energies that involve product channels of electron transfer and vibrational excitation, as well as total

* Corresponding author. E-mail: ohrn@qtp.ufl.edu. Fax: 352-392-8722.

breakup, with water molecules⁹ and with methane molecules.¹⁰ Also, H_2^+ collisions with hydrogen molecules have been studied.¹¹

Model systems exhibiting intramolecular electron transfer have been treated within the simplest END approach¹² with promising results. Also, the relationship between vibrational modes of positively charged polyacetylene oligomers and soliton dynamics of polyacetylene chains has been studied.¹³

2. Electron–Nuclear Dynamics Theory

The ideas behind electron–nuclear dynamics (END) are straightforward. The theory is discussed in great detail elsewhere.¹² However, the details of the discussion so far have been limited to the simplest model, which describes the electrons by a coherent state family of determinantal wave functions and uses classical nuclei. Therefore, there is room for an explanation of the generality of the END theory attempted here.

Both the power and the limitation of END lie in the choice of the family of wave functions employed in the time-dependent variational principle (TDVP).¹⁴ The correct choice permits the selection and emphasis of the important degrees of freedom for a given process, but any choice, of course, limits what can be achieved to that space of wave functions. Too much detail, e.g. a full representation on a grid, may lead to intractable computations, while too restrictive a choice, say classical nuclei, prohibits the description of some important aspects of the dynamics, such as multichannel dynamical branching. The flexibility of the END theory permits a balanced choice to be made for each problem studied.

The END for general reactions using a full quantum description is given in this section in a form that permits the identification of the more approximate implementation presented before as a special case.

Two rather basic observations for the choice of families of variational wave functions can be made based on experience: (1) The electronic wave function of a molecular system is approximated remarkably well by a single determinantal wave function, but the flexibility to use multiple configurations is essential. (2) The nuclei behave quite classically in many respects; however, for multichannel processes the molecular wave function must be capable of splitting into multiple packets in accordance with the superposition principle.

Our experience has shown that nonlinear families of wave functions, rather than those formed by linear superposition, often provide accurate results with greater efficiency versus effort. Although identical nuclei should be given wave functions of correct permutational symmetry, the discussion below will not treat the symmetry of the nuclei. Our own experience is that the numerical effects of nuclear permutation symmetry are often negligible and the notation becomes unduly cluttered. The expressions are easily adapted for such symmetry, when needed.

For a didactic presentation of a general framework for simultaneous dynamics of electrons and nuclei, the coordinates and the basis functions of choice could be different from those commonly used in other approaches. This does not mean that the particular choice used here is believed to perform better or worse in numerical computations, but rather that it clarifies the similarity and differences between nuclear and electronic degrees of freedom.

The symbol Ψ is used for molecular wave functions, Φ for electronic wave functions, Ξ for nuclear wave functions. A

molecular wave function is given in terms of the Born–Huang¹⁵ expansion

$$\Psi(X, x, c, f, d, e, z, R, P) = \sum_n c_n \Xi_n(X, f, d, R, P) \Phi_n(x, e, z, R, P) \quad (1)$$

where the various parameters are time-dependent and explained below.

Nuclear Wave Function. Each nuclear wave function in the above expansion represents all nuclei in the system and is a sum

$$\Xi_n(X, f, d, R, P) = \sum_{(\pi)} f_n(\pi) \prod_{l=1}^{N_{at}} \chi_{\pi(l)}(\vec{X}_l, d, \vec{R}_l, \vec{P}_l) \quad (2)$$

of products of orbitals

$$\chi_l(\vec{X}, d, \vec{R}, \vec{P}) = \sum_j d_{lj} X^{k_{lj}} Y^{m_{lj}} Z^{n_{lj}} \exp[-\alpha_{lj}(\vec{X} - \vec{R})^2 - i\vec{P} \cdot \vec{X}] \quad (3)$$

centered on average locations R with average momenta P . The index (π) stands for the set of indices π_l , $l = 1, \dots, N_{at}$ with N_{at} the number of atomic nuclei. This sum describes the correlation between the nuclei.

It is well-known that the major part of this correlation for any bound subsystem is described by vibrational eigenstates of normal-mode coordinates. For example, for a diatomic molecule in the vibrational groundstate with a sharp localization in orientation (θ, φ) , the wave function has the form

$$\begin{aligned} \exp[-\alpha(\vec{X}_{cm} - \vec{C})^2 - \beta(X_{rel} - D)^2] f(\theta, \varphi) = \\ \exp[-\alpha(\vec{X}_{cm} - \vec{C})^2 - \beta(\vec{X}_{rel} - \vec{D})^2] = \exp[-\gamma(\vec{X}_1 - \vec{R}_1)^2 - \\ \gamma(\vec{X}_2 - \vec{R}_2)^2 - \delta(\vec{X}_1 - \vec{R}_1) \cdot (\vec{X}_2 - \vec{R}_2)] = \\ \exp[-\gamma(\vec{X}_1 - \vec{R}_1)^2] \exp[-\gamma(\vec{X}_2 - \vec{R}_2)^2] \sum_n [-\delta(\vec{X}_1 - \vec{R}_1) \cdot \\ (\vec{X}_2 - \vec{R}_2)]^n / n! \quad (4) \end{aligned}$$

where in the second step the angular localization is given a Gaussian form, and where

$$\begin{aligned} \gamma = \alpha/4 + \beta, \quad \delta = \alpha/2 - \beta \\ \vec{C} = (\vec{R}_1 + \vec{R}_2)/2, \quad \vec{D} = \vec{R}_1 - \vec{R}_2 \quad (5) \end{aligned}$$

This shows the sum in terms of products of orbitals for nuclei. The correlation can be seen to need basis functions with high angular momentum components k , m , and n for eq 3 to converge.

Quantum mechanical treatments of nuclear dynamics on molecular potential energy surfaces often employ basis functions in internal coordinates that are carefully chosen to be close, but not identical, to normal modes so as to accelerate convergence. For example, the discrete variable representation (DVR) method typically selects from 6 to 12 discretization points in angular variables, which corresponds to a polynomial fit of the same order. This would in the above expansion correspond to basis functions with $k + m + n$ ranging from 6 to 12 or more, because the generic basis functions (eq 3) are not as optimal as is customary with internal variables for quantum molecular dynamics.

Electronic Wave Function. Each electronic wave function in the expansion (1) may be represented as a sum of determinants

$$\Phi_n(x, e, z, R, P) = \sum_{(\pi)} e_{n(\pi)} \det[\varphi_{\pi(h)}(\vec{x}_g, z, \vec{R}, \vec{P})] \quad (6)$$

built of orbitals

$$\varphi_h(\vec{x}, z, \vec{R}, \vec{P}) = \sum_p z_{ph} x^{k_{ph}} y^{m_{ph}} z^{n_{ph}} \exp[-\alpha(\vec{x} - \vec{R})^2] \quad (7)$$

centered on average nuclear positions R moving with the same average velocity P/M as the nuclei. The symbol (π) is a configuration label and runs over the list of configurations. The sum describes the correlation between electrons.

It is well-known that the best single determinant, constructed with the self-consistent field (SCF) method, provides a reasonable description for most systems. For computational efficiency we choose Gaussian type orbitals, but obviously it is possible to use other types of orbitals, even numerical representations on a grid, if that is needed and judged to be computationally feasible for the problem under consideration. It is not unusual in correlated electronic structure theory to use angular momentum basis functions through f and g types or higher and to use basis sets of so-called double-zeta, triple-zeta, or even better quality. The questions of the quality of basis set needed for END applications to reach converged results are largely still unanswered, but initial studies on systems with first-row elements seem to indicate that converged results are obtained with quite limited basis sets. Further studies are needed of the behavior of the calculated results as functions of increasing electronic basis.

Molecular Wave Function. In some general approach to determine a total molecular wave function, the coefficients d and c of the nuclear wave function could be determined to a good approximation, for instance, by finding the eigenstates in nuclear normal coordinates, while the coefficients e and z of the electronic wave function could be obtained by SCF plus any one of a number of well-proven correlated electronic structure methods. It must be emphasized that this is *not* what END does, as elaborated below.

The sum in the wave function equation (1) describes the correlation between the electrons and the nuclei. It is well-known that the Born–Oppenheimer (BO) approximation provides an excellent first term in the sum. In that case the electronic wave function is the eigenfunction with eigenvalue $V(X)$ of the electronic problem with the nuclei frozen at the geometry X . And the nuclear wave function is the vibrational–rotational eigenfunction of the nuclei moving on the molecular potential surface $V(X)$. Because of the overwhelming success of the BO approximation, most approaches to molecular dynamics include the construction of the potential energy surface to some acceptable level of accuracy.

Because it is technically not (yet) feasible to express the matrix elements of the nuclear Hamiltonian in the BO approximation directly in terms of the nuclear basis functions (eq 3) and the electronic basis functions (eq 7), all molecular dynamics methods proceed through fitting some analytic function to the potential energy surface. This is already starting to change, as shown by the popularity of gradient-driven molecular dynamics and Car–Parinello-like methods. These methods employ classical (Newtonian) dynamics of the nuclei but use gradients supplied directly by electronic structure methods rather than from analytic fitted forms as was still the norm only a decade ago.

Instead of the classical Born–Oppenheimer or adiabatic form of the wave function

$$\Psi(X, x, f, d, e, z, R, P) = \Xi(X, f, d, R, P) \Phi(x, e, z, X) \quad (8)$$

where the electronic wave function depends parametrically on

the nuclear dynamical variables X , END considers a sum (eq 1) of less tightly coupled products of nuclear and electronic wave functions where the BO approximation and potential energy surface are only defined for the average nuclear positions R and momenta P . This series bears some resemblance to the diabatic form of the Born–Huang expansion, which is known to be formally equivalent to the adiabatic or BO form and to be more rapidly converging near avoided crossings of surfaces.

Electron–Nuclear Dynamics. Because the goal is to study dynamics in a time-dependent method, it is not necessary to require the convergence of both the electronic and the nuclear wave functions in each molecular term separately. Rather, it is sufficient to consider convergence for the electron nuclear dynamics of the molecular system with a wave function expressed directly as a sum of basic configurations

$$\Psi(X, z, c, d, z, R, P) = \sum_{(\pi)} c_{(\pi)} \prod_{i=1}^{N_{\text{el}}} \chi_{\pi(i)}(\vec{X}_i, d, \vec{R}_i, \vec{P}_i) \times \det[\varphi_{\pi(h)}(\vec{x}_g, z, \vec{R}, \vec{P})] \quad (9)$$

where the symbol (π) now runs over all combined electron–nuclear configurations.

The coefficients c now describe the correlation among electrons (MCSCF), among the nuclei (normal-mode states), and between electrons and nuclei (Born–Oppenheimer states) and become (time-dependent) dynamical variables. Note that the entire wave function depends parametrically on the average nuclear positions R and momenta P . When the basis is complete, this is largely irrelevant as the average values can be computed from the wave function. It is a well-known technique for accelerating convergence of numerical solutions of differential equations, to make the basis-function placement part of the solution method. Examples are found in the placing of the electronic basis functions on the nuclear centers in electronic structure, or using carefully chosen internal coordinates in quantum molecular dynamics, or employing adaptive grid methods in fluid dynamics. By making the parameters R and P dynamical variables, the basis functions are made to follow the flow of the dynamics such that accurate solutions can be constructed with a more limited basis set.

Analogous to the classical mechanics, there is a quantum mechanical “Hamilton’s principle” or time-dependent variational principle (TDVP). The quantum mechanical action¹⁴ is defined to be

$$A = \int_{t_1}^{t_2} L(\Psi^*, \Psi) dt \quad (10)$$

where the quantum mechanical Lagrangian is

$$L(\Psi^*, \Psi) = \left\langle \Psi \left| i \frac{\partial}{\partial t} - H \right| \Psi \right\rangle / \langle \Psi | \Psi \rangle \quad (11)$$

and H is the quantum mechanical Hamiltonian of the system. The many-body wave function Ψ is subject to the boundary conditions

$$\delta |\Psi\rangle = \delta \langle \Psi| = 0 \quad (12)$$

at $t = t_1$ and t_2 . TDVP yields the time-dependent Schrödinger equation if Ψ is varied in the full Hilbert space. If, however, the variations are restricted to a predetermined region of Hilbert space, as it would be for a Ψ chosen to be of a specific form, then the Lagrangian will generate an approximate time evolution. The notation $\Psi \equiv \Psi(\xi) \equiv |\xi\rangle$ is introduced, with $\xi = \{\xi_1, \xi_2,$

..., $\xi_M\}$ being a (column) array of complex parameters $\xi_\alpha \equiv \xi_\alpha(t)$ depending on the time parameter t .

The variation principle states that

$$\delta A = \delta \int_{t_1}^{t_2} L dt = 0 \quad (13)$$

and using integration by parts and the boundary conditions (12), the surviving terms of δL can be written as

$$\frac{\langle \delta \xi | \dot{\xi} \rangle}{\langle \xi | \xi \rangle} - \frac{\langle \delta \xi | H \xi \rangle}{\langle \xi | \xi \rangle} - i \frac{\langle \delta \xi | \xi \rangle}{\langle \xi | \xi \rangle^2} \langle \xi | \dot{\xi} \rangle + \frac{\langle \delta \xi | \xi \rangle}{\langle \xi | \xi \rangle^2} \langle \xi | H \xi \rangle + \text{complex conjugate} \quad (14)$$

where the notation $d\xi/dt = \dot{\xi}$ is used.

In order to obtain the dynamical equations, the notations $S(\xi^*, \xi) = \langle \xi | \xi \rangle$ and $E(\xi^*, \xi) = \langle \xi | H \xi \rangle / \langle \xi | \xi \rangle$ are introduced, which lead to

$$\delta A = \int_{t_1}^{t_2} \left\{ \sum_{\beta} \left[-i \sum_{\alpha} \left(\frac{\partial^2 \ln S}{\partial \xi_{\alpha}^* \partial \xi_{\beta}} \dot{\xi}_{\alpha}^* - \frac{\partial E}{\partial \xi_{\beta}} \right) \delta \xi_{\beta} + i \sum_{\alpha} \left(\frac{\partial^2 \ln S}{\partial \xi_{\alpha} \partial \xi_{\beta}^*} \dot{\xi}_{\alpha} - \frac{\partial E}{\partial \xi_{\beta}^*} \right) \delta \xi_{\beta}^* \right] \right\} dt = 0 \quad (15)$$

and since $\delta \xi_{\beta}$ and $\delta \xi_{\beta}^*$ are independent variations one can write

$$i \sum_{\beta} C_{\alpha\beta} \dot{\xi}_{\beta} = \frac{\partial E}{\partial \xi_{\alpha}^*} \quad (16)$$

where the complex Hermitian matrix $\mathbf{C} = \{C_{\alpha\beta}\}$ with elements $C_{\alpha\beta} = \partial^2 \ln S / \partial \xi_{\alpha}^* \partial \xi_{\beta}$.

For two differentiable functions $f(\xi, \xi^*)$ and $g(\xi, \xi^*)$ the generalized Poisson bracket

$$\{f, g\} = -i \sum_{\alpha, \beta} \left[\frac{\partial f}{\partial \xi_{\alpha}} (\mathbf{C}^{-1})_{\alpha\beta} \frac{\partial g}{\partial \xi_{\beta}^*} - \frac{\partial g}{\partial \xi_{\alpha}} (\mathbf{C}^{-1})_{\alpha\beta} \frac{\partial f}{\partial \xi_{\beta}^*} \right] \quad (17)$$

is defined. It follows that $\dot{\xi} = \{\xi, E\}$ and $\dot{\xi}^* = \{\xi^*, E\}$, i.e., the time evolution of wave function parameters is governed by Hamilton-like equations.

The generalized phase space and the associated Poisson bracket (eq 17) permit the relations

$$\{\xi_{\alpha}, \xi_{\beta}\} = \{\xi_{\alpha}^*, \xi_{\beta}^*\} = 0; \quad \{\xi_{\alpha}, \xi_{\beta}^*\} = -i(\mathbf{C}^{-1})_{\alpha\beta} \quad (18)$$

which show that ξ^* and ξ behave as "classical" coordinates and momenta. If the matrix \mathbf{C} was the unit matrix the corresponding phase space would be canonical or "flat". However, in general this generalized phase space is curved.

Dynamical Variables and Wave Function Parameters. The wave function parameters are the dynamical variables, the evolution of which is governed by the dynamical equations. Because of this it is essential that the parametrization is nonredundant, that the parameter manifold is continuous, and that it is complete. Such requirements lead to the consideration of coherent states¹⁶ or at least to families of state vectors whose parameters have these properties. The completeness of a family of state vectors $|\xi\rangle$ can be expressed through the resolution of the identity I

$$\int |\xi\rangle \langle \xi| d\xi = I \quad (19)$$

with some appropriate positive measure $d\xi$ defined on the parameter space.

The importance of this type of parametrization and an important consequence of the completeness is that during the evolution the dynamics should, if required, be able to pass through any one of the members of the family $|\xi\rangle$. In order to accomplish this in practice one needs the capability to switch from a current local parametrization or chart that for some reason has led to, say, too large parameter values and therefore numerically unstable dynamical equations, to another chart that is more suitable for that part of the dynamics. Such switching of charts must be done without any artificial discontinuities in trajectories and various properties, a behavior that can be guaranteed with appropriate parametrization. An example of this is a Thouless parametrization of a determinantal electronic wave function $|\mathbf{z}\rangle = \det\{\chi_i(x_i)\}$, with the spin orbitals expressed in terms of atomic spin orbitals $\{u_k(x_i)\}$ centered on the various nuclei, as

$$\chi_i = u_i + \sum_j u_j z_{ji} \quad (20)$$

with time-dependent complex coefficients z_{ji} being the dynamical variables. This parametrization guarantees that all possible determinants in terms of the atomic orbitals is accessible during a dynamical evolution.

As an example of how this works we consider a particular trajectory of the $\text{H} + \text{H}_2(0,0) \rightarrow \text{H}_2(v,j) + \text{H}$ exchange reaction at an energy of 1.2 eV in the center of mass frame. Using an atomic orbital basis and a representation of the electronic state in terms of a Thouless determinant and a classical description of the protons, the leading term of the electronic state of the reactants is

$$|(1s_1 + 1s_2)\alpha(1s_1 + 1s_2)\beta_1 s_3 \alpha| \quad (21)$$

where 1 and 2 label the protons of the reactant molecule, 3 denotes that of the projectile atom, and $1s_i$ is an atomic orbital centered on proton i .

The reactive trajectory proceeds by exchange of protons 2 and 3, making the leading term of the product electronic state

$$|(1s_1 + 1s_3)\alpha(1s_1 + 1s_3)\beta_1 s_2 \alpha| \quad (22)$$

The original chart or Thouless parametrization

$$\begin{aligned} &1s_1\alpha + 1s_2\alpha z_1 + 2s_1\alpha z'_1 + \dots \\ &1s_2\beta + 1s_1\beta z_2 + 1s_3\beta z'_2 + \dots \\ &1s_3\alpha + 1s_2\alpha z_3 + 2s_1\alpha z'_3 + \dots \end{aligned} \quad (23)$$

will then become unsuitable since, say, the absolute value of the z -coefficients of the $1s_2\alpha$ spin orbital become large in comparison to unity, making the integration of the dynamical equations less accurate. The ENDyne code which implements the END theory automatically switches to a new chart with the new coefficients suitable for the product side. Although the leading determinant in the basis thus has changed, the total END wave function is the same and the resulting trajectory shows no discontinuous behavior.

3. Implementation of the Electron–Nuclear Dynamics Theory

The integration of the END equations from a given set of initial conditions, the projection of the evolved state vector on a given (final) state to obtain state to state transition probabilities,

the calculation of cross sections (differential and integrated) including the semiclassical corrections to classical results, and the necessary interface to provide graphic representations of the evolution of various properties are all accomplished within the ENDyne code.¹⁷

As seen in the previous section, the TDVP produces an approximation to the time-dependent Schrödinger equation in the form of a system of coupled first-order ordinary differential equations. Methods for integrating such systems are available in the literature¹⁸ and the modification and implementation of such techniques in the ENDyne code has been discussed in some detail elsewhere.¹²

An initial molecular state is usually determined by an optimization algorithm to determine the initial values of the electronic and nuclear parameters. For instance, the optimal Thouless parametrization of an electronic state is one for which the z -parameters are as small as possible. Here one should note that the initial state of the total system can contain a projectile moiety with both nuclei and electrons being translated toward a target molecule. This requires some care in specifying the initial conditions in order to obtain a proper dynamics.

When electrons are also allowed to evolve dynamically, i.e., without the use of a precalculated or fitted potential energy surface, then a basis set, much like in electronic structure theory, is used. It was shown some time ago¹⁹ how to account for the electron dynamics when an atom or molecule is in motion. The idea is to use an exponential factor in the atomic or molecular orbital basis to account for the momentum of the electrons explicitly. The exponential factors are called electron translation factors (ETF). A simple example is that of the ground state of a moving H atom (using atomic units)

$$\psi(\vec{r}) = \exp(i\vec{v} \cdot \vec{r} - i(\vec{v}^2/2 - \epsilon_{1s}))\phi_{1s}(\vec{r} - \vec{R}) \quad (24)$$

which satisfies the time-dependent Schrödinger equation. In order to use ETF's for computations in the dynamics studies of molecular systems, a general, high-quality integral package must be written which includes basis orbitals with ETF's such as the following Gaussian basis set

$$\varphi_h(\vec{x}, z, \vec{R}, \vec{P}) = \sum_p z_{ph} x^{k_{ph}} y^{m_{ph}} z^{n_{ph}} \exp[-\alpha(\vec{x} - \vec{R})^2 - \text{im}/M\vec{P} \cdot \vec{x}] \quad (25)$$

Such a tool does not yet exist, although some attempts have been made to produce a general integral package.²⁰ Much work continues to be done on the topic of ETF's in the area of atomic and molecular collisions. It is not the purpose of this paper to review the important advances made in this area, but to explain the different approach to the challenge of ETF's adopted in the current implementation of the END theory using standard integral packages such as HERMIT.^{21,22}

We review the END equations for the simplest model of classical nuclei and a single complex determinantal wave function for the electrons, and we identify the electron-nuclear couplings which are responsible for the need to introduce ETF's. The modified Fock operator with these couplings included yields an equation that determines atomic or molecular orbitals with the correct translational properties within the given basis. This equation is the "boosted SCF" equation. The solutions are complex, linear combinations of atomic basis functions, which constitute the best approximation to the ETF's within the basis and have the property of not changing in time as long as they are in inertial motion.

ETF's are always needed, even for low energies, to obtain correct dynamics. However, they can be introduced as a complex expansion in terms of real orbitals or as explicit exponential factors multiplying the atomic or molecular orbitals. When the original (real) orbitals basis is small, the explicit factor provides more accurate results and the complex expansion needs a larger basis to get to the same level of accuracy. This becomes increasingly relevant for high kinetic energies, say above a few keV. For most processes at kinetic energies in the range up to few hundred eV's, the complex expansion approach within a modest basis set provides an excellent dynamical description.

END uses the time-dependent variational principle as a unifying principle to derive the dynamic equations for the wave function parameters, which as shown above constitute the dynamical variables of the system. The use of the TDVP allows the equations of motion to apply not only for a fully quantal or completely classical treatment but also for a mixed quantum-classical description. For basis functions which depend, in some form, on the classical dynamical variables (e.g. basis functions centered on classical nuclei and thus depend on their positions and momenta), this approach explicitly introduces all nonadiabatic couplings between the classical and quantum degrees of freedom. These couplings are essential for satisfying conservation theorems and for correct behavior of many observable quantities.^{5,23}

Approximate dynamical equations are obtained by making specific choices of the form of wave function to use and which degrees of freedom to treat classically. For this argument we choose classical atomic nuclei and position electronic basis functions on the dynamically moving nuclei. A single Thouless determinant²⁴ is used to describe the electrons.

The Lagrangian that encompasses these approximations is

$$L = \frac{1}{2} \sum_k (\vec{P}_k \cdot \dot{\vec{R}}_k - \dot{\vec{P}}_k \cdot \vec{R}_k) - \sum_k \frac{\vec{P}_k^2}{2M_k} + \left\langle z \left| \frac{i}{2} \left(\frac{d}{dt} - \frac{\vec{d}}{dt} \right) - H_{el} \right| z \right\rangle \quad \langle z | z \rangle \quad (26)$$

where the symmetric form of the time derivative includes the operator \vec{d}/dt acting on the bra and where the electronic Hamiltonian H_{el} contains the nuclear-nuclear repulsion potential energy. The symbols \vec{R}_k , \vec{P}_k , and M_k denote the position, momentum, and mass, respectively, of nucleus k , while \vec{R} and \vec{P} are the time derivatives of said quantities. The electronic wave function $|z\rangle$ depends on a number of complex parameters, such as molecular orbital coefficients, collectively denoted by z . The TDVP means that the action must be stationary as expressed by eq 13.

In order for the phase space of the electrons to be well-defined and so the electron can carry momentum the wave function must be complex. Standard normalized molecular orbital (MO) coefficients are redundant, which can be seen from the fact that rotations separately among occupied and unoccupied states do not change the state. Such a choice of MO coefficients as dynamical parameters makes the equations singular. Thouless²⁴ developed a set of nonredundant parameters z for a single determinant. They turn out to be the coset representatives of the unitary group $U(K)$ and belong to the coset space $U(K)/U(N) \times U(K-N)$, where N is the number of electrons and K is the rank of the basis. Single determinants parametrized this way are coherent states.^{12,14,16} The important features of these parameters from the point of view of dynamics is that they provide a complex, continuous, nonredundant wave function parametrization. The complex parameters are actually dynamical

variables and form a (generalized) phase space with a nonunit metric and a generalized Poisson bracket.¹⁴

In terms of a given spin orbital basis set $\{\phi_i; i = 1, K\}$ centered on the nuclei, the occupied orbitals of the determinant are

$$\chi_h = \phi_h + \sum_{p=N+1}^K z_{ph} \phi_p \quad (27)$$

The first N orbitals ϕ_h form the reference determinant. If the basis is orthogonal, the virtual dynamical orbitals are written in terms of the same coefficients as

$$\chi_p = \phi_p - \sum_{h=1}^N z_{ph}^* \phi_h \quad (28)$$

In terms of a nonorthogonal basis the virtual dynamical orbitals are

$$\chi_p = \phi_p + \sum_{h=1}^N v_{hp}^* \phi_h \quad (29)$$

where the v coefficients are functions of the complex, time-dependent z -coefficients.^{3,12} The orbitals χ_h are mutually non-orthogonal as are the χ_p , but they satisfy $\langle \chi_p | \chi_h \rangle = 0$.

In terms of these dynamical parameters for electrons and nuclei, the TDVP yields the dynamical equations in matrix form

$$\begin{pmatrix} iC & 0 & iC_R & 0 \\ 0 & -iC^* & -iC_R^* & 0 \\ iC_R^\dagger & -iC^T & C_{RR} & -I \\ 0 & 0 & I & 0 \end{pmatrix} \begin{pmatrix} \dot{z} \\ \dot{z}^* \\ \dot{\vec{R}} \\ \dot{\vec{P}} \end{pmatrix} = \begin{pmatrix} \partial E / \partial z^* \\ \partial E / \partial z \\ \partial E / \partial \vec{R} \\ \partial E / \partial \vec{P} \end{pmatrix} \quad (30)$$

where the total energy is

$$E = \sum_k \frac{P_k^2}{2M_k} + \frac{\langle z | H_{el} | z \rangle}{\langle z | z \rangle} \quad (31)$$

The coupling elements in eq 30 are

$$\begin{aligned} C &= \frac{\partial^2 \ln S(z^*, \vec{R}', z, \vec{R})}{\partial z^* \partial z} \Big|_{\vec{R}=\vec{R}'} \\ C_R &= \frac{\partial^2 \ln S(z^*, \vec{R}', z, \vec{R})}{\partial z^* \partial \vec{R}} \Big|_{\vec{R}=\vec{R}'} \\ C_{RR} &= -2 \operatorname{Im} \frac{\partial^2 \ln S(z^*, \vec{R}', z, \vec{R})}{\partial \vec{R}' \partial \vec{R}} \Big|_{\vec{R}=\vec{R}'} \end{aligned} \quad (32)$$

They are derived from the overlap

$$S(z^*, \vec{R}', z, \vec{R}) = \langle z; \vec{R}' | z; \vec{R} \rangle \quad (33)$$

formed between Thouless determinants at two different geometries \vec{R}' and \vec{R} .

It is noteworthy that using the TDVP ensures the conservation of important physical quantities such as total energy, total momentum, and total angular momentum.^{3,12} The coupling terms in the dynamical metric play a crucial role in this connection. An SCF approach that includes the coupling terms C_R can be introduced. For a molecule or atom in inertial motion, the nuclear acceleration will be zero, but \vec{R} will not be. Thus, if initial z coefficients corresponding to some stationary state are

used, they will change in time because of the electron–nuclear coupling C_R . When ETF's are explicit factors built into the basis, extra terms appear on the right side of the electronic equations which cancel these coupling terms.¹⁹ In most current approaches the ETF's are dropped in the evaluation of the two-electron Coulomb repulsion integrals, a procedure that can often be justified as long as the electron deBroglie wavelength is long compared to the orbital size. Alternatively, by allowing for complex orbital coefficients, as is done in the END theory, one relies on the basis to approximate the ETF's and then the ETF is included in all integrals.

A straightforward way to see how the coupling terms generate the ETF is in the SCF approach that includes the coupling terms. Phrasing the problem in this way means that a set of z 's are sought that for given velocities $\vec{R}_k = \vec{V}_k$ satisfy $\dot{z}_{ph} = 0$. Imposing this condition means that the equations to be solved are

$$i \sum_k C_{R_k} \cdot \vec{V}_k = \partial E / \partial z^* \quad (34)$$

which can be written in matrix form as¹²

$$0 = (-\mathbf{z} \quad \mathbf{I}^0) \{ \langle \phi_i | \hat{F} - i \sum_k \vec{V}_k \cdot \nabla_{\vec{R}_k} | \phi_j \rangle \} \begin{pmatrix} \mathbf{r} \\ \mathbf{z} \end{pmatrix} \quad (35)$$

where \hat{F} is the ordinary Fock operator, ϕ_k are the basis functions, assumed for present purposes with no loss of generality to be orthonormal, the columns of the partitioned matrix

$$\begin{pmatrix} \mathbf{r} \\ \mathbf{z} \end{pmatrix}$$

are the occupied molecular orbital coefficients, and the columns of

$$(-\mathbf{z} \quad \mathbf{I}^0)^\dagger = \begin{pmatrix} -\mathbf{z}^\dagger \\ \mathbf{I}^0 \end{pmatrix}$$

are the virtual molecular orbital coefficients. The symbols \mathbf{r} and \mathbf{I}^0 denote the unit matrices of dimension N and $K - N$, respectively.

Without the nuclear gradient term, this is precisely the SCF equation of electronic structure theory. The added term produces an SCF scheme in a Galilei boosted frame when all velocities \vec{V}_k are equal. Obviously, the extra terms will make the molecular coefficients complex. If the velocities of all the atoms are the same, then the new operator, $\hat{F} - i \vec{V} \cdot \sum_k \nabla_{\vec{R}_k}$ is Hermitian. If for some reason one wanted to find a state in initial electronic equilibrium (i.e. $\dot{z}_{ph} = 0$) but with atoms with different velocities, then the new operator would not be Hermitian, unless the overlap vanishes between orbitals belonging to nuclei with different velocities. Equation 35 with this modified Fock operator is called the boosted SCF equation.

Solution procedures for the boosted SCF equations have been added to the ENDyne code.¹⁷ This provides the facility to obtain properly boosted starting z -coefficients. Analogous treatment can be adopted for more general wave functions.

References and Notes

- (1) Car, R.; Parrinello, M. *Phys. Rev. Lett.* **1985**, *55*, 2471.
- (2) Öhrn, Y.; Deumens, E.; Diz, A.; Longo, R.; Oreiro, J.; Taylor, H. In *Time-Dependent Quantum Molecular Dynamics*; Broeckhove, J., Lathouwers, L., Eds.; Plenum: New York, 1992; pp 279–292.
- (3) Deumens, E.; Diz, A.; Taylor, H.; Öhrn, Y. *J. Chem. Phys.* **1992**, *96*, 6820.

- (4) Longo, R.; Deumens, E.; Öhrn, Y. *J. Chem. Phys.* **1993**, *99*, 4554–4565.
- (5) Longo, R.; Diz, A.; Deumens, E.; Öhrn, Y. *Chem. Phys. Lett.* **1994**, *220*, 305–311.
- (6) Hedström, M.; Deumens, E.; Öhrn, Y. *Phys. Rev. A* **1998**, *57*, 2625.
- (7) Diz, A.; Öhrn, Y.; Sabin, J. R. *Nucl. Instrum. Methods B* **1995**, *B96*, 633.
- (8) Morales, J. A.; Diz, A. C.; Deumens, E.; Öhrn, Y. *J. Chem. Phys.* **1995**, *103*, 9968–9980.
- (9) Hedström, M.; Morales, J. A.; Deumens, E.; Öhrn, Y. *Chem. Phys. Lett.* **1997**, *279*, 241.
- (10) Jacquemin, D.; Morales, J. A.; Deumens, E.; Öhrn, Y. *J. Chem. Phys.* **1997**, *107*, 6146–6155.
- (11) Öhrn, Y.; Oreiro, J.; Deumens, E. *Int. J. Quantum Chem.* **1996**, *58*, 583.
- (12) Deumens, E.; Diz, A.; Longo, R.; Öhrn, Y. *Rev. Mod. Phys.* **1994**, *66*, 917–983.
- (13) Champagne, B.; Deumens, E.; Öhrn, Y. *J. Chem. Phys.* **1997**, *107*, 5433.
- (14) Kramer, P.; Saraceno, M. *Geometry of the Time-Dependent Variational Principle in Quantum Mechanics*; Springer: New York, 1981.
- (15) Born, M.; Huang, K. *Dynamical Theory of Crystal Lattices*; Clarendon: Oxford, UK, 1954.
- (16) Klauder, J. R.; Skagerstam, B.-S. *Coherent States, Applications in Physics and Mathematical Physics*; World Scientific: Singapore, 1985.
- (17) Deumens, E.; Helgaker, T.; Diz, A.; Taylor, H.; Oreiro, J.; Morales, J. A.; Longo, R.; *ENDyne version 2.7 Software for Electron Nuclear Dynamics*; Quantum Theory Project, University of Florida, Gainesville, FL 32611–8435, 1998.
- (18) Press, W. H.; Flannery, B. P.; Teutolsky, S. A.; Vetterling, W. T. *Numerical Recipes: The Art of Scientific Computing*; Cambridge University: New York, 1986.
- (19) Delos, J. B. *Rev. Mod. Phys.* **1981**, *58*, 287.
- (20) Riera, A. In *Time-Dependent Quantum Molecular Dynamics*; Broeckhove, J., Lathouwers, L., Eds.; Plenum: New York, 1992; pp 311–346.
- (21) Helgaker, T. U.; Jensen, H. J. A.; Jørgensen, P. *J. Chem. Phys.* **1986**, *84*, 6280.
- (22) Helgaker, T.; Taylor, P. R. *Theor. Chim. Acta* **1992**.
- (23) Diz, A.; Öhrn, Y. *Int. J. Quantum Chem.* **1994**, *S28*, 11.
- (24) Thouless, D. J. *Nucl. Phys.* **1960**, *21*, 225.

Vibrational Dynamics of the I₃ Radical: A Semiempirical Potential Surface, and Semiclassical Calculation of the Anion Photoelectron Spectrum

C. J. Margulis, D. A. Horner, S. Bonella, and D. F. Coker*

Department of Chemistry, Boston University, 590 Commonwealth Avenue, Boston, Massachusetts 02215

Received: July 26, 1999; In Final Form: September 24, 1999

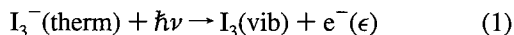
The semiempirical diatomics in molecules (DIM) approach is used to model the potential surface for ground-state vibration of a linear I₃ molecule. We use this system to explore semiclassical methods for treating quantal nuclear vibrations by computing the photoelectron spectrum of I₃[−] which produces vibrationally excited I₃. We compare semiclassical results with full quantum calculations and experimental results recently reported by Neumark and co-workers. (Taylor, T. R.; Asmis, K.R.; Zanni, M. T.; Neumark, D. M. *J. Chem. Phys.* 1999, 110, 7607.)

1. Introduction

Since the 1950s the existence of the triiodide radical has been proposed as an intermediate species to explain how iodine atoms, produced by photodissociating I₂, can recombine in the gas phase to reproduce the diatomic species. The accepted mechanism involves an I[•] radical first colliding I₂ to form stable I₃ which subsequently undergoes collision with another I[•] radical, then this collision complex breaks apart to give two I₂ molecules. Despite its proposed importance in this most fundamental reaction of gas-phase chemical kinetics, direct experimental observation of the I₃ molecule has only very recently been accomplished in the high-resolution photoelectron spectroscopy studies of Neumark and co-workers.¹

The first goal of this paper is to demonstrate that a very simple description of the I₃ molecule offered by the semiempirical diatomics-in-molecules (DIM) approach is actually capable of providing a very reliable representation of this molecule, reproducing the recently measured binding energies, and vibrational frequencies with surprising accuracy.

Next we summarize how time dependent perturbation theory can be used to compute the distribution of ejected photoelectron kinetic energy $P_{\beta}(\epsilon)$ in the thermal equilibrium photoelectron spectrum of I₃[−] in which vibrationally hot I₃ is produced according to the following process:



Finally we will compare the results of fully quantum dynamical calculations of this photoelectron spectrum, with classical and semiclassical calculations of the I₃ vibrational dynamics probed by these measurements, and we compare our theoretical results with the experimental photoelectron spectrum of Neumark and co-workers.¹

2. Methods

2.1. A DIM Potential Model for Ground Electronic State Intramolecular Vibrations of I₃. The model assumes that the I₃ molecule is linear, hence the projection of the total angular momentum of the system into the molecular axis is a good quantum number. Following the same scheme used in previous work² we write the basis set as Hund's case C kets

$$|J_1 m_{j1}\rangle |J_2 m_{j2}\rangle |J_3 m_{j3}\rangle = |J_1 m_{j1}, J_2 m_{j2}, J_3 m_{j3}\rangle$$

where J_k and m_{jk} are the total angular momentum and its projection on the molecular axis for each of the iodine atoms. Our purpose in this paper is to focus on the properties of the ground electronic state of I₃, hence we will reduce our basis set to a minimum subspace that will include only the necessary kets mixing to form this lowest energy eigenstate. Thus the approach we present here will not produce all the subsequent excited states, but only some of them.

We suppose that the ground-state eigenket has total angular momentum projection

$$M_J = \sum_{k=1}^3 m_{jk} = \pm 1/2$$

so only kets satisfying this condition will combine to generate this assumed lowest energy eigenstate.³ Our knowledge of the ground-state dissociation limits of the I₃ radical can be used to further limit the basis set. Thus if one of the bonds is stretched, the molecule should dissociate to ground-state I₂ and an I[•] radical species. The ground state of I₂ in our representation is

$$1/\sqrt{2}(|^3/2, ^1/2\rangle |^3/2, -1/2\rangle - |^3/2, -1/2\rangle |^3/2, ^1/2\rangle)$$

and the I[•] radical ground state is

$$|^3/2 \pm 1/2\rangle$$

These considerations thus enable us to limit the basis kets to only those having all the $J_k = 3/2$ and the $m_{jk} = \pm 1/2$. This procedure is only valid in the gas phase, in solution other states that we are not including in the calculations described here will be coupled by anisotropic interactions with the solvent and thus make contributions to the lowest energy solution phase eigenket, but this is beyond the scope of the current paper.

The DIM Hamiltonian operator has the form^{4,5}

$$\sum_{i < j} \hat{H}_{i,j} - n \sum_i \hat{H}_i \quad (2)$$

and we choose the zero in energy to be that of the isolated I[•] radicals; therefore, the second sum in the above expression can be disregarded. For convenience in the notation we will drop the J index in the angular momentum expression since it is the

same for all iodine atoms and we will only label them by their values of m_{jk} .

In the gas phase the I₃ ground state can have total $M_J = \pm 1/2$, both angular momentum orientation states are degenerate and uncoupled, thus we need only consider the one with total $M_J = 1/2$. The only basis kets to consider now are the following:

$$\{|^{-1/2, 1/2, 1/2}\rangle; |^{1/2, -1/2, 1/2}\rangle; |^{1/2, 1/2, -1/2}\rangle\}$$

Any matrix element between them will be of the form

$$\langle m_{j1}, m_{j2}, m_{j3} | \hat{H}_{l,m} | m'_{j1}, m'_{j2}, m'_{j3} \rangle = \langle m_{j1}, m_{j2} | \hat{H}_{l,m} | m'_{j1}, m'_{j2} \rangle \times \langle m_{j3} | m'_{j3} \rangle$$

i.e., an I₂ matrix element times a $\delta(m_j, m'_j)$.

The full electronic Hamiltonian matrix thus becomes

$$\langle ^{-1/2, 1/2, 1/2} | \hat{H} | ^{-1/2, 1/2, 1/2} \rangle = \langle ^{-1/2, 1/2} | \hat{H}_{R1} | ^{-1/2, 1/2} \rangle + \langle ^{1/2, 1/2} | \hat{H}_{R2} | ^{1/2, 1/2} \rangle + \langle ^{-1/2, 1/2} | \hat{H}_{R3} | ^{-1/2, 1/2} \rangle$$

$$\langle ^{1/2, -1/2, 1/2} | \hat{H} | ^{1/2, -1/2, 1/2} \rangle = \langle ^{1/2, -1/2} | \hat{H}_{R1} | ^{1/2, -1/2} \rangle + \langle ^{-1/2, 1/2} | \hat{H}_{R2} | ^{-1/2, 1/2} \rangle + \langle ^{1/2, 1/2} | \hat{H}_{R3} | ^{1/2, 1/2} \rangle$$

$$\langle ^{1/2, 1/2, -1/2} | \hat{H} | ^{1/2, 1/2, -1/2} \rangle = \langle ^{1/2, 1/2} | \hat{H}_{R1} | ^{1/2, 1/2} \rangle + \langle ^{1/2, -1/2} | \hat{H}_{R2} | ^{1/2, -1/2} \rangle + \langle ^{-1/2, 1/2} | \hat{H}_{R3} | ^{-1/2, 1/2} \rangle$$

$$\langle ^{-1/2, 1/2, 1/2} | \hat{H} | ^{1/2, -1/2, 1/2} \rangle = \langle ^{-1/2, 1/2} | \hat{H}_{R1} | ^{1/2, -1/2} \rangle$$

$$\langle ^{-1/2, 1/2, 1/2} | \hat{H} | ^{1/2, 1/2, -1/2} \rangle = \langle ^{-1/2, 1/2} | \hat{H}_{R3} | ^{1/2, -1/2} \rangle$$

$$\langle ^{1/2, -1/2, 1/2} | \hat{H} | ^{1/2, 1/2, -1/2} \rangle = \langle ^{1/2, -1/2} | \hat{H}_{R2} | ^{1/2, -1/2} \rangle$$

Where R1 is the distance from the I atom at one end of the molecule to the central one, R2 is the distance from the I atom at the other end to the central atom, and R3 is the distance between the two I atoms at opposite ends of the molecule. Using Table 1 in ref 2 and performing some simple algebra we find the matrix elements to be

$$\langle ^{-1/2, 1/2} | \hat{H} | ^{-1/2, 1/2} \rangle = {}^1I_2(E(1^3\Sigma_u^+) + E(X))$$

$$\langle ^{1/2, 1/2} | \hat{H} | ^{1/2, 1/2} \rangle = E(1^1\Pi_u)$$

for which experimental values are available in Batista and Coker's² paper and the references therein.

The electronic ground-state surface of I₃ is thus obtained by simply diagonalizing the 3 × 3 matrix whose elements are summarized above and selecting the lowest energy eigenvalue. In Figure 1 we display the elements of our reduced DIM Hamiltonian matrix as functions of R1 and R2 while Figure 2 shows the electronic ground state of I₃ calculated from these matrix elements as described above. Table 1 summarizes various properties of this ground-state I₃ potential and compares these results with the experimental values.¹ This table also summarizes various properties of the I₃⁻ potential which we need to prepare the initial state for our photoelectron spectrum studies.

The symmetric stretch frequency of I₃ obtained from these calculations is about 10% too high, and the dissociation energy to I₂ and an I• radical is also a little high but with in the reported experimental uncertainty. Given the shapes of the various diabats and coupling matrix elements presented in Figure 1, the accuracy

TABLE 1: Comparison of Properties of Calculated DIM Surface for I₃ with Experimental Results^a

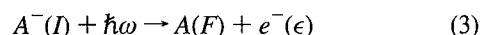
item	parameters and results	
	this paper	Neumark's results
symmetric frequency	126.1 cm ⁻¹	115 ± 5 cm ⁻¹
antisymmetric frequency	163.7 cm ⁻¹	
dissociation energy I ₃ → I ₂ + I•	0.19157 eV	0.143 ± 0.06 eV
dissociation energy I ₃ → 3 I•	1.74723 eV	
I ₃ equilibrium bond length	2.762 Å	
I ₃ adiabatic EA	4.226 eV	4.226 eV
I ₃ ⁻ symmetric frequency ^b	106.7 cm ⁻¹	112 cm ⁻¹
I ₃ ⁻ antisymmetric frequency	122.2 cm ⁻¹	
-I ₃ ⁻ bond length	2.85 Å	
τ	100 fs	
ħω	4.657 eV	4.657 eV

^a The I₃⁻ potential is assumed to be quadratic in both symmetric and antisymmetric coordinates to simplify the calculations. ^b Different values for the symmetric and antisymmetric frequencies can be found in the literature. See refs 6 and 7 and references therein.

with which our DIM ground-state surface reproduces experimental values is quite remarkable.

Our calculations assume that the I₃ molecule is linear and symmetric just like I₃⁻. Thus the fact that the equilibrium bond length we find for our model I₃ molecule is about 0.1 Å shorter than that of the parent I₃⁻ means that when we photoionize the anion via a vertical Franck-Condon excitation we will extend the symmetric stretch mode of the resulting I₃. As we shall see in the detailed analysis of our calculated signals we present in section 3, antisymmetric stretch components can enter our signals through thermal populations of ground electronic state antisymmetric stretch motions or through nonlinear couplings between the symmetric and antisymmetric modes as a result of motion over our fully nonlinearly coupled I₃ potential surface.

2.2. Semiclassical Computation of the Photoelectron Spectrum. For our purposes we view the photoionization reaction



as a process which takes the molecular ion system A⁻ from a discrete electronic state Φ_I to a continuum molecular ion electronic state Φ_{Fε} by absorption of a photon. The final continuum state is really a neutral molecule A in one of its discrete states Φ_F and an ejected free electron with continuous kinetic energy ε. In the appendix we outline the time dependent perturbation theory approach to computing the probability of observing ejected photoelectrons with kinetic energy ε obtained by ionizing molecules prepared in a thermal distribution of vibrational states moving on the ground electronic surface of I₃⁻ (state I) and producing ground-state neutrals (state F). There we show that if we assume that the dipole matrix elements connecting states I and F depend weakly on nuclear coordinates and vary slowly with electronic kinetic energy, ε, (see appendix for details), this probability is obtained as

$$P_{\beta}^{IF}(\epsilon) \sim \text{Re} \left\{ \int_0^\infty dt \phi_{IF}(t; \beta) \exp \left[-\frac{i}{\hbar} (\epsilon - \hbar\omega) t \right] \exp \left[-\frac{t^2}{4\tau^2} \right] \right\} \quad (4)$$

where the thermally averaged dynamical correlation function appearing in this expression is given by

$$\phi_{IF}(t; \beta) = \sum_v \exp[-\beta E_{Iv}] \exp \left[\frac{i}{\hbar} E_{Iv} t \right] f_{F, Iv}(t) \quad (5)$$

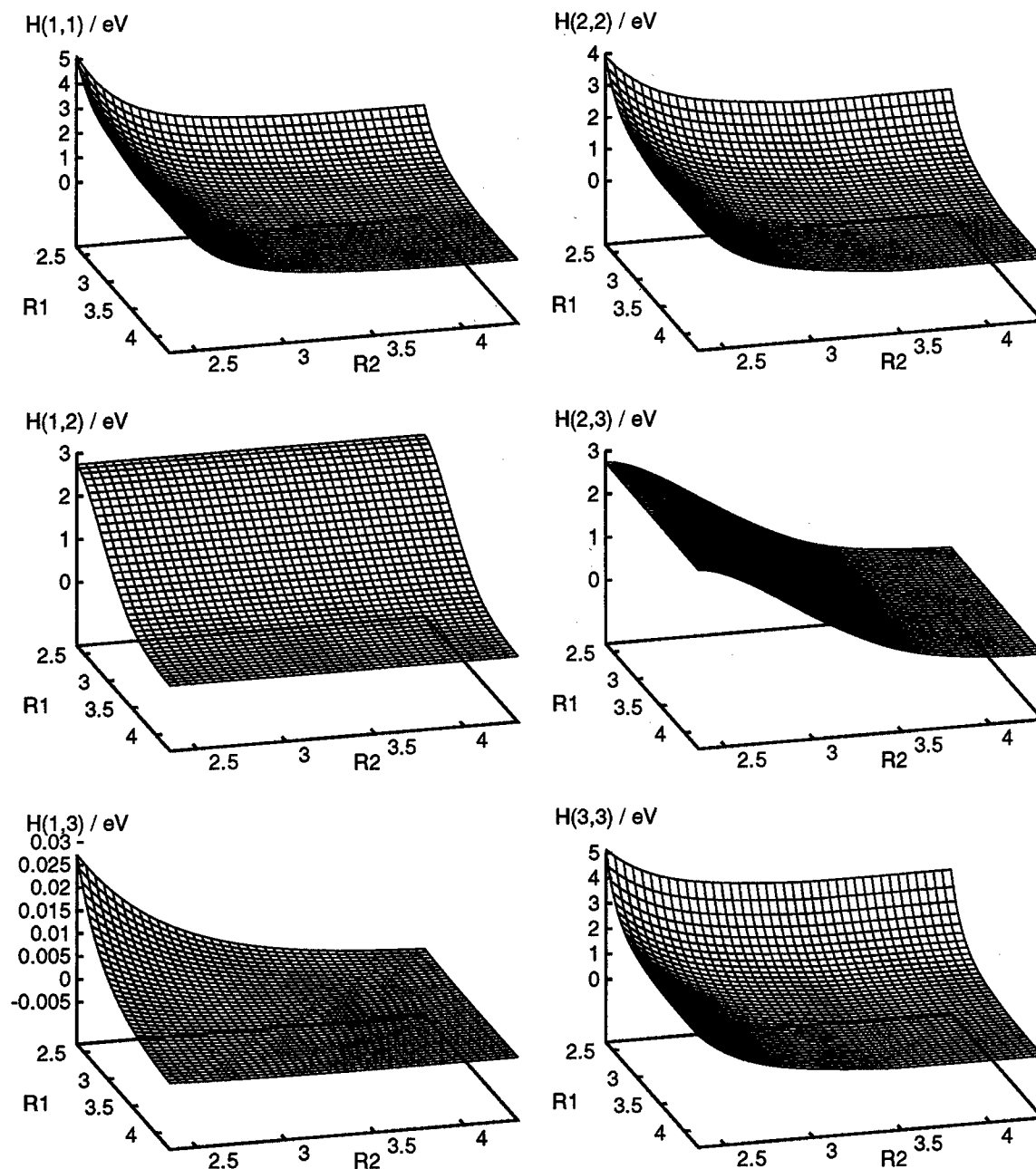


Figure 1. Elements of the DIM Hamiltonian used in our calculation of the collinear ground state electronic surface of I_3 as a function of bond lengths in Ångströms.

Energy / eV

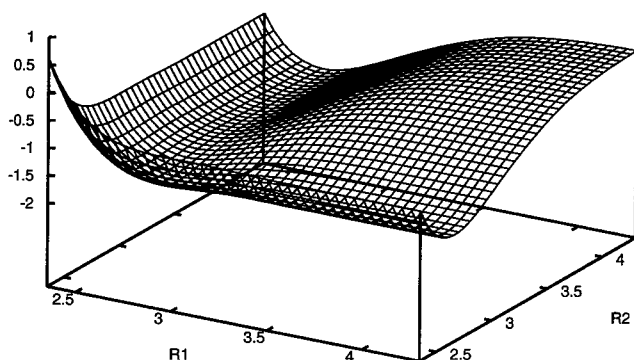


Figure 2. DIM Ground-state electronic surface of I_3 as a function of bond lengths in Ångströms.

Here E_{ν} is the energy of the ν th vibrational eigenstate on the initial electronic surface I , $\chi_{\nu}(\mathbf{Q})$ is the corresponding nuclear

vibrational eigenstate on this surface, and the individual vibrational component, excited electronic state propagated correlation functions are

$$f_{F,\nu}(t) = \langle \chi_{\nu} | \exp \left[-\frac{i}{\hbar} \hat{H}_F t \right] | \chi_{\nu} \rangle \quad (6)$$

where \hat{H}_F is the Hamiltonian governing nuclear dynamics over the excited electronic state potential F . This correlation function thus involves propagating the nuclear vibrational eigenstates of the initial electronic surface over the final excited-state surface and measuring the overlap of these propagated function at time t with the initial wave function.

In our studies we will assume that the initial electronic surface of the I_3^- can be approximated harmonically around its equilibrium geometry and that this approximation will be reliable for all the thermally accessible initial vibrational states at the temperatures of interest. This approximation is expected to be

reasonable for the deep I₃⁻ ground-state surface. However, vibrations on the I₃ excited state surface are expected to be highly anharmonic as motion on this surface is only very weakly bound along certain directions as seen in Figure 2.

To simplify our calculations, we further assume that the bending of the I₃ molecule is not excited in these experiments and that rotation-vibration coupling can be ignored. Thus we need only the symmetric and antisymmetric stretch coordinates to describe the anharmonic intramolecular vibrational dynamics on the I₃ potential surface. This reduces our intramolecular vibrational problem to just two dimensions. We thus employ the initial ground state normal mode coordinates of the system in our quantum and semiclassical propagation calculations detailed below.

The individual vibrational correlation functions given in eq 6 can be computed exactly using standard FFT grid propagation methods^{8,9} and the results added according to eq 5 to give the required thermal average correlation function. Such methods are, however, generally only viable for systems of few dimensions. Semiclassical methods based on propagating swarms of classical trajectories and carefully adding up the semiclassical phases associated with these trajectories to compute the approximate semiclassical dynamical wave function are in principle applicable to systems with many more dimensions.

We now consider the implementation of the Herman-Kluk, coherent state semiclassical propagator¹⁰⁻¹⁶ to compute the correlation functions given above. With this approach the propagator describing nuclear vibrations on surface F has the form

$$\exp\left[-\frac{i}{\hbar}\hat{H}_F t\right] = \int \frac{d\mathbf{P}}{(2\pi\hbar)^d} d\mathbf{Q} |\mathbf{P}, \mathbf{Q}_i\rangle C(\mathbf{P}, \mathbf{Q}, t) \exp\left[\frac{i}{\hbar} S(\mathbf{P}, \mathbf{Q}, t)\right] \langle \mathbf{PQ} | \quad (7)$$

where the coordinate state representation of the time dependent coherent state basis set elements used in this description are the Gaussian functions

$$\langle \mathbf{x} | \mathbf{P}, \mathbf{Q}_i \rangle = \left(\frac{2\gamma}{\pi}\right)^{d/4} \exp\left[-\gamma(\mathbf{x} - \mathbf{Q}_i)^2 + \frac{i}{\hbar} \mathbf{P}_i \cdot (\mathbf{x} - \mathbf{Q}_i)\right] \quad (8)$$

whose time dependent center position \mathbf{Q}_i , and phase \mathbf{P}_i parameters are the positions and momenta of simple classical trajectories, γ is a constant arbitrary width parameter, $S(\mathbf{P}, \mathbf{Q}, t) = \int d\mathbf{r} \mathbf{P}_i^2(\mathbf{P}, \mathbf{Q})/2M - E_F(\mathbf{Q}_i(\mathbf{P}, \mathbf{Q}))$ is the classical action along the trajectory propagated over our final state surface, which depends on the initial position \mathbf{Q} , and phase (momentum) \mathbf{P} of the given basis function, and the function $C(\mathbf{P}, \mathbf{Q}, t)$ is related to the stability of the classical trajectory with respect to variations in initial conditions as measured by the so-called monodromy matrixes whose elements have the form $\mathbf{M}_{PQ}^{(ij)}(\mathbf{P}, \mathbf{Q}, t) = [\partial P_i^j / \partial Q^j](\mathbf{P}, \mathbf{Q}, t)$, for example. In all the calculations reported in this paper we have used ensembles containing 1000 trajectories. The quantity $C(\mathbf{P}, \mathbf{Q}, t)$ which weights each trajectory's contribution to the semiclassical propagator in eq 7 is found to have the form

$$C(\mathbf{P}, \mathbf{Q}, t) = \left\{ \det \left[\frac{1}{2} (\mathbf{M}_{PP} + \mathbf{M}_{QQ} - 2\gamma i \hbar \mathbf{M}_{QP} + \frac{i}{2\gamma \hbar} \mathbf{M}_{PQ}) \right] \right\}^{1/2} \quad (9)$$

The monodromy matrixes can be computed by integrating the following auxiliary equations of motion which are determined by the time dependent local curvature of the potential along the classical trajectory

$$\dot{\mathbf{M}}_{QQ} = \mathbf{N} \mathbf{M}_{PQ} \quad \dot{\mathbf{M}}_{PQ} = -\mathbf{D}(t) \mathbf{M}_{QQ} \quad (10)$$

$$\dot{\mathbf{M}}_{QP} = \mathbf{N} \mathbf{M}_{PP} \quad \dot{\mathbf{M}}_{PP} = -\mathbf{D}(t) \mathbf{M}_{QP} \quad (11)$$

Where \mathbf{N} is a diagonal matrix with elements equal to the inverses of the masses associated with the different particle coordinates, and $\mathbf{D}(t)$ is the time dependent Hessian matrix $D^{(ij)}(t) = [\partial^2 V / \partial Q^i \partial Q^j](\mathbf{Q}_i)$ computed at points along the classical trajectory.

Using the excited-state semiclassical nuclear propagator in eq 7 we can express the correlation functions in eq 6 as

$$f_{F,IV}^{SC}(t) = \int \frac{d\mathbf{P}}{(2\pi\hbar)^d} d\mathbf{Q} \langle \chi_{IV} | \mathbf{P}, \mathbf{Q}_i \rangle C(\mathbf{P}, \mathbf{Q}, t) \times \exp\left[\frac{i}{\hbar} S(\mathbf{P}, \mathbf{Q}, t)\right] \langle \mathbf{PQ} | \chi_{IV} \rangle \quad (12)$$

Here the classical trajectories swarm over the potential surface associated with the final electronic state F .

With the assumptions described earlier, our vibrational eigenstates on surface I are products of harmonic oscillator eigenfunctions in the symmetric and antisymmetric coordinates. We can readily calculate the projections of these states onto our coherent state basis set in these coordinates and after some algebra we find for a given mode

$$\langle PQ | \chi_{IV} \rangle = \frac{N_v}{\alpha} \left(\frac{2\gamma}{\pi}\right)^{1/4} \exp[-\gamma \alpha^2 \delta (Q - X_0)^2] \times \exp[-\delta P^2 / 2\hbar^2] \exp[i\alpha^2 \delta P(Q - X_0)] \sum_{n=0}^v (\alpha^2 \delta)^{(n+1)/2} c_n P_n(g) \quad (13)$$

where the harmonic oscillator wave functions have the form $\psi_v(x) = N_v H_v(\alpha(x - x_0)) \exp[-\alpha^2(x - x_0)^2/2]$ with $\alpha = \sqrt{m\omega/\hbar}$, $N_v = (\alpha\sqrt{\pi}2^v v!)^{-1/2}$ is a normalization constant, $H_v(y) = \sum_{n=0}^v c_n y^n$ are the hermite polynomials, and $\delta = (2\gamma + \alpha^2)^{-1}$. The polynomials $P_n(g)$ result from the integrations and generally satisfy the recursion relation $P_{n+1}(g) = gP_n(g) + (n - 1)P_{n-1}(g)$ with $P_0 = 1$ and $P_1 = g$ and $g = \sqrt{\delta}[2\gamma(Q - x_0) - iP/\hbar]$.

Despite the appeal of obtaining semiclassical quantum dynamical effects by just averaging various dynamical quantities over an ensemble of classically propagating trajectories labeled by their initial conditions as, for example, in eq 12, the implementation of such semiclassical expressions is plagued with many serious numerical "traps for new players". In the discussion that follows we show how these problems arise in our application to the dynamics of I₃ excited in the photoelectron ejection experiments on I₃⁻.

The main difficulty with implementing these semiclassical methods arises due to the rapid oscillation of the integrand in eq 12, for example, between positive and negative values in various regions of initial phase space point (\mathbf{P}, \mathbf{Q}) . In these rapidly oscillatory regions contributions from near-by trajectories should add destructively to give only a vanishingly small contribution to the final integral. The integration over points (\mathbf{P}, \mathbf{Q}) which we accomplish by summing over the ensemble of trajectories thus requires a sufficiently dense packing of trajectories in such regions to accurately represent this cancellation. The primitive implementation of a grid or Monte Carlo based approach thus wastes much effort propagating trajectories from such regions only to have them add destructively to represent zero.

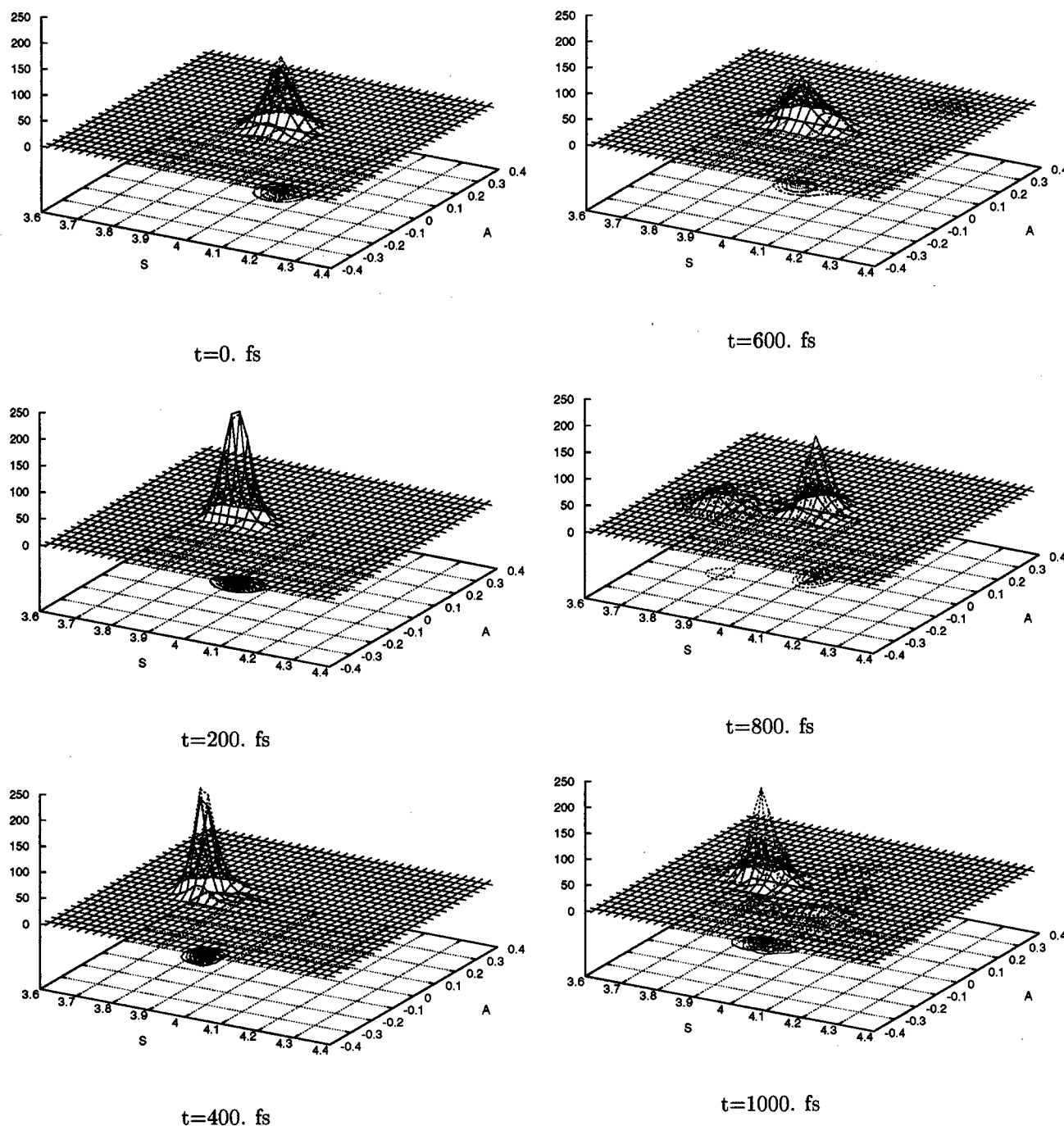


Figure 3. Propagation of initial harmonic I_3^- ground vibrational state on the photoexcited I_3 DIM potential surface. Surface of solid lines is propagated using the bare Herman-Kluk semiclassical algorithm. The dashed surface is the full quantum wave function propagated using split operator FFT methods. The wave functions are plotted as functions of symmetric and antisymmetric stretch normal modes in Ångströms.

The situation with a semiclassical integrand like that in eq 12 is even more troublesome. The phase factor in the integrand $\exp[i\theta(\mathbf{P},\mathbf{Q})/\hbar]$, say, becomes a rapidly oscillatory function of (\mathbf{P},\mathbf{Q}) because the phase, $\theta(\mathbf{P},\mathbf{Q})$, varies with (\mathbf{P},\mathbf{Q}) and dividing by a small \hbar amplifies these variations into rapid oscillations of the phase factor. In stationary phase regions where the rate of change of $\theta(\mathbf{P},\mathbf{Q})$ with (\mathbf{P},\mathbf{Q}) remains sufficiently small there will be constructive interference between trajectories giving nonvanishing contributions. Outside these stationary phase regions, however, the phase starts to change and the lowest order variation in phase is easily shown to be determined by the monodromy matrixes $M_{Q,P} = \partial Q/\partial P$, for example. In the classical dynamics of anharmonic many-body systems such quantities can become very large very quickly as trajectories become exponentially unstable with respect to variations in their

initial conditions in classically chaotic regions.^{4,17-26} Semiclassical expressions like that in eq 12 usually involve weighting trajectory contributions by quantities such as $C(\mathbf{P},\mathbf{Q})$ which depend on potentially diverging monodromy factors. As discussed above these explosive monodromy factors also appear exponentially in the phase factor so the cancellation of their contribution is crucial.

Several approaches for handling the cancellation of nonstationary trajectories and removing their explosive consequences in systems exhibiting strongly chaotic classical dynamics have recently been presented.^{14,18-25} All these methods are based on the ideas of stationary phase filtering which were developed during the 1980's when attempts were made to use path integral Monte Carlo methods to compute fully quantum real time correlation functions.²⁷⁻³¹

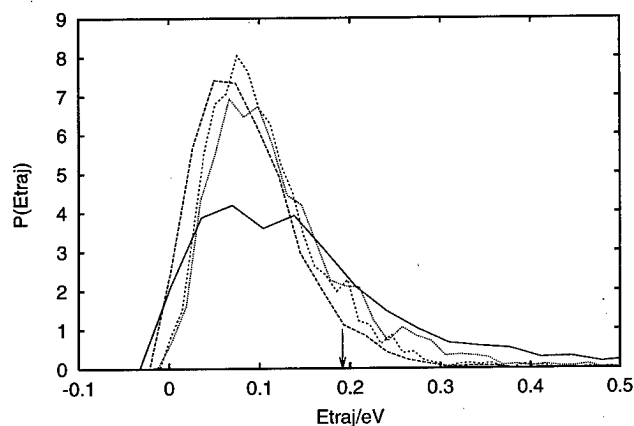


Figure 4. Classical trajectory energy distributions for various values of coherent state parameter γ for propagation on I_3 surface. The I_3 potential minimum is zero energy and the negative energies are due to the low energy resolution of our histogram. The dissociation energy of our model is indicated by the arrow. Values of γ in \AA^{-2} displayed are $\gamma = 25$. (solid), $\gamma = 125$. (long dashes), $\gamma = 525$. (short dashes), $\gamma = 825$. (dots). In our calculations we employ a value of $\gamma = 125$, which gives a trajectory energy distribution with a smaller high energy tail to reduce the rapid growth of chaotic trajectories in our ensemble.

The particular method we have found convenient to implement is that due to Herman^{22,23} and we now present a brief summary of the approach and demonstrate how it remedies the serious problems arising from classical chaos even in a system as simple as the two coupled anharmonic stretching modes of I_3 .

The disastrous effects of classical chaos on the straightforward implementation of semiclassical expressions such as that in eq 12 for I_3 can be seen very clearly in Figure 3 where we compare the full quantum and semiclassical time dependent normalized wave function densities for symmetric and antisymmetric stretch coordinates of I_3 produced after photoelectric ejection from I_3^- . The initial Gaussian density produced during the Franck-Condon excitation of our harmonic model of I_3^- starts out on the attractive wall of the I_3 surface with the symmetric stretch coordinate extended relative to the equilibrium geometry of I_3 due to the differences in equilibrium bondlength for the ionic and neutral species which are accurately produced by our model surfaces.

This nonequilibrium excited state distribution thus first compresses in the symmetric stretch and then as it extends in this direction the density also shows elongation in the antisymmetric stretch direction due to the strong anharmonic couplings between these modes present in our DIM model I_3 surface.

In Figure 4 we present the distribution of classical trajectory energies for various coherent state basis set width parameters γ . We see that as this basis set width parameter is varied, the energy distribution of our classical trajectory ensemble changes considerably. The value of this parameter we used in most of our calculations was $\gamma = 125 \text{ \AA}^{-2}$. This value gives a narrow energy distribution with a small tail extending above the smallest dissociation energy of our potential ($D_{\text{anti}} \sim 0.2 \text{ eV}$).

The longer time wave functions ($t > 400 \text{ fs}$) presented in Figure 3 show a serious discrepancy between the wave function obtained from the bare application of the semiclassical coherent state basis set approach and the exact wave function. These semiclassical results at the longer times show wave function fragmentation resulting from a few trajectories in the high energy tail of the distribution in Figure 4 exhibiting large amplitude motions. These high energy trajectories rapidly become unstable with respect to variations in their initial conditions so the

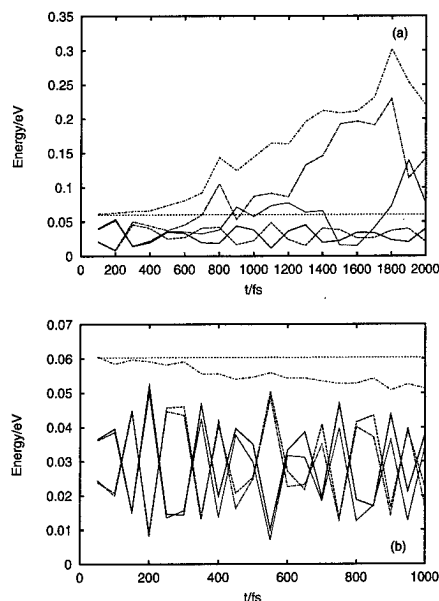


Figure 5. (a) Comparison of time dependence of total quantum system energy and kinetic and potential components computed using full quantum propagation (curves add to give total energy conservation), and results computed using the bare Herman-Kluk semiclassical approach which show serious energy conservation problems and divergence from exact quantum results beyond 300–400 fs. (b) Similar comparison to a only here results from preaveraging semiclassical calculations show much better energy conservation and comparison with full quantum results.

magnitudes of their $C(\mathbf{P}, \mathbf{Q}, t)$ weights in the bare semiclassical expression (eq 12) become overwhelming. In Figure 5a we show the time history of the kinetic, potential, and total energy computed using the bare semiclassical wave function and the fully quantum result. As expected, beyond 400 fs, the semiclassical components deviate dramatically from the exact results and the total energy of the bare semiclassical propagated wave function shows serious conservation problems. Not surprisingly, since the ensemble average is becoming dominated by the unstable high energy components due to their rapidly growing $C(\mathbf{P}, \mathbf{Q}, t)$ factors, the energy trends upward to the average of these high energy trajectories (see Figure 4).

If we were free to increase the ensemble size without bound the contribution from these unstable trajectories would eventually be approximately canceled by interference with other unstable trajectories since they emanate from nonstationary regions of phase space as discussed earlier. Such an approach is in general numerically impractical as it requires the cancellation of very large weights with different signs.

The approach adopted in the so-called “interfering condition” or “preaveraging” methods attempts to average these large interfering weights over many close lying trajectories by assuming a linear or quadratic variation of the phase around a trajectory, and within this approximation integrating the weight analytically to obtain a “pre-averaged” weight which no longer oscillates wildly.^{18,19–21,23,32,33} Typically these methods first multiply the integral being evaluated by unity represented as a normalized integral of a Gaussian in the difference between the original integration variables and the preaveraging Gaussian integral variables. If the widths of these preaveraging Gaussians are made small enough, the phase of the original integrand can be expanded to low order in the difference variables and the resulting Gaussian integrals performed analytically to give an averaged weight (see for example refs 22 and 23 for details).

The main advantage of the specific preaveraging approach developed by Herman^{22,23} is that it preserves the shape of the fixed width coherent state basis set used to represent the time evolving wave function. This is accomplished by changing the integration variables in the semiclassical expression like eq 12 from the trajectory initial phase space point (\mathbf{P}, \mathbf{Q}) to the final point variables $(\mathbf{P}_t, \mathbf{Q}_t)$, the Jacobian of this transformation is unity. The integrand conditioning Gaussian integrals are then introduced in displacements of the final points of the trajectories. Thus we multiply our semiclassical expression by the following representation of unity

$$\prod_{k=1}^d \left(\frac{c_P^k c_Q^k}{\pi^2} \right)^{1/2} \int d\mathbf{p}_t \int d\mathbf{q}_t \exp[-c_P^k (\mathbf{p}_t^k - \mathbf{p}_i^k)^2] \times \exp[-c_Q^k (\mathbf{q}_t^k - \mathbf{q}_i^k)^2] = 1 \quad (14)$$

By choosing these preaveraging Gaussians to be sufficiently narrow (making the c_P^k and c_Q^k appropriately large for the various degrees of freedom, k) we can truncate the expansion of the phase of the semiclassical integrand in final point displacements to low order and perform the preaveraging integrals analytically. The final result is obtained by returning to an expression involving integrals over trajectory initial conditions but the weights of the different trajectories must be determined by reverse propagating the auxiliary trajectory stability equations from the final points reached by each trajectory. For the results reported here we have employed Herman's first order preaveraging form in which an initial function whose coherent state representation has the form $\langle \mathbf{PQ} | \psi_0 \rangle = |\langle \mathbf{PQ} | \psi_0 \rangle| \exp[i\theta_0/\hbar]$ is propagated according to the result

$$|\psi_t\rangle = \int \frac{d\mathbf{P}}{(2\pi\hbar)^d} d\mathbf{Q} |\mathbf{P}_t, \mathbf{Q}_t\rangle C(\mathbf{P}, \mathbf{Q}, t) \exp\left[\frac{i}{\hbar} S(\mathbf{P}, \mathbf{Q}, t)\right] \times \exp[-\Delta\theta^2(\mathbf{P}, \mathbf{Q}, t)] \langle \mathbf{PQ} | \psi_0 \rangle \quad (15)$$

Here the exponent in the preaveraging weight factor has the form

$$\Delta\theta^2(\mathbf{P}, \mathbf{Q}, t) = \sum_{k=1}^d \left\{ \left(\frac{1}{4\hbar^2 c_P^k} \right) \left(\frac{\partial\theta}{\partial\mathbf{P}_t^k} \right)^2 (\mathbf{P}, \mathbf{Q}, t) + \left(\frac{1}{4\hbar^2 c_Q^k} \right) \left(\frac{\partial\theta}{\partial\mathbf{Q}_t^k} \right)^2 (\mathbf{P}, \mathbf{Q}, t) \right\} \quad (16)$$

For the coherent state basis set we find that the phase derivatives in the above expression are the components of the following vectors

$$\frac{\partial\theta}{\partial\mathbf{Q}_t} = \left(\frac{\partial\theta_0}{\partial\mathbf{Q}} - \mathbf{P} \right)^T \frac{\partial\mathbf{Q}}{\partial\mathbf{Q}_t} + \left(\frac{\partial\theta_0}{\partial\mathbf{P}} \right)^T \frac{\partial\mathbf{P}}{\partial\mathbf{Q}_t} \quad (17)$$

and

$$\frac{\partial\theta}{\partial\mathbf{P}_t} = \left(\frac{\partial\theta_0}{\partial\mathbf{Q}} - \mathbf{P} \right)^T \frac{\partial\mathbf{Q}}{\partial\mathbf{P}_t} + \left(\frac{\partial\theta_0}{\partial\mathbf{P}} \right)^T \frac{\partial\mathbf{P}}{\partial\mathbf{P}_t} \quad (18)$$

In these expressions we assume that all terms which do not contain the time reversed monodromy matrixes $(\partial\mathbf{Q}/\partial\mathbf{P}_t)$, for example) are small and can be ignored compared to these factors which grow exponentially in systems exhibiting chaotic dynamics.

The more conventional approach,²⁰ on the other hand, introduces the preaveraging Gaussians in initial point displacements

resulting in a travelling coherent state basis set in which the coherent state widths vary in different ways along different trajectories. If the coherent state basis elements get very narrow many trajectories may be needed to represent the dynamical wave function in these regions. Generally with this approach, however, the preaveraged weights of the trajectories associated with these narrow coherent state basis elements are small so they make little contribution anyway. This deterioration of the basis set is avoided with Herman's frozen Gaussian approach.

The approach we use to implement preaveraging can thus be summarized as follows: (1) Trajectory initial conditions (\mathbf{P}, \mathbf{Q}) are first sampled from the distribution $|\langle \mathbf{PQ} | \psi_0 \rangle|$. Each initial condition generated in this way is given an initial weight $\exp[i\theta_0(\mathbf{P}, \mathbf{Q})/\hbar]$. (2) Next these trajectories are evolved classically to phase space points $(\mathbf{P}_t, \mathbf{Q}_t)$ at time t . At this point we evaluate the coherent state representation of whatever function concerns us for our time correlation function. Along each trajectory we compute the classical action S and weight each trajectory's contribution by $\exp[iS/\hbar]$. (3) Now we must compute the preaveraging weight based on the time reversed monodromy factors appearing in eq 17. This is accomplished by setting the monodromy matrixes to the appropriate unit or zero matrixes at time t and reverse time integrating eq 10 back $t = 0$. This reverse time integration requires the evaluation of the Hessian at all points along each classical trajectory. It can be shown^{23,34} that the $C(\mathbf{P}, \mathbf{Q}, t)$ weighting factors can be computed from these reverse propagated monodromy matrixes according to the following result

$$C(\mathbf{P}, \mathbf{Q}, t) = \left\{ \det \left[\frac{1}{2} (\tilde{\mathbf{M}}_{PP} + \tilde{\mathbf{M}}_{QQ} + 2\gamma i \hbar \tilde{\mathbf{M}}_{QP} - \frac{i}{2\gamma \hbar} \tilde{\mathbf{M}}_{PQ}) \right] \right\}^{1/2} \quad (19)$$

with $\tilde{\mathbf{M}}_{QP}^{(ij)} = \partial Q^i / \partial P_t^j$ for example. With this result the monodromy matrixes need only be propagated in the reverse direction. We can thus finally weight each trajectory's contribution by the $C(\mathbf{P}, \mathbf{Q}, t)$ and preaveraging weight factors according to eq 15 to obtain our final results.

In strongly chaotic systems it may prove more fruitful to incorporate the positive definite, rapidly damping preaveraging weight factor $\exp[-\Delta\theta^2(\mathbf{P}, \mathbf{Q})]$ into the importance sampling Monte Carlo procedure which we use to integrate over trajectory initial conditions. We are currently exploring such an approach for application to many body systems.

For studying our excited I_3 vibrational dynamics probed in I_3^- photodetachment experiments; however, the straightforward preaverage weighting procedure described above provides a reliable way to implement semiclassical expressions. In Figure 6, for example, we show that the spurious fragmentation of the wave function observed with the bare application of semiclassical propagation is completely remedied by use of the preaveraging procedures discussed above. The spurious effects of the high energy components of our ensemble which should be controlled by interference are effectively removed by the preaverage weighting procedure. We also see from Figure 5b a dramatic improvement in the time dependence of the energy components, and in energy conservation using this preaveraging approach.

We conclude this section with an observation on the relative amount of work involved in the semiclassical calculation of the thermal averaged time correlation given in eqs 5 and 12 as compared to its fully quantum mechanical calculation. As a result of our assumption that the initial states are prepared by exciting a thermal distribution of harmonic oscillator vibrational states in the ground electronic state well, each of these initial states has the form of a product of Gaussians times polynomials

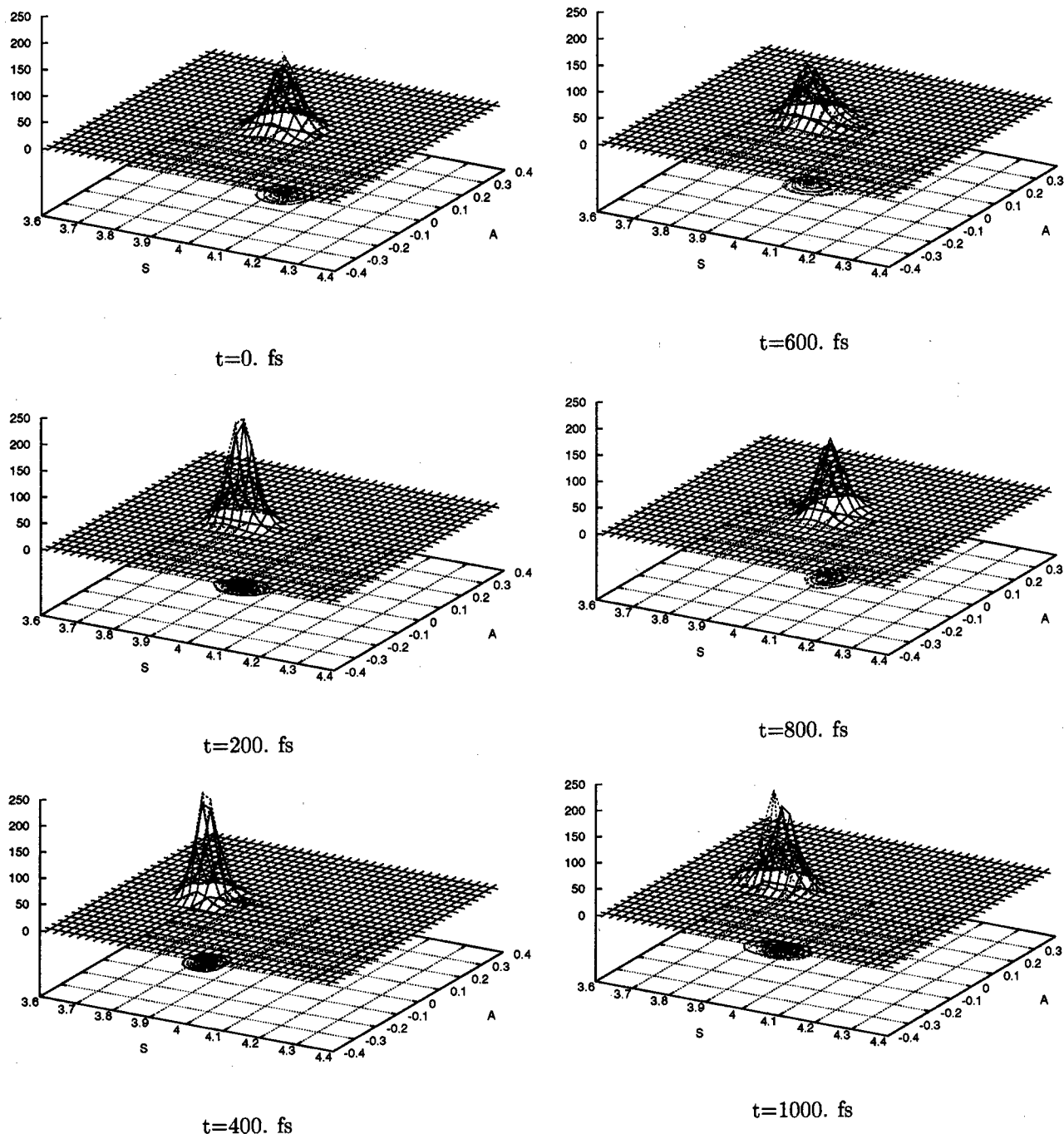


Figure 6. Propagation of initial harmonic I_3^- ground vibrational state on the photoexcited I_3 DIM potential surface. Surface of solid lines is propagated using the preaveraging approach for semiclassical algorithm. The dashed surface is the full quantum wavefunction propagated using split operator FFT methods. The wavefunctions are plotted as functions of symmetric and antisymmetric stretch normal modes in Angstroms.

in the various normal modes of the ground state surface. For the full quantum calculation of the thermally weighted sum of correlation functions in eq 5 we must take each of the different thermally accessible initial states, evolve them subject to the nuclear Hamiltonian of the excited electronic state, and finally overlap the evolved function at time t with its initial state to obtain the component signal associated with this particular initial state. Correlation functions computed in this way must finally be weighted with the appropriate Boltzman factors and added to give the total correlation function as in eq 5. Thus if there are n thermally accessible states, we need to perform n propagations to construct our fully quantum thermal average.

For the semiclassical calculation described above, on the other hand, the propagation of all the different harmonic oscillator

initial states can be accomplished by a SINGLE semiclassical propagation from the product Gaussian ground state initial distribution of position and momentum parameters (see the exponential factors in eq 13). Each of the different state contributions in this semiclassical representation of the dynamics is simply obtained by multiplying each trajectory's contribution by the appropriate product polynomials (see the polynomial factors in eq 13), and their complex conjugates, in the initial and final phase space points of the given trajectory and adding these trajectory contributions to the ensemble average. There is thus a qualitatively different amount of effort required for these quantal and semiclassical calculations due to fundamental differences in the nature of the quantal and semiclassical propagators and how they evolve wave functions. The same potential for savings

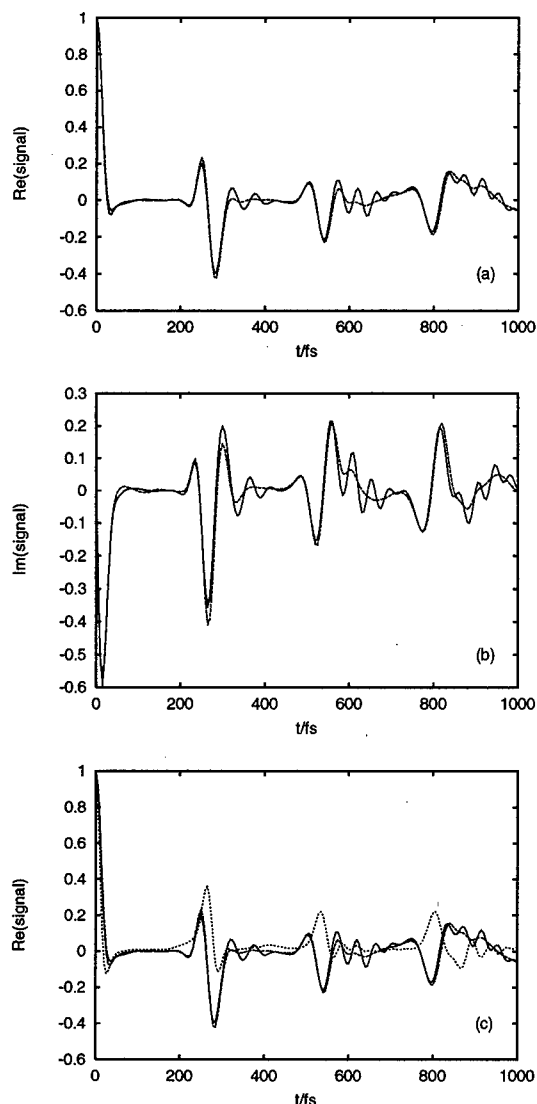


Figure 7. Parts a and b show real and imaginary parts of thermal averaged time correlation function $\phi_{IF}(t;\beta)$ defined in eq 5 for $T = 205$ K. Solid curves are full quantum calculations and dashed curves are preaveraged semiclassical calculations. Part c compares real part of correlation function computed with full quantum (solid curve), preaveraged semiclassical (dashed curve), and results obtained when the trajectory stability factors are ignored (dotted curve).

in the semiclassical calculation of thermal averaged time correlation functions exists when ever the initial states can be written as a product of functions in the various coordinates and fast varying pieces of these functions can be pulled out as an initial phase space distribution for the parameters in a coherent state basis set representation and the remainder of the initial state functions are incorporated in multiplicative quantities to be averaged over initial and final points of classical trajectories as in eq 12. In future work we will explore the application of these ideas to study rotational dynamics.³⁵

3. Results and Discussion

In Figure 7 we present our calculated thermal averaged time correlation functions as defined in eq 5 for the ground-state I_3 vibrational dynamics excited as a result of photoelectron detachment from ground-state I_3^- . For comparison we present the correlation function obtained from full quantum calculations as well as our preaverage weighted semiclassical results. Generally, the agreement between these calculated correlation functions is very good with the semiclassical results reproducing

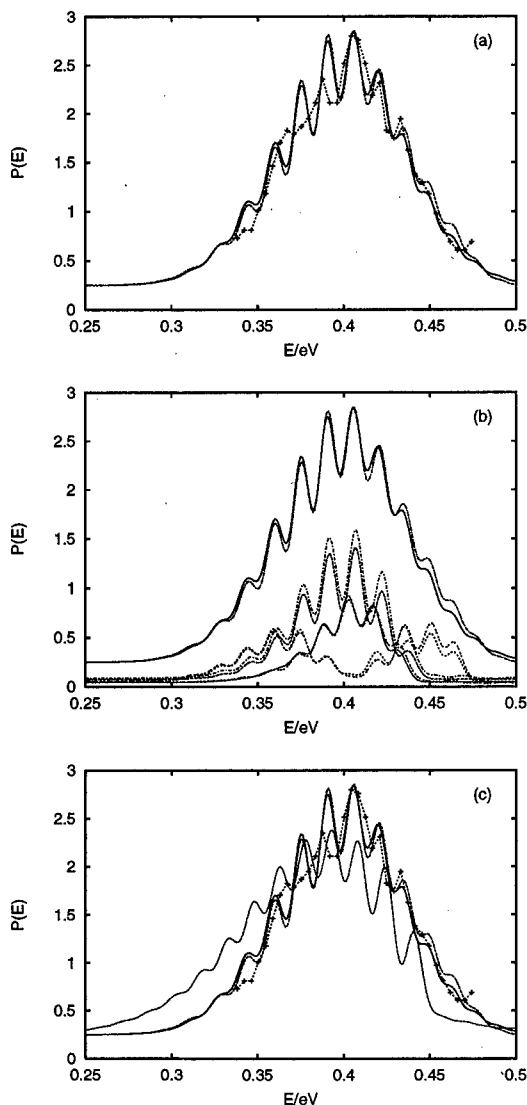


Figure 8. (a) Comparison of I_3^- photoelectron spectrum calculated with full quantum nuclear propagation (solid curve), preaveraged semiclassical nuclear propagation (dashed curve), and experimental curves (dotted curve with + symbols). (b) Comparison of full quantum and preaveraged semiclassical contributions to total signal. Upper curves are total signals, the three sets of component curves below these are contributions starting from the ground vibrational state $(S,A) = (0,0)$ (largest components), contributions from low initial symmetric stretch excitations, i.e., $\sum_{n=1}^3(n,0)$ (bimodal contributions), and contributions from low initial anti-symmetric stretch excitations, i.e., $\sum_{n=1}^3(0,n)$ (band with shifted peaks). (c) Same as that in part a only here we also include the result obtained when trajectory stability factors are ignored (shifted dotted curve).

the general periodicity very accurately and smoothing out some of the finer details of the fully quantum signal. In the bottom part c of this figure we also compare the real part of the correlation function obtained by setting the C factor trajectory stability weights to unity. This is a commonly used approximation³⁶⁻³⁸ which gives considerable numerical savings in semiclassical calculations. Unfortunately, as we see from this figure, the time correlation function obtained with this approximation for the vibrational dynamics of our I_3 system is really quite poor.

The time signals presented in Figure 7 can be transformed to energy space according to eq 4 giving the distributions of photoejected electron kinetic energies which we compare with the experimental results of Neumark and co-workers in Figure 8a. The calculated spectra presented in this figure were generated

assuming a Gaussian photoexcitation pulse width of $\tau = 100$ fs. The peak positions and band shape of the full quantum and semiclassical results agree with one another very closely and the overall shape of these calculated curves is in near quantitative agreement with the experimental results. The main deviations between the calculated and experimental results apparent in this figure are on the low energy side of the band where the calculated curves display a little too much structure and the peak positions may be shifted slightly. Generally, however, the close agreement with experiment is quite good.

In part b of Figure 8 we show a break down of our calculated signals into contributions from various initial states with in the thermal distribution. We see that the general shape of the final band results not only from contributions from the ($S = 0, A = 0$) or (0,0) ground vibrational state but there are also significant contributions from symmetric stretch excitations ($n,0$) which tend to broaden the band as they give contributions on either side of band center, and antisymmetric stretch excitations (0, n) which give slightly shifted contributions near the middle of the band. On the basis of these observations it is clear that several factors could be contributing to the small differences between the experimental and calculated spectra described above: First, with in the harmonic I_3^- initial surface approximation the hot bands line up, rather than being displaced due to anharmonicities. This will of course result in too much structure in the final spectrum. Next, uncertainty in the difference between the symmetric and antisymmetric stretch frequencies of the I_3^- initial surface can lead to an inaccurate representation of the interference between the peaks and troughs of the various contributions to the spectrum. Further, we have ignored the bending motions of the molecule and overlapping different bend vibration progressions could easily fill in the spaces between the bands we see in our restricted calculation results, thus smearing much of the detailed structure we observe. Our neglect of molecular rotations of course has a similar effect and including such motions would further smear out the features leading to closer agreement with experiment. Finally, if the shape of our DIM I_3 surface was inaccurate, our dynamics over this surface would fail give a good representation of the Franck-Condon factors responsible for controlling the amplitude of the various hot band contributions to the spectrum. Given all these potential problems, the fact that we get a spectrum which so closely resembles the experimental results is quite remarkable.

In the bottom part c of Figure 8 we compare the spectra from our quantum and semiclassical calculations with that obtained from ignoring the C trajectory stability factors. Not surprisingly, just as with the time correlation functions, leaving out these factors which account for the variation in semiclassical path space volume around each classical trajectory leads to significant errors.

4. Conclusions

In this paper we have presented a model potential describing the symmetric and antisymmetric stretch motions of a linear I_3 molecule obtained from a semiempirical diatomics-in-molecules approach. This model system has been employed as a test of various semiclassical methods for propagating nuclear vibrational wavefunctions over this highly anharmonic, weakly bound potential surface.

We have demonstrated the problems with implementing a bare semiclassical approach which involves a straightforward weighting of the contributions from various trajectories by a semiclassical approximation to the volume of path space around each classical trajectory. These approximate path space volumes

are related to trajectory stability with respect to changes in initial conditions. In regions where the classical trajectories become chaotic this semiclassical approximation to the local path space volume thus diverges and we have demonstrated the disastrous effect of these chaotic trajectories at longer times in the application of the bare semiclassical approach with a finite ensemble of trajectories to this realistic two-dimensional model problem.

Contributions from these unstable trajectories should interfere destructively with other trajectories emanating from these chaotic regions as the integrand is highly nonstationary with respect to variations in trajectory initial conditions over which we integrate to obtain the semiclassical propagator. We have shown through comparison with exact full quantum calculations that the first order stationary phase filtering or preaveraging approach proposed by Herman^{22,23} provides a simple to implement, potentially quite general, and extremely effective solution to this problem for our model system. We have further shown that the alternative approach to handling the contributions from chaotic trajectories in which we simply assume that the path space volume associated with all trajectories is a constant, independent of trajectory, yields poor dynamical results for this realistic problem.

Finally by comparing the ejected photoelectron kinetic energy distributions calculated from our semiclassical and quantum calculations with the experimental results of Neumark¹ we have demonstrated the remarkable accuracy of our semiempirical I_3 potential which gives reasonable estimates of the binding energies and stretch vibrational frequencies with no adjustable parameters.

5. Acknowledgment

We are grateful to Prof. Ruth Lynden-Bell for important discussions on limiting the DIM basis set size through symmetry requirements. We gratefully acknowledge financial support for this work from the National Science Foundation (Grant CHE9521793) and the Petroleum Research Fund of the American Chemical Society (Grant 34927-AC6). We also acknowledge a generous allocation of supercomputer time from the Boston University's center for Scientific Computing and Visualization.

6. Appendix

The time dependent perturbation theory approach we outline here to obtain the expression we use to calculate the photoelectron spectrum is very similar to that presented by Heller for the calculation of the Raman spectrum.³⁹ This approach is commonly used in many spectroscopic applications.⁴⁰

The time dependent Hamiltonian describing the molecular ion in a classical radiation field is $\hat{H}(t) = \hat{H}_{\text{molec}} - \hat{\mu} \cdot \epsilon(t)$ where $\hat{\mu}$, for our molecular photoionization example, is the molecular ion dipole operator, $\epsilon(t)$ is the time dependent electric field, and $\hat{H}_{\text{molec}} = \hat{K}_N(\hat{\mathbf{P}}) + \hat{H}_{\text{el}}(\hat{\mathbf{p}}, \hat{\mathbf{r}}; \hat{\mathbf{R}})$ is the molecular ion Hamiltonian composed of the usual nuclear kinetic and electronic contributions. As usual we employ the Born-Oppenheimer adiabatic electronic eigenstates $\Phi_j(\mathbf{r}, \mathbf{R})$ defined for a given nuclear configuration by $\hat{H}_{\text{el}}(\hat{\mathbf{p}}, \hat{\mathbf{r}}; \mathbf{R})\Phi_j(\mathbf{r}, \mathbf{R}) = E_j(\mathbf{R})\Phi_j(\mathbf{r}, \mathbf{R})$ as a basis set to represent the electronic distribution for nuclear configuration \mathbf{R} .

The time dependent wave function of the molecular ion coupled to the radiation field $\Psi(\mathbf{r}, \mathbf{R}, t)$ satisfies

$$i\hbar \frac{\partial}{\partial t} \Psi(\mathbf{r}, \mathbf{R}, t) = \hat{H}(t) \Psi(\mathbf{r}, \mathbf{R}, t) \quad (20)$$

Writing the solution of this equation in terms of the above adiabatic electronic basis set as

$$\Psi(\mathbf{r}, \mathbf{R}, t) = \sum_f \chi_f(\mathbf{R}, t) \Phi_f(\mathbf{r}, \mathbf{R}) \quad (21)$$

and making the Born–Oppenheimer approximation we find that if we arrange the nuclear coefficient functions $\chi_f(\mathbf{R}, t)$ into a vector $\mathbf{X}(\mathbf{R}, t)$ they satisfy the following matrix equation

$$i\hbar \frac{\partial}{\partial t} \mathbf{X}(\mathbf{R}, t) = \hat{\mathbf{H}}(t) \mathbf{X}(\mathbf{R}, t) \quad (22)$$

where $\hat{\mathbf{H}}(t) = \hat{\mathbf{H}}_0 + \mathbf{V}(t)$ is a matrix of nuclear Hamiltonians, the time independent part of which has elements $[\hat{\mathbf{H}}_0]_{IK} = \hat{H}_K \delta_{IK}$ where $\hat{H}_K = \hat{K}_N + E_K(\mathbf{R})$ is the Hamiltonian governing nuclear motion over the Born–Oppenheimer surface $E_K(\mathbf{R})$. The time dependent part of the matrix has elements $[\mathbf{V}(t)]_{IK} = -\epsilon(t) \cdot \mathbf{M}_{IK}(\mathbf{R})$ which describe how the radiation field couples the nuclear coefficient functions on different electronic surfaces. Here $\mathbf{M}_{IK}(\mathbf{R}) = \langle \Phi_I | \hat{\mu} | \Phi_K \rangle(\mathbf{R})$.

The first order time dependent perturbation theory solution of this system of equations is readily obtained as

$$\mathbf{X}(\mathbf{R}, t) = \exp\left[-\frac{i}{\hbar} \hat{\mathbf{H}}_0(t - t_0)\right] \mathbf{X}(\mathbf{R}, t_0) + \frac{1}{i\hbar} \int_{t_0}^t dt' \times \\ \exp\left[-\frac{i}{\hbar} \hat{\mathbf{H}}_0(t - t')\right] \mathbf{V}(t') \exp\left[-\frac{i}{\hbar} \hat{\mathbf{H}}_0(t' - t_0)\right] \mathbf{X}(\mathbf{R}, t_0) \quad (23)$$

We assume that the system is prepared in some initial Born–Oppenheimer vibronic eigenstate $\chi_{Iv}(\mathbf{R}) \Phi_I(\mathbf{r}, \mathbf{R})$ where χ_{Iv} are the vibrational eigenstates of the nuclear Hamiltonian (specified by the vector \mathbf{v} of vibrational quantum numbers) for electronic state I , i.e., $\hat{H}_I(\mathbf{R}) \chi_{Iv}(\mathbf{R}) = E_{Iv} \chi_{Iv}(\mathbf{R})$ so the initial nuclear coefficient vector, $\mathbf{X}(\mathbf{R}, 0)$ has only a single nonzero entry, $\chi_{Iv}(\mathbf{R})$ as the I th component function. Thus to first order in perturbation theory eq 23 gives that the nuclear coefficient function for the J th electronic state at time t will be

$$\chi_{Jv}(\mathbf{R}, t) = \exp\left[-\frac{i}{\hbar} \hat{H}_J(t - t_0)\right] \chi_{Iv}(\mathbf{R}) \delta_{IJ} + \frac{1}{i\hbar} \int_{t_0}^t dt' \times \\ \exp\left[-\frac{i}{\hbar} \hat{H}_J(t - t')\right] V_{JI}(t') \exp\left[-\frac{i}{\hbar} \hat{H}_I(t' - t_0)\right] \chi_{Iv}(\mathbf{R}) \quad (24)$$

For our photoelectron experiment described in subsection 2.2 $\Phi_J = \Phi_{F\epsilon}$ so $\hat{H}_J(\mathbf{R}) = \hat{H}_F(\mathbf{R}) + \epsilon$. Thus the probability of observing a photoelectron with kinetic energy ϵ and depositing the system in neutral state F at time t from a molecular ion prepared in state Iv before time t_0 when a radiation field was applied is obtained from the square of the above amplitude as

$$P(F\epsilon, Iv, t) = \\ \frac{1}{\hbar^2} \int_{t_0}^t dt' \int_{t_0}^{t'} dt'' \exp\left[-\frac{i}{\hbar} (\epsilon - E_{Iv})(t'' - t')\right] V_{IF\epsilon}(t'') V_{FI\epsilon}(t') \times \\ \left\langle \chi_{Iv} \left| \exp\left[-\frac{i}{\hbar} \hat{H}_F(t'' - t')\right] \right| \chi_{Iv} \right\rangle \quad (25)$$

In writing this result we have made the Condon approximation and assumed that the dipole matrix elements vary weakly with nuclear configuration so $V_{IF\epsilon}$, etc., is approximately independent of \mathbf{R} .

We further suppose that the excitation pulse at frequency ω has a Gaussian time profile with experimental width parameter τ , so that $V_{IF\epsilon}(t) = A_{IF\epsilon} \exp[-t^2/2\tau^2] \cos \omega t$. Transforming the double time integral to sum and difference times, and extending

t_0 to $-t$, we can perform the integration over the sum variable analytically and keeping only the resonant term we find the infinite time probability of observing a photoelectron with energy ϵ resulting from the transition $F \leftarrow Iv$ is obtained as

$$P(F\epsilon, Iv, \infty) \sim \frac{|A_{IF\epsilon}|^2}{\hbar^2} \text{Re} \left\{ \int_0^\infty ds \exp\left[-\frac{i}{\hbar} (\epsilon - E_{Iv} - \hbar\omega)s\right] \times \right. \\ \left. \exp\left[-\frac{s^2}{4\tau^2}\right] \left\langle \chi_{Iv} \left| \exp\left[-\frac{i}{\hbar} \hat{H}_F s\right] \right| \chi_{Iv} \right\rangle \right\} \quad (26)$$

Finally the total probability, $P_\beta(\epsilon)$ of observing ejected photoelectrons with kinetic energy ϵ at long time if the molecules are initially in thermal equilibrium at a temperature T , which is proportional to the signal in these experiments, is obtained by summing over a Boltzman distribution of initial states and adding the signal contributions from all possible final states, thus

$$P_\beta(\epsilon) = \sum_{Iv} \exp[-\beta E_{Iv}] \sum_F P(F\epsilon, Iv, \infty) \quad (27)$$

where $\beta = 1/k_B T$.

In our calculations we assume that the ground electronic state of our molecular anion system is well separated from any excited electronic states so the Boltzman contributions from these higher energy electronic states can be ignored and we need only sum over initial excited vibrational states on the ground electronic state surface. Further, we will suppose that the final excited electronic states of interest, which involve only the ground state of the neutral molecule and the ejected electron with various amounts of kinetic energy, are sufficiently well separated from other excited neutral states so these higher excited final states can be neglected for the ground-state to ground-state band we wish to study.

Note in this work we assume that the quantities $|A_{IF\epsilon}|^2$ are weakly varying functions of electronic kinetic energy ϵ , compared to the time integral in eq 26. Finally, we have adjusted our calculated spectrum so that its peak amplitude matches experiment for purpose of comparison.

References and Notes

- (1) Taylor, T. R.; Asmis, K. R.; Zanni, M. T.; Neumark, D. M. *J. Chem. Phys.* **1999**, *110*, 7607.
- (2) Batista, V. S.; Coker, D. F. *J. Chem. Phys.* **1996**, *105* 4033.
- (3) It is possible that the ground state of I_3 has $M_J = \pm 3/2$. Some of the states with this angular momentum projection will have the same dissociation limit as the $M_J = \pm 1/2$ which we assume to be the ground state in this analysis. These states are currently under investigation and may lie close in energy to our assumed ground state. The experiments may probe a statistical distribution of the various states.
- (4) Ellison, F. O. *J. Am. Chem. Soc.* **1963**, *85*, 3540.
- (5) Tully, J. C. In *Semiempirical Methods of Electronic Structure Calculation, Part A: Techniques*; Segal, L. A., Ed.; Plenum: New York, 1977.
- (6) Ruhman, S.; Lynden-Bell, R.; Kosloff, R.; Vala, J. *J. Chem. Phys.* **1998**, *109*, 9928.
- (7) Sato, H.; Hirata, F.; Myers, A. B. *J. Phys. Chem. A* **1998**, *102*, 2065.
- (8) Feit, M. D., Jr.; Fleck, J. A.; Steiger, A. *J. Comput. Phys.* **1982**, *47*, 412.
- (9) Kosloff, R. *J. Phys. Chem.* **1988**, *92*, 2087.
- (10) Herman, M. F.; Kluk, E. *Chem. Phys.* **1984**, *91*, 27.
- (11) Kluk, E.; Herman, M. F.; Davis, H. L. *J. Chem. Phys.* **1986**, *84*, 326.
- (12) Kay, K. G. *J. Chem. Phys.* **1994**, *100*, 4377.
- (13) Kay, K. G. *J. Chem. Phys.* **1994**, *100*, 4432.
- (14) Kay, K. G. *J. Chem. Phys.* **1994**, *101*, 2250.
- (15) Kay, K. G. *J. Chem. Phys.* **1997**, *107*, 2313.
- (16) Madhusoodanan, M.; Kay, K. G. *J. Chem. Phys.* **1998**, *109*, 2644.

- (17) Lichtenberg, L.; Lieberman, M. In *Computer Simulation in Chemical Physics*; Springer-Verlag: New York, 1983.
- (18) Heller, E. J. *J. Chem. Phys.* **1991**, *94*, 2723.
- (19) Walton, A. R.; Manolopoulos, D. E. *Chem. Phys. Lett.* **1995**, *244*, 448.
- (20) Walton, A. R.; Manolopoulos, D. E. *Mol. Phys.* **1996**, *87*, 961.
- (21) Hulme, J.; Brewer, M.; Manolopoulos, D. E. *J. Chem. Phys.* **1997**, *106*, 4832.
- (22) Herman, M. F.; Guerin, B. *Chem. Phys. Lett.* **1998**, *286*, 361.
- (23) Herman, M. F. *Chem. Phys. Lett.* **1997**, *275*, 445.
- (24) Campolieti, G.; Brumer, P. *J. Chem. Phys.* **1998**, *109*, 2999.
- (25) Elran, Y.; Kay, K. G. *J. Chem. Phys.* **1990**, *110*, 3653.
- (26) Herman, M. F.; Coker, D. F. *J. Chem. Phys.* **1999**, *111*, 1801.
- (27) Filinov, V. S. *Nucl. Phys. B* **1986**, *271*, 717.
- (28) Makri, N.; Miller, W. H. *Chem. Phys. Lett.* **1987**, *139*, 10.
- (29) Makri, N.; Miller, W. H. *J. Chem. Phys.* **1988**, *89*, 2170.
- (30) Coalson, R. D.; Freeman, D. L.; Doll, J. D. *J. Chem. Phys.* **1986**, *85*, 4567.
- (31) Doll, J. D.; Freeman, D. L.; Gillan, M. J. *Chem. Phys. Lett.* **1988**, *143*, 277.
- (32) Spath, B. W.; Miller, W. H. *J. Chem. Phys.* **1996**, *104*, 95.
- (33) Garashchuk, S.; Tannor, D. J. *Chem. Phys. Lett.* **1996**, *262*, 477.
- (34) Herman, M. F. *J. Chem. Phys.* **1986**, *85*, 2069.
- (35) Xiong Sun; Miller, W. H. *J. Chem. Phys.* **1998**, *108*, 8870.
- (36) Ovchinnikov, M.; Apkarian, V. A. *J. Chem. Phys.* **1997**, *106*, 5775.
- (37) Ovchinnikov, M.; Apkarian, V. A. *J. Chem. Phys.* **1998**, *108*, 2277.
- (38) Ovchinnikov, M.; Apkarian, V. A. *J. Chem. Phys.* **1996**, *105*, 10312.
- (39) Lee, S. Y.; Heller, E. J. *J. Chem. Phys.* **1979**, *71*, 4777.
- (40) Batista, V. S.; Zanni, M. T.; Greenblatt, B. J.; Neumark, D. M.; Miller, W. H. *J. Chem. Phys.* **1999**, *110*, 3736.

Experience chemistry as it happens...

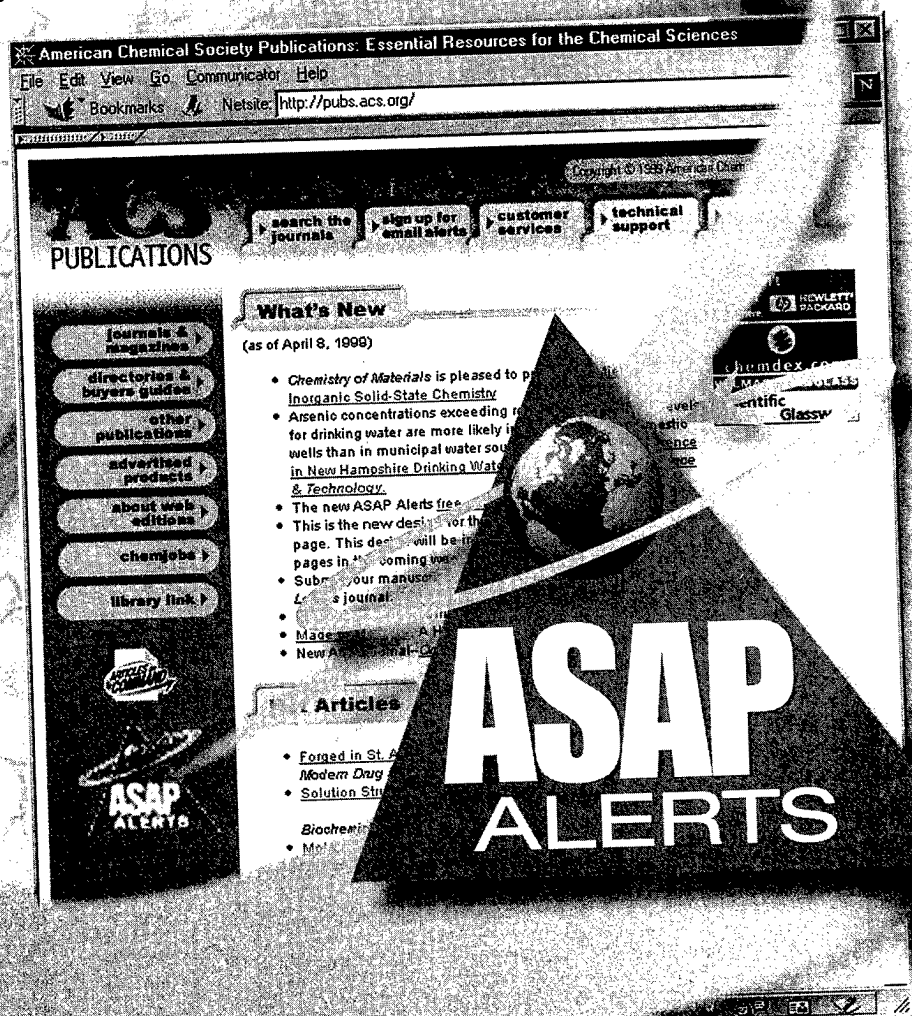
Introducing **ASAP Alerts** - a new **FREE** e-mail alert service from ACS Publications. This new service will send you the latest research posted to Articles A.S.A.P.SM (As Soon As Publishable) - a compilation of peer-reviewed, fully edited articles published two to eleven weeks prior to print.

The e-mail message will include:

- The Journal Name, Article Title, and Author Name(s)
- Official Web Publication Date
- A direct URL link to the full-text article - subscribers to the Web Edition will access the full-text article, while non-subscribers may purchase the full-text article using our Articles on Command service.

ASAP Alerts

delivers information either daily or weekly from one or all of the ACS Web Editions - you choose.



*Just think, cutting-edge
research delivered right*

Sign Up Today!



AMERICAN CHEMICAL SOCIETY

Science That Matters.

**How can ACS Web Edition subscribers
instantly access abstracts of article
references from the CAS database?**

[CAS]



just click this

Now, ACS Web Edition subscribers can immediately link from references in all ACS Web Edition articles to the relevant Chemical Abstracts Service (CAS) record, gaining instant access to the abstract and bibliographic information, regardless of article publisher.

Available exclusively from the American Chemical Society, this new capability greatly enriches and extends the value of the original article, enabling scientists, librarians and academicians to achieve significantly faster and more productive results.

Visit an article from the first edition
of *Organic Letters* today at
<http://pubs.acs.org/reflink>
and simply click on the CAS tag in the
references to try out this exciting new feature.

It's that easy.

ACS Web Edition Subscribers: use the HTML
version to avail of this new reference-linking
capability—available now for all ACS Web Editions.

ACS  WEB EDITIONS

Know it Now!

<http://pubs.acs.org>

American Chemical Society Publications Division

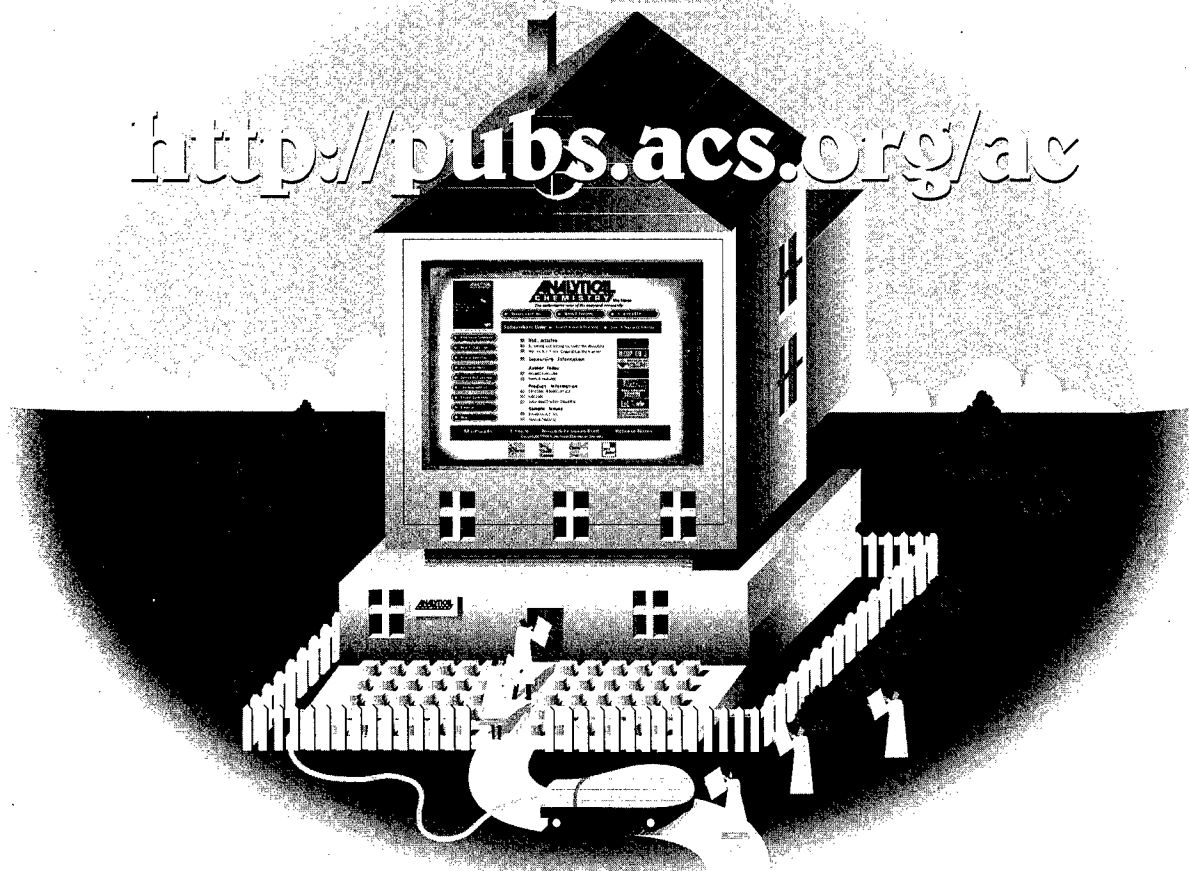
Member & Subscriber Services, P.O. Box 3337, Columbus, OH 43210

Phone: (800) 333-9511 (US & Canada); (614) 447-3776

Fax: (614) 447-3671 • E-mail: service@acs.org • <http://pubs.acs.org>

Here's the address of the ideal research assistant

<http://pubs.acs.org/ac>



DROP IN AND GET ACQUAINTED

Your whole career, you've been looking for the perfect research assistant – *Analytical Chemistry Web Edition*.

This is an assistant that will be there for you 24 hours a day. One that's always up on the latest progress and innovation. Incredibly easy to work with and never too tired to dig right in.

Most impressive of all, your new assistant can access cutting-edge research from 1996 to the present; search materials by authors, subjects, keywords and more; and deliver hard copy — including all the same text and graphics as in the print edition of *Analytical Chemistry* — in a matter of seconds.

GIVE YOUR NEW ASSISTANT A TRIAL RUN

There's a FREE sample waiting online. Just check in at <http://pubs.acs.org/ac>. Here on our home page find all the information you need to order.

Soon you'll be reviewing the very latest in ground breaking research through *Articles ASAP*SM — meaning as soon as it's been peer-reviewed, edited and approved for publication (up to 4 weeks before the print edition cover date!) And your assistant will also keep you current in the analytical field with the latest articles, news and product reviews.

It all will be possible thanks to your innovative new research assistant... *Analytical Chemistry Web Edition*.

**ANALYTICAL
CHEMISTRY**

PUBLISHED BY THE AMERICAN CHEMICAL SOCIETY

Web Edition... *Your Online Connection to the Number One Research Authority*

Choosing a graduate school?

Need to know who's doing research critical to yours?

The ACS Directory of Graduate Research 1997

is the most current source of information on chemical research and researchers at universities in the United States and Canada. The directory

- lists universities with names and biographical information for all faculty members; their areas of specialization; titles of all papers published within the last two years; and individual telephone numbers, fax numbers, and computer addresses; and
- provides a statistical summary of academic chemical research, with information by department on numbers of full- and part-time faculty, postdoctoral appointments, graduate students, and M.S. and Ph.D. degrees granted.

Inside, you'll find information on

✓692 academic departments ✓12,030 faculty members ✓91,515 publication citations

New! DGRweb, a searchable database on the Web. Go to ChemCenter for more details: <http://www.chemcenter.org>.

No academic institution or chemically oriented business can afford to be without the ACS Directory of Graduate Research 1997! Order today by calling toll-free, (800) 227-9919, or dialing direct, (202) 776-8100. Or, use the coupon below. Fax your order to (202) 872-6067.

The directory has listings for

- chemistry
- chemical engineering
- biochemistry
- medicinal/pharmaceutical chemistry
- clinical chemistry
- polymer science
- food science
- forensic science
- marine science
- toxicology
- materials science
- environmental science

Please send me _____ copy(ies) of the ACS Directory of Graduate Research 1997.

Price: U.S. & Canada, \$65 Export, \$78

☐ Payment enclosed (make payable to American Chemical Society)

☐ Purchase order enclosed, P.O. # _____

Charge my: ☐ MasterCard/VISA ☐ American Express

Account # _____ Expires _____

Signature _____

Phone _____

Ship books to:

Name _____

Address _____

City, State, ZIP _____

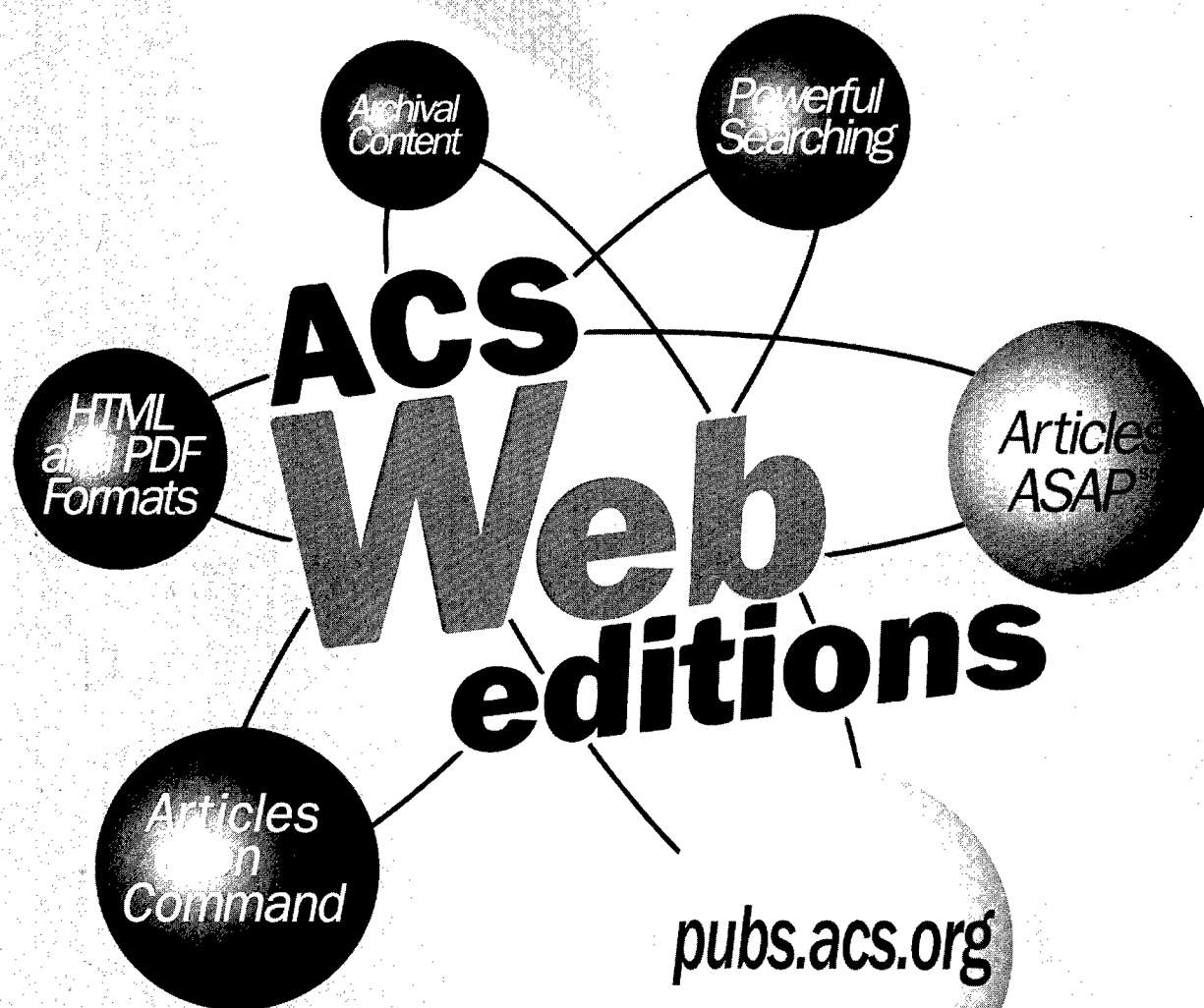
ORDERS FROM INDIVIDUALS MUST BE PREPAID.

Please allow 4-6 weeks for delivery.

Prices are quoted in U.S. dollars. Mail this order form with your payment or purchase order to: American Chemical Society, Attn:

Customer Service & Sales, P.O. Box 57136, Washington, DC 20037-0136.

**Today's Research...
Tomorrow's Discoveries...**



Know It NOW.

Get a jump on significant new findings—two weeks to almost 3 months before they appear in print—with Articles ASAP (As Soon As Publishable). Fully approved for publication, Articles ASAP are ready for your immediate use...all that's missing is the wait.

Draw on a rich, fast-growing archive of material. View articles in HTML or PDF format...as an abstract or full text. Link to interactive scientific databases. Even manipulate molecular structures and other three-dimensional models.

Access a free sample Web Edition of your favorite ACS journal at pubs.acs.org to experience real-time science. Why wait for mail when you can *know it now* with Web Editions?

pubs.acs.org
ACS PUBLICATIONS

**American Chemical Society
Member & Subscriber Services**

P.O.Box 3337
Columbus, Ohio, 43210 USA
1-800-333-9511 (US and Canada)
1-614-447-3776
Fax: 1-614-447-3671
service@acs.org